TECHNISCHE UNIVERSITÄT MÜNCHEN
Fakultät für Chemie
Lehrstuhl I für Technische Chemie

# $CO_x$ Methanation over Ni-Al-Based Catalysts: Development of $CO_2$ Methanation Catalysts and Kinetic Modeling

Thomas Burger

Vollständiger Abdruck der von der Fakultät für Chemie der Technischen Universität München zur Erlangung des akademischen Grades eines

Doktor-Ingenieurs (Dr.-Ing.)

genehmigten Dissertation.

| | |
|---|---|
| Vorsitzender: | Prof. Dr. Klaus Köhler |
| Prüfer der Dissertation | 1. Prof. Dr.-Ing. Kai-Olaf Martin Hinrichsen |
| | 2. Prof. Dr.-Ing. Hartmut Spliethoff |
| | 3. Prof. Dr. Luca Lietti |

Die Dissertation wurde am 23.09.2020 bei der Technischen Universität München eingereicht und durch die Fakultät für Chemie am 23.02.2021 angenommen.

*So eine Arbeit wird eigentlich nie fertig,*
*man muß sie für fertig erklären,*
*wenn man nach Zeit und Umständen*
*das mögliche getan hat.*

Johann-Wolfgang von Goethe, Italienische Reise (1787)

# Danksagung

An dieser Stelle möchte ich mich bei all Jenen bedanken, die mich während meines Promotionsstudiums unterstützt haben.

Besonderer Dank gilt meinem Doktorvater, Herrn Prof. Dr.-Ing. Kai-Olaf Hinrichsen, für die Betreuung des Promotionsstudiums in seiner Arbeitsgruppe. Besonders angenehm war die Möglichkeit, innerhalb des Forschungsthemas eigene Schwerpunkte zu setzen und dabei Interessen und Ideen zu verfolgen. Ich möchte Herrn Prof. Dr. Klaus Köhler für die vielen ausgiebigen fachlichen Diskussionen über Forschungsfragestellungen, nicht nur auf dem Gebiet der ferromagnetischen Resonanzspektroskopie, danken, Dr. Carmen Haeßner für ihre Hilfe bei der Erfassung von EPR/FMR-Daten und Prof. Dr. Tom Nilges für den Zugang zum ICP-OES-Instrument in seiner Gruppe. Darüber hinaus möchte ich Prof. Dr. Fritz Wagner für seine Expertise und seine Hilfe bei der Mössbauer-Spektroskopie sowie Dr. Markus Döblinger, Prof. Dr. Josef Zweck und Felix Schwarzhuber für die Aufnahme von EDX-STEM- und TEM-Daten von Katalysatorproben danken. Bei Hannah Augenstein und Oliver Thomys möchte ich mich für die gute Zusammenarbeit über den Arbeitskreis hinaus bedanken. Großer Dank gilt auch meinem Bruder Stefan Burger und seinem Gruppenleiter Dr. Gregor Kieslich für ihre Mithilfe bei Untersuchungen zur Struktur einiger Katalysatormaterialien. Außerdem möchte ich Tim Kratky und Prof. Dr. Sebastian Günther für ihre Hilfe auf dem Gebiet der XPS-Spektroskopie danken. Darüber hinaus möchte ich Christoph Denk und PD Dr. Andreas Jentys für Zugang zum IR-Spektroskop danken. Besonderer Dank gilt den Mitarbeitern der Mechanik- und Elektronikwerkstatt, die bei Problemen immer tatkräftig und engagiert zur Seite standen. Zudem möchte ich mich beim Team für Ver- und Entsorgung der Fakultät für Chemie bedanken, insbesondere bei Daniel Lemma und Cihangir Agacdeviren.

Vor allem jedoch möchte ich mich bei den Kollegen und Kolleginnen am Lehrstuhl bedanken. Franz, Stefan, Philipp, Sebastian, Chris, Moritz, My, Tabea, Matthias, Johanna, Julia, Daniel, Franz, Florian und Jennie, ihr wart bei Problemen immer zur Stelle. Es war mir jederzeit eine Freude, mit euch zusammenzuarbeiten. Ich möchte auch Heidi und Thomas für die Übernahme vieler Verwaltungsarbeiten danken. Im Laufe meines Promotionsstudiums durfte ich eine Vielzahl von studentischen Arbeiten betreuen. Ich möchte mich hierfür bei Andreas, Ang Shieh, Anne, Carolin, Deborah, Fengmin, Franziska, Heike, Katja, Keng, Matthias, Moritz, Philip, Roberta, Tan und Kai für ihr Interesse und ihre Leistungen bedanken.

Ein besonderer Dank gilt meiner Familie, meiner Freundin sowie Freunden, die mich während der gesamten Arbeit sehr unterstützt haben.

# Abstract

The power-to-gas concept is one of the chemical approaches to convert and utilize $CO_2$, and ultimately prevent their release to the atmosphere, which is linked to global warming leading to a number of secondary effects on world climate and environment. $CO_2$ is converted to synthetic natural gas (SNG) *via* the methanation reaction, using renewable power for $H_2$ generation. SNG then can be re-used for power generation or stored in the natural gas grid and serve as long-term chemical energy storage. The methanation reaction is usually heterogeneously catalyzed and carried out in fixed bed reactors. The process thereby needs to be designed as cost-effective as possible, since SNG needs to compete with natural gas in the natural gas market, and as efficient as possible to meet the specifications of natural gas quality.

On catalyst scale, an efficient methanation catalyst should feature a high intrinsic activity to achieve high $CH_4$ yields at low temperature and low materials usage, but also high stability and resistance against deactivation processes common at high temperature and elevated pressure in reaction gas atmosphere to achieve a long catalyst life-time.

In the first part of this thesis, the promoters Mn and Fe are introduced and their effects on a state-of-the-art, co-precipitated $NiAlO_x$ catalyst in the $CO_2$ methanation are investigated. The methanation experiments are carried out at steady state, a total pressure of 8 bar, and stoichiometric feed gas composition. Mn is found to enhance the intrinsic catalytic activity of a co-precipitated $NiAlO_x$ catalyst by increasing the density of medium basic sites necessary for $CO_2$ pre-activation and by modifying the $CO_2$ adsorption strength on these sites. Besides, Mn species may additionally alter the electronic properties of neighbored Ni sites. At a $n_{Ni}/n_{Mn}$ ratio of approximately 5, the low-temperature activity of $NiAlO_x$ is significantly improved, leading to nearly doubled $CO_2$ conversion rates in the kinetic regime while keeping the selectivity to methane at more than 99.2 % away from thermodynamic equilibrium. Fe doping, in contrast, strongly improves the apparent thermal stability of the catalyst, proved by an aging treatment at 500 °C and a total pressure of 8 bar. Aging of $NiAO_x$ under these harsh conditions provokes deactivation mechanisms like particle and oxide phase sintering, resulting in a decrease of metal surface area, BET surface area, and basic site density. For an aging time of 32 h, the decrease of catalyst activity in the kinetic regime is reduced to only about 1/3 at an optimized $n_{Ni}/n_{Fe}$ ratio of 5.5. Besides, Fe doping is accompanied by an improvement of the intrinsic activity of $NiAlO_x$. Fe thereby is co-reduced with Ni during the catalyst activation treatment, forming Ni-Fe alloy particles. This may result in a modification of methanation kinetics by electronic effects, possibly by ameliorating the C-O dissociation properties.

The beneficial effects of Mn and Fe on the performance of $NiAlO_x$ can be combined. By co-doping Fe and Mn, catalysts with a significantly improved apparent stability and intrinsic activity can be synthesized. Besides co-doping during co-precipitation, it is shown that the promoter effects of Mn and Fe on $NiAlO_x$ can also be achieved when doping the co-precipitated $NiAlO_x$ catalyst by incipient wetness impregnation. For bi-doped catalysts, thereby the catalyst performance depends on the doping order. With this toolbox, the activity-stability behavior of a $NiAlO_x$ catalyst can be tailored to specific requirements. The combined effects of Fe and Mn suggest a bifunctional-type methanation mechanism, where the methanation takes place at the perimeter of metal particle and oxidic phase.

In the second part of the thesis it is focused on the dynamics of the Fe promoter effect on $NiAlO_x$ under $CO_2$ methanation conditions. Pre- and post-reaction characterization studies on the catalyst samples show that the enhanced apparent stability of the Fe-doped catalysts can be related to the *in situ* segregation of the Ni-Fe alloy particles under aging conditions, coupled with the oxidation of Fe, possibly forming a wüstite phase in close neighborhood to the active Ni sites. It is shown that the improved apparent stability is caused by a temporal increase of the catalytic activity due to this segregation process. The importance of the close proximity of Fe species to the Ni sites for its promoter effect in $NiAlO_x$ catalysts is demonstrated by introducing Fe species *via* a surface redox reaction technique.

The third part deals with the development of an intrinsic, thermodynamically consistent kinetic model for the co-methanation of CO and $CO_2$ over $NiAlO_x$. Kinetic models are indispensable for reactor modeling, especially important for the highly exothermal methanation reactions with respect to safety issues, and may further give insights into possible reaction mechanisms and relevant kinetic parameters. Unlike approaches available in literature, the kinetic model derived in this thesis describes the methanation reactions of CO and $CO_2$ over one shared rate-determining step by implementing competitive CO and $CO_2$ adsorption. More than 1700 responses for $CH_4$, $CO_2$, and CO based on kinetic data on $CO_x$ methanation, water-gas shift reaction, and steam reforming gathered under a wide range of industrial-type operating conditions were used for model discrimination and parameter estimation. In accordance with steady-state $D_2$ isotope experiments, model discrimination suggests that the dissociation of a hydrogenated $COH_y$ surface complex is the kinetically relevant step in $CO_x$ methanation, assuming a hydrogen-assisted $CO_2$ adsorption mechanism. The best fit was obtained for a discrete value of $y = 2$. The estimated parameters in the derived model give a good average on co-methanation kinetics. They are thermodynamically consistent, statistically relevant, and physically meaningful.

# Contents

# 1 Introduction

## 1.1 Motivation

Global warming, caused by the rising $CO_2$ levels in the atmosphere, originating from extensive utilization and exploitation of fossil energy carriers over the last decades, has led to strong interest in politics and society for the development of sustainable and green power generation methods. To the year 2020, a world temperature increase of about 1.1 K, based on land and ocean data, has been calculated compared to the average of the years from 1951 to 1980, illustrated in Figure 1.1 [1, 2]. This is related to a number of direct and indirect consequences on nature and environment. World temperature rise leads to pole melting, the melting of glaciers and ice caps as well as thermal expansion of the oceans, causing rising sea levels [3]. The effects of climate change, e.g. the acidification of the sea by rising $CO_2$ levels [4], are expected to have extensive impact on marine life [5, 6]. Weather phenomena like cyclones, thunderstorms, and intense rainfall leading to floodings [7] may become more severe and more common. At the same time, drought periods may get longer and hotter, resulting in a decline of natural fresh water resources and changing ecosystems [8, 9].

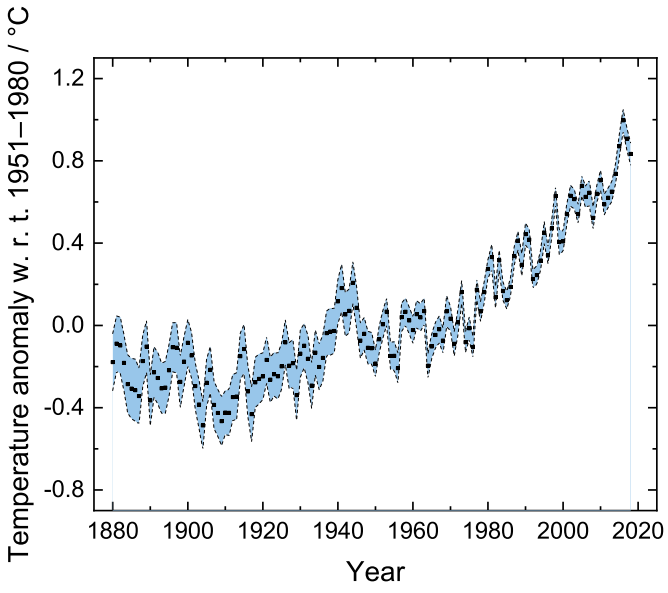


**Figure 1.1:** Average year temperature anomaly with respect to 1951 to 1980, based on land and ocean data. Blue error band marks the 95 % confidence interval, data taken from [1], uncertainty according to [2].

To contain global warming in order to limit the global temperature increase and the resulting consequences on nature and mankind, the European Union aims to reach climate-neutrality by the year 2050, which shall be achieved by the reduction of greenhouse gas emissions by 80 to 95 % [10]. As reference for the climate goals, the year 1990 is defined. To the year 2030, the following climate goals have been declared [11]:

- reduction of greenhouse gas emissions by at least 40 %
- expansion of the renewable energy share in the energy mix to at least 32 %
- increase of energy efficiency by minimum 32.5 %.

In a more stringent approach, Germany committed to reducing greenhouse gas emissions by at least 55 % to the year 2030 [12]. This includes a fast transition from conventional fossil-based power sources to renewable energy. One of the main challenges, however, are the regional and temporal dependencies of renewable power generation, such as wind and solar power. In Germany, climatic conditions, geography, and economy lead to a special situation. Congested areas and energy-consuming industry, majorly located in mid-Germany, require high power demand throughout the year. However, areas with highest potential for wind power generation are located offshore in northern Germany, areas most suitable for solar power generation in the south and southwest of Germany. This situation is further complicated by seasonal fluctuations in the power output of renewables, where peaks arise in windy autumns and sunny summers, respectively. To implement a high share of renewable energy in the energy mix, the fluctuations need to be buffered. Therefore, efficient power storage and distribution systems need to be developed.

Among others, critical parameters for suitable energy storage systems are capacity and storage time in combination with minimum storage losses (conversion and re-conversion efficiency). In increasing order in terms of capacity and storage time, one can distinguish between [13]

- electrical (e.g. capacitors)
- electrochemical (e.g. batteries)
- mechanical (e.g. compressed air storage systems)
- thermal (e.g. sensitive heat storage, latent heat storage)
- chemical (e.g. $H_2$, SNG)

energy storage systems. In a recent analysis, in Germany only the chemical energy storage systems were considered adequate to buffer the fluctuations of renewable energy generation over a sufficiently long period of time to overcome cold spells as well as times of high energy demand and low renewable energy generation [14].

One of the innovative energy concepts for chemical energy storage is the power-to-gas process. Hydrogen supplied by electrolysis using surplus renewable energy is converted with $CO_2$, which may originate from waste gas steams, carbon capture, coal, or biomass, to SNG, which is then stored and distributed in the natural gas grid and used for power generation on demand [15]. Three main benefits of this technology can be distinguished:

- $CO_2$-neutral technology for power supply
- Utilization of surplus electrical energy for hydrogen production in times of high renewable energy production
- Establishment of a chemical energy storage system to buffer discrepancies between energy demand and renewable energy production.

A schematic overview of the power-to-gas concept is provided in Figure 1.2 [15]. The capacity of SNG storage in Germany amounts to 260 TW $h_{th}$, compared to an electrical storage capacity of only 0.04 TW $h_{el}$ [14]. Underground gas storage facilities can be depleted gas or oil reservoirs, aquifers or salt caverns [16]. In depleted reservoirs and aquifers, SNG is stored inside the porous rocks under pressure application. Slippage is prohibited by gas-tight clay and salt layers. These pore storages typically feature a high storage capacity. Salt caverns, in contrast, are artificially created underground cavities in salt stocks. In contrast to pore storages, gas injection and withdrawal can occur very fast, predestining this kind of storage system for buffering short-term fluctuations in energy demand [16].

The main drawback linked to the power-to-gas technology, however, are losses during the conversion processes. Maximum efficiency factors are 70 % for $H_2O$ electrolysis and 76 % for $CO_2$ methanation (on the basis of uncompressed $CO_2$), resulting in an overall efficiency of 53 % of the primary energy [17, 18]. Directly utilizing $H_2$ as chemical energy carrier, however, is hindered by strong material requirements on storage and transportation due to its high diffusivity. Since it is highly explosive, also severe safety aspects need to be considered. For SNG,

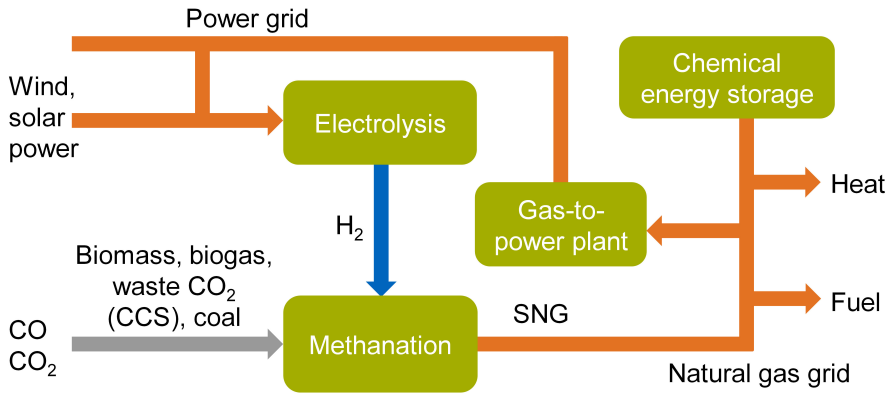


**Figure 1.2:** Schematic overview of the power-to-gas concept, adapted from [15].

in contrast, infrastructure, the natural gas grid, already exists and safety measures in handling are well-established. SNG can be used as car fuel, or be burned in gas power plants or domestic heating units in end-user applications.

In recent times, also the methanation of $CO_2$ directly from the atmosphere is under research [19]. The main challenge in this technology is the comparatively low partial pressure of $CO_2$ in the atmosphere (approx. 400 ppm), which leads to high $CO_2$ separation costs [20, 21].

Besides $CO_2$, also CO can be converted to $CH_4$. The methanation reactions therefore can be utilized to convert CO-rich biomass gasification streams into easily accessible SNG (biomass-to-gas process) [22, 23].

## 1.2 Outline

This work focuses on the development of next-generation $CO_2$ methanation catalysts for potential application in the power-to-gas process. Material properties are altered to improve the performance of a state-of-the-art, industrial-type $NiAlO_x$ catalyst, with the focus on enhancing the intrinsic catalytic activity and the thermal stability. Mn and Fe, respectively, have been identified as suitable promoters to improve catalyst performance. By understanding the underlying promoter working mechanisms and deducing the structure-activity relationships, the catalyst can be optimized to exploit the promoter effects. Besides, an intrinsic kinetic model for CO methanation, $CO_2$ methanation, and the water-gas shift reaction on the basis of investigations on $CO_2$ methanation in [24] and own experiments is derived to predict $CH_4$ formation rates under a wide range of industrially relevant operating conditions over $NiAlO_x$.

- **Chapter 2** deals with the fundamentals of the methanation reaction, from the state-of-the-art technology and challenges in the methanation process to the underlying principles in catalysis.
- **Chapter 3** focuses on the description of the methodology and principles for catalyst synthesis and characterization applied in this work.
- **Chapter 4** illustrates the effects of doping Fe and Mn, respectively, to the co-precipitated industrial-type $NiAlO_x$ catalyst to improve two critical requirements in $CO_2$ fixed bed methanation, thermal stability and intrinsic activity of the catalyst.

  This chapter is based on:

  T. Burger[1], F. Koschany[1], O. Thomys, K. Köhler, O. Hinrichsen, "$CO_2$ methanation over Fe- and Mn-promoted co-precipitated Ni-Al catalysts: Synthesis, characterization and catalysis study", Applied Catalysis A: General, 2018, *558*, 44–54, DOI 10.1016/j.apcata.2018.03.021

[1] The authors equally contributed to this work.

- **Chapter 5** shows that both promoter effects on the catalytic performance of $NiAlO_x$ in the $CO_2$ methanation reaction can be combined by co-doping Fe and Mn. It is demonstrated that catalyst performance (catalytic activity and thermal stability) of $NiFeMnAlO_x$ can be tailored by adjusting the preparation procedure.

  This chapter is based on:

  T. Burger, F. Koschany, A. Wenng, O. Thomys, K. Köhler, O. Hinrichsen, "Simultaneous activity and stability increase of co-precipitated Ni-Al $CO_2$ methanation catalysts by synergistic effects of Fe an Mn promoters", Catalysis Science & Technology, 2018, *8*, 5920–5932, DOI 10.1039/C8CY01834K

- **Chapter 6** investigates the importance of the location of the Fe promoter on the Ni catalyst for its promoter effect. A $NiAlO_x$ and a $Ni/Al_2O_3$ catalyst are selectively doped at the Ni centers by the surface redox reduction technique. It is demonstrated that the beneficial effect of Fe on the stability of the $NiAlO_x$ catalyst is linked to the formation of ($\gamma$Fe,Ni) particles on the catalyst surface.

  This chapter is based on:

  T. Burger, H. M. S. Augenstein, F. Hnyk, M. Döblinger, K. Köhler, O. Hinrichsen, "Targeted Fe-Doping of Ni-Al Catalysts *via* the Surface Redox Reaction Technique for Unravelling its Promoter Effect in the $CO_2$ Methanation Reaction", ChemCatChem, 2020, *12*, 649–662, DOI 10.1002/cctc.201901331

- **Chapter 7** highlights the beneficial effect of Fe onto the apparent stability of $NiAlO_x$. Time-resolved aging and characterization studies are utilized to draw the structure-activity relationship for the improved stability of $NiFeAlO_x$ catalysts and shine light onto the dynamical interactions between Fe and the active Ni sites under $CO_2$ methanation conditions.

  This chapter is based on:

  T. Burger, S. Ewald, A. Niederdränk, O. Hinrichsen, "Enhanced activity of co-precipitated $NiFeAlO_x$ in $CO_2$ methanation by segregation and oxidation of Fe", Applied Catalysis A: General, 2020, *604*, 117778, DOI 10.1016/j.apcata.2020.117778

- **Chapter 8** focuses on the derivation of a kinetic model for the co-methanation of CO and $CO_2$ over a co-precipitated $NiAlO_x$ catalyst ($w_{Ni}$ = 44 wt.%) *via* a common kinetically relevant surface methanation step, the decomposition of a $COH_y$ surface complex. The resulting model fully describes the reaction system CO, $CO_2$, $H_2$, $H_2O$, $CH_4$ over $NiAlO_x$ in a thermodynamically consistent kinetic model.

  This chapter is based on:

  T. Burger[1], P. J. Donaubauer[1], O. Hinrichsen, "On the kinetics of the co-methanation of CO and $CO_2$", Applied Catalysis B: Environmental, 2020, *282*, 119408, DOI 10.1016/j.apcatb.2020.119408

# 2 Theoretical and Technological Background on the Methanation Reactions

## 2.1 Thermodynamic Considerations

The methanation reactions were discovered in 1902 by Sabatier and Senderens, who converted CO (*cf.* Reaction 2.I) and $CO_2$ (*cf.* Reaction 2.II), respectively, with $H_2$ to substitute natural gas (SNG) over a Ni catalyst [25]. The methanation reactions are linked *via* the water-gas shift reaction, which describes the conversion of CO to $CO_2$ (*cf.* Reaction 2.III). At standard conditions, all three reactions are exothermal and exergonic.

$$CO + 3\,H_2 \rightleftharpoons CH_4 + H_2O \qquad \Delta_R H^o = -206.3\,kJ\,mol^{-1} \quad \Delta_R G^o = -142.2\,kJ\,mol^{-1} \tag{2.I}$$

$$CO_2 + 4\,H_2 \rightleftharpoons CH_4 + 2\,H_2O \qquad \Delta_R H^o = -165.1\,kJ\,mol^{-1} \quad \Delta_R G^o = -113.5\,kJ\,mol^{-1} \tag{2.II}$$

$$CO + H_2O \rightleftharpoons CO_2 + H_2 \qquad \Delta_R H^o = -41.2\,kJ\,mol^{-1} \quad \Delta_R G^o = -27.7\,kJ\,mol^{-1} \tag{2.III}$$

Both methanation reactions are volume contracting. According to Le Chatelier's principle, an increase in pressure therefore shifts the thermodynamic equilibrium to the reaction products. Similarly, due to their exothermal character, high reaction temperatures negatively affect the maximum thermodynamically feasible $CH_4$ yield. The detrimental effect of reaction temperature and the beneficial effect of reaction pressure on the thermodynamically feasible carbon oxides conversion is stronger in $CO_2$ methanation than in CO methanation due to the additional mole $H_2O$ formed per mole $CH_4$ in $CO_2$ methanation (*cf.* Reactions 2.I and 2.II).

Besides, depending on the catalyst system, the Fischer-Tropsch reaction (*cf.* Reaction 2.IV) as well as $CH_3OH$ formation (*cf.* Reactions. 2.V and 2.VI) may take place [26]. In addition, at under-stoichiometric $H_2/CO_x$ feed gas ratio (with respect to Reactions 2.I and 2.II), CO may undergo disproportionation according to the Boudouard reaction (*cf.* Reaction 2.VII) [27], leading to carbon deposition on the catalyst, which can ultimately result in catalyst deactivation over time [28]. Depending on the catalyst, varying selectivities to Fischer-Tropsch reaction products [29, 30], $CH_3OH$ [31], or $CH_4$ [25] can be observed when hydrogenating $CO_x$ [26, 32]. Due

to the manifold reactions possibly taking place, the optimum reaction conditions are catalyst-dependent and must be chosen adequately to ensure that the final product gas composition (dry gas) fulfills the specifications suitable for feeding into the natural gas grid or direct utilization as fuels after purification. This does not only include the heating value of the produced SNG, but also impurities such as sulfur-containing substances, typically present in $CO_x$ streams derived from biomass [33].

$$n\mathrm{CO} + (2n+1)\mathrm{H_2} \rightleftharpoons \mathrm{C}_n\mathrm{H}_{2n+2} + n\,\mathrm{H_2O} \tag{2.IV}$$

$$\mathrm{CO} + 2\,\mathrm{H_2} \rightleftharpoons \mathrm{CH_3OH} \qquad \Delta_\mathrm{R}H^\mathrm{o} = -90.8\,\mathrm{kJ\,mol^{-1}} \tag{2.V}$$

$$\mathrm{CO_2} + 3\,\mathrm{H_2} \rightleftharpoons \mathrm{CH_3OH} + \mathrm{H_2O} \qquad \Delta_\mathrm{R}H^\mathrm{o} = -49.6\,\mathrm{kJ\,mol^{-1}} \tag{2.VI}$$

$$2\,\mathrm{CO} \rightleftharpoons \mathrm{CO_2} + \mathrm{C} \qquad \Delta_\mathrm{R}H^\mathrm{o} = -172.5\,\mathrm{kJ\,mol^{-1}} \tag{2.VII}$$

The chemical composition of natural gas varies depending on the natural gas reserve [34]. Table 2.1 lists a typical composition and properties of refined and unrefined natural gas [35].

Besides impurities, $H_2$ is one of the critical components in SNG. In DIN EN 16723-2, the maximum $H_2$ content for feeding biogas to the natural gas grid is defined to 2 % [36]. The limiting application thereby is the utilization of SNG in gas engines for transportation. Furthermore, for some gas turbines that feature premix burners, as well as for gas storage tanks, the maximum $H_2$ content is restricted to 1 vol.% [37]. The maximum permitted amount of sulfur in biogas (non-odorized) for feed-in is set to 20 mg m$^{-3}$ according to DIN EN 16723-2 [38]). To achieve low $H_2$ contents in the methanation product gas, gas purification and high $CO_2$ and

**Table 2.1:** Typical composition and properties of unrefined (left) and refined (right) natural gas, adapted from Speight *et al.* [35].

| | |
|---|---|
| Relative molar mass | 20–16 |
| Carbon content (wt.%) | 73–75 |
| Hydrogen content (wt.%) | 27–25 |
| Oxygen content (wt.%) | 0.4–0 |
| Hydrogen-to-carbon atomic ratio | 3.5–4 |
| Density relative to air (at 15 °C) | 1.5–0.6 |
| Boiling temperature (°C, at 1 atm) | –162 |
| Autoignition temperature (°C) | 540–560 |
| Octane number | 120–130 |
| Methane number | 69–99 |
| Vapor flammability limits (vol.%) | 5–15 |
| Flammability limits (vol.%) | 0.7–2.1 |
| Lower heating/calorific value (BTU) | 900 |
| Methane concentration (vol.%) | 80–100 |
| Ethane concentration (vol.%) | 5–0 |
| Nitrogen concentration (vol.%) | 15–0 |
| Carbon dioxide concentration (vol.%) | 5–0 |
| Sulfur concentration (ppm, wt.) | 5–0 |

$H_2$ conversion levels are required. Figure 2.1 A illustrates the effect of the operating pressure on the thermodynamically feasible $CO_2$ conversion and $CH_4$ yield as a function of temperature at a stoichiometric $H_2/CO_2$ ratio of 4. Figure 2.1 B shows the corresponding results for CO methanation ($H_2/CO = 3$). At stoichiometric feed gas composition and 10 bar, for example, in $CO_2$ methanation the reaction temperature needs to be below 295 °C to obtain a $CH_4$ yield of at least 98 %. The thermodynamic $CH_4$ yields can be further increased by raising the $H_2/CO_x$ ratio. Since, however, $H_2$ is the limiting resource in the power-to-gas concept and excess $H_2$ furthermore requires separation in the product gas, this effect is usually not utilized. Figure 2.2 illustrates the influence of the $H_2/CO_x$ feed gas ratio on the thermodynamic $CO_x$ conversion and $CH_4$ yield as a function of temperature, exemplary at a pressure of $p = 10$ bar, for $CO_2$ methanation (A) and CO methanation (B).

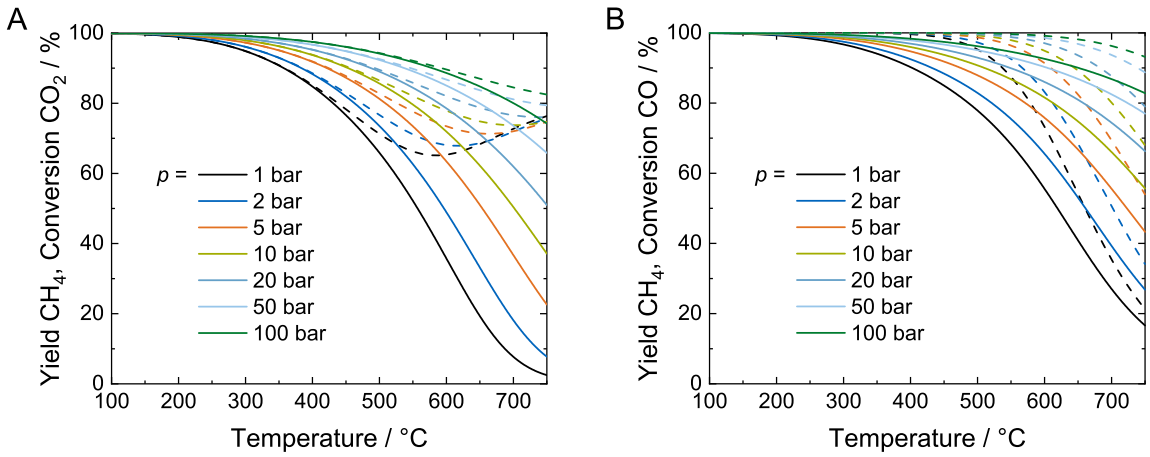


**Figure 2.1:** Effect of the operating pressure on the thermodynamic $CO_x$ conversion (dashed lines) and $CH_4$ yield (solid lines) for a feed gas composition of $H_2/CO_2 = 4$ (A) and $H_2/CO = 3$ (B) as a function of temperature, calculated using the $\Delta G$ minimization method (*cf.* Appendix C).

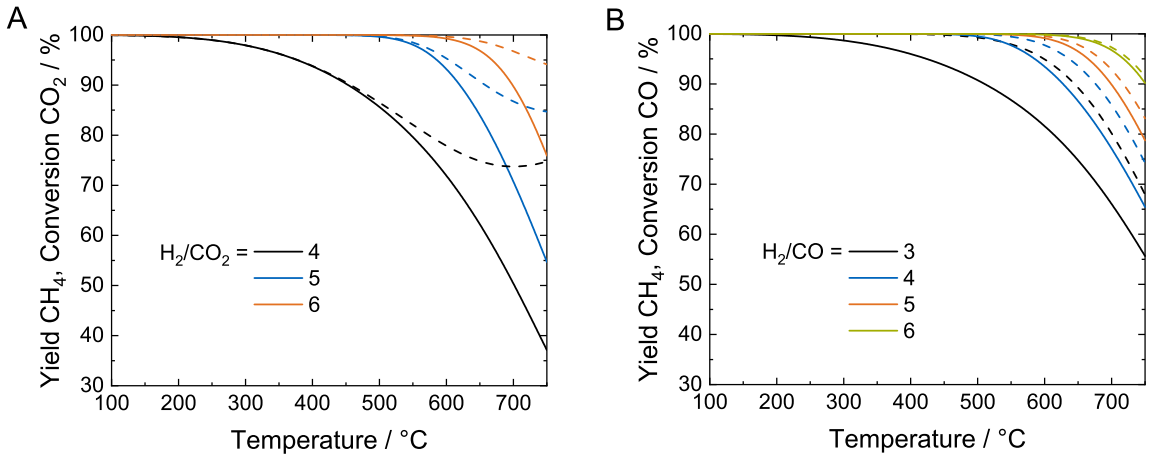


**Figure 2.2:** Effect of the $H_2/CO_x$ feed gas ratio on the thermodynamic $CO_x$ conversion (dashed lines) and $CH_4$ yield (solid lines) in $CO_2$ (A) and CO (B) methanation at an operating pressure of $p = 10$ bar as a function of temperature, calculated using the $\Delta G$ minimization method (*cf.* Appendix C).

## 2.2 State of the Art in $CO_x$ Methanation

### 2.2.1 Methanation Technologies

Advances have been made in biological and catalytic methanation. In biological methanation, first found in 1906 [39], $CH_4$ is generated by methanogenic microorganisms (type archea) under anaerobic conditions at 20 to 70 °C. Usually, $CO_2$ feed stock is derived from biomass that is hydrolyzed to monosaccharides, amino acids, and fatty acids in the first step, which are subsequently converted to $H_2$, $CO_2$, and acetate. Biological methanation takes place in the liquid phase. Biomass hydrolysis, acidogenesis, and acetogenesis, however, results in product gas with an under-stoichiometric $H_2/CO_2$ ratio. Therefore, $H_2$ needs to be co-fed. SNG formation is controlled by mass transport of $H_2$ into the aqueous reaction phase and can be enhanced by increasing the operating pressure or the mass transfer coefficient. When carrying out the reaction in a continuous stirred tank reactor, the latter can be realized by increasing the agitator speed, which typically makes up a majority of the additional energy input. Another problem results from the effect of $CO_2$ concentration on the pH of the reaction phase, impacting the performance of the microorganisms. Therefore, pressure, $CO_2$ concentration, and agitator speed need to be finely tuned for optimum performance. Furthermore, the SNG formation rate per reactor volume is rather low compared to catalytic methanation [17].

Catalytic methanation is commonly carried out in fixed bed, fluidized bed, or three-phase slurry reactors. Fixed-bed methanation concepts include adiabatic or cooled reactors. Due to the highly exothermal character of the methanation reactions, the major problem in fixed-bed methanation results from hotspot formation accompanied by sintering of the catalytically active sites, causing catalyst deactivation over time. In fluidized-bed methanation, in comparison, excessive active site sintering can be circumvented by a strongly improved heat transfer, establishing isothermal-like conditions [17]. However, the particles may suffer from intra-particle and particle-wall attrition, ultimately leading to catalyst deactivation by loss of active surface area due to mechanical-induced crushing of the catalyst particles and loss of catalytic material by abrasion [40]. Three-phase methanation involves a liquid phase, typically a thermal oil, to ensure isothermal-like conditions. The catalyst particles are suspended in the liquid phase, the gas flow ensures vigorous mixing. Similar to biological methanation, the critical step is the mass transfer of hydrogen into the liquid phase. In addition, decomposition and evaporation of the liquid may occur [17].

In recent years, also structured reactors, such as monolith [41], honeycomb [42, 43] or microstructured reactors [44] have been brought up to cope with the difficulties arising from the strongly exothermal character of the methanation reactions and high pressure drops in fixed-bed applications. The catalyst is coated onto the metallic walls, which significantly enhances radial heat transport. However, replacement of the catalyst, once it is deactivated, is expensive [17].

### 2.2.2 Fixed Bed Reactor Concepts

For fixed-bed methanation, different reactor concepts have been developed to deal with temperature hotspots and their effect on catalyst life-time and thermodynamic limitations on the maximum $CH_4$ yield in the product gas. In terms of economics, besides, recuperation of energy from the generated steam is essential to improve the efficiency of the reactor concept.

In general, the reaction can be carried out in adiabatic or cooled reactors. Recycle of product gas streams helps to decrease the temperature in the reaction zone. Often, multi-reactor concepts are applied, in which most of the $CO_2$ is converted in a first step at high temperatures in an adiabatic reactor (preferentially over a catalyst that features high thermal stability), while the remaining $CO_2$ in the product gas is converted in a second step, maybe even after $H_2O$ separation, using a highly active catalyst to obtain high $CH_4$ yields at low temperature. Different commercially available methanation reactor concepts are exemplarily shown in Figure 2.3.

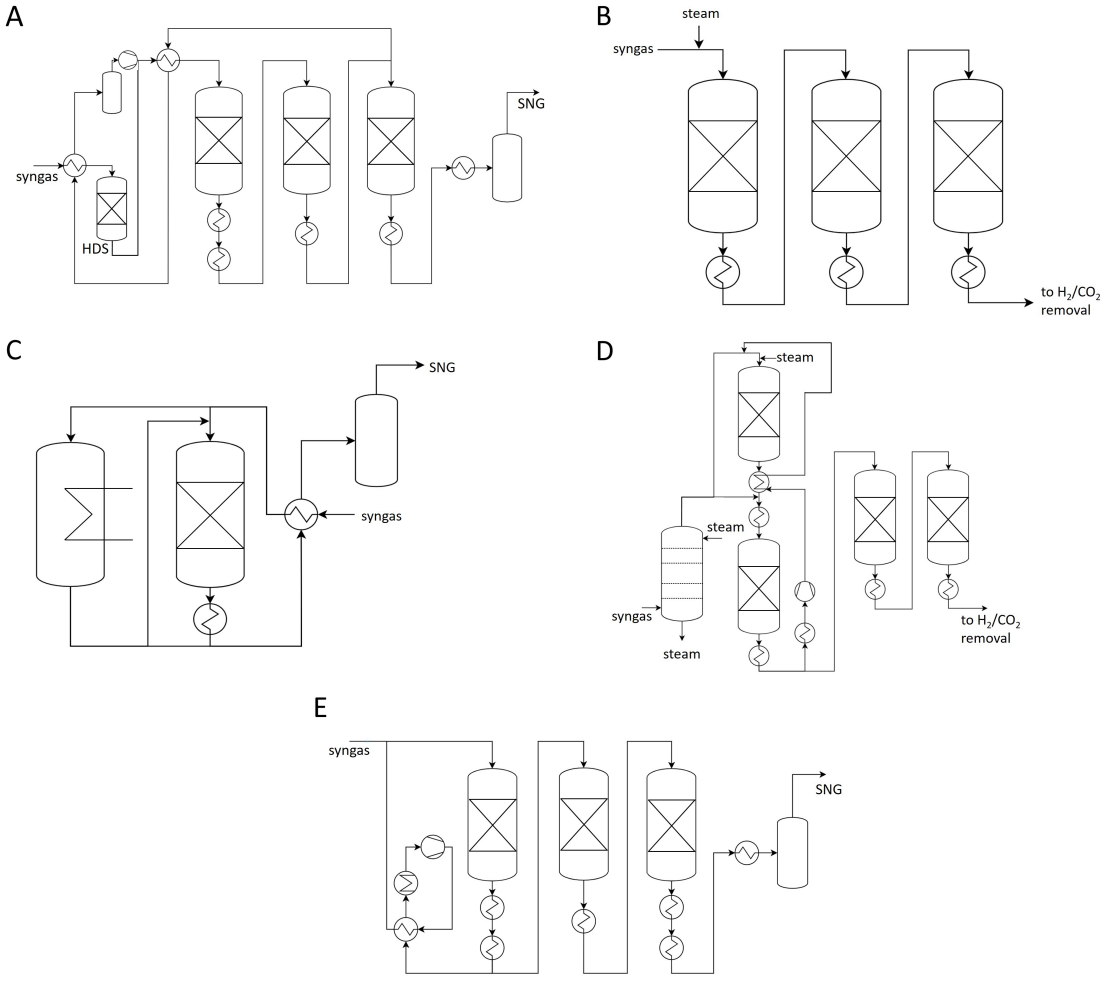


**Figure 2.3:** Reactor concepts for $CO_x$ methanation, Lurgi/BASF, adapted from [45] (A), ICI, adapted from [46, 47] (B), Linde, adapted from [48] (C), HICOM, adapted from [46, 47] (D), TREMP, adapted from [47, 49] (E).

In the Lurgi/BASF process, methanation is carried out in three serial fixed bed reactors. It includes a recycle stream after the second reactor [45]. The process developed by ICI (Imperial Chemical Industries), in comparison, consists of three serial adiabatic fixed bed reactors with intermediate gas cooling units [46]. In the Linde process, an adiabatic and an isothermal reactor are utilized. The reactors are set in series or parallel (split flow), depending on conditions and requirements [48]. In the HICOM process, steam is co-fed to the feed gas in a counter-current fixed bed before the reaction mixture enters the methanation reactor. Some of the product gas is recycled after cooling, the remaining part is passed through further fixed bed reactors, that are operated at low temperature to achieve a high $CH_4$ yield [46]. The TREMP (Haldor Topsøe) process comprises sequential adiabatic fixed bed reactors. It includes a minimum recycle after the first methanation unit for cooling. The enthalpy flow of the reactants exiting the first methanation stage is used for the generation of high pressure super-heated steam [50].

An alternative approach that recently gained interest is the so-called sorption-enhanced methanation concept [51, 52]. Therein, steam generated during the reaction is adsorbed on the oxidic phase of the catalyst or an additionally added adsorbent placed within the methanation reactor, which, according to Le-Chatelier principle, re-defines the conditions for thermodynamic equilibrium and leads to higher thermodynamically feasible $CH_4$ yields. However, the problems arising from heat generation may be even more dominant due to the heat of adsorption of $H_2O$ being released.

## 2.2.3 Methanation Catalysts

### 2.2.3.1 Active Metals

The methanation reaction is catalyzed by group VIII to group X transition metals. Most studies include noble metals (Ru [53–59], Rh [60–65]) and base metals (Ni [24, 66–74], Co [75, 76]). For $Al_2O_3$-supported catalyst systems, Vannice and Bartholomew [77] reported the specific activity order $Ir/Al_2O_3 < Pt/Al_2O_3 < Pd/Al_2O_3 < Rh/Al_2O_3 < Co/Al_2O_3 < Ni/Al_2O_3 < Fe/Al_2O_3 < Ru/Al_2O_3$ in CO methanation. Besides activity, the selectivity is an important factor when selecting an appropriate catalyst. The molecular weight of the hydrocarbon reaction products in [77] was in the order $Ru/Al_2O_3 > Fe/Al_2O_3 > Co/Al_2O_3 > Rh/Al_2O_3 > Ni/Al_2O_3 > Ir/Al_2O_3 > Pt/Al_2O_3 > Pd/Al_2O_3$.

Karn *et al.* showed that 0.5 wt.% $Ru/Al_2O_3$ is active in $CO_2$ and CO methanation [78]. A first detailed kinetic data set for $CO_2$ methanation over the same type of catalyst was supplied by Lunde and Kester [79], who found an apparent activation energy of 70 kJ mol$^{-1}$. Solymosi *et al.* [58] deduced from IR studies that the prominent methanation pathway over 5 wt.% $Ru/Al_2O_3$ involves H*-assisted adsorption of $CO_2$, which then decomposes to C* on Ru. C* is then subsequently hydrogenated to $CH_4$. The apparent activation energy was 67 kJ mol$^{-1}$. Scire *et al.* [54] compared a Ru/H-ZSM-5 and a $Ru/SiO_2$ catalyst in $CO_2$ methanation. While both catalysts were very active, Ru/H-ZSM-5 featured a higher selectivity to $CH_4$ formation. Based

on IR studies on CO and $CO_2$ adsorption, this was explained from a higher positive polarization of Ru on the zeolite, causing a weaker Ru-CO bond and therefore a higher H* surface coverage. Vannice *et al.* [77], however, observed significant formation of $C_2$ to $C_5^+$ species at 275 °C, reaching a $CH_4$ selectivity of only about 60 %. Garbarino *et. al* [55] reported activation energies in the range of 60 to 75 kJ mol$^{-1}$ for $CO_2$ methanation over 3 wt.% $Ru/Al_2O_3$. They observed that even after activation in $H_2$ high oxidation state Ru oxide species are present on the catalyst. For methanation in $H_2$-rich streams, Kowalczyk *et al.* [59] gave an activity order of $Ru/C < Ru/MgO < Ru/MgAl_2O_4 < Ru/Al_2O_3$ for both CO and $CO_2$ methanation. Eckle *et al.* [80] investigated 2.2 to 5 wt.% Ru/zeolite catalysts in CO and $CO_2$ methanation by DRIFTS and SSITKA experiments and deduced that HCO* is an important reaction intermediate for CO methanation. $CO_2$ methanation was found to proceed *via* a carbonyl intermediate, while formate is considered to be a spectator species. This reaction mechanism is consistent to an IR study by Falbo *et al.* [57] over $Ru/Al_2O_3$, who proposed that CO adsorbs on the active Ni sites, while $CO_2$ is pre-activated on the alumina support and subsequently hydrogenated on Ru *via* formate and carbonyl intermediates. The latter are hydrogenated on the Ru sites to yield $CH_4$. For high CO concentrations in the feed gas, catalyst deactivation was observed, assigned to the presence of carboxylate species blocking adsorption and reaction sites. In a DFT approach on Ru (0001), Zhang *et al.* [56] proposed that $CO_2$ and CO methanation occurs *via* a CHO* and/or COH* intermediate, respectively, and that the selectivity is governed by the competition of CH* reacting with H* or CH*. Porta *et al.* [81] prepared 0.5 wt.% $Ru/SiO_2$ egg-shell catalyst particles by incipient wetness impregnation and showed that these can be used even for 2300 µm pellets without obvious internal diffusion limitations.

Also, Rh was investigated in detail for $CO_x$ methanation. Solymosi *et al.* [60] tested different supports in $CO_2$ methanation and deduced an activity order of $Rh/TiO_2 > Rh/Al_2O_3 > Rh/SiO_2$. The superior activity of $Rh/TiO_2$ with an apparent activation energy of 81 kJ mol$^{-1}$ was attributed to electronic interactions between the Rh particles and the $TiO_2$ support, which was further evaluated by doping $TiO_2$ with lower and higher valency ions [61]. It was also observed that the methanation of $CO_2$ occurred at a faster rate than the methanation of CO, which was explained by the low carbonyl and high hydrogen coverages under $H_2/CO_2$, leading to rapid hydrogenation [60]. The authors concluded that the high carbonyl coverage under $H_2$/CO feed gas results in the formation of aged C* species, which are less reactive and whose hydrogenation require a higher activation energy. Based on observations in DRIFT experiments [62], Beuls *et al.* [65] further investigated $CO_2$ methanation at temperatures between 50 and 150 °C over $Rh/Al_2O_3$. They found that $CO_2$ oxidizes Rh under reaction conditions and that the type of adsorbed species, Rh-CO or $Rh(CO)_2$ depends on the Rh oxidation state. Novák *et al.* [82] observed that the initial catalyst activity of 1 wt.% $Rh/Al_2O_3$ depends on the reduction temperature, while under steady-state conditions this effect vanished. It was claimed that oxygen vacancies are formed on the perimeter of the Rh-$TiO_2$ interphase during reduction, that are removed over time on stream by re-oxidation involving $CO_2$ and $H_2O$. Karelovic and Ruiz [63] observed a distinct particle size dependence of the apparent activation energy and the

apparent reaction order in low-temperature $CO_2$ methanation by varying Rh loading on $TiO_2$. For small Rh particles in the range of 2 nm, higher activation energies up to 120 kJ mol$^{-1}$ were observed, whereas for Rh particles larger than 7 nm the apparent activation energy decreased to a minimum of 71 kJ mol$^{-1}$. It was hypothesized that, while the C-O dissociation energy is not a function of particle size, CO* is bound more strongly to small Rh particles. Similar trends of particle size dependence of the apparent activation energy was found for Rh/$\gamma$-$Al_2O_3$ [64], suggesting structure-sensitivity of $CO_2$ methanation over these kinds of catalysts. In this context, Matsubu *et al.* [83] investigated isolated Rh sites on $TiO_2$ and found that these sites exhibit activity for the reverse water-gas shift reaction rather than the methanation and that the fractions of isolated sites and nanoparticle-type sites changed under reaction conditions. In an DFT approach on $Rh_1/TiO_2$, Ma *et al.* [84] supported these observations. It was proposed that CO* bound to Rh blocks further adsorption of $H_2$ and therefore also the hydrogenation of CO*. From studies on Rh/$SiO_2$ it was concluded that for small Rh loadings CO* on Rh clusters is surrounded by hydroxyl groups on $SiO_2$, resulting in low $H_2$ adsorption and therefore high selectivity to CO. At higher loadings, the $H_2$ uptake is significantly enlarged, leading to a selectivity shift towards $CH_4$.

Besides its activity in the Fischer-Tropsch reaction [29], Co can also be applied for CO methanation. Le *et al.* [76] concluded from SSITKA experiments over Pt-promoted Co/$SiO_2$ that the reaction kinetics over Co are governed by the rate of $CH_x$ hydrogenation rather than CO dissociation. Among the supports $\gamma$-$Al_2O_3$, $SiO_2$, $TiO_2$, $CeO_2$, and $ZrO_2$, Co/$CeO_2$ was found to be the most active catalyst in both CO and $CO_2$ methanation.

Due to high availability and comparatively low costs [85], high catalytic activity, and excellent $CH_4$ selectivity [86, 87], in general, Ni is the preferred active component in methanation catalysts [88]. The most common support materials for Ni-based methanation catalysts are $Al_2O_3$ [64, 68, 89–106], $SiO_2$ [87, 107, 108], $ZrO_2$ [109–112], $CeO_2$ [43, 66, 113], and $TiO_2$ [114]. For $CO_2$ methanation, Vannice *et al.* [87] reported an activity order Ni/$SiO_2$ < Ni/$Al_2O_3$ < Ni/$TiO_2$.

Weatherbee and Bartholomew investigated a Ni/$SiO_2$ catalyst for CO and $CO_2$ methanation. In the temperature range from 500 to 750 K, the methanation of CO occurred at a faster rate than the methanation of $CO_2$ for constant reaction conditions. The apparent activation energy of $CO_2$ methanation was 80 kJ mol$^{-1}$, while CO methanation exhibited a higher temperature dependence with an apparent energy of 96 kJ mol$^{-1}$. Falconer and Zagli [115] deduced from $CO_2$ adsorption and methanation experiments over Ni/$SiO_2$ that the methanation of CO and $CO_2$ proceed *via* the same mechanism. Due to activated $CO_2$ adsorption, the ratio of H* to CO* on the catalyst surface was estimated higher in $CO_2$ than in CO methanation, resulting in a higher $CH_4$ selectivity for $CO_2$ methanation than for CO hydrogenation. Guo *et al.* [116] found superior $CO_2$ methanation performance of impregnated Ni/ZSM-5 compared to Ni/$Al_2O_3$, Ni/$SiO_2$, Ni/MCM-41, and Ni/SBA-15, which they attributed to improved basicity and metal-support interactions. Aziz *et al.* [117] studied Ni-doped mesoporous nanostructured

silica nanoparticles (MSN) in low-temperature $CO_2$ methanation and found a specific activity order of Ni/MSN > Ni/MCM-41 > Ni/HY > Ni/$SiO_2$ > Ni/$\gamma$-$Al_2O_3$ for a Ni loading of 5 wt.%. The superior performance of Ni/MSN was assigned to high basic site density and defect sites or oxygen vacancies in MSN that provide CO* species adsorbed on MSN. These are hydrogenated by H* supplied on Ni [117, 118]. Crystallinity, surface area, and basic site density decreased with rising Ni loading. Therefore, for 5 wt.% and 10 wt.% Ni similar catalytic activity was observed. Du *et al.* [119] found that the $CH_4$ selectivity over MCM-41-supported Ni catalysts increases from 1 to 3 wt.% and that the activity strongly depends on the activation temperature. The best activity was observed when activating the catalyst at 973 K. The optimized catalyst additionally featured high thermal stability. Schüler *et al.* [120] investigated chemical vapor deposition (CVD) as a promising technique to prepare $SiO_2$-supported nickel catalysts. A so-prepared 10 wt.% Ni/$SiO_2$ catalyst outperformed a benchmark catalyst prepared by impregnation and featured a $CO_2$ methanation activity similar to a co-precipitated Ni-Al catalyst, which was attributed to the high dispersion of Ni. Yan *et al.* [121] developed 2D nanocomposites of Ni nanoparticles and siloxene nanosheets. It was found that catalyst performance and reaction pathway strongly depend on the location of the nanoparticles, which could by controlled by synthesis parameters such as the solvent used in nucleation and growth of the siloxene nanosheets. Also, methanation studies on Ni supported on hierarchical silica microspheres were carried out [122].

Due to its ability to form oxygen vacancies, $CeO_2$ is a widely used support material for Ni-based $CO_2$ methanation catalysts [66, 123–125]. Tada *et al.* compared Ni/$CeO_2$, Ni/$TiO_2$, Ni/MgO, and Ni/$\alpha$-$Al_2O_3$ (Ni loading 10 wt.%) in $CO_2$ methanation at atmospheric pressure. Ni/$CeO_2$ featured a selectivity to $CH_4$ close to 100 % and exhibited much higher activity than the reference catalysts. Zhou *et al.* [123] assigned the high activity of Ni/$CeO_2$ to surface oxygen vacancies that are active in generating surface-bound CO* species, in addition to $CO_2$ activation on Ni. $CO_2$ activation on $CeO_2$ (*via* hydrocarbonate and formate intermediates) was confirmed by Konishcheva *et al.* [124] in an IR study. When using $NiCl_2$ as precursor during catalyst synthesis, the active sites on ceria were blocked by $Cl^-$, consequently catalyst activity declined. CO methanation, in contrast, was found to predominantly take place on the Ni sites.

In numerous studies, $CeO_2$ was promoted with $ZrO_2$ [126–130]. Zirconia is known to improve oxygen vacancy formation and increase oxygen mobility in $CeO_2$ [131]. Ocampo *et al.* [129] prepared a Zr-Ce mixed metal oxide *via* the sol-gel method for $CO_2$ methanation. At a composition of $Ce_{0.72}Zr_{0.28}O_2$, an optimum Ni loading of 10 wt.% was reported. Later, the Zr-Ce composition was optimized to a 40/60 ratio for a Ni loading of 5 wt.% [130]. $Ni^{2+}$ incorporated in the oxidic CeZr fluorite structure was found to improve the specific catalyst activity. Pan *et al.* investigated Ni/$Ce_{0.5}Zr_{0.5}O_2$ catalysts in detail [126–128]. High nickel surface area, high densities of basic sites, and oxygen vacancies as well as high concentrations of Ce(III) were identified as the decisive parameters for high catalytic activity in $CO_2$ methanation [127]. $CO_2$ was proposed to preferentially adsorb on surface oxygen sites adjacent to Ce(III) [126]. The hydrogenation of monodentate carbonates on Ce(III) was found to take place more facile

than the hydrogenation of monodentate carbonates formed on Ce(IV). Formate was suggested as the main intermediate species along the reaction pathway. The improved performance of $Ni/Ce_{0.5}Zr_{0.5}O_2$ compared to $Ni/Al_2O_3$ was assigned to a higher density of medium basic sites on $Ce_{0.5}Zr_{0.5}O_2$, resulting in a higher coverage of monodentate carbonate [128]. It was assumed that monodentate formate derived from hydrogenation of monodentate carbonate could be hydrogenated faster than bidentate formate from hydrogen carbonate, while $CO_2$ bound to strong basic sites does not participate in the reaction. Abate *et al.* [132] developed a quaternary nanocomposite support system consisting of $\gamma$-$Al_2O_3$, $ZrO_2$, $TiO_2$, and $CeO_2$, using a impregnation-precipitation technique. Ni was added *via* impregnation to achieve a total Ni loading of 20 wt.%. The highest $CO_2$ methanation activity was obtained for a composition of $Al_2O_3/ZrO_2/TiO_2/CeO_2$ = 55/15/15/15.

Concerning Ni-Al catalyst systems, supported $Ni/Al_2O_3$ catalysts and co-precipitated Ni-Al mixed metal oxide catalysts can be distinguished. Aksyolu *et al.* [70] investigated co-precipitated Ni-Al mixed metal oxide catalyst with Ni loadings up to 25 wt.%. The $CO_2$ conversion increased with rising Ni content. However, the methane formation rate per metal surface area was highest for low Ni contents, which was assigned to inefficiencies linked to the formation of nickel aluminate. While the Ni surface area increased almost linearly with the Ni loading, the total surface area exhibited a maximum at a Ni loading of about 15 wt.%, indicating a distinct effect of the Ni content on the catalyst structure. Later, they compared the performance of co-precipitated Ni-Al and impregnated $Ni/Al_2O_3$ catalysts at constant Ni loadings up to 16.5 wt.% and tested the catalysts in CO and $CO_2$ methanation, respectively [68]. From CO methanation experiments, they deduced that the specific activity decreases with rising Ni loadings for co-precipitated catalysts, but increases for impregnated, supported $Ni/Al_2O_3$ catalysts. This phenomenon was attributed to spillover and reverse spillover effects of CO for highly loaded impregnated and lowly loaded co-precipitated Ni-Al catalysts. The co-precipitated Ni-Al catalysts were found to feature a higher specific activity in $CO_2$ methanation, which was confirmed in [133] and [134]. Abate *et al.* [135] varied pH during co-precipitation ($n_{Ni}/n_{Al}$ = 3) and found that high reducibility of nickel and high metal surface area are crucial for high catalyst activity. Koschany *et al.* [24] synthesized Ni-Al mixed metal oxide catalysts in molar ratios of $n_{Ni}/n_{Al}$ = 0.2, 0.33, 1, 3, and 5 and highlighted the influence of the $n_{Ni}/n_{Al}$ ratio on the structure of the catalyst. Characterization data, however, was limited to the calcined rather than the activated catalysts. In contrast to Aksoylu *et al.* [70], they found a nearly linear relationship between metal surface area and weight time yield of $CH_4$. However, they did not observe any bulk nickel aluminate formation at the chosen calcination temperature of 450 °C. Abello *et al.* [136] reported the optimum $n_{Ni}/n_{Al}$ molar ratio for $CO_2$ methanation activity, stability, and $CH_4$ selectivity ($\approx$ 98.7 %) at 2. It was claimed that the Ni particles are dispersed on a $NiAl_2O_4$ spinel matrix. Gabrovska *et al.* [137] synthesized catalysts with molar ratios of $n_{Ni}/n_{Al}$ = 3, 1.5, and 0.5, and showed that the activation temperature has a significant influence on catalyst performance. The catalyst with the composition $n_{Ni}/n_{Al}$ = 3 performed best when

activation was carried out at 400 to 450 °C. The catalyst with $n_{Ni}/n_{Al}$ = 0.5, in contrast, prevailed when activation was carried out at 530 to 600 °C. Catalyst reducibility, however, strongly depends on the synthesis procedure as well as pretreatment and calcination steps, which can be attributed to complex interactions between Ni and Al in the mixed metal oxide depending on synthesis and treatment parameters [138–140]. Ewald *et al.* [141] investigated the interaction of $H_2$ with catalysts similar to the ones used in [24] and two $Ni/Al_2O_3$ catalysts (9 and 17 wt.% Ni) prepared by incipient wetness impregnation using transient measurement techniques. In an aging study [134], the influence of Ni loading on BET surface area found in [70] was confirmed: the maximum BET surface area was found at a $n_{Ni}/n_{Al}$ ratio of 1. Moreover, it was shown that the aging behavior of co-precipitated Ni-Al catalysts in the $CO_2$ methanation reaction strongly depends on the Ni loading. The relative deactivation, assigned to metal particle sintering, loss of basic sites, especially medium basic sites, accompanied by loss of BET surface area, increased with rising Ni loading. At the same time, catalyst activity increased with Ni loading. A comprehensive study on Ni-Al catalysts for $CO_2$ methanation was carried out by Beierlein *et al.* [142]. By comparing the $CO_2$ methanation activities of several $Ni/Al_2O_3$ catalysts, prepared by incipient impregnation, wet impregnation, and deposition-precipitation, as well as of co-precipitated $NiAlO_x$ catalysts, the authors deduced that $CO_2$ methanation over Ni-Al catalysts is a structure-insensitive reaction. In accordance with [24], a linear correlation between Ni surface area and $CO_2$ methanation activity was observed, while the selectivity decreased with rising Ni loading. From the correlation of the $CO_2$ turnovers per metal surface area to the metal particle diameters for all the differently prepared catalysts the authors concluded that terrace atoms were the active sites in $CO_2$ methanation.

#### 2.2.3.2 Promoters for Ni-Al catalysts

Ni-Al-based catalysts are commonly doped with promoters such as Ce [71, 91, 132, 143–145], La [71, 99, 144, 145], Mn [71, 94, 99, 104, 146, 147], or Fe [144, 147–153] to improve their performance in $CO_x$ methanation.

Rahmani *et al.* [71] investigated the impact of Ce, Mn, La, and Zr dopants on a 20 wt.% $Ni/Al_2O_3$ reference catalyst in the $CO_2$ methanation reaction. The catalysts were synthesized by subsequent impregnation of an $Al_2O_3$ support prepared by the sol-gel method. Among the tested catalysts, the Ce-promoted sample featured the highest catalytic activity, while the La- and the Zr-promoted catalysts performed worse than the reference catalyst. The highest activity was found for a Ce loading of 2 wt.%, and it decreased with rising Ce content. The promoter influence was mainly ascribed to modified nickel-support interactions: for Mn and Ce promoters, a decrease of the NiO and $NiAl_2O_4$ reduction temperature was found, thus increasing catalytic activity. Wu *et al.* [143] prepared $Ni/Al_2O_3$-$CeO_2$ catalysts in a one-pot sol-gel procedure. During catalyst activation, $Ce^{3+}$ was formed, introducing oxygen vacancies into the catalyst system. Besides, an increase in NiO reducibility, in accordance with [71], was observed. Over the Ce-promoted catalysts, an enhanced $CO_2$ conversion at an improved

$CH_4$ selectivity was found. The best performance was achieved for a 1:1 molar ratio of Al and Ce in the mixed oxide. It was hypothesized that for highly dispersed Ni particles the oxygen vacancies trigger an additional pathway for the activation of $CO_2$ and provide carbon species under reaction conditions that can be hydrogenated by H* provided on the Ni surface. Xavier *et al.* [91] doped 10 to 20 wt.% $Ni/Al_2O_3$ catalysts with 0.5 to 2 wt.% Ce. All Ce-containing catalyst samples exhibited an improved activity in CO methanation (feed gas $H_2/CO = 99$). The optimum Ce loading was determined at 1.5 wt.%. The beneficial effect of Ce was attributed to several effects, such as higher reducibility of NiO and a significantly improved Ni particle dispersion. In addition, the authors supposed that $Ce^{3+}$ sites induce electron back donation to the anti-bonding orbitals of chemisorbed CO, thus facilitating CO dissociation.

The promoting influence of La was investigated by A. Zhao *et al.* [99]. The dispersion of Ni particles on a 24 wt.% $Ni/Al_2O_3$ catalyst was improved when doping 2 wt.% of La. In accordance with [71], La addition resulted in a shift of the NiO reduction signal to higher temperature. This indicates that the higher Ni dispersion results from stronger metal-support interactions. In contrast to [71], however, in $CO_2$ methanation the La-doped catalyst exhibited a higher activity than the $Ni/Al_2O_3$ reference catalyst. For CO methanation, La-doped $Ni/Al_2O_3$ featured a significantly higher activity than $Ni/Al_2O_3$. Znak *et al.* [145] found in $H_2$-TPD and TPH of adsorbed oxygen that the state of hydrogen adsorbed on Ni in La-, Ce-, and Zr-doped $Ni/Al_2O_3$ catalysts is very similar. The increased CO and $CO_2$ methanation activity of La- and Ce-promoted catalysts was assigned to a beneficial promoter effect on CO dissociation.

Mn was found to improve the Ni particle dispersion in $Ni/Al_2O_3$ [99]. In contrast to promotion with La, Mn addition caused a decrease of the NiO reduction signal, indicating an improved reducibility [94, 99]. With increasing Mn loading, a higher proportion of NiO weakly interacting with the support was observed [94]. The Mn-doped $Ni/Al_2O_3$ catalyst showed a higher activity than $Ni/Al_2O_3$ in CO methanation, and significantly outperformed $Ni\text{-}La/Al_2O_3$ and $Ni\text{-}La\text{-}Mn/Al_2O_3$ in $CO_2$ methanation [99]. From aging experiments at 450 °C in syngas ($CO/CO_2/H_2 = 6.6/1.8/67.8$), a higher stability of the Mn-doped catalysts was deduced [94]. K. Zhao *et al.* [104] confirmed these findings over Mn-doped 15 wt.% $Ni/Al_2O_3$. The beneficial effect of Mn was assigned to a higher number of $CO_2$ adsorption sites, combined with an increased Ni dispersion and weakened Ni-support interactions. The involvement of basic sites would also explain the higher impact of Mn on $CO_2$ methanation compared to CO methanation. Thomys [147] doped $Ni/Al_2O_3$ catalysts with Mn in various composition and impregnation orders. All Mn-doped catalyst samples featured a higher $CO_2$ methanation activity compared to the benchmark catalyst. The impact of the promoter strongly depended on the calcination and activation temperature. The highest impact was observed when calcination was performed at low temperature.

The suitability of Fe to promote on Ni-based CO methanation catalysts was highlighted by Nørskov and co-workers [148, 154]. By introducing a descriptor that can be calculated by density functional theory, for CO hydrogenation namely the (adsorbed) CO dissociation energy,

and linking this descriptor to experimental data, preliminary screening of suitable intermetallic alloys can be performed [148]. It was shown that the best catalysts for CO methanation feature dissociative adsorption energies in the range of −1 to −1.6 eV [155]. High activity of alloyed NiFe and $Ni_3Fe$ were predicted in theoretical DFT studies and confirmed in experimental studies [148, 153]. Moreover, Kustov *et al.* [153] found that $MgAl_2O_4$ is a decent support for Ni-Fe particles at low metal loadings (2.5 wt.%, 25Fe75Ni), while for higher metal loadings (10 wt.%, 50Fe50Ni) $Al_2O_3$- and $MgAl_2O_4$-supported catalysts featured a higher activity, which was ascribed to differences in reducibility. Hwang *et al.* investigated Fe-, La, Ce-, and Zr-doped 30 wt.% $Ni/Al_2O_3$ xerogel catalysts in CO methanation [144]. From temperature-programmed surface reaction studies, where the Fe-doped catalyst exhibited the $CH_4$ production peak at the lowest temperature, it was concluded that $Ni\text{-}Fe/Al_2O_3$ features the most favorable CO dissociation energy for CO methanation among the tested dopants. In XRD and XPS experiments, the formation of Ni-Fe alloy particles was found. In addition, the Ni-Fe catalyst featured the highest $H_2$ uptake. The authors reported the same findings over a Fe-doped (5 wt.%) 35 wt.% $Ni/Al_2O_3$ catalyst in $CO_2$ methanation [151]. $CO_2$-TPD suggested that the Fe-doped catalyst featured a lower $CO_2$ adsorption capacity than Mg-, Y-, and Zr-doped samples, which the authors related to weak metal support-interactions. Meng *et al.* [149] prepared 16 wt.% $Ni/Al_2O_3$ catalysts with Fe loadings from 1 to 8 wt.% and tested them for CO methanation in a slurry bed reactor. Starting from a Fe loading of 2 wt.%, the formation of Ni-Fe alloy particles was observed, which was given as main reason for the improved CO methanation activity. Besides, the authors reported reduced metal-support interactions, evident from a decrease of the $H_2$ consumption signal during activation to lower temperatures. At high Fe loadings, the catalytic activity decreased, though, and the selectivity to $CO_2$ formation *via* the water-gas shift reaction increased. Pandey and Deo [156] synthesized Ni-Fe-based catalysts with various $n_{Ni}/n_{Fe}$ ratios, supported on $Al_2O_3$ and $SiO_2$, respectively. The best activity in $CO_2$ formation was observed for $n_{Ni}/n_{Fe} = 3$. On both supports, the formation of Ni-Fe alloy particles was observed. Compared to $Ni\text{-}Fe/Al_2O_3$, $Ni\text{-}Fe/SiO_2$ was less active in $CO_2$ methanation. The beneficial effect of Fe on $CO_2$ conversion was discussed to originate from the formation of a suitable Ni-Fe alloy, an increase of active sites by an improved metal particle dispersion, for $Al_2O_3$ furthermore the generation of basic sites (by unreduced Fe species in $Fe_3O_4$) for $CO_2$ adsorption, or a combination of these factors. In studies with various support materials [157] (total Ni-Fe loading 10 wt.%) and $n_{Ni}/n_{Fe} = 3$, the activity order $Ni\text{-}Fe/Al_2O_3 > Ni\text{-}Fe/ZrO_2 > Ni\text{-}Fe/TiO_2 > Ni\text{-}Fe/SiO_2 > Ni\text{-}Fe/Nb_2O_5$ was found. The authors did not find a correlation between specific activity and particle size, surface area, or the degree of reduction, and assigned the activity improval to the formation of alloyed Ni-Fe particles in a composition beneficial for methanation as well as the $CO_2$ adsorption capacity. Li *et al.* [158] prepared $Ni\text{-}Fe/Al_2O_3$ catalysts with various Ni and Fe loadings. The best $CO_2$ methanation performance was found for a Ni loading of 12 wt.% and a Fe loading of 3 wt.%, while a 15 wt.% Fe catalyst featured poor activity and high selectivity to CO. The promoter effect of Fe was described by a facilitated reducibility and an electronic effect of Fe. For Fe and Ni loadings of 12 wt.%, however, a reduced catalytic activity was found, which

was hypothesized to arise from excess FeO on the catalyst surface. A $Ni_3Fe/Al_2O_3$ catalyst prepared by deposition-precipitation with a total metal loading of 17 wt.% was investigated in $CO_2$ methanation by Mutz *et al.* [152]. The $Ni_3Fe$ alloy particles featured a higher low-temperature methanation activity compared to the nickel reference catalyst. In addition, the catalyst exhibited high stability at 358 °C. Yet, at low temperature, severe deactivation was observed, accompanied by a decrease of $CH_4$ selectivity and CO formation. The loss in activity was attributed to carbon deposition on the catalyst, promoted by Fe. Later, Serrer *et al.* [159] investigated the $CO_2$ methanation performance of a similarly prepared $Ni_{3.2}Fe/Al_2O_3$ catalyst under dynamic feed gas conditions. For a simulated $H_2$ dropout in the feed-gas, oxidation of Fe was observed, protecting the Ni particles from oxidation in intermittent catalyst operation in $CO_2$-rich atmosphere. For an unpromoted $Ni/Al_2O_3$ catalyst, $H_2$ dropout in the feed gas resulted in Ni surface oxidation and catalyst deactivation [160].

Regarding co-precipitated Fe-doped Ni-Al catalysts, Hwang *et al.* [150] studied the influence of precipitation agents on catalyst properties and $CO_2$ methanation performance (Ni loading 30 %, Fe loading of 5 %). The metal particle size increased in the order $NiFeAl-NaOH > NiFeAl-NH_4OH > NiFeAl-Na_2CO_3 > NiFeAl-(NH_4)_2CO_3$, the trend of $CO_2$ conversion *vice versa*. The selectivity at a $CO_2$ conversion of about 50 % was higher than 99 % for all catalysts. Mebrahtu *et al.* [161] synthesized Ni-Fe/(Mg, Al)$O_x$ catalysts with various Fe/(Ni+Fe) ratios. The Ni/(Mg, Al)$O_x$ reference catalysts as well as the catalysts featuring $n_{Fe}/n_{Ni}$ ratios higher than 0.5 showed low $CH_4$ selectivities (ranging from 0 to 55 % at 335 °C and atmospheric pressure), which was ascribed to metal particle size effects. With rising metal particle size, the selectivity to CO increased. The best performance was found for a $n_{Fe}/n_{Ni}$ ratio of 0.1 with a $CH_4$ selectivity of 90 %. They concluded that high surface basicity, high nanoparticle dispersion, and an optimum CO dissociation energy (modified by the formation of Ni-Fe alloy particles verified by STEM-EDS, in accordance with theoretical investigations [148, 162]) were the key descriptors for high catalytic activity in $CO_2$ methanation.

### 2.2.4 Reaction Mechanisms

Although catalysts for the methanation reactions are well-explored, there is still dissent on the reaction mechanism, the rate-determining step, and the reaction pathway. Two different mechanisms have been proposed for CO and $CO_2$ methanation each, the so-called associative and dissociative methanation pathways.

In the associative $CO_2$ methanation mechanism, deduced from observations on a $Ni/CeO_2$-$ZrO_2$ catalyst [163], $CO_2$ is suggested to adsorb associatively on basic sites on the perimeter of the Ni particles in the form of carbonate, which is then hydrogenated by H* adatoms, that are dissociatively adsorbed on the active Ni sites. The so-formed formate intermediates are supposed to be consecutively hydrogenated to $CH_4$ by H*. To explain carbonyl bands experimentally observed in infrared spectroscopy, it was suggested that CO is formed from $CO_2$ reduction by

$Ce^{3+}$ *via* CO* and adsorbs on Ni. Similar studies were carried out by Pan *et al.* [126], who assumed that the formate species are mainly formed *via* hydrogenation of hydrogen carbonates and monodentate carbonates, which originate from $CO_2$ adsorption on surface hydroxyls and surface oxygen sites on the $CeO_2$-$ZrO_2$ mixed oxide. Studies by Westermann *et al.* [164], carried out over Ni/USY, confirm the formation of formate in the methanation reaction, but indicate that CO*, stemming from formate decomposition on the Ni sites, may be the main intermediate of both reaction products, $CH_4$ and CO.

In the dissociative methanation pathway, in contrast, $CO_2$ directly dissociates to CO* and O* during adsorption. CO* then dissociates to C* and O*, or is hydrogenated to a hydrogen-containing reaction intermediate ($COH_y$* or CHO*), as shown by SSITKA analysis over $Ru/Al_2O_3$ by Eckle *et al.* [80]. In this approach, formate is considered as a spectator species. De Leitenburg *et al.* [165] concluded from TPD experiments over $CeO_2$-supported noble metal catalysts that $CO_2$ can also directly dissociate on $Ce^{3+}$ sites *via* a redox mechanism involving the re-oxidation of $Ce^{3+}$. The dissociative methanation pathway was computationally confirmed by Akamaru *et al.* in DFT studies over $Ni/TiO_2$ [166]. An overview of generalized associative and dissociative $CO_2$ methanation pathways (extracted from the research articles cited in this section, as well as [73] and references therein) is schematically shown in Table 2.2.

Miao *et al.* [167] tried to resolve this discrepancy between experimental observations that give hints for the associative or dissociative mechanism, respectively, by referring to the respective reaction conditions, mainly temperature window and $H_2/CO_2$ stoichiometric ratio. They concluded that the dissociative reaction mechanism may be favored at low temperature and in $H_2$-rich feed gas, while the associative mechanism may be preferred at higher temperatures and under-stoichiometric feed gas composition. Moreover, the oxidic support $CeO_2$, especially due to its redox properties [71, 91, 165], may play a critical role in the $CO_2$ activation pathway.

**Table 2.2:** Schematic associative and dissociative $CO_2$ methanation pathways proposed in literature, extended by a dual site mechanism. For reasons of readability, not all possible intermediates are listed.

| Step | Associative (H*-assisted) | | | | Dissociative | | |
|---|---|---|---|---|---|---|---|
| 1 | $CO_{2(g)} + {}^{\#}/*$ | $\rightleftharpoons$ | $CO_2{}^{\#}/*$ | | $CO_{2(g)} + 2\,*$ | $\rightleftharpoons$ | CO* + O* |
| 2 | | | $H_{2(g)} + 2\,*$ | $\rightleftharpoons$ | 2H* | | |
| 3 | $CO_2{}^{\#}/* + H*$ | $\rightleftharpoons$ | $HCO_2{}^{\#}/* + *$ | | O* + H* | $\rightleftharpoons$ | OH* + * |
| 4 | $HCO_2{}^{\#}/* + H*$ | $\rightleftharpoons$ | $HCO^{\#}/* + OH*$ | | *cf.* Table 2.3 steps 3 to 5 | | |
| 5 | $HCO^{\#}/* + H*$ | $\rightleftharpoons$ | $CH* + OH^{\#}/*$ | | | | |
| 6 | | | $CH_z* + (4-z)\,H*$ | $\rightleftharpoons$ | $CH_4* + (4-z)\,*$ | | |
| 7 | | | $CH_4*$ | $\rightleftharpoons$ | $CH_{4(g)} + *$ | | |
| 8 | | | $OH^{\#}/* + H*$ | $\rightleftharpoons$ | $H_2O* + {}^{\#}/*$ | | |
| 9 | | | $H_2O*$ | $\rightleftharpoons$ | $H_2O_{(g)} + *$ | | |

$y$ = 1, 2, or 3; $z$ = ($y$-1) or $y$.
* free metal center, # free surface center on the oxidic (support) phase.

**Table 2.3:** Schematic associative and dissociative CO methanation pathways proposed in literature. For reasons of readability, not all possible intermediates are listed.

| Step | Associative (H*-assisted) | | | Dissociative | | |
|---|---|---|---|---|---|---|
| 1 | | $CO_{(g)} + *$ | $\rightleftharpoons$ | $CO*$ | | |
| 2 | | $H_{2(g)} + 2*$ | $\rightleftharpoons$ | $2H*$ | | |
| 3 | $CO* + y\,H*$ | $COH_y* + y\,*$ | | $CO* + *$ | $\rightleftharpoons$ | $C* + O*$ |
| 4 | $COH_y* + *$ | $\rightleftharpoons$ $CH_{y-1}* + OH*$ *or* | | $O* + H*$ | $\rightleftharpoons$ | $OH* + *$ |
| 5 | $COH_y* + H*$ | $\rightleftharpoons$ $CH_y* + OH*$ | | $C* + y\,H*$ | $\rightleftharpoons$ | $CH_y* + y*$ |
| 6 | | $CH_z* + (4-z)\,H*$ | $\rightleftharpoons$ | $CH_4* + (4-z)\,*$ | | |
| 7 | | $CH_4*$ | $\rightleftharpoons$ | $CH_{4(g)} + *$ | | |
| 8 | | $OH* + H*$ | $\rightleftharpoons$ | $H_2O* + *$ | | |
| 9 | | $H_2O*$ | $\rightleftharpoons$ | $H_2O_{(g)} + *$ | | |

$y$ = 1, 2, or 3; $z$ = ($y$-1) or $y$
* free metal center

Similarly, the mechanism of CO methanation is discussed controversially. Two different mechanisms have been proposed over the last 50 years. CO* may either react with H* to form HCO* or $COH_y*$ ($y$ = 1 to 3) reaction intermediates, that are subsequently decomposed or hydrogenated to $CH_z*$ species [80, 166, 168–175], or CO* directly dissociates to C* and O* species, which are then stepwise hydrogenated [176–179]. Confirmation of the hydrogen-assisted methanation pathway (associative CO methanation) was given by numerous computational studies [101, 180–182]. It was consistently found that the activation barrier for CO bond cleavage is lowest when assuming a hydrogen-containing reaction species (CHO* or $COH_y*$) as reaction intermediate. The different proposed reaction schemes for CO methanation are schematically illustrated in Table 2.3 (extracted from [73] and references therein).

### 2.2.5 Kinetic Models

Kinetic models available in literature comprise power-law models but also intrinsic kinetic models, which, in a more sophisticated approach, consider a reaction mechanism and are based on assuming one reaction step as rate-determining. The latter are usually derived by applying Langmuir-Hinshelwood-Hougen-Watson (LHHW) [183], Mars-van-Krevelen [184], or Eley-Rideal [185] theory to experimental observations. An overview of the kinetic models discussed in this section is given in Table 2.4.

In pioneer work, Xu and Froment [186] developed a kinetic model for the steam reforming reaction over a 15.2 wt.% $Ni/MgAl_2O_4$ catalyst. The data range covered the temperature range from 573 to 673 K for experiments on the reverse of the water-gas shift reaction and methanation, and 773 to 848 K for steam reforming experiments in the pressure range from 3 to 10 bar. The reported rate equations were discriminated from 21 sets of three rate equations.

Hou and Hughes [187] performed kinetic measurements for methane steam reforming accompanied by the water-gas shift reaction over a $\alpha$-$Al_2O_3$-supported Ni catalyst with a NiO loading of 15 to 17 wt.%. Both CO and $CO_2$ were found to be primary reaction products, but the rate of $CO_2$ formation was much faster than the one of CO formation. The kinetic data points were fitted to Langmuir-Hinshelwood-Hougen-Watson models coupled with a Freundlich-type adsorption approach [188]. The mechanism plausible from model discrimination was the same as the one found by Xu and Froment [186]. The exponents of the partial pressures in the kinetic term [189], however, were treated as additional fitting parameters to ensure thermodynamic consistency of the kinetic model.

Klose and Baerns [190] derived a kinetic model for CO methanation over a commercial 18 wt.% Ni/alumina catalyst from experiments at 453 to 557 K and reaction pressures between 1 and 25 bar. Deactivation due to carbon deposition during the kinetic measurements was compensated by correcting the data to the state after catalyst conditioning in an approach similar to [186]. The best fit was obtained when assuming the reaction between C* and 2 H* as rate-limiting step. In addition, a kinetic expression for $C_2H_6$ formation was provided.

Zhang *et al.* [74] employed the kinetic model derived by Xu and Froment and fitted data gathered over a commercial 50 wt.% catalyst in the temperature range from 250 to 360 °C and the pressure range from 1 to 5 bar. In a first approach, the kinetic parameters of the rate equations derived by Xu and Froment [186] for steam reforming and water-gas shift reaction were fitted to their data, while the adsorption parameters were kept constant. The fitted activation energy for steam reforming was 248 kJ mol$^{-1}$, the one of the water-gas shift reaction 62 kJ mol$^{-1}$. In a second approach, the data was fitted to the rate equation of CO methanation derived by Klose and Bearns [190] by adjusting the kinetic parameters, while the adsorption parameters were taken from [190]. For describing the water-gas shift reaction, again the rate equation given by Xu and Froment [186] was applied. The activation energy was fitted to 103 kJ mol$^{-1}$.

Kopyscinski *et al.* [73] performed spatially resolved CO methanation measurements in a plate reactor and fitted kinetic models to the axial concentration profiles. Temperature was tracked by infrared thermography. Kinetic data points were collected over a commercial 50 wt.% Ni/$Al_2O_3$ catalyst between 280 and 360 °C at a total pressure of 2 bar. Rate equations were formulated for CO methanation and the water-gas shift reaction to account for $CO_2$ byproduct formation. $CO_2$ and $CH_4$ were observed to not hinder the reaction rate. Three sets of rate equations, that could not be further statistically discriminated, described the kinetic data well. Plausible rate-determining steps, based on model-discrimination, were a) the surface hydrogenation of C*, b) the surface hydrogenation of CH*, and c) the surface hydrogenation of a HCO* surface complex. For water-gas shift, the reaction of CO* and OH* was treated as kinetically relevant. However, for all models neither the equilibrium constant of $H_2$ adsorption nor the one of CO adsorption could be estimated. In addition, no rate equation for $CO_2$ methanation was supplied. Exemplarily, the rate equations and activation energies assuming the hydrogenation of C* to be rate-limiting in CO methanation are shown in Table 2.4.

Recently, Lalinde *et al.* [191] transferred this approach to describe $CO_2$ methanation and the reverse of the water-gas shift reaction over an ordered mesoporous 30 wt.% $NiO/Al_2O_3$ catalyst in the temperature range from 320 to 420 °C and the pressure range from 1.2 to 7.2 bar. Two sets of rate equations were found plausible to describe the data points, assuming the decomposition of COH* or HCOO* over a surface center or their reaction with H* as the rate-determining step in $CO_2$ methanation. The inhibiting effect of steam on $CO_2$ methanation kinetics was modelled *via* a hydroxyl adsorption term, while no impact of $CH_4$ on reaction kinetics could be observed. For the reverse of the water-gas shift reaction, the surface reaction of $CO_2$* and H* was assumed to be the kinetically limiting step. Exemplarily, model 11 from [191] is shown in Table 2.4.

Koschany *et al.* [24] developed a kinetic model for $CO_2$ solo-methanation over a co-precipitated Ni-Al catalyst ($n_{Ni}/n_{Al}$ = 1). The catalyst was subjected to an aging treatment for 320 h at 380 °C, 7 bar, and a feed gas ratio simulating a $CO_2$ conversion of 56 % at the reactor inlet to accelerate aging and decouple catalyst deactivation from kinetic data gathering. Parameter estimation was based on 258 responses for the methane formation rate in the temperature range from 180 to 340 °C and the pressure range from 1 to 15 bar. Among LHHW approaches, the best fit was obtained for a kinetic model assuming the hydrogenation of CO*, stemming from dissociative adsorption of $CO_2$, being rate-limiting. The inhibiting effect of steam was considered to arise from active site blockage by OH*. Furthermore, the surface hydrogenation of O* was treated as irreversible.

The adequacy of this kinetic expression for the description of the $CH_4$ formation rate in $CO_2$ methanation was confirmed by Marocco *et al.* [192] (co-precipitated Ni-Al catalyst with $n_{Ni}/n_{Al}$ = 3). While Koschany *et al.* did not investigate the influence of CO due to the high selectivity of $CO_2$ methanation in the investigated parameter range [24] and therefore did not include the reverse of the water-gas shift reaction or CO methanation in their study, Marocco *et al.* [192] combined the rate equation of $CO_2$ methanation with a power-law model for the reverse of the water-gas shift reaction. $CO_2$ methanation was investigated from 270 to 390 °C at atmospheric pressure.

A similar study was carried out by Champon *et al.* [193] over a 14 to 17 wt.% $Ni/Al_2O_3$ catalyst. The temperature for the kinetic data points ranged from 623 to 723 K at atmospheric pressure. $CO_2$ methanation was aimed to be described *via* a direct and an indirect pathway (reverse of the water-gas shift reaction followed by CO methanation). Model derivation, however, was not based on theoretical studies assuming kinetically relevant steps in the reaction network, but on literature kinetic models, which were modified depending on empiric observations.

Alstrup [179] constructed a kinetic model for CO methanation based on the assumption of a constant C* coverage in the investigated temperature range. The kinetic model considers the hydrogenation of an active C* species to be rate-limiting and describes data reported by Goodman *et al.* [195] over Ni(100) and Polizzotti and Schwarz [196] over Ni foil adequately.

Weatherbee and Bartholomew [194] investigated $CO_2$ methanation and the influence of CO on the reaction kinetics. Kinetic data points were gathered over a 3 % $Ni/SiO_2$ catalyst in the

**Table 2.4:** Kinetic models on the reaction system CO, $CO_2$, $CH_4$, $H_2$, and $H_2O$ over Ni-based catalysts available in literature.

| Catalyst | Reaction | Kinetic equation | Rate-determining step | Activation energy | Reference |
|---|---|---|---|---|---|
| 15.2 wt.%Ni/$MgAl_2O_4$ | steam reforming | $r_1 = \frac{k_1}{p_{H_2}^{2.5}} \cdot \frac{p_{CH_4} \cdot p_{H_2O} - \frac{p_{H_2}^3 \cdot p_{CO}}{K_{eq,1}}}{\left(1 + K_{CO} \cdot p_{CO} + K_{H_2} \cdot p_{H_2} + K_{CH_4} \cdot p_{CH_4} + K_{H_2O} \cdot \frac{p_{H_2O}}{p_{H_2}}\right)^2}$ | CHO* + * $\rightleftharpoons$ CO* + H* | 240.1 kJ mol$^{-1}$ | [186] |
| | water-gas shift | $r_2 = \frac{k_2}{p_{H_2}} \cdot \frac{p_{CO} \cdot p_{H_2O} - \frac{p_{H_2} \cdot p_{CO_2}}{K_{eq,2}}}{\left(1 + K_{CO} \cdot p_{CO} + K_{H_2} \cdot p_{H_2} + K_{CH_4} \cdot p_{CH_4} + K_{H_2O} \cdot \frac{p_{H_2O}}{p_{H_2}}\right)^2}$ | CO* + O* $\rightleftharpoons$ $CO_2$* + * | 67.1 kJ mol$^{-1}$ | |
| | reverse of $CO_2$ methanation | $r_3 = \frac{k_3}{p_{H_2}^{3.5}} \cdot \frac{p_{CH_4} \cdot p_{H_2O}^2 - \frac{p_{H_2}^4 \cdot p_{CO_2}}{K_{eq,3}}}{\left(1 + K_{CO} \cdot p_{CO} + K_{H_2} \cdot p_{H_2} + K_{CH_4} \cdot p_{CH_4} + K_{H_2O} \cdot \frac{p_{H_2O}}{p_{H_2}}\right)^2}$ | CHO* + O* $\rightleftharpoons$ $CO_2$* + H* | 243.9 kJ mol$^{-1}$ | |
| 15 to 17 wt.%NiO/$\alpha$-$Al_2O_3$ | steam reforming | $r_1 = k_1 \cdot \frac{p_{CH_4} \cdot p_{H_2O}^{0.5} \cdot \left(1 - \frac{p_{H_2}^3 \cdot p_{CO}}{K_{eq,1} \cdot p_{CH_4} \cdot p_{H_2O}}\right)}{p_{H_2}^{1.25} \cdot \left(1 + K_{CO} \cdot p_{CO} + K_H \cdot p_{H_2}^{0.5} + K_{H_2O} \cdot \frac{p_{H_2O}}{p_{H_2}}\right)^2}$ | CHO* + * $\rightleftharpoons$ CO* + H* | 209.2 kJ mol$^{-1}$ | [187] |
| | water-gas shift | $r_2 = k_2 \cdot \frac{p_{CO} \cdot p_{H_2O}^{0.5} \cdot \left(1 - \frac{p_{H_2} \cdot p_{CO_2}}{K_{eq,2} \cdot p_{CO} \cdot p_{H_2O}}\right)}{p_{H_2}^{0.5} \cdot \left(1 + K_{CO} \cdot p_{CO} + K_H \cdot p_{H_2}^{0.5} + K_{H_2O} \cdot \frac{p_{H_2O}}{p_{H_2}}\right)^2}$ | CO* + O* $\rightleftharpoons$ $CO_2$* + * | 15.4 kJ mol$^{-1}$ | |
| | reverse of $CO_2$ methanation | $r_3 = k_3 \cdot \frac{p_{CH_4} \cdot p_{H_2O} \cdot \left(1 - \frac{p_{H_2}^4 \cdot p_{CO_2}}{K_{eq,3} \cdot p_{CH_4} \cdot p_{H_2O}^2}\right)}{p_{H_2}^{1.75} \cdot \left(1 + K_{CO} \cdot p_{CO} + K_H \cdot p_{H_2}^{0.5} + K_{H_2O} \cdot \frac{p_{H_2O}}{p_{H_2}}\right)^2}$ | CHO* + O* $\rightleftharpoons$ $CO_2$* + H* | 109.4 kJ mol$^{-1}$ | |
| $NiAlO_x$ ($n_{Ni}/n_{Al} = 1$) | $CO_2$ methanation | $r = k \cdot \frac{p_{CO_2}^{0.5} \cdot p_{H_2}^{0.5} \cdot \left(1 - \frac{p_{CH_4} \cdot p_{H_2O}^2}{K_{eq} \cdot p_{CO_2} \cdot p_{H_2}^4}\right)}{\left(1 + K_{H_2} \cdot p_{H_2}^{0.5} + K_{mix} \cdot p_{CO_2}^{0.5} + K_{OH} \cdot \frac{p_{H_2O}}{p_{H_2}^{0.5}}\right)^2}$ | CO* + H* $\rightleftharpoons$ HCO* + * | 77.5 kJ mol$^{-1}$ | [24] |
| $NiAlO_x$ ($n_{Ni}/n_{Al} = 3$) | $CO_2$ methanation | $r_1 = k_1 \cdot \frac{p_{CO_2}^{0.5} \cdot p_{H_2}^{0.5} \cdot \left(1 - \frac{p_{CH_4} \cdot p_{H_2O}^2}{K_{eq,1} \cdot p_{CO_2} \cdot p_{H_2}^4}\right)}{\left(1 + K_{H_2}^{0.5} \cdot p_{H_2}^{0.5} + K_{mix} \cdot p_{CO_2}^{0.5} + K_{OH} \cdot \frac{p_{H_2O}}{p_{H_2}^{0.5}}\right)^2}$ | CO* + H* $\rightleftharpoons$ HCO* + * | 74.9 kJ mol$^{-1}$ [a]/ 65.2 kJ mol$^{-1}$ [b] | [192] |
| | reverse of water-gas shift | $r_2 = k_2 \cdot p_{H_2}^{\gamma} \cdot p_{CO_2}^{\delta} \cdot \left(1 - \frac{p_{CO} \cdot p_{H_2O}}{K_{eq,2} \cdot p_{CO_2} \cdot p_{H_2}}\right)$ | n.d. | 85.3 kJ mol$^{-1}$ | |

[a] considering only the rate law for $CO_2$ methanation.
[b] considering the rate laws for $CO_2$ methanation and the reverse of the water-gas shift reaction.

| Catalyst | Reaction | Kinetic equation | Rate-determining step | Activation energy | Reference |
|---|---|---|---|---|---|
| 50 wt.%Ni/$Al_2O_3$ | CO methanation | $r_1 = k_1 \cdot \frac{K_C \cdot p_{CO}^{0.5} \cdot p_{H_2}^{0.5}}{\left(1+K_C \cdot p_{CO}+K_{OH} \cdot \frac{p_{H_2O}}{p_{H_2}^{0.5}}\right)^2}$ | C* + H* $\rightleftharpoons$ CH* + * | 74.1 kJ mol$^{-1}$ | [73] |
| | water-gas shift | $r_2 = k_2 \cdot \frac{K_\alpha \cdot p_{CO} \cdot p_{H_2O} - \frac{p_{CO_2} \cdot p_{H_2}}{K_{eq,2}}}{p_{H_2}^{0.5} \cdot \left(1+K_C \cdot p_{CO}+K_{OH} \cdot \frac{p_{H_2O}}{p_{H_2}^{0.5}}\right)^2}$ [a] | CO* + OH* $\rightleftharpoons$ $CO_2$* + H* | 161.6 kJ mol$^{-1}$ | |
| 18 wt.% Ni/alumina | CO methanation | $r = k_{CH_2} \cdot \frac{K_C \cdot K_H^2 \cdot p_{CO}^{0.5} \cdot p_{H_2}}{\left(1+K_C \cdot p_{CO}^{0.5}+K_H \cdot p_{H_2}^{0.5}\right)^3}$ | C* + 2H* $\rightleftharpoons$ $CH_2$* + 2* | 103 kJ mol$^{-1}$ | [190] |
| 30 wt.%NiO/$Al_2O_3$ | $CO_2$ methanation | $r_1 = k_1 \cdot \frac{K_{COH} \cdot p_{CO_2}^{0.5} \cdot K_{H_2} \cdot p_{H_2} \cdot \left(1-\frac{p_{CH_4} \cdot p_{H_2O}^2}{K_{eq,1} \cdot p_{CO_2} \cdot p_{H_2}^4}\right)}{\left(1+K_{COH} \cdot p_{CO_2}^{0.5} \cdot K_{H_2}^{0.5} \cdot p_{H_2}^{0.5}+K_{H_2}^{0.5} \cdot p_{H_2}^{0.5}+K_{OH} \cdot \frac{p_{H_2O}}{p_{H_2}^{0.5}}\right)^2}$ [b] | COH* + H* $\rightleftharpoons$ CH* + OH* | 79.7 kJ mol$^{-1}$ | [191] |
| | reverse of water-gas shift | $r_2 = k_2 \cdot \frac{p_{CO_2} \cdot K_{H_2}^{0.5} \cdot p_{H_2}^{0.5} \cdot \left(1-K_\beta \cdot \frac{p_{CO} \cdot p_{H_2O}}{K_{eq,2} \cdot p_{CO_2} \cdot p_{H_2}}\right)}{\left(1+K_{COH} \cdot p_{CO_2}^{0.5} \cdot K_{H_2}^{0.5} \cdot p_{H_2}^{0.5}+K_{H_2}^{0.5} \cdot p_{H_2}^{0.5}+K_{OH} \cdot \frac{p_{H_2O}}{p_{H_2}^{0.5}}\right)^2}$ | $CO_2$* + H* $\rightleftharpoons$ CO* + OH* | 194.7 kJ mol$^{-1}$ | |
| 14 to 17 wt.%Ni/$Al_2O_3$ | $CO_2$ methanation | $r_1 = k_1 \cdot \frac{K_{CO_2} \cdot p_{CO_2} \cdot K_{H_2} \cdot p_{H_2} \cdot \left(1-\frac{p_{CH_4} \cdot p_{H_2O}^2}{K_{eq,1} \cdot p_{CO_2} \cdot p_{H_2}^4}\right)}{\left(1+K_{CO_2} \cdot p_{CO_2}+K_{H_2} \cdot p_{H_2}+K_{H_2O} \cdot p_{H_2O}+K_{CO} \cdot p_{CO}\right)^2}$ | $CO_2$* + $H_2$* $\rightleftharpoons$ CO* + $H_2O$* | 110 kJ mol$^{-1}$ | [193] |
| | reverse of water-gas shift | $r_2 = k_2 \cdot \frac{K_{CO_2} \cdot p_{CO_2} \cdot \left(1-\frac{p_{CO} \cdot p_{H_2O}}{K_{eq,2} \cdot p_{CO_2} \cdot p_{H_2}}\right)}{\left(1+K_{CO_2} \cdot p_{CO_2}+K_{H_2} \cdot p_{H_2}+K_{H_2O} \cdot p_{H_2O}+K_{CO} \cdot p_{CO}\right)^2}$ | $CO_2$* + * $\rightleftharpoons$ CO* + O* | 97.1 kJ mol$^{-1}$ | |
| | CO methanation | $r_3 = k_3 \cdot \frac{K_{CO} \cdot p_{CO} \cdot K_{H_2} \cdot p_{H_2} \cdot \left(1-\frac{p_{CH_4} \cdot p_{H_2O}}{K_{eq,3} \cdot p_{CO} \cdot p_{H_2}^3}\right)}{\left(1+K_{CO_2} \cdot p_{CO_2}+K_{H_2} \cdot p_{H_2}+K_{H_2O} \cdot p_{H_2O}+K_{CO} \cdot p_{CO}\right)^2}$ | n.d. | 97.3 kJ mol$^{-1}$ | |
| 3 wt.% Ni/$SiO_2$ | $CO_2$ methanation | $r = k' \cdot N_S^2 \cdot \frac{p_{CO_2}^{0.5} \cdot p_{H_2}^{0.5}}{\left(1+K' \cdot \frac{p_{CO_2}^{0.5}}{p_{H_2}^{0.5}}+K'' \cdot p_{CO_2}^{0.5} \cdot p_{H_2}^{0.5}+\frac{p_{CO}}{K'''}\right)^2}$ [c] | CO* + * $\rightleftharpoons$ C* + O* | 94 kJ mol$^{-1}$ | [194] |

[a] $K_\alpha$: combination of adsorption equilibrium constants.

[b] $K_\beta$: additional van't Hoff-type fitting parameter.

[c] $k'$, $K'$, $K''$, and $K'''$: lumped kinetic and adsorption constants; rate equation gives molecules of $CH_4$ produced per second and surface site. $N_S$ is normalized to the total number of sites determined by $H_2$ chemisorption and therefore is unity in the above expression [194].

temperature range from 500 to 600 K at 1.4 bar. $CO_2$ methanation was discussed to occur *via* dissociative adsorption of $CO_2$, followed by CO* dissociation, which was regarded as the rate-limiting step. C* is subsequently hydrogenated to $CH_4$. The higher $CH_4$ selectivity in $CO_2$ methanation was explained by a higher CO* coverage under CO methanation conditions, leading to a lower H*/CO* ratio on the catalyst surface, ultimately causing a lower selectivity to $CH_4$. In their kinetic model (*cf.* Table 2.4) they considered the inhibiting effect of CO by introducing an additional adsorption term.

These kinetic approaches do not consider that, from a microkinetic point of view, CO* adsorbed on the catalyst surface may react to $CH_4$ with the same kinetics, independent from the gas phase precursor molecule, CO or $CO_2$ (assuming no adsorbate interactions and that alternated surface coverages do not change the methanation mechanism). Hints for a common reaction mechanism in CO and $CO_2$ methanation were found by Falconer and Zagli [115], who observed identical $CH_4$ and $H_2O$ peaks in temperature-programmed heating in $H_2$ for CO and $CO_2$ pre-adsorption. Weatherbee and Bartholomew found that at low reaction temperature (525 K) the turnover numbers for CO and $CO_2$ methanation were the same [107]. The experimentally observed inhibiting effect of CO on $CO_2$ methanation is commonly ascribed to weaker adsorption of $CO_2$ or slower adsorption compared to CO [168, 169, 194]. In the presence of CO, therefore, $CO_2$ adsorption or dissociation may become kinetically relevant, and the original rate equation for $CO_2$ solo-methanation developed for a different rate-determining step can no longer be applied. This issue can be resolved when considering competitive rather than quasi-equilibrated adsorption of CO and $CO_2$ on the catalyst surface. Inoue and Funakashi [176] developed kinetic models for CO and $CO_2$ solo-methanation over a tube wall nickel catalyst. For co-methanation of CO and $CO_2$, they coupled the adsorption of CO and $CO_2$ with CO* dissociation on the catalyst surface. For both reactions, the conversion of C* with $H_2$ in an Eley-Rideal-type mechanism was modelled as the rate-limiting step. The water-gas shift reaction was not considered. Even under these simplifications, however, the kinetic model could not be explicitly solved to provide a kinetic expression for the co-methanation of CO and $CO_2$.

## 2.3 Catalyst Development for $CO_2$ Methanation

From the thermodynamic considerations in Section 2.1, basic requirements on catalyst systems for fixed-bed methanation processes can be deduced. Since the excessive heat release due to the exothermicity of the methanation reactions inevitably leads to catalyst deactivation by sintering processes or carbon deposition, the catalyst should be inexpensive to replace, which is a major criterion against the application of noble metal catalysts [85]. However, one of the main disadvantages of utilizing affordable and available base metals like Ni or Co is their low resistance against particle sintering compared to noble metals (sintering susceptibility can be estimated by the Hüttig temperature $T_{\text{Hüttig}} = 0.3 \cdot T_{\text{m}}$, the temperature at which surface atoms start to diffuse, and the Tammann temperature $T_{\text{Tamman}} = 0.5 \cdot T_{\text{m}}$, temperature at which bulk atoms

start to diffuse [197, 198], e.g. $T_{Tammann,Ni} = 863\ K \ll T_{Tammann,Ru} = 1362\ K$ [198]). Therefore, one approach for the development of novel catalysts is to enhance the sintering resistance of preferentially applied base metal nanoparticles. Slower deactivation rates eventually lead to longer catalyst life-time, ultimately decreasing operational costs. The second main requirement is high catalyst activity. As exemplarily shown in Figure 2.1, high pressure needs to be applied to achieve high $CH_4$ yields in single-pass operation. Gas compression, inevitable for feed-in into the gas grid or storage, is an additional cost factor for methanation units. When applying the compression step downstream the SNG unit after $H_2O$ separation and carrying out methanation at low pressure, energy losses for the compression of the $H_2O$ equivalents can be circumvented. The utilization of highly active catalysts to achieve high $CH_4$ yields at mild conditions therefore can reduce the operational costs.

The main role of the support material or oxidic phase of a catalyst is to provide a high surface area for the stabilization of well-dispersed metal nanoparticles (*via* metal-support interactions). Moreover, the oxidic material should feature sufficient thermal and mechanical stability to prevent rapid catalyst deactivation [40]. Depending on the reaction and the catalyst system, besides the active metal sites, also sites on the oxidic phase may play a significant role in the reaction mechanism (bi-functional catalysts) [199]. This is especially true for $CeO_2$ due to its redox properties and oxygen vacancies, offering oxygen storage capacity under reaction conditions, which can be beneficial for $CO_2$ activation [66, 113, 143, 200–202].

Most commonly, methanation reactions are carried out over oxide-supported metal catalysts or mixed metal oxide catalysts. The latter typically feature high metal contents, but still highly dispersed metal particles [203]. Oxide-supported metal catalysts are most commonly prepared by impregnation of an oxide with a metal salt solution, or by precipitation or deposition-precipitation of the metal precursor onto the oxidic support material. Mixed metal oxide catalysts, in contrast, can be prepared *via* co-precipitation of the metal salts [204].

For altering catalyst properties, different techniques can be utilized, such as varying the oxidic support or oxidic phase, or doping additional promoters to the catalyst. Promoters may lead to electronic modification of the active sites (binding modifiers), altering enthalpies and entropies of adsorption of reactants and reaction intermediates and/or activation energies. Besides, they may alter the structural properties of the catalyst (structural promoter), which may affect the pore system, catalyst surface, crystallinity, and nanoparticle dispersion [205]. Promoters may also affect product selectivity and catalyst life-time, e.g. by altering the resistance against gas impurities and catalyst poisons such as $H_2S$ [205, 206].

# 3 Methodology

This chapter provides the basic principles of the methodologies for catalyst synthesis, catalyst characterization, and the catalytic measurements applied in this study. The specific experimental procedures including the experimental parameters are given in the respective Chapters 4 to 8.

## 3.1 Catalyst Synthesis by Co-Precipitation

In this thesis, it is focused on co-precipitated catalysts. The catalytic material thereby is obtained by calcination and reduction of a precipitate.

Precipitation is usually carried out discontinuously in a batch reactor. In a one-pot synthesis, aqueous salt solutions of the metals that should be contained in the later catalyst are mixed in the desired stoichiometry. Often, nitrate or carbonate salts are used, since these anions can be easily removed by washing of the precipitate and/or calcination. Due to low costs, commonly $Na_2CO_3$, $K_2CO_3$, NaOH, and/or KOH are used as precipitation agents.

The driving force for precipitation is the supersaturation of the solution [207], which, in catalyst synthesis, results from a chemical reaction between metal ion and the anion of the precipitation agent. Batch precipitation can be carried out in three different modes [208]:

- **forward precipitation**: The alkaline precipitation agent is drop-wise added to the metal salt solution, causing the pH to increase, inducing precipitation.
- **reverse co-precipitation**: The metal salt solution is added drop-wise to a solution containing the alkaline precipitation agent. The pH decreases during precipitation.
- **precipitation at constant pH**: Throughout the precipitation process, the pH is held constant. Acidic metal solution and alkaline precipitation agent are added simultaneously.

The properties of the precipitate are governed by primary and secondary processes occurring during the synthesis process, which can be adjusted by the synthesis parameters. Often, the precipitate is aged in the mother liquor to provoke secondary processes. The main processes are [207]:

- **nucleation**: the rate of nucleation is determined by the degree of supersaturation

- **crystal growth**: controlled by bulk diffusion of the crystallizing material or by the surface integration process. Depending on the conditions, also the Gibbs-Thompson effect, or, in highly concentrated suspensions, the particle "crowding" effect, may play a role.
- **Ostwald ripening**: thermodynamically driven reduction of the interfacial area *via* the dissolution of small crystallites and the growth of larger crystallites
- **aggregation**: agglomeration (flocculation or coalescence) of particles depending on attractive or repulsive forces.

Delayed bases like $CO(NH_2)_2$ have special importance in precipitation processes. $CO(NH_2)_2$ can be mixed with the metal ions, but precipitation is only induced by heating above 60 °C, which causes $CO(NH_2)_2$ to decompose, accompanied by the formation $NH_3$. This technique mostly finds application in the deposition-precipitation technique, where mixing and diffusion of the ions and the precursor of the precipitation agent into the pores of an oxidic support material then can be separated from basification, ultimately leading to nucleation [209, 210].

## 3.2 Catalyst Material Characterization

The catalysts synthesized in this study were characterized by various material chacterization techniques to get insights into composition, structure, and morphology of the material, the composition and size of the metal nanoparticles and the oxidic phase, catalyst surface properties, and the reduction behavior.

### 3.2.1 Inductively Coupled Plasma-Optical Emission Spectroscopy

Inductively-coupled plasma-optical emission spectroscopy (ICP-OES) is a method to be determine the bulk composition of a material.

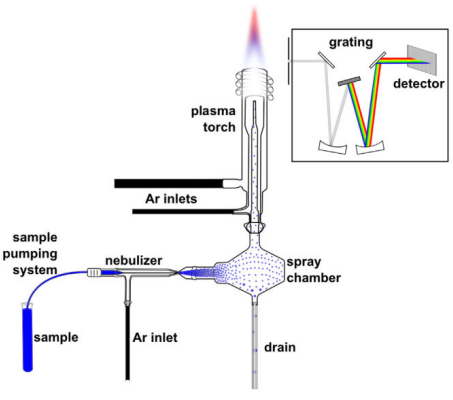


**Figure 3.1:** Experimental setup for ICP-OES, taken from [211]. Reprint with permission from Elsevier.

The experimental setup is shown in Figure 3.1 [211]. The sample is either completely digested in an appropriate aqueous solvent, or the components to analyze are leached from the material before filtering the suspension to obtain a metal ion solution. After nebulizing the solution in Ar, the aerosol is injected into Ar plasma, where the valence electrons of the different atoms are excited. During relaxation, photons in element-characteristic wavelengths are emitted. The photons are split in a polychromator and, after passing a photoelectron multiplier, are captured by the detector [212].

### 3.2.2 X-ray Powder Diffraction

X-ray powder diffraction (XRD) is utilized to analyze the crystalline phases of a crystalline material in terms of type, purity, and composition as well as quantity. X-rays from an appropriate source, usually Cu or Mo, are scattered by the atoms in the sample, majorly by their electrons. When the scattered X-rays and the incident X-rays are in phase, diffraction beams can be observed [213]. By identification of the diffraction angles as well as the intensities of these diffracted X-rays, information on the three-dimensional order of the atoms can be deduced.

The $d$ spacing is defined as the distance between diffraction planes. The relation between the $d$ spacing and the diffraction angle $2\theta$ is given by Bragg's law in Eq. 3.1 [213].

$$2 \cdot d \cdot \sin\theta = n \cdot \lambda \tag{3.1}$$

$n$ denotes the order of the maximum, $\lambda$ the wavelength of the X-rays. With the Miller indizes ($h$, $k$, $l$) of the diffraction planes, the unit cell parameters $a$, $b$, $c$ can be calculated from the $d$ spacing. For a cubic crystal ($a = b = c$, $\alpha = \beta = \gamma = 90°$) (e.g. fcc Ni), the unit cell parameter $a$ can be computed according to Eq. 3.2 [214].

$$d = a \cdot \sqrt{h^2 + k^2 + l^2} \tag{3.2}$$

For a hexagonal crystal structure ($a = b \neq c$, $\alpha = \beta = 90°$, $\gamma = 120°$) (e.g. takovite), the correlation between $a$ and $c$ and the diffraction angle $2\theta$ is given in Eq. 3.3 [214].

$$sin^2(\theta) = \frac{\lambda^2}{4} \cdot \left( \frac{4}{3} \cdot \frac{h^2 + k^2 + h \cdot k}{a^2} + \frac{l^2}{c^2} \right) \tag{3.3}$$

Diffraction in small crystallites (crystallite size $d_C$ « 100 to 200 nm) [215] leads to broadening of the corresponding reflections. Under these circumstances, the crystallite size $d_C$ can be calculated according to the Scherrer equation as shown in Eq. 3.4 [215, 216].

$$d_C = \frac{K \cdot \lambda}{\beta \cdot \cos\theta} \tag{3.4}$$

$K$ is the shape factor of the crystallite and typically has values of about 0.9 [215], $\beta$ is the full width at half maximum of the reflection. Since further peak broadening may arise from instrument effects, inhomogeneous microstrain in the crystal, and crystal lattice defects [215], the crystallite size determined by the Scherrer equation $d_C$ is a lower bound for the size of the scattering domain and is usually smaller than the particle diameter $d_P$.

### 3.2.3 Temperature-Programmed Reduction

Temperature-programmed reduction (TPR) is a tool to investigate the reducibility of oxidic components in a material. The oxidic material is heated in reductive atmosphere with a linear heating rate. The content of the reducing agent in the gas exiting the reactor is tracked by an appropriate method, such as mass spectrometry or a thermal conductivity detector (TCD) [217].

To minimize effects of side products, such as $CO_2$ evolved from the decomposition of carbonates or $H_2O$ produced during reduction, on the TPR signal (especially when using a thermal conductivity detector), a cold trap with a suitable cryogenic slurry can be used. The residence time should be kept low to minimize temperature offsets and dispersion effects. Malet and Caballero [218] as well as Monti and Baiker [219] developed experimental criteria for the measurement conditions to draw reliable conclusions from TPR patterns.

### 3.2.4 Temperature-Programmed Desorption

Temperature-programmed desorption (TPD) is an instationary technique to analyze the surface of a material and identify as well as quantify surface centers by surface-adsorbate interactions. After cleaning the material surface by a heating or degassing step, an appropriate gas is adsorbed on the material at a specific temperature. After flushing the material with an inert gas at this specific temperature to remove all weakly bound adsorbates, the temperature is linearly increased. Depending on the binding energy of the adsorbate to specific surface sites in a specific binding mode, the energy input leads to the desorption of the gas at a specific temperature [220]. Gas desorption is tracked, e.g. by mass spectrometry or a thermal conductivity detector. To minimize dispersion effects and temperature offsets in the TPD pattern, the residence time should be held as small as possible.

### 3.2.5 $N_2$ Physisorption

$N_2$ physisorption is a sorption technique commonly used to get insights into the total surface area, the pore volume $V_{Pore}$, and the pore diameter ($d_{Pore}$) distribution of a solid material. After degassing to clean the surface from adsorbates, in static (volumetric) physisorption $N_2$ is dosed to the material that is kept at the saturation temperature of liquid nitrogen ($T$ = 77 K at atmospheric pressure) by stepwise increasing the pressure from vacuum to the reference

pressure (saturation pressure of liquid nitrogen at liquid nitrogen temperature). Depending on the structure of the material, different $N_2$ sorption isotherms can be distinguished. They are classified by IUPAC and illustrated in Figure 3.2 [221]:

- **Type I isotherms** are typical for microporous materials that feature a low external surface area. $N_2$ uptake majorly accounts for micropore filling than for adsorption on the surface area.
- **Type II isotherms** are common for non-porous or macroporous solids. At the point B, the transition from mono- to multilayer adsorption can be identified.
- **Type III isotherm** materials exhibit heats of adsorption that are lower than the heat of liquefaction of the adsorbate, in contrast to materials that feature type II isotherms. The materials are non-porous or macroporous.
- **Type IV isotherms** are characteristic for mesoporous materials. The hysteresis loop between the adsorption and desorption isotherm is caused by capillary condensation of the adsorbate in the mesopores.
- **Type V isotherms** are similar to type IV isotherms, but (as for type III isotherms) no clear transition from monolayer to multilayer adsorption can be identified. This is typical for mesoporous materials where the heat of liquefaction of the adsorbate is higher than the heat of adsorption.

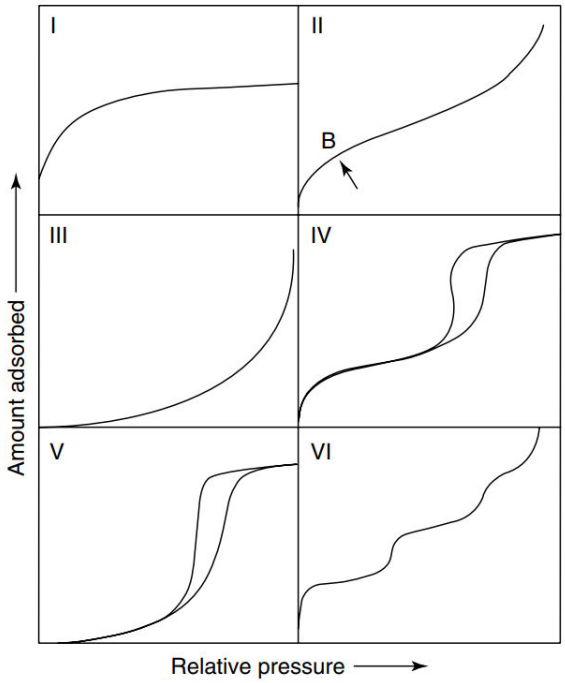


**Figure 3.2:** IUPAC isotherm types, taken from [222], reprint with permission from John Wiley and Sons.

- **Type VI isotherms** arise from stepwise multilayer adsorption on a uniform, non-porous surface.

The surface area of a material can be determined by models that give access to the monolayer uptake, such as the Langmuir or BET theory. For the application of the Langmuir theory,

- monolayer adsorption
- an energetically uniform surface
- absence of interactions between adsorbed species

are assumed [223]. This implies that its application is restricted to materials that feature type I isotherms only. The basic assumptions for the BET theory are [224]:

- multilayer adsorption
- adsorption of the first layer is described by the Langmuir theory
- adsorption of all further layers is described by condensation of gas onto liquid
- The heat of adsorption of the first layer molecules $\Delta H_{ads,1}$ is higher than the one of the molecules in the further layers, which equals the heat of condensation $\Delta H_L$.

The monolayer volume $V_{ML}$ can be determined from the linear form of the BET equation (*cf.* Eq. 3.5). $V_{ads}$ describes the volume adsorbed at the relative pressure $p/p_0$ [224].

$$\frac{1}{V_{ads} \cdot \left(\frac{p_0}{p} - 1\right)} = \frac{C-1}{V_{ML} \cdot C} \cdot \left(\frac{p}{p_0}\right) + \frac{1}{V_{ML} \cdot C} \tag{3.5}$$

$C$ is the BET constant, which can be calculated from the adsorption enthalpy of the first layer $\Delta H_{ads,1}$ and all following layers $\Delta H_L$ shown in Eq. 3.6 [224].

$$C = \exp\left(\frac{\Delta H_{ads,1} - \Delta H_L}{R \cdot T}\right) \tag{3.6}$$

From the monolayer volume $V_{ML}$ and the cross-sectional area of the adsorptive $\sigma_i$, the specific BET surface area $S_{BET}$ can be calculated using Eq. 3.7. $N_A$ denotes Avogadro's constant.

$$S_{BET} = \frac{V_{ML} \cdot N_A \cdot \sigma_i}{V_m \cdot m_{cat}} \tag{3.7}$$

$m_{cat}$ denotes the catalyst mass, $V_m$ the molar volume. The BET equation is usually applied in the $p/p_0$ range from 0.05 to 0.3 [225], which is the relative pressure region in the range of complete monolayers. The limited applicability at $p/p_0 > 0.3$ can be explained by polarization forces, leading to a higher heat of adsorption in the second layer than in all further layers [224].

Moreover, it needs to be considered that micropore filling may falsify the determination of the surface area by the BET method [225, 226].

Materials applied in catalysis often feature mesoporous pore structure. These pores provide a high internal surface area, on which metal nanoparticles can be finely dispersed. Depending on the structure of the mesoporous material, different hysteresis types can be distinguished (*cf.* Figure 3.3) [225]:

- **H1 hysteresis**: The material consists of agglomerates or spherical particles that are arranged in a fairly uniform way, the pores are cylindrical with relatively high pore size uniformity and facile pore connectivity.
- **H2 hysteresis**: This hysteresis type is caused by ink-bottle pores or pore networks that feature connectivity effects. The shape of the hysteresis results from pore blocking and percolation effects during evaporation.
- **H3 hysteresis**: The material is a loose assemblage of aggregates of plate-like particles, leading to the formation of slit-like pores.
- **H4 hysteresis**: The material features narrow slit-like pores or consists of particles with internal voids of irregular shape and broad pore size distribution.

Low pressure hystereses (dashed lines in Figure 3.3) may result from swelling of non-rigid pores, irreversible uptake of the adsorbent, or chemisorption [225] and hinder accurate determination of the pore size distribution. Depending on the isotherm and hysteresis type, different

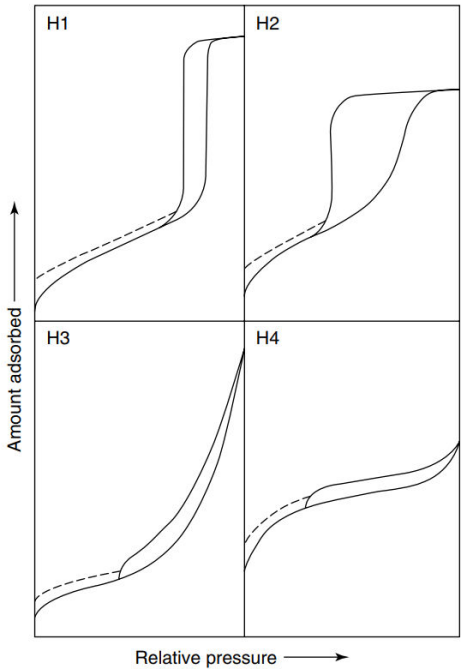


**Figure 3.3:** Hysteresis types, taken from [222], reprint with permission from John Wiley and Sons.

theories can be applied to calculate the pore volume and the pore diameter distribution [225].

For cylindrical pores, the mean pore diameter $d_{\mathrm{Pore}}$ can be computed from the total pore volume $V_{\mathrm{Pore}}$ and the BET surface area $S_{\mathrm{BET}}$ according to Eq. 3.8.

$$d_{\mathrm{Pore}} = 2 \cdot r_{\mathrm{Pore}} = \frac{4 \cdot V_{\mathrm{Pore}}}{S_{\mathrm{BET}}} \tag{3.8}$$

In the mesopore or small macropore range, the BJH (Barret-Joyner-Halenda) method [227] can be applied for the determination of the pore size distribution. It is based on the pore filling model described by the Kelvin equation. Therein, the adsorbed amount results from adsorption on the walls and pore filling. A cylindrical pore shape is assumed. Depending on the hysteresis type, the pore size distribution is extracted from the adsorption or desorption branch [225].

### 3.2.6 Chemisorption

Unlike physisorption, where surface adsorbate interactions result from van der Waals interactions, chemisorption leads to the formation of chemical bonds. Chemisorption techniques are applied to get insights into the metallic surface area rather than the total surface area (as measured by $N_2$ physisorption). Chemisorption experiments can either be carried out statically (volumetrically) or dynamically (pulse chemisorption). Depending on the metal, different adsorptives may be applied. Basic requirements are a known adsorption stoichiometry of the adsorptive onto a surface atom *s*, sensitive binding to the metal sites (no spill-over to the oxidic phase [228, 229]), as well as inert character with respect to the surface atoms to prevent bulk oxidation or any other chemical reaction (such as $Ni(CO)_4$ formation).

For Ni catalysts, chemisorption experiments are usually carried out with $H_2$. In static chemisorption, the catalyst is reduced *in situ* before the sample cell containing the catalyst is evacuated at elevated temperature to free the surface from adsorbates. At a chosen chemisorption temperature, the pressure inside the sample cell is stepwise increased. The molar uptakes at each dosing pressure are determined by pressure measurements. The resulting adsorption isotherm reflects the amount cumulatively adsorbed by chemi- and physisorption at the respective pressure.

Depending on the material, there are different methods for calculating the chemisorbed amount from the cumulative (combined) adsorption isotherm. The physisorbed and weakly chemisorbed adsorbate can be removed by an evacuation step at the adsorption temperature. Stepwise readsorption at this temperature then exclusively yields the isotherm for physisorbed and weakly chemisorbed adsorbate (weak isotherm). The difference between the combined and the weak isotherm results in the so-called strong isotherm, that gives access to the chemisorbed amount of adsorbate.

For Ni, however, the recommended method (DIN 66136-2) [230] is to extrapolate the linear part of the combined isotherm to zero pressure. The chemisorbed amount can then be regarded as the pressure independent uptake at the respective adsorption temperature and is given by the

$y$-intercept.

From the chemisorbed molar amount $n_m$, the number of surface atoms $N_{S,M}$ can be calculated according to Eq. 3.9.

$$N_{S,M} = n_m \cdot s \cdot N_A \tag{3.9}$$

With the area occupied by a surface atom, $A_{S,M}$, and the catalyst mass $m_{cat}$, the specific metal surface area $S_M$ can be calculated.

$$S_M = \frac{N_{S,M} \cdot A_{S,M}}{m_{cat}} \tag{3.10}$$

The metal dispersion $D_M$ is defined as the ratio of exposed number of metal atoms $N_{S,M}$ to the total number of the respective metal atoms, that can be determined from catalyst mass, metal loading $l_M$, the molar mass of the metal $M_M$, and Avogadro's constant.

$$D_M = \frac{N_{S,M}}{\frac{l_M \cdot m_{cat}}{M_M} \cdot N_A} \tag{3.11}$$

The metal dispersion is indirectly proportional to the mean metal particle diameter, as shown in Eq. 3.12. For the calculation, the degree of reduction $d_{red}$ of the respective metal needs to be taken into account.

$$d_{VA,M} = K \cdot \frac{V_{B,M}}{D_M \cdot A_{S,M}} \cdot d_{red} = K \cdot \frac{M_M}{D_M \cdot A_{S,M} \cdot N_A \cdot \rho_M} \cdot d_{red} \tag{3.12}$$

The shape factor $K$ is 6 for spherical particles. The volume of a bulk metal atom $V_{B,M}$ can be calculated from its molar mass, Avogadro's constant, and bulk metal density $\rho_M$.

### 3.2.7 Fourier Transform Infrared Spectroscopy

Infrared radiation is capable to excite chemical bond vibrations in molecules as well as functional groups. Precondition for the IR activity of a chemical bond is a change in dipole moment or the induction of a dipole moment during vibration. Since the vibrational modes of a chemical bond are discrete, the energy absorbed during excitation can be written as [231]

$$\Delta E = h \cdot \nu = h \cdot c \cdot \tilde{\nu}. \tag{3.13}$$

$\nu$ is the frequency of the electromagnetic wave, $c$ denotes the velocity of light, $h$ denotes Planck's constant. The wavenumber $\tilde{\nu}$ thereby is characteristic for the molecule or functional group as well as the specific vibration. IR spectroscopy therefore can be applied for qualitative and quantitative analysis. In surface analytics, IR spectroscopy is applied to investigate strength and concentration of specific sites on a material (e.g. basic sites). Suitable probe molecules are

adsorbed on these sites, IR radiation in characteristic wavelength then excites their vibration modes [232]. Compared to dispersive IR instruments, where the radiation is monochromatic and the wavenumber is stepwise varied, in FTIR instruments interferograms are measured with a polychromatic light source, which are then processed to the transmission spectrum by Fourier transformation [233].

### 3.2.8 Paramagnetic/Ferromagnetic Resonance Spectroscopy

Ferromagnetic resonance spectroscopy is an analysis tool for ferromagnetic materials relying on resonance absorption of electromagnetic radiation. It can be utilized to determine the gyromagnetic ratio, the magnetization, the anisotropy field, and the damping constant of a ferromagnetic material [234].

The ferromagnetic sample is placed between the poles of an electromagnet and irradiated with constant microwave energy in the super high frequency band, while the magnetic field strength is varied. The microwaves are captured by a detector.

Due to the external magnetic field, the magnetic moments in the sample are forced to precess with the so-called precession frequency that depends on the properties of the sample, temperature, and the external magnetic field $B$. Resonance occurs when the precession frequency is the same as the frequency of the microwave radiation, leading to absorption and a decrease in intensity in the detector [234].

### 3.2.9 Mössbauer Spectroscopy

Mössbauer spectroscopy is a nondestructive material characterization technique based on recoil-free emission and absorption of $\gamma$ radiation in solids. It is very sensitive to the chemically environment of the nuclei. Therefore, it can not only be applied for qualitative and quantitative elemental analysis, but also for the identification of oxidation states and magnetic behavior. The element to analyze in the sample thereby contains the same isotopes as the radiation source. For Fe spectroscopy, a $^{57}$Co source is utilized. The process used for Mössbauer spectroscopy is the transition of $^{57}_{26}$Fe from $I = 3/2$ to $I = 1/2$ (energy release: 14.41 keV). An overview of Mössbauer-active elements is provided in Figure 3.4 A [235].

A finely modulated beam of $\gamma$ radiation is generated by moving the radiator, utilizing the Doppler effect. The solid is exposed to the radiation, leading to the absorption of $\gamma$ quants. The transmission is captured by a detector. A typical experimental setup is depicted in Figure 3.4 B. Three types of interactions can be distinguished [235]:

- **isomer shift**: energy shift due to Coulomb interactions between the charge distribution of the Fe nucleus and the electron charge density, also influenced by shielding effects of higher orbitals
- **quadrupole splitting**: hyperfine interaction due to electric quadrupole interactions between the electric quadrupole moment of the nucleus and the electrical field gradient due to the surrounding electrons
- **magnetic hyperfine splitting**: magnetic dipole interaction between the nulear spin moment and the internal magnetic field based on the Zeeman effect, often accompanied by electric field splitting.

The interactions, the splitting of the nuclear energy levels, and the corresponding Mössbauer spectra are schematically illustrated in Figure 3.4 C [235]. Spectrum analysis is usually carried out using a fitting software and comparison to reference materials.

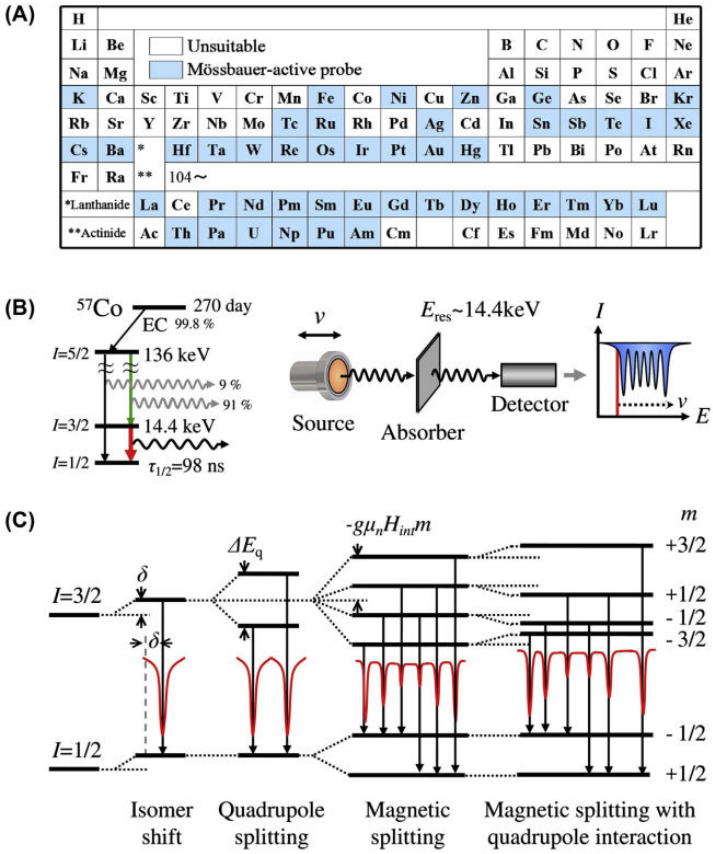


**Figure 3.4:** Fundamentals of $^{57}$Fe Mössbauer spectroscopy: Mössbauer-active elements (A), experimental setup (B), hyperfine splitting of the nuclear energy levels and schematic Mössbauer spectra (C); $\delta$ is the isomer shift, $\Delta E_q$ is the quadrupole splitting, $g$ is the nuclear $g$-factor, $m_n$ is the nuclear Bohr magneton, $H_{int}$ is the internal magnetic field, and $m$ is the nuclear magnetic spin quantum number. Taken from [235], reprint with permission from Elsevier.

### 3.2.10 X-ray Photoelectron Spectroscopy

X-ray photoelectron spectroscopy is a surface-sensitive material characterization technique applied under ultra high vacuum conditions. It is based on the photoelectric effect. X-ray radiation (typically from a Al or Mg electrode) causes electrons to be detached from the inner orbitals of the atoms in an irradiated material. To release the electron from the orbital, the binding energy $E_{bin}$ (with respect to the Fermi level) needs to be overcome. The work function $\Phi$ describes the energy that is necessary to transfer the electron from the solid to the gas phase. The kinetic energy of the electron leaving the material $E_{kin}$ therefore can be described by the energy difference of the X-ray radiation, the work function of the material surface, and the binding energy, as shown in Eq. 3.14 [236].

$$E_{kin} = h \cdot \nu - E_{bin} - \Phi \tag{3.14}$$

In practice, the kinetic energy $E_{kin}$ is measured with respect to the vacuum level of the electron energy analyzer, which means that the work function of the analyzer, which is an instrument-dependent parameter, rather than the work function of the irradiated material needs to be considered in Eq. 3.14 [236].

The photoelectrons are captured by an electron energy analyzer and processed in a secondary electron multiplier. From signal intensity at different kinetic energies, quantitative information on the elemental distribution at the material surface can be deduced. Since, moreover, the binding energies of electrons in the inner shells vary with the chemical state (chemical shift), also the oxidation and binding states of the atoms can be investigated. In addition, spin orbit-coupling is evident [236].

The photoelectric effect is superimposed by the Auger effect. The electron vacancy generated in the inner shells by the photoelectric effect can be filled with an electron from a higher shell, leading to the release of the respective energy. This energy is transferred to one of the outer electrons, which itself leaves the orbital with the energy $E_{kin,Au}$. This kinetic energy depends on the initial electron transition energy and the ionization energy of the electron released from the outer shell and is therefore specific for the material. Unlike the kinetic energy of the photoelectrons (*cf.* Eq. 3.14), the kinetic energies of the Auger electrons thus do not vary with the energy of the X-ray source [236].

### 3.2.11 Scanning Transmission Electron Microscopy / Energy-Dispersive X-ray Spectroscopy

Transmission electron microscopy can be applied to analyze the structure and chemical composition of materials on nanometer scale. The sample (thickness in the range of 100 nm) is irradiated with electrons that feature an energy of 200 to 300 keV. The interactions between the sample atoms and the irradiated electrons are manifold, such as elastic and inelastic scattering,

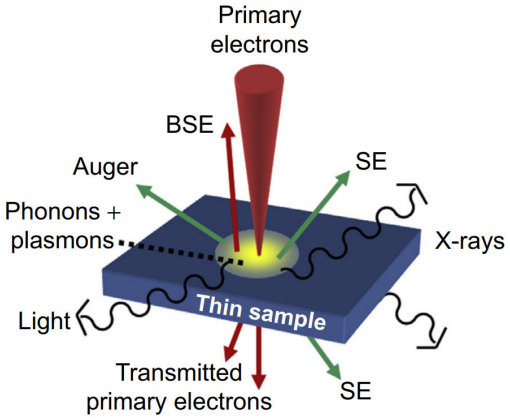


**Figure 3.5:** Electron interaction with a material. SE: secondary electrons, BSE: backscattered electrons. Taken from [237], reprint with permission from Elsevier.

backscattering of primary electrons, generation of Auger electrons, and characteristic X-ray radiation (*cf.* Figure 3.5) [237]. For imaging, the elastically scattered electrons are utilized. From TEM images, particle size distributions of nanoparticles can be obtained. By high resolution transmission electron spectroscopy (HR-TEM), the atomar structures of a material (e.g. defects in nanometer-sized crystals) can be resolved.

Energy-dispersive X-ray (EDX) spectroscopy can be utilized to, qualitatively and quantitatively, visualize the local element distribution [237]. Sample irradiation with high energy primary electrons leads to the removal of electrons from the inner atom shells. These vacancies are filled with electrons from higher shells. To compensate the energy difference, X-ray radiation with an energy specific for the respective element according to Mosley's law is emitted.

## 3.3 Test Setup for Methanation Experiments

The experiments are carried out in two parallel lines equipped with glass-lined tubular fixed bed reactors (inner tube diameter 4 mm) that have their own gas line supply. The reactors can be pressurized up to 20 bar and heated up to 600 °C. The reaction temperature is tracked by a thermocouple placed within the catalyst bed. For reactor line 1, $H_2O$, which is evaporated in a 1/16" capillary, can be fed to the gas stream with a maximum flow rate of 50 mL min$^{-1}$. All tubing is heated to 200 °C to prevent $H_2O$ condensation. The gas flow exiting the backpressure regulator is diluted with Ar (volumetric flow rate $\dot{V}_{dil}$) to obtain a volumetric flow of 500 mL min$^{-1}$ entering analytics. An Emerson MTL-4 gas process analyzer (PGA) is used for online tracking of the molar gas composition (IR spectroscopy for $CO_2$, CO, $CH_4$, $H_2O$, and TCD detector for $H_2$). Byproduct analysis is performed on a Perkin Elmer Clarus 580 gas chromatograph (GC) equipped with two columns and flame ionization detectors (FIDs). A schematic overview of the setup is shown in Figure 3.6.

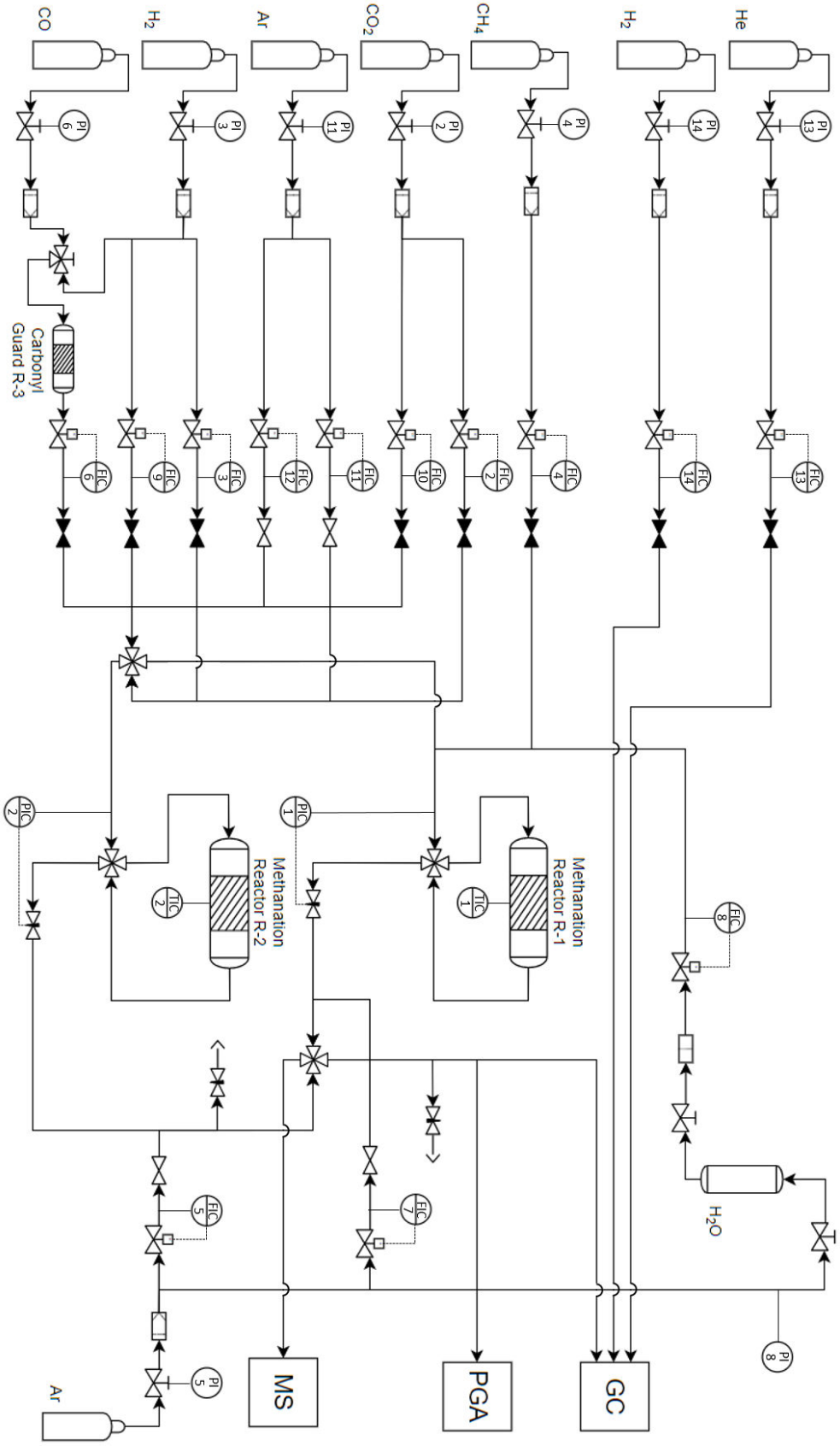


**Figure 3.6:** Scheme of the experimental setup.

The net rate of formation of species *i* is expressed *via* the difference of the molar flow of species *i* (*i* = $CO_2$, CO, $CH_4$, $H_2O$, $H_2$) leaving the reactor, $\dot{n}_{out}(i)$, and entering the reactor, $\dot{n}_{in}(i)$. The molar flow rates of the species *i* are calculated from the overall volumetric flow rates for bypass and reactor measurement entering the PGA ($\dot{V}_{PGA,in}$ and $\dot{V}_{PGA,out}$, respectively), the volumetric concentration determined by the PGA $x_{PGA}$, and the molar volume $V_m$, assuming ideal gas behavior. Since the methanation reactions are accompanied by volume contraction ($\Delta n_{CO_2Met} = \Delta n_{COMet} = -2$, *cf.* Reactions 2.I and 2.II), the volumetric flow rate is not constant.

Neglecting the concentration of $C_xH_y$ in the product gas, which is a valid assumption based on the high selectivity of CO and $CO_2$ methanation to $CH_4$ observed in all experiments, the volume contraction in the methanation reactions $\dot{V}_{cont}$ can be described by Eq. 3.15.

$$\dot{V}_{cont} = \dot{V}_{PGA,in} - \dot{V}_{PGA,out} = \dot{V}_{PGA,in} \cdot 2 \cdot \left(x_{PGA,out}(CO_2) + x_{PGA,out}(CO)\right) \cdot \frac{\dot{n}_{PGA,out}(CH_4) - \dot{n}_{PGA,in}(CH_4)}{\dot{n}_{PGA,in}(CO_2) + \dot{n}_{PGA,in}(CO)} \tag{3.15}$$

For the exiting volumetric flow rate in a reactor measurement $\dot{V}_{PGA,out}$, this yields Eq. 3.16 for methanation experiments.

$$\dot{V}_{PGA,out} = \frac{\sum x_{PGA,in}(CO_x) + 2 \cdot \sum x_{PGA,in}(CO_x) \cdot x_{PGA,in}(CH_4)}{\sum x_{PGA,in}(CO_x) + 2 \cdot \sum x_{PGA,in}(CO_x) \cdot x_{PGA,out}(CH_4)} \cdot \dot{V}_{PGA,in} \tag{3.16}$$

In analogy to Eq. 3.15, the volume expansion in the steam reforming reactions can be described:

$$\dot{V}_{exp} = \dot{V}_{PGA,out} - \dot{V}_{PGA,in} = \dot{V}_{PGA,in} \cdot 2 \cdot x_{PGA,out}(CH_4) \cdot \frac{\dot{n}_{PGA,out}(CO_2) - \dot{n}_{PGA,in}(CO_2) + \dot{n}_{PGA,out}(CO) - \dot{n}_{PGA,in}(CO)}{\dot{n}_{PGA,in}(CH_4)}. \tag{3.17}$$

The corresponding flow rate entering the PGA for a reactor measurement is described in Eq. 3.18.

$$\dot{V}_{PGA,out} = \frac{1 - 2 \cdot x_{PGA,in}(CO) - 2 \cdot x_{PGA,in}(CO_2)}{1 - 2 \cdot x_{PGA,out}(CO) - 2 \cdot x_{PGA,out}(CO_2)} \cdot \dot{V}_{PGA,in} \tag{3.18}$$

Conversions *X* and yields *Y* are calculated according to Eqs. 3.19 to 3.20.

$$X(i) = \frac{\dot{n}_{in}(i) - \dot{n}_{out}(i)}{\dot{n}_{in}(i)} = \frac{x_{PGA,in}(i) \cdot \dot{V}_{PGA,in} - x_{PGA,out}(i) \cdot \dot{V}_{PGA,out}}{x_{PGA,in}(i) \cdot \dot{V}_{PGA,in}}, \quad i = CO_2, CO, CH_4, H_2O, H_2 \tag{3.19}$$

$$Y(i) = \frac{\dot{n}_{\text{out}}(i) - \dot{n}_{\text{in}}(i)}{\dot{n}_{\text{in}}(j)} = \frac{x_{\text{PGA,out}}(i) \cdot \dot{V}_{\text{PGA,out}} - x_{\text{PGA,in}}(i) \cdot \dot{V}_{\text{PGA,in}}}{x_{\text{PGA,in}}(\text{j}) \cdot \dot{V}_{\text{PGA,in}}},$$
$$i = \text{CO}, \text{CO}_2, j = \text{CO}, \text{CO}_2, \text{CH}_4; j \neq i \tag{3.20}$$

The yield of $CH_4$ in co-methanation experiments is defined on the basis of $CO_2$ and CO, shown in Eq. 3.21.

$$Y(\text{CH}_4) = \frac{\dot{n}_{\text{out}}(\text{CH}_4) - \dot{n}_{\text{in}}(\text{CH}_4)}{\dot{n}_{\text{in}}(\text{CO}_2) + \dot{n}_{\text{in}}(\text{CO})} =$$
$$= \frac{x_{\text{PGA,out}}(\text{CH}_4) \cdot \dot{V}_{\text{PGA,out}} - x_{\text{PGA,in}}(\text{CH}_4) \cdot \dot{V}_{\text{PGA,in}}}{x_{\text{PGA,in}}(\text{CO}_2) \cdot \dot{V}_{\text{PGA,in}} + x_{\text{PGA,in}}(\text{CO}) \cdot \dot{V}_{\text{PGA,in}}} \tag{3.21}$$

Yields of the hydrocarbon byproducts (also based on the CO and $CO_2$ inlet flows) are calculated from the FID response corrected by the sensitivity factors [238]. Hydrocarbon ($C_xH_y$) selectivities are calculated according to Eq. 3.22 with the respective stoichiometric factor $\nu_{\text{CO}} = \nu_{\text{CO}_2} = x$.

$$S(\text{C}_x\text{H}_y) = \frac{\dot{n}_{\text{out}}\left(\text{C}_x\text{H}_y\right) - \dot{n}_{\text{in}}\left(\text{C}_x\text{H}_y\right)}{(\dot{n}_{\text{in}}(\text{CO}_2) - \dot{n}_{\text{out}}(\text{CO}_2)) + (\dot{n}_{\text{in}}(\text{CO}) - \dot{n}_{\text{out}}(\text{CO}))} \cdot \nu_{\text{CO,CO}_2} \tag{3.22}$$

Carbon mass balance $mb$(C) on the basis of all carbon-containing molar streams is given in Eq. 3.23. For data validity, the criterion $97\,\% \leq mb(\text{C}) \leq 103\,\%$ is defined.

$$mb(\text{C}) = \frac{\dot{n}_{\text{out}}(\text{CO}_2) + \dot{n}_{\text{out}}(\text{CO}) + \dot{n}_{\text{out}}(\text{CH}_4) + \sum \dot{n}_{\text{out}}\left(\text{C}_x\text{H}_y\right)}{\dot{n}_{\text{in}}(\text{CO}_2) + \dot{n}_{\text{in}}(\text{CO}) + \dot{n}_{\text{in}}(\text{CH}_4) + \sum \dot{n}_{\text{in}}\left(\text{C}_x\text{H}_y\right)} \tag{3.23}$$

Alternatively, exiting volumetric flow rates $\dot{V}_{\text{out}}$ in Eq. 3.16 and Eq. 3.18 could be calculated by mass balance. However, in this case corrupt data cannot be identified by an independent closing criterion.

Enthalpy and entropy data for the calculation of equilibrium data are derived from the Shomate equation according to Appendix B. The calculation itself was carried out by the $\Delta G$ minimization method (*cf.* Appendix C).

# 4 $CO_2$ Methanation over Fe- and Mn-Promoted Co-Precipitated Ni-Al Catalysts: Synthesis, Characterization, and Catalysis Study

This chapter was published in similar form in

T. Burger[1], F. Koschany[1], O. Thomys, K. Köhler, O. Hinrichsen, "$CO_2$ methanation over Fe- and Mn-promoted co-precipitated Ni-Al catalysts: Synthesis, characterization and catalysis study", *Applied Catalysis A: General*, 2018, *558*, 44–54, DOI 10.1016/j.apcata.2018.03.021

 Part was also published in:

K. Köhler, O. Thomys, K.-O. Hinrichsen, F. Koschany, T. Burger, "Manganese-doped nickel-methanation catalysts", European Patent Office, 2018, publication number WO/2018/141649, international application number PCT/EP2018/051996[1]

and

K. Köhler, O. Thomys, K.-O. Hinrichsen, F. Koschany, T. Burger, "Iron-doped nickel methanation catalysts", European Patent Office, publication number WO/2018/141648, international application number PCT/EP2018/051995.[1]

Parts of this chapter include findings from [239]

T. Burger, "Experimental and theoretical investigations on the methanation reaction of $CO_2$", *not published*, Master's Thesis, Technical University of Munich, Munich, DE, **2015**.

[1] The authors equally contributed to this work.

## Abstract

The methanation reaction of $CO_2$ is in discussion to be a sustainable pathway to address future questions arising from limited primary energy feedstock and the accumulation of $CO_2$ in the atmosphere. Therefore, the development of highly active and thermostable catalysts for this reaction is an indispensable matter of research. For this reason, an equimolar $NiAlO_x$ benchmark catalyst (44 wt.% Ni loading) was synthesized and modified by doping with Fe or Mn up to 10 wt.% of promoter by co-precipitation at constant pH 9. Their activity and stability performances in the $CO_2$ methanation reaction were evaluated by comparing the conversion vs. temperature characteristics before and after an aging period of 32 h at 500 °C. Material characterization studies comprising BET, XRD, *in situ* IR spectroscopy, XPS, $H_2$ and $CO_2$ chemisorption, and EPR/FMR contributed to derive structure-activity relationships and to obtain a deeper understanding of the catalytic behavior. Promotion with Mn led to a significant enhancement of the catalytic activity. This is assumed to be caused by a higher density of medium basic sites and an enhanced $CO_2$ adsorption capacity on the activated catalyst related to interactions between Mn oxide species and the mixed oxide phase, in combination with a stabilization of the Ni surface area at moderate Mn loadings. Promotion with Fe increased the thermal stability of the catalyst, which is attributed to the formation of a Ni-Fe alloy during catalyst activation. For both phenomena, the optimum molar Ni to promoter ratio for co-precipitated catalysts was found to be around 5.


## 4.1 Introduction

The increasing primary energy consumption in the world, caused by rising population and improved standards of living, as well as the limited worldwide natural crude oil stocks result in a major task for research and development in the fields of energy science and technology. In the future, the focus has to be set on new, sustainable pathways to secure both feedstock for chemical industries and primary energy supply. The main problems in conventional energy generation technologies based on the combustion of fossils arise from $CO_2$, which is released in enormous amounts and thereby largely contributes to the world exhaust gas emissions and the greenhouse effect [240]. The generation of synthetic natural gas (SNG) *via* the methanation of $CO_2$ with $H_2$, which can be supplied by electrolysis using surplus energy from renewable sources, is considered to be a possible approach to cope with both issues to a large scale. The most important benefit, however, is considered to be the fact that SNG, storable in an already existing infrastructure [241], can serve as a long-term energy buffer system for renewables. The methanation reaction therefore may be a key technology in the energy transition from fossil fuels to renewables [242, 243] in order to overcome the local and temporal discrepancies in energy production from renewables and energy consumption. The methanation reaction of $CO_2$

is a commonly heterogeneously catalyzed and highly exothermal reaction [244]. It has been known as the Sabatier reaction since the beginning of the 20th century [25].

$$CO_2 + 4\,H_2 \rightleftharpoons CH_4 + 2\,H_2O \quad \Delta_R H^o = -165.1\,kJ\,mol^{-1} \quad \Delta_R G^o = -113.5\,kJ\,mol^{-1} \qquad (4.I)$$

Following the principle of Le Chatelier, high pressures and low temperatures are beneficial for the equilibrium conversion of $CO_2$ in this volume contracting reaction. From thermodynamic calculations it can be deduced that a $CH_4$ yield of 95 % at nearly 100 % selectivity using stoichiometric feed gas composition at a total pressure of 1 bar and a temperature of 300 °C can be gained. Up to 400 °C, CO formation in equilibrium due to the Boudouard reaction remains at very low rates resulting in less than 100 ppm in the product gas [27]. Therefore, the development of highly active and selective catalysts is indispensable. In addition, the exothermal character of the reaction can cause severe hotspot formation, especially in fixed-bed reactor operation [245]. The deactivation mechanism of thermal sintering has been extensively discussed in literature [246, 247]. Furthermore, the formed $H_2O$, especially in combination with heat, can cause severe deactivation of the catalyst [24], e.g. by modification of the alumina phase [248]. For this reason, the development of thermostable catalysts is of high interest for industrial reaction processing.

In recent years, research on $CO_2$ methanation catalysts has attracted high attention. Due to their advantages in metal costs and availability [85], the focus in this work is placed on NiAl-based catalysts. In contrast to impregnated $Ni/Al_2O_3$ catalysts, co-precipitated $NiAlO_x$ catalysts commonly feature high Ni loadings and are the catalysts of choice for the methanation reaction with respect to activity and stability [203]. Unpromoted $NiAlO_x$ catalysts have been investigated in several studies [135, 137, 249]. In this work, in contrast, the effects of iron (Fe) or manganese (Mn) on the activity and stability under reaction conditions of a co-precipitated $NiAlO_x$ catalyst are investigated. Doping effects of Fe on $Ni/Al_2O_3$ catalysts have already been widely discussed in literature [150, 250]. Hwang *et al.* prepared a Ni(30 wt.%)Fe(5 wt.%)/$Al_2O_3$ catalyst by co-precipitation, analyzing the impact of different precipitation agents. A maximum $CO_2$ conversion of around 60 % was reached at 220 °C and 10 bar in a single-pass fixed bed reactor, while the $CH_4$ selectivity remained high at 99 %. In particular, no Fischer-Tropsch byproducts were observed. The beneficial effect of Fe oxide promotion was reported to be caused by an alleviated reducibility of the active Ni phase. In addition, an increase of Ni particle dispersion upon the introduction of Fe oxide was claimed [150]. Concerning the selectivity towards $CH_4$, similar results were found by Jiang *et al.* [250], who investigated $Ni/Al_2O_3$ catalysts promoted with 0.5 wt.% Fe in the CO methanation reaction. The high activity of Fe-doped Ni catalysts was mainly attributed to the formation of a Ni-Fe alloy, with Ni(50 %)Fe(50 %) being the most active catalyst at high metal loadings [153].

However, studies on Fe-promoted Ni-based catalysts are mostly limited to the evaluation of the catalytic activity so far. Studies on the thermal stability under industrially relevant hydrothermal conditions at high $CO_2$ conversions and harsh conditions, where hotspots can reach 500 °C and more [251], and in particular the evaluation of the degree of deactivation at conditions away

from thermodynamic equilibrium are scarce. Mutz *et al.* [152] investigated the performance of a $Ni_3Fe$ catalyst prepared by homogeneous deposition-precipitation. The $Ni_3Fe/Al_2O_3$ catalyst exhibited a higher activity than their benchmark Ni catalyst, but featured a much lower selectivity towards $CH_4$ at low temperatures (< 60 % selectivity to $CH_4$ at 10 % $CO_2$ conversion). They also claimed a higher stability for $Ni_3Fe/Al_2O_3$, but the stability testing was only carried out at temperatures as low as 360 °C for a duration of 44 h. Most noteworthy, the $Ni_3Fe/Al_2O_3$ suffered from severe deactivation at low temperatures (< 260 °C), which they hypothesized to be possibly caused by carbon formation *via* CO dissociation.

Apart from Fe, Mn has been described to be an effective promoter in the $CO_2$ methanation reaction [94, 146]. Zhao *et al.* [94] demonstrated an increase in catalytic activity in syngas methanation for Mn-promoted $Ni/Al_2O_3$ catalysts synthesized by co-impregnation compared to a $Ni/Al_2O_3$ system. They assumed that Mn stabilizes the particle dispersion of Ni on the surface, resulting in an enhancement of the catalytic activity. Recently, Mn was additionally found to increase the number of medium basic sites in $Ni/Al_2O_3$, which led to an enhancement of the $CO_2$ uptake capacity [104]. However, studies investigating Mn promotion are limited to the impregnation technique, while Mn has not been added to co-precipitated $NiAlO_x$ catalysts yet.

Therefore, a state-of-the-art $NiAlO_x$ catalyst is modified by the introduction of Fe and Mn to systematically investigate their influence on catalyst activity and stability under hydrothermal (500 °C) conditions. Further questions addressed concern the optimum Ni/promoter ratios. Detailed characterization studies, including Brunauer-Emmett-Teller analysis (BET), X-ray photoelectron spectroscopy (XPS), X-ray powder diffraction analysis (XRD), *in situ* infrared (IR) spectroscopy, temperature-programmed desorption of $CO_2$ ($CO_2$-TPD), paramagnetic/ferromagnetic resonance (EPR/FMR) spectroscopy, as well as $H_2$ and $CO_2$ chemisorption were performed to obtain insights into the electronic state of the promoters and into structure-activity relationships.

## 4.2 Experimental

### 4.2.1 Catalyst Synthesis

The co-precipitation route at constant pH 9 follows the synthesis described in [24] and was carried out in a 3 L double-walled glass vessel. All catalysts were based on an equal Ni/Al molar ratio of 1. For doping, Fe or Mn with a definite molar Ni/promoter ratio (29.5, 9.5, 5.5, 3.5, 2.8 for Mn) were added. 120 mL of the mixed 1 M metal nitrate solutions of $Ni(NO_3)_2 \cdot 6\,H_2O$ (Merck), $Al(NO_3)_3 \cdot 9\,H_2O$ (Sigma-Aldrich), $Fe(NO_3)_3 \cdot 9\,H_2O$ (Merck), and $Mn(NO_3)_2 \cdot 4\,H_2O$ (Merck), respectively, were fed to 1 L of bi-distilled $H_2O$ with a flow rate of 2.3 mL $min^{-1}$. Simultaneously, a solution of 0.5 M NaOH (Merck) and 0.5 M $Na_2CO_3$ (Sigma-Aldrich) was dosed by a Titrino Autotitrator 716DMS (Methrom) to keep the pH constant at 9 ± 0.1 during

precipitation (overall volume approx. 360 mL). All reagents were pro analysis (*p.a.*) purity. The slurry was kept at 30 °C and stirred by a KPG stirrer at 150 rpm. To improve mixing, two flow breakers were inserted. The suspension was aged for 18 h at 30 °C in the mother liquor while further stirring. Afterwards, the precipitate was filtered and washed until pH 7. The washing procedure comprised five cycles of re-dispersing the filter cake in DI water and filtering. The filter cake was then dried overnight at 80 °C. For calcination, the precursors were heated to 450 °C with a constant heating rate of 5 K $min^{-1}$ under flowing synthetic air and kept there for 6 h. The calcined catalyst powder was pelletized manually using a Lightpath LP-15 laboratory hydraulic press. Pellet diameter was 2 cm and the pressure was kept as low as 450 N $cm^{-2}$. For pressures higher than 700 N $cm^{-2}$, a gradual loss of the BET surface area could be observed. The pellet was ground in a mortar and manually sieved to the particle fraction of 150 to 200 µm.

In the following, NiAl represents the $NiAlO_x$ benchmark catalyst system, which already exhibits excellent activity and sintering properties in this reaction [203]. The promoted NiAl catalysts are denoted as "NiPX", where P indicates the promoter and X its weight fraction in percent. Repetition of catalyst synthesis yielded in similar catalyst composition and characterization data. Especially the effects of Fe and Mn were reproducible. Extensive series of DoE-plans in combination with parallel syntheses and parallel catalytic testing devices confirm all conclusions on the effects of the iron as well as the manganese promoter [147].

## 4.2.2 Catalyst Characterization

### 4.2.2.1 Elemental Analysis

Catalyst composition was determined by inductively coupled plasma-optical emission spectroscopy (ICP-OES) using an Agilent 700. 50 mg of catalyst powder were dissolved in 1 M $H_3PO_4$ (Alfa Aesar, *p.a.*) and sonicated at 60 °C. To dissolve insoluble $MnO_2$ formed in acidic environment, 50 mg of $Na_2SO_3$ (Merck, *p.a.*) were added. After cooling down, the solutions were diluted 1 to 10 with bi-distilled $H_2O$ and filtered using 0.45 µm syringe filters (Pall). Metal standards were prepared for 1, 10, and 50 mg $L^{-1}$ in the same matrix. Wavelengths used for data evaluation were 230.299 nm (Ni), 396.152 nm (Al), 259.372 nm (Mn), and 238.204 nm (Fe). All data were collected five times. Metal signal superimpositions were excluded. In reference experiments (no addition of $Na_2SO_3$) also the Na signal (568.263 nm) was checked to exclude Na poisoning of the catalysts.

### 4.2.2.2 X-ray Photoelectron Spectroscopy

XPS results were obtained on a Leibold Heraeus LHS 10 using Al-$K_\alpha$ radiation. Approximately 300 mg of the catalyst precursor samples were calcined and degassed overnight. After a full spectrum scan, spectra in the definite binding energy ranges from 885 to 845 eV, 740 to 710 eV, and 665 to 635 eV were collected. Peak positions were corrected to the aliphatic C signal.

#### 4.2.2.3 X-ray Powder Diffraction

For X-ray powder diffraction analysis, a Philips X'pert with Cu-K$\alpha$ radiation and a monochromator was used. Diffractograms of catalyst precursors were obtained by scanning with 0.013° per step and 250 steps $min^{-1}$. For *in situ* XRD measurements, the catalyst was scanned with 0.017 ° $step^{-1}$ and 50 steps $min^{-1}$ before and after a reduction treatment in 5 % $H_2$ in $N_2$ at 485 °C for 8 h at a heating rate of 2 K $min^{-1}$. Interplanar distances $d$ were calculated according to Bragg's law (*cf.* Eq. 3.1). Rather than using transmission electron spectroscopy (TEM), crystallite diameters were determined using the Scherrer equation (*cf.* Eq. 3.4) from *in situ* XRD measurements, since the Ni particles were found to readily oxidize in air.

#### 4.2.2.4 $N_2$ Physisorption

BET analysis was carried out on a NOVA 4000e (Quantachrome) by $N_2$ adsorption at 77 K. After activation at 485 °C in 5 % $H_2$ in Ar for 5 h, the samples were vacuum degassed at 485 °C for 1 h. The $p/p_0$ range between 0.05 and 0.3 was used for determining the BET surface area $S_{BET}$. The total pore volume $V_{Pore}$ was calculated from the data point at $p/p_0$ = 0.995. Under the assumption of cylindrical pores, the mean pore radius $r_{Pore}$ can be calculated from $V_{Pore}$ and $S_{BET}$ (*cf.* Eq. 3.8).

#### 4.2.2.5 $H_2$ and $CO_2$ Chemisorption

Chemisorption experiments with $H_2$ and $CO_2$ were performed using an Autosorb 1 C (Quantachrome) at 35 °C after activation as mentioned above (5 % $H_2$ in $N_2$ at a heating rate of 2 K $min^{-1}$ to 485 °C). An equilibration time of 2 min ($H_2$) and 10 min ($CO_2$), respectively, was applied. A dissociative adsorption mechanism of $H_2$ on Ni with one H atom adsorbing per Ni atom was applied for the calculation of the specific metal area [252], assuming that $H_2$ adsorption only occurs on Ni and not on Fe. This procedure is approved in literature, since only insignificant amounts of $H_2$ are reported to be chemisorbed on Fe under the chosen conditions [253, 254]. $H_2$ adsorption measurements at 200 °C as suggested by Topsøe *et al.* [255] resulted in $H_2$ spillover onto the aluminum-containing oxide phase. Moreover, the determination of Fe surface atoms by CO chemisorption is further complicated since the adsorption stoichiometry is known to be structure-dependent [255, 256]. In contrast to literature [115, 257], the adsorption of $CO_2$ at the chosen conditions was proved to be not kinetically hindered on the samples. For all sorption techniques the errors in repetition experiments were within the error range of the instrument (±4 %, data provided by Quantachrome).

#### 4.2.2.6 Fourier Transform Infrared Spectroscopy

*In situ* infrared spectroscopy was carried out on a Bruker Vertex 70 spectrometer equipped with $CaF_2$ windows. A catalyst pellet of 1 cm diameter was heated to 450 °C with a rate of 5 K $min^{-1}$ in $H_2$ flow and *in situ* activated at this temperature for 5 h. Subsequently, the cell was evacuated

and, after cool-down to 40 °C, kept at $10^{-7}$ mbar for 18 h. $CO_2$ was dosed into the cell to a pressure of 1 mbar. After 10 min of equilibration, the cell was evacuated again for 30 min at $10^{-7}$ mbar before the IR spectrum was recorded. The background was collected after pellet removal.

#### 4.2.2.7 Temperature-Programmed Desorption of $CO_2$

For temperature-programmed desorption of $CO_2$ ($CO_2$-TPD), 50 mg of catalyst were reduced *in situ* in 5 % $H_2$ in He at 480 °C for a duration of 8 h. The heating rate was 2 K min$^{-1}$. The catalyst bed was purged with He at 480 °C for 1 h. After cooling down to 35 °C, $CO_2$ was adsorbed for 30 min with a flow rate of 50 mL min$^{-1}$. To remove weakly adsorbed $CO_2$, the catalyst was post-flushed with He for 30 min. TPD was carried out from 35 °C to 480 °C with a heating rate of 6 K min$^{-1}$ in He (volumetric flow rate 100 mL min$^{-1}$). The $CO_2$ signal was tracked on a mass spectrometer (Pfeiffer Vacuum, OmniStar). $CO_2$ signal fitting was omitted due to unknown desorption kinetics.

#### 4.2.2.8 Temperature-Programmed Reduction

Temperature-programmed reduction (TPR) studies were conducted with 5 % $H_2$ in Ar with a total flow of 20 mL min$^{-1}$ and a heating rate of 2 K min$^{-1}$ to 485 °C. Hydrogen consumption was tracked with an online mass spectrometer (OmniStar GSD 320, Pfeiffer Vacuum). TPR measurements up to 1000 °C were carried out on a ChemStar TPx (Quantachrome). 60 mg of the calcined catalyst powders were heated in 5 % $H_2$ in Ar using a total volumetric flow rate of 100 mL min$^{-1}$. Hydrogen consumption was tracked using a TCD detector. Evolving $H_2O$ and $CO_2$ were frozen out using an acetone/liquid $N_2$ frigorific mixture.

#### 4.2.2.9 Temperature-Programmed Oxidation

Temperature-programmed oxidation (TPO) was applied to check for carbon residues on the catalyst after testing. The spent catalyst was heated *in situ* to 500 °C in Ar (100 mL min$^{-1}$), held at this temperature for 4 h, and cooled down to room temperature in Ar. Subsequently, the catalyst was heated in 5 % synthetic air in Ar with a heating rate of 5 K min$^{-1}$ to 500 °C at a total flow rate of 100 mL min$^{-1}$. A mass spectrometer (OmniStar GSD 320, Pfeiffer Vacuum) was used to track CO and $CO_2$ signals during heating.

#### 4.2.2.10 Paramagnetic/Ferromagnetic Resonance Spectroscopy

Paramagnetic and ferromagnetic resonance (EPR/FMR) spectra of the activated catalysts were recorded on a JEOL JES-RE 2X at X-band frequency at temperatures between 113 and 473 K, microwave frequency 9.4 GHz, microwave power < 0.2 mW, modulation frequency 100 kHz. The microwave frequency was measured with a microwave frequency counter Advantest R5372. The catalyst samples were reduced at 450 °C in $H_2$ for 2 h and measured in this particular

capillary reactor without contact to air. The integrated intensity was determined by double integration of the resonance signals of a weighed catalyst sample calibrated to a known standard ($Mn^{2+}$/MgO). For the Fe-doped catalyst, the significance of intensities/magnetizations measured below 273 K are of limited value due to substantial integrated intensity at zero field for X-band frequency. The spectra and magnetic data derived have been compared to the calcined catalysts (before reduction) and to model iron oxide catalysts with (potentially) ferromagnetic properties. The supported iron oxides particles showed at least one to two orders of magnitudes lower magnetizations (integrated intensities) and magnetic anisotropies clearly different from the Ni and Ni-Fe systems. Thus, their contribution to the ferromagnetic resonance spectra of the reduced catalysts can be neglected for these particular samples.

### 4.2.3 Experimental Setup and Activity Measurements

The setup as described in Section 3.3 and [24] was used for catalyst testing. 25 mg catalyst with a particle size from 150 to 200 µm were diluted with 225 mg purified SiC (ESK) and plugged with quartz wool in the isothermal zone of a 4 mm diameter glass-lined reactor tube. Reaction temperature was measured by a thermocouple placed in the outlet of the catalyst bed. Gases were supplied by Westfalen with a purity of 5.0 and 6.0 for $H_2$, respectively. The product gas exiting the back pressure regulators was diluted with Ar in a ratio of 1 to 8. In addition, all tubing was heated to prevent $H_2O$ condensation.

All catalysts were treated following the procedure applying the process parameters listed in Table 4.1. Catalyst activation was carried out *in situ* at 485 °C and ambient pressure for 8 h at a heating rate of 2 K $min^{-1}$ in 5 % $H_2$ in Ar at a flow rate of 50 mL $min^{-1}$. The gas hourly space velocity (*GHSV*) was set to 200.000 $h^{-1}$ with stoichiometric feed gas composition and an Ar dilution of 50 %. After a start-up period of 24 h at 250 °C at 7 bar, the conversion of $CO_2$ was determined stepwise every 25 K in the temperature range between 175 and 500 °C at 8 bar, denoted as $S_1$. This was followed by an aging period under harsh hydrothermal conditions at 500 °C and 7 bar for 32 h in thermodynamic equilibrium (partial pressure of steam 1.6 bar). These industrially relevant specifications were chosen to simulate catalyst deactivation occurring during possible hotspot formation. In addition, in a second temperature variation cycle $S_2$,

**Table 4.1:** Variation of process parameters for the determination of catalyst activity and thermal stability.

| | Feed $H_2/CO_2$/Ar | $Q$ / NL $g_{cat}^{-1}$ $h^{-1}$ | $T$ / °C | $p$ / bar | $t$ / h |
|---|---|---|---|---|---|
| Activation | 5/0/95 | 130 | 485 | 1 | 8 |
| Start-up | 4/1/5 | 150 | 260 | 7 | 24 |
| $S_1$ | 4/1/5 | 150 | 175–500 | 8 | 11 |
| Aging | 4/1/5 | 150 | 500 | 7 | 32 |
| $S_2$ | 4/1/5 | 150 | 175–500 | 8 | 11 |

data indicating the thermal stability of the catalyst away from thermodynamic equilibrium was recorded. This rapid aging technique proved to be advantageous since at 300 °C (isothermal bed conditions) and high partial pressure of steam ($p(H_2O)$ approx. 1.6 bar, $X(CO_2)$ = 80 %) over 250 h time on stream (TOS) no deactivation could be observed even for the benchmark catalyst NiAl (*cf.* Figure 4.14). At higher temperatures, potential activity loss due to catalyst deactivation could not be tracked due to equilibrium product gas composition.

In advance, detailed studies to exclude heat and mass transport limitations for conditions away from thermodynamic equilibrium were carried out. The pressure drop due to the catalyst bed at the volumetric flow rate applied was below 0.1 bar and, at a total pressure of 8 bar, therefore negligible.

For $CO_2$, $CH_4$, CO, $H_2$, and $H_2O$, gas composition was determined using an Emerson MTL-4 online process gas analyzer (PGA). Further byproduct analysis was carried out on a PerkinElmer gas chromatograph Clarus 580, equipped with two columns and FID detectors. For every temperature, the conditions were kept stable for 45 min to ensure the achievement of steady-state conditions. Gas composition was monitored by the PGA, which recorded gas composition once per second. For data evaluation, the concentrations indicated by the PGA were averaged over the last 2.5 min. Thereafter, GC analysis was started. Volume contraction (*cf.* Eq. 3.15) was included in the calculations for conversions, yields and selectivities. Closed C, O, and H balances (±3 %) proved data reliability. For conversions and yields, the errors in repeated experiments were ±2 % rel.

To compare all catalysts regarding activity and stability at industrially relevant conversions away from equilibrium and from differential conditions, $T_{50}$, the temperature required to achieve 50 % $CO_2$ conversion, was determined for every catalyst in $S_1$ and $S_2$. $T_{50}$ during $S_1$ serves as a measure for catalyst activity, the ratios of $T_{50}$ of $S_2$ and $S_1$ for thermal stability. By normalization to the activity and stability data of the benchmark NiAl catalyst as shown in Eqs. 4.1 and 4.2, the results directly serve as a measure for the influences of the promoters on catalyst performance.

$$\text{Normalized activity} = \frac{T_{50,S_1}(\text{NiAl})}{T_{50,S_1}(\text{doped cat.})} \tag{4.1}$$

$$\text{Normalized stability} = \frac{\frac{T_{50,S_2}(\text{NiAl})}{T_{50,S_1}(\text{NiAl})}}{\frac{T_{50,S_2}(\text{doped cat.})}{T_{50,S_1}(\text{doped cat.})}} \tag{4.2}$$

Thermodynamic calculations were carried out using the $\Delta G$ minimization method (*cf.* Appendix C). Enthalpy and entropy values of $CO_2$, CO, $CH_4$, $H_2O$, and $H_2$ were determined using the Shomate equation (*cf.* Appendix B).

# 4.3 Results and Discussion

## 4.3.1 Material Characterization

### 4.3.1.1 Elemental Analysis

The catalysts were prepared by co-precipitation at a constant pH 9 for Ni/promoter molar ratios of 29.5, 9.5, 5.5, 3.5, and 2.8 for Mn. Rather than keeping the Ni content constant, the $n_{Ni}/n_{Al}$ ratio was fixed to 1, since the structure of the precipitates and catalysts after calcination was found to strongly depend on the Ni/Al molar ratio [24, 139, 258]. The metal contents of the calcined materials are summarized in Table 4.2.

The undoped NiAl catalyst features a Ni content of 44.3 wt.%. By promoting this system with Fe, the Ni loading drops from 44.3 to 40 wt.%, but stays at around 40 wt.% independent from the Fe fraction, which rises from 1.7 to 7 wt.%. With further increasing amount of Fe (> 7 wt.%), the Ni loading (36 wt.%) decreases. In comparison, the Ni loading is always lower for similar Mn weight fractions, which might suggest a competitive incorporation of Ni and Mn in the crystal structure. The originally inserted $n_{Ni}/n_{Al}$ ratio of 1 is recovered in the calcined catalyst for both, NiFe and NiMn with a deviation of $\pm 6$ %.

In the reference experiments with no $Na_2SO_3$ being added to the ICP solutions, Na signals were below the detection limit (< $10^{-3}$ wt.%), meaning that Na poisoning of the catalysts can be excluded.

**Table 4.2:** Elemental composition of the catalysts after calcination obtained by ICP-OES.

| | $l$ / wt.% | | | |
|---|---|---|---|---|
| Sample | Ni | Al | Fe | Mn |
| NiAl | 44.3 | 19.8 | - | - |
| NiFe2 | 40.0 | 19.4 | 1.7 | - |
| NiFe4 | 39.7 | 17.8 | 4.3 | - |
| NiFe7 | 39.6 | 16.0 | 6.9 | - |
| NiFe10 | 36.1 | 17.4 | 10.1 | - |
| NiMn1 | 38.7 | 18.0 | - | 1.3 |
| NiMn4 | 38.9 | 18.2 | - | 3.7 |
| NiMn6 | 36.3 | 15.5 | - | 6.1 |
| NiMn8 | 31.9 | 15.2 | - | 8.3 |
| NiMn11 | 34.1 | 16.6 | - | 10.8 |

### 4.3.1.2 X-ray Photoelectron Spectroscopy

XPS studies were carried out on NiAl, NiMn8 and NiFe10 to determine the oxidation state of the metals in the calcined catalyst. When comparing the full survey spectra in Figure 4.7 A, no clear differences are observable. Figure 4.7 B illustrates the XPS spectrum of NiAl. Distinct

signals can be observed for Ni-$2p^{3/2}$ at 854.9 eV, for Ni-$2p^{1/2}$ at 872.6 eV, as well as for the satellite peaks at 862.2 and 879.2 eV. Peak shapes are consistent with results from a detailed study on co-precipitated NiAl catalysts conducted by Shalvoy *et al.* [259], who concluded that spinel phase $NiAl_2O_4$ is present on the catalyst surface, since the peak attributed to Ni-$2p^{3/2}$ should feature a characteristic doublet structure for NiO. However, it needs to be mentioned that peak positions in this study are shifted to lower binding energies compared to spinel phase Ni-$2p^{3/2}$, which in contrast is an indicator for NiO rather than for $NiAl_2O_4$ [259].

As shown in Figure 4.7 C, for NiFe10 a characteristic peak can be observed at $E_{bin}$ = 723.9 eV, identifying the Fe species on the catalyst surface as $Fe_2O_3$ ($2p^{1/2}$) [260]. The corresponding peak for $2p^{3/2}$ is hidden by Ni Auger electrons. Regarding NiMn8 (*cf.* Figure 4.7 D), two differences can be observed in comparison to the NiAl catalyst. The signal at $E_{bin}$ = 653.1 eV can be attributed to $Mn_3O_4$ ($2p^{1/2}$) [261]. The peak caused by $2p^{3/2}$ is superimposed by Ni Auger electrons, but still can be identified at 641.8 eV, which can also be attributed to $Mn_3O_4$ [262]. Small shifts in binding energies in the XPS spectra would indicate a different oxidation state. Therefore, analytical investigations have been carried out (*cf.* Section 4.5.2), which show results that are consistent to XPS.

#### 4.3.1.3 X-ray Powder Diffraction Analysis

XRD patterns of the catalyst precursors are shown and discussed in detail in Section 4.5.3 (*cf.* Figure 4.8). For all catalyst precursors, a modified takovite structure is found. As displayed in Figure 4.1, the XRD patterns for all catalysts after calcination are similar. Reflexes can neither be assigned to pure NiO (bunsenite) nor to $Al_2O_3$. Also, the XRD patterns show that no bulk

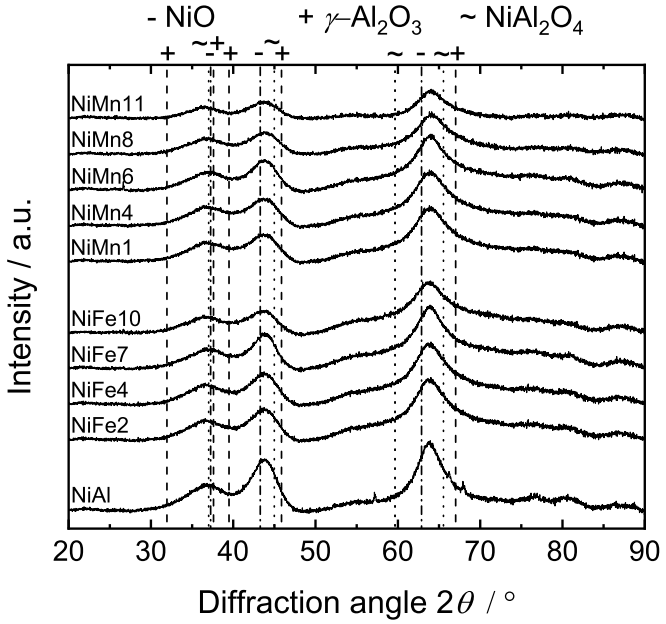


**Figure 4.1:** XRD patterns of catalyst after calcination (JCPDS: NiO 78-0429, $\gamma$-$Al_2O_3$ 10-0425, $NiAl_2O_4$ 10-0339).

$NiAl_2O_4$ spinel phase is present. This indicates that a mixed oxide phase containing NiO and $AlO_x$ is formed. The positions of the reflexes suggest plane distances between the ones of NiO and $Al_2O_3$. The shift of the reflex attributed to the (220) plane of NiO at $2\theta = 63.76°$ reveals that, compared to pure NiO, the lattice constant $a_c$ is decreased from 4.177 Å (JCPDS: 78-0429) to 4.125 Å. This indicates that $Al^{3+}$ ions are incorporated into the NiO crystal lattice, leading to a decrease of the lattice constant $a_c$. Calcined NiAl hydrotalcites have been investigated in a variety of studies, but the structures are still under discussion [139, 258, 263].

It is well-known that low temperature calcination of those materials results in the generation of metastable mixed oxides [258, 263], while at high calcination temperatures phase separation into NiO and $NiAl_2O_4$ [139], or $NiAl_2O_4$ and two different NiO phases, with one of them containing $Al^{3+}$ ions, might occur [258]. In addition, the structure is highly dependent on the $n_{Ni}/n_{Al}$ ratio [24, 139, 258]. Alzamora *et al.* [139] suggested that the hydrotalcites calcined at low temperatures consist of two separate phases, one crystalline NiO phase, which contains $Al^{3+}$ ions, and an amorphous alumina phase, which might contain $Ni^{2+}$ ions. The evolution of a crystalline Al-containing NiO phase is in concordance with the results shown in Figure 4.1. No impact of Fe or Mn on the structure of the calcined catalysts can be observed. This indicates that the promoters are incorporated into the modified NiO phase, without a significant change of the lattice constants, present as amorphous phase, or incorporated in an amorphous alumina phase. For the Fe-promoted catalysts, also the formation of some X-ray amorphous $NiFe_2O_4$ during calcination cannot be excluded. The precipitated NiFeAl hydrotalcite catalyst systems prepared by Yu *et al.* [253] exhibit similar XRD patterns, with an observable impact of Fe promotion on the NiAl structure starting from at least 20 wt.% Fe for catalysts calcined at 480 °C.

However, promoter-induced modifications of the catalyst structure emerge in the XRD patterns of the reduced catalysts. As displayed in Figure 4.2, fcc metallic Ni reflexes emerge at $2\theta = 44.5$ (111), 51.9 (200) and 76.4° (220) due to the reduction of NiO. As a result, the former crystalline

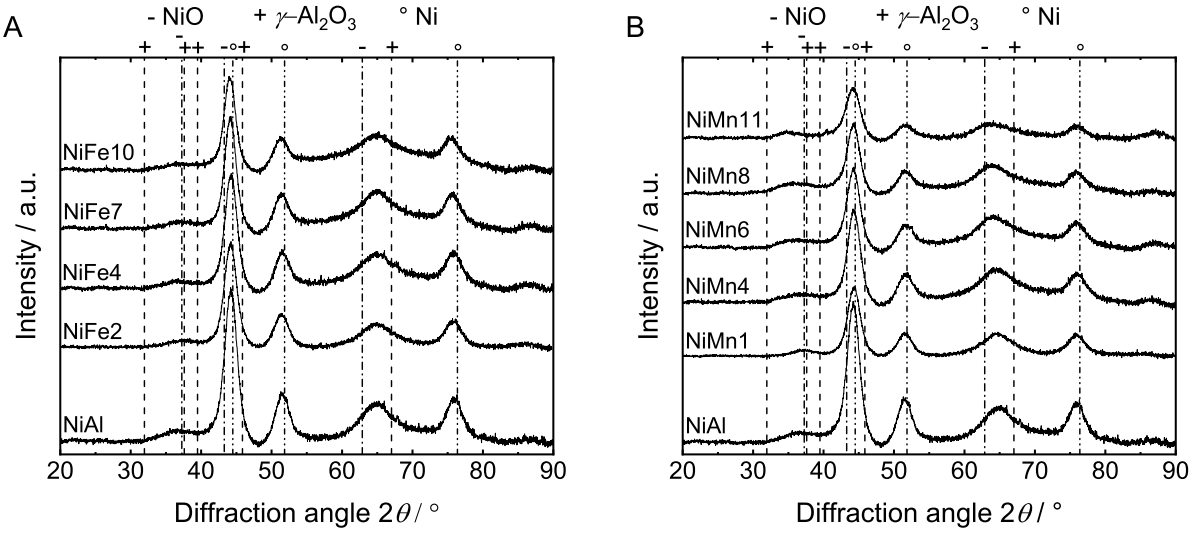


**Figure 4.2:** XRD patterns of the reduced Fe-promoted (A) and Mn-promoted (B) catalysts (JCPDS: NiO 78-0429, $\gamma$-$Al_2O_3$ 10-0425, Ni 87-0712.)

mixed oxide phase is shifted towards the reflexes of $\gamma$-$Al_2O_3$, accounting for the higher Al content. Compared to the reference patterns, the reflexes show a systematic shift towards larger lattice constants, which is caused by thermal expansion, since the XRD patterns were collected at 485 °C [264]. Similar to the calcined materials, the structure of reduced NiAl hydrotalcites, with the focus on the role of Al, has been extensively discussed in literature. Two different models have been developed for hydrotalcites calcined at low temperatures (below 600 °C). Alzamora *et al.* [139] suggested that Ni particles nucleate on the surface of the Al-containing NiO phase, with Al hindering excessive Ni particle growth. During reaction, the $Al^{3+}$ ions are supposed to diffuse to the nucleated Ni particles, leading to the formation of alumina phases. In contrast, similar to co-precipitated Cu/ZnO/$Al_2O_3$ catalyst systems, Wright *et al.* [263] showed that the Ni particles form a paracrystalline phase, caused by the incorporation of Al, possibly in the form of $AlO_2^-$ [265].

For the Fe-promoted catalysts in Figure 4.2 A, the reflexes corresponding to the fcc metallic Ni planes at Fe loadings higher than 4 wt.% are shifted to larger lattice constants as compared to the benchmark NiAl system, the extent increasing with rising Fe weight fraction. It is concluded that Fe is also reduced and interacts with the metallic Ni phase, leading to Ni lattice distortion by the formation of a Ni-Fe alloy. Similar results are reported by Yu *et al.* [253] and Reshetenko *et al.* [266] for co-precipitated NiFeAl catalysts, as well as by Meng *et al.* [149] for impregnated Fe-Ni/$\gamma$-$Al_2O_3$ catalysts.

In contrast, as shown in Figure 4.2 B, Mn does not seem to interact with the metallic Ni, but with the former mixed oxide phase instead. The reflexes of the former mixed oxide phase, which for NiAl appear at $2\theta$ = 36.4 and 65.0°, are shifted to lower diffraction angles with higher Mn content. The fact that these shifts are not visible for the calcined sample in Figure 4.1 indicates that, during the (partial) reduction of NiO, Mn species might be incorporated into the former NiO-rich matrix or that the Mn species are modified under reduction conditions, leading to a change of the lattice constant of the former mixed oxide phase. No separate Mn oxide phase was detected in XRD, but the presence of X-ray amorphous Mn oxide species on the catalyst surface cannot be excluded. The comparison of Figures 4.1 and 4.2 shows that, despite the reflex shift of the mixed oxide phase upon the removal and reduction of NiO, the reflexes of the former mixed oxide phase in Figure 4.2 do not match to the diffraction pattern of $\gamma$-$Al_2O_3$. This either indicates that no pure $\gamma$-$Al_2O_3$ phase is formed or, as common for co-precipitated $NiAlO_x$ catalysts [139], that after the reduction process still some NiO is present in the oxide phase, meaning that the reduction of NiO does not take place quantitatively.

#### 4.3.1.4 Material Properties

As shown in Table 4.3, a BET surface area of 294 $m^2\,g_{cat}^{-1}$ was obtained for the NiAl system, which is 32 % higher than for $Al_2O_3$. For NiAl catalysts prepared by co-precipitation the specific surface is reported to range from 100 to 300 $m^2\,g_{cat}^{-1}$ [203]. Promoting with Fe reduces the overall surface area to a minimum at NiFe7, from whereon it starts to increase again. Similar

**Table 4.3:** Catalyst characterization data including results from $N_2$ physisorption as well as $H_2$ and $CO_2$ chemisorption.

| Catalyst | $S_{BET}$ / $m^2\,g_{cat}^{-1}$ | $V_{Pore}$ / / $mL\,g_{cat}^{-1}$ | $r_{Pore}$ / nm | $S_{Ni}^{a}$ / $m^2\,g_{cat}^{-1}$ | $D_{Ni}^{a}$ / % | $d_{C}^{b}$ / nm | $U(CO_2)$ / $\mu mol\,g_{cat}^{-1}$ |
|---|---|---|---|---|---|---|---|
| NiAl | 294 | 0.68 | 4.6 | 21.1 | 7.1 | 3.4 | 172 |
| NiFe2 | 302 | 0.75 | 5.0 | 19.8 | 7.4 | 3.8 | 199 |
| NiFe4 | 283 | 0.84 | 5.9 | 18.3 | 6.9 | 3.7 | 198 |
| NiFe7 | 214 | 0.89 | 8.3 | 11.4 | 4.3 | 3.4 | 196 |
| NiFe10 | 240 | 0.80 | 6.7 | 9.4 | 3.9 | 3.5 | 188 |
| NiMn1 | 301 | 080 | 5.4 | 19.2 | 7.4 | 3.2 | 197 |
| NiMn4 | 254 | 0.64 | 5.0 | 20.1 | 7.7 | 3.3 | 215 |
| NiMn6 | 254 | 0.59 | 4.7 | 20.0 | 8.2 | 3.2 | 244 |
| NiMn8 | 262 | 0.69 | 5.3 | 17.6 | 8.3 | 3.2 | 240 |
| NiMn11 | 282 | 0.69 | 4.9 | 13.4 | 5.9 | 3.2 | 282 |
| NiO | - | - | - | 1.2 | - | - | 240 |
| $Al_2O_3$ | 223 | 0.49 | 4.4 | - | - | - | 282 |

[a] from $H_2$ chemisorption (*cf.* Eq. 3.11).
[b] from XRD analyzing the Ni(-Fe) reflection at $2\theta$ = 51.3 to 51.7° applying the Scherrer equation (*cf.* Eq. 3.4).

trends can be observed for the Mn-promoted catalysts. The minimum specific surface areas are found for NiMn4 and NiMn6 (254 $m^2\,g_{cat}^{-1}$). Adsorption and desorption isotherms suggest a mesoporous structure for all catalysts. Compared to literature data, the BET surface area obtained for the NiAl catalyst is slightly higher than reported by Abello *et al.* [136], which also applies to NiFe7 [150]. Literature studies suggest that synthesis parameters like temperature, pH during precipitation [139], or the $n_{Ni}/n_{Al}$ ratio [24, 136] affect the BET surface area more severely than promotion with further metals. The total pore volume is 0.68 $mL\,g_{cat}^{-1}$ for NiAl and increases with rising Fe content to 0.89 $mL\,g_{cat}^{-1}$ for NiFe7. This trend is similar to the average pore radius, which is highest for NiFe7 (8.3 nm). For higher Fe contents, both the total pore volume and the average pore radius decrease. For the Mn-promoted samples, in contrast, the changes for both the total pore volume and the average pore radius are less pronounced. At low Mn loadings in NiMn1 both the total pore volume and the average pore radius show the highest values, but are only slightly increased compared to NiAl. The lowest total pore volume is found for NiMn6. At higher Mn loadings (8 to 11 wt.%) it reaches a constant level at 0.69 $mL\,g_{cat}^{-1}$. The average pore radius stays approximately constant at $5 \pm 0.4$ nm for all Mn-promoted catalysts.

A specific Ni metal surface area of 21.1 $m^2\,g_{cat}^{-1}$ is obtained for the benchmark NiAl catalyst. The addition of Fe from 1.7 to 10.1 wt.% causes a continuous decrease of the specific Ni area from 19.8 to 9.4 $m^2\,g_{cat}^{-1}$. The decreasing metal surface area with increasing Fe content at high Fe loadings indicates an interaction between metallic Ni and metallic Fe, with the $H_2$ adsorption capacity of the latter being known to be negligible under the chosen conditions [253]. This

furthermore implies that the Fe atoms are concentrated on the catalyst surface, forming a Ni-Fe surface alloy, which is consistent to the findings in XRD in Figure 4.2 A, *i.e.* to increasing lattice constants with increasing Fe content. The difference between NiFe4 (18.3 $m^2\,g_{cat}^{-1}$) and NiFe7 (11.4 $m^2\,g_{cat}^{-1}$) can be directly correlated to the reflex shift of the Ni phase in Figure 4.2 A. On the contrary, for small Mn loadings the specific Ni surface stays approximately constant, leading to an increase of Ni dispersion from 7.1 to 8.3 %. The reason for this might be a support-stabilizing effect by the interactions of Mn with the mixed oxide phase as shown in XRD analysis. At high Mn loadings (> 6 wt.%), however, a decline of the Ni surface area can be observed. Ni dispersion values were calculated on the assumption that $H_2$ adsorption takes place on Ni only. The mean crystallite diameters were calculated from XRD rather than $H_2$ chemisorption, since it is known that in co-precipitated NiAl mixed oxide systems Ni activation does not take place quantitatively under the chosen reduction conditions [139]. For the benchmark NiAl catalyst, the mean crystallite diameter is found to be 3.4 nm. Upon promotion with Fe, the mean diameter slightly rises to 3.7 to 3.8 nm for Fe contents up to 4 wt.%, before it decreases to its initial value for NiFe7 and NiFe10, for which interactions between metallic Fe phase and metallic Ni were found in Figure 4.2 A. This indicates a beneficial effect of metallic Fe on the crystallite diameter. In contrast, for the Mn-promoted catalysts the Ni crystallite diameter stays nearly constant at 3.2 nm. However, it needs to be mentioned that the differences in the calculated crystallite diameters are rather small and too low to draw further conclusions. In addition, exact determination of the crystallite sizes might be influenced by their possibly paracrystalline character as discussed in Section 4.3.1.3. Nevertheless, within this study the results are comparable, and the order of magnitude matches well to literature, where, depending on the precipitation procedure, particle sizes of approximately 5 nm are reported for NiAl catalysts [203].

For the evaluation of the $CO_2$ adsorption capacities, the molar amounts of adsorbed $CO_2$ ($U(CO_2)$) are compared in Table 4.3. The exact adsorption stoichiometry of $CO_2$ on Ni depends on dissociation behavior and whether CO is bound linearly, bridged, or as a subcarbonyl [252]. The benchmark NiAl catalyst exhibits a $CO_2$ adsorption capacity of 172 $\mu mol\,g_{cat}^{-1}$. The amount of adsorbed $CO_2$ increases to 199 $\mu mol\,g_{cat}^{-1}$ at promotion with 2 wt.% Fe. In contrast to the trend in $H_2$ adsorption capacity, this level is approximately maintained until 7 wt.% Fe and slightly decreases at 10 wt.% Fe. Mn promotion greatly enhances the $CO_2$ adsorption capacity with increasing promoter weight fraction from 197 $\mu mol\,g_{cat}^{-1}$ at 1 wt.% Mn to 240 $\mu mol\,g_{cat}^{-1}$ at 8 wt.% Mn. It is hypothesized that the increase of $CO_2$ adsorption capacity is caused by the modification of the catalyst surface by introducing Mn, which rises the basic character of the catalyst [104, 267]. This leads to a facilitated chemisorption of the acidic $CO_2$ molecule, which preferentially adsorbs on basic sites [157, 268].

Figure 4.3 shows the infrared spectra of the activated NiAl, NiFe7, and NiMn6 catalysts, on which $CO_2$ was adsorbed with a pressure of 1 mbar. Three different basic sites on the oxide phase can be distinguished: bicarbonate, monodentate carbonate, and bidentate carbonate. Overall, NiAl and NiFe7 feature a similar density of basic sites. For NiFe7, the density of medium basic sites (binding bidentate carbonate [269] at $\nu$ = 1590 $cm^{-1}$ and $\nu$ = 1340 to 1320 $cm^{-1}$ and

strong basic sites (binding monodentate carbonate [269] at $\nu$ = 1560 to 1510 $cm^{-1}$ and $\nu$ = 1400 to 1360 $cm^{-1}$) seems to be slightly decreased, whereas the density of weak basic sites (binding bicarbonate [269] at $\nu$ = 1650, 1450, and 1230 $cm^{-1}$) is higher. This is consistent to the similar $CO_2$ uptake capacities of NiAl and the Fe-promoted catalysts. The slightly increased number for Fe-promoted catalysts might arise from different $CO_2$ sorption and dissociation properties of Ni and Ni-Fe [156]. However, in accordance with the enhanced $CO_2$ uptake capacity of the Mn-promoted catalysts shown in Table 4.3, the number of basic sites is much higher on NiMn6 compared to NiAl. Especially the density of medium basic and strong basic sites [269] is increased. For the $CO_2$ methanation reaction, especially a high density of medium basic sites was claimed to be beneficial for high catalyst activity [128]. It was thereby assumed that monodentate formate originating from monodentate carbonate species is quickly hydrogenated [128]. The elevated number of medium basic sites on NiMn6 compared to NiAl is supported by recent studies of Zhao *et al.*, who found that Mn introduction in $Ni/Al_2O_3$ catalysts by incipient wetness impregnation increases the number of medium basic sites [104].

For the sake of comparison, characterization data of NiO and $Al_2O_3$ are shown in Table 4.3. The high $CO_2$ uptake of $Al_2O_3$ (437 µmol $g_{cat}^{-1}$) and the low value of NiO (5.4 µmol $g_{cat}^{-1}$) indicate that in co-precipitated $NiAlO_x$ samples the majority of the $CO_2$ adsorbed binds onto the oxide phase. This confirms that the increasing $CO_2$ uptakes upon Mn promotion are caused by the dopants, since the general trend of Al content with increasing dopant loading decreases. Pandey and Deo [157] reported a $CO_2$ uptake of 838 µmol $g_{cat}^{-1}$ for commercial $Al_2O_3$ (Sasol) and directly correlated the $CO_2$ uptake for NiFe catalysts supported on different oxide materials to their activity in $CO_2$ methanation. Both activity and $CO_2$ uptake values increased in the order $SiO_2 < TiO_2 < Nb_2O_5 < ZrO_2 < Al_2O_3$. The higher $CO_2$ uptake of the commercial $Al_2O_3$ compared to 4.3 may originate from differences in the preparation procedures, in particular the thermal treatments.

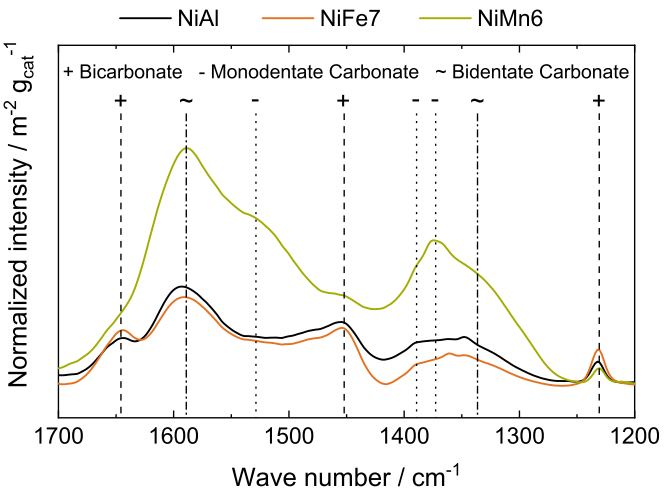


**Figure 4.3:** Infrared spectra of the reduced NiAl, NiFe7, and NiMn6 catalysts, adsorption pressure $p(CO_2)$ = 1 mbar, $T$ = 40 °C, references from Di Cosimo *et al.* [269].

Temperature-programmed desorption experiments contribute to derive information on the binding strengths of the carbonates observed in Figure 4.3. Figure 4.10 illustrates the $CO_2$-TPD profiles of the reduced NiAl, NiFe7, and NiMn6 catalysts. For NiAl, the signals can be assigned to $CO_2$ originating from weakly-bound bicarbonate (50 to 125 °C), medium strength bidentate carbonate (50 to 200 °C), strongly bound monodentate carbonate (80 to 300 °C), and bridged carbonate species (250 to 480 °C) [270], that could not be identified in IR experiments in Figure 4.3 (at approx. 970 $cm^{-1}$ [270], absorption by $CaF_2$ windows). For NiFe7 and NiMn6, the signals assigned to medium strength bidentate carbonate and strongly bound monodentate carbonate are shifted to lower temperatures by approximately 20 K, which indicates a lower binding strength of these species on the promoted catalysts. Also, the broad high-temperature desorption signal originating from bridged carbonate at 370 °C is shifted to lower temperatures. For NiFe7 and NiMn6, one might suspect the presence of low amounts of an additional, differently stabilized carbonate species desorbing at temperatures around 400 °C. However, one might also argue that the decrease of the $CO_2$ desorption signal trend might be an artifact of Ni(-Fe) surface passivation by desorbing $CO_2$ [160], since CO was observed at these temperatures. For a definite statement, additional studies are required. Overall, the results are in concordance with the IR spectra in Figure 4.3. NiAl and NiFe7 show similar $CO_2$ uptakes, while for NiMn6 the uptake is increased. Especially the densities of weak basic, medium basic, and strong basic sites seem to be higher. From the shifts of the desorption signals for NiFe7 one can deduce that some Fe species might still interact with the oxide phase after catalyst reduction. This implies that the reduction of $Fe^{3+}$ to Fe proved by XRD in Figure 4.2 A and FMR studies does not take place quantitatively.

#### 4.3.1.5 Temperature-Programmed Reduction

For examination of catalyst reducibility, $H_2$ consumption during catalyst activation was recorded by mass spectrometry. As shown in Figure 4.9, the NiAl benchmark catalyst exhibits a clear reduction peak at 460 °C, attributed to the reduction of NiO [24]. In addition, a small peak appears at 170 °C, which has previously been assigned to the presence of small amounts of $Ni^{3+}$ in the external layers of the solid [271]. Promotion with Fe (*cf.* Figure 4.9 A) leads to a shift of the main $H_2$ consumption peak to lower temperatures, which is attributed to the reduction of Ni at lower temperatures, indicating that the reduction features a lower activation barrier compared to NiAl. This observation is in concordance with literature studies [149]. For NiFe10, the peak is shifted by -30 K to 430 °C. Additionally, a shoulder appears in the temperature range between 250 and 350 °C. The asymmetric peak shape indicates that different reduction processes are hidden under the NiO reduction peak. Literature suggests that for Fe-doped $Ni/Al_2O_3$ the reduction of Fe from $Fe_2O_3$ *via* FeO to metallic Fe occurs in the temperature range from 200 to 440 °C, whereas the activation temperature decreases with increasing Fe content [149]. Therefore, the appearance of this Fe reduction peak is only visible for NiFe10. This supports the hypothesis of the formation of a metallic Ni-Fe alloy, in concordance with XRD analysis and $H_2$ chemisorption data.

For the Mn-promoted catalyst, similar peak shifts can be observed, but to a smaller extent as compared to the Fe-promoted catalysts (*cf.* Figure 4.9 B). For NiMn4, for example, a peak shift of the NiO reduction signal by -10 K can be observed. However, a second peak emerges at 150 °C, rising in intensity with increasing Mn loading, that is systematically shifted to higher temperatures, with its maximum at 175 °C for NiMn8. It is supposed that the emerging $H_2$ consumption peak is attributed to the reduction of $Mn_3O_4$ to MnO. Similar temperature regions for the reduction of manganese oxides have been found for $Pd/Mn/Al_2O_3$ [272]. The increased surface basicity of the Mn-promoted catalysts, which was found in $CO_2$ chemisorption experiments, $CO_2$-TPD, and *in situ* IR spectroscopy, and which is in accordance with literature studies [104, 267], therefore may be caused by X-ray amorphous strongly basic MnO [273] present on the catalyst surface. At higher Mn loadings, the peak seems to split into a low temperature (160 °C) and high temperature (290 °C) peak, which might be ascribed to the presence of two different Mn species. The TPRs shown in Figure 4.9 A and 4.9 B reflect the actual hydrogen uptake of the catalysts prior to catalyst testing. To check for high temperature reduction signals, TPRs were also performed to 1000 °C. Figure 4.9 C shows the TPR patterns for NiAl, NiFe7 and NiMn6. For all samples, a shoulder at 580 °C is observed. This reduction signal may be attributed to $Ni^{2+}$ species that strongly interact with Al in the mixed NiAl oxide or, as discussed in Section 4.3.1.3, from $Ni^{2+}$ species incorporated in a possibly X-ray amorphous alumina type phase [137]. Resolution of the high temperature signal, also by varying the heating rate, could not be achieved.

#### 4.3.1.6 Paramagnetic/Ferromagnetic Resonance Experiments

EPR/FMR measurements on NiAl, NiFe10 and NiMn8 confirm the observations from XRD analysis (*cf.* Section 4.3.1.3). The FMR spectra (*cf.* Figures 4.11 and 4.12) are illustrated and discussed in detail in Section 4.5.6. Compared to NiAl, for NiFe10 a strong increase of the ferromagnetic characteristics could be found, which supports the assumption of Ni-Fe alloy particles after reduction. For NiMn8, the ferromagnetic characteristics were slightly reduced compared to NiAl, which might originate for the lower Ni loading as seen in Table 4.2. This is an indicator that after catalyst activation Mn species interact with the oxide phase, which is in agreement to XRD.

### 4.3.2 Tests on Catalytic Activity and Thermal Stability

#### 4.3.2.1 Activity Tests

The $CO_2$ methanation activities of all catalysts were determined following the test procedure mentioned in Table 4.1. The results are displayed in Figure 4.4. For temperatures higher than 400 °C, thermodynamic equilibrium was achieved for all catalysts. The slight increase of $CO_2$ conversion at temperatures below 220 °C is followed by a steep growth of the reaction rate. The approach to equilibrium at conversions higher than 80 % slows down, as product gas,

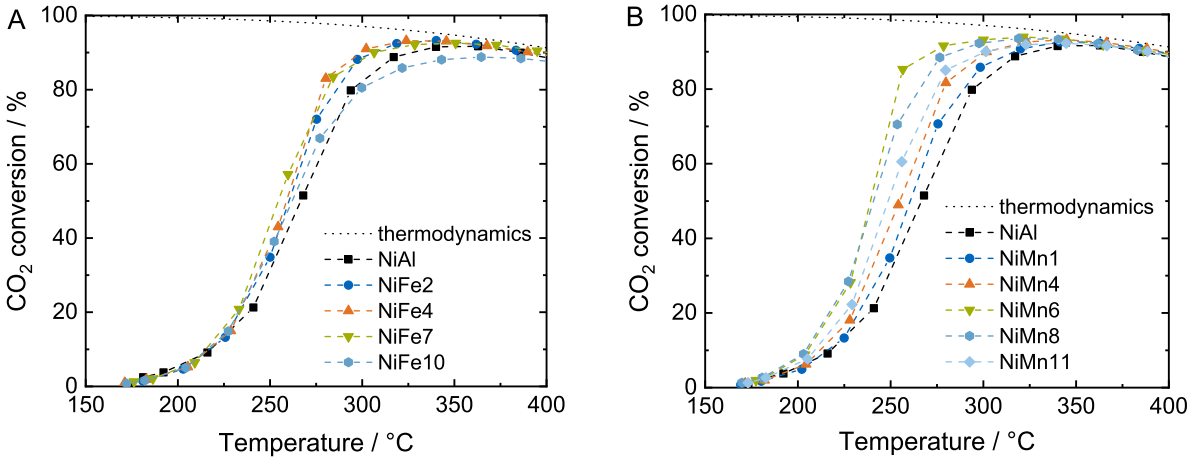


**Figure 4.4:** $CO_2$ conversion vs. reaction temperature plots: Fe-promoted catalysts (A), Mn-promoted catalysts (B). Reaction conditions: $H_2/CO_2/Ar = 4/1/5$, $Q = 150\,\mathrm{NL\,h^{-1}\,g_{cat}^{-1}}$, $m_{cat} = 25\,\mathrm{mg}$, $p = 8\,\mathrm{bar}$.

in particular $H_2O$, inhibits the conversion of $CO_2$ close to thermodynamic equilibrium [24]. Regarding the Fe-promoted catalysts (*cf.* Figure 4.4 A), no differences in their catalytic activities are recognizable for $CO_2$ conversions below 20 %. At higher temperatures, the following activity order can be determined by $T_{50}$: NiFe7 > NiFe4 > NiFe2 > NiFe10. Most noteworthy, all Fe-promoted catalysts show higher activity in the $CO_2$ methanation reaction than the benchmark NiAl catalyst. This result confirms literature findings with regard to the enhancement of the catalytic activity of NiAl methanation catalysts by Fe promotion [150, 250]. According to Tables 4.2 and 4.3, the Ni loadings and, above all, the Ni surface areas decrease with increasing promoter loading. The fact that NiFe7 with a metal surface area of $9.2\,\mathrm{m^2\,g_{cat}^{-1}}$, which is 50 % of the benchmark $NiAlO_x$ system, shows the best activity performance, indicates that the state of the active phase is changed by the introduction of Fe. It is hypothesized that Fe acts as an electronic promoter, which modifies the properties of the active Ni phase and thus increases the catalytic activity.

Similar observations have been made in CO methanation. Kustov *et al.* [153] investigated series of Ni, NiFe, and Fe catalysts supported on $Al_2O_3$ and $MgAl_2O_4$ spinel phase and found higher activity for alloyed Ni-Fe catalysts. The rate of CO dissociation and the stability of intermediates have been reported to be crucial for decent CO methanation rates [148, 155, 274]. Bligaard *et al.* [155] correlated catalyst activity in the CO methanation reaction and the energy of dissociative CO adsorption on stepped metal surfaces with DFT studies, finding that, for Fe, binding energies of C* and O* are rather high, limiting further reaction processing, while on Ni CO* dissociation is kinetically hindered. Both effects decrease the CO methanation rate. According to the Sabatier theory, the formation of a Ni-Fe alloy accelerates both rate limiting steps and thus increases the catalytic activity [148, 274]. With regard to this, Weatherbee and Bartholomew reported that CO dissociation is also the rate-limiting step in $CO_2$ methanation [194]. At approach to thermodynamic equilibrium, starting with $CO_2$ conversions higher than

50 %, the differences between the Fe-promoted catalysts in Figure 4.4 A become more significant. The slope for NiFe10 decreases in comparison to smaller Fe contents. It is supposed that already during $S_1$, apparent by the comparatively slow approach to equilibrium, catalyst deactivation takes place for NiFe10, possibly promoted by the high partial pressure of $H_2O$ at high $CO_2$ conversion values. From literature it is known that steam promotes particle-particle bridge bonding due to hydroxylation and dehydroxylation processes [275]. In particular, this has been observed for Fe/$Fe_xO_y$-containing catalyst systems [276, 277].

Pan *et al.* [128] linked the catalyst activity in the $CO_2$ methanation reaction to the density of medium basic sites. They assumed that monodentate formate originating from monodentate carbonate could be hydrogenated faster than bidentate formate from bicarbonate species [128]. As discussed in Section 4.3.1.4, NiFe7 features a similar amount of medium and lower amount of strong basic sites, but the binding strengths of $CO_2$ on the medium and strong basic sites seems to be lower compared to NiAl (*cf.* Section 4.10). Therefore, a beneficial effect of the lower binding strength of monodentate carbonate species cannot be excluded. Mn-promoted catalysts feature a much higher enhancement of the $CO_2$ conversion trends than observed for the Fe-promoted catalysts.

In Table 4.4, for the Mn-doped catalysts, the weight time yields (*WTY*) of $CH_4$ formation at $T$ = 200 °C are normalized to the metal surface areas. For NiAl, 0.46 µmol $s^{-1}$ $m_{Ni}{}^{-2}$ are obtained. This specific *WTY* stays approximately constant up to moderate Mn loadings, then rises to 0.58 µmol $s^{-1}$ $m_{Ni}{}^{-2}$ for NiMn6 and 0.84 µmol $s^{-1}$ $m_{Ni}{}^{-2}$ for NiMn8, respectively. For higher Mn loadings, it seems to be constant again. However, despite the fact that metal dispersion is known to be an important parameter in the $CO_2$ methanation reaction [278], these data need to be handled with care, since the rates were normalized to the Ni metal surface areas in Table 4.3, which are not necessarily equal to the active sites in the $CO_2$ methanation reaction, meaning that the support and the metal-support interface may play a crucial role [128, 278]. Moreover, this consideration cannot be carried out for the Fe-promoted catalysts, since, as discussed in Section 4.3.1.4, the number of surface Fe atoms could not be determined. Due to the industrial relevance of integral reactor operation for the $CO_2$ methanation reaction, in the following $T_{50}$ rather than differential conversions is used to compare the catalyst performances. As illustrated

**Table 4.4:** Nickel surface-normalized $CH_4$ weight time yields $WTY(CH_4)$ $S_{Ni}^{-1}$ at $T$ = 200 °C, $p(CO_2)$ = 0.8 bar, $H_2/CO_2$ = 4/1.

| Catalyst | $WTY(CH_4)$ $S_{Ni}^{-1}$ / µmol $s^{-1}$ $m_{Ni}{}^{-2}$ |
|---|---|
| Ni44 | 0.46 |
| NiMn1 | 0.44 |
| NiMn4 | 0.48 |
| NiMn6 | 0.58 |
| NiMn8 | 0.84 |
| NiMn11 | 0.88 |

in Figure 4.4 B, catalytic activities clearly differ over the whole temperature range depending on promoter loading. At $T_{50}$, NiMn6 is the most active catalyst, comparable to NiMn8, followed by NiMn11, NiMn4 and NiMn1. Obviously, the strong increase in catalytic activity for catalysts comprising a Mn weight fraction between 4 and 6 wt.% is followed by a decline in activity for the catalysts featuring Mn weight fractions higher than 8 wt.%.

It is suggested that the high activity increase can be directly correlated to the increased $CO_2$ uptake shown in Table 4.3, and the higher density of medium basic sites illustrated in Figure 4.3. Different mechanisms of $CO_2$ methanation have been developed in literature [169, 180, 186, 194, 279]. Both the adsorption of $CO_2$ [169] and, for the methanation pathway *via* CO dissociation [115, 194], the CO dissociation rate [194] are discussed to be rate-limiting. This indicates that promotion of the specific $CO_2$ uptake can be a simple method to successfully increase the methanation activity of the $Ni/Al_2O_3$ catalyst. Although the Ni metal surface area decreases from NiMn4 to higher Mn loadings, the activity increases with rising $CO_2$ uptake until NiMn6, from where on the Ni surface area seems to become limiting for the specific methanation rate. Therefore, it is hypothesized that there exists an optimum ratio of $H_2$ and $CO_2$ uptake. However, besides a high $CO_2$ uptake, there might also be an optimum of catalyst activity in dependence of the $CO_2$ binding energy. As seen in $CO_2$-TPD experiments, besides a higher amount of medium and strong basic sites also the binding strengths of $CO_2$ on these sites are decreased for NiMn6 compared to NiAl. The fact that $CO_2$ seems to preferentially adsorb on the Mn-modified oxide phase implies that the energy barrier for the reverse spillover of $CO_2$ to the active metal sites might be sufficiently low or that the reaction takes place on the interface of the Ni particles and the oxide phase. Consequently, it is hypothesized that for highly-loaded $NiAlO_x$ the supply of $CO_2$ at the reaction site is limiting the methanation rate. The $S_1$ curves suggest an optimum molar Ni/promoter ratio of about 5 for both Mn and Fe promotion. In this context it needs to be mentioned that also for Fe promotion an increase in $CO_2$ uptake was observed. However, the extent of increase is less severe (8 to 13 %), but could also contribute to the activity enhancement.

Figure 4.13 exemplarily illustrates the product yields for NiAl, NiFe7 and NiMn6. Besides $CH_4$ and CO, some $C_2H_6$ and $C_3H_8$ formation can be observed. For all catalysts, the selectivity towards $CH_4$ formation was higher than 99 % at temperatures between 250 and 400 °C. At higher temperatures, CO formation slightly increases, following the thermodynamic equilibrium at these temperatures [27] and reaching a maximum selectivity of 4 % at 500 °C. The low temperature CO formation at 175 to 325 °C is supposed to originate from the reverse of the water-gas shift reaction and is most pronounced for the benchmark NiAl, but the yields are below 1 % for all catalysts. Most noteworthy, no increased CO byproduct formation was observed over the Fe-promoted catalyst other than reported by Mutz *et al.* [152], whose catalyst suffered from severe deactivation when running at 20 % $CO_2$ conversion. Consequently, proved in the start-up period as illustrated in Table 4.1, for the catalysts no deactivation could be observed within 24 h at a temperature of 250 °C ($CO_2$ conversions approx. 25 %), highlighting the superior performance of the co-precipitated $NiFeAlO_x$ catalysts. $C_2H_6$ and $C_3H_8$ are only

observed in traces (selectivities < 1 %) at $CO_2$ conversions around 30 to 60 %. The benchmark NiAl catalyst features the lowest alkane formation. Further hydrocarbons, particularly Fischer-Tropsch products, were not observed, although Fe is known for its Fischer-Tropsch activity [280].

#### 4.3.2.2 Tests on Thermal Stability

Figure 4.14 illustrates the time-on-stream (TOS) behavior of the benchmark catalyst NiAl. Over 250 h on stream, the $CO_2$ conversion stays constant at 80.1 ± 0.25 %, while the selectivity towards $CH_4$ is maintained between 99.1 and 99.6 %, the only side product being CO. In Figure 4.5 A, the $S_1$ and $S_2$ measurements for the benchmark NiAl catalyst are illustrated. Due to deactivation during the applied aging period at 500 °C, the trend in $S_2$ is shifted towards higher temperatures as compared to the $S_1$ curve. Accordingly, a subsequent reduction after $S_2$ under the conditions mentioned above, as well as an oxidation and reduction treatment at 485 °C did not restore the initial activity recorded in $S_1$. The comparatively small enhancement of catalytic

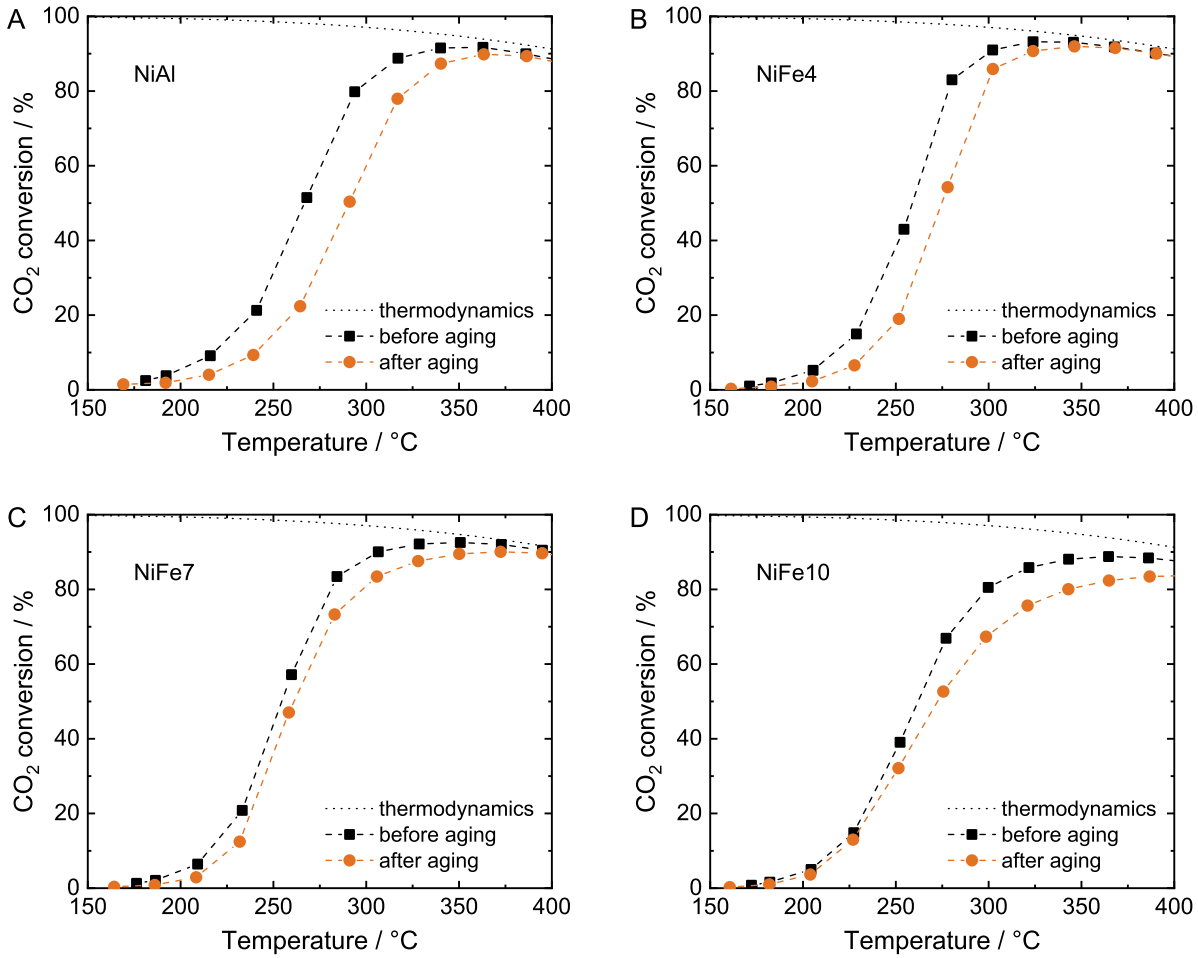


**Figure 4.5:** $CO_2$ conversion vs. reaction temperature plots: influence of aging on $CO_2$ conversion for NiAl (A), NiFe4 (B), NiFe7 (C), NiFe10 (D). Reaction conditions: $H_2/CO_2/Ar$ = 4/1/5, $Q$ = 150 NL $h^{-1}$ $g_{cat}^{-1}$, $m_{cat}$ = 25 mg, $p$ = 8 bar, aging for $t_a$ = 32 h at $T_a$ = 500 °C, $p$ = 7 bar.

activity for the Fe-doped catalysts is accompanied by a strong increase in thermal stability, which, as shown in Figure 4.5 B–D increases in the order NiAl < NiFe4 < NiFe10 < NiFe7. As already mentioned for catalyst activity, also for the thermal stability the optimum Ni/promoter molar ratio is approximately 5. It is supposed that the rising stability is strongly linked to the interactions of metallic Ni and Fe as shown in Figure 4.2 A. The shifts of the Ni-Fe reflexes indicate that within the investigated loading ranges the degree of alloy formation increases with rising Fe content. For NiFe4, no alloy formation could be proved by XRD, and its activity decay is only slightly improved compared to NiAl. In contrast, the impact of the aging treatment on NiFe7, for which *in situ* XRD analysis suggests the formation of a Ni-Fe alloy, is much lower, indicating a higher thermal stability. However, as already discussed, high Fe loadings seem to promote sintering processes. Therefore, it is consistent that NiFe10 shows stronger deactivation during the aging period, especially when evaluated at high temperatures, than NiFe7, for which the particles seem to be much more stabilized. However, it needs to be mentioned that NiFe10 maintains its low temperature activity.

Detailed investigations of possible deactivation mechanisms can be found in [134] and Chapter 7. Carbon deposition as deactivation mechanism has been excluded. In TPO experiments over NiAl, NiFe7, and NiMn6 immediately carried out after $S_2$, no CO or $CO_2$ could be detected. In a previous study, however, it was found that the partial pressure of the reaction product water has a direct influence on the deactivation kinetics, indicating that deactivation is mostly due to hydrothermal sintering [24]. In an additional study, the improvement of the thermal stability by Fe promotion was also verified under undiluted feed gas conditions. Detailed aging studies that contribute to a deeper understanding of the beneficial effect of Fe on the hydrothermal stability of the $NiAlO_x$ catalyst can be found in Chapter 7. Therein, catalyst performance data is linked to characterization data by investigating the state of the active phase for different times on stream and aging temperatures to gain information on structure-activity relationships.

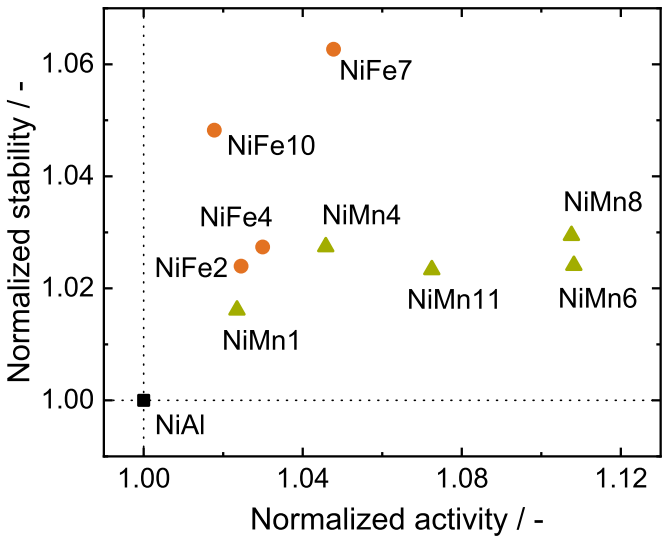


**Figure 4.6:** Normalized stability vs. normalized activity for the synthesized catalysts, determined by using the temperatures at 50 % $CO_2$ conversion.

In Figure 4.6, the activity-stability characteristics of the catalysts are compared using $T_{50}$ obtained from $S_1$ and $S_2$ and the normalization method described in Section 4.2.3. Most noteworthy, all doped catalyst samples are more active and more stable than the NiAl benchmark system. Doping Fe with a $n_{Ni}/n_{Fe}$ ratio of 5.5 increases the normalized thermal stability by 7 % and activity by 5 %. In contrast, Mn leads mainly to a higher normalized catalyst activity by 11 %, but also the normalized thermal stability is increased by 3 % as compared to the co-precipitated NiAl benchmark catalyst system.

## 4.4 Conclusion

Mn- and Fe-promoted $NiAlO_x$ catalysts with improved activity and high thermal stability, two basic requirements on catalysts for industrial application of the $CO_2$ methanation technology, were synthesized by co-precipitation. Characterization data revealed that promotion with Mn leads to an increase of the $CO_2$ adsorption capacity, while the specific Ni metal surface area, which is stabilized by a mixed metal oxide of Mn, Al, and Ni, is maintained. The combination of both effects results in an increased catalytic activity compared to the simple NiAl catalyst, with its maximum at a Ni/Mn molar ratio of around 5. It is supposed that high methanation activity for those Mn-promoted catalysts can be gained by optimally adjusting the values of $CO_2$ uptake and metal surface area. Regarding Fe-promoted catalysts, Fe increases the activity up to 5 wt.% by formation of a surface Ni-Fe alloy and a slight increase of the $CO_2$ uptake capacity. In addition, the interaction between Ni and Fe leads to a strong increase of the thermal stability, proved by an aging period of 32 h at 500 °C under hydrothermal conditions, with the optimum molar Ni/Fe ratio at approximately 5. For higher Fe loadings, the catalyst is less active at high temperatures after the aging treatment, but retains its low temperature methanation activity. Further investigations will include the combination of activity and stability improvement in one catalyst by promoting the $NiAlO_x$ system with both Fe and Mn. In addition, detailed investigations of the deactivation behavior of co-precipitated $NiAlO_x$ and Fe-promoted $NiAlO_x$ catalysts might help to further elucidate the deactivation mechanisms and phenomena.

# 4.5 Supplementary Material

## 4.5.1 X-ray Photoelectron Spectroscopy

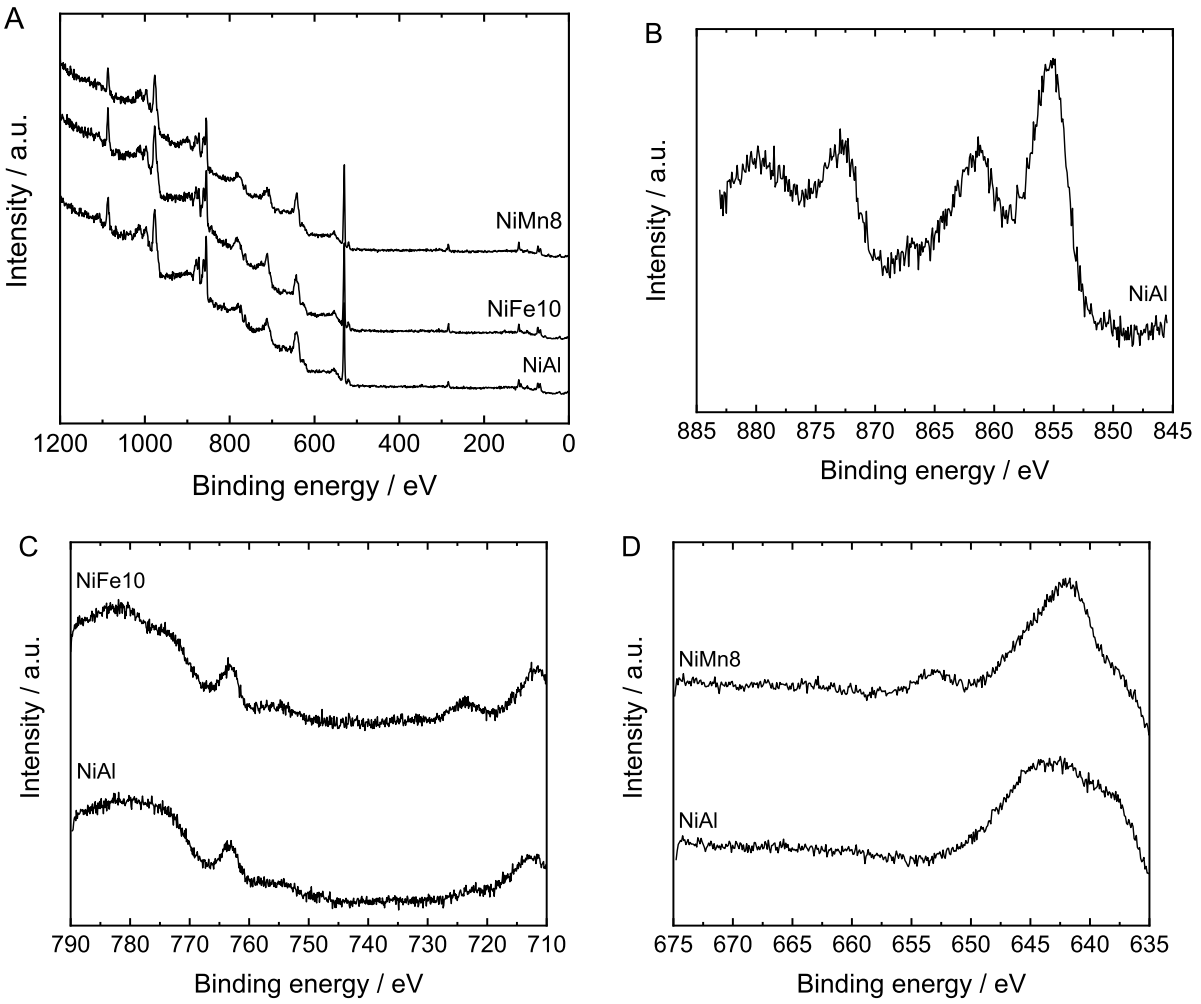


**Figure 4.7:** Selected binding energy ranges in the XPS spectra for the determination of the oxidation states of Ni, Fe, and Mn in the calcined NiAl, NiFe10, and NiMn8 catalysts.

## 4.5.2 Analytical Investigations on the Oxidation States of Fe and Mn

The oxidation state of Fe was further analyzed by leaching the catalysts in 1 M HCl (Merck, *p.a.*) and adding potassium ferricyanide. A color change to blue affirmed the presence of $Fe^{3+}$ ions [281], while the addition of potassium ferrocyanide resulted in no color change. This reveals the presence of $Fe^{3+}$ on the catalyst, which is consistent to the preparation procedure starting from $Fe(NO_3)_3 \cdot 9\,H_2O$. Regarding NiMn6, the solubility of Mn species in 1 M HCl was investigated [282]. ICP-OES measurements of samples leached in HCl revealed that the ratio of Mn in solution and the total content of Mn in NiMn6 is equal to the stoichiometric ratio of Mn(II) and Mn(IV) in $Mn_3O_4$.

### 4.5.3 X-ray Powder Diffraction Analysis

Figure 4.8 illustrates the XRD patterns for the catalyst precursors. The reflexes for the NiAl catalyst are in good agreement with the ones of the crystal structure of takovite, a mineral belonging to the hydrotalcite group that crystallizes in trigonal structure (JCPDS 15-0087). Small shifts in reflex position as well as the absence of the takovite reflexes at 39.7 and 61.2° originate from the chosen $n_{Ni}/n_{Al}$ ratio of 1 rather than 3 [24]. Also, the intensities are lower compared to catalysts featuring a $n_{Ni}/n_{Al}$ ratio of 3, suggesting a lower degree of crystallinity.

Takovite consists of $Al^{3+}$ and $Ni^{2+}$ mixed hydroxide layers, which are separated by $CO_3^{2-}$ and $H_2O$ [283]. The ratio of $n_{Ni}/n_{Al}$ in those compounds is reported variable between 1 and 5.6 [258]. Also, the anions between the layers are replaceable and not necessarily carbonate. As a function of precipitation agent and pH value, also the anions of the metal salt precursors and hydroxide might supply charge compensation, which, in turn, would also affect layer distances, lattice constants, as well as Ni particle size and Ni surface area after calcination and reduction [139, 284]. $Fe^{n+}$ or $Mn^{n+}$ ($n$ = 2, 3) as well as other cations like $Mg^{2+}$, $Cu^{2+}$, or $Zn^{2+}$ can be incorporated in the structure replacing $Ni^{2+}$ or $Al^{3+}$ without changing the characteristic hydrotalcite structure [285]. The XRD reflexes at $2\theta$ = 11.4 and 22.9° arise from X-ray diffraction on the basal (003) and (006) planes, respectively. Evaluating the mean of the reflexes of the (006) and the (003) planes for the benchmark NiAl system indicates an increase of the interlayer distance $c$ from 22.595 Å (takovite, JCPDS: 15-0087) to 23.43 Å. In contrast, the lattice constant of the brucite-like layer slightly decreases from 3.025 Å (JCPDS: 15-0087) to 2.98 Å when evaluating the (110) reflex at $2\theta$ = 62.3°. The decrease of the lattice constant $a$ may be explained by the replacement of $Ni^{2+}$ by $Al^{3+}$ compared to takovite, which results in attraction of the octahedrally coordinated $OH^-$ groups. However, the excess of positive charge in the brucite-like layers may be compensated by an increased amount of anions located in the interlayers, effectively leading to an increase of the interlayer distance. With rising weight

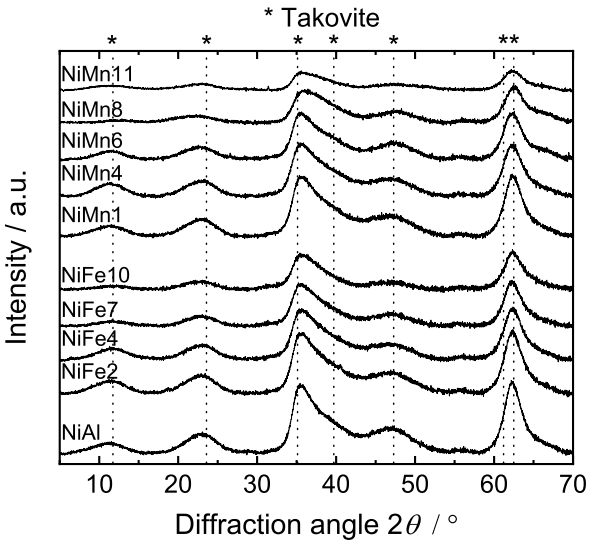


**Figure 4.8:** XRD patterns of catalysts before calcination (JCPDS: Takovite 15-0087).

fraction of the promoters, the basal reflexes vanish, indicating a decrease of the crystallinity. In addition, for high manganese loadings in NiMn8, the reflex at $2\theta = 22.9°$, marking the (006) plane, is shifted to $2\theta = 22.4°$. However, the reflex corresponding to the (003) plane is shifted to higher diffraction angles. While no clear statement on the reflex shift at $2\theta = 35.6°$ can be made, since reflexes of both (012) and (015) are superimposed, the reflex caused by diffraction on the (110) plane at $2\theta = 62.3°$ is shifted to $2\theta = 62.6°$ for NiMn8. Similar shifts can be observed for all other reflexes. This indicates that, for high Mn loadings, $Mn^{n+}$ might disturb the regular arrangement of $Ni(OH)_6^{4-}$ and $Al(OH)_6^{3-}$ octahedra, possibly by replacement of some $Ni^{2+}$ or $Al^{3+}$. In contrast, no clear influence of Fe on the hydrotalcite structure can be observed in Figure 4.8. The difference of the hydrotalcite structures prepared for $n_{Ni}/n_{Al} = 1$ and $n_{Ni}/n_{Al} = 3$ justifies the choice of a constant $n_{Ni}/n_{Al}$ ratio, taking different Ni loadings for all catalysts into account.

### 4.5.4 Temperature-Programmed Reduction

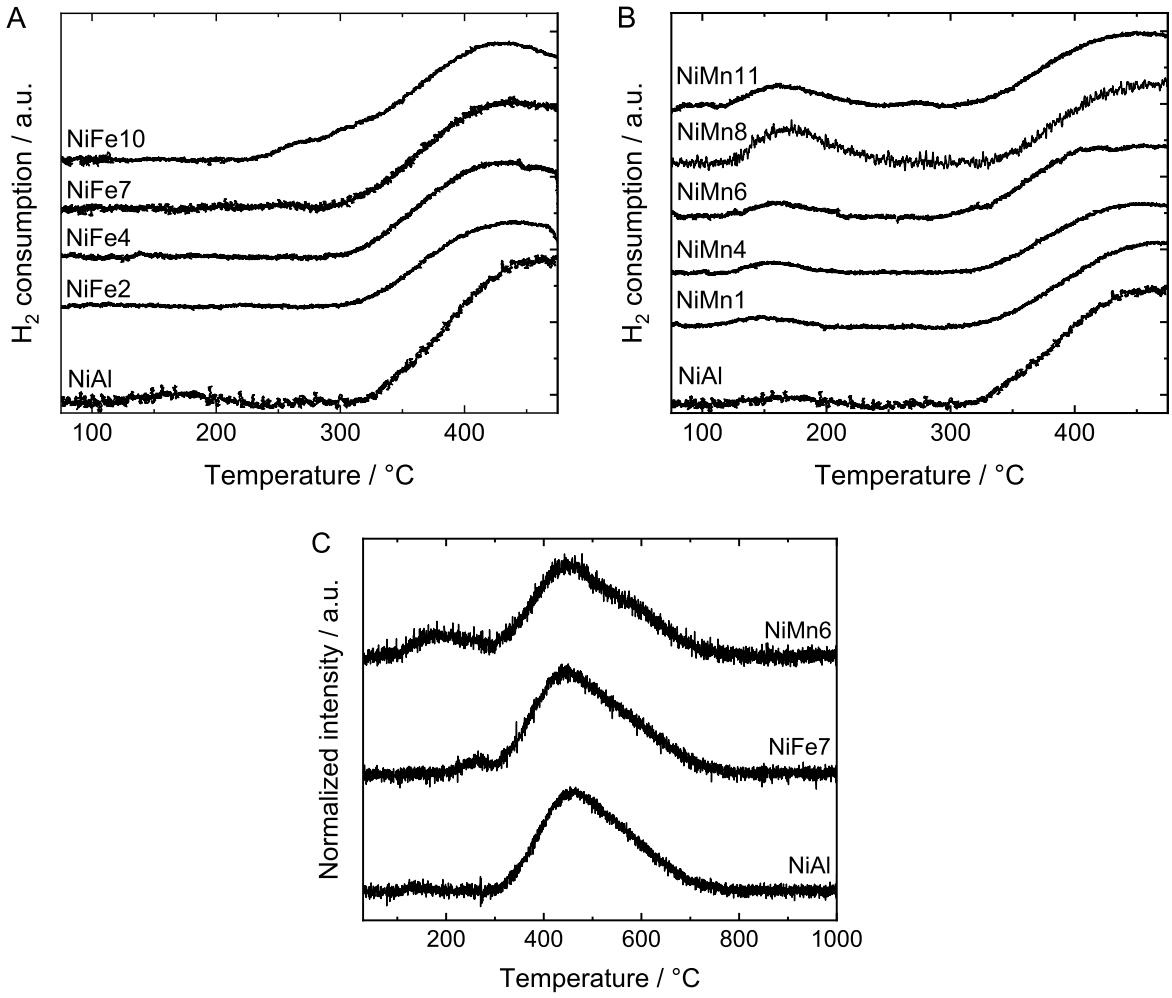


**Figure 4.9:** $H_2$ consumption during TPR measurements to 485 °C for NiAl and Fe-promoted (A), and Mn-promoted (B) catalysts, and $H_2$ consumption during TPR measurements to 1000 °C for NiAl, NiFe7, and NiMn6 (C).

### 4.5.5 Temperature-Programmed Desorption of $CO_2$

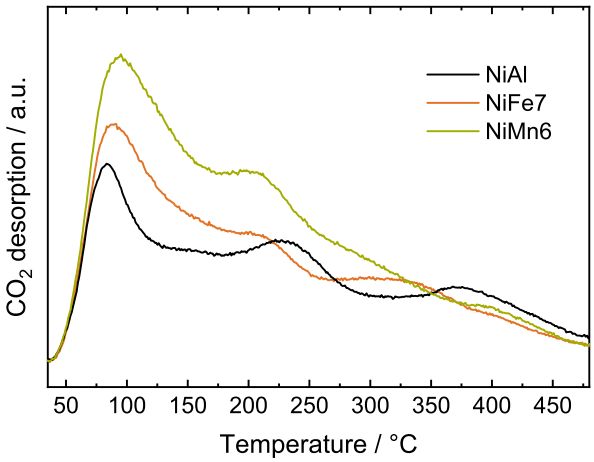


**Figure 4.10:** $CO_2$-TPD profiles of reduced NiAl, NiFe7, and NiMn6.

### 4.5.6 Magnetic Resonance Investigations

Due to the specific magnetic properties of Ni, Fe, and Mn, a magnetic resonance investigation could deliver additional information on the potential interaction or electronic properties in particular within the NiFe and NiMn catalysts in their active form. Therefore, paramagnetic/ferromagnetic resonance experiments (EPR, FMR) have been performed with the activated catalysts NiAl, NiMn8, and NiFe10 as a function of temperature (thermomagnetic investigations). The EPR/FMR spectra are given in Figure 4.11 for the three catalysts as a function of the recording temperatures. The temperature dependencies of the integrated intensity between 473 and 273 K normalized to the one of the NiFe10 catalyst at $T = 273$ K (Figure 4.12 A) show linear or concave curvatures (increasing with decreasing $T$) for all samples investigated. The absolute values of the integrated intensities of the samples of identical weight are found to be substantially different. A relation of 2:1:5 is found for NiAl:NiMn8:NiFe10. The temperature dependence of the linewidths $\Delta B_{pp}$ is given in Figure 4.12 B and the shift of the $g$ values at 293 to 273 K is found to be 2.240 $\rightarrow$ 2.245 (for NiAl), 2.046 $\rightarrow$ 2.054 (for NiFe10), and 2.198 $\rightarrow$ 2.193 (for NiMn8).

All these data imply consistently a contrary effect of both promoters on the ferromagnetic properties of the Ni nanoparticles in the benchmark NiAl catalyst. The thermomagnetic curves of the pure Ni and of the Mn-promoted catalyst qualitatively agree well with those reported for metallic Ni nanoparticles supported on (diamagnetic) oxide [286–288]. Differences in the magnetizations ($I_{rel}$, *cf.* Figure 4.12 A), $\Delta B_{pp}$, shift of $g$ values, or anisotropy of the FMR spectra are described in the literature by variations of the Ni particle size and interactions with the support or adsorbed molecules [289–291]. The slightly reduced ferromagnetic characteristics ($I_{rel}$, $\Delta B_{pp}$, $\Delta g$) of the Mn-promoted catalyst can be explained by the reduced total Ni amount in the NiMn8 catalyst or by modified Ni-oxide phase interactions in agreement with the XRD results

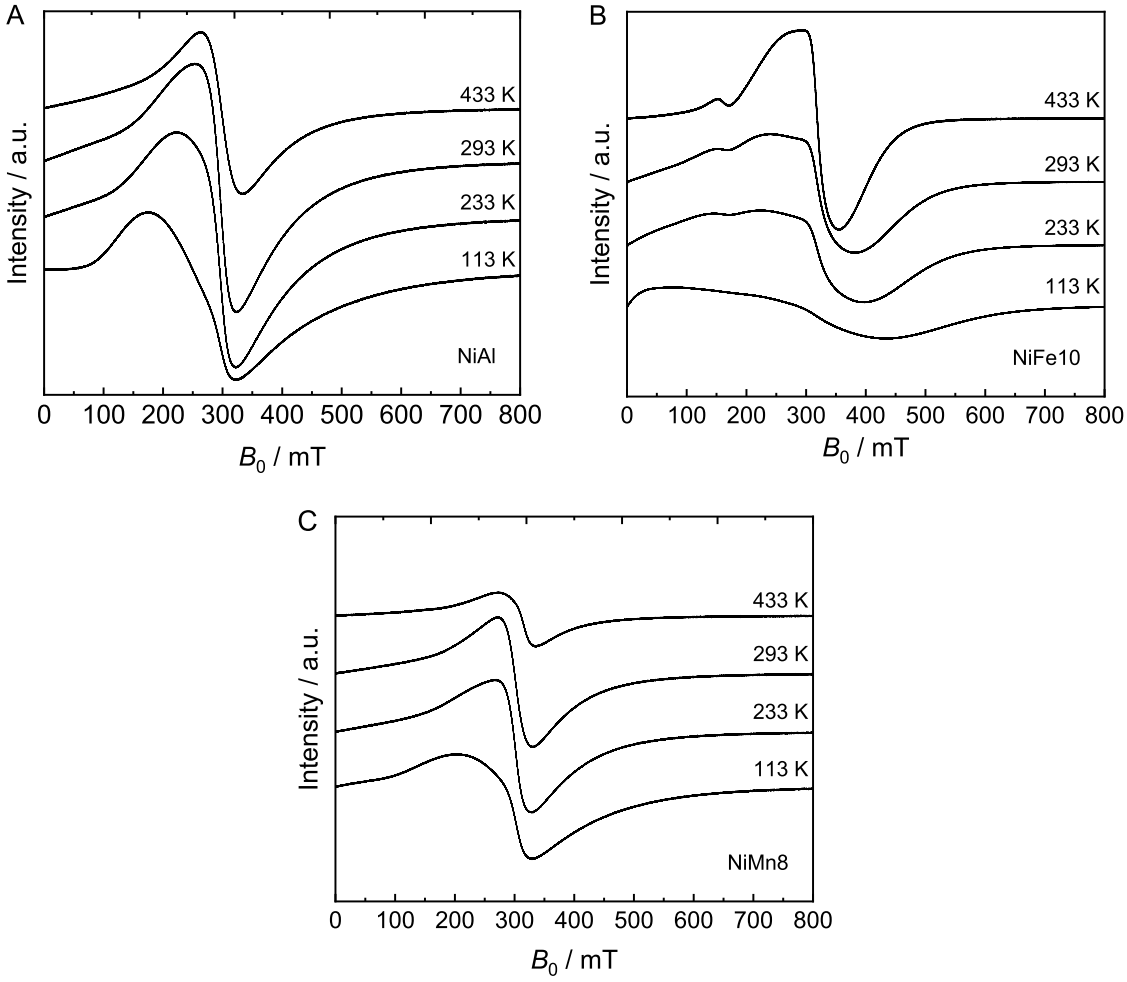


**Figure 4.11:** Ferromagnetic resonance spectra of the activated NiAl (A), NiFe10 (B), and NiMn8 (C) catalysts for different recording temperatures at X-band frequency ($\nu$ = 9.4 GHz).

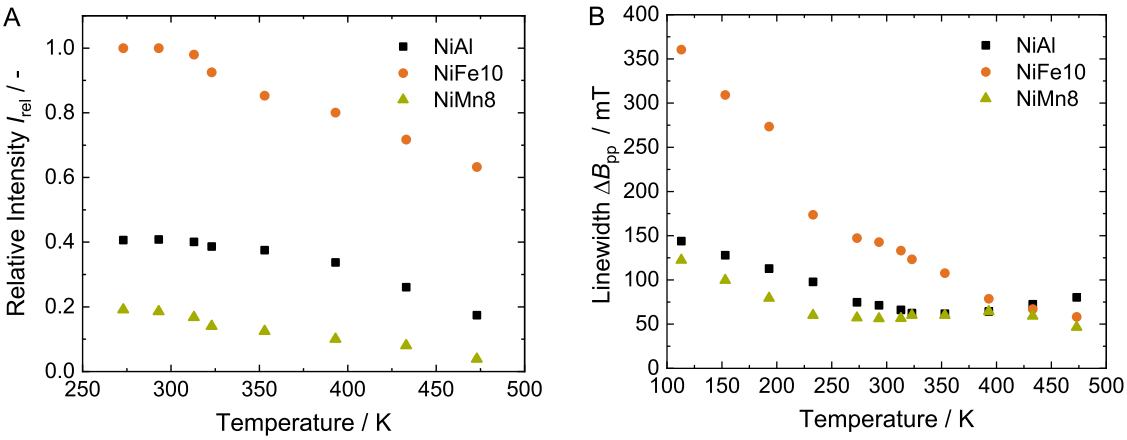


**Figure 4.12:** Temperature dependencies of the integrated intensities ('magnetizations'), normalized to $I_{rel}$ = 1 for NiFe10 at $T$ = 273 K (A), and temperature dependencies of the experimental peak-to-peak linewidths $\Delta B_{pp}$ of the FMR spectra of the activated NiAl, NiFe10, and NiMn8 catalysts (B).

in Figure 4.2 B. Alternative interpretations such as a weakening influence by antiferromagnetic MnO particles ($T_{Néel}$ = 122 K [292]) can be regarded as less probable.

In summary, it is concluded that no (or very weak) interactions and influence of Ni particles and the Mn promoter are indicated. In contrast, the drastic changes of the ferromagnetic characteristics of the NiAl catalyst by doping with Fe after activation can only be explained by a substantial ferromagnetic contribution of metallic Fe and is in very good agreement with XRD results in Figure 4.2 A and the assumption of the formation of Ni-Fe alloy particles. This is reflected by the strong increase of all relevant criteria as anisotropy of the FMR spectra and $\Delta g$, magnetization ($I_{rel}$), and $\Delta B_{pp}$ for NiFe10. Additional magnetic measurements with the calcined catalysts (before reduction) and with alumina-supported iron oxide model compounds indicate that only small, negligible ferrimagnetic proportions could be expected from iron oxide magnetism to the FMR spectra.

### 4.5.7 Yield-Temperature Plots

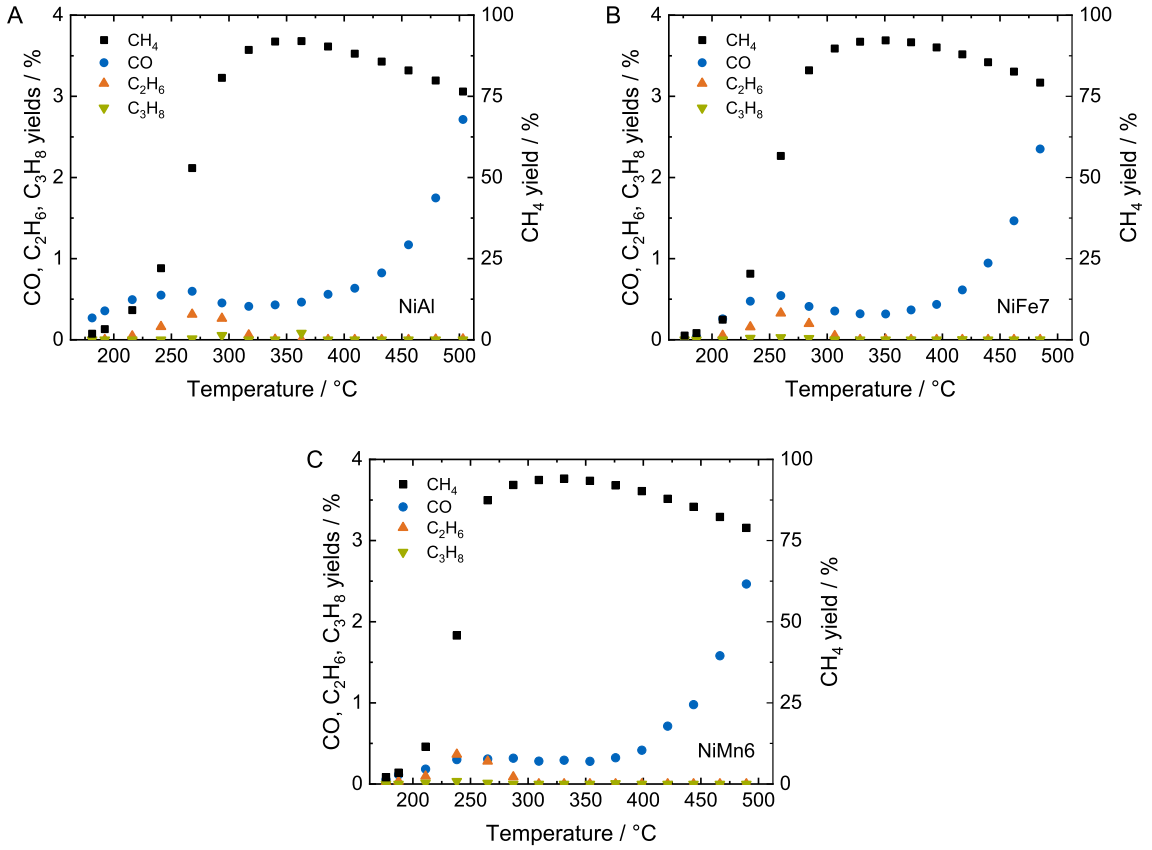


**Figure 4.13:** $CH_4$, CO, $C_2H_6$, and $C_3H_8$ yields for NiAl (A), NiFe7 (B), and NiMn6 (C).

### 4.5.8 Time-on-Stream Behavior of NiAl

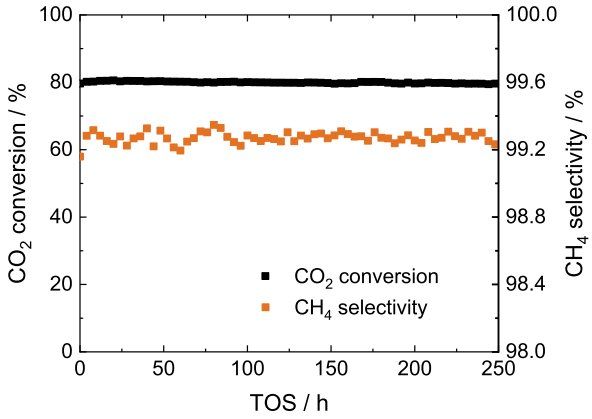


**Figure 4.14:** Time on stream behavior of NiAl. Reaction conditions: $H_2/CO_2/Ar = 4/1/5$, $Q = 150\,\mathrm{NL\,h^{-1}\,g_{cat}^{-1}}$, $m_{cat} = 25\,\mathrm{mg}$, $p = 7\,\mathrm{bar}$, $T = 300\,°\mathrm{C}$.

# 5 Simultaneous Activity and Stability Increase of Co-Precipitated Ni-Al $CO_2$ Methanation Catalysts by Synergistic Effects of Fe and Mn Promoters

This chapter was published in similar form in

T. Burger, F. Koschany, A. Wenng, O. Thomys, K. Köhler, O. Hinrichsen, "Simultaneous activity and stability increase of co-precipitated Ni-Al $CO_2$ methanation catalysts by synergistic effects of Fe an Mn promoters", *Catalysis Science & Technology*, 2018, *8*, 5920–5932, DOI 10.1039/C8CY01834K.

 Part was also published in:

K. Köhler, O. Thomys, K.-O. Hinrichsen, F. Koschany, T. Burger, "Nickel methanation catalysts doped with iron and manganese", European Patent Office, publication number WO/2018/141646, international application number PCT/EP2018/051993.[1]

Parts of this chapter include findings from [239]

T. Burger, "Experimental and theoretical investigations on the methanation reaction of $CO_2$", *not published*, Master's Thesis, Technical University of Munich, Munich, DE, **2015**.

## Abstract

For $CO_2$ methanation, the development of highly active and thermostable catalysts is indispensable to cope with the demands of SNG purity in single-pass fixed-bed operation and the exothermal character of the reaction. In this chapter, a co-precipitated $NiAlO_x$ catalyst with an equimolar Ni/Al ratio is modified by the two promoters Mn and Fe. The combination of both dopants can be used to synthesize highly thermostable catalysts with an enhanced catalytic activity. The activity-stability performance is strongly dependent on the Ni/promoter ratios, with $n_{Ni}/n_{Mn}$ = 9.5 and $n_{Ni}/n_{Fe}$ = 7 performing best. Besides doping already during

[1] The authors equally contributed to this work.

co-precipitation, it is shown that for doping *via* impregnation the activity-stability performance for a constant $n_{Ni}/n_{Fe}/n_{Mn}$ ratio can be influenced by the preparation procedure. This offers the unique opportunity to target the activity-stability behavior of a co-precipitated $NiAlO_x$ catalyst as required.

## 5.1 Introduction

The power-to-gas concept is one of the most promising techniques to contribute to coping with problems arising from depleting fossil resources, global warming, and the demand for energy storage systems. Therein, $CO_2$ is converted to synthetic natural gas (SNG) using $H_2$, which can be derived from $H_2O$ by electrolysis using surplus electrical energy from renewables [293, 294]. SNG can be handled easily and stored as well as distributed in an already existing infrastructure. Burning it on demand or converting it as platform chemical in industrial processes closes the $CO_2$-neutral cycle. The methanation reaction was first discovered by Sabatier and Senderens in 1902 [25].

$$CO_2 + 4\,H_2 \rightleftharpoons CH_4 + 2\,H_2O \quad \Delta_R H^o = -165.1\,kJ\,mol^{-1} \quad \Delta_R G^o = -113.5\,kJ\,mol^{-1} \qquad (5.I)$$

The most challenging feature of this generally heterogeneously catalyzed, volume contracting reaction is its highly exothermal character. First, it limits the equilibrium conversion of $CO_2$ at high temperatures. However, for successful implementation of the power-to-gas concept, a high SNG purity after $H_2O$ removal is desired. For this reason, the reaction is commonly carried out at harsh conditions at elevated pressures. Second, heat generation is a major issue for reaction control in fixed bed reactor systems, since hotspots can be formed [245], that may significantly harm the catalyst performance, e.g. by particle sintering [247, 295]. Consequently, for potential commercialization, two of the major demands on the catalyst evolve, which are catalytic activity to obtain high conversions at low temperatures and to decrease the necessary operating pressure, as well as thermal stability of the catalyst to increase catalyst life-time.

For Ni-based catalysts, a number of different promoters have been claimed to increase the specific surface area of the catalyst, e.g. Mn [71, 99, 104], Fe [150, 151, 250], Ce [71, 91], La [71, 99, 296], and $ZrO_2$ [71]. The promoters Fe [149, 253], Mn [94], and Ce [91] were reported to alleviate the reducibility of the active nickel phase. Ce promoted both activity and stability of the methanation catalyst [71]. Zhao *et al.* investigated the impact of Mn on impregnated $Ni/Al_2O_3$ catalysts and found that the addition of Mn has an influence on the type of NiO species [94]. Recently, Zhao *et al.* linked the improved activity observed for Mn-doped $Ni/Al_2O_3$ catalysts to the increase of the number of medium basic sites necessary to activate $CO_2$ [104]. Hwang *et al.* [150] for the first time used the co-precipitation method to add Fe and investigated the influence of different precipitation agents on the performance of Ni-Fe-$Al_2O_3$ catalysts. Despite the known activity of Fe in the Fischer-Tropsch reaction [280], $CH_4$

selectivities higher than 99.4 % at 220 °C and 10 bar ($CO_2$ conversion about 50 %) were found for all catalysts. However, with 9.6 NL $g_{cat}^{-1}$ $h^{-1}$, the feed rate was chosen very low. Furthermore, other studies are limited to the (incipient) wetness impregnation technique, which results in maximum Ni loadings of around 20 wt.%, and often do not include detailed information on catalyst performance after aging, or conclusions on catalyst stability are affected by measuring gas compositions under thermodynamic equilibrium conditions.

It is widely known that metal doping can greatly modify the textural and electronic properties of catalysts [297], which can be used to design catalysts with specific characteristics depending on the requirements. In Chapter 4, the effect of doping Mn to a $NiAlO_x$ catalyst ($n_{Ni}/n_{Al}$ = 1) onto the catalytic activity using the co-precipitation technique was shown. In addition, Fe was brought up as a promoter to significantly increase the thermal stability of the $NiAlO_x$ system, and both single effects were linked to detailed characterization data. Catalyst testing had been carried out at a pressure of 8 bar in the temperature range from 175 to 500 °C using stoichiometric feed gas composition at 150 NL $g_{cat}^{-1}$ $h^{-1}$, and included activity validation after an aging treatment under harsh, hydrothermal conditions (7 bar, 500 °C, 32 h, $p(H_2O)$ = 1.6 bar).

In this chapter, in contrast, it is investigated how the simultaneous doping of Mn and Fe during co-precipitation influences the catalytic performance of an equimolar $NiAlO_x$ catalyst to introduce a new generation of catalysts featuring significantly improved activity and thermal stability that may meet the requirements for commercialization of the $CO_2$ methanation process. Increased chances of independent promoter effects of Fe and Mn in bi-doped $NiAlO_x$ catalysts are thereby given by differences in the nature of their working mechanisms proposed in Chapter 4 (Fe interacting with the metallic Ni particles and Mn with the oxidic phase). In addition, in contrast to promotion already during co-precipitation, a co-precipitated calcined $NiAlO_x$ catalyst, which is known to feature improved catalytic activity and stability compared to its $Ni/Al_2O_3$ counterpart [133, 147, 203], is subsequently impregnated with $Fe(NO_3)_3$ and $Mn(NO_3)_2$. Despite the additional effort in catalyst synthesis, this approach may help to control the location of the promoters. Variation of the impregnation order may provide some insights into the importance of phase and promoter distribution on the surface of bi-doped $NiAlO_x$ catalysts. Investigating the interactions of the two promoters may further elucidate their mode of operation.

## 5.2 Experimental

### 5.2.1 Catalyst Synthesis

The catalysts were prepared by co-precipitation at a constant pH of 9 and 30 °C. 1 M solutions of $Ni(NO_3)_2 \cdot 6H_2O$ (Merck), $Al(NO_3)_3 \cdot 9H_2O$ (Merck), $Fe(NO_3)_3 \cdot 9H_2O$ (Sigma-Aldrich), and $Mn(NO_3)_2 \cdot 4H_2O$ (Merck) were mixed to a total volume of 120 mL. The molar ratios were 1 for Ni/Al, 9.5, 7, and 5.5 for Ni/Fe, and 29.5, 9.5, and 5.5 for Ni/Mn, respectively. The purity of

all chemicals was pro analysis (*p.a.*). Co-precipitation was carried out in a double-walled stirred tank reactor with an overall volume of 3 L equipped with a KPG stirrer and two flow breakers. For pH adjustment before and pH maintenance during co-precipitation, an equimolar mixture of 1 M $Na_2CO_3$ (Sigma-Aldrich, *p.a.*) and NaOH (Merck, *p.a.*) was automatically added using a 1 A (Schott) titrator. 1 L of bi-distilled water was adjusted to pH 9 and heated to 30 °C. The nitrate salt solution was added with a volume flow of 2.3 mL $min^{-1}$ using a peristaltic pump (Metrohm). In the following, the slurry was aged at pH 9 and 30 °C for a duration of 18 h. After filtration, the filter cake was deeply washed to remove $Na^+$ and $NO_3^-$ residues until a pH of 7 had been reached, before the precipitate was dried in air at 80 °C for 18 h. Calcination was carried out by heating up in flowing synthetic air with a linear heating rate of 5 K $min^{-1}$ and holding at 450 °C.

After calcination, a Ni-Al catalyst was modified by incipient wetness impregnation. 1 g of the calcined catalyst was ground under dropwise addition of 1 mL of solutions of $Fe(NO_3)_3 \cdot 9\,H_2O$ (Sigma-Aldrich, *p.a.*), $Mn(NO_3)_2 \cdot 4\,H_2O$ (Merck, *p.a.*), or both metal salts. The metal concentrations in these solutions had been adjusted to meet ratios of $n_{Ni}/n_{Mn}$ = 9 and $n_{Ni}/n_{Fe}$ = 6.5, respectively, in the final catalysts. The as-synthesized catalyst precursors were dried in air at 80 °C for 18 h, before the single metal impregnated catalysts underwent a subsequent impregnation step with the other metal salt solution, followed by further drying under the conditions described above. All impregnated catalysts were calcined again following the procedure described above.

The promoted NiAl catalysts are denoted as "NiP*X*", where P indicates the promoter and *X* its weight fraction in percent. The catalysts used for or modified by impregnation are denoted with index $_i$ and the impregnation order is indicated by $_{(I)}$ or $_{(II)}$. All catalysts were shaped to pellets of 1 cm diameter using a Lightpath LP-15 hydraulic laboratory press (pressure 450 N $cm^{-2}$). The pellets were ground and sieved to obtain the particle fraction of 150 to 200 µm, which was used for all further analyses.

## 5.2.2 Catalyst Characterization

The materials were characterized by static $H_2$ and $CO_2$ chemisorption, $N_2$ physisorption, *in situ* X-ray powder diffraction (XRD) analysis, temperature-programmed reduction (TPR), temperature-programmed desorption of $CO_2$ ($CO_2$-TPD), and inductively coupled plasma-optical emission spectroscopy (ICP-OES).

### 5.2.2.1 Elemental Analysis

For the investigation of the composition of the calcined catalysts, elemental analysis was carried out by ICP-OES on an Agilent 700. Approximately 50 mg of catalyst powder were suspended in 1 M $H_3PO_4$ (VWR, *p.a.*). 50 mg $Na_2SO_3$ (SigmaAldrich, *p.a.*) were added to reduce insoluble $MnO_2$ formed in acidic media. The suspensions were sonicated for 4 h at 60 °C, filled to an

overall volume of 50 mL, diluted with bi-distilled water in a ratio of 1 to 10 and filtered using 0.45 µm syringe filters (Pall). Calibration standards were prepared for 1, 10, and 50 mg $L^{-1}$ of metal ion concentrations using a 1000 mg $L^{-1}$ ICP multi-element standard (standard IV, Merck). Phosphate matrix effects were excluded. ICP data was averaged over five measurements. The wavelengths tracked for data processing were 230.299 nm (Ni), 396.152 nm (Al), 238.204 nm (Fe), and 257.610 nm (Mn). Metal signal superimpositions were excluded. In reference experiments without adding $Na_2SO_3$, also the Na (568.263 nm) content of the catalyst samples was checked to exclude Na poisoning of the catalysts.

#### 5.2.2.2 X-ray Powder Diffraction

For *in situ* XRD studies, the calcined catalyst powders were heated in 5 % $H_2$ in Ar to 480 °C with a linear heating rate of 2 K $min^{-1}$ and held there for 8 h. Two XRD patterns were recorded with 0.017° per step and 50 steps per min, one at room temperature under the specified $H_2$ flow before initiating the heating procedure and one at 480 °C after the reduction had been completed. Crystallite sizes $d_C$ were calculated using the Scherrer equation (*cf.* Eq. 3.4).

#### 5.2.2.3 Temperature-Programmed Reduction

Temperature-programmed reduction (TPR) studies were carried out on a ChemStar TPx (Quantachrome). The calcined catalyst was heated to 850 °C in 10 % $H_2$ in He with a total flow of 50 mL $min^{-1}$ and a linear heating rate of 5 K $min^{-1}$. Catalyst masses were chosen to obtain $P$ values of about 6 K [218]. $H_2$ consumption was tracked using a thermal conductivity detector (TCD). Evolving $H_2O$, $CO_2$, and $CH_4$ were removed from the gas stream by a liquid $N_2$ trap upstream the TCD. The TCD signals were smoothed applying the Lowess method with a span of 0.1.

#### 5.2.2.4 $H_2$ and $CO_2$ Chemisorption

$H_2$ and $CO_2$ chemisorption experiments were performed using an Autosorb 1 C (Quantachrome). Approximately 100 mg of calcined catalyst were heated up in 5 % $H_2$ in Ar to 500 °C with a linear heating rate of 2 K $min^{-1}$ and held there for 5 h. Afterwards, the sample cell was evacuated for 1 h, cooled down in vacuum and evacuated for another 15 min. The adsorption isotherm was recorded from 40 to 800 Torr at a temperature of 35 °C. Sorption equilibration time was 2 min for $H_2$ and 10 min for $CO_2$. The adsorbed gas volume was calculated *via* the extrapolation method. For Ni, a dissociative mechanism with one H atom adsorbing per Ni atom was applied [252]. Fe is known to not adsorb $H_2$ under the chosen conditions [253, 254], which means that the metal surface area can be set equal to the Ni surface area. $H_2$ adsorption at a recommended temperature of 200 °C [255], however, resulted in $H_2$ spill-over onto the Al-containing oxide material. Prior to $CO_2$ chemisorption experiments, it was proved that the adsorption of $CO_2$ is not kinetically hindered under the chosen conditions.

#### 5.2.2.5 $N_2$ Physisorption

The specific surface areas of the catalysts were determined by $N_2$ physisorption according to the BET method on a Quantachrome NOVAtouch. Adsorption and desorption isotherms of the reduced catalysts (procedure *cf.* Section 5.2.2.4) were recorded in the $p/p_0$ range from 0.007 to 0.995. For determination of the BET surface area, the $p/p_0$ range from 0.05 to 0.3 was used. The total pore volume $V_{Pore}$ was calculated based on the $N_2$ uptake at $p/p_0 = 0.995$. The mean pore radius $r_{Pore}$ was calculated on the assumption of cylindrical pores based on the total pore volume and the specific BET surface area (*cf.* Eq. 3.8).

#### 5.2.2.6 Temperature-Programmed Desorption of $CO_2$

Temperature-programmed desorption of $CO_2$ ($CO_2$-TPD) was carried out in a setup described elsewhere [141]. 50 mg of catalyst were reduced *in situ* in 5 % $H_2$ in He at 480 °C for 8 h (heating rate 2 K min$^{-1}$) and purged with He for 1 h. After cooling down to 35 °C, $CO_2$ was adsorbed for 30 min with a flow rate of 50 mL min$^{-1}$. The catalyst was flushed with He for 30 min to remove weakly adsorbed $CO_2$ species. During the TPD, the catalyst was heated in He (100 mL min$^{-1}$) from 35 to 480 °C with a heating rate of 6 K min$^{-1}$. The $CO_2$ and CO signals were tracked by a mass spectrometer (Pfeiffer Vacuum, OmniStar). Signal fitting was omitted due to unknown desorption kinetics.

### 5.2.3 Experimental Setup and Activity Measurements

25 mg of catalyst with a particle size from 150 to 200 µm were diluted with purified SiC (ESK) in a mass ratio of 1 to 9 and placed in the isothermal zone of a glass-lined tube reactor with an inner diameter of 4 mm. The axial position of the bed was fixed by two quartz wool plugs with a length of 4 mm each. A thermocouple was placed at the end of the catalyst bed to track the reaction temperature. The setup described in [24] and Section 3.3 was used for catalyst testing. Gases were supplied by Westfalen with a purity of 5.0. The product gas exiting the pressure regulators was diluted with Ar in a ratio of 1 to 8. In addition, all tubing was heated to prevent water condensation. All catalysts were treated following the procedure applying the process parameters listed in Table 5.1.

After reduction at ambient pressure and a start-up period for 24 h at 250 °C and 7 bar, $CO_2$ conversion was determined stepwise every 25 K in the temperature range between 175 to 500 °C at 8 bar, denoted as $S_1$. This treatment was followed by an aging period at 500 °C for 32 h to simulate deactivation in hotspot conditions occurring in industrial fixed bed reactors. In a second temperature variation cycle $S_2$ the temperature-conversion characteristics were recorded again to resolve data away from thermodynamic equilibrium, indicating the thermal stability of the catalyst. Beforehand, heat and mass transfer limitations under the chosen conditions in the kinetic regime away from thermodynamic equilibrium conditions had been excluded.

**Table 5.1:** Variation of process parameters for the determination of catalyst activity and thermal stability.

| | Feed $H_2/CO_2/Ar$ | $Q$ / NL $g_{cat}^{-1}$ $h^{-1}$ | $T$ / °C | $p$ / bar | $t$ / h |
|---|---|---|---|---|---|
| Activation | 5/0/95 | 130 | 485 | 1 | 8 |
| Start-up | 4/1/5 | 150 | 260 | 7 | 24 |
| $S_1$ | 4/1/5 | 150 | 175–500 | 8 | 11 |
| Aging | 4/1/5 | 150 | 500 | 7 | 32 |
| $S_2$ | 4/1/5 | 150 | 175–500 | 8 | 11 |

The gas concentrations of $CO_2$, $CH_4$, CO, $H_2$, and $H_2O$ were tracked using an online Emerson MTL-4 process gas analyzer (PGA). Parameters were kept constant for 45 min while online tracking to ensure steady-state conditions. For data evaluation, 150 data points were averaged over 150 s. A PerkinElmer gas chromatograph Clarus 500 equipped with two columns and FID detectors was used for byproduct analysis. Data reliability was confirmed by closed molar C, H, and O balances (±3 %). Conversion, yields and selectivities were calculated the taking volume contraction into account (*cf.* Eq. 3.15). For reasons of comparison, the temperature necessary for obtaining 50 % $CO_2$ conversion in $S_1$ was interpolated, marked as $T_{50,S_1}$. By normalizing it to $T_{50,S_1}$ (NiAl), this may serve as a measure for the relative catalyst activity. Similarly, the ratios of $T_{50,S_2}$ and $T_{50,S_1}$ describe the relative stabilities of the catalysts.

$$\text{Normalized activity} = \frac{T_{50,S_1}(\text{NiAl})}{T_{50,S_1}(\text{doped cat.})} \tag{5.1}$$

$$\text{Normalized stability} = \frac{\frac{T_{50,S_2}(\text{NiAl})}{T_{50,S_1}(\text{NiAl})}}{\frac{T_{50,S_2}(\text{doped cat.})}{T_{50,S_1}(\text{doped cat.})}} \tag{5.2}$$

Thermodynamic equilibrium data for $CO_2$, $CH_4$, CO, $H_2$, and $H_2O$ were calculated using the $\Delta G$ minimization method (*cf.* Appendix C). Enthalpy and entropy values were calculated by the Shomate equation (*cf.* Appendix B).

## 5.3 Results and Discussion

In this study, the simultaneous effects of Fe and Mn promotion of a co-precipitated $NiAlO_x$ catalyst on catalyst performance in the methanation reaction of $CO_2$ are investigated. Instead of keeping the Ni content in all catalysts constant, the $n_{Ni}/n_{Al}$ ratio is set constant to 1, since the structures of the precipitate and the oxide after calcination are known to strongly depend on the $n_{Ni}/n_{Al}$ ratio [24, 139, 258]. In addition to adding the dopants already during co-precipitation and optimizing the promoter loadings, in a further sub-study the promoters are added on the benchmark $NiAlO_x$ by incipient wetness impregnation. Despite the obvious additional effort in

catalyst synthesis, this technique may help to control the location of the dopants and contribute to gain additional information on structure-activity relationships in these bi-doped $NiAlO_x$ catalysts.

## 5.3.1 Material Characterization

### 5.3.1.1 Elemental Analysis

The metal loadings and molar metal ratios obtained from ICP-OES are shown in Table 5.2. In concordance with Chapter 4, high Mn loadings seem to have a repressive effect on the Ni content of the material, which suggests a competitive incorporation of Ni and Mn into the precipitate. In contrast, Ni loading is only slightly influenced by adding Fe. The high Ni loadings of the impregnated samples are artifacts of the second calcination step. It is known that co-precipitated Ni-Al precursors contain high amounts of $H_2O$, $OH^-$, and $CO_3^{2-}$, that might not be completely removed after calcination at 450 °C [24, 298]. Therefore, their content might be decreased by the second calcination step.

**Table 5.2:** Mass fractions and molar metal ratios obtained from ICP-OES.

| | Mass fraction after calcination / wt.% | | | | Molar ratios / - | | |
|---|---|---|---|---|---|---|---|
| Sample | Ni | Al | Fe | Mn | $n_{Ni}/n_{Al}$ | $n_{Ni}/n_{Fe}$ | $n_{Ni}/n_{Mn}$ |
| *Co-precipitated catalysts* | | | | | | | |
| Ni44 | 44.3 | 19.8 | - | - | 1.03 | - | - |
| NiFe4Mn1 | 39.5 | 17.7 | 3.9 | 1.3 | 1.03 | 9.7 | 28.9 |
| NiFe4Mn4 | 39.9 | 17.8 | 4.0 | 4.2 | 1.03 | 9.5 | 9.0 |
| NiFe3Mn6 | 35.6 | 16.0 | 3.4 | 6.0 | 1.02 | 10.0 | 5.6 |
| NiFe5Mn1 | 38.7 | 17.4 | 5.3 | 1.2 | 1.02 | 6.9 | 29.5 |
| NiFe5Mn4 | 38.1 | 17.3 | 5.3 | 3.8 | 1.01 | 6.8 | 9.4 |
| NiFe5Mn6 | 36.3 | 16.6 | 4.8 | 6.1 | 1.01 | 7.2 | 5.5 |
| NiFe7Mn1 | 37.2 | 16.0 | 6.5 | 1.3 | 1.07 | 5.4 | 26.5 |
| NiFe6Mn4 | 36.9 | 18.2 | 6.2 | 3.5 | 0.93 | 5.6 | 9.8 |
| NiFe6Mn6 | 34.1 | 16.8 | 5.9 | 5.8 | 0.93 | 5.5 | 5.5 |
| *Co-precipitated + impregnated catalysts* | | | | | | | |
| $Ni45_i$ | 45.4 | 19.1 | - | - | 1.09 | - | - |
| $Ni58_i$ | 58.5 | 25.6 | - | - | 1.05 | - | - |
| $NiFe7_i$ | 48.4 | 20.7 | 7.1 | - | 1.08 | 6.5 | - |
| $NiMn6_i$ | 50.2 | 21.4 | - | 5.6 | 1.08 | - | 8.4 |
| $NiFe7Mn5_i$ | 43.8 | 18.7 | 6.5 | 4.6 | 1.08 | 6.4 | 9.0 |
| $NiFe6_{(I)}Mn5_{(II)i}$ | 40.0 | 16.9 | 6.1 | 4.3 | 1.09 | 6.2 | 8.7 |
| $NiFe6_{(II)}Mn4_{(I)i}$ | 44.3 | 18.7 | 7.0 | 4.9 | 1.09 | 6.0 | 8.5 |

### 5.3.1.2 X-ray Powder Diffraction Analysis

The XRD patterns of the co-precipitated catalyst precursors are compared in Figure 5.1. For all samples, distinct reflexes appear at $2\theta$ = 35.6, 47.7, 62.4, and 73.8°. In addition, the benchmark

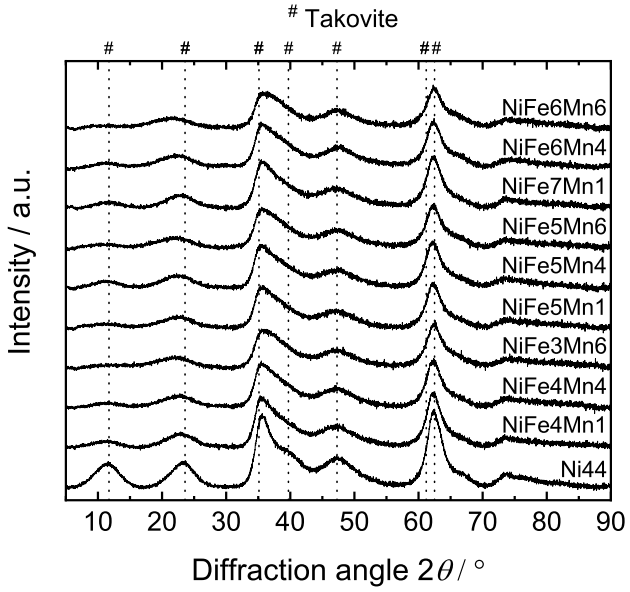


**Figure 5.1:** XRD patterns of the co-precipitated catalysts before calcination (JCPDS reference: takovite 15-0087).

Ni44 catalyst precursor causes reflexes at $2\theta$ = 11.6, 23.3, 39.7, and 67.0°, which lose in intensity for the promoted catalysts, indicating a lower degree of crystallinity. The positions of the reflexes suggest the evolution of a layered double hydroxide (LDH) phase, similar to takovite, a natural hydrotalcite with a $n_{Ni}/n_{Al}$ ratio of 3. LDHs consist of brucite-like hydroxide layers with the cations being inserted in the octahedral gaps. Charge compensation arising from the exchange of $Ni^{2+}$ with $Al^{3+}$ is supplied by $CO_3{}^{2-}$ anions located in the interlayers. In addition, the interlayers contain loosely bound $H_2O$ molecules, which prevent inter-anion repulsion. The common formula for such precipitates is $[Ni_{1-x}Al_x(OH)_2][(CO_3)_{0.5x}{\cdot}nH_2O]$ [299]. The reflexes at $2\theta$ = 11.6, 23.4, and 34.4° mark the reflexes of the basal (003), (006), and (009) planes, which, for Ni44, are in good agreement with takovite (JCPDS: 15-0087). Therefore, it is concluded that the interlayer distances hardly depend on the replacement of some $Ni^{2+}$ by $Al^{3+}$ from 3/1 to 1/1 $n_{Ni}/n_{Al}$ stoichiometry. Contraction due to stronger attraction caused by electrostatic forces might be compensated by space requirements for additional $CO_3{}^{2-}$ for charge compensation. However, the reflex intensity compared to takovite is much smaller, possibly caused by a lower degree of crystallinity. The diffraction angles of the (003) and (006) planes are proportional, which indicates that the ordered basal structure is still maintained. In addition, while constant for all other reflexes, the reflex at 23.3° caused by the basal (006) plane is shifted to lower diffraction angles, especially for NiFe3Mn6, NiFe6Mn4, NiFe6Mn6, NiFe5Mn4, and NiFe5Mn6, being more sensitive to Mn loading than to Fe loading. This is consistent with results reported for Mn-single-doped and Fe-single-doped catalyst systems in Chapter 4, where for Mn loadings higher than 6 wt.% a shift of the basal reflexes to lower diffraction angles could be observed. The reflex shifts in Figure 5.1 seem to correlate with the amount of dopant added. Assuming that $Fe^{3+}$ and $Mn^{n+}$ ($n$ = 2, 3) are preferentially placed in the octahedral gaps of brucite layers, this might indicate that, once a maximum replacement in the brucite layers is reached, Mn might

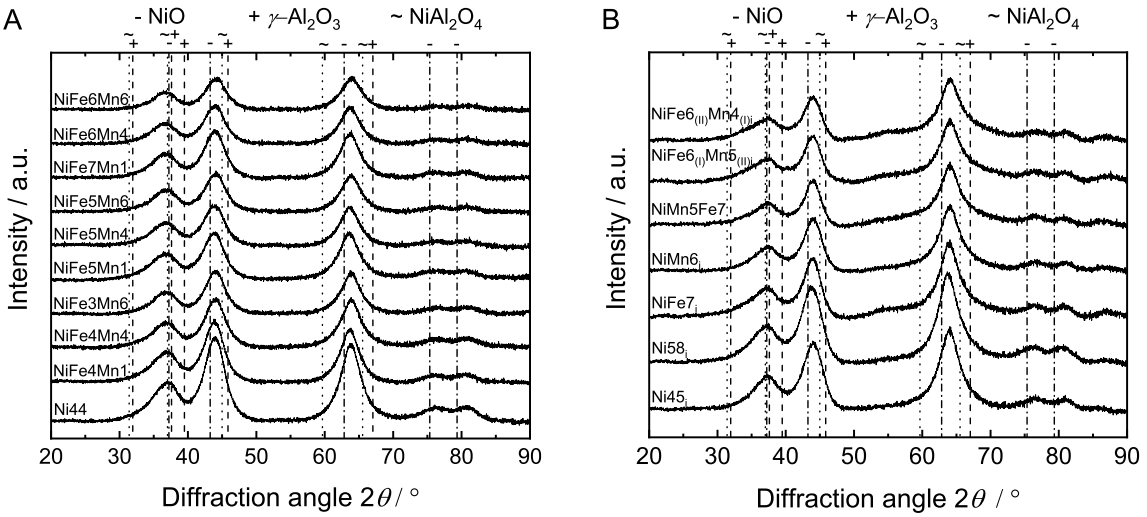


**Figure 5.2:** XRD patterns of the co-precipitated (A) and impregnated (B) calcined catalysts (JCPDS references: NiO 78-0429, $\gamma$-$Al_2O_3$ 10-0425, $NiAl_2O_4$ 10-0339).

be incorporated in the interlayer, leading to an increase of the interlayer distance *c*.

After calcination (*cf.* Figure 5.2), the diffraction reflexes appear between NiO and $\gamma$-$Al_2O_3$ ($2\theta$ = 37.1, 44.0, 63.8, 76.3, and 80.8°), suggesting the formation of a $NiAlO_x$ mixed oxide. Such metastable mixed oxide structures are discussed to originate from low-temperature calcination of Ni-Al hydrotalcites [258, 263]. The reflexes are supposed to originate from crystalline NiO containing $Al^{3+}$ ions, leading to lattice distortion. Besides, Alzamora *et al.* suggested that in addition to the NiO phase an amorphous alumina phase is formed, which, on the contrary, might contain $Ni^{2+}$ ions [139]. Most noteworthy, no bulk $NiAl_2O_4$ spinel phase can be detected by XRD.

For the co-precipitated samples in Figure 5.2 A, the reflex intensities decrease with increasing promoter loading, resulting from lower NiO loading (*cf.* Table 5.2) or reduced crystallinity. While, upon promotion, no additional reflexes evolve, systematic shifts in reflex positions of the modified NiO structure to lower diffraction angles with increasing Fe weight fraction can be observed. This is in contrast to single metal doping (*cf.* Chapter 4). However, for samples with high Fe and Mn loadings, especially for NiFe6Mn6, the reflexes at $2\theta$ = 44.0 and 63.8° return to their original positions. This indicates that a competitive insertion of Mn and Fe into the modified NiO structure takes place, where insertion of Fe leads to an additional lattice expansion, whilst the preferentially incorporated Mn does not seem to lead to any additional lattice distortion. The shift of the reflex at $2\theta$ = 37.1° for catalysts containing high Fe loadings (NiFe6Mn6, NiFe6Mn4, and NiFe7Mn1) therefore might indicate the evolution of an additional $Fe_2O_3$ phase. Figure 5.2 B illustrates the XRD patterns of the catalysts prepared by impregnation and the benchmark systems, respectively. For the benchmark $Ni58_i$, the diffraction reflexes of the Al-containing NiO phase are shifted to smaller diffraction angles, indicating a decrease of the amount of $Al^{3+}$ being incorporated in the crystalline NiO phase and possibly a higher amount of amorphous alumina. This trend might be caused by the repeated calcination step.

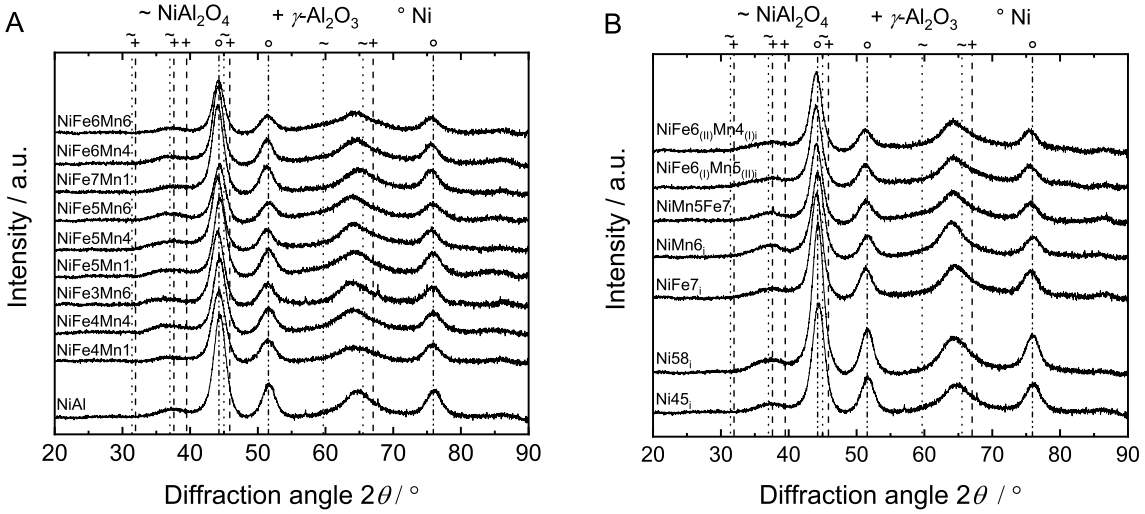


**Figure 5.3:** XRD patterns of *in situ* reduced co-precipitated (A) and impregnated (B) and catalyst samples (JCPDS references: Ni 87-0712, $NiAl_2O_4$ 10-0339, $\gamma$-$Al_2O_3$ 10-0425).

Koschany *et al.* [24] found similar results when increasing the calcination temperature, with a distinct evolution of a $NiAl_2O_4$ phase at 800 °C. In addition, reflex intensity grows from $Ni45_i$ to $Ni58_i$. Besides a decrease of reflex intensity with decreasing nickel loading, no changes in reflex shape or position can be found for the catalyst samples prepared by impregnation, suggesting that the promoter oxide species are present as X-ray amorphous particles on the catalyst surface.

During activation, a crystalline Ni phase is formed, leading to diffraction reflexes at $2\theta$ = 44.3, 51.7, and 76.1°, shown in Figure 5.3. Consequently, the reflexes attributed to the former mixed oxide $NiAlO_x$ phase are shifted to higher diffraction angles towards $\gamma$-$Al_2O_3$, which is supposed to be caused by the decreased amount of $Ni^{2+}$ in the mixed oxide phase. With increasing Fe loading, the reflexes caused by metallic Ni are systematically shifted towards lower diffraction angles, indicating lattice distortion due to the formation of a Ni-Fe alloy phase. The extent of the reflex shift increases with rising Fe fraction. Similar reflex shifts caused by Ni-Fe formation have been reported in literature [149, 152, 253] and Chapter 4. In contrast, with rising Mn fraction, the reflex of the former Ni-Al mixed oxide phase is shifted to lower diffraction angles as compared to the activated benchmark catalyst system. This suggests that Mn is incorporated into the former mixed oxide phase, replacing $Ni^{2+}$, or that Mn species undergo a reduction process during activation of the Ni phase, as proposed for mono-doped co-precipitated NiMnAl catalyst systems. From XPS and TPR studies it had been deduced that Mn is reduced from $Mn_3O_4$ to MnO during Ni activation (*cf.* Chapter 4). Comparable results are obtained for the catalysts prepared by subsequent impregnation. For the single-doped catalysts $NiFe7_i$ and $NiMn6_i$, only the effect corresponding to the respective promoter can be observed. Among the bi-doped catalysts, prepared by co- and subsequent impregnation, no differences can be found, in agreement with the similar elemental compositions shown in Table 5.2, which suggests that during catalyst activation similar processes take place.

#### 5.3.1.3 Temperature-Programmed Reduction

TPR profiles of the catalysts are illustrated in Figure 5.8. Ni44 and $Ni45_i$ feature broad reduction signals from 350 to 750 °C, which is typical for co-precipitated catalysts due to the strong interactions of Ni and Al in the mixed oxide phase after calcination [137]. One can distinguish between a peak centered at around 520 °C, which is supposed to arise from the reduction of $Ni^{2+}$ from the Al-containing NiO phase, and a high-temperature peak at around 650 °C, which may belong to the reduction of the $Ni^{2+}$ located in the amorphous Al-rich phase. The splitting into these two $Ni^{2+}$ species can be observed for all catalysts. In accordance with the findings from XRD in Figure 5.2 B, $Ni^{2+}$ in $Ni58_i$ seems to be more difficult to reduce than in $Ni45_i$, which is supposed to be caused by increased NiO-$AlO_x$ interactions by the repeated calcination procedure.

This effect is also observed for all impregnated catalyst samples in Figure 5.8 B. For $NiMn6_i$ and the bi-doped catalysts in Figure 5.8 B, a low-temperature signal at 175 to 320 °C can be observed, which, in analogy to the co-precipitated mono-doped catalysts, is attributed to the reduction of $Mn_3O_4$ to MnO (*cf.* Chapter 4). The peak area thereby consistently increases with rising Mn content in the catalyst samples. In addition, for high Mn loadings (approx. 6 wt.%) the shoulder at 600 to 700 °C is more distinct. It should be noted that the $Ni^{2+}$ species that cause this shoulder are most probably not reduced under reaction conditions (activation at 485 °C for 8 h). This distinct shoulder indicates that MnO decreases the reducibility of $Ni^{2+}$ in the mixed oxide. This modification might be caused by interactions of $Ni^{2+}$, $Mn^{2+}$, and $Al^{3+}$ and be the reason for the shifted XRD reflex of the mixed oxide phase remaining after catalyst activation at 485 °C in Figure 5.3. The reduction of $Fe^{3+}$ is apparent from shoulders starting at approx. 300 °C [149]. In addition, the main NiO reduction peak previously centered at 505 °C in Ni44 is shifted to lower reduction temperatures, the extent increasing with rising Fe content to a minimum of 460 °C for NiFe7Mn1. This feature might arise from a synergistic effect of Fe reduction, leading to the formation of a Ni-Fe alloy [253, 300, 301], as observed in XRD analysis in Figure 5.3. The additional shoulder observed for NiFe6Mn6 at 240 and 360 °C might be caused by the presence of an additional $Fe_2O_3$ phase as suggested by XRD in Figure 5.2 A. The effect of Fe promotion on the TPR profiles of the impregnated catalysts in Figure 5.8 B is analogous. However, the shift of the main reduction signal to lower temperatures due to Ni(-Fe) formation is superimposed by a shift to higher temperatures caused by the repeated calcination step, in accordance with the difference between $Ni45_i$ and $Ni58_i$. It is noteworthy that, despite their difference in the impregnation order, the TPR profiles for the catalysts $NiFe7Mn5_i$, $NiFe6_{(I)}Mn5_{(II)i}$, and $NiFe6_{(II)}Mn4_{(I)i}$ are very similar. The estimation of the degrees of reduction was omitted due to several overlapping (partial) reduction processes of Ni, Fe, and Mn.

#### 5.3.1.4 Sorption Properties of the Catalysts

Table 5.3 illustrates the gas sorption properties of the co-precipitated catalysts. The highest Ni surface area is obtained for the benchmark Ni44 catalyst (21.1 $m^2\,g_{cat}^{-1}$). Upon promotion, the nickel surface area decreases. NiFe6Mn6 features the lowest nickel surface area (5.5 $m^2\,g_{cat}^{-1}$). When comparing the Ni surface areas and the Ni dispersions (taking the Ni loading into account), several effects can be distinguished. First, at low Mn and Fe loadings, the Ni dispersion is approximately constant at 5 to 7 %, which means that the loss of the Ni surface area is mainly caused by the decreasing Ni content. At high Fe loadings, Fe clearly has a negative influence on the $H_2$ surface area, most probably due to the generation of a Ni-Fe alloy (*cf.* Figure 5.3), limiting the number of Ni atoms being accessible by $H_2$. Fe is known to adsorb only insignificant amounts of $H_2$ under the chosen conditions [253, 254]. However, for these samples, increasing Mn loading (especially for NiFe7Mn1, NiFe6Mn4, and NiFe6Mn6) leads to a decrease of both the Ni surface area and the Ni dispersion, while the mean crystallite size $d_C$ remains in the range of 3.6 to 3.8 nm. This observation can be linked to the TPR profiles shown in Figure 5.8 A, where a negative effect of Mn on the reducibility of $Ni^{2+}$ was found. The decrease of the Ni surface area at high Mn loadings is in accordance with studies on the

**Table 5.3:** Characterization data including results from BET as well as $H_2$ and $CO_2$ chemisorption.

| Catalyst | $S_{Ni}$ / $m^2\,g_{cat}^{-1}$ | $D_{Ni}$ / % | $d_C^a$ / nm | $S_{BET}$ / $m^2\,g_{cat}^{-1}$ | $V_{Pore}$ / $mL\,g_{cat}^{-1}$ | $r_{Pore}$ / nm | $U(CO_2)$ / $\mu mol\,g_{cat}^{-1}$ |
|---|---|---|---|---|---|---|---|
| *Co-precipitated catalysts* | | | | | | | |
| Ni44 | 21.1 | 7.1 | 3.4 | 294 | 0.68 | 4.6 | 172 |
| NiFe4Mn1 | 16.1 | 6.1 | 3.5 | 284 | 0.74 | 5.2 | 204 |
| NiFe4Mn4 | 12.9 | 4.8 | 3.3 | 286 | 0.78 | 5.5 | 345 |
| NiFe3Mn6 | 11.9 | 5.0 | 3.5 | 273 | 0.77 | 5.6 | 221 |
| NiFe5Mn1 | 17.6 | 6.8 | 3.7 | 286 | 0.73 | 5.1 | 269 |
| NiFe5Mn4 | 17.8 | 7.0 | 3.8 | 282 | 0.78 | 6.3 | 298 |
| NiFe5Mn6 | 15.8 | 6.5 | 3.8 | 257 | 0.81 | 6.3 | 327 |
| NiFe7Mn1 | 11.2 | 4.5 | 3.8 | 269 | 0.77 | 5.7 | 223 |
| NiFe6Mn4 | 7.6 | 3.1 | 3.8 | 269 | 0.85 | 6.4 | 276 |
| NiFe6Mn6 | 5.5 | 2.4 | 3.6 | 238 | 0.94 | 7.9 | 322 |
| *Co-precipitated + impregnated catalysts* | | | | | | | |
| $Ni45_i$ | 26.8 | 8.8 | 3.6 | 280 | 0.62 | 4.5 | 202 |
| $Ni58_i$ | 25.6 | 6.5 | 3.6 | 235 | 0.34 | 2.9 | 180 |
| $NiFe7_i$ | 14.8 | 4.6 | 3.8 | 223 | 0.48 | 4.3 | 194 |
| $NiMn6_i$ | 23.1 | 6.9 | 3.7 | 233 | 0.52 | 4.5 | 230 |
| $NiFe7Mn5_i$ | 13.2 | 4.5 | 4.0 | 255 | 0.62 | 4.9 | 226 |
| $NiFe6_{(I)}Mn5_{(II)i}$ | 11.4 | 4.3 | 4.0 | 188 | 0.44 | 4.7 | 243 |
| $NiFe6_{(II)}Mn4_{(I)i}$ | 13.0 | 4.4 | 3.8 | 228 | 0.60 | 5.2 | 242 |

[a] from XRD analyzing the Ni(-Fe) reflex at $2\theta$ = 51.3 to 51.7° using the Scherrer equation (*cf.* Eq. 3.4).

single Mn-doped co-precipitated Ni-Al catalysts (*cf.* Chapter 4). The mean crystallite sizes average between 3.4 to 4.0 nm for all catalysts. Since line broadening is evident, the values should not be over-interpreted, but are in line with literature studies on co-precipitated Ni-Al catalysts [136, 203]. In addition, it should be noted that line profiling was carried out on the assumption of only one kind of Ni-Fe species being present. Transmission electron spectroscopy for crystallite size determination was omitted due to strong ferromagnetic properties of the reduced and subsequently passivated catalyst samples.

The BET surface areas of the co-precipitated catalysts range from approx. 240 to 290 $m^2\,g_{cat}^{-1}$ and can be correlated to the total promoter loading. Ni44 features the highest BET surface area (294 $m^2\,g_{cat}^{-1}$). Low promoter loadings (Fe up to 5 wt.%, Mn up to 4 wt.%) hardly affect the BET surface area, but higher promoter loadings lead to a slight decrease. The lowest BET surface area is obtained for NiFe6Mn6 (238 $m^2\,g_{cat}^{-1}$). All samples exhibit mesoporous structure. The high BET surface areas are caused by the release of $H_2O$ and $CO_2$ during calcination of the hydrotalcites [298]. Fe and Mn generally can be incorporated into the hydrotalcite structure [285], but, as seen from the XRD patterns in Figure 5.1, high Fe and/or Mn loadings seem to modify the hydrotalcite structure. Besides the reduced content of Ni and Al and the correlated decrease of structural $CO_3^{2-}$ and $H_2O$ per mass, this modification may be the reason for the decreased BET surface area for high promoter loadings. In addition, as seen in the XRD patterns of the oxidized and reduced catalysts in Figure 5.2 and 5.3, both Fe and Mn seem to be incorporated in the Ni-Al mixed oxide structure after calcination and therefore are part of the porous system, but undergo (partial) reduction and therefore may be released from the porous system, leading to pore destabilization and collapse. This is in agreement to an increase of the pore radii from 4.6 nm for Ni44 with increasing promoter loading to a maximum of 7.9 nm for NiFe6Mn6, effectively leading to higher total pore volumes (*cf.* Table 5.3).

Except for NiFe3Mn6, the $CO_2$ uptake increases with rising Mn loading for constant Fe contents. This is in agreement with the impact of doping Mn alone to a co-precipitated $NiAlO_x$ catalyst (*cf.* Chapter 4). Mn seems to enhance the $CO_2$ uptake capacity providing additional basic adsorption sites for the acidic $CO_2$ molecule [157, 268]. Similar conclusions can be drawn from the data of the impregnated catalysts. Compared to $Ni45_i$, the Ni surface area, BET surface area, and the $CO_2$ uptake decrease, which might be an effect of the second calcination treatment. The additional treatment might lead to phase separation and weaker Ni-Al interactions in the mixed oxide phase (*cf.* Figure 5.2), resulting in a decreased Ni dispersion on the reduced catalyst. In comparison to $Ni58_i$, again Fe doping in $NiFe7_i$ decreases the Ni surface area due to Ni-Fe alloy formation (*cf.* Figure 5.3 B), while on $NiMn6_i$ the Ni surface area is slightly increased. In contrast, the impregnation procedure leads to reduced BET surface areas. This might be caused by water contact and the drying process. In accordance with previous results, Mn doping in $NiMn6_i$ rises the $CO_2$ uptake by 28 %, Fe in $NiFe7_i$ by 8 %. For the bi-doped impregnated catalysts, the Ni dispersion stays constant around 4.4 %. The approximately 1.5 $m^2\,g_{cat}^{-1}$ lower Ni surface area of $NiFe6_{(I)}Mn5_{(II)i}$ therefore seems to be an artifact from the comparatively lower Ni metal loading in $NiFe6_{(I)}Mn5_{(II)i}$ shown in Table 5.2. For the co-impregnated $NiFe7Mn5_i$

catalyst, a BET surface area of 255 $m^2\ g_{cat}^{-1}$ is achieved, while the sequentially impregnated samples feature a further decrease of the BET surface area. Interestingly, the $CO_2$ uptakes of the sequentially impregnated systems are similar, while for the co-impregnated sample it decreases by 11 %. However, it is still 26 % higher than the $CO_2$ uptake of the benchmark $Ni58_i$.

Potential differences in $CO_2$ binding strengths are evaluated by $CO_2$-TPD. The patterns are illustrated in Figure 5.9 and discussed in Section 5.5.2. In summary, three basic observations from the $CO_2$-TPD patterns can be made: first, both Fe and Mn lead to a decrease of the binding energies of $CO_2$ in monodentate carbonate. The effect of Fe on the basic site density of the oxide material suggests that $Fe^{3+}$ is not reduced quantitatively. Second, at low Fe loadings in NiFe4Mn1, NiFe4Mn4, and NiFe3Mn6, rising Mn loading leads to a further decrease of those binding energies. Third, at moderate and high Fe loadings, increasing Mn loading majorly leads to an increase of the basic site density, especially for weak and medium basic sites. The binding strengths of $CO_2$ on the basic sites of the co-doped $NiFe7Mn5_i$, $NiFe6_{(I)}Mn5_{(II)i}$, and $NiFe6_{(II)}Mn4_{(I)i}$ catalysts seem to be very similar, which is in accordance with their almost identical elemental compositions (*cf.* Table 5.2).

## 5.3.2 Tests on Catalyst Performance

### 5.3.2.1 Activity Tests

The $CO_2$ conversion-temperature characteristics of the co-precipitated bi-doped catalysts are illustrated in Figure 5.4, grouped for approximately constant $n_{Ni}/n_{Fe}$ ratios in A–C. All catalysts show improved activity compared to the benchmark Ni44. For low Fe loadings (Figure 5.4 A and B), increasing Mn loadings enhance the catalytic activity. When comparing Figure 5.4 A–C, it becomes obvious that Mn loading becomes less significant with increasing Fe loading, meaning that the impact of Mn is more pronounced at low Fe loadings. As a result, rising Mn loadings hardly influence catalyst activity for a $n_{Ni}/n_{Fe}$ ratio of approximately 5.5 in Figure 5.4 C. The increase of catalytic activity by Mn promotion has extensively been discussed in Chapter 4. The main reason was found to be an increase of the density of medium basic sites for $CO_2$ adsorption and utilization as well as a reduction of the binding energy of $CO_2$ on these sites. Similar observations can be made for the bi-doped co-precipitated catalysts, apparent from the $CO_2$ uptake measured by static chemisorption in Table 5.3 and the $CO_2$-TPD patterns (*cf.* Figure 5.9).

Pan *et al.* showed that on $Ni/Ce_{0.5}Zr_{0.5}$ catalysts monodentate formate derived from monodentate carbonate on medium basic sites could be hydrogenated quicker than bidentate formate derived from bicarbonate [128]. This indicates that the activity of Ni-based catalysts can be increased by rising their medium basic site density. $CO_2$-TPD suggests an increase of the number of medium basic sites from NiFe5Mn1 to NiFe5Mn6 and from NiFe7Mn1 to NiFe6Mn6 with rising Mn content, which also follows the trend of their activity. However, it is supposed that these medium basic sites need to be located close to the Ni centers, which supply H* for hydrogenation. For high Fe loadings, the hydrogenation properties of the Ni centers might be

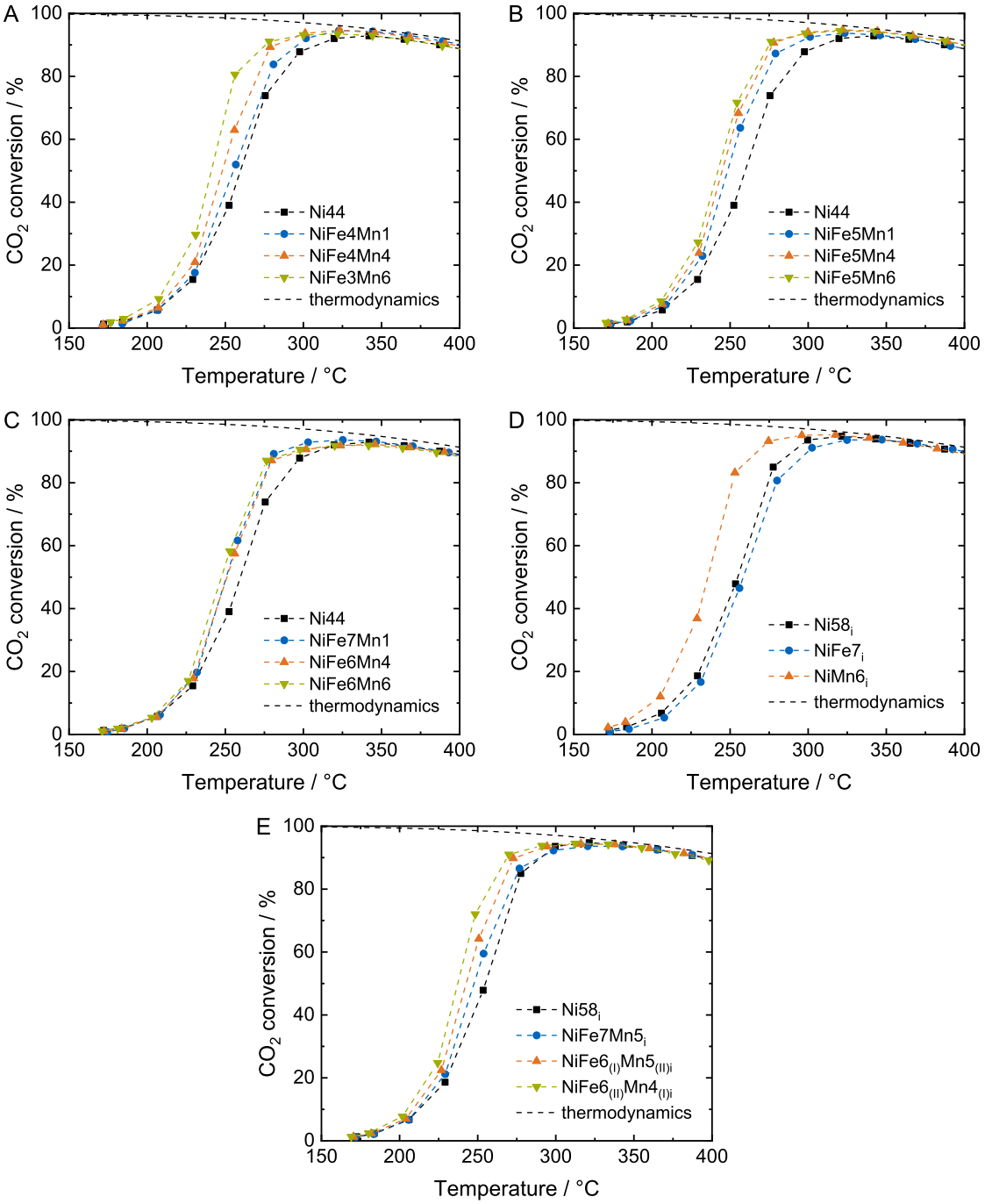


**Figure 5.4:** $CO_2$ conversion vs. reaction temperature plots for Ni44, NiFe4Mn1, NiFe4Mn4, and NiFe3Mn6 (A), Ni44, NiFe5Mn1, NiFe5Mn4, and NiFe5Mn6 (B), Ni44, NiFe7Mn1, NiFe6Mn4, and NiFe6Mn6 (C), $Ni58_i$, $NiFe7_i$, and $NiMn6_i$ (D), $Ni58_i$, $NiFe7Mn5_i$, $NiFe6_{(I)}Mn5_{(II)i}$, and $NiFe6_{(II)}Mn4_{(I)i}$ (E). Reaction conditions: $H_2/CO_2/Ar$ = 4/1/5, $Q$ = 150 NL $g_{cat}^{-1}$ $h^{-1}$, $m_{cat}$ = 25 mg, $p$ = 8 bar.

modified by Ni-Fe alloy formation, which would explain the diminished effect of Mn at high Fe loadings (*cf.* Figure 5.4 C). For low Fe loadings, though, the beneficial effect of Mn doping on the catalytic activity is clearly observable (*cf.* Figure 5.4 A). Figure 5.9 A suggests that NiFe3Mn6 features the lowest density of medium basic sites among NiFe4Mn1, NiFe4Mn4,

and NiFe3Mn6. However, the $CO_2$ desorption signals are systematically shifted to lower temperatures, which indicates a lower binding energy of $CO_2$ adsorbed on these sites. This suggests that, besides their density, also the decreased binding energy of $CO_2$ on medium basic sites might be beneficial for high methanation activity.

At high promoter loadings, a decrease of the catalytic activity is observed. For example, the characteristic temperature for 50 % $CO_2$ conversion increases from 245 °C for NiFe5Mn4 to 251 °C for NiFe6Mn4. This may be explained by the decreased Ni surface areas (due to reduced Ni contents, *cf.* Tables 5.2 and 5.3) and the repressive effect of Mn on the reducibility of $Ni^{2+}$ found by TPR in Figure 5.8 A, but also indicates that Fe dominates at high loadings and therefore represses the promoting effect of Mn. NiFe7Mn1, NiFe6Mn4, and NiFe6Mn6 feature similar catalytic activities, while for Ni5Mn1, Ni5Mn4, and NiFe5Mn6 a beneficial Mn promoter effect is still evident. This suggests that the effect of Mn cannot be exploited for high Fe loadings.

The catalytic activities of the Mn- and Fe-impregnated catalysts are depicted in Figure 5.4 D–E. Figure 5.4 D compares the catalytic activities of the mono-doped catalysts in the temperature variation cycle before aging ($S_1$). Mn raises the catalytic activity compared to the benchmark $Ni58_i$, leading to an approximately doubled $CO_2$ conversion up to 260 °C. This is supposed to be caused by an improved $CO_2$ management on the catalyst surface, obvious from an increased $CO_2$ uptake capacity shown in Table 5.3, which originates from a higher density of medium basic sites (*cf.* Figure 5.9 D and Chapter 4), while, at the same time, the Ni dispersion is increased by 6 %. The fact that the overall Ni metal surface area is decreased by 10 % indicates that an improved $CO_2$ management is more significant under the chosen conditions. $NiFe7_i$, in contrast, features a slightly deteriorated activity.

The effects of Fe- and Mn-doped in impregnated $NiAlO_x$ catalysts can be transferred to bi-doped impregnated catalyst systems. All bi-doped catalysts show an improved activity compared to the benchmark $Ni58_i$ (*cf.* Figure 5.4 E). In addition, catalyst behavior seems to be strongly dependent on the synthesis procedure. The characteristic temperature value of 50 % $CO_2$ conversion decreases from 254.9 °C for the benchmark $Ni58_i$ to 247.7 °C for the co-impregnated $NiFe7Mn5_i$. Not only the sequentially impregnated catalysts show comparatively improved activity, but also the impregnation order seems to have an influence. For $NiFe6_{(I)}Mn5_{(II)i}$, 50 % $CO_2$ conversion are obtained at 242.6 °C, while, when impregnating Mn first, Fe second, another temperature reduction by 5.4 K can be achieved. As stated for the Mn-doped catalyst sample, $CO_2$ management seems to play a major role in the $CO_2$ methanation reaction, leading to an increase of catalytic activity. Consequently, $NiFe6_{(II)}Mn4_{(I)i}$, featuring a $CO_2$ uptake of 242 µmol $g_{cat}^{-1}$, and $NiFe6_{(I)}Mn5_{(II)i}$ (243 µmol $g_{cat}^{-1}$) show the highest activity. However, in $CO_2$ methanation, both $CO_2$ uptake and Ni surface area need to be considered. Therefore, the fact that, despite the similar $CO_2$ uptake, $NiFe6_{(II)}Mn4_{(I)i}$ shows an improved activity compared to $NiFe6_{(I)}Mn5_{(II)i}$ may be explained by the decrease of Ni surface area from 13.0 to 11.4 $m^2\,g_{cat}^{-1}$. In contrast, for $NiFe7Mn5_i$, at a Ni surface area of 13.2 $m^2\,g_{cat}^{-1}$,

the $CO_2$ uptake seems to become limiting again. According to Figure 5.9, the nature of the bidentate and monodentate carbonate sites seems to be similar, though. Most noteworthy, all catalysts show selectivities higher than 99 % towards $CH_4$ formation in the temperature range from 200 to 400 °C, the major byproduct being $C_2H_6$ with a maximum yield of 0.5 % at 30 % $CO_2$ conversion.

#### 5.3.2.2 Tests on the Thermal Stability of the Impregnated Catalysts

Figure 5.5 displays the temperature-conversion characteristics of the impregnated catalysts before and after the aging treatment. While the thermal stability of $Ni58_i$ (*cf.* Figure 5.5 A) is hardly influenced by Mn promotion (*cf.* Figure 5.5 C), Fe doping (*cf.* Figure 5.5 B) results in an enhancement of the thermal stability of the catalyst system. Increase of thermal stability by Fe promotion and enhancement of catalytic activity by Mn doping, respectively, are consistent with effects shown in Chapter 4 for Mn- and Fe-doped $NiAlO_x$ catalysts prepared by co-precipitation. For the bi-doped impregnated samples (Figure 5.5 D–F), the thermal stability compared to the benchmark $Ni58_i$ is improved for all samples, indicating the beneficial effect of Fe. The aging treatment results in a temperature difference of 23.5 K between $S_1$ and $S_2$ for 50 % $CO_2$ conversion for the $Ni58_i$ benchmark catalyst, 13.1 K for $NiFe7Mn5_i$, 16.3 K for $NiFe6_{(I)}Mn5_{(II)i}$, and 18.4 K for $NiFe6_{(II)}Mn4_{(I)i}$. This means that the catalytic activity and the thermal stability of the bi-doped impregnated catalysts behave countervailing. Analysis of the reasons for the improved temperature stability of these Fe-promoted $NiAlO_x$ requires detailed investigation of used catalyst samples under inert conditions to draw conclusions on the role of Fe and to derive the structure-activity relationship.

### 5.3.3 Discussion of the Experimental Data

As illustrated in Figure 5.9 E, the $CO_2$ binding strength on medium basic sites, which are discussed to be essential in the $CO_2$ methanation reaction [128], are similar for the bi-doped impregnated catalysts. In addition, the TPR results in Figure 5.8 show the same characteristics. Therefore, the differences in the catalytic performances observed in Figure 5.4 E may be ascribed to distinct locations of the promoters relative to the active Ni sites in dependence of the preparation procedure.

The Ni-Al mixed oxide, from which, upon catalyst activation, Ni is removed, forming dispersed Ni particles on the catalyst surface, is the base material for all the impregnated catalysts. By varying the impregnation order, the location of the dopants related to the Ni particles after activation might be controlled, assuming that the metal nitrate species are deposited majorly in the pores on the surface of the calcined Ni-Al mixed oxide. When impregnating the $NiAlO_x$ catalyst with $Mn(NO_3)_2$ nitrate, during the drying process dispersed $Mn(NO_3)_2$ crystals are formed on the mixed oxide surface. It is supposed that in the subsequent impregnation step with $Fe(NO_3)_3$ preferably $Fe(NO_3)_3$ crystallites in vicinity to manganese nitrate crystals are formed,

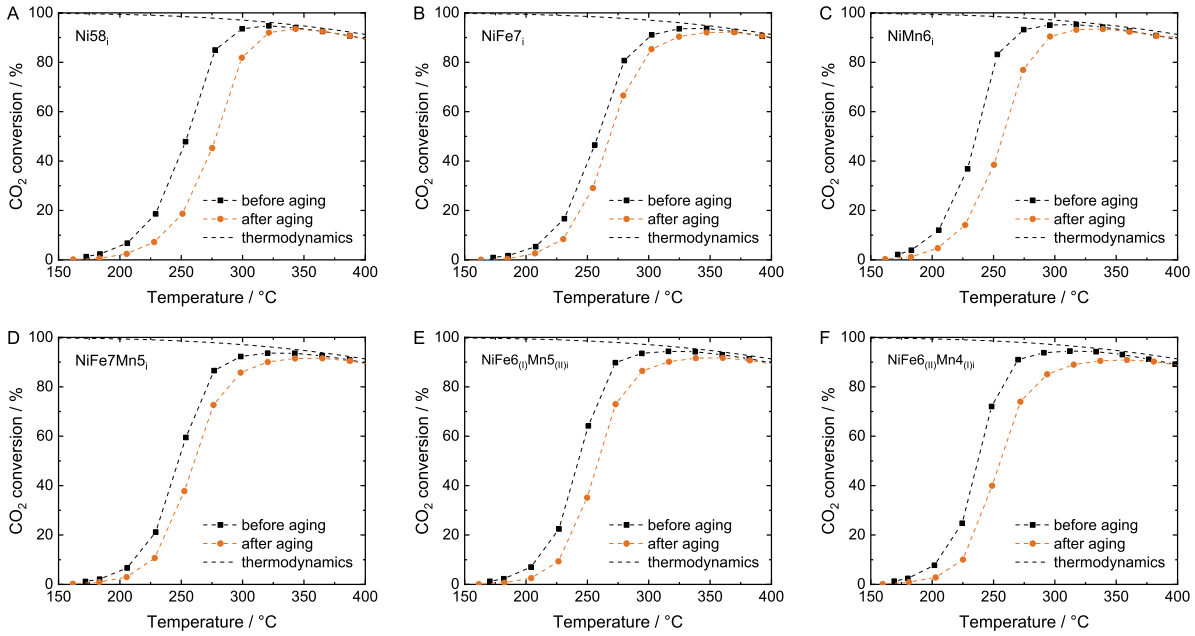


**Figure 5.5:** $CO_2$ conversion vs. reaction temperature plots before and after aging treatment for $Ni58_i$ (A), $NiFe7_i$ (B), $NiMn6_i$ (C), $NiFe7Mn5_i$ (D), $NiFe6_{(I)}Mn5_{(II)i}$ (E), and $NiFe6_{(II)}Mn4_{(I)i}$ (F). Reaction conditions: $H_2/CO_2/Ar$ = 4/1/5, $Q$ = 150 NL $g_{cat}^{-1}$ $h^{-1}$, $m_{cat}$ = 25 mg, $p$ = 8 bar.

the latter serving as crystal nuclei during the drying process. Consequently, when Ni is removed from the mixed oxide phase, it first gets in contact with the element deposited first, in this case Mn, which means that on the activated catalyst Mn species are located next to Ni particles, while the interactions between Fe and Ni are less pronounced. This is in concordance to the increased Ni surface area shown in Table 5.3, which indicates that the interactions between Ni and Fe on the Ni surface are less distinct compared to $NiFe7Mn5_i$ and $NiFe6_{(I)}Mn5_{(II)i}$. $CO_2$ adsorbed on the modified $NiMnAlO_x$ phase is in vicinity to $H_2$ adsorbed on Ni particles and therefore can efficiently react, leading to an enhancement of the methanation rate. As seen for the Mn-doped catalyst system in Figure 5.4, this leads to an increase of the catalytic activity. The influence of Fe is low but becomes obvious in a slight increase of the thermal stability of such catalyst systems.

In contrast, when impregnating with $Fe(NO_3)_3$ first, $Fe(NO_3)_3$ crystals might serve as nuclei for the crystallization of $Mn(NO_3)_2$. After Ni activation, this may lead to more pronounced interactions between Ni and Fe, becoming evident in the decreased Ni surface area shown in Table 5.3. The high $CO_2$ uptake, nevertheless, indicates that a similar $NiMnAlO_x$ oxide phase is formed. However, the adsorbed $CO_2$ might not be fully utilized, since Fe might not supply the H* atoms necessary for methanation taking place, which leads to a decrease of the methanation activity of $NiFe6_{(I)}Mn5_{(II)i}$ compared to $NiFe6_{(II)}Mn4_{(I)i}$. However, the interactions with Fe result in an increase of the thermal stability. Adding both dopants at the same time in theory leads to homogeneous mixing and distribution of both elements. It is apparent from Figure 5.5 that for such a system the influence of Fe prevails, while the increase of the catalytic activity caused by Mn is comparatively low. Also, the $CO_2$ uptake capacity is decreased, maybe due to

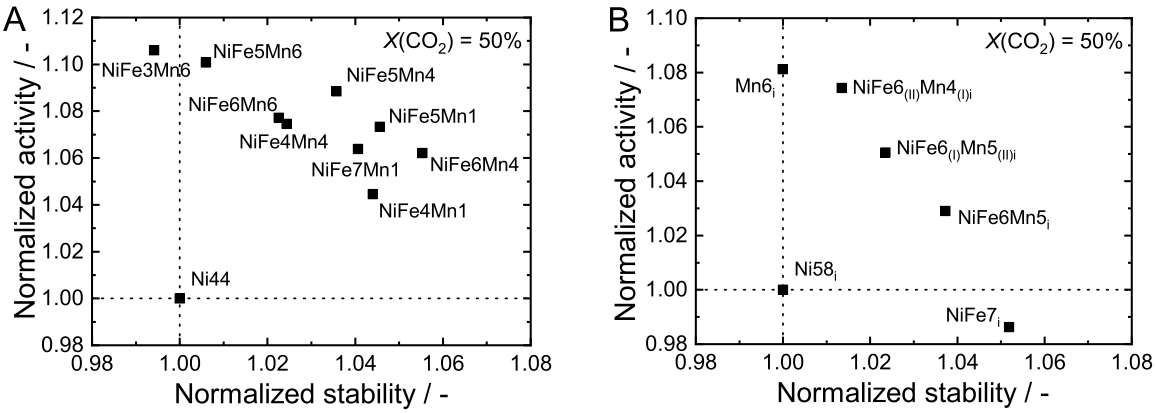


**Figure 5.6:** Activity vs. stability diagram at 50 % conversion of $CO_2$ for co-precipitated (A) and impregnated (B) catalyst systems.

the mixing of Fe and Mn in those samples. In addition, again, the potential supply of $CO_2$ might not be fully exploited since some Fe particles hinder the contact between H* supplied at the Ni particles and $CO_2$ adsorbed on the Mn-rich phase, leading to a decreased activity compared to $NiFe6_{(II)}Mn4_{(I)i}$.

Figure 5.6 comprehensively shows the activity and stability enhancements of the doped catalysts with respect to their $NiAlO_x$ benchmark systems. For the co-precipitated samples in Figure 5.6 A, the activity-stability characteristics are highly dependent on the promoter weight fraction and on the $n_{Mn}/n_{Fe}$ ratio. With respect to an increased catalyst activity at enhanced thermal stability, Fe5Mn4, Fe5Mn1, and Fe6Mn4 perform best. Interestingly, NiFe4Mn4 and NiFe6Mn6 feature very similar performance, indicating that the $n_{Mn}/n_{Fe}$ ratio is a more sensitive parameter during synthesis than the total content of Fe and Mn. For those catalyst samples featuring a higher Mn than Fe loading, no significant improvement, or even a deterioration of the thermal stability can be observed. Figure 5.6 B illustrates that the catalyst characteristics of the impregnated catalysts are approximately circularly arranged around the reference catalyst $Ni58_i$. In this consideration, it must be mentioned that the absolute values in Figure 5.6 A and B cannot be transferred to each other due to different benchmark catalyst systems. All in all, the fact that both effects, the increase of activity by Mn promotion and the enhancement of the thermal stability by doping Fe are no linear combination suggests an intense competition between Fe and Mn, and that both promoters act at similar locations in vicinity to the active Ni sites. Since Mn clearly interacts with the oxide matrix, while Fe seems to modify the metallic Ni particles, it is supposed that both dopants act on the interface of the Ni particles and the oxide matrix. Ni-Fe alloy formation leads to an improvement of catalyst stability under reaction conditions, while Mn increases the density of medium basic sites and thereby the amount of $CO_2$ being supplied for hydrogenation as well as the binding energy of $CO_2$ on these sites, resulting in an enhancement of the methanation activity. Besides $CO_2$ supply, however, an electronic effect of Mn oxide species on the closely located Ni sites cannot be excluded. It is therefore hypothesized that methanation preferentially takes places at potent perimeter sites. The proposed elemental distribution of Ni, Fe, Mn, and Al after reduction is illustrated in

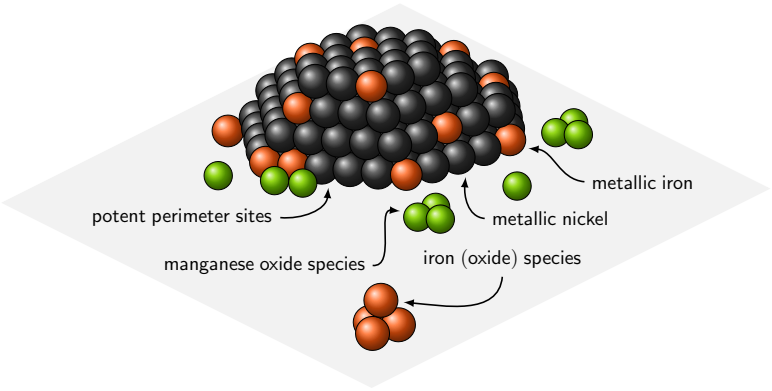


**Figure 5.7:** Proposed schematic elemental distributions of Ni, Fe, and Mn on a bi-doped co-precipitated $NiAlO_x$ catalyst after reduction, background: Ni-containing aluminum oxide phase.

Figure 5.7.

Despite the additional effort in catalyst preparation, two advantages of impregnating $NiAlO_x$ catalysts were found. First, $NiMn6_i$ features a slightly improved activity compared to the co-precipitated $NiMnAlO_x$ catalyst (*cf.* Chapter 4), which might be caused by a better utilization of Mn that is selectively doped on the surface of the mixed oxide catalyst rather than its unselective distribution within the oxide matrix for the co-precipitated catalyst. Second, in contrast to co-precipitated catalysts, for which the activity-stability performance is dictated by the elemental composition of the catalysts, the activity and stability behavior for a constant $n_{Ni}/n_{Fe}/n_{Mn}/n_{Al}$ ratio can be adjusted when doping a $NiAlO_x$ catalyst *via* impregnation.

## 5.4 Conclusion

By co-doping Fe and Mn onto an equimolar co-precipitated $NiAlO_x$ benchmark catalyst, catalysts that feature increased activity in $CO_2$ methanation, due to the effect of Mn, and, at the same time, an enhanced stability under reaction conditions, caused by Fe promotion, can be synthesized. The best performance was found for nickel-to-promoter ratios of $n_{Ni}/n_{Mn}$ = 9.5 and $n_{Ni}/n_{Fe}$ = 7. The enhanced activity by Mn promotion is attributed to an increase of the density of medium basic sites and the reduction of the $CO_2$ binding energy on those sites, while the improved stability is assigned to the formation of Ni-Fe alloy particles at high Fe loadings. While for co-precipitation the activity-stability performance is highly dependent on the molar Fe/Mn and Ni/promoter ratios, the performance at a fixed elemental composition can be adjusted by varying the impregnation order of Mn and Fe using the incipient wetness impregnation technique, where the effect of the element deposited first prevails. This can be used to selectively target a certain catalyst behavior for a fixed elemental composition. From the interference of stability and activity effects it is concluded that Fe and Mn species compete for active sites on the reduced catalyst. Since Mn interacts with the oxide phase, while Fe is

contacted to the metallic Ni particles, it is supposed that both dopants act at the interface of the Ni particles and the oxide matrix. Studies resolving structural changes during time on stream could contribute to gain further insights and to possibly understand the role of the promoters and promoter interaction.

## 5.5 Supplementary Material

### 5.5.1 Temperature-Programmed Reduction

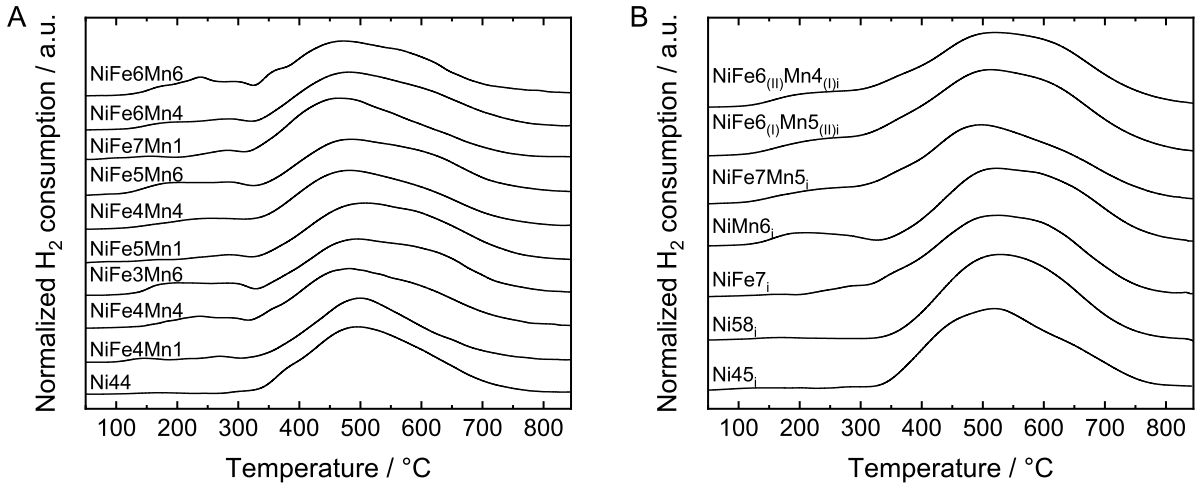


**Figure 5.8:** TPR profiles of the co-precipitated (A) and impregnated (B) catalysts and their benchmark catalysts.

### 5.5.2 Temperature-Programmed Desorption of $CO_2$

Four different $CO_2$ signals originating from different carbonate species can be distinguished for the Ni-Al catalyst in Figure 5.9 D: bicarbonate (centered around 90 °C), binding on weak basic sites, bidentate carbonate (centered around 150 °C), monodentate carbonate (centered around 220 °C), binding on medium strength basic sites, and bridged/organic-like carbonate species, binding on strong basic sites and featuring a broad high-temperature desorption signal [270].

The $CO_2$-TPD patterns for NiFe4Mn1, NiFe4Mn4, and NiFe3Mn6 are illustrated in Figure 5.9 A. Compared to the pattern of the Ni-Al catalyst, the peaks attributed to $CO_2$ from bicarbonate and bidentate carbonate merge. With increasing Mn loading, the signal assigned to $CO_2$ originating from monodentate carbonate shifts to lower temperature, which indicates a decrease of the binding strength of $CO_2$ on the medium basic sites with increasing Mn loading. The high $CO_2$ uptake of NiFe4Mn4, also found by static $CO_2$ chemisorption measurements (*cf.* Table 5.3), seems to arise from an increased density of weak basic sites. The TPD patterns of the catalysts featuring a Fe loading of 5 wt.% are illustrated in Figure 5.9 B. For these catalysts,

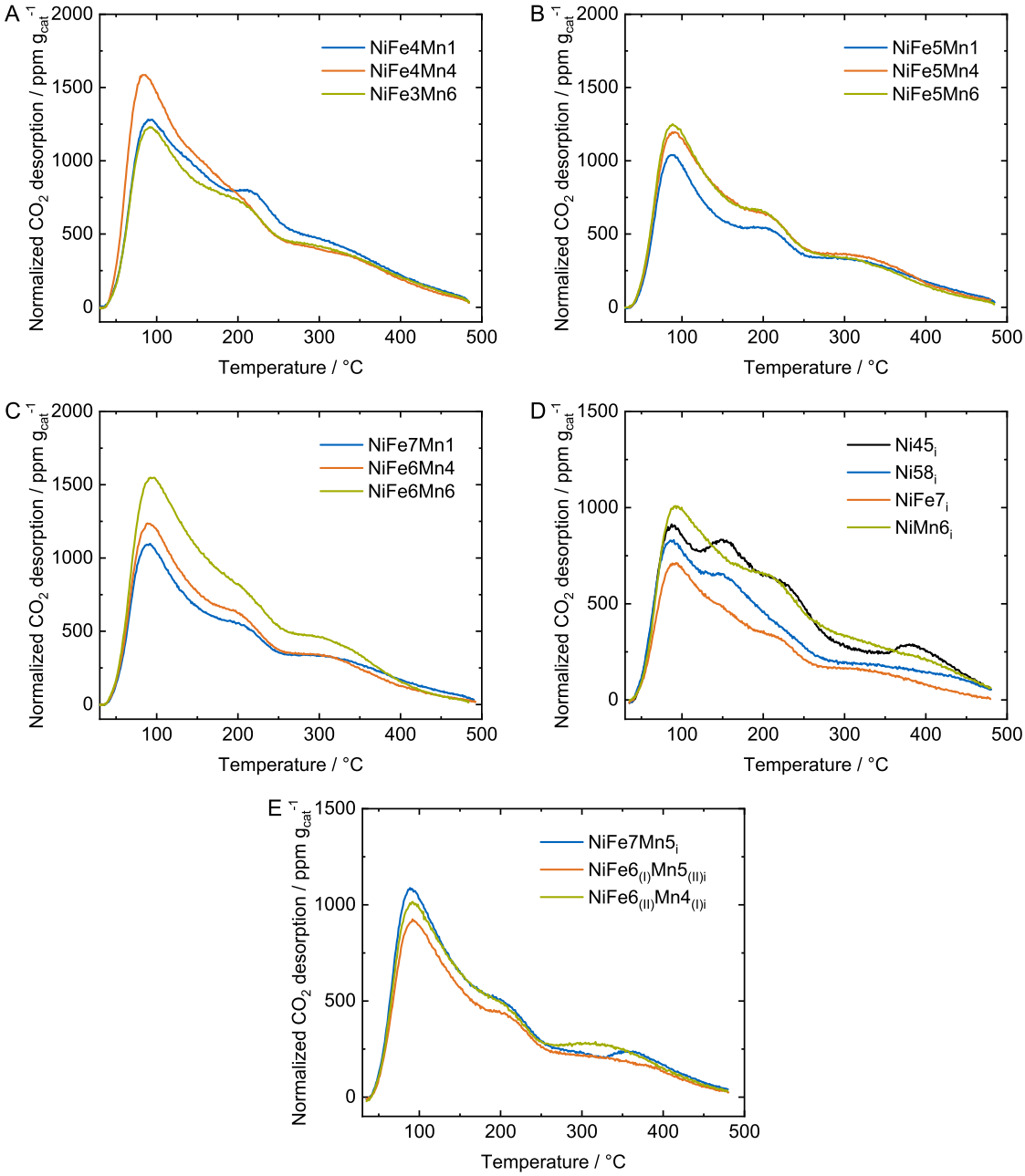


**Figure 5.9:** TPD profiles: NiFe4Mn1, NiFe4Mn4, NiFe3Mn6 (A), NiFe5Mn1, NiFe5Mn4, NiFe5Mn6 (B), NiFe7Mn1, NiFe6Mn4, NiFe6Mn6 (C), $Ni45_i$, $Ni58_i$, $NiFe7_i$, $NiMn6_i$ (D), and $NiFe7Mn5_i$, $NiFe6_{(I)}Mn5_{(II)i}$, $NiFe6_{(II)}Mn4_{(I)i}$ (E).

no peak shifts can be observed, but with rising Mn content an increased density of weak and medium basic sites is found.

The same observation can be made for NiFe7Mn1, NiFe6Mn4, and NiFe6Mn6 (*cf.* Figure 5.9 C). The TPD pattern for the latter also indicates a higher amount of strong basic sites. Especially the densities of strong and the medium basic sites are negatively affected by the re-calcination of the Ni-Al catalyst ($Ni58_i$, *cf.* Figure 5.9 D). No distinct signal arising from monodentate carbonate can be observed for $Ni58_i$. For $NiMn6_i$ and $NiFe7_i$ (Figure 5.9 D), the desorption peaks attributed to $CO_2$ from monodentate carbonate species are shifted to lower

desorption temperatures, indicating a lower binding strength of $CO_2$ on medium basic sites, while for $NiMn6_i$ additionally a higher basic site density can be observed for all species. The effects of Fe and Mn are similar to the co-precipitated counterpart catalysts (*cf.* Chapter 4).

Figure 5.9 E illustrates the TPD patterns of the co-doped catalysts $NiFe7Mn5_i$, $NiFe6_{(I)}Mn5_{(II)i}$, and $NiFe6_{(II)}Mn4_{(I)i}$. These catalysts feature almost identical elemental compositions (*cf.* Table 5.2). It is noteworthy that, besides the high-temperature signal assigned to $CO_2$ from bridged carbonate species, the $CO_2$ binding strengths on the basic sites on these catalysts seem to be very similar. No temperature shifts in the desorption signals can be observed.

The high-temperature signal should not be over-interpreted, since at these conditions CO evolution, probably caused by the oxidation of Ni and Fe, was observed, leading to pressure changes in the mass spectrometer. Overall, the static $CO_2$ uptakes reported in Table 5.3 correlate well with the basic site densities found by $CO_2$-TPD.

# 6 Targeted Fe-Doping of Ni-Al Catalysts *via* the Surface Redox Reaction Technique for Unravelling its Promoter Effect in the $CO_2$ Methanation Reaction

This chapter was published in similar form in

T. Burger, H. M. S. Augenstein, F. Hnyk, M. Döblinger, K. Köhler, O. Hinrichsen, "Targeted Fe-Doping of Ni-Al Catalysts *via* the Surface Redox Reaction Technique for Unravelling its Promoter Effect in the $CO_2$ Methanation Reaction", *ChemCatChem*, 2020, *12*, 649–662, DOI 10.1002/cctc.201901331.



## Abstract

In promoted catalyst systems, the location of dopants is of very high interest to investigate promoter effects. A $Ni/Al_2O_3$ catalyst ($w_{Ni}$ = 11 wt.%) prepared by deposition-precipitation and a co-precipitated $NiAlO_x$ ($n_{Ni}/n_{Al}$ = 1) catalyst are modified with Fe by means of the surface redox reaction technique and tested for activity under differential and integral conditions and for thermal stability (aging at 500 °C, 8 bar, 32 h) in the methanation reaction of $CO_2$. By applying detailed material characterization studies comprising $H_2$ and $CO_2$ chemisorption, ICP-OES, XRD, STEM-EDX, FMR, and BET, it is shown that the surface deposition techniques can be used to selectively deposit Fe in the vicinity of Ni nanoparticles. Doping with Fe leads to an increase of the catalytic activity, attributed to electronic effects through the formation of surface Ni-Fe alloys, and, for the co-precipitated Ni-Al catalyst, to an enhancement of the apparent thermal stability at higher Fe loadings, which is assumed to be caused by a dynamic variation of Ni, Fe, and Al interactions depending on the reaction conditions.

## 6.1 Introduction

The $CO_2$ methanation reaction has recently gained interest for its role in the power-to-gas concept [15]. Synthetic natural gas (SNG) can be stored and distributed in the natural gas grid and therefore serve as a chemical energy storage to buffer fluctuations as well as regional and seasonal dependencies of energy supply by renewables. The highly exothermal character of the $CO_2$ methanation reaction ($\Delta_R H^o$ = -165.1 kJ mol$^{-1}$) leads to a demand for both high catalytic activity to achieve high $CH_4$ yields at mild operating conditions and high thermal stability to increase catalyst life-time by avoiding excessive catalyst deactivation, e.g. by sintering processes [40], in industrial fixed-bed application.

Due to its high abundancy and low costs [85] as well as its high selectivity to methane formation [296], Ni [25, 115, 302–304] is preferred over other active metals like Rh [60], Pd [305], Ru [55], Pt, or Ir [306]. Fe has been claimed to enhance the activity of Ni-based catalyst systems by electronic modification of the active Ni centers, forming Ni-Fe alloy particles (*cf.* [151, 152, 156, 157, 161] and Chapter 4). The effect of Fe on methanation kinetics, however, is not conclusively clarified yet. In literature, the associative and the dissociative methanation pathways are controversially discussed [167]. In associative methanation, $CO_2$ adsorbs on the catalyst surface on basic sites and undergoes hydrogenation at the interface of the Ni particles, where H* is supplied [128, 163, 164, 304]. Therein, catalyst performance is critical to the density and distribution of basic sites [128]. In the dissociative mechanism, both $H_2$ and $CO_2$ adsorb dissociatively [80, 166]. In this case, it is generally accepted that C-O bond cleavage is rate-determining [170, 180, 307]. The reported effects of Fe, however, are manifold. Mebrahtu *et al.* showed that the surface basicity can be tuned by varying the Fe loading in $NiMgAlO_x$ catalysts [161]. The Nørskov group showed in a Brønsted-Evans-Polanyi relation approach that Ni-Fe alloys feature improved C-O dissociation energies, leading to an improved methanation performance [148, 155]. The computational approach was also transferred to experimental studies [153] and is in line with the findings for co-precipitated $NiFeAlO_x$ catalysts (*cf.* Chapters 4 and 5) and results from Hwang *et al.*, who also claimed that Fe doping to Ni-Al xerogel catalysts decreases the metal-support interactions [151]. In addition, beneficial effects of Fe on the reducibility of NiO (*cf.* [149] and Chapter 4) and the Ni dispersion [149] were reported.

Besides the positive effect of Fe on the methanation activity, in Chapter 4 an enhancement of the apparent thermal stability under aging conditions for co-precipitated $NiFeAlO_x$ catalysts at sufficiently high $n_{Fe}/n_{Ni}$ ratios was proved. However, the reasons for the stability improvement are not clear yet. When applying conventional catalyst preparation techniques like impregnation or (co-)precipitation for metal doping, the promoter may be distributed on the catalyst surface or within the catalyst structure, and the location of the promoter relative to the active metal centers is usually unknown. In addition, for its redox properties especially true for Fe, the promoter may be present in different oxidation states (possibly also depending on its location), complicating conclusive decisions on its effect and the structure-activity relationship. Therefore, this chapter addresses the investigation of the promoting effect of Fe on Ni-Al catalysts selectively doped

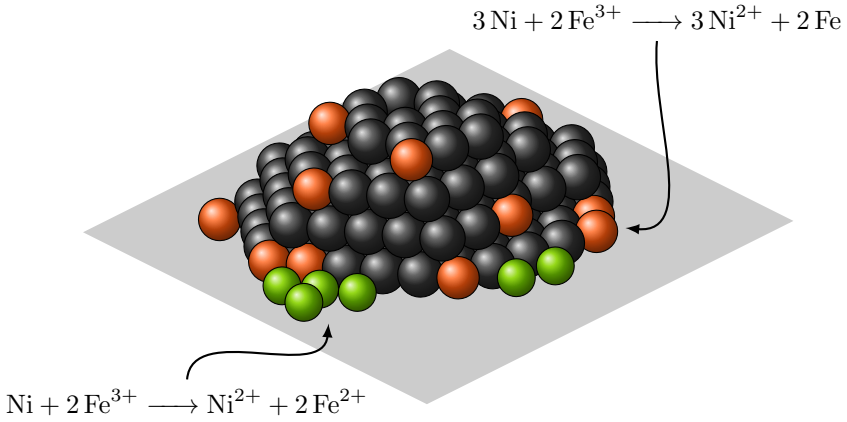


**Figure 6.1:** Doping of an activated Ni-Al catalyst with Fe by means of the surface redox reaction method, black: Ni, orange: Fe, green: $Fe^{2+}$, grey: oxidic Al-rich phase.

at the Ni centers by means of the surface redox reaction (SRR) method to better understand the effect of Fe on Ni-Al catalysts in the $CO_2$ methanation reaction exclusively on the Ni centers.

The surface redox reaction (SRR) method is a known material preparation procedure [308, 309], but rather rarely used and has not been applied to Ni-Fe-Al systems in $CO_2$ methanation so far. It can be applied to selectively replace metal atoms on a material by atoms of a different metal with a lower reduction potential in an appropriate solvent. In this work, $Fe^{3+}$ ions dissolved in EtOH are used to oxidize Ni atoms on an activated Ni-Al catalyst. Figure 6.1 illustrates the reactions possible on a Ni particle under the chosen conditions. The Fe species are deposited at the location where the electrons are supplied in the form of $Fe^0$ or $Fe^{2+}$, or maintain in solution as $Fe^{2+}$, while the generated $Ni^{2+}$ ions go into solution. The synthesis procedure is very sensitive to the washing process after the surface redox reaction to avoid any formation of clusters of the oxidizing or oxidized ion species by adsorption from the liquid phase or by impregnation during the drying process.

A $Ni/Al_2O_3$ catalyst prepared by deposition-precipitation and a co-precipitated $NiAlO_x$ catalyst were taken as the template catalysts for the surface redox reaction. Besides the approach of doping Fe in a selective manner to the Ni nanoparticles, the comparison of the impact of Fe on two differently synthesized Ni-Al template catalysts that vary in structure and sorption properties may shine some light on the importance of particle-support interactions and morphology on the promoter effect of Fe. The Ni loading of the precipitated $Ni/Al_2O_3$ catalyst was set to a typical value of 11 wt.%. For the co-precipitated benchmark catalyst, the $n_{Ni}/n_{Al}$ ratio was set to 1 to provide data comparable to Chapter 4. The catalysts are labeled $NiY_xFeZ$, where $Y$ and $Z$, respectively, denote the metal loadings, subscript $x$ indicates that the catalyst was derived from the co-precipitated $NiAlO_x$ catalyst.

## 6.2 Experimental

### 6.2.1 Preparation of Template Catalysts

The $Ni/Al_2O_3$ template catalyst was prepared by deposition-precipitation. 200 mL of a 0.02 M aqueous solution of $Ni(NO_3)_2 \cdot 6H_2O$ (*p.a.*, Merck) and of 1.3 M ammonia were added to 2.0 g $Al_2O_3$ (Sasol) in an open 500 mL Erlenmeyer flask with baffles. The suspension was mixed on a rotary platform shaker (Heidolph) with 150 rpm at room temperature for 48 h. The suspension was decanted and the solid was washed with DI water two times. After drying at room temperature for 18 h, the catalyst precursor was calcined at 450 °C for 3 h with a heating rate of 5 K $min^{-1}$. For activation, the $Ni/Al_2O_3$ template catalyst was heated from room temperature to 500 °C (at a linear heating rate of 2 K $min^{-1}$) in 50 % $H_2$ in Ar and held there for 1 h, before switching to a flow of 100 % $H_2$ for another hour.

The $NiAlO_x$ template catalyst was prepared by co-precipitation at a constant pH of 9. 120 mL of 1 M aqueous solutions of $Ni(NO_3)_2 \cdot 6H_2O$ (*p.a.*, Merck) and $Al(NO_3)_3 \cdot 9H_2O$ (*p.a.*, Sigma-Aldrich) were mixed and dropwise added to a 3 L double-walled glass vessel (volumetric flow rate 2.5 mL $min^{-1}$) containing 1 L of bi-distilled water stirred at 150 rpm. Two flow breakers were positioned in the vessel for secondary mixing. The temperature was pre-adjusted to 30 °C and kept constant during the synthesis by a thermostat, the pH was pre-adjusted to 9 by adding a 0.5 M mixture of 1 M solutions of $Na_2CO_3$ (Sigma-Aldrich) and NaOH (Merck). An Alphaline Titrino Plus (Schott) was used to keep the pH constant at $9 \pm 0.1$ by adding the precipitation agent throughout the synthesis. The suspension was aged for 18 h in the mother liquor at pH 9 and 30 °C while further stirring. Afterwards, the suspension was vacuum-filtered and the filter cake was washed until the conductivity of the filtrate was similar to DI water. The filter cake was dried at 80 °C for 18 h.

The catalyst was calcined in flowing synthetic air at 450 °C for 6 h with a linear heating rate of 5 K $min^{-1}$. The catalyst powder was pelletized with a pressure of 450 N $cm^{-2}$, ground and sieved to obtain a particle fraction of 150 to 200 µm. Detrimental effects on the porosity and the surface area of the catalysts at this pelletizing pressure were experimentally ruled out. The $NiAlO_x$ template catalyst was reduced in $H_2$ at 500 °C for 5 h with a linear heating rate of 2 K $min^{-1}$.

### 6.2.2 Doping of the Template Catalysts with Fe

For both template catalysts, three SRR-modified catalysts were synthesized. For doping by means of the surface redox reaction technique, the activated catalyst was evacuated at $10^{-6}$ mbar at the reduction temperature for 1 h to free the Ni sites from H* species and cooled down to room temperature at $10^{-6}$ mbar. $Fe(NO_3)_3 \cdot 9H_2O$ (*p.a.*, Merck) was dissolved in degassed and dried EtOH (*p.a.*, Merck) before the solution was added to the activated catalyst under Ar (purity

**Table 6.1:** Catalyst and precursor masses as well as solvent volumes used for the surface redox reaction.

| Catalyst | $m_{cat}$ / g | $m(Fe(NO_3)_3 \cdot 9\ H_2O)$ / g | $V_{EtOH}$ / mL |
|---|---|---|---|
| *Precipitated template catalyst $Ni/Al_2O_3$* | | | |
| Ni11-EtOH | 1.0 | - | 25 |
| Ni9Fe0.5 | 0.83 | 0.13 | 25 |
| Ni7Fe1 | 0.83 | 0.81 | 25 |
| Ni5Fe2 | 0.83 | 1.5 | 25 |
| *Co-precipitated template catalyst $NiAlO_x$* | | | |
| $Ni48_x$-EtOH | 1.0 | - | 20 |
| $Ni39_x$Fe4 | 1.0 | 3.8 | 20 |
| $Ni36_x$Fe6 | 1.0 | 6.1 | 20 |
| $Ni27_x$Fe9 | 1.0 | 8.6 | 20 |

5.0) atmosphere. The synthesis parameters are listed in Table 6.1. The suspension was stirred at 300 rpm for 10 min. After filtration under Ar atmosphere, the catalyst was washed five times with degassed DI water. The catalyst was then vacuum-degassed at room temperature for 1 h, at 80 °C for 1 h and then at 250 °C for another 3 h.

For better comparison, the template catalysts were subjected to the same procedure without Fe being added, labeled -EtOH. The so modified catalysts Ni11-EtOH and $Ni48_x$-EtOH serve as benchmark catalysts throughout the studies. Catalyst testing and material characterization was carried out on the SRR-modified catalysts as well as their benchmark catalysts, respectively. An impact of EtOH on the physiochemical, morphological, and catalytic properties of the Ni-Al catalysts has been excluded by blank experiments.

## 6.2.3 Material Characterization

### 6.2.3.1 Elemental Analysis

Elemental analysis was carried out *via* inductively coupled plasma-optical emission spectroscopy (ICP-OES) on an Agilent 700. For sample preparation, approximately 50 mg of the catalyst were dissolved in 50 mL of 1 M $H_3PO_4$ by sonication for 2 h at 60 °C. The samples were cooled down and diluted in a ratio of 1 to 10 with bi-distilled water. The solutions were filtered using 0.45 µm syringe filters (Pall). The multi-element standard IV (Merck) was used to prepare metal standard solutions for 1, 10, and 50 ppm metal ion concentrations. Matrix interactions and metal signal interference were excluded. The wavelengths tracked for quantification were 230.299 nm (Ni), 396.152 nm (Al), 238.204 nm (Fe), and 568.263 nm (Na). All data were averaged over five measurements. The Na signal in all samples was below the detection limit (corresponding to a Na loading $w_{Na} < 10^{-3}$ wt.%), meaning that Na poisoning by the co-precipitation agent can be excluded.

#### 6.2.3.2 X-ray Powder Diffraction Analysis

Ambient X-ray powder diffraction (XRD) was carried out on a Philips X'pert equipped with Cu-$K_\alpha$ radiation and a monochromator. The powders were scanned with $0.017\,°\,\text{step}^{-1}$ and $83\,\text{steps}\,\text{min}^{-1}$. XRD on reduced and spent catalyst samples was carried out on a STOE Stadi P diffractometer using Cu-$K_\alpha$ radiation, a Ge(111) monochromator and a Dectris MYTHEN 1K detector. Approximately 5 mg of catalyst was transferred into glass capillaries (outer diameter 0.5 mm) under Ar atmosphere. Diffractograms were taken in the range of $2\theta = 5$ to 90° with $0.015\,°\,\text{step}^{-1}$ and a stepping rate of $45\,\text{steps}\,\text{min}^{-1}$. The mean particle diameters were calculated by line profiling (Pseudo Voigt function) using Highscore 3.0d, evaluating the reflex caused by X-ray diffraction on the (020) plane at $2\theta = 51.5$ to 51.8° of Ni or ($\gamma$Fe,Ni) crystallites, respectively. Nomenclature for Ni-Fe alloys was taken from Swatzendruber *et al.* [310]. Estimation of the ($\gamma$Fe,Ni) alloy particle composition was carried out by comparing the calculated cell parameter of the fcc crystal lattice $a$, determined from the reflection caused by diffraction at the (020) plane at $2\theta = 51.5$ to 51.8°, to tabulated values [310]. From the XRD step-width, the absolute error in the atomar Ni/Fe composition of the ($\gamma$Fe,Ni) crystallites can be estimated to $\pm 0.7$ at.%.

#### 6.2.3.3 Scanning Transmission Electron Microscopy / Energy-Dispersive X-ray Spectroscopy

To evaluate the relative positions of Fe and Ni on the oxidized SRR-modified catalysts, energy dispersive X-ray (EDX) spectroscopy in scanning transmission electron microscopy (STEM) mode was carried out at 300 kV on a FEI Titan Themis microscope equipped with a Super-X EDX detector. 1 mg of catalyst powder was dispersed in bi-distilled $H_2O$ and sonicated for 10 min. After sedimentation of the larger particles, 3 µL of the suspension were dropped onto a carbon film coated copper grid. The droplet was removed after an adsorption time of 10 s using filter paper.

#### 6.2.3.4 Temperature-Programmed Reduction

Temperature-programmed reduction (TPR) profiles were recorded by thermal gravimetric analysis/mass spectrometry (TG-MS) on a NETZSCH ST 409. The parameters were chosen in accordance with Malet and Caballero [218] and Monti and Baiker [219]. 50 mg of catalyst were heated in a flow of $60\,\text{mL}\,\text{min}^{-1}$ Ar to 350 °C with a linear heating rate of $5\,\text{K}\,\text{min}^{-1}$. After cooling down to room temperature, the sample was heated to 850 °C in 5 % $H_2$ in Ar with a total volumetric flow rate of $70\,\text{mL}\,\text{min}^{-1}$ and a linear heating rate of $5\,\text{K}\,\text{min}^{-1}$. To gather the TPD patterns, the $H_2O$ signal at $m/z$ 18 was evaluated. Data was smoothed using a Loess filter with a span of 0.03. For determination of the reduction temperatures, the signals were deconvoluted by Gaussian peak fitting.

#### $N_2$ Physisorption

$N_2$ physisorption experiments on activated and spent catalyst samples were carried out at 77 K samples on a Quantachrome NOVAtouch. For the determination of the BET surface area, the $p/p_0$ range between 0.05 and 0.3 was taken for evaluation. For the catalysts derived from the precipitated $Ni/Al_2O_3$ catalyst, the total pore volume was taken from the data point at $p/p_0$ = 0.995. For the $Al_2O_3$-based catalysts, the pore size distribution was determined applying the BJH method on the adsorption branch since the samples exhibited type IV isotherms featuring a H2 hysteresis. The $N_2$ physisorption characteristics of the samples derived from the co-precipitated template catalyst can be classified into type IV isotherms featuring a H3 hysteresis, which is a hint for plate-like particles or slit-like pores. Therefore, the conventional theories on the pore volume and pore sizes determination cannot be applied [221]. For this reason, reporting of the total pore volumes and the pore size distributions for the $NiAlO_x$-based catalyst is omitted.

#### 6.2.3.5 $H_2$ and $CO_2$ Chemisorption

$H_2$ and $CO_2$ chemisorption experiments were conducted on an Autosorb 1C (Quantachrome). For the pre-treatment, the fresh catalysts were activated in $H_2$ at 500 °C for 5 h (linear heating rate 2 K $min^{-1}$). Adsorption equilibration time was set 2 min ($H_2$) and 10 min ($CO_2$), respectively. A dissociative adsorption mechanism of $H_2$ on Ni was applied for the calculation of the specific metal surface area [252]. As generally accepted in literature [253, 254], it was assumed that under the chosen conditions $H_2$ exclusively adsorbs on Ni and not on Fe. Furthermore, in preliminary studies it was ensured that the adsorption of $CO_2$ at the chosen conditions was not kinetically hindered on the samples.

#### 6.2.3.6 Paramagnetic/Ferromagnetic Resonance Spectroscopy

Paramagnetic/ferromagnetic resonance (EPR/FMR) spectra of the activated catalysts were recorded on a JEOL JES-RE 2X at X-band frequency at temperatures between 113 and 473 K, a microwave frequency of 9.4 GHz, a microwave power < 0.2 mW, and a modulation frequency of 100 kHz. The microwave frequency was measured with a microwave frequency counter Advantest R5372. The catalyst samples were transferred into glass capillaries (diameter 0.5 mm) after activation (fresh catalyst samples) without contact to air. The integrated intensity was determined by double integration of the resonance signals of a weighed catalyst sample calibrated to a known standard ($Mn^{2+}$/MgO). Conclusions on FMR data of the aged catalyst samples are difficult to interpret due to factors like particle size and shape [287] (owed to possibly different susceptibilities to sintering), possible adsorbates on the catalyst surface [290] as well as modified particle-support interactions [289] during aging, influencing ferromagnetic characteristics like magnetic intensity and anisotropy.

#### 6.2.3.7 Temperature-Programmed Desorption of $CO_2$

$CO_2$-TPD was carried out in a setup described elsewhere [134]. 50 mg of catalyst powder was reduced at 480 °C in 5 % $H_2$ in He for 5 h (linear heating rate 2 K min$^{-1}$). After purging with He for 1 h, the catalyst bed was cooled down to 35 °C in He. The catalyst was treated with $CO_2$ for 30 min at 35 °C, before weakly adsorbed $CO_2$ was removed by purging with He for 30 min. The TPD was carried out from 35 °C to 480 °C with a linear heating rate of 6 K min$^{-1}$ using He (Westfalen, 6.0) carrier gas (100 mL min$^{-1}$). Due to unknown adsorption and desorption kinetics, fitting of the $CO_2$ desorption signal was omitted.

### 6.2.4 Catalyst Testing Procedure

Catalyst testing was carried out in a setup described in [24] and Section 3.3. 50 mg of catalyst in the particle size fraction from 150 to 200 µm were thoroughly mixed with 450 mg purified SiC (ESK) and placed in the isothermal zone of a 4 mm diameter glass-lined tube reactor. The absence of heat and mass transfer limitations for this specific particle size range under the chosen conditions had been excluded beforehand, both experimentally and by evaluating heat and mass transport criteria (*cf.* Appendix A) [24, 311–313]. The axial position of the catalyst bed was fixed by 4 mm quartz wool plugs. To track bed temperature during reaction, a thermocouple was placed at the end of the diluted catalyst bed. The catalysts were activated *in situ* in $H_2$ ($Q$ = 60 NL $g_{cat}^{-1}$ h$^{-1}$) by heating to 500 °C with a linear heating rate of 2 K min$^{-1}$ and holding this temperature for 5 h. Initially, the catalyst was subjected to methanation conditions at 8 bar and 250 °C at 150 NL $g_{cat}^{-1}$ h$^{-1}$ ($H_2/CO_2/Ar$ = 4/1/5) for 2 h. After this start-up phase, the temperature was varied stepwise from 175 to 500 °C at 8 bar to resolve data on the activity of the catalyst in the form of its $CO_2$ conversion vs. temperature characteristics (labeled $S_1$). In the following, the catalyst was subjected to an aging treatment at 500 °C and 8 bar for a duration of 32 h. After this artificial aging treatment, a second temperature variation cycle ($S_2$) was carried out in order to resolve data indicating the apparent thermal stability of the catalyst under reaction conditions. The temperature program is shown in Figure 6.10. Data accuracy was checked in replicate experiments. To provide a clean surface prior the characterization of spent samples, the catalyst bed was heated up to 350 °C in Ar ($Q$ = 60 NL $g_{cat}^{-1}$ h$^{-1}$) and held there for 1 h. Furthermore, after cool-down, the sample was removed from the setup under inert atmosphere and vacuum-degassed at 350 °C for 1 h.

The activation energies for $CH_4$ formation before and after aging were determined under differential conditions with the $CO_2$ conversion ranging from 2 to 10 % by evaluating the slope of the logarithmic $CH_4$ formation rate plotted against 1/$T$. In advance, it was checked that the reaction orders of $H_2$ and $CO_2$ do not change in this regime. Experimental errors were calculated by Gaussian error propagation. The calculated and reported errors were higher than the errors observed in replicate experiments. The purity of all gases (Westfalen) was 5.0. The gas flow exiting the backpressure regulator was diluted with Ar in a ratio of 1 to 8.

All tubing was heated to prevent water from condensation. An Emerson MTL-4 gas process analyzer was used for online tracking of the molar gas composition ($CO_2$, CO, $H_2O$, $CH_4$, and $H_2$). For each measurement point, the parameters were kept constant for 45 min. Steady-state conditions were reached after 20 min. The actual product gas composition was averaged over 150 s (300 data points). Byproduct analysis was performed on a PerkinElmer Clarus 580 gas chromatograph equipped with two columns and FID detectors. C, H, and O balances were closed by $\pm 3$ wt.%. Conversions $X$ and yields $Y$ were calculated according to Eqs. 6.1 to 6.3, taking volume contraction into account according to Eq. 6.4 (derived from Section 3.3 on the basis of $CO_2$). Yields of the hydrocarbon byproducts were calculated from the FID response corrected by the sensitivity factors [238]. Selectivities were calculated according to Eq. 6.5. Enthalpy and entropy data for the calculation of equilibrium data were determined from the Shomate equation (*cf.* Appendix B) The calculation itself was carried out by the $\Delta G$ minimization method (*cf.* Appendix C).

$$X(j) = \frac{\dot{n}_{\mathrm{in}}(j) - \dot{n}_{\mathrm{out}}(j)}{\dot{n}_{\mathrm{in}}(j)} = \frac{x_{\mathrm{PGA,in}}(j) \cdot \left(\dot{V}_{\mathrm{in}} + \dot{V}_{\mathrm{dil}}\right) - x_{\mathrm{PGA,out}}(j) \cdot \left(\dot{V}_{\mathrm{out}} + \dot{V}_{\mathrm{dil}}\right)}{x_{\mathrm{PGA,in}}(j) \cdot \left(\dot{V}_{\mathrm{in}} + \dot{V}_{\mathrm{dil}}\right)}, j = \mathrm{CO_2}, \mathrm{H_2} \tag{6.1}$$

$$Y(i) = \frac{x_{\mathrm{PGA,out}}(i) \cdot \left(\dot{V}_{\mathrm{out}} + \dot{V}_{\mathrm{dil}}\right)}{x_{\mathrm{PGA,in}}(\mathrm{CO_2}) \cdot \left(\dot{V}_{\mathrm{in}} + \dot{V}_{\mathrm{dil}}\right)}, i = \mathrm{CH_4}, \mathrm{CO} \tag{6.2}$$

$$Y(\mathrm{H_2O}) = 2 \cdot \frac{x_{\mathrm{PGA,out}}(\mathrm{H_2O}) \cdot \left(\dot{V}_{\mathrm{out}} + \dot{V}_{\mathrm{dil}}\right)}{x_{\mathrm{PGA,in}}(\mathrm{H_2}) \cdot \left(\dot{V}_{\mathrm{in}} + \dot{V}_{\mathrm{dil}}\right)} \tag{6.3}$$

$$\dot{V}_{\mathrm{out}} = \frac{\dot{V}_{\mathrm{in}} \cdot \left(1 - 2 \cdot x_{\mathrm{PGA,in}}(\mathrm{CO_2})\right) + 2 \cdot \dot{V}_{\mathrm{dil}} \cdot \left(x_{\mathrm{PGA,out}}(\mathrm{CO_2}) - x_{\mathrm{PGA,in}}(\mathrm{CO_2})\right)}{1 - 2 \cdot x_{\mathrm{PGA,out}}(\mathrm{CO_2})} \tag{6.4}$$

$$S(k) = \frac{Y(k)}{X(\mathrm{CO_2})}, k = \mathrm{C}_x\mathrm{H}_y, \mathrm{CO} \tag{6.5}$$

## 6.3 Results and Discussion

### 6.3.1 Evaluation of Fe Deposition During the Surface Redox Reaction

The metal loadings and the molar element ratios of the catalysts prepared from the template catalysts are listed in Table 6.2. For all SRR-modified catalysts, the amount of the Fe precursor substance $Fe(NO_3)_3 \cdot 9\ H_2O$ used during synthesis (*cf.* Table 6.1) correlates well with the Fe loading on the catalyst. At the same time, a decrease of the Ni loading is observed, owed to the exchange of Ni with Fe. The catalysts originating from the co-precipitated $NiAlO_x$ catalyst feature $n_{\mathrm{Ni}}/n_{\mathrm{Fe}}$ ratios of 9.3, 5.7, and 3.0, respectively, making them comparable to the co-precipitated $NiFeAlO_x$ catalysts prepared in Chapter 4.

The exchange ratio $\Delta N_{\mathrm{Fe}}/\Delta N_{\mathrm{Ni}}$ describes the number of Fe atoms that are deposited on the catalyst per removed Ni atom. As depicted in Figure 6.1, two competing reaction mechanisms need to be considered: $Fe^{3+}$ may either be reduced to $Fe^0$ ($\Delta N_{\mathrm{Fe}}/\Delta N_{\mathrm{Ni}} = 2/3$), which is deposited

**Table 6.2:** Metal loadings and elemental ratios determined by ICP-OES.

| Catalyst | $w_{Ni}$ / wt.% | $w_{Fe}$ / wt.% | $n_{Fe}/n_{Ni}$ / - | $n_{Ni}/n_{Al}$ / - | $n_{Fe}/n_{Al}$ / - | $\Delta N_{Fe}/\Delta N_{Ni}$ / - |
|---|---|---|---|---|---|---|
| *Precipitated template catalyst $Ni/Al_2O_3$* | | | | | | |
| Ni11-EtOH | 11.0 | - | - | 0.114 | - | - |
| Ni9Fe0.5 | 8.7 | 0.5 | 17.2 | 0.095 | 0.006 | 0.31 |
| Ni7Fe1 | 6.6 | 1.0 | 6.0 | 0.073 | 0.012 | 0.31 |
| Ni5Fe2 | 5.3 | 1.8 | 2.8 | 0.054 | 0.019 | 0.32 |
| *Co-precipitated template catalyst $NiAlO_x$* | | | | | | |
| $Ni48_x$-EtOH | 48.1 | - | - | 1.04 | - | - |
| $Ni39_x$Fe4 | 38.7 | 3.6 | 10.3 | 0.84 | 0.08 | 0.39 |
| $Ni36_x$Fe6 | 36.4 | 6.1 | 5.7 | 0.74 | 0.13 | 0.42 |
| $Ni27_x$Fe9 | 27.5 | 8.6 | 3.0 | 0.58 | 0.19 | 0.41 |

on top or the perimeter of the Ni particle, or to $Fe^{2+}$, which may either be deposited on perimeter sites ($\Delta N_{Fe}/\Delta N_{Ni} = 2$), or stay in solution.

The second pathway seems to be the prominent one in this approach, since, for all catalysts, $\Delta N_{Fe}/\Delta N_{Ni}$ is lower than the expected minimum value of 2/3. This also indicates that a considerate amount of $Fe^{3+}$ is reduced to $Fe^{2+}$, remaining in solution rather than being deposited on the surface. In agreement, the presence of $Fe^{2+}$ in the solution was experimentally qualitatively proved by Turnbull's blue formation after adding $[Fe(CN)_6]^{3-}$ (Merck, *p.a.*). The molar amount of Al in the samples stayed constant in all catalysts, no $Al^{3+}$ leaching in EtOH could be observed by ICP-OES. Suspending the samples in $H_2O$, in contrast, led to significant leaching of $Al^{3+}$ as well as $\gamma$-AlO(OH) formation (proved by XRD, not shown) for experiment times exceeding 24 h, which is consistent to processes occurring during hydrothermal treatments, however, reported in literature [248]. Therefore, the washing times after the SRR treatment in $H_2O$ were kept as short as 2 min. Washing the catalysts five times in fresh degassed water, however, proved to be crucial to wash away redundant $Fe^{n+}$ ($n$ = 2, 3) and $Ni^{2+}$ species from the liquid phase, and to re-dissolve clusters nucleated on the Al-containing oxide surface. The Fe and Ni contents in the fifth washing filtrate were checked to be below 0.05 mg $g_{cat}^{-1}$ by ICP-OES, highlighting that both the amount of Fe species being adsorbed on the surface and the amount of Ni and Fe being re-impregnated on the catalyst surface during drying can be neglected. Besides, the combination of this washing procedure and the degassing at 250 °C ensured that no remaining C species originating from EtOH remained on the catalyst, as checked by BET and CHN analysis in pre-studies.

The constant exchange ratios of $\Delta N_{Fe}/\Delta N_{Ni}$ (0.31 to 0.32) for the catalysts originating from the precipitated $Ni/Al_2O_3$ template catalyst and 0.39 to 0.42 for the ones stemming from the co-precipitated $NiAlO_x$ template catalyst prove that the doping process *via* the SRR technique is reproducible. The offset of about 0.1 between the template catalysts may result from the differences in the Ni particle size (e.g. accessible Ni sites) and morphological properties.

### 6.3.2 Scanning Transmission Electron Microscopy / Energy-Dispersive X-ray Spectroscopy

Due to their strong ferromagnetic character after reduction (*cf.* also Section 6.3.4), no STEM images or EDX data of the activated or aged catalyst samples could be collected. The local atomic distributions of Ni, Fe, and Al in calcined Ni5Fe2, resolved by STEM-EDX, are exemplarily shown in Figure 6.11, local intensity distributions of Ni-$K_\alpha$, Al-$K_\alpha$, and Fe-$K_\alpha$ in Figure 6.2. As expected for a classical supported $Ni/Al_2O_3$ catalyst, clear NiO clusters in the range of 6 nm can be observed. Fe is not statistically distributed on the surface, but rather located on concentrated spots in close neighborhood to Ni-rich sites (*cf.* Figure 6.2 A). On the Fe-rich spots, the Ni signal is reduced (e.g. Figure 6.11, Area 1), which is consistent to the replacement mechanism proposed in Figure 6.1. As apparent from Figure 6.2 B and Figure 6.12, on $Ni27_xFe9$, in contrast, Ni and Al are more homogeneously distributed. The central areas in Figure 6.12 A and 6.12 B feature a very homogeneous distribution of both Al and Ni. No distinct NiO clusters can be observed, which highlights the different morphologies of a supported $Ni/Al_2O_3$ and a co-precipitated $NiAlO_x$ catalyst. Moreover, Figure 6.12 C indicates that different phases exist, one that is rich in $Ni^{2+}$ and one that is rich in $Al^{3+}$ and poor in $Ni^{2+}$. Fe, again, seems to be co-localized rather with $Ni^{2+}$ than with $Al^{3+}$. Elemental analysis data (by EDX) of selected spots in Figure 6.2 are shown in Section 6.5.2. Based on the STEM-EDX observations on the Ni5Fe2 and $Ni27_xFe9$ samples and on the strong correlation of $\Delta N_{Fe}/\Delta N_{Ni}$, one can conclude that the replacement mechanism proposed in Figure 6.1 is valid.

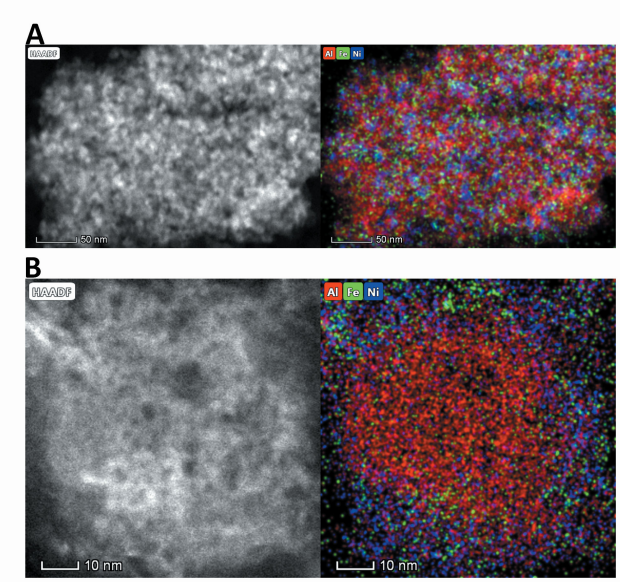


**Figure 6.2:** HAADF-STEM image and local EDX intensity distribution of Ni-$K_\alpha$ (blue), Al-$K_\alpha$ (red), and Fe-$K_\alpha$ (green) in the Ni5Fe2 (A) and $Ni27_xFe9$ (B) catalysts in their calcined (oxidized) state.

### 6.3.3 Structural Characterization

The uncalcined $NiAlO_x$ template catalyst features a hydrotalcite structure. The structural and morphological properties of this takovite-like $[Ni_{0.5}Al_{0.5}(OH)_2][(CO_3)_{0.25}\cdot n H_2O]$ material have been extensively discussed in Chapter 4 and 5 as well as [284].

Figure 6.3 shows the XRD patterns of the calcined Ni-Al catalysts prior to the SRR treatment. For the calcined $Ni/Al_2O_3$, the characteristic $\gamma$-$Al_2O_3$ reflections appear at $2\theta$ = 37.6, 39.5, 45.9, and 67.0° (JCPDS 10-0475), the NiO reflections at $2\theta$ = 37.3, 43.3, 61.9, 75.4, and 79.4° (JCPDS 78-4029). The presence of these two crystalline phases in the precipitated catalyst is typical for a classical supported catalyst, where NiO clusters are dispersed on the $Al_2O_3$ support, in accordance with STEM-EDX. In contrast, for the co-precipitated $NiAlO_x$ catalyst the reflections attributed to NiO are shifted towards the respective peaks of $\gamma$-$Al_2O_3$, which indicates that $Al^{3+}$ is incorporated into the NiO crystal lattice, leading to lattice shrinkage ($2\theta$ = 36.9, 44.1, 63.9, 76.2, and 81.0°).

Besides the obvious presence of this crystalline NiO-rich phase, Alzamora *et al.* proposed the co-existence of a second X-ray amorphous Al-rich Ni-containing alumina-like phase [139], which is consistent to the previously discussed observations from STEM-EDX in Figure 6.12. This structure is common to hydrotalcite-derived materials [139, 314] and greatly varies from the one of the precipitated $Ni/Al_2O_3$ catalyst. Noteworthy, no bulk $NiAl_2O_4$ spinel phase can be found by XRD for any of the catalysts.

The XRD patterns of the reduced reference catalysts Ni11-EtOH and $Ni48_x$-EtOH are shown in Figure 6.4. The characteristic fcc Ni peaks evolve at $2\theta$ = 44.50, 51.85, and 76.38°. From the Scherrer equation (*cf.* Eq. 3.4), the Ni crystallite sizes can be estimated to 6.1 nm for

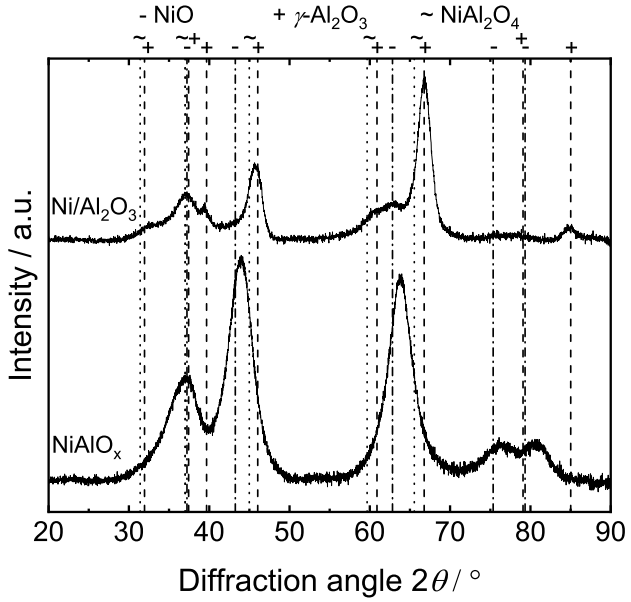


**Figure 6.3:** XRD patterns of the $Ni/Al_2O_3$ and the $NiAlO_x$ catalyst after calcination (NiO JCPDS 78-4029, $\gamma$-$Al_2O_3$ JCPDS 10-0475, $NiAl_2O_4$ JCPDS 10-0339).

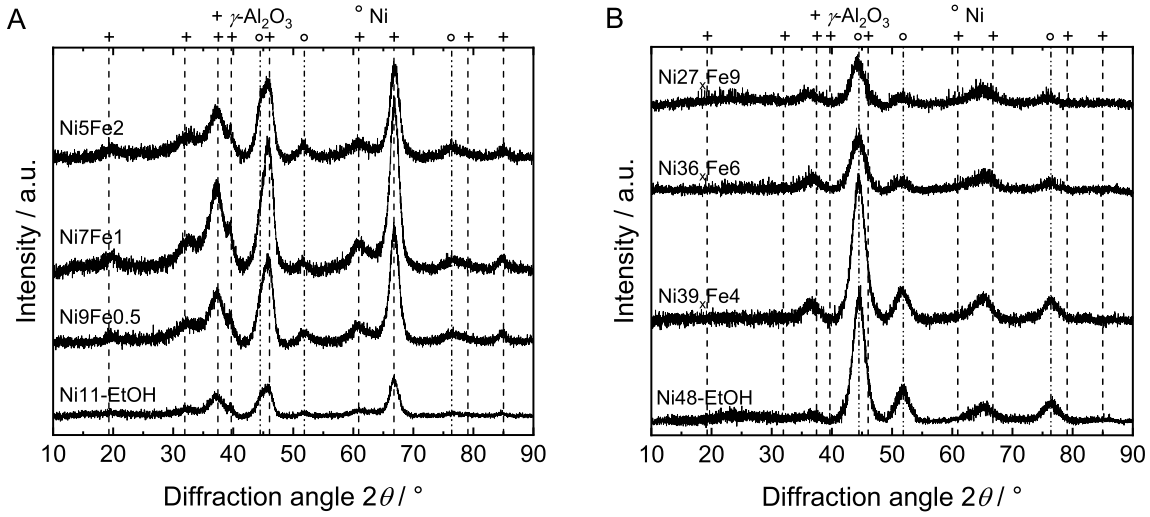


**Figure 6.4:** XRD patterns of the Ni11-EtOH reference catalyst as well as the $Ni/Al_2O_3$-derived Fe-doped catalyst samples after activation (A) and the $Ni48_x$-EtOH reference catalyst as well as the $NiAlO_x$-derived Fe-doped catalyst samples after activation (B) (Ni ICCD 96-901-3002, $\gamma$-$Al_2O_3$ JCPDS 10-0475).

$Ni/Al_2O_3$-EtOH and 3.4 nm for $Ni48_x$-EtOH. It needs to be mentioned that this low particle diameter for the co-precipitated catalyst is close to the application limit of the Scherrer equation, but nevertheless is consistent with particle size distributions obtained by transmission electron microscopy studies in literature [136, 203].

The catalyst samples are not reduced quantitatively. While the remaining NiO species seem to be X-ray amorphous or too little to be detected by XRD for Ni11-EtOH in Figure 6.4 A, their presence in $Ni48_x$-EtOH is still evident from Figure 6.4 B. Albeit the reflections caused by the NiO-rich mixed oxide shift towards alumina during reduction (*cf.* Figure 6.4 B, reflections at $2\theta$ = 36 and 66°), which indicates the partial removal of $Ni^{2+}$ during catalyst activation, some $Ni^{2+}$ remains in this freshly formed crystalline $Al^{3+}$-rich oxide phase, since its changed reflection signal still does not meet the reflection positions of $\gamma$-$Al_2O_3$.

For all Fe-promoted samples, no distinct reflexes caused by Fe species can be observed in the XRD patterns. However, with increasing Fe loading, for both the catalysts derived from the $Ni/Al_2O_3$ (*cf.* Figure 6.4 A) and the $NiAlO_x$ (*cf.* Figure 6.4 B) template catalysts, shifts of the 111, 200, and 220 fcc Ni reflexes to lower diffraction angles can be observed. The corresponding increase of the lattice constant $a$ can be explained by the insertion of Fe atoms into the crystal lattice of fcc Ni, effectively leading to the formation of ($\gamma$Fe,Ni) alloy particles [253]. The bulk composition of the alloy particles can be estimated by line profiling and comparison to tabulated values [310]. From the step width, an absolute error of 0.7 % can be assumed for $x_{Fe}$, detailed data is given in Table 6.9. While for Ni9Fe0.5 the bulk of the particles only contains 2.5 at.% Fe, the Fe content stepwise increases to 4 at.% for Ni7Fe1 and 8 at.% for Ni5Fe2. Comparison to the overall $n_{Ni}/n_{Fe}$ ratios in the catalyst (*cf.* Table 6.2) shows that the $n_{Ni}/n_{Fe}$ ratio in the bulk alloy particles is significantly higher, which suggests that the majority of Fe atoms is located on the outer surface in vicinity to or on top of the Ni-rich ($\gamma$Fe,Ni) particles, in the form of a Ni-Fe

surface alloy or $Fe^{2+}$, not contributing to the alloy formation in the bulk of the particles.

A similar picture is found for the catalysts derived from the $NiAlO_x$ template catalyst. However, the degree of bulk alloying is significantly higher. For $Ni39_xFe4$, the bulk of the ($\gamma$Fe,Ni) particles contains 11 at.% Fe, which further increases to 15.5 at.% for $Ni36_xFe6$ and 21 at.% for $Ni27_xFe9$. The molar Ni/Fe ratios in the particles are much closer to the overall $n_{Ni}/n_{Fe}$ ratios listed in Table 6.2. These observations suggest that for the $NiAlO_x$-derived (co-precipitated) catalysts Ni-Fe alloy formation under reductive conditions (500 °C, $H_2$) seems to be preferred compared to $Ni/Al_2O_3$-derived (precipitated) catalysts, which might be caused by particle size effects or different stabilization of the particles on the oxidic phases.

### 6.3.4 Paramagnetic/Ferromagnetic Resonance Spectroscopy

A further indicator for the composition of the metal particles on the reduced catalysts is the change of the magnetic properties resolved by paramagnetic/ferromagnetic resonance spectroscopy (FMR). All activated catalyst samples show spectra, line intensities, and thermomagnetic behavior typical for ferromagnetic particles, but with varying parameters for the different iron contents. These differences in the magnetizations ($I_{rel}$), $\Delta B_{pp}$, shift of $g$ values, or anisotropy of the FMR spectra are described in the literature by variations of the Ni particle size and interactions with the support or adsorbed molecules [287, 289, 290].

Ni11-EtOH (*cf.* Figure 6.13 A) features a significantly higher anisotropy (at $T$ = 133 K) of the FMR spectrum compared to $Ni48_x$-EtOH (*cf.* Figure 6.14 A). For Ni5Fe2 (*cf.* Figure 6.13 B), a severe impact of Fe can be observed. The anisotropy of the FMR spectrum, evident from the decrease of $\Delta B_{pp}$ (at 133 K, *cf.* Figure 6.13 C) is significantly reduced, while the magnetization ($I_{rel}$) increases. This behavior can be explained by the interference of the ferromagnetic characteristics of Ni and metallic Fe, possibly by Fe atoms located on the surface of Ni particles.

The drastic changes of the ferromagnetic characteristics between the activated $Ni48_x$-EtOH (*cf.* Figure 6.13 A) and $Ni27_xFe9$ (*cf.* Figure 6.14 B) are absolutely analogous to the co-precipitated Ni-Fe-Al catalyst (*cf.* Chapter 4) and can only be explained by a substantial ferromagnetic contribution of metallic Fe and the assumption of the formation of Ni-Fe alloy particles. This is reflected by the strong increase of all relevant criteria as anisotropy of the FMR spectra and $\Delta g$, of magnetization ($I_{rel}$), and $\Delta B_{pp}$ (at 133 K, *cf.* Figure 6.14 C) for $Ni27_xFe9$ and is reported in detail in Chapter 4 (and literature cited therein) and in Section 6.5.4.

### 6.3.5 Catalyst Reducibility

Figure 6.5 A illustrates the TPR profiles for the $Ni/Al_2O_3$-derived catalysts, Figure 6.5 B the ones of the $NiAlO_x$-derived catalysts. For $Ni/Al_2O_3$, a broad asymmetric reduction signal ranging from 360 to 760 °C, caused by two overlapping reduction peaks centered at 520 and 615 °C, respectively, and a shoulder at 780 °C can be observed. The peak at 520 °C can be

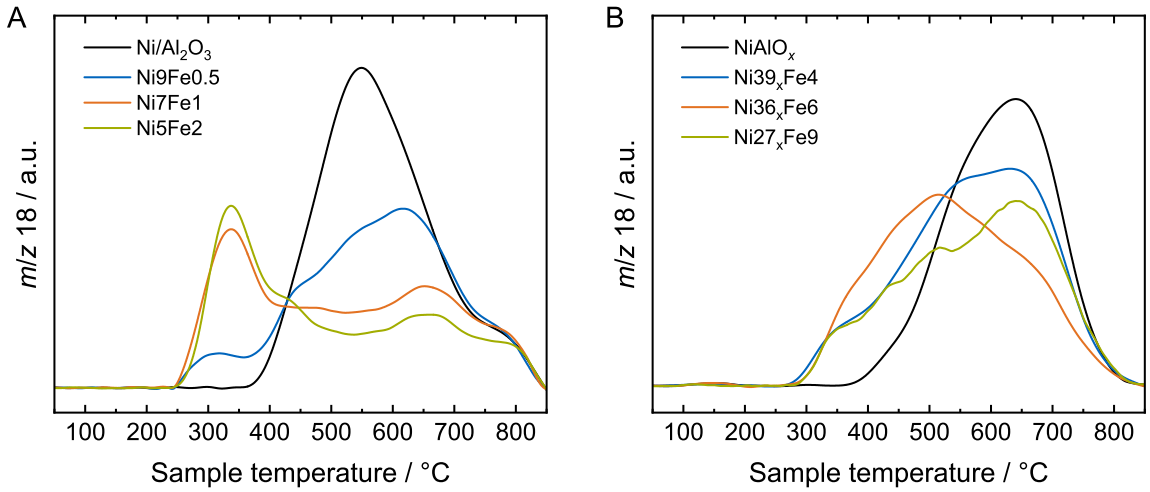


**Figure 6.5:** TPR profiles of the $Ni/Al_2O_3$ template catalyst as well as the $Ni/Al_2O_3$-derived Fe-doped catalyst samples (A) and the $NiAlO_x$ template catalyst as well as the $NiAlO_x$-derived Fe-doped catalyst samples (B).

attributed to the reduction of $Ni^{2+}$ weakly interacting with $\gamma$-$Al_2O_3$, while the peak centered at 615 °C is supposed to be caused by the reduction of $Ni^{2+}$ that more strongly interacts with $\gamma$-$Al_2O_3$ [94]. The third, high-temperature peak at 780 °C indicates the presence of $Ni^{2+}$ possibly captured in a spinel-like structure [104]. Thereby, the presence of such $Ni^{2+}$ species seems to be limited to the catalyst surface, as significant amounts of bulk spinel formation can be excluded on the basis of XRD shown in Figure 6.3. The $NiAlO_x$ template catalyst features three reduction signals. The small low-temperature signal at $T$ = 150 °C has previously been assigned to $Ni^{3+}$ in the outer layers of the catalyst structure [253]. In addition, two overlapping high temperature signals can be observed. The larger reduction signal centered at 585 °C originates from the reduction of $Al^{3+}$-containing NiO, while the smaller signal at higher temperature (680 °C) is caused by the reduction of $Ni^{2+}$ incorporated in the $Al^{3+}$-rich oxide phase [137, 315, 316].

For all Fe-doped catalysts, clear signals that can be assigned to the stepwise reduction of $Fe^{3+}$ to Fe can be found. This suggests that the SRR-modified catalysts get re-oxidized in the degassing step by $NO_3^-$, that probably forms the counter ion of $Fe^{2+}$ species located near the perimeter of the metal particles, but also indicates the presence of metallic Fe on the catalysts after reduction at 500 °C. The reduction of $Fe^{3+}$ on the Fe-promoted $Ni/Al_2O_3$-derived catalysts occurs in the temperature range between 250 to 500 °C. The first peak centered at 330 °C corresponds to the reduction of $Fe^{3+}$ to $Fe^{2+}$, the shoulder at 420 °C marks the reduction of $Fe^{2+}$ to $Fe^0$. The reduction signals of Fe are superimposed by the three reduction signals of NiO previously discussed and increase with rising Fe loading.

Similar observations can be made for the Fe-doped $NiAlO_x$-derived catalysts. The shoulders at 350 and 410 °C can be attributed to the reduction of $Fe^{3+}$ and $Fe^{2+}$, respectively. The reduction peaks, however, are further superimposed by the reduction of $Ni^{2+}$ from the Ni-rich Ni-Al mixed oxide, that is shifted to lower temperature with decreasing Ni loading. The decrease

of the reduction signal from $Ni36_xFe6$ to $Ni27_xFe9$ is caused by the decrease in Ni loading, superimposing the reduction signal of $Fe^{3+}$.

## 6.3.6 Catalyst Sorption Properties

### 6.3.6.1 $N_2$ Physisorption

The catalysts derived from the precipitated $Ni/Al_2O_3$ template catalysts feature type IV $N_2$ adsorption isotherms with H2 hysteresis loops. The BET surface area amounts to $182\,m^2\,g_{cat}^{-1}$ for the Ni11-EtOH reference catalyst. With increasing Fe content, the BET surface area stepwise increases to a maximum of $198\,m^2\,g_{cat}^{-1}$ for Ni5Fe2 (*cf.* Table 6.3, index 1: before aging). The pore diameter first stays constant at 7.8 nm, but increases to 8.6 nm for Ni5Fe2. At the same time, for Ni5Fe2 a slightly increased pore volume ($0.43\,mL\,g_{cat}^{-1}$ compared to 0.39 to $0.40\,mL\,g_{cat}^{-1}$) is observed. Despite the approach of a mild drying process (*cf.* Section 6.2.1), this increase in porosity can be attributed to the rapid evolution of $NO_x$ during degassing after the surface redox reaction inside the pores, which may lead to further pore formation or rupture of small pores. The amount of $NO_x$ released during the degassing step (which is proportional to the Fe loading) can be correlated to the increase of the BET surface area and the pore volume.

The BET surface areas of the hydrotalcite-derived catalysts are significantly higher. For the reference $Ni48_x$-EtOH catalyst, a BET surface area of $263\,m^2\,g_{cat}^{-1}$ is obtained. For all Fe-modified catalysts, the BET surface area stays constant at $300\,m^2\,g_{cat}^{-1}$. The lower BET surface area of $Ni48_x$-EtOH can be explained by the difference in the processes occurring during the thermal pre-treatments. While the Fe-modified catalyst samples are re-oxidized during the degassing by $NO_2$ as stated above, $Ni48_x$-EtOH stays in its reduced state. In the second reduction treatment, $Ni48_x$-EtOH seems to undergo some aging, leading to a decrease of the specific BET surface area. For the Fe-modified catalysts, in contrast, the mixed oxide phase is reconstructed during oxidation, and re-reduction leads to a similar BET surface area as obtained after the first reduction step. In accordance with this hypothesis, the specific BET surface area of the $NiAlO_x$ template catalyst after the first reduction amounts to $300\,m^2\,g_{cat}^{-1}$. This indicates that (a) Fe does not have an influence on the structural characteristics of the oxidic phase after catalyst activation and that (b), within the investigated range, the $n_{Ni}/n_{Al}$ ratio, which decreases with increasing Fe loading from $Ni48_x$-EtOH to $Ni27_xFe9$ according to Table 6.2, does not have a significant impact on the porosity and the characteristics of the oxidic phase after reduction.

In summary, the results from material characterization are in line with the proposed pathway for the surface redox reaction and support the hypothesis that, after catalyst activation, the Fe species interact with the Ni particles rather than with the oxidic phase.

### 6.3.6.2 $H_2$ Chemisorption

The metal surface area determined by $H_2$ chemisorption is set equal to the Ni surface area (*cf.* Table 6.3, index 1: before aging), since $H_2$ adsorption on Fe can be neglected under the chosen

conditions [253, 254]. $H_2$ adsorption at a recommended temperature of 200 °C to account for exposed Fe atoms [255], moreover, resulted in significant $H_2$ spill-over, making the determination of the metal surface area impossible. Moreover, CO chemisorption could not be applied, since the adsorption stoichiometry of CO on Fe is known to be structure-dependent [255, 256] and therefore *a priori* unknown.

For Ni11-EtOH, a Ni surface area of 7.7 $m^2\ g_{cat}^{-1}$ is found. With increasing Fe loading, the Ni surface area decreases, reaching a minimum of 2.3 $m^2\ g_{cat}^{-1}$ for Ni5Fe2. This trend is consistent with the $NiAlO_x$-derived catalyst samples. The very high Ni surface area of $Ni48_x$-EtOH ($S_{Ni}$ = 42.5 $m^2\ g_{cat}^{-1}$) strongly decreases with the introduction of Fe as a function of Fe loading. $Ni27_xFe9$ features a Ni surface area of 8.2 $m^2\ g_{cat}^{-1}$. Based on this trend, three major conclusions can be drawn: first, the samples prepared from the co-precipitated $NiAlO_x$ template catalyst show much higher Ni surface areas compared to the classical supported $Ni/Al_2O_3$-based catalysts, which has its reason in the unique characteristics of the hydrotalcite-derived oxide, leading to the stabilization of small Ni particles even at high Ni loadings [203]. Second, with increasing Fe loading, also the amount of Fe species exposed on the surface, blocking $H_2$ adsorption sites on Ni, is likely to increase for each template catalyst. This trend in the $H_2$ adsorption capacity is a typical feature for Ni-Fe alloy particles [253] and therefore consistent with the presence of ($\gamma$Fe,Ni) nanoparticles supported by XRD and FMR. Analogous findings were made for co-precipitated Ni-Fe-Al catalysts for a $n_{Ni}/n_{Fe}$ ratio > 6 (*cf.* Chapter 4 and 5). Finally, the effect of Fe on the Ni surface area is consistent with the assumption that the Fe atoms were deposited in the neighborhood of the Ni sites during the surface redox reaction.

#### 6.3.6.3 $CO_2$ Chemisorption and Temperature-Programmed Desorption

The surface basicity of the catalyst materials as well as the $CO_2$ binding strength are important parameters in catalyst development for the activation of $CO_2$. Especially medium basic sites were proposed to play an important role in $CO_2$ processing under the assumption of an associative $CO_2$ methanation pathway *via* hydrogenation of $CO_2$ adsorbed on the support material at the particle-support interphase [128]. In this study, the overall $CO_2$ uptake of the catalysts is determined by static $CO_2$ chemisorption, while the binding strength and basic site distribution is investigated by $CO_2$-TPD. It should be mentioned that the total $CO_2$ uptake does not completely match the uptake determined by $CO_2$-TPD, since some of the weakly adsorbed $CO_2$, which is accounted for in static chemisorption experiments, is already removed during the initial purging step prior to the TPD. As shown in Table 6.3, the total $CO_2$ uptake for the catalysts derived from $Ni/Al_2O_3$ is approx. 230 µmol $g_{cat}^{-1}$, independent from the Fe loading. Since the total $CO_2$ uptake primarily mirrors the $CO_2$ adsorbed basic sites of the oxidic phase, this is a hint that Fe species do not modify the surface basicity of the $Al_2O_3$ support, but rather interact with the Ni particles in accordance with XRD, FMR, and $H_2$ chemisorption.

Figure 6.6 A illustrates the corresponding temperature-programmed desorption patterns for the $Ni/Al_2O_3$-derived catalysts. Four $CO_2$ desorption signals can be distinguished: $CO_2$ bound to

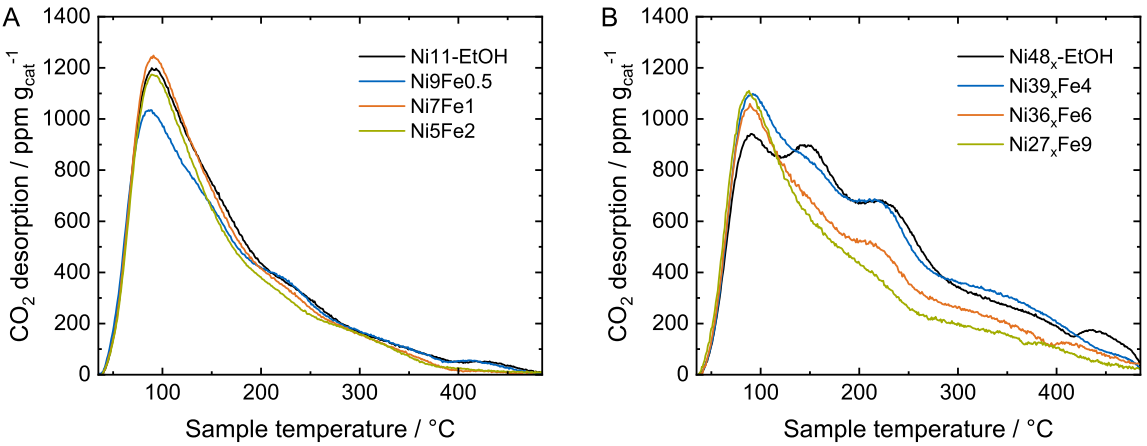


**Figure 6.6:** $CO_2$-TPD patterns of the Ni11-EtOH reference catalyst as well as the $Ni/Al_2O_3$-derived Fe-doped catalyst samples (A) and the $Ni48_x$-EtOH reference catalyst as well as the $NiAlO_x$-derived Fe-doped catalyst samples (B).

weak basic sites (peak centered at 90°), $CO_2$ bound to medium basic sites as bidentate carbonate (maximum desorption peak at 150 °C) and monodentate carbonate (desorption peak at 225 °C) as well as $CO_2$ adsorbed on strong basic sites in the form of "organic-like" carbonates with the maximum desorption signal at 320 °C (*cf.* [270]). The disturbed desorption signal at 390 to 410 °C stems from a negative contribution of $CO_2$ oxidizing the surface of the metal particles, leading to CO formation.

Within the error range, the TPD patterns of the Fe-doped $Ni/Al_2O_3$-derived catalysts are very similar, which is especially true for the distribution of basic sites. The majority of $CO_2$ is bound as bicarbonate on weak basic sites. With decreasing Ni loading, the density of monodentate carbonate sites slightly decreases. The formation of these basic sites is known to be promoted by remaining $Ni^{2+}$ in the catalyst structure [141]. The declining density of these sites therefore may go hand in hand with the decrease of $Ni^{2+}$ remaining unreduced during catalyst activation with increasing Fe loading due to the surface redox reaction.

The $CO_2$ adsorption characteristics of the $NiAlO_x$-derived catalysts depicted in Figure 6.6 B, in contrast, differ significantly. For the reference $Ni48_x$-EtOH, the total $CO_2$ uptake is 261 µmol $g_{cat}^{-1}$. Rising Fe loading and decreasing Ni loading then result in a decrease of the $CO_2$ uptake, reaching a minimum of 167 µmol $g_{cat}^{-1}$ for $Ni27_xFe9$. This behavior can be explained from the $CO_2$ desorption patterns in Figure 6.6 B. For the $Ni48_x$-EtOH reference catalyst, four distinct $CO_2$ desorption signals can be found. With increasing Fe loading, one can observe a stepwise decrease of the medium and strong basic sites, while the density of weak basic sites increases only slightly. As stated above, $Ni^{2+}$ is known to be responsible for the formation of medium and strong basic sites on $AlO_x$. With an increasing degree of Ni replacement by the introduction of Fe during the surface redox reaction, the effective $n_{Ni}/n_{Al}$ ratio in the mixed oxide phase after catalyst activation continuously decreases with rising Fe loading, effectively leading to a lower density of medium and strong basic sites. The binding strength of $CO_2$ on those sites, however, seems to be unaffected. The decrease of the total $CO_2$ uptake capacity for

the hydrotalcite-derived catalysts therefore can be considered as an artifact from the surface redox reaction and is supposed to be caused by the decreasing $n_{Ni}/n_{Al}$ ratio rather than a detrimental effect of Fe.

### 6.3.7 Catalyst Performance

The activity for $CO_2$ methanation was determined under integral as well as under differential conditions. Figure 6.7 illustrates the $CO_2$ conversion vs. temperature characteristics ($S_1$) for the catalysts derived from the precipitated Ni/$Al_2O_3$ (A) and the co-precipitated $NiAlO_x$ (B) catalysts. For all catalysts, thermodynamic equilibrium gas composition is achieved at 400 °C. All catalysts exhibited excellent selectivity towards methane formation (*cf.* Figure 6.16 and 6.17). For the Ni/$Al_2O_3$-based catalysts, the maximum selectivities to $C_2H_6$ (0.4 %), $C_3H_8$ (0.1 %), and CO (2.8 %) were found at approx. 50 % $CO_2$ conversion. Due to their higher activity, for the catalysts based on $NiAlO_x$, the maximum selectivities (also in the $CO_2$ conversion range from 50 to 60 %) were 0.9 % towards $C_2H_6$, 0.2 % towards $C_3H_8$ and 2.5 % towards CO, merely independent from the Fe content of the catalyst.

To compare the activities of the catalysts under integral conditions, the characteristic temperature necessary to obtain a $CO_2$ conversion of 50 % can be evaluated. Based on this consideration, the activity rises in the order Ni11-EtOH (321.7 °C) < Ni9Fe0.5 (320.9 °C) < Ni7Fe1 (317.5 °C) < Ni5Fe2 (311.9 °C). This order is opposed to the trends of both the Ni loading (*cf.* Table 6.2) and the Ni surface area (*cf.* Table 6.3). Moreover, since properties like the $CO_2$ uptake/basic site density and $CO_2$ binding strength as well as the characteristics of the $Al_2O_3$ support stay constant, this trend can only be explained by the effect of the Fe promoter on the active sites during $CO_2$ methanation in accordance with the theory of ($\gamma$Fe,Ni) nanoparticle formation. Fe may tune the C-O dissociation ability of the active sites, as found in computational

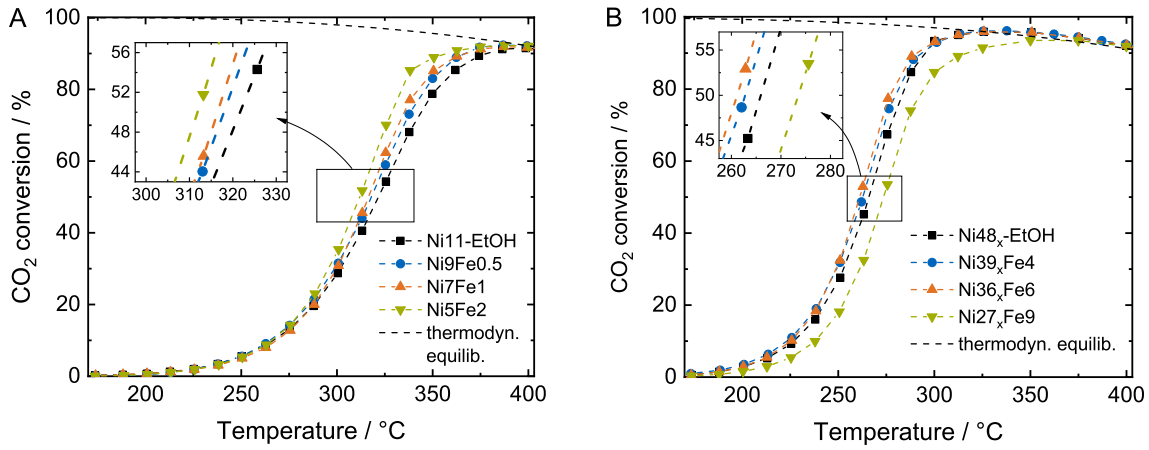


**Figure 6.7:** $CO_2$ conversion vs. temperature plots for the Ni11-EtOH reference catalyst as well as the Ni/$Al_2O_3$-derived Fe-doped catalyst samples (A) and for the $Ni48_x$-EtOH reference catalyst as well as the $NiAlO_x$-derived Fe-doped catalyst samples (B).

analyses based on a Brønsted-Evans-Polanyi approach on the most active nanoparticle step sites by Andersson *et al.* for CO methanation [148, 154] and $CO_2$ methanation [154]. Thereby, it is assumed, in agreement to the general opinion in literature, that the cleavage of the C-O bond (hydrogen-assisted or *via* direct C-O dissociation) is the rate-determining step in the methanation reaction [24, 148, 154, 180]. Their investigations are limited to the assumption of a constant bulk composition of the nanoparticles, which, however, may undergo changes under aging conditions.

Interestingly, the behavior under differential conditions suggests a different trend. As shown in Table 6.3, the apparent activation energy increases with rising Fe loading from 72.5 kJ mol$^{-1}$ for Ni11-EtOH to 76.9 kJ mol$^{-1}$ for Ni7Fe1 and 84.0 kJ mol$^{-1}$ for Ni5Fe2, which is a clear indicator for the modification of the active sites by the introduction of Fe. The unexpected coupling of a rising activity despite an increasing apparent activation energy can be explained by a distinct compensation effect [317]. The increase in the apparent activation energy can thereby be caused by an increase of the change of the entropy of the transition complex according to Eyring's theory [318, 319], or, more likely, by the simultaneous occurrence of $CO_2$ methanation on surface centers that involve different activation energies. In the latter case, the determination of the activation energy based on the Arrhenius equation would then yield an average activation energy over all active sites.

The catalytic activities of the $NiAlO_x$ derived catalysts can be explained in a similar manner. The activity under integral conditions rises in the order $Ni27_xFe9$ (273.5 °C) < $Ni48_x$-EtOH (265.9 °C) < $Ni39_xFe4$ (262.8 °C) < $Ni36_xFe6$ (261.2 °C). For $Ni27_xFe9$, obviously, the beneficial effect of the Fe promoter can no longer compensate the decrease of the Ni surface area and the $CO_2$ uptake due to the loss of medium basic sites, which are characteristics that were proved to be essential for high methanation activity over co-precipitated catalysts [134]. This effectively leads to a decrease of catalyst activity. A picture similar to $Ni/Al_2O_3$ can be drawn when evaluating the activity behavior under differential conditions. Here, the apparent activation energy increases from 75.5 kJ mol$^{-1}$ for $Ni48_x$-EtOH to 85.6 kJ mol$^{-1}$ for $Ni36_xFe6$ and 89.7 kJ mol$^{-1}$ for $Ni27_xFe9$. It is noteworthy that, compared to the $Ni/Al_2O_3$-derived catalysts, the activation energies of the $NiAlO_x$-derived catalysts for a constant $n_{Ni}/n_{Fe}$ molar ratio seem to be systematically increased by approx. 4 kJ mol$^{-1}$, which might have its reason in different characteristics of the nanoparticles depending on the synthesis procedure. Wright *et al.* [263], for example, showed that in reduced co-precipitated Ni-Al catalysts Al, possibly in the form of $(AlO_2)^-$ [265], may be incorporated in the nanoparticles, forming a paracrystalline Ni phase, which might modify the properties compared to crystalline Ni. At this point, it should be mentioned that the calculation of *TOF* values to compare the intrinsic activities of the catalysts was omitted since the number of active sites could not be determined (*cf.* Section 6.3.6.2).

### 6.3.8 Stability of the Catalysts under Aging Conditions

To test the stability of the catalysts under harsh methanation conditions at high temperature and elevated pressure, the catalysts were subjected to an aging treatment in thermodynamic equilibrium at 500 °C and 8 bar for a duration of 32 h. To evaluate the activity after the aging treatment and to resolve data on catalyst stability, thereafter the $CO_2$ conversion vs. temperature characteristics were recorded again ($S_2$).

Figure 6.8 A–D illustrates the $CO_2$ conversion vs. temperature characteristics before and after the aging treatment for the catalysts derived from the precipitated $Ni/Al_2O_3$ catalyst. With increasing Fe loading, the curve recorded after aging is shifted further to higher temperatures. The difference between the characteristic temperatures necessary to obtain a $CO_2$ conversion of 50 % , $\Delta T$ ($X(CO_2)$ = 50 %), can serve as a measure for the apparent stability of the catalyst. $\Delta T$ increases from 18.3 K for Ni11-EtOH to 23 K for Ni9Fe0.5, 25.7 K for Ni7Fe1, and 30.8 K for Ni7Fe2. The reference catalyst Ni11-EtOH is the most stable one, and the apparent stability decreases the higher the Fe loading.

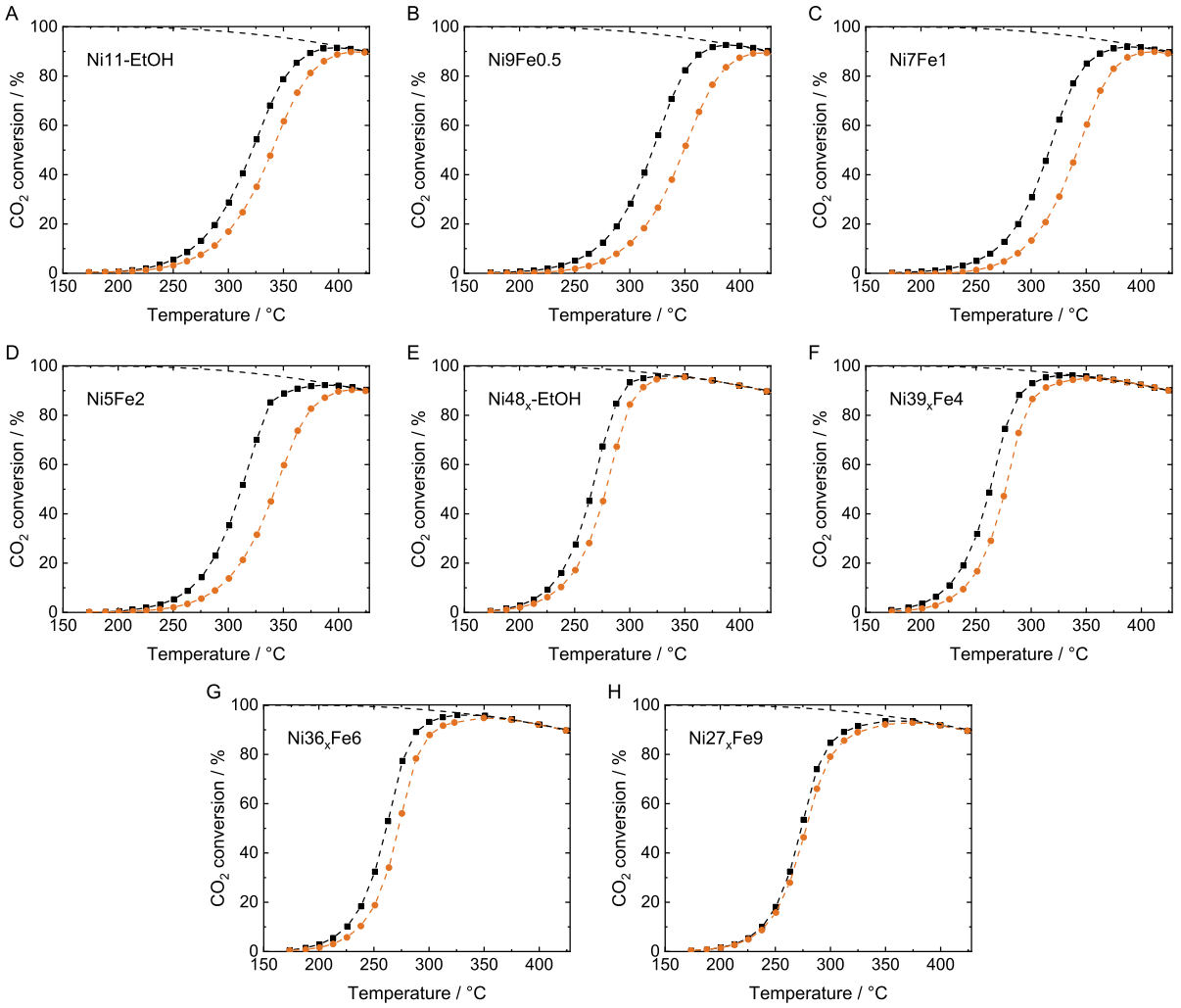


**Figure 6.8:** $CO_2$ conversion vs. temperature plots for the $Ni/Al_2O_3$- (A-D) and $NiAlO_x$-based (E-G) catalysts before (black squares) and after aging (orange circles).

The material properties after aging are listed in Table 6.3 (index 2: after aging). The $CO_2$ uptakes after aging are in the same order of magnitude and range from 119 µmol $g_{cat}^{-1}$ for Ni11-EtOH to 135 µmol $g_{cat}^{-1}$ for Ni7Fe1. The BET surface areas decrease to approx. 146 $m^2$ $g_{cat}^{-1}$ for all catalysts, while the total pore volumes stay approximately constant. The mean pore diameter increases to 10.9 nm for all catalysts. As shown in Table 6.3, for all $Ni/Al_2O_3$-based catalysts, the Ni surface area decreases significantly during aging. The decrease amounts to 75 % for Ni11-EtOH and Ni9Fe0.5, 70 % for Ni7Fe1, and 60 % for Ni5Fe2.

At the same time, evaluation of the XRD patterns after reduction reveals that the bulk composition of the (γFe,Ni) particles is altered during aging, leading to a slightly higher degree of alloying. For these samples, the molar Ni/Fe ratio in the Ni-Fe alloy after aging is closer to the total molar $n_{Ni}/n_{Fe}$ ratio, which is shown in Table 6.2. For Ni9Fe0.5, the alloy contains 4.5 at.% Fe (previously 2.5 at.%), for Ni7Fe1 6 at.% (previously 4 at.%), while it increases from 8 at.% to 10.5 at.% for Ni5Fe2. The activation energies stay approximately constant; one could, however, suspect a small decrease at high Fe loadings. By a slightly higher degree of alloying, the surface concentration of the Fe-modified active sites might decrease (extent increasing with rising Fe loading), effectively leading to a decrease of the activity after aging, opposite to the trend in initial activity of the Fe-doped $Ni/Al_2O_3$-based catalysts.

The catalysts derived from the precipitated $NiAlO_x$ catalysts (*cf.* Figure 6.8 E-H) feature a significantly different behavior. The differences of the characteristic temperatures necessary for 50 % $CO_2$ conversion before and after aging amount to 12.6 K for $Ni48_x$-EtOH, 13.9 K for $Ni39_xFe4$, 11.0 K for $Ni36_xFe6$, and 4.4 K for $Ni27_xFe9$. Similar to the $Ni/Al_2O_3$-based catalyst, the properties of the oxidic phase, BET surface area (approx. 125 $m^2$ $g_{cat}^{-1}$) and the total $CO_2$ uptake (approx. 125 $m^2$ $g_{cat}^{-1}$) decrease to the same values for all catalysts. The loss of Ni surface area ascribed to sintering can be calculated to 56 % for $Ni48_x$-EtOH. For $Ni39_xFe4$, it amounts to 56 %, 53 % for $Ni36_xFe6$, and only 24 % for $Ni27_xFe9$. The change in Ni surface area can be ascribed to two different effects: first, particle sintering may occur, as evident from the increase of the (γFe,Ni) crystallite size shown in Table 6.3, but also to a redistribution of the Fe centers on the metal surface, blocking or releasing $H_2$ adsorption sites on Ni. The bulk composition of the (γFe,Ni) particles undergoes significant changes during aging: for the Fe-containing $NiAlO_x$-based catalysts, the Ni/Fe ratios within the bulk alloy decrease. XRD analysis suggests that after the aging treatment the bulk of the (γFe,Ni) alloy particles contains 6.5 at.% Fe in $Ni39_xFe4$ (previously 11 at.%), 9 at.% Fe in $Ni36_xFe6$ (previously 15.5 at.%), and 11 at.% Fe in $Ni27_xFe9$ (previously 21 at.%), which can be interpreted as partial de-alloying of the metal particles [320].

To confirm the effect of the aging treatment on the composition of the metal particles, FMR was exemplarily carried out on the aged $Ni27_xFe9$ catalyst. The aging procedure led to clear changes in the ferromagnetic characteristics, reflected in particular by a strong decrease in anisotropy

**Table 6.3:** Material characterization data and apparent activation energies, determined before (1) and after aging (2).

| Catalyst | $S_{Ni}$ / $m^2\ g_{cat}^{-1}$ | | $d_C^a$ / nm | | $U(CO_2)$ / $\mu mol\ g_{cat}^{-1}$ | | $S_{BET}$ / $m^2\ g_{cat}^{-1}$ | | $V_{Pore}$ / $mL\ g_{cat}^{-1}$ | | $d_p$ / nm | | $E_{A,app}$ / $kJ\ mol^{-1}$ | |
|---|---|---|---|---|---|---|---|---|---|---|---|---|---|---|
| | 1 | 2 | 1 | 2 | 1 | 2 | 1 | 2 | 1 | 2 | 1 | 2 | 1 | 2 |
| *Precipitated template catalyst $Ni/Al_2O_3$* | | | | | | | | | | | | | | |
| Ni11-EtOH | 7.7 | 1.9 | 5.2 | 6.4 | 230 | 119 | 182 | 146 | 0.40 | 0.39 | 7.7 | 10.9 | $72.5 \pm 0.6$ | $73.1 \pm 0.2$ |
| Ni9Fe0.5 | 7.3 | 1.8 | 4.8 | 5.4 | 228 | 129 | 186 | 149 | 0.41 | 0.39 | 7.8 | 10.9 | $74.5 \pm 0.5$ | $75.4 \pm 0.3$ |
| Ni7Fe1 | 5.2 | 1.6 | 4.5 | 5.2 | 227 | 135 | 192 | 145 | 0.41 | 0.42 | 7.8 | 10.9 | $76.9 \pm 1.9$ | $76.5 \pm 1.0$ |
| Ni5Fe2 | 2.3 | 0.9 | 4.4 | 5.5 | 234 | 132 | 199 | 146 | 0.44 | 0.41 | 8.6 | 10.9 | $84.0 \pm 3.1$ | $80.2 \pm 1.1$ |
| *Co-precipitated template catalyst $NiAlO_x$* | | | | | | | | | | | | | | |
| $Ni48_x$-EtOH | 42.5 | 18.6 | 3.4 | 4.2 | 216 | 129 | 263 | 127 | - | - | - | - | $75.7 \pm 0.6$ | $76.3 \pm 1.0$ |
| $Ni39_xFe4$ | 25.9 | 11.2 | 3.4 | 4.5 | 255 | 123 | 300 | 129 | - | - | - | - | $81.6 \pm 0.5$ | $81.6 \pm 1.8$ |
| $Ni36_xFe6$ | 22.2 | 10.5 | 3.9 | 4.5 | 220 | 126 | 300 | 127 | - | - | - | - | $85.6 \pm 0.8$ | $89.7 \pm 1.5$ |
| $Ni27_xFe9$ | 8.2 | 6.2 | 4.1 | 4.4 | 167 | 122 | 300 | 123 | - | - | - | - | $89.7 \pm 1.4$ | $97.1 \pm 0.3$ |

1 before aging. 2 after aging.

[a] determined from the Ni, ($\gamma$Fe,Ni) diffraction reflex at $2\theta$ = 51.5 to 51.8° by the Scherrer equation (*cf.* Eq. 3.4).

($\Delta B_{pp}$) and $\Delta g$ of the main component, while a remaining background indicates residual Ni-Fe alloyed particles. The ferromagnetic contribution of iron is clearly reduced indicating de-alloying and possibly partial oxidation of Fe. Due to the complex interactions of metal particle sintering (*cf.* Table 6.3), particle composition, as well as possible changes of metal particle shape and particle stabilization effects on the oxidic phase over aging, however, conclusive statements or interpretations are not possible at the current state.

In accordance with the change in the alloy bulk composition over aging, differences in the apparent activation energies can be observed. While the apparent activation energy is constant for $Ni48_x$-EtOH and $Ni39_xFe4$, where the influence of Fe, in line with studies using co-precipitated Ni-Fe-Al catalysts (*cf.* Chapter 4), might be too low, it increases by 4.1 kJ mol$^{-1}$ for $Ni36_xFe6$ and 7.4 kJ mol$^{-1}$ for $Ni27_xFe9$ over the aging treatment. These drastic changes once more indicate the presence of a compensation effect, caused by the change in the concentrations of exposed Fe sites due to dynamic variation of the ($\gamma$Fe,Ni) bulk composition under aging conditions. At the same time, the segregation process may lead to (a) the generation of new active sites and (b) a decrease in the sintering rate of the Ni sites, resulting in an improved apparent catalyst stability. A decisive statement on the exact composition of the active sites and the role of possible $Fe^{2+}$ formation [320] during the segregation process, however, cannot be made.

Detailed time-resolved studies on catalyst activity as a function of aging time, coupled with detailed material characterization under inert conditions to further resolve structure-activity relationships are carried out in Chapter 7. With respect to this, it should be noted that the selectivities towards $CH_4$ or any of the by-products remained merely unchanged over aging, which is an indicator that no isolated Fe clusters on the catalyst surface were formed caused by the (partial) segregation of Ni-Fe during aging (*cf.* Figure 6.17).

### 6.3.9 Effect of Catalyst Aging on ($\gamma$Fe,Ni) Nanoparticle Composition and Fe Surface Enrichment on the Catalytic Activity

It can be concluded that, depending on the nature of the oxidic phase, the composition of the ($\gamma$Fe,Ni) nanoparticles can undergo changes under harsh methanation conditions. These modifications influence the nature and the number of active sites, leading to (a) differences in catalyst activity and (b) changes of the (apparent) stability under methanation conditions. Within the investigated $n_{Ni}/n_{Fe}$ range, a high surface concentration of exposed Fe atoms, either for the freshly activated catalyst or by (partial) segregation of a Ni-Fe alloy, leads to an enhancement of the catalytic activity of the material. This increase in activity is accompanied by an increase in the apparent activation energy, caused by the modification of the active sites.

In fact, for each state, a relation between the apparent activation energy and the bulk ($\gamma$Fe,Ni) nanoparticle composition can be found, which is depicted in Figure 6.9. With increasing Fe

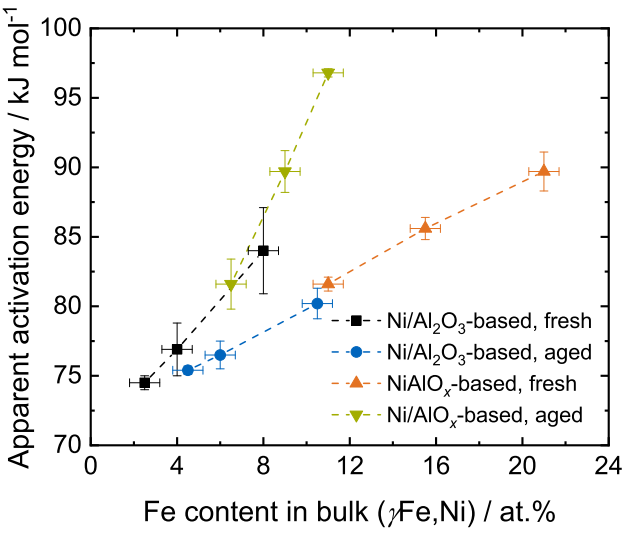


**Figure 6.9:** Trend of the apparent activation energy with ($\gamma$Fe,Ni) bulk composition. Dashed lines are a guide to the eye.

content in ($\gamma$Fe,Ni), the apparent activation energy rises for both the $Ni/Al_2O_3$- and the $NiAlO_x$-based catalysts. The (partial) segregation of the Ni-Fe particles during aging of the $NiAlO_x$-based catalysts leads to an increase of Fe sites on the surface and consequently to an increase of the apparent activation energy.

## 6.4 Conclusion

The surface redox reaction was successfully applied to selectively dope metallic Ni centers with Fe on a classical supported $Ni/Al_2O_3$ catalyst prepared by deposition-precipitation and a co-precipitated $NiAlO_x$ catalyst. Activity and (apparent) catalyst stability were found to strongly depend on the surface concentration of Fe species on alloyed ($\gamma$Fe,Ni) nanoparticles formed after catalyst activation.

For the $Ni/Al_2O_3$-derived catalysts, an increase of the catalytic activity with increasing Fe loading was found, but aging revealed a decrease of the (apparent) stability under methanation conditions, possibly caused by a slightly deeper degree of alloying after aging. For the $NiAlO_x$-derived catalysts, in contrast, a substantial enhancement of the apparent thermal stability upon an aging treatment with increasing Fe loading was found, linked to the (partial) segregation of the previously alloyed Ni-Fe particles. For all catalysts containing Fe in considerate amounts ($n_{Ni}/n_{Fe}$ approx. 6), a distinct compensation effect regarding the apparent activation energy was observed, strongly dependent on the surface concentration of Fe and most likely caused by the simultaneous occurrence of the methanation reactions over different active sites.

Further studies will focus on the time resolution of the deactivation behavior and modification of the aging conditions to decouple sintering and de-alloying effects. Material characterization

studies under inert conditions at different states of deactivation may contribute to further elucidate the structure of the active sites on the (partly) deactivated Fe-promoted $NiAlO_x$ catalysts. Besides the surface redox reaction technique, also organometallic approaches may allow to draw a comprehensive picture of the deactivation behavior of Fe-promoted Ni-Al catalysts.

## 6.5 Supplementary Material

### 6.5.1 Experimental Setup, Activity, and Stability Measurements

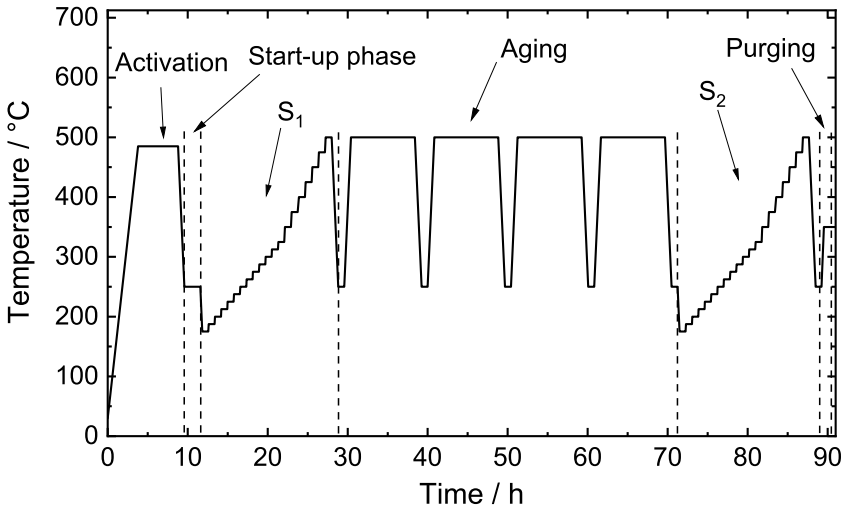


**Figure 6.10:** Temperature program for catalyst reduction and testing.

Conditions:

- Activation: $Q = 60\,\mathrm{NL\,g_{cat}^{-1}\,h^{-1}}$, $H_2$, $t = 5\,\mathrm{h}$, $5\,\mathrm{K\,min^{-1}}$
- Start-up phase: $Q = 150\,\mathrm{NL\,g_{cat}^{-1}\,h^{-1}}$, $Ar/H_2/CO_2 = 5/4/1$, $p = 8\,\mathrm{bar}$
- $S_1$: $Q = 150\,\mathrm{NL\,g_{cat}^{-1}\,h^{-1}}$, $Ar/H_2/CO_2 = 5/4/1$, $p = 8\,\mathrm{bar}$
- Aging: $Q = 150\,\mathrm{NL\,g_{cat}^{-1}\,h^{-1}}$, $Ar/H_2/CO_2 = 5/4/1$, $p = 8\,\mathrm{bar}$
- $S_2$: $Q = 150\,\mathrm{NL\,g_{cat}^{-1}\,h^{-1}}$, $Ar/H_2/CO_2 = 5/4/1$, $p = 8\,\mathrm{bar}$
- Purging: $Q = 60\,\mathrm{NL\,g_{cat}^{-1}\,h^{-1}}$, Ar, $t = 1\,\mathrm{h}$, $p = 1\,\mathrm{bar}$

### 6.5.2 Scanning Transmission Electron Microscopy / Energy-Dispersive X-ray Analysis

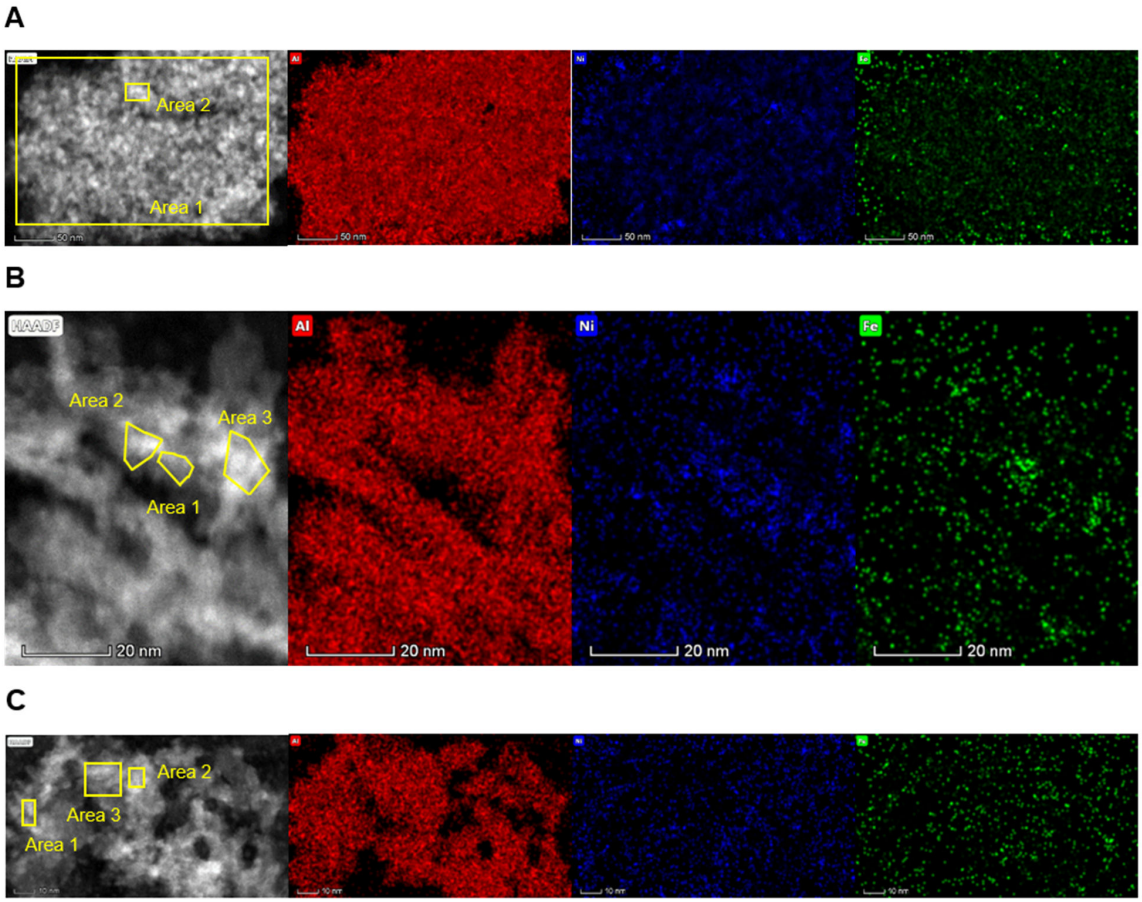


**Figure 6.11:** STEM-EDX images of Ni5Fe2 catalyst: HAADF image, atomic distributions of Al (red), Ni (blue), and Fe (green).

**Table 6.4:** Fractions determined by EDX from STEM images for Figure 6.11 A.

| Catalyst | Atomic fraction / % | Atomic error / % | Mass fraction / % | Mass error / % | Fit error / % |
|---|---|---|---|---|---|
| *Area 1* | | | | | |
| O | 61.40 | 7.44 | 46.77 | 3.43 | 0.44 |
| Al | 31.59 | 7.32 | 35.57 | 7.49 | 0.67 |
| Ni | 5.81 | 1.05 | 14.80 | 2.25 | 0.24 |
| Fe | 1.21 | 0.22 | 2.86 | 0.43 | 0.50 |
| *Area 2* | | | | | |
| O | 60.40 | 6.81 | 43.44 | 2.99 | 1.17 |
| Al | 28.63 | 6.51 | 30.44 | 6.36 | 0.84 |
| Ni | 19.41 | 1.64 | 22.63 | 3.40 | 1.22 |
| Fe | 1.56 | 0.28 | 3.49 | 0.55 | 5.24 |

**Table 6.5:** Fractions determined by EDX from STEM images for Figure 6.11 B.

| Catalyst | Atomic fraction / % | Atomic error / % | Mass fraction / % | Mass error / % | Fit error / % |
|---|---|---|---|---|---|
| *Area 1* | | | | | |
| O | 69.83 | 8.23 | 58.74 | 4.37 | 2.43 |
| Al | 27.30 | 6.30 | 33.79 | 7.17 | 3.17 |
| Ni | 1.43 | 0.44 | 4.00 | 1.17 | 24.98 |
| Fe | 1.44 | 0.43 | 3.74 | 1.06 | 23.99 |
| *Area 2* | | | | | |
| O | 66.51 | 7.71 | 53.47 | 3.83 | 1.47 |
| Al | 28.89 | 6.61 | 34.33 | 7.21 | 1.45 |
| Ni | 3.74 | 0.69 | 10.05 | 1.61 | 5.52 |
| Fe | 0.86 | 0.22 | 2.14 | 0.52 | 19.29 |
| *Area 3* | | | | | |
| O | 62.69 | 8.89 | 51.89 | 4.52 | 0.85 |
| Al | 35.66 | 8.68 | 43.64 | 9.43 | 1.37 |
| Ni | 1.18 | 0.24 | 3.27 | 0.56 | 6.41 |
| Fe | 0.47 | 0.11 | 1.20 | 0.25 | 13.94 |

**Table 6.6:** Fractions determined by EDX from STEM images for Figure 6.11 C.

| Catalyst | Atomic fraction / % | Atomic error / % | Mass fraction / % | Mass error / % | Fit error / % |
|---|---|---|---|---|---|
| *Area 1* | | | | | |
| O | 65.77 | 8.08 | 53.37 | 4.05 | 1.57 |
| Al | 30.49 | 71.0 | 36.58 | 7.75 | 1.91 |
| Ni | 3.21 | 0.62 | 8.72 | 1.45 | 6.54 |
| Fe | 0.53 | 0.20 | 1.33 | 0.49 | 33.67 |
| *Area 2* | | | | | |
| O | 66.88 | 8.48 | 56.02 | 4.40 | 1.41 |
| Al | 31.13 | 7.31 | 38.54 | 8.21 | 1.90 |
| Ni | 1.29 | 0.29 | 3.61 | 1.73 | 13.28 |
| Fe | 0.70 | 0.21 | 1.83 | 0.51 | 23.44 |
| *Area 3* | | | | | |
| O | 66.46 | 8.31 | 55.10 | 4.26 | 1.41 |
| Al | 30.90 | 7.23 | 37.87 | 8.05 | 1.89 |
| Ni | 1.18 | 0.27 | 3.27 | 0.68 | 14.13 |
| Fe | 1.46 | 0.32 | 3.76 | 0.73 | 11.85 |

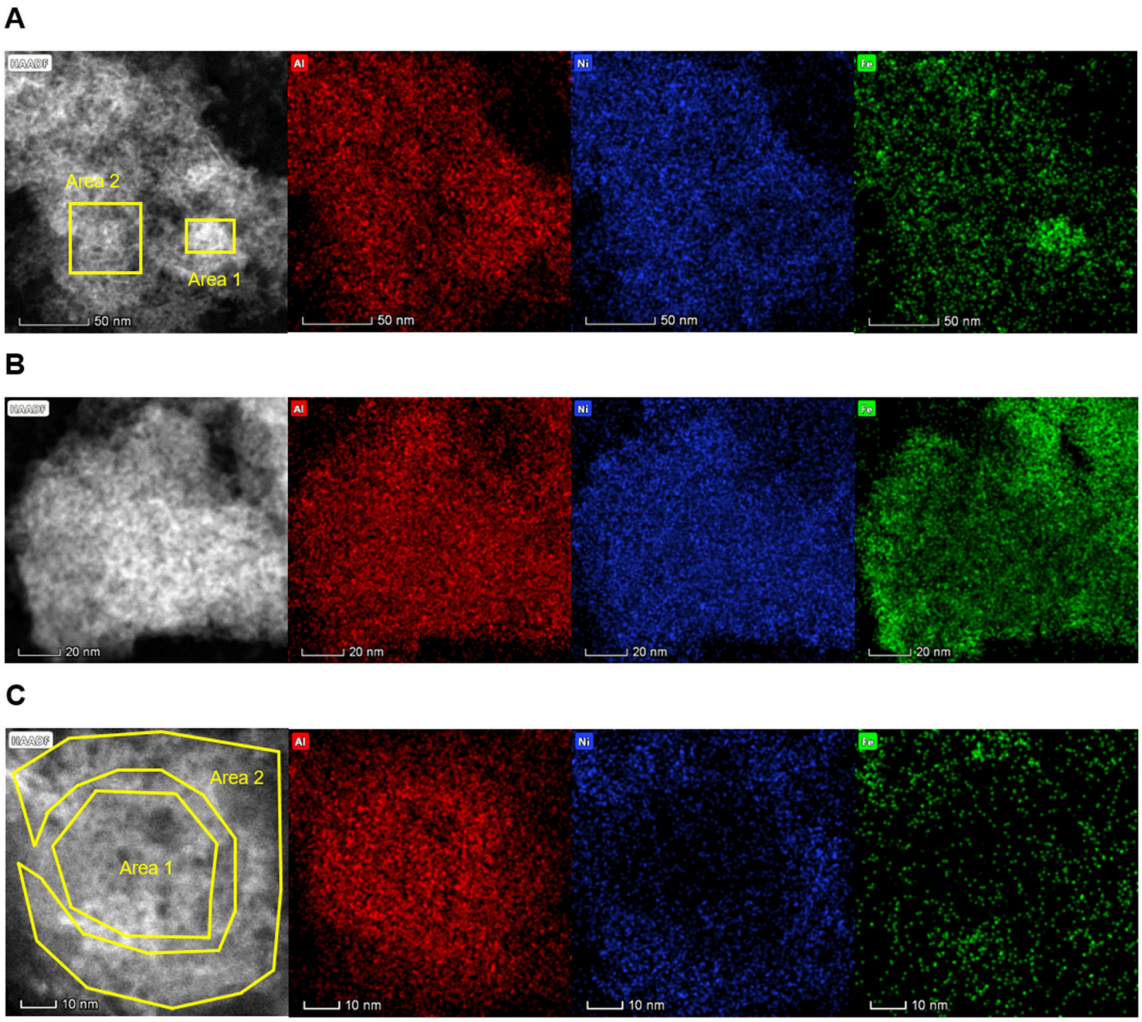


**Figure 6.12:** STEM-EDX images of $Ni27_xFe9$ catalyst: HAADF image, atomic distributions of Al (red), Ni (blue), and Fe (green).

**Table 6.7:** Fractions determined by EDX from STEM images for Figure 6.12 A.

| Catalyst | Atomic fraction / % | Atomic error / % | Mass fraction / % | Mass error / % | Fit error / % |
|---|---|---|---|---|---|
| *Area 1* | | | | | |
| O | 61.68 | 5.60 | 41.80 | 2.33 | 0.85 |
| Al | 21.44 | 4.66 | 21.48 | 4.41 | 1.15 |
| Ni | 7.53 | 1.22 | 17.07 | 2.48 | 1.79 |
| Fe | 9.34 | 1.51 | 19.64 | 2.85 | 1.78 |
| *Area 2* | | | | | |
| O | 61.23 | 5.94 | 40.58 | 2.46 | 0.82 |
| Al | 21.04 | 4.63 | 20.62 | 4.26 | 0.73 |
| Ni | 14.56 | 2.40 | 32.37 | 4.72 | 0.50 |
| Fe | 3.17 | 0.52 | 6.52 | 0.96 | 1.43 |

**Table 6.8:** Fractions determined by EDX from STEM images for Figure 6.12 C.

| Catalyst | Atomic fraction / % | Atomic error / % | Mass fraction / % | Mass error / % | Fit error / % |
|---|---|---|---|---|---|
| *Area 1* | | | | | |
| O | 61.18 | 8.71 | 49.75 | 4.32 | 0.36 |
| Al | 36.39 | 8.86 | 43.75 | 9.45 | 1.00 |
| Ni | 1.87 | 0.37 | 5.10 | 0.81 | 1.41 |
| Fe | 0.56 | 0.11 | 1.40 | 0.23 | 3.38 |
| *Area 2* | | | | | |
| O | 64.61 | 6.59 | 47.87 | 2.98 | 0.68 |
| Al | 25.53 | 5.67 | 27.96 | 5.79 | 0.82 |
| Ni | 8.25 | 1.39 | 20.46 | 3.01 | 0.51 |
| Fe | 1.61 | 0.27 | 3.70 | 0.55 | 1.41 |

### 6.5.3 X-ray Diffraction Analysis: Composition of ($\gamma$Fe,Ni) Nanoparticles

**Table 6.9:** Atomar particle composition of fresh and aged catalysts according to the 200 reflection position, estimated absolute error of $x_{Fe}$ based on $\Delta 2\theta$/step = 0.015°: ±0.7 at.%.

| Catalyst | fresh | | | | aged | | | |
|---|---|---|---|---|---|---|---|---|
| | $2\theta$ / ° | $a$ / Å | $x_{Fe}$ / at.% | Ni/Fe / - | $2\theta$ / ° | $a$ / Å | $x_{Fe}$ / at.% | Ni/Fe / - |
| *Precipitated template catalyst $Ni/Al_2O_3$* | | | | | | | | |
| Ni9Fe0.5 | 51.82 | 3.525 | 2.5 | 39 | 51.76 | 3.530 | 4.5 | 21.2 |
| Ni7Fe1 | 51.78 | 3.528 | 4 | 24 | 51.73 | 3.531 | 6 | 15.7 |
| Ni5Fe2 | 51.70 | 3.533 | 8 | 11.5 | 51.66 | 3.536 | 10.5 | 8.5 |
| *Co-precipitated template catalyst $NiAlO_x$* | | | | | | | | |
| $Ni39_xFe4$ | 51.63 | 3.538 | 11 | 8.1 | 51.71 | 3.533 | 6.5 | 14.4 |
| $Ni36_xFe6$ | 51.56 | 3.542 | 15.5 | 5.5 | 51.68 | 3.535 | 9 | 10.1 |
| $Ni27_xFe9$ | 51.47 | 3.548 | 21 | 3.8 | 51.64 | 3.537 | 11 | 8.1 |

### 6.5.4 Paramagnetic/Ferromagnetic Resonance Spectroscopy

As stated in Section 4.2.2.10, for the Fe-doped catalyst, the significance of intensities/magnetizations measured below 273 K are of limited value due to substantial integrated intensity at zero field for X-band frequency. The spectra and magnetic data derived have been compared to the calcined catalysts (before reduction) with (potentially) ferromagnetic properties. The oxidized samples showed at least two orders of magnitudes lower magnetizations (integrated intensities) and magnetic anisotropies clearly different from the Ni and Ni-Fe systems. Thus, their contribution to the ferromagnetic resonance spectra of the reduced catalysts can be neglected for these particular samples. The thermomagnetic curves of the pure Ni alumina catalyst qualitatively

agree well with those reported for metallic Ni nanoparticles supported on (diamagnetic) oxides [286–288]. The FMR spectra after activation are illustrated in Figure 6.13 A for the Ni11-EtOH reference catalyst and Figure 6.13 B for Ni5Fe2. Figure 6.13 C compares the $\Delta B_{pp}$ values for both catalysts reflecting the changes in the magnetic anisotropy. The corresponding characteristics for $Ni48_x$-EtOH and $Ni27_xFe9$ are shown in Figure 6.14. Figure 6.15 shows the FMR spectra and the $\Delta B_{pp}$ values as a function of recording temperature for the aged $Ni27_xFe9$ catalyst.

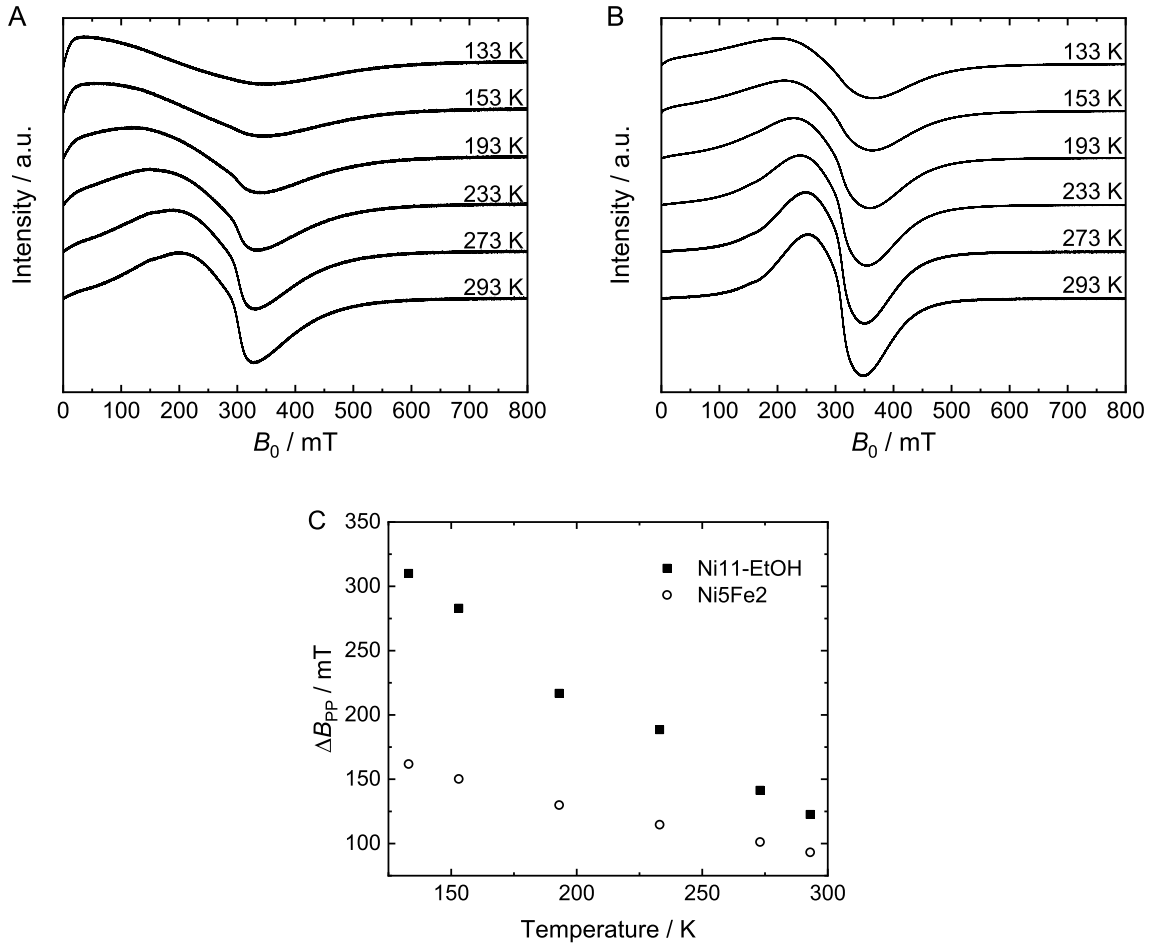


**Figure 6.13:** EPR/FMR spectra of the catalysts Ni11-EtOH (A) and Ni5Fe2 (B) after activation; $\Delta B_{pp}$ values for both catalysts as function of the recording temperature (C).

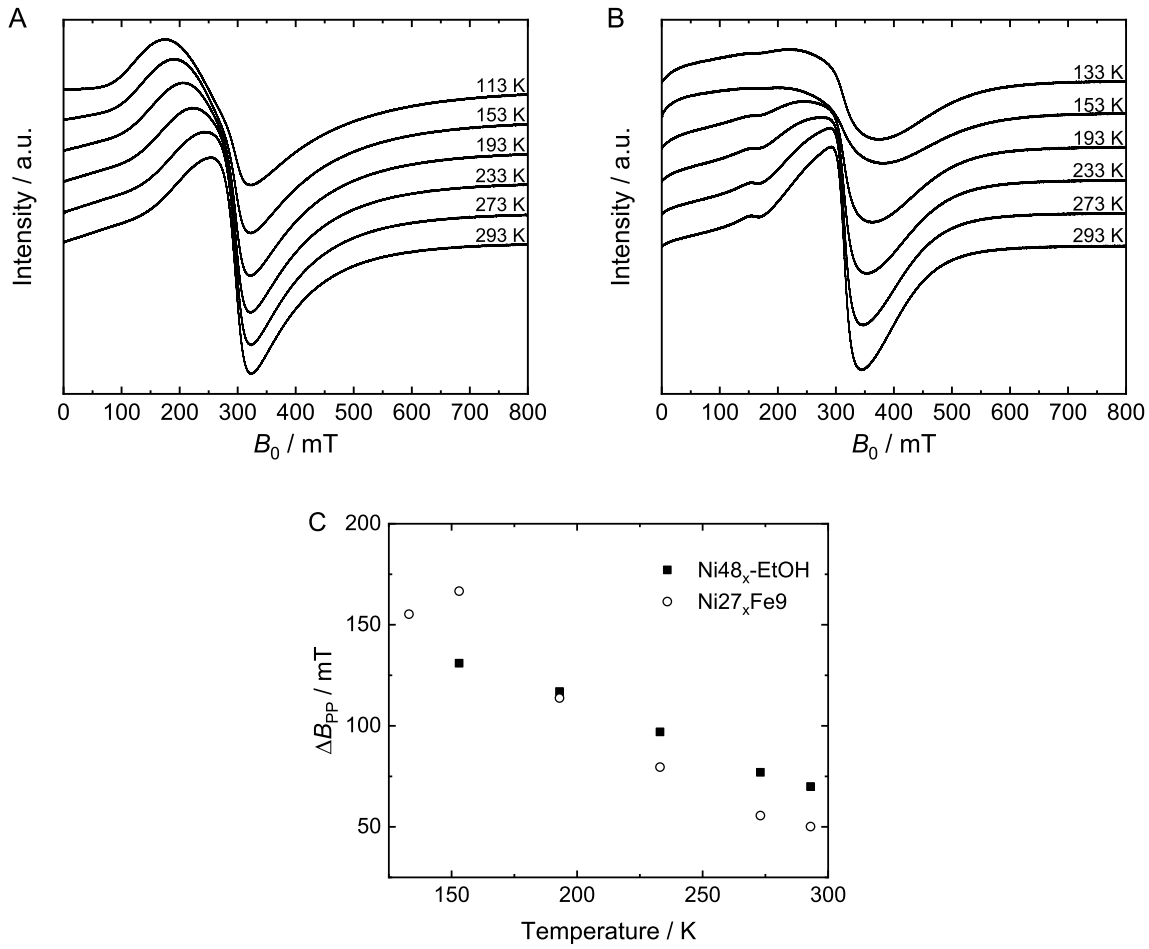


**Figure 6.14:** EPR/FMR spectra of the catalysts Ni48$_x$-EtOH (A) and Ni27$_x$Fe9 (B) after activation; $\Delta B_{pp}$ values for both catalysts as function of the recording temperature (C).

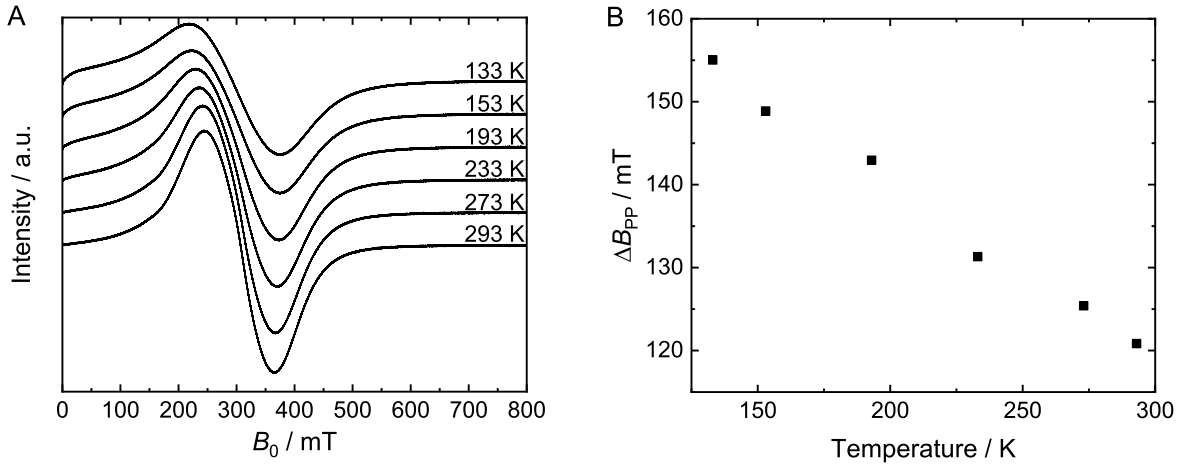


**Figure 6.15:** EPR/FMR spectra (A) and $\Delta B_{pp}$ values as function of the recording temperature (B) for Ni27$_x$Fe9 after aging (500 °C, 8 bar, 32 h, Ar/$H_2$/$CO_2$ = 5/4/1).

### 6.5.5 Byproduct Formation

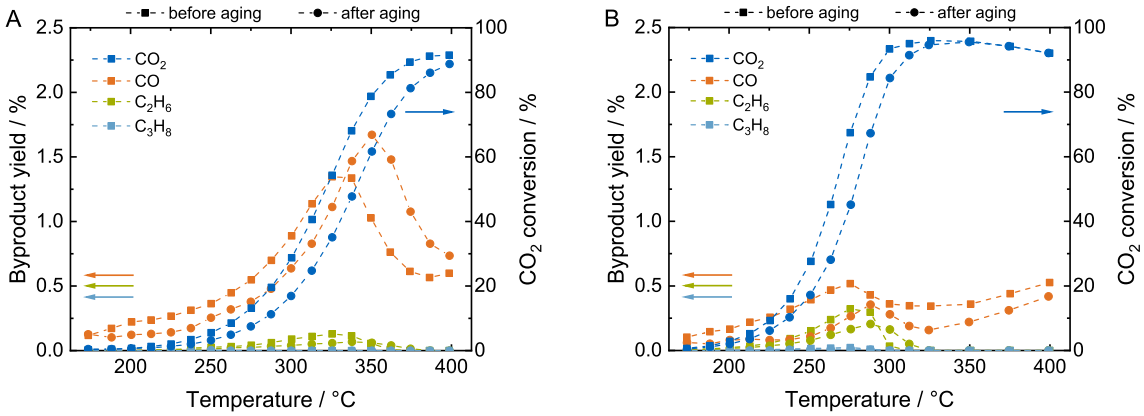


**Figure 6.16:** $CO_2$ conversion and yields of $C_2H_6$, $C_3H_8$, and CO for Ni11-EtOH (A) and $Ni48_x$-EtOH (B).

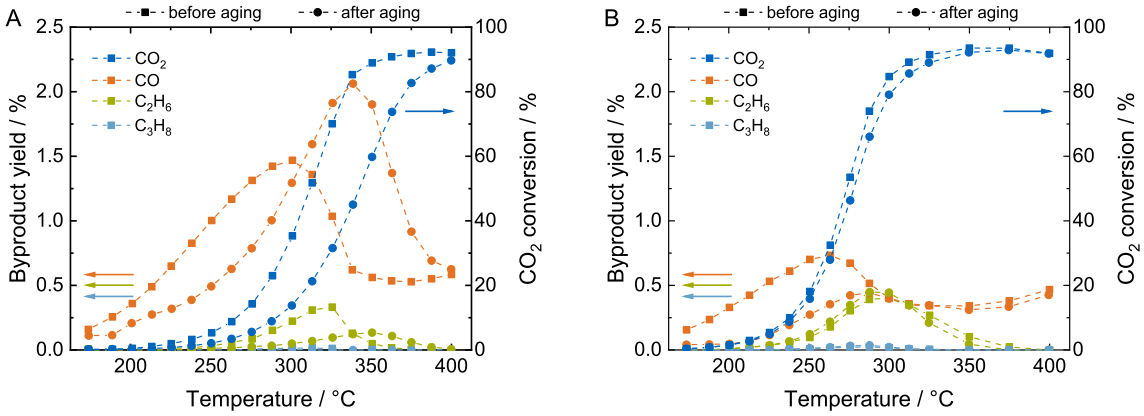


**Figure 6.17:** $CO_2$ conversion and yields of $C_2H_6$, $C_3H_8$, and CO for Ni5Fe2 (A) and $Ni27_xFe9$ (B).

# 7 Enhanced Activity of Co-Precipitated $NiFeAlO_x$ in $CO_2$ Methanation by Segregation and Oxidation of Fe

This chapter was published in similar form in

T. Burger, S. Ewald, A. Niederdränk, O. Hinrichsen, Enhanced activity of co-precipitated $NiFeAlO_x$ in $CO_2$ methanation by segregation and oxidation of Fe, *Applied Catalysis A: General*, 2020, *604*, 117778, DOI 10.1016/j.apcata.2020.117778



## Abstract

Commercial application of the $CO_2$ methanation reaction demands for the development of catalysts that feature an enhanced stability under hydrothermal reaction conditions to increase catalyst lifetime. By time-resolved aging studies, it is shown that the improved deactivation resistance of co-precipitated $NiFeAlO_x$ catalysts compared to $NiAlO_x$ is obtained by a temporal increase of the intrinsic catalytic activity of $NiFeAlO_x$, provoked by aging at elevated temperature and pressure in thermodynamic equilibrium. Detailed structural characterization of freshly reduced and aged catalysts resolves that aging triggers the partial segregation of ($\gamma$Fe,Ni) nanoparticles initially formed during catalyst activation, accompanied by the oxidation of Fe. Thereby, the intrinsic catalytic activity increases, which can be explained by the generation of redox-active $Fe^{2+}$ sites that offer an additional reaction pathway for $CO_2$ activation. The deactivation behavior of a $NiFeAlO_x$ catalyst can be described by a superimposition of activity increase related to $Fe^{2+}$ site formation and activity decrease due to the loss of active sites by particle and oxide phase sintering.

## 7.1 Introduction

As one of the key technologies in the power-to-gas process, the methanation reaction of $CO_2$ has been brought up as a possible approach to generate substitute natural gas (SNG), which can be stored in the existing natural gas grid and used for power generation on demand [241]. Therein, surplus energy from renewables is used for hydrogen production by water electrolysis, which is then reacted with $CO_2$, e.g. stemming from conventional power plants based on fossils, to form SNG.

Since the $CO_2$ methanation reaction is accompanied by volume contraction, it is usually carried out at elevated pressure to achieve high yields of $CH_4$ in thermodynamic equilibrium.

$$CO_2 + 4\,H_2 \rightleftharpoons CH_4 + 2\,H_2O \quad \Delta_R H^o = -165.1\,kJ\,mol^{-1} \quad \Delta_R G^o = -113.5\,kJ\,mol^{-1} \qquad (7.I)$$

Ni [87, 303, 321], Ru [306, 322], and Rh [60, 306] have been reported to be active in catalyzing $CO_2$ methanation. Most often, Ni-based catalysts are applied for reasons of metal cost and availability [85]. Besides, Ni features a very high selectivity towards $CH_4$ formation (*cf.* [24, 296, 323] and Chapters 4 to 6. Commonly utilized promoters to enhance the activity of Ni-based catalysts are $CeO_2$ [71, 91], $ZrO_2$ [71], $La_2O_3$ [99] and $MnO_x$ (*cf.* [94, 99, 324] and Chapter 4 and 5). Moreover, beneficial effects of Fe promotion on catalyst activity have been reported [150–152, 161], but the reasons for this effect have not been fully understood yet. Increased reducibility [149], improved metal-support interactions, and optimization of the CO dissociation energy by electronic effects [151, 161], caused by the formation of Ni-Fe alloy particles (*cf.* [109, 150, 152] and Chapter 4, 5, and 6) have been suggested to explain this phenomenon. The experimentally observed activity enhancement has also been confirmed in computational studies [154]. Despite the known activity of Fe and Ni-Fe in the Fischer-Tropsch reaction [108], in most studies no significant negative impact of Fe on the selectivity towards $CH_4$ formation has been observed for $n_{Ni}/n_{Fe}$ ratios higher than 2 (*cf.* [154, 161] and Chapter 4). Mutz *et al.* [152], however, experienced significant CO selectivities (up to 30 %) at $CO_2$ conversions less than 20 % over a 17 % $Ni_3Fe$ catalyst prepared by deposition-precipitation.

Fe has also been tested as active component in the methanation reactions. Vannice *et al.* [77] compared the specific activities of different $Al_2O_3$-supported catalysts in CO methanation and found a higher specific activity of $Fe/Al_2O_3$ compared to $Ni/Al_2O_3$. However, at a $CH_4$ selectivity of about 70 %, significant hydrocarbon byproduct formation was observed, and the high specific activity of Fe resulted from a very low metal surface area. Kirchner *et al.* [325] studied various iron oxide catalyst samples in $CO_2$ methanation and found that, depending on feed gas composition and iron oxide modification, $CO_2$ methanation is accompanied by carbonization of Fe. The catalytic activity of $\gamma$-$Fe_2O_3$ was ascribed to $\gamma$-$Fe_3C$ and $\chi$-$Fe_5C_2$ build-up. Yet, strong CO formation was accompanied with the carbonization process; at a *GHSV* of 30 000 $h^{-1}$, the selectivity to $CH_4$ was between 8 to 20 %, decreasing with rising *GHSV*. $Fe_5C_2$ formation in plain Fe (oxide) catalysts under methanation conditions was also found in [326, 327].

The highly exothermal character of the $CO_2$ methanation reaction leads to a demand for highly thermostable catalysts to resist deactivation phenomena caused by hotspot formation in industrial fixed-bed application. Hotspot formation leads to rapid establishment of thermodynamic equilibrium gas composition due to the high reaction rate, resulting in high steam contents that may further promote (irreversible) changes of catalyst structure and deactivation. For Ni-Al-based catalyst systems, possible deactivation phenomena may comprise hydrothermal sintering of Ni crystallites [134] as well as modification of the alumina phase [134, 248]. In addition, for alloyed bimetallic catalysts, surface segregation and/or partial oxidation of the metals under reaction conditions may occur [328].

Besides the increase of the methanation activity, in Chapter 4 it was shown that Fe doping enhances the apparent stability of co-precipitated $NiAlO_x$ catalysts, with an optimum promoter effect at a $n_{Ni}/n_{Fe}$ ratio around 5. Moreover, the promoter effect of Fe selectively doped on the Ni sites on a classical supported $Ni/Al_2O_3$ and a co-precipitated $NiAlO_x$ catalyst were compared by introducing the surface redox reaction method for $CO_2$ methanation catalysts. In Chapter 6 it was illustrated that apparent thermal stability of co-precipitated $NiAlO_x$ depends on the composition of the active Ni-Fe nanoparticles and the dynamic change of elemental metal particle composition over aging. Kim *et al.* [320] and Theofanidis *et al.* [329] found that Fe improves the stability of $Ni/MgAlO_x$ dry reforming catalysts by reducing the C* deposition rate on the active sites *via* a $FeO_x$-Fe redox mechanism, highlighting the distinct dynamics of $FeO_x$ surface species in syngas chemistry. Serrer *et al.* [159] investigated a 17 % $Ni_{3.2}Fe$ catalyst and deduced from experiments under dynamic reaction conditions that Fe protects the Ni sites from oxidation in a $H_2$ dropout scenario.

This chapter deals with the fundamental understanding of the aging behavior of a co-precipitated, highly-loaded, industrial-type $NiFeAlO_x$ catalyst ($n_{Ni}/n_{Fe}/n_{Al}$ = 5.5/1/5.5) by linking detailed and time-resolved characterization studies to kinetic data. To draw conclusions on the improved apparent stability of Fe-doped $NiAlO_x$ catalysts and the underlying structure-activity relationship, the catalysts are thoroughly characterized after certain times on stream without exposure to air. The study gives new insights into the dynamically changing role and working mechanism of the Fe promoter and into structural changes taking place under methanation conditions, as a function of aging time and temperature. It illustrates the dynamics of active sites under reaction conditions and consequences on catalytic activity and may be transferred to similar reactions carried out over Ni-Fe catalysts.

## 7.2 Materials and Methods

### 7.2.1 Catalyst Synthesis

A $NiFeAlO_x$ and a reference $NiAlO_x$ catalyst were prepared from the respective nitrate salts by co-precipitation at pH 9 and 30 °C, using a 1 M mixture of $Na_2CO_3$ and NaOH. The catalysts were prepared similarly to the catalysts in Chapter 4 with a molar $n_{Ni}/n_{Fe}/n_{Al}$ ratio of 5.5/1/5.5. The detailed synthesis procedure can be found in Section 7.5.1. In the following, the two catalysts are referred to as $NiAlO_x$ and $NiFeAlO_x$.

### 7.2.2 Catalyst Characterization

Catalyst composition was determined by inductively coupled plasma-optical emission spectroscopy (ICP-OES). The basic material properties like metal surface area, reducibility, basic site density and distribution, as well as structure and morphology of the two catalysts were evaluated by $H_2$ chemisorption, transmission electron microscopy (TEM), temperature-programmed reduction (TPR), $CO_2$ chemisorption, temperature-programmed desorption of $CO_2$ ($CO_2$-TPD), $N_2$ physisorption, and X-ray powder diffraction (XRD).

To develop an understanding of the promotional effect of Fe on the apparent thermal stability of co-precipitated $NiFeAlO_x$ observed in Chapter 4, the catalysts were subjected to methanation feed gas at the temperature $T_a$ for the time $t_a$ and re-characterized by $H_2$ chemisorption, TEM, $N_2$ physisorption, and $CO_2$ chemisorption. To get specifically insights into the composition of the active metal particles, the catalysts were further characterized by XRD, ferromagnetic/paramagnetic resonance (FMR), and Mössbauer spectroscopy before and after aging. The detailed characterization procedure for each technique is reported in Section 7.5.2.

### 7.2.3 Experimental Setup, Evaluation of Activity, and Catalyst Aging

50 mg of the calcined catalyst with a particle diameter from 150 to 200 µm were thoroughly mixed with 450 mg of purified SiC (ESK) and put into a glass-lined tube reactor with 4 mm diameter. The catalyst bed was fixed by quartz wool plugs and placed in the isothermal zone of a tube furnace. The setup described in [24] and Section 3.3 was used for catalyst testing. A thermocouple was placed in the catalyst bed to track the reaction temperature.

To ensure the catalysts are compared under differential conditions ($X(CO_2) < 15\,\%$) free from influence of thermodynamics (neglection of the backwards reaction), the catalysts were subjected to a well-defined temperature program, which is listed in Table 7.1 and illustrated in Figure 7.6. For activation, the catalyst was heated from room temperature to 485 °C with a linear rate of 2 K min$^{-1}$ in 5 % $H_2$ in Ar (50 mL min$^{-1}$) and held there for 5 h. After cooling down to 230 °C in 5 % $H_2$ in Ar, the initial catalyst activity after reduction was measured under

**Table 7.1:** Variation of process parameters for the determination of catalyst activity and aging.

| | Feed ($H_2/CO_2/Ar$) | $Q$ / NL $g_{cat}^{-1}$ $h^{-1}$ | $T$ / °C | $p$ / bar | $t$ / h |
|---|---|---|---|---|---|
| Activation | 5/0/95 | 130 | 485 | 1 | 5 |
| Activity test | 4/1/75 | 600 | 230–210 | 4 | 1 |
| Aging | 4/1/5 | 18 | 350, 400, 450 | 8 | 0, 6, 40, 72 |

differential reaction conditions at 4 bar and 600 NL $g_{cat}^{-1}$ $h^{-1}$ ($H_2/CO_2/Ar$ = 4/1/75, $GHSV$ = 800 000 $h^{-1}$). These conditions are used as reference point for all kinetic data reported in this chapter. Intra- and inter-particle heat and mass transport limitations were checked to be negligible under these conditions, both experimentally and theoretically (*via* the respective criterion equations [311–313]) (*cf.* Section 7.5.4).

To trigger deactivation processes, the catalyst was heated with a linear rate of 5 K $min^{-1}$ to the respective aging temperature (350, 400, and 450 °C) at 8 bar and held there for 2 h in the initial deactivation treatment and for 4 h in all further aging treatments. To age the whole catalyst bed under $H_2O$- and $CH_4$-rich gas while keeping realistic $H_2/CO_2/Ar$ = 4/1/5 feed gas composition, the space velocity was reduced to 18 NL $g_{cat}^{-1}$ $h^{-1}$ ($GHSV$ = 24 000 $h^{-1}$). In reference experiments at 450 °C, it was checked that under these conditions thermodynamic equilibrium was achieved after approx. 10 % of catalyst bed, so 90 % of the catalyst bed were aged under the same (thermodynamically governed) $H_2O$- and $CH_4$-rich gas composition.

To re-evaluate catalyst activity in the kinetic regime under conditions free from product or equilibrium limitations and to resolve the effect of aging on the intrinsic catalyst activity, the catalyst bed was then cooled back down to 230 °C to the reference point conditions. This procedure was repeated to obtain catalysts aged for 0, 6, 40, and 72 h. The heating and activity measurement procedure were checked to have no notable influence on the aging behavior of the catalyst.

All gases were supplied by Westfalen with a purity of 5.0. Online gas analysis was carried out using an Emerson MTL-4 process gas analyzer (IR for $CO_2$, CO, $CH_4$, and $H_2O$, TCD for $H_2$). Downstream the backpressure regulator, Ar (volume flow $\dot{V}_{dil}$) was dosed to the volume flow $\dot{V}_{in}$ entering or $\dot{V}_{out}$ leaving the reactor, respectively, to obtain an overall volume flow of approx. 500 mL $min^{-1}$ entering the process gas analyzer (PGA). Data points for volume concentrations $x_{PGA}$ for feed and product gas species were taken at steady state conditions (waiting time 45 min, monitored by the PGA) and averaged over the last 150 s (300 data points). To prevent water condensation, all tubing was heated to 200 °C. For Fischer-Tropsch byproduct analysis, a Clarus 580 (PerkinElmer) gas chromatograph equipped with two flame ionization detectors and columns was used. Element balances (C, H, and O) were closed by ±3 %. Volume contraction due to the conversion of 5 moles to 3 moles (*cf.* Reaction 7.I) was taken into account (*cf.* Eq. 7.1 to 7.4). The selectivity $S$ of C-containing products (*cf.* Eq. 7.5) was calculated from their yield $Y$ (*cf.* Eq. 7.2) and the $CO_2$ conversion $X(CO_2)$ (*cf.* Eq. 7.1).

$$X(j) = \frac{\dot{n}_{\text{in}}(j) - \dot{n}_{\text{out}}(j)}{\dot{n}_{in}(j)} = \frac{x_{\text{PGA,in}}(j) \cdot \left(\dot{V}_{\text{in}} + \dot{V}_{\text{dil}}\right) - x_{\text{PGA,out}}(j) \cdot \left(\dot{V}_{\text{out}} + \dot{V}_{\text{dil}}\right)}{x_{\text{PGA,in}}(j) \cdot \left(\dot{V}_{\text{in}} + \dot{V}_{\text{dil}}\right)}, j = \text{CO}_2, \text{H}_2 \tag{7.1}$$

$$Y(i) = \frac{x_{\text{PGA,out}}(i) \cdot \left(\dot{V}_{\text{out}} + \dot{V}_{\text{dil}}\right)}{x_{\text{PGA,in}}(\text{CO}_2) \cdot \left(\dot{V}_{\text{in}} + \dot{V}_{\text{dil}}\right)}, i = \text{CH}_4, \text{CO} \tag{7.2}$$

$$Y(\text{H}_2\text{O}) = 2 \cdot \frac{x_{\text{PGA,out}}(\text{H}_2\text{O}) \cdot \left(\dot{V}_{\text{out}} + \dot{V}_{\text{dil}}\right)}{x_{\text{PGA,in}}(\text{H}_2) \cdot \left(\dot{V}_{\text{in}} + \dot{V}_{\text{dil}}\right)} \tag{7.3}$$

$$\dot{V}_{\text{out}} = \frac{\dot{V}_{\text{in}} \cdot \left(1 + 2 \cdot x_{\text{PGA,in}}(\text{CH}_4)\right) + \dot{V}_{\text{dil}} \cdot \left(2 \cdot x_{\text{PGA,in}}(\text{CH}_4) - 2 \cdot x_{\text{PGA,out}}(\text{CH}_4)\right)}{1 + 2 \cdot x_{\text{PGA,out}}(\text{CH}_4)} \tag{7.4}$$

$$S(k) = \frac{Y(k)}{X(\text{CO}_2)}, k = \text{C}_x\text{H}_y, \text{CO} \tag{7.5}$$

Catalyst activity was tracked *via* the weight time yield of $CH_4$ $WTY(CH_4)(t_a)$, calculated from the differential net production rate of $CH_4$ $\dot{n}(CH_4)(t_a)$ at the reference point according to Eq. 7.6. For better comparison, the $WTY(CH_4)(t_a)$ is normalized to the weight time yield initially obtained after catalyst activation, $WTY(CH_4)(t_a = 0\,\text{h})$.

$$WTY(\text{CH}_4)(t_a) = \frac{\dot{n}(\text{CH}_4)(t_a)}{m_{\text{cat}}} \tag{7.6}$$

Before removing the aged samples from the setup, the apparent activation energy was determined by measuring the net production rates of $CH_4$ under differential conditions ($X(CO_2) < 15\,\%$) from 230 to 210 °C in 5 K steps (holding time 60 min each). The apparent activation energy was obtained from the linear form of the general rate law. Errors were calculated based on Gaussian error propagation. Validity was checked by replicate experiments.

To free the catalyst surface from adsorbates, the catalyst was then flushed in Ar at 350 °C for 1 h. The aged catalysts were removed from the setup under Ar atmosphere and stored in a glovebox to prevent oxidation or surface passivation of the nanoparticles. The transfer to all characterization units was carried out under Ar atmosphere.

## 7.3 Results and Discussion

### 7.3.1 Characterization Prior to Catalysis and Aging Tests

Since for co-precipitated catalysts the structure and the morphology of the precipitate as well as of the final catalyst is well-known to strongly depend on the $n_{Ni}/n_{Al}$ ratio [24, 258], both catalysts were prepared with a $n_{Ni}/n_{Al}$ ratio of 1 rather than preparing catalysts with a constant Ni loading.

A Ni loading of 36.8 wt.% in the calcined $NiAlO_x$ catalyst was determined by ICP-OES. For $NiFeAlO_x$, a Ni loading of 34.9 wt.% and a Fe loading 4.8 wt.% was found, resulting in a $n_{Ni}/n_{Al}$ ratio of 5.5 as desired. The $Na^+$ content was below the detection limit ($< 10^{-3}$ wt.%) for both samples, indicating that the washing procedure was sufficient to quantitatively remove $Na^+$ from the precipitates. Therefore, any effect of $Na^+$ on the catalytic performance can be excluded. The co-precipitated catalyst precursors feature a distorted takovite-like structure $[Ni_{0.5}Fe_yAl_{0.5}(OH)_{2+2y}][(CO_3)_{0.25+y/2} \cdot n\,H_2O]$ ($y$ = 0 for $NiAlO_x$, 0.09 for $NiFeAlO_x$) (*cf.* Section 7.5.5.1 and Chapter 4). During calcination at 450 °C, mixed metal oxide structures were formed for both catalysts. XRD (*cf.* Section 7.5.5.1 and Chapter 4) and TPR (*cf.* Section 7.5.5.2 and Chapter 4) indicate that a crystalline NiO phase, distorted by the incorporation of $Al^{3+}$ and, for $NiFeAlO_x$, possibly also $Fe^{3+}$, co-exists with an amorphous Ni-containing $Al^{3+}$-rich phase.

During catalyst activation, Ni particles were formed for $NiAlO_x$, evident from the evolution of fcc Ni reflexes in the XRD pattern in Figure 7.10. The degree of reduction of $Ni^{2+}$ at 485 °C can be calculated to 57 % from TPR (*cf.* Section 7.5.5.2). The incomplete reduction of $Ni^{2+}$ is in line with X-ray diffraction, which shows the presence of a $Ni^{2+}$-poor Ni-Al mixed metal oxide after catalyst activation (*cf.* Figure 7.10). From the Scherrer equation, applied to the 200 Ni reflection at $2\theta = 51.84°$, a mean metal crystallite size of 3.2 nm can be determined. In good agreement, evaluation of the metal particle size distribution by TEM (*cf.* Figure 7.14 A) yields a mean Ni particle size of 4.2 ± 1.3 nm. The Ni surface area calculated from $H_2$ chemisorption is 30.1 $m^2\,g_{cat}^{-1}$. For $NiFeAlO_x$, in contrast, XRD data suggest the formation of ($\gamma$Fe,Ni) metal nanoparticles during activation at 485 °C, evident from a shift of the fcc Ni reflections to lower diffraction angles (*cf.* Figure 7.10). From the 200 fcc ($\gamma$Fe,Ni) reflection at $2\theta = 51.34°$, the Fe content in the bulk of ($\gamma$Fe,Ni) after activation at 485 °C can be estimated to 28 at.% [310]. This is in line with TPR, where, compared to $NiAlO_x$, an additional reduction signal at 280 °C can be assigned to the reduction of $Fe^{3+}$ to $Fe^{2+}$. $Fe^{2+}$ is subsequently reduced to Fe, possibly alleviating the reduction process of $Ni^{2+}$ [149], which is evident from a shift of the $Ni^{2+}$ reduction peak to lower temperature (*cf.* Figure 7.11). The overall degree of reduction of $Ni^{2+}$ and $Fe^{3+}$ can be calculated to 60 %. Similar to $NiAlO_x$, the mean crystallite size (by XRD) is estimated to 3.2 nm, the mean particle size (by TEM, *cf.* Figure 7.14 C) 4.3 ± 1.3 nm. The $H_2$ chemisorption gives a Ni surface area of 20.1 $m^2\,g_{cat}^{-1}$, which suggests that part of the Fe atoms is exposed, since $H_2$ adsorption on Fe is negligible at 35 °C [253, 254].

Both activated catalysts feature type IV isotherms with a H3 hysteresis, which is typical for aggregates of plate-like particles giving rise to slit-shaped pores [225]. The specific BET surface area of the activated $NiAlO_x$ catalyst is 293 $m^2\,g_{cat}^{-1}$, the one of $NiFeAlO_x$ 266 $m^2\,g_{cat}^{-1}$. The total $CO_2$ uptake capacity determined by static $CO_2$ chemisorption amounts to 199 µmol $g_{cat}^{-1}$ for $NiAlO_x$ and 219 µmol $g_{cat}^{-1}$ for $NiFeAlO_x$. $CO_2$-TPD (*cf.* Figure 7.13) suggests the presence of weak ($CO_2$ bound as bicarbonate), medium ($CO_2$ bound as mono- and bidentate carbonate) and strong ($CO_2$ bound in a bridged, organic-like carbonate) basic sites. For $NiFeAlO_x$, the density of medium basic sites is decreased, while the density of weak basic sites is higher compared to

$NiAlO_x$. Besides, for $NiFeAlO_x$ the signals are shifted to lower desorption temperatures, which indicates a lower binding strength of $CO_2$ on the respective sites. The clear effect of Fe on the basic density and strength may be caused by un- or partly reduced $Fe^{n+}$ ($n$ = 2, 3) species interacting with and modifying the $CO_2$ binding sites on the oxidic phase. This observation is in accordance with infrared spectroscopy (*cf.* Figure 7.12), where, for $NiFeAlO_x$, increased bicarbonate and decreased mono- and bidentate carbonate bands are found. Besides, the spectra show distinct bands in the 2100 to 1700 $cm^{-1}$ region, which can be assigned to carbonyl bound linearly (approx. 2010 to 2000 $cm^{-1}$), bridged (approx. 1890 $cm^{-1}$), and in a three- or fourfold hollow mode (approx. 1860 to 1800 $cm^{-1}$) to metal centers. This suggests that Ni and ($\gamma$Fe,Ni) are able to dissociate $CO_2$ already at 40 °C [330]. DFT studies show that the ability for $CO_2$ adsorption and dissociation on Ni surfaces is in the order Ni(110) > Ni(100) > Ni(111) [331]. The kinetic barrier for the dissociation of $CO_2$ on Ni(100) thereby is reported to be 0.33 eV [330]. The intensities of the carbonyl bands in the IR spectra are much higher for $NiFeAlO_x$, especially the band assigned to linearly bound carbonyl, which is a hint that Fe significantly contributes to $CO_2$ adsorption and dissociation and/or modifies the adsorption and dissociation properties of Ni. In this context, Liu *et al.* found in DFT studies that the adsorption of $CO_2$ on a (100) surface is more favorable on Fe than on Ni [332].

## 7.3.2 Catalyst Performance

Figure 7.1 A illustrates the trend of weight time yields of $CH_4$ ($WTY(CH_4)$) over $NiAlO_x$ and $NiFeAlO_x$, aged at 450 °C. For $NiAlO_x$, with a fast initial deactivation in the first 2 h to 76 %, an exponential-like decrease of $WTY(CH_4)$ can be observed, levelling out at 50 % of the initial

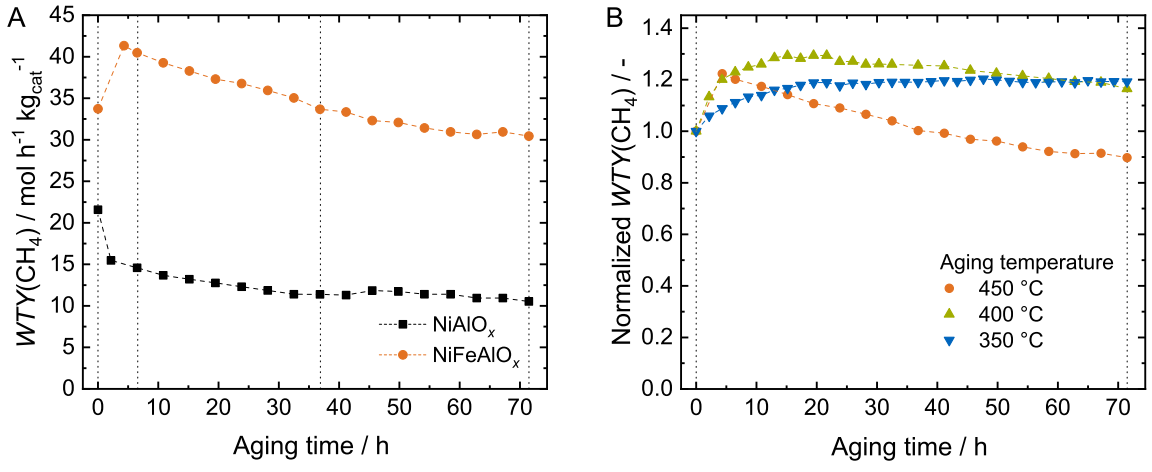


**Figure 7.1:** $WTY(CH_4)$ vs. aging time for $NiAlO_x$ compared to $NiFeAlO_x$, recorded under differential conditions at 230 °C, 4 bar, 600 NL $g_{cat}^{-1}$ $h^{-1}$, $H_2/CO_2/Ar$ = 4/1/75, and aged at 450 °C, 8 bar, 18 NL $g_{cat}^{-1}$ $h^{-1}$, $H_2/CO_2/Ar$ = 4/1/5 (A); $WTY(CH_4)$ over $NiFeAlO_x$ as a function of aging time, recorded under differential reaction conditions at 230 °C, 4 bar, 600 NL $g_{cat}^{-1}$ $h^{-1}$, $H_2/CO_2/Ar$ = 4/1/75, and aged at different temperatures, 8 bar, 18 NL $g_{cat}^{-1}$ $h^{-1}$, $H_2/CO_2/Ar$ = 4/1/5, normalized to $WTY(CH_4)$($t_a$ = 0 h) (B).

$WTY(CH_4)$ after 32 h aging time. In contrast, for $NiFeAlO_x$, first a substantial increase of the $WTY(CH_4)$ over the first 6 h to 122 % takes place. From 6 h onwards, a decrease similar to $NiAlO_x$ takes place, but 90 % of the initial activity are still maintained after 72 h aging time.

Figure 7.1 B displays the temperature dependence of the aging behavior for $NiFeAlO_x$. In contrast to aging at 450 °C, the activity increase is even higher when aging at 400 °C, where the catalyst reaches the highest normalized $WTY(CH_4)$ (129 % of the initial value) after 16 h, slightly decreasing to 116 % when aging up to 72 h. For an aging temperature of 350 °C, the activity increase takes place even slower, reaching 119 % after an aging time of 20 h, from where this level is maintained up to 72 h. Based on these results, it can be concluded that, in contrast to $NiAlO_x$, where a monotonous decrease of catalyst activity induced by deactivation processes can be observed for all aging temperatures, for $NiFeAlO_x$ a second process takes place. Since this phenomenon exhibits a distinct temperature dependence, it can be regarded as an activated kinetic process. However, also the extent of the activity increase varies with aging temperature. At elevated temperature, deactivation processes similar to $NiAlO_x$ in Figure 7.1 A are promoted. As seen in Figure 7.1 B, during aging at 350 °C no apparent catalyst deactivation can be observed, but deactivation is fast when aging at 450 °C. At 350 °C aging temperature, the loss of catalyst activity due to the deactivation processes seems to be cancelled out by the activity increase provoked by the Fe promoter.

The selectivity to $CH_4$ formation was higher than 95 % for all data points. Besides CO formation, owed to the reverse of the water-gas shift reaction at high *GHSV* [333], no other reaction products were observed. In Chapter 4, it was shown that at a lower *GHSV* (200 000 $h^{-1}$, based on the total gas flow of $H_2/CO_2/Ar$ = 5/4/1), allowing integral rather than differential reactor operation, the yield of CO remained below 0.7 % between 175 to 400 °C in the whole conversion range up to thermodynamic equilibrium, before CO yield rises due to thermodynamics. Similar to Chapter 4, the Fe-doped catalyst did not feature an enhanced activity to CO formation compared to $NiAlO_x$. Sehested *et al.* [154] and Mebrahtu *et al.* [161] consistently found a significant negative impact of Fe on $CH_4$ selectivity for $n_{Ni}/n_{Fe}$ ratios less than 2, which is much lower than the $n_{Ni}/n_{Fe}$ ratio of 5.5 applied in this study.

### 7.3.3 Evolution of Catalyst Properties under $CO_2$ Methanation Reaction Conditions

Figure 7.2 illustrates the XRD patterns of the catalysts in their initial ($t_a$ = 0 h) and deactivated ($t_a$ = 6, 40, and 72 h) states. For $NiAlO_x$, upon aging an increase of the Ni reflections at $2\theta$ = 44.4, 51.8, and 76.4° can be observed. Crystallite size analysis indicates that this is caused by a rise of $d_C$ from 3.2 to 4.8 nm (*cf.* Table 7.2) during the first 40 h of aging, suggesting that Ni particle sintering is one of the deactivation processes contributing to the loss of activity shown in Figure 7.1 A. This is in line with the trend of the Ni surface area (*cf.* Table 7.2), which drops by approx. 50 % during the first 6 h and remains at about 12 $m^2\,g_{cat}^{-1}$ after 40 h

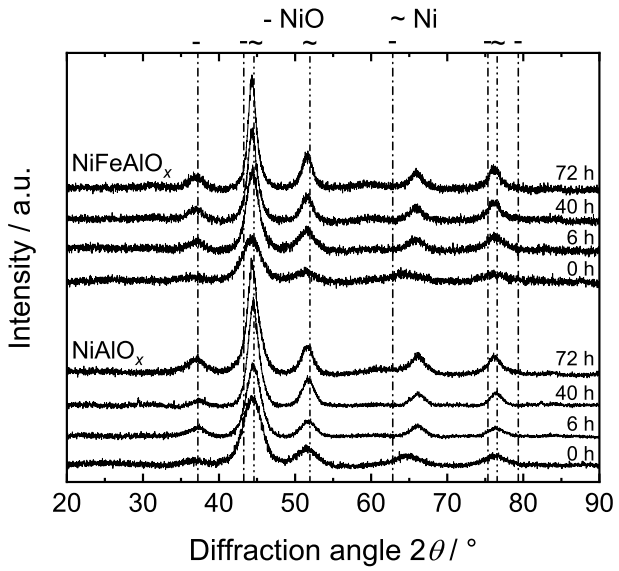


**Figure 7.2:** X-ray diffractograms of the activated and deactivated $NiAlO_x$ and $NiFeAlO_x$ catalysts aged at $T_a$ = 450 °C for varying aging times (JCPDS: NiO 78-0429, Ni 87-0712).

aging time. Particle size analysis by TEM (*cf.* Figure 7.14 A, B) confirms an increase of the mean Ni particle diameter from initially 4.2 ± 1.3 nm to 10.1 ± 1.2 nm after aging for 72 h. Besides, the reflection assigned to the mixed oxide phase shifts from $2\theta$ = 64.8° for the fresh catalyst to $2\theta$ = 66.1°, which indicates a further phase transformation. This might be caused by segregation through the additional removal of $Ni^{2+}$ ions from the mixed oxide structure, leading to the formation of an alumina-like structure. $N_2$ physisorption (*cf.* Table 7.2) indicates that this potential segregation process in the mixed oxide phase is accompanied by oxide phase sintering.

**Table 7.2:** Catalyst characterization data including results from BET as well as $H_2$ and $CO_2$ chemisorption for different aging times: Ni surface area $S_{Ni}$, dispersion of Ni $D_{Ni}$, mean crystallite size $d_C$, mean metal particle size $d_P$, BET surface area $S_{BET}$, and $CO_2$ uptake $U(CO_2)$.

| Catalyst | $t_a$ / h | $T_a$ / °C | $S_{Ni}$ / $m^2\,g_{cat}^{-1}$ | $D_{Ni}$ / % | $d_C^a$ / nm | $d_P^b$ / nm | $S_{BET}$ / $m^2\,g_{cat}^{-1}$ | $U_{CO_2}$ / $\mu mol\,g_{cat}^{-1}$ |
|---|---|---|---|---|---|---|---|---|
| $NiAlO_x$ | 0 | - | 30.1 | 12.2 | 3.2 | 4.2 ± 1.3 | 293 | 199 |
| | 6 | 450 | 15.3 | 6.2 | 4.2 | n. d. | 207 | 123 |
| | 40 | 450 | 12.2 | 5.0 | 4.8 | n. d. | 131 | 84 |
| | 72 | 450 | 12.1 | 4.9 | 4.8 | 10.1 ± 1.2 | 132 | 82 |
| $NiFeAlO_x$ | 0 | 450 | 20.1 | 8.6 | 3.2 | 4.3 ± 1.3 | 266 | 219 |
| | 6 | 450 | 13.4 | 5.8 | 3.7 | 6.6 ± 1.2 | 130 | 121 |
| | 40 | 450 | 6.8 | 2.9 | 4.4 | 9.0 ± 1.2 | 110 | 87 |
| | 72 | 450 | 5.4 | 2.3 | 5.3 | 10.3 ± 1.2 | 108 | 84 |
| | 72 | 350 | 9.0 | 3.9 | 4.0 | n. d. | 191 | 140 |
| | 72 | 400 | 8.1 | 3.5 | 4.7 | n. d. | 131 | 109 |

[a] mean crystallite diameter $d_C$ determined from XRD, ($\gamma$Fe,Ni) reflection at $2\theta$ = 51.3 to 51.8°.
[b] mean particle size $d_P$ obtained from fitting a lognormal distribution to TEM data (*cf.* Figure 7.14).

A strong decrease of the BET surface area from initially 293 to 132 $m^2\ g_{cat}^{-1}$ after aging for 72 h can be observed. Simultaneously, the $CO_2$ uptake capacity decreases from 199 to 82 $m^2\ g_{cat}^{-1}$, which indicates that aging under these hydrothermal-like conditions leads to a drastic decrease of basic site density. Compared to Figure 7.1 A, the trend of $WTY(CH_4)$ over time qualitatively follows the decrease of the Ni surface area, the BET surface area, and the $CO_2$ uptake capacity, but none of these parameters is linearly correlated to $WTY(CH_4)$. Interestingly, however, for constant catalyst activity after 40 h of aging, all these three catalyst property descriptors also remain constant. It is therefore hypothesized that, although the loss of Ni surface area may merely contribute to deactivation, catalyst activity of $NiAlO_x$ also depends on the properties of the oxidic phase. It is an indicator that the sites active for $CO_2$ methanation might be located at the interphase of Ni particles and the oxidic phase (*cf.* Chapter 5). The trends of catalytic activity and the material descriptors of the reference $NiAlO_x$ catalyst are qualitatively in line with a study on Ni-Al catalysts [134]. The Ni surface area of the $NiFeAlO_x$ catalyst drops from 20.1 to 13.4 $m^2\ g_{cat}^{-1}$ during the first 6 h of aging. In contrast to $NiAlO_x$, where the Ni surface area stays constant from 40 h of aging onwards, for $NiFeAlO_x$ the Ni surface area undergoes a further decrease from 6.8 $m^2\ g_{cat}^{-1}$ after 40 h to 5.4 $m^2\ g_{cat}^{-1}$ after 72 h of aging. This decrease is in accordance with an increase of the crystallite size $d_C$ determined from XRD (*cf.* Figure 7.2), as well as the mean metal particle size $d_P$ from TEM (*cf.* Table 7.2, Figure 7.14 C–E). Similar to the unpromoted reference catalyst, the BET surface area and the $CO_2$ adsorption capacity of $NiFeAlO_x$ remain approximately constant from 40 h of aging onwards. The further drop in activity from 40 to 72 h therefore can be ascribed to metal particle sintering.

As deduced from XRD (*cf.* Figure 7.2), the reduction of $NiFeAlO_x$ leads to the formation of ($\gamma$Fe,Ni) alloy particles. With increasing aging time, however, the initial 200 reflection position ($2\theta$ = 51.34°) shifts to higher diffraction angles, illustrated in Figure 7.2. After 6 h of aging, the 200 reflection appears at $2\theta$ = 51.5°, after 72 h of aging at $2\theta$ = 51.59°. This is a strong hint that the Fe content in the bulk of the alloy is stepwise reduced during aging by (partial) segregation of the ($\gamma$Fe,Ni) particles. From comparison of the reflection positions to tabulated data [310], one can deduce that the Fe content in the bulk of the ($\gamma$Fe,Ni) particles gradually decreases from initially 28 at.% to 19.5 at.% after 6 h of aging, 17 at.% after 40 h, and 14.5 at.% after 72 h of aging. Besides, the reflection of the former crystalline mixed oxidic phase at $2\theta$ = 64.8° (*cf.* Figure 7.2) is shifted to $2\theta$ = 66.1°, in analogy to $NiAlO_x$, which indicates that the transformation processes of the oxidic phase occurring during aging are similar for $NiAlO_x$ and $NiFeAlO_x$.

For further investigations on the nature of the Fe species after activation and after aging for 6 h, Mössbauer spectra of the catalyst samples were taken under inert conditions. The spectra are shown in Figure 7.15. After reduction, in accordance with XRD results, 28 % of the Fe species are observed to be metallic with a hyperfine field of 28.6 T and an isomer shift of –0.12 mm $s^{-1}$, typical for Fe incorporated an Ni-Fe alloy [334]. The magnetically split broad signal is most probably caused by $Fe^{3+}$ (47 %), which, similar to the calcined catalyst, might still interact with the oxidic phase after reduction. Besides, a third, broad component with an isomer shift of

about 1 mm $s^{-1}$ is required to describe the spectrum, fitted as a magnetically split sextet with a hyperfine field of about 10 T. From the isomer shift it can be deduced that this signal originates from $Fe^{2+}$ species (25 %). In an oxidic system, the $Fe^{2+}$ might form wüstite ($Fe_yO$), which orders at low temperatures and then gives rise to complicated, unresolved magnetic hyperfine spectra [335–337]. After 6 h under aging conditions, the spectrum changes significantly. The amount of $Fe^{3+}$ stays constant, but the average hyperfine field increases from 36 to 39 T. This indicates a change in the environment of the $Fe^{3+}$ species and, assuming that $Fe^{3+}$ is present in the oxide phase after catalyst activation, might be caused by the phase transformation of the $Al^{3+}$-rich oxidic phase during aging observed in Figure 7.2. In contrast, the spectrum shows a lower amount of metallic Fe (19 %), which means that about a third of the metallic Fe species got oxidized during 6 h of aging, forming $Fe^{2+}$ species (34 %) on the surface of the catalysts, most likely in close neighborhood to the metal particles. The amount of Fe getting oxidized during 6 h at 450 °C in reactant gas can be calculated to 0.43 wt.% (based on the calcined material). The ratio of the freshly formed $Fe^{2+}$ within the first 6 h to the exposed Ni atoms (with a dispersion of 5.8 %, *cf.* Table 7.2) can be calculated to 0.2, the ratio to the Ni perimeter sites (assuming hemispheres with a diameter of 6.6 nm, *cf.* Table 7.2) 0.7. This indicates that an increase of $Fe^{2+}$ by 9 % may have a significant impact on the active sites of the catalyst. The hyperfine field of the metallic Fe slightly decreases to 28.3 T, which may be due to a slight decrease of the Fe/Ni ratio in the alloy [334]. Therefore, Mössbauer analysis confirms the observation of ($\gamma$Fe,Ni) segregation from XRD and suggests that Fe is partially oxidized during aging. To get further experimental proof of $Fe^{2+}$ on the aged catalyst systems, total X-ray scattering experiments were carried out for $NiFeAlO_x$ aged for 0, 6, 40, and 72 h, shown in Figure 7.3.

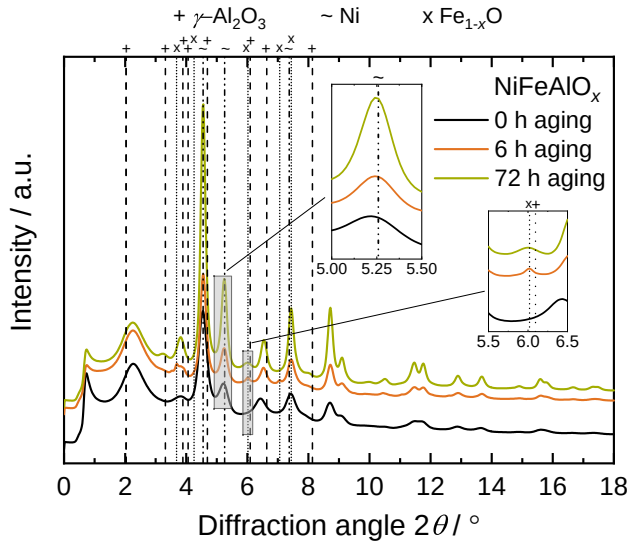


**Figure 7.3:** Total X-ray scattering data collected for the activated (0 h aging) and aged (6 and 72 h aging) $NiFeAlO_x$ catalyst samples, aging temperature $T_a$ = 450 °C, $\lambda$ = 0.161 669 Å (Ni: JCPDS 87-0712, $Fe_{1-x}O$: ICDD 01-079-1971, $\gamma$-$Al_2O_3$: JCPDS 10-0425).

Upon aging for 6 h, reflection signals appear at $2\theta = 3.69$, 6.01, and 7.06°, suggesting the formation of disordered wüstite ($Fe_{1-x}O$, ICDD 01-079-1971) species. Noteworthy, the reflections get more diffuse upon further aging and do not follow the trend of particle sintering evident from the intensity increase of all other reflections. This could be interpreted as a hint that wüstite formation takes place in a thin, film-like structure on the outer catalyst surface, since it does not feature sintering characteristics of typical crystal particles. The absence of diffractions in standard XRD in Figure 7.2 suggests that the crystallites are very small, low in quantity or located on the outer surface of the catalyst. The appearance of the wüstite reflections goes hand in hand with the shift in the reflection positions of ($\gamma$Fe,Ni). After reduction, the reflection attributed to the (200) plane of ($\gamma$Fe,Ni) appears at $2\theta = 5.21°$. After 6 h aging time, it is shifted to $2\theta = 5.24°$, after 72 h aging time to $2\theta = 5.25°$. This confirms the findings of partial ($\gamma$Fe,Ni) segregation under aging conditions from standard XRD shown in Figure 7.2 and the formation of $Fe^{2+}$ species found by Mössbauer spectroscopy.

The evolution of the ferromagnetic properties of $NiAlO_x$ and $NiFeAlO_x$ over aging, resolved by FMR, are shown in Figure 7.16 and 7.17, respectively. After reduction, $NiFeAlO_x$ features a higher magnetic anisotropy than $NiAlO_x$, evident from the higher linewidths $\Delta B_{pp}$ for $NiFeAlO_x$ (260 mT vs. 145 mT for $NiAlO_x$, at $T = -140$ °C, *cf.* Table 7.4). In combination with the difference in magnetic intensity by a factor of two, this can be interpreted by the formation of alloyed Ni-Fe particles. Over aging, the normalized intensity increases to a factor of four after 6 h and five after 40 h, before it decreases back to four after 72 h. The changes in the magnetic intensity indicate a change in the Ni-Fe particle composition, while for $NiAlO_x$, the magnetic intensity remains constant. Guirado-Lopez *et al.* showed that the magnetic properties of Ni-Fe clusters strongly depend on the atomic composition and chemical order. Reduced magnetizations were found for particles that feature Fe-rich cores, while random alloys and core-shell configurations with a Ni-rich core featured high magnetizations [338]. This observation is in line with the theory of the decreasing Fe concentration in the bulk of the ($\gamma$Fe,Ni) particles evident from XRD in Figure 7.2 and total X-ray scattering in Figure 7.3. The complex trend of the magnetic intensity in Table 7.4 therefore may be explained by a superimposition of an intensity increase caused by structural changes and rearrangement of Fe in the metal particles due to Fe enrichment on the surface, and a decline, originating from the oxidation of Fe. At the same time, the magnetic anisotropy changes over aging. For $NiFeAlO_x$, $\Delta B_{pp}$ decreases from 260 mT after reduction to 230 mT after 40 h, and ultimately to 170 mT after 72 h. For $NiAlO_x$, in contrast, one can monitor an increase from 145 to 270 mT. At this point, it needs to be mentioned that the reasons for anisotropy changes can be manifold. Possible explanations are changes in metal particle size or shape [287] as well as particle-support interactions [289], i.e. parameters that may change over aging. Also, remaining adsorbates on the metal surface were found to have an influence on the magnetic anisotropy [290]. Therefore, conclusive statements on the exact reasons for the anisotropy change are not possible at the current state, but the effects may be manifold and opposing each other.

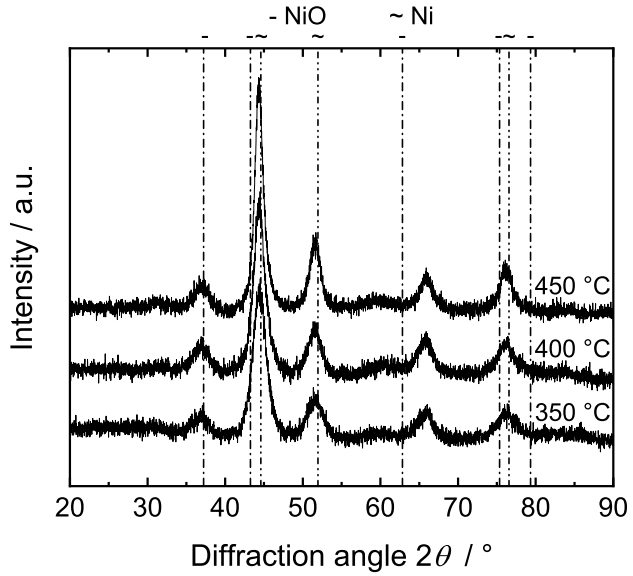


**Figure 7.4:** X-ray diffractograms of $NiFeAlO_x$ aged for $t_a$ = 72 h at different temperatures.

In Figure 7.4, the XRD patterns of the $NiFeAlO_x$ catalysts aged for 72 h at different temperatures are compared. Also for the samples aged at 350 and 400 °C, shifts of the reflections assigned to the oxide phase and metal phase similar to Figure 7.2 can be observed, which suggests that Ni-Fe alloy segregation already takes place at aging temperatures as low as 350 °C. The bulk of the ($\gamma$Fe,Ni) particles is estimated to contain 14 at.% Fe after aging at 350 °C for 72 h and 17 at.% Fe after aging at 400 °C, respectively. The intensities of the reflections in Figure 7.4 rise with aging temperature, suggesting an increase of crystallinity of the metal particles. The crystallite size $d_C$ rises from 4.0 nm ($T_a$ = 350 °C) over 4.7 nm ($T_a$ = 400 °C) to 5.3 nm ($T_a$ = 450 °C), clearly showing the temperature influence of crystallite size growth and only a small growth rate at an aging temperature of 350 °C. In accordance, the declining Ni surface area, BET surface area as well as $CO_2$ uptake capacity (*cf.* Table 7.2) during aging follow the same trend, which indicates that aging at lower temperatures provokes the same aging mechanisms as aging at 450 °C, but slows down the deactivation rate. Most noteworthy, the FMR spectra of the catalyst aged for 72 h at 400 °C (*cf.* Figure 7.17 E) look very similar to the ones of the catalyst aged for 6 h (*cf.* Figure 7.17 B) and 40 h at 450 °C (*cf.* Figure 7.17 C), which clearly shows that the changes of the ($\gamma$Fe,Ni) particles over aging time is an activated process, therefore being facilitated at higher temperatures. The decrease of basic site density, however, seems to be more temperature-sensitive than the decrease of the Ni surface area as well as of the BET surface area.

Table 7.3 lists the apparent activation energies for $NiAlO_x$ and $NiFeAlO_x$, determined from an Arrhenius approach after different aging times as indicated in Figure 7.1 A. For $NiAlO_x$, the apparent activation energy remains constant at around 75 kJ mol$^{-1}$, which is a typical value for $CO_2$ methanation over Ni-based catalysts [87]. The constant value over aging is a hint that the nature of active sites does not change during aging and that the decrease of the methanation rate can be related to a decrease of the Arrhenius pre-factor by common deactivation mechanisms

**Table 7.3:** Apparent activation energies after different aging times.

| Catalyst | $t_a$ / h | $T_a$ / °C | $E_{A,app}$ / kJ mol$^{-1}$ |
|---|---|---|---|
| $NiAlO_x$ | 0 | - | 76.2 ± 1.4 |
| | 6 | 450 | 73.9 ± 3.6 |
| | 40 | 450 | 75.0 ± 2.5 |
| | 72 | 450 | 73.7 ± 2.1 |
| $NiFeAlO_x$ | 0 | - | 89.5 ± 1.4 |
| | 6 | 450 | 104.8 ± 3.8 |
| | 40 | 450 | 104.2 ± 2.7 |
| | 72 | 450 | 101.9 ± 1.2 |
| | 72 | 350 | 99.7 ± 1.9 |
| | 72 | 400 | 102.3 ± 0.9 |

like the loss of active sites due to sintering processes, as shown in Table 7.2. In contrast, for $NiFeAlO_x$ an apparent activation energy of 90 kJ mol$^{-1}$ is found after reduction. Moreover, the apparent activation energy rises to approximately 102 kJ mol$^{-1}$ within the first 6 h of aging, from where it stays constant. For the catalyst samples aged for 72 h at different temperatures, similar apparent activation energies of about 102 kJ mol$^{-1}$ were found. The increase of intrinsic catalytic activity of $NiFeAlO_x$ during the first 6 h shown in Figure 7.1 A appears to be in strong contrast to the observed increase of the activation energy by 11 %. In an Arrhenius approach, three possible reasons for this behavior (compensation effect) were suggested [317]: a) compensation of a lower energy of adsorption of the educts by an easier excitation of the bonds between the activated complex and the catalyst, b) the presence of at least two types of active sites that feature different activation energies, and a changing composition thereof, c) compensation effect due to a tunnel effect. For case b), the overall rate constant can be written as linear combination of Arrhenius approaches for different active sites. If the density of the more active sites decreases, e.g. by a thermal treatment, compensation effects may occur [317]. The appearance of a distinct compensation effect for $NiFeAlO_x$ therefore suggests that aging promotes the formation of new active sites, which contribute to the $CH_4$ formation rate, most probably by offering an additional reaction pathway. These *in situ* formed sites obviously feature a higher activation barrier for $CO_2$ methanation compared to methanation over conventional Ni or ($\gamma$Fe,Ni) particles (*cf.* Table 7.3).

### 7.3.4 Re-activation of $NiFeAlO_x$

In Figure 7.10, it is shown that re-reduction of a re-calcined $NiFeAlO_x$ catalyst restores the original ($\gamma$Fe,Ni) metal particle composition and crystallite size. To investigate the influence of a re-reduction process on partially segregated Ni-Fe alloy particles, a catalyst sample aged for 6 h was re-reduced in 5 % $H_2$ in Ar for 5 h before re-evaluating its catalytic performance. This procedure was repeated two times. The trend of $WTY(CH_4)$ over aging time, normalized to the initial $WTY(CH_4)$ obtained after the first reduction process, is shown in Figure 7.5.

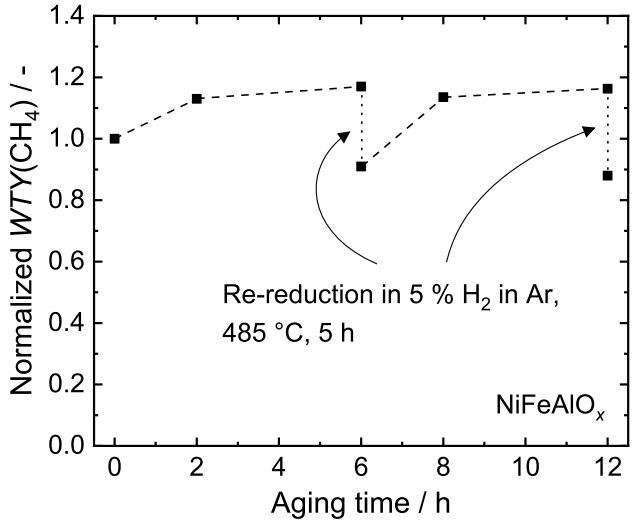


**Figure 7.5:** Cycles of tracking the $WTY(CH_4)$ over $NiFeAlO_x$ at $T$ = 230 °C with intermediate aging at $T_a$ = 450 °C for 6 h, then re-activation in 5 % $H_2$ in Ar.

During the first 6 h, the intrinsic catalytic activity increases consistent to Figure 7.1, reaching a normalized $WTY(CH_4)$ of 1.17. After 6 h, the catalyst was re-reduced, resulting in a drop of the normalized $WTY(CH_4)$ to 0.91. In a second aging cycle for 6 h, the normalized $WTY(CH_4)$ increases back to 1.16. A second re-reduction step decreases the $WTY(CH_4)$ to 0.87. The enhanced catalytic activity, in agreement to Figure 7.1 and Table 7.3, is accompanied by an increase of the apparent activation energy. From initially 88.4 $\pm$ 1.7 kJ mol$^{-1}$, it increases to 99.9 $\pm$ 1.0 kJ mol$^{-1}$, after re-activation it is reduced back to 88.4 $\pm$ 1.7 kJ mol$^{-1}$. The second 6 h aging treatment leads to an increase back to 99.1 $\pm$ 1.6 kJ mol$^{-1}$. After the second re-activation step (85.4 $\pm$ 0.6 kJ mol$^{-1}$), the initial activation energy is approximately restored.

To track the changes in ($\gamma$Fe,Ni) particle composition and crystallite size, the X-ray diffraction pattern of the $NiFeAlO_x$ catalyst re-reduced two times is shown in Figure 7.18. The reflection signal of the (200) plane appears at $2\theta$ = 51.6°, which corresponds to a Fe content of 14.5 at.%. This composition is similar to the catalyst sample aged for 72 h at 450 °C (*cf.* Table 7.2) and clearly suggests that the initial ($\gamma$Fe,Ni) bulk particle composition (28 at.% Fe) is not restored. Instead, it seems to be unaffected by the re-activation treatment. Therefore, it is safe to conclude that the increase of the intrinsic activity and the activation energy are not directly correlated to the ($\gamma$Fe,Ni) particle bulk composition (also some minor impact might exist), but to the formation of the $Fe^{2+}$ species as found in total X-ray scattering experiments in Figure 7.3 and Mössbauer spectroscopy in Figure 7.15 B.

The decrease of the normalized $WTY(CH_4)$ from 1 to 0.91 can be attributed to (under the chosen re-activation conditions comprising no intermediate re-calcination step) irreversible sintering processes, as evident from the increase of the mean crystallite diameter $d_C$ from 3.2 to 4.2 Å (*cf.* Figure 7.18). The mean crystallite size of 4.2 Å fits well to the data in Table 7.2 and indicates that re-reduction (without intermediate calcination) does not lead to re-dispersion of the ($\gamma$Fe,Ni) particles.

### 7.3.5 Discussion of the Promotional Effect of Fe in the $CO_2$ Methanation Reaction

It is generally accepted that the rate-determining step in CO and $CO_2$ methanation involves the dissociation of the C-O bond. The C-O bond cleavage thereby can either run H*-assisted (*via* $COH_x$ intermediates) [170, 171, 180], or directly without H* being involved [176–178, 307]. However, some studies also give hints that the hydrogenation of C* is rate-limiting [176, 190].

It was found that Fe has several effects on the macroscopic catalytic performance of $NiAlO_x$ catalysts. First, doping with Fe leads to an increase of the apparent catalyst activity. The higher apparent activation energy over $NiFeAlO_x$ after reduction indicates that Fe modifies the active sites of the catalysts, evident from the formation of ($\gamma$Fe,Ni) particles. This may also influence the reaction mechanism. In a Brønsted-Evans-Polanyi approach investigating steps on closed packed surfaces, Bligaard *et al.* [155] and Andersson [148] *et al.* found that, due to the comparatively weak CO adsorption, for Ni C-O dissociation (which can be H*-assisted [180]) is rate-limiting, while the stronger adsorption of CO on Fe leads to rate limitation by the hydrogenation of C* and O*. In a volcano approach, Ni-Fe alloys feature higher activity compared to Ni and Fe by a trade-off between the activation energy of C-O dissociation and the (adsorbed) CO dissociation energy [148]. Since the adsorption of CO is stronger on Ni-Fe than on Ni [148], the higher apparent activation energy over Ni-Fe compared to Ni (*cf.* Table 7.3, aging time 0 h) can be explained by an increasing impact of C* and O* hydrogenation to the kinetics of the overall process.

Catalyst characterization by total X-ray scattering, Mössbauer spectroscopy and FMR showed a decrease of the alloying of the bulk of the ($\gamma$Fe,Ni) particles, leading to surface enrichment with Fe and its partial oxidation, forming a wüstite phase. It is well known that wüstite is a non-stoichiometric structure consisting of $Fe^{2+}$, $Fe^{3+}$ and $O^{2-}$ and is generally described as $Fe_yO$, with $y$ ranging from 0.88 to 0.95 at atmospheric pressure [339]. $y$ also depends on temperature and gas atmosphere [340]. The $Fe^{2+}$ deficit is compensated by the incorporation of $Fe^{3+}$, resulting in a defect structure. However, the observed lattice parameter of 4.36 Å (*cf.* Figure 7.3) is larger than expected for a structure with the composition $Fe_yO$ ($y$ = 0.9 to 1) [339]. This may indicate that besides $Fe^{n+}$ ($n$ = 2, 3) some $Ni^{2+}$ ions are incorporated in the structure, possibly stemming from the co-oxidation of Ni closely interacting with Fe after reduction or unreduced $Ni^{2+}$ species, leading to lattice expansion.

The Tamaura group showed that $H_2$-reduced magnetite ($M_xFe_{3-x}O_{4-\delta}$, M = Fe, Co, Ni [341], $\delta$ denoting the degree of reduction) is able to decompose $CO_2$ to carbon and oxygen [342–347]. They proposed a redox mechanism, in which carbon is deposited on the surface, related to the oxidation of $Fe^{2+}$ to $Fe^{3+}$, while $O^{2-}$ is incorporated into the cation-excess crystal lattice [345]. It was hypothesized that the high reduction potential of $Fe^{2+}$ for $CO_2$ is directly correlated to the mobility of $O^{2-}$ in the iron oxide [342, 345]. Carbon adsorbed on the surface is subsequently hydrogenated to $CH_4$ [341, 346, 347]. The original state is then restored by the re-reduction of

$Fe^{3+}$ and the formation of $H_2O$. Other than in the studies of Tamaura *et al.*, who used $H_2$-treated magnetite for the generation of those active $Fe^{2+}$ sites, in this study these active sites seem to be generated by the partial segregation and oxidation of Fe from the ($\gamma$Fe,Ni) nanoparticles.

Similarly, Kim *et al.* [320] and Theofanidis *et al.* [329] found that $Fe^{2+}$ segregated from Ni-Fe alloy particles is able to remove C* deposited on Ni(Fe) sites in dry reforming by $CO_x$ formation *via* $Fe^{2+}$-$Fe^{3+}$ redox chemistry in $Fe_yO$. It can be hypothesized that in $CO_2$ methanation atmosphere the reverse reaction, resulting in $CO_2$ activation on $Fe_yO$, takes place. The hypothesis of redox-active $Fe^{2+}$ sites participating in the methanation reaction and contributing to the overall reaction rate is consistent to the observed compensation effect [317]. Regeneration of $NiFeAlO_x$ after 6 h of aging causes $Fe^{2+}$ to be re-reduced to metallic Fe, which closes the additional reaction pathway provided by $Fe^{2+}$ (evident from the decrease of the activation energy), leading to a decrease of catalyst activity (*cf.* Figure 7.1).

The high activation energy of the $Fe^{2+}$ promoted reaction pathway is supposed to arise from an unfavorable kinetic barrier of the hydrogenation step of carbon adsorbed on these sites and the involvement of a solid-gas reaction. Since Mössbauer spectroscopy (*cf.* Figure 7.15) suggests the presence of a small part of $Fe^{2+}$ already after catalyst activation, the complete absence of these additional reaction sites directly after catalyst activation cannot be excluded. However, due to lower percentage of $Fe^{2+}$ as well as their unknown location, their contribution, if present, is supposed to only play a minor role compared to $CO_2$ methanation over ($\gamma$Fe,Ni).

## 7.4 Conclusion

The improved apparent stability of Fe-promoted co-precipitated $NiAlO_x$ catalysts in the $CO_2$ methanation reaction was shown to be caused by a temporal increase of the intrinsic catalytic activity triggered by catalyst exposure to aging conditions, resolved by intermediate kinetic measurements away from equilibrium conditions. The increase in intrinsic activity is provoked by the simultaneous (partial) segregation of ($\gamma$Fe,Ni) particles initially formed during catalyst activation and *in situ* formation of active $Fe^{2+}$ sites under aging conditions, as proved by XRD analysis and Mössbauer spectroscopy. These sites are hypothesized to provide an additional, alternative reaction pathway *via* $CO_2$ activation on disordered $Fe_yO$. Since sintering effects, which lead to a decrease of the metal surface area, $CO_2$ adsorption capacity, and the BET surface area, cause a countervailing reduction of catalyst activity, aging of $NiFeAlO_x$ at a moderate temperature of 400 °C resulted in the highest temporal activity increase. This highlights that the promotional effect of Fe on the methanation activity of co-precipitated $NiAlO_x$ is highly sensitive to the pretreatment procedure and implies that the activity of co-precipitated $NiFeAlO_x$ can be enhanced by a suitable temperature program.

# 7.5 Supplementary Material

## 7.5.1 Catalyst Synthesis

The catalysts were prepared by co-precipitation at constant pH 9. 1 M solutions of $Ni(NO_3)_2$ ($Ni(NO_3)_2 \cdot 6H_2O$, Merck), $Al(NO_3)_3$ ($Al(NO_3)_3 \cdot 9H_2O$, Merck), and $Fe(NO_3)_3$ ($Fe(NO_3)_3 \cdot 9H_2O$, Merck), respectively, were mixed to an overall volume of 120 mL. The mixture was fed with a flow rate of 2.5 mL $min^{-1}$ to a 3 L-sized glass vessel, which contained 1 L of bi-distilled water at pH 9 and 30 °C. The precipitation agent, an equimolar mixture of 1 M NaOH (Merck) and 1 M $Na_2CO_3$ (Merck), was automatically dosed by a titrator (Alphaline Titrino Plus, Schott) to keep the pH constant at 9 ± 0.1. All reagents were *p.a.* purity. After aging at pH 9 and 30 °C for 18 h in the mother liquor, the suspension was vacuum-filtered and washed until the pH of the fresh filtrate was 7 and the conductivities of the fresh filtrate and of bi-distilled water were in the same order of magnitude. The filter cake was dried at 80 °C for 18 h in air, before it was calcined in flowing synthetic air at 450 °C for 6 h (linear heating rate 5 K $min^{-1}$). For all further studies, the particle fraction from 150 to 200 µm was used, obtained by pelletizing (pressure 450 N $cm^{-2}$), grinding and sieving. Any effects of the pelletizing process on the porous structures of the catalysts were excluded beforehand.

## 7.5.2 Catalyst Characterization

### 7.5.2.1 Inductively Coupled Plasma-Optical Emission Spectroscopy

Elemental analysis was carried out by inductively coupled plasma-optical emission spectroscopy (ICP-OES) on an Agilent 700. Approximately 50 mg of the calcined catalyst samples were sonicated in 1 M $H_3PO_4$ for 4 h. After cooling down, the volume was adjusted to 50 mL and the solutions were diluted 1 to 10 with bi-distilled water, before filtering using 0.45 µm filters (Pall). Multi-element standards (ICP standard IV, Merck) were prepared for 50, 10, 1, and 0.1 ppm metal ion concentrations. Matrix effects and metal signal superimpositions were excluded. The wavelengths used for data evaluation were 230.299 nm (Ni), 396.152 nm (Al), 238.204 nm (Fe), and, to check the Na content of the catalysts, 588.995 nm (Na). All data were collected five times.

### 7.5.2.2 Temperature-Programmed Reduction

Temperature-programmed reduction (TPR) experiments were conducted using a Quantachrome ChemStar TPx. Approximately 50 mg of catalyst were positioned in a U-shaped quartz reactor with a thermocouple placed in the catalyst bed. The procedure included heating to 485 °C (2 K $min^{-1}$) in 5 % $H_2$ in Ar (100 mL $min^{-1}$), holding for 5 h, and cooling down to room temperature in He. For temperature-programmed oxidation, the activated catalyst was heated in 10 % synthetic air in He (50 mL $min^{-1}$) to 450 °C (5 K $min^{-1}$) and held there for 6 h before

cooling down to room temperature in Ar. The whole TPR process was repeated with a fresh catalyst, heating up to 1000 °C and holding 30 min. $H_2$ consumption was tracked using a thermal conductivity detector (TCD). Evolving $H_2O$ and $CO_2$ were frozen out in an acetone / liquid $N_2$ slurry trap. Degrees of reduction were calculated from the integral $H_2$ consumption using CuO for TCD calibration, assuming all nickel and iron species in the calcined catalysts were initially present in the form of $Ni^{2+}$ and $Fe^{3+}$ (*cf.* Chapter 4). The reduction signals were fitted using Gaussian peak functions.

#### 7.5.2.3 $H_2$ and $CO_2$ Chemisorption

$H_2$ and $CO_2$ chemisorption experiments were carried out on a Quantachrome Autosorb 1 at 35 °C. Before and after each measurement, the reduced and deactivated catalysts were vacuum-degassed at 350 °C for 1 h (heating rate 5 K $min^{-1}$). Sorption equilibration time was set 2 min for $H_2$ chemisorption and 10 min for $CO_2$ chemisorption. The extrapolation method to zero pressure was used for the calculation of the metal surface area (from $H_2$ chemisorption) and the $CO_2$ uptake, respectively. For $H_2$ adsorption, a dissociative adsorption mechanism with one H atom adsorbing on one Ni atom was assumed [252]. $H_2$ adsorption on Fe under the chosen conditions was neglected due to its kinetic limitation [253, 254]. $H_2$ chemisorption at a recommended temperature of 200 °C to track Fe sites [255] resulted in significant spillover onto the $Al^{3+}$-containing oxidic phase and was therefore omitted. Metal surface area determination by CO chemisorption was also omitted, since adsorption of CO on Fe is known to be structure-dependent [255, 256] and therefore allows no conclusion on the metal surface area. The Ni dispersion was calculated from the specific $H_2$ uptake $U(H_2)$, the Ni loading $l_{Ni}$, and the molar mass of Ni $M_{Ni}$.

$$D_{Ni} = \frac{N_{Ni,ex}}{N_{Ni}} = \frac{2 \cdot U_{H_2}}{\frac{l_{Ni}}{M_{Ni}}} \tag{7.7}$$

#### 7.5.2.4 $N_2$ Physisorption

The total surface area was calculated from $N_2$ physisorption data recorded on a NOVA 4000e (Quantachrome) at 77 K, applying the BET method in the $p/p_0$ range from 0.05 to 0.3. The reduced and deactivated catalysts were vacuum-degassed for 1 h at 350 °C (heating rate 5 K $min^{-1}$) beforehand. Sorption equilibration time was 3 min. Since the catalysts exhibited type IV isotherms featuring type H3 hystereses, care must be taken in the evaluation of mean pore diameters and the pore volumes [221, 225].

#### 7.5.2.5 X-ray Powder Diffraction Analysis

X-ray powder diffraction (XRD) analysis for the calcined samples was carried out on a Philips X'pert using Cu-$K_\alpha$ radiation, a Ni filter, and a monochromator. For *in situ* measurements, the sample was heated in 5 % $H_2$ in $N_2$ to 480 °C with a linear heating rate of 2 K $min^{-1}$, held there

for 5 h and cooled down to room temperature. Afterwards, the sample was heated to 450 °C with a linear heating rate of 5 K $min^{-1}$ in synthetic air and held there for 6 h. After cooling down, a second reduction treatment was performed. Diffractograms were taken in the scanning range from $2\theta$ = 5 – 90° with 0.02 ° $step^{-1}$ and 50 steps $min^{-1}$. XRD analyses for reduced and deactivated catalyst samples were carried out on a STOE Stadi P diffractometer using Cu-$K_\alpha$ radiation, a Ge(111) monochromator, and a Dectris MYTHEN 1K detector. 5 mg of the catalyst sample were transferred into glass capillaries (diameter 0.5 mm, WJM-Glas) in Ar atmosphere and sealed. Data were recorded for $2\theta$ = 5 – 90° with 0.015 ° $step^{-1}$ and 45 steps $min^{-1}$. For selected catalyst samples, total X-ray scattering data were collected at I15 at the Diamond Light Source with a fixed energy of 76.69 eV (wavelength of 0.161 669 Å). Line profiling was carried out using Pseudo Voigt functions (Highscore 3.0d). Interplanar distances $d$ were calculated according to Bragg's law (*cf.* Eq. 3.1). Mean crystallite sizes were obtained evaluating the 200 reflection of the metal crystallites (*cf.* Eq. 3.4). The calculated cell parameters were compared to tabulated values [310] to estimate the respective composition of the Fe-Ni alloy particles. Based on the step width during the diffraction measurements, the absolute error in the estimated Ni/Fe composition can be estimated to be 0.7 at.%.

#### 7.5.2.6 Transmission Electron Spectroscopy

For transmission electron spectroscopy (TEM), approx. 1 mg of the catalyst samples were suspended in bi-distilled $H_2O$ and sonicated for 10 min. After sedimentation of the larger particles, 3 µL of the suspension were dropped onto a copper grid coated with carbon film. The droplet was removed using a filter paper after 10 s. TEM was carried out on a Tecnai F30 with an acceleration voltage of 300 kV. The measured particle diameters were fitted to lognormal distributions to obtain data on average particle diameters and standard deviations.

#### 7.5.2.7 Fourier Transform Infrared spectroscopy

Fourier transform infrared spectroscopy for $CO_2$ adsorption on the activated catalysts was carried out on a Bruker Vertex 70 spectrometer. The calcined catalyst powder was shaped to a pellet of 1 cm diameter and activated *in situ* at 450 °C for 5 h (linear heating rate 5 K $min^{-1}$). Subsequently, the chamber was evacuated and kept at $10^{-7}$ mbar for 18 h. $CO_2$ was dosed into the cell to the desired pressure (0.1, 1, and 10 mbar). For each pressure, the cell was evacuated to $10^{-7}$ mbar after 10 min of equilibration before the IR spectrum was recorded. After pellet removal, the background was collected.

#### 7.5.2.8 Temperature-Programmed Desorption of $CO_2$

The freshly reduced catalysts were studied by temperature-programmed desorption of $CO_2$ ($CO_2$-TPD). 50 mg of catalyst were activated *in situ* in 5 % $H_2$ in He by heating to 485 °C with a linear rate of 2 K $min^{-1}$ and kept there for 5 h. Then, the catalyst was purged with He for 1 h. After cool-down to 35 °C, $CO_2$ was adsorbed for a duration of 30 min with a flow rate

of 50 mL $min^{-1}$. To remove any physisorbed $CO_2$, the catalyst bed was purged with He for another 30 min. TPD was performed in a stream of 100 mL $min^{-1}$ He with a linear heating rate of 6 K $min^{-1}$ up to 480 °C. The signals of CO and $CO_2$ fragments were tracked online *via* an OmniStar mass spectrometer (Pfeiffer Vacuum). Due to unknown ad- and desorption kinetics, fitting of the desorption signals was omitted.

#### 7.5.2.9 Ferromagnetic/Paramagnetic Resonance Spectroscopy

Ferromagnetic and paramagnetic resonance spectra of the reduced and deactivated catalysts were recorded on a JEOL JES-RE 2X at X-band frequency at temperatures between 113 to 473 K, microwave frequency 9.4 GHz, microwave power < 0.2 mW, and a modulation frequency of 100 kHz. The microwave frequency was measured with a microwave frequency counter Advantest R5372. For the Fe-containing catalysts, the significance of intensities/magnetizations measured below 273 K are of limited value due to substantial integrated intensity at zero field for X-band frequency.

#### 7.5.2.10 Mössbauer Spectroscopy

$^{57}Fe$ Mössbauer measurements were performed in transmission geometry with a source of $^{57}Co$ in a rhodium matrix at 4.2 K in a liquid helium bath cryostat. The Mössbauer absorbers were prepared in $N_2$ atmosphere and transferred into the liquid helium bath of the cryostat without exposure to air. Mössbauer spectra were fitted with Lorentzian lines grouped into appropriate patterns. In addition to magnetic sextets and electric quadruple doublets, patterns corresponding to Gaussian distributions of magnetic hyperfine fields were used. Isomer shifts are given as measured with respect to the source having the same temperature as the absorber. For the conversion to isomer shifts with respect to metallic iron at room temperature, 0.245 mm $s^{-1}$ have to be added to these values.

### 7.5.3 Temperature Program for Catalyst Activity Tracking over Aging

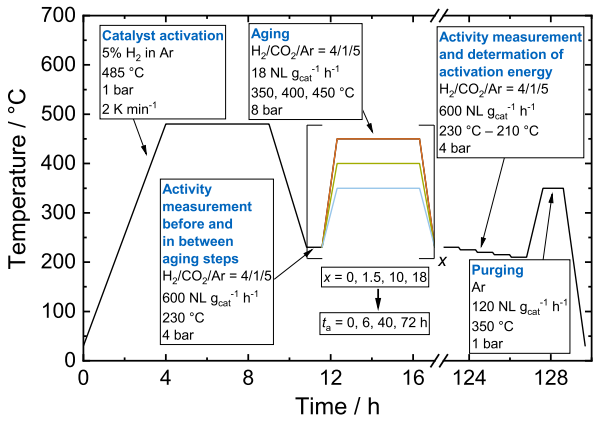


**Figure 7.6:** Temperature program for the time-resolved aging study.

## 7.5.4 Exclusion of Heat and Mass Transport Effects on Kinetic Data

### 7.5.4.1 Theoretical Proof of the Absence of Heat and Mass Transport Limitations

To theoretically evaluate possible influence of internal and external heat and mass transport effects on the reported apparent weight time yields of $CH_4$, the respective heat and mass transport criteria (Eqs. A.1 to A.4, *cf.* Appendix A) were checked. Although Koschany *et al.* recently showed that the reaction orders of $CO_2$ and $H_2$ in $CO_2$ methanation over the Ni-Al catalyst are well below 1 in the investigated temperature window [24], $n$ is set 1 in this consideration in a conservative approach for all species $i$. The maximum catalyst particle diameter used in the experimental was 200 µm. The activation energy was conservatively set 120 kJ mol$^{-1}$ [24, 87]. The catalyst bulk density was measured to be 500 kg m$^{-3}$. This low bulk density is an artifact from the low pelletizing pressure, chosen at 450 N cm$^{-2}$. At higher pressures, an impact on pore volume and BET surface area was observed in $N_2$ physisorption measurements. From the total pore volume, approximated from $N_2$ physisorption at $p/p_0$ = 0.995, and the catalyst bulk density, the internal catalyst pellet porosity was calculated. Bed voidage was set 0.45, the tortuosity was set 4 in a conservative approach. Catalyst pellet conductivity was estimated to be 0.15 W m$^{-1}$ K$^{-1}$ [24], a very conservative value regarding the metal loading of about 50 wt.% of the reduced catalyst. From characterization data and theoretical investigations it was deduced that the initial state of the catalyst is most sensitive to potential internal limitation effects, since during aging the pore size increases due to pore rupture, leading to a smaller impact of Knudsen diffusion and therefore faster intra-particle mass transport (*cf.* Eq. A.6). From $N_2$ physisorption measurements, the average pore diameter was approximated to 12.2 nm. All four criteria (*cf.* Eq. A.1 to A.4) were fulfilled under the chosen experimental conditions, justifying the assumption that heat and mass transport effects can be excluded and that the reported data reflect the kinetic properties of the catalyst. The most critical effect was found to be intra-particle mass transport limitation for $CO_2$. The Weisz-Prater criterion for intra-particle mass transport (*cf.* Eq. A.3) of $CO_2$ reached a maximum value of $0.21 < 1$ in this conservative assumption. All other criteria were fulfilled by a factor of at least 15.

### 7.5.4.2 Experimental Proof of the Absence of Heat and Mass Transport Limitations

Internal and external transport effects were also checked experimentally by altering catalyst particle diameter at high space velocities as well as volumetric flow rate at fixed space velocities, respectively. For the evaluation of possible intra-particle heat and mass transport limitations, the $NiFeAlO_x$ catalyst (higher activity) was pelletized, crushed and sieved to particle fractions of 100 to 150 µm, 150 to 200 µm, 200 to 250 µm, and 250 to 355 µm. Possible limitation was evaluated by comparing the yields of $CH_4$ at the conditions shown in Table 7.1 (total volumetric flow rate 500 mL min$^{-1}$, $H_2/CO_2/Ar$ = 4/1/75, 50 mg catalyst, 230 °C, 4 bar) for the different catalyst particle fractions. Figure 7.7 illustrates the obtained $CH_4$ yields as a function of the maximum particle diameter in the corresponding particle fraction. The standard deviation of the

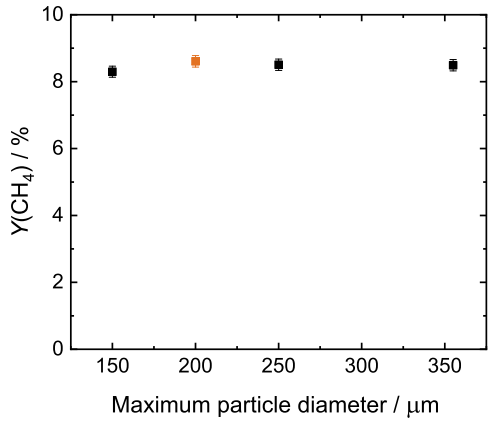


**Figure 7.7:** Yield of $CH_4$ for different maximum particle diameters (100 to 150 µm, 150 to 200 µm, 200 to 250 µm, and 250 to 355 µm), orange marks the data point used for the kinetic measurement.

$CH_4$ yields amounts to 1.3 % rel., which means that internal mass and heat transport limitations can be ruled out.

For the evaluation of the possible impact of inter-particle heat and mass transport effects on the reported data, the volumetric flow rate was varied from 300 to 500 mL $min^{-1}$ while keeping the space velocity constant by varying the catalyst bed length accordingly (30 to 50 mg catalyst). The particle fraction used was 150 to 200 µm. Feed gas composition was $H_2/CO_2/Ar$ = 4/1/75, the temperature was set 230 °C, the total pressure 4 bar. The yields of $CH_4$ as a function of the total volumetric flow rate are illustrated in Figure 7.8. No effect of the flow rate on the yield of $CH_4$ can be observed, which means that the reported data is not affected by external heat or mass transport effects. The standard deviation amounts to 1.3 % rel. In both experimental series no impact on $CH_4$ formation was observed, confirming that any heat and mass transport effects, both intra- and inter-particle, on the kinetic data ($WTY(CH_4)$) and the activation energies (under differential measurement conditions at $T$ = 230 °C and high space velocity) can be ruled out.

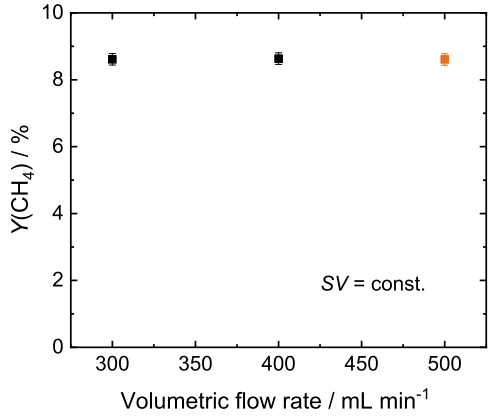


**Figure 7.8:** Yield of $CH_4$ as a function of total volumetric flow rate at constant space velocity *SV*, orange marks the data point used for the kinetic measurement.

## 7.5.5 Characterization Results and Discussion

### 7.5.5.1 X-ray Powder Diffraction

#### Structure of the Precipitate

Figure 7.9 illustrates the XRD patterns of the co-precipitated $[Ni_{0.5}Fe_yAl_{0.5}(OH)_{2+2y}][(CO_3)_{0.25+y/2} \cdot n\,H_2O]$ ($y$ = 0, 0.09) catalyst precursors. The XRD reflections indicate the formation of a modified takovite structure, where $Al^{3+}$ ions partly replace $Ni^{2+}$ ions in hydroxide octahedra. Charge compensation is supplied by the incorporation of $CO_3^{2-}$ in the interlayers. Shifts in the position of the reflections relative to takovite (JCPDS: 15-0087) are caused by the deviation of the $n_{Ni}/n_{Al}$ ratio from 3 [24]. For $NiAlO_x$, the positions of the basal 003 and 006 reflections appear at $2\theta$ = 11.76 and 23.08°, which indicates some distortion of the interlayer between the brucite-like layers, even more pronounced for $NiFeAlO_x$ ($2\theta$ = 11.68 and 22.91°). Evaluation of the mean values of the 003 and 006 reflections reveals a mean interlayer distance $c$ of 22.8 Å for $NiAlO_x$ and 23.0 Å for $NiFeAlO_x$, respectively. The difference in the interlayer distance suggests that the excess of positive charge by the partial replacement of some $Ni^{2+}$ by $Fe^{3+}$ in the gaps of the $OH^-$ octahedra might be compensated by an increased amount of $CO_3^{2-}$ located in the interlayers, leading to a slight increase of the interlayer distance. Evaluation of the 110 reflections at $2\theta$ = 62.36° results in a lattice parameter $a$ of 2.976 Å for both samples, indicating that the replacement of $Ni^{2+}$ and $Al^{3+}$ by $Fe^{3+}$ in the brucite-like layers does not have a significant impact on the mean lattice parameter $a$. The results from XRD on the precipitates are consistent to Chapter 4.

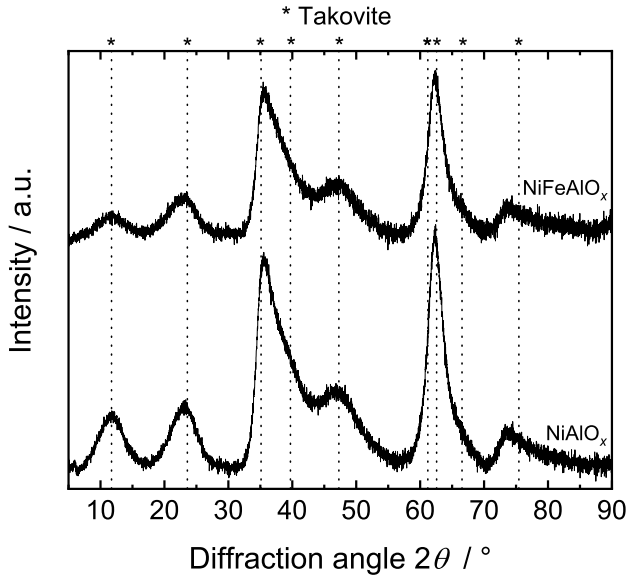


**Figure 7.9:** XRD patterns of the co-precipitated catalyst precursors (JCPDS: Takovite 15-0087).

### Structure of the Calcined and Reduced Catalyst Materials

Figure 7.10 illustrates XRD patterns of the two catalysts in their oxidized and reduced states. During calcination (A), for $NiAlO_x$ a mixed oxide phase of Ni and Al is formed, becoming evident from shifts of the NiO reflections towards the reflections of $\gamma$-$Al_2O_3$ (JCPDS 10-0425). Evaluation of the 220 reflection at $2\theta = 63.80°$ indicates a lattice constant of $a_c = 4.12$ Å for the modified cubic NiO crystal lattice. For $NiFeAlO_x$, a slight systematic shift to lower diffraction angels can be observed, possibly caused by the incorporation of $Fe^{3+}$ ions into the mixed oxide lattice [253]. Therefore, a minimal increase of the lattice parameter $a_c$ to 4.13 Å is found.

Activation (B) of $NiAlO_x$ leads to the formation of metallic Ni crystallites, evident from reflections at $2\theta = 44.56$, 51.84, and 76.50°. In addition, the positions of the reflections caused by the former mixed oxide are further shifted towards $\gamma$-$Al_2O_3$, indicating a decrease of the $Ni^{2+}$ content in the mixed oxide. However, the reflection positions do not meet any pure aluminum oxide phase, which suggests that $Ni^{2+}$ is not removed quantitatively from the bulk of the mixed oxide. Similar observations can be made for $NiFeAlO_x$. However, for the reduced $NiFeAlO_x$, the diffraction signals attributed to the metallic Ni reflections are shifted to lower diffraction angles, e.g. from $2\theta = 51.84°$ (200 fcc Ni reflection) to $2\theta = 51.34°$. This implies that some lattice expansion by the incorporation of metallic Fe into Ni takes place, suggesting that under the chosen activation conditions ($\gamma$Fe,Ni) alloy particles [310] are formed. From the reflection position, the Fe content in the bulk of the ($\gamma$Fe,Ni) alloy particles can be estimated to be 28 at.% [310]. In addition, the reflection positions of the former mixed oxide phase change similar to the ones of $NiAlO_x$. The mean metal crystallite sizes $d_C$ estimated applying the Scherrer equation (*cf.* Eq. 3.4) to the 200 reflections are 3.2 nm for both catalysts.

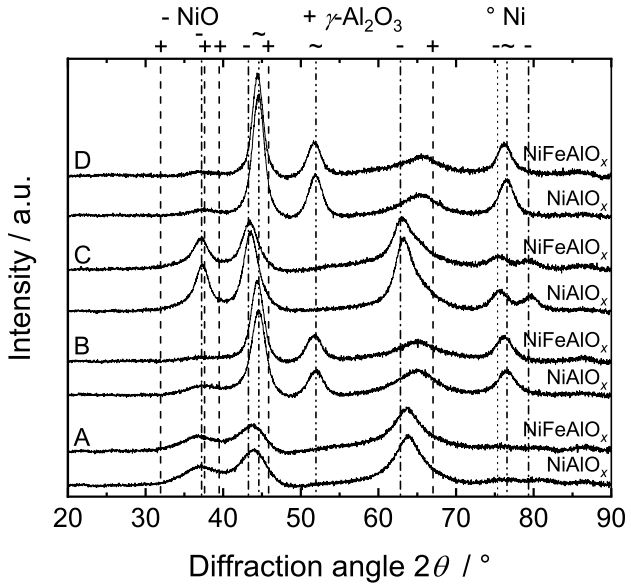


**Figure 7.10:** XRD patterns of the co-precipitated precursors after calcination (A), reduction (B), second calcination (C), second reduction (D) (JCPDS: NiO 78-0429, Ni 87-0712, $\gamma$-$Al_2O_3$ 10-0425).

A second oxidation treatment at 450 °C (C) results in the re-formation of the mixed oxide phase (A). The reflections caused by the metal particles disappear, indicating quantitative oxidation. However, in comparison to (A), for both materials the reflections attributed to the mixed Ni-Al oxide are shifted further towards NiO, which suggests that the amounts of $Al^{3+}$ in the Ni(Fe)$AlO_x$ crystal lattice in the re-oxidized samples are lower than before the initial reduction treatment. This can be interpreted that oxidation of the Ni particles led to the formation of NiO-rich domains in the mixed oxides, containing less $Al^{3+}$ than in the initial calcined catalysts (A). As a consequence of mass balance, this is a strong indicator that, in addition to the mixed oxide phase being evident from XRD, a second amorphous $Al^{3+}$-containing phase, which might also contain $Ni^{2+}$ ions, might be present in the calcined catalyst. This is consistent to a structural model by Alzamora *et al.* [139] derived for hydrotalcites calcined at low temperature. In addition, the intensity of the reflections is higher than in (A), which might arise from an increased degree of crystallinity, possibly attributed to less lattice distortion by $Al^{3+}$ or increased crystallite sizes.

For $NiAlO_x$, a second activation treatment (D) restores the state of the initially reduced catalyst (B). The comparison of diffractogram (D) and (B) shows that the increased crystallinity due to the changed structure of the oxidic catalyst does not have a notable impact on the Ni crystallite size of the reduced catalyst. In addition, this might indicate that for these mixed oxide-derived catalysts a re-dispersion of the Ni particles by oxidation and reduction may be possible. In contrast, for $NiFeAlO_x$, a shift of the reflection for the mixed oxide phase from $2\theta = 65.1°$ (B) to $2\theta = 65.5°$ (D) can be observed, which may result from partial segregation of $Ni^{2+}$, $Fe^{3+}$, and $Al^{3+}$ in the mixed oxide phase during re-oxidation in (C). However, the initial composition of the ($\gamma$Fe,Ni) particles (28 at.% Fe) is restored. The mean crystallite size $d_C$ is 3.2 nm for both catalysts. Most noteworthy, in all diffractograms no reflections corresponding to bulk spinel $NiAl_2O_4$ can be detected.

#### 7.5.5.2 Catalyst Reducibility

Figure 7.11 illustrates the TPR profiles of $NiFeAlO_x$ and the reference $NiAlO_x$, which are consistent to Chapter 4 and 5. Both catalysts exhibit broad reduction signals ranging from 300 to 750 °C. The non-symmetric shapes suggest the co-reduction of differently stabilized $Ni^{2+}$ species in both samples. As claimed by Puxley *et al.* [138], this peak shape might be caused by the reduction of $Ni^{2+}$ from an $Al^{3+}$-containing NiO phase (with the Gaussian peak maximum at 438 °C, 41 %) and $Ni^{2+}$ incorporated in an aluminum oxide phase (Gaussian peak maximum at 540 °C, 58 %) as discussed in Section 7.5.5.1.

For $NiAlO_x$, an additional weak reduction signal appears at 140 °C, which has previously been assigned to small amounts of $Ni^{3+}$ species in external layers [253]. In accordance to its absence in the diffractograms in Figure 7.10, no reduction signal for spinel $NiAl_2O_4$, which would be expected at temperatures higher than 800 °C according to literature [92, 348, 349], can be detected.

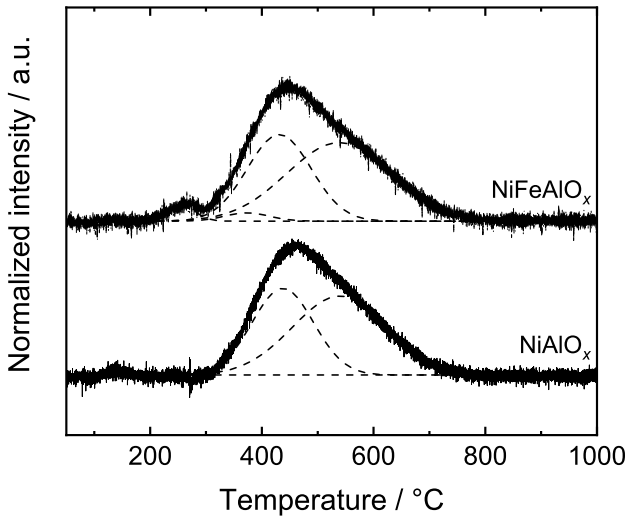


**Figure 7.11:** Temperature-programmed reduction patterns for $NiAlO_x$ and $NiFeAlO_x$, normalized to catalyst mass.

For $NiFeAlO_x$, an additional reduction signal with the maximum at 257 °C appears, that can be assigned to the reduction of $Fe^{3+}$ to $Fe^{2+}$. According to literature [253], the $Fe^{2+}$ species are subsequently reduced to $Fe^0$, with the $H_2$ consumption peak hidden under the broad $Ni^{2+}$ reduction signal. Gaussian peak fitting resolves the maximum of the $Fe^{2+}$ reduction signal at 373 °C. Compared to $NiAlO_x$, the fitted peak of the $Ni^{2+}$ reduction signal from the low-temperature signal is shifted to 431 °C, indicating that the presence of Fe species alleviates the reduction of the nickel oxide phase [149], possibly by interaction with Ni species through the formation of ($\gamma$Fe,Ni) alloy phase as evident from XRD in Figure 7.10 [253].

Comparison of the areas of the reduction signals obtained for the activation conditions applied in the catalytic tests (485 °C, 5 h) reveals that the degree of reduction is 57 % for $NiAlO_x$ and 60 % for $NiFeAlO_x$. The low degree of $Ni^{2+}$ reduction in both catalysts is attributed to incomplete activation of $Ni^{2+}$ incorporated in the $Al^{3+}$-rich oxidic phase (high-temperature reduction peak in Figure 7.11) and is in line with XRD in Section 7.5.5.1.

#### 7.5.5.3 Basicity of the Catalysts

In Figure 7.12 A, the IR spectra of the activated $NiAlO_x$ and $NiFeAlO_x$ catalyst are compared. The carbonate species adsorbed on basic sites of the amphoteric oxide phase are merely similar for both catalysts. For $NiFeAlO_x$, to the detriment of monodentate (1560 to 1510 $cm^{-1}$, 1400 to 1360 $cm^{-1}$) and bidentate carbonate (1630 to 1610 $cm^{-1}$, 1340 to 1320 $cm^{-1}$), a slightly higher amount of bicarbonate species (1650, 1480, and 1220 $cm^{-1}$) [269] can be observed. In literature, a high $CO_2$ uptake capacity of the oxide phase has been shown to be beneficial for $CO_2$ methanation (*cf.* [157] and Chapter 4), with medium basic sites (mono- and bidentate carbonate) [269] being most important [69, 128]. Thereby, an associative methanation pathway is assumed, in which monodentate formate stemming from monodentate carbonate can be hydrogenated faster than bidentate formate originating from bicarbonate [128].

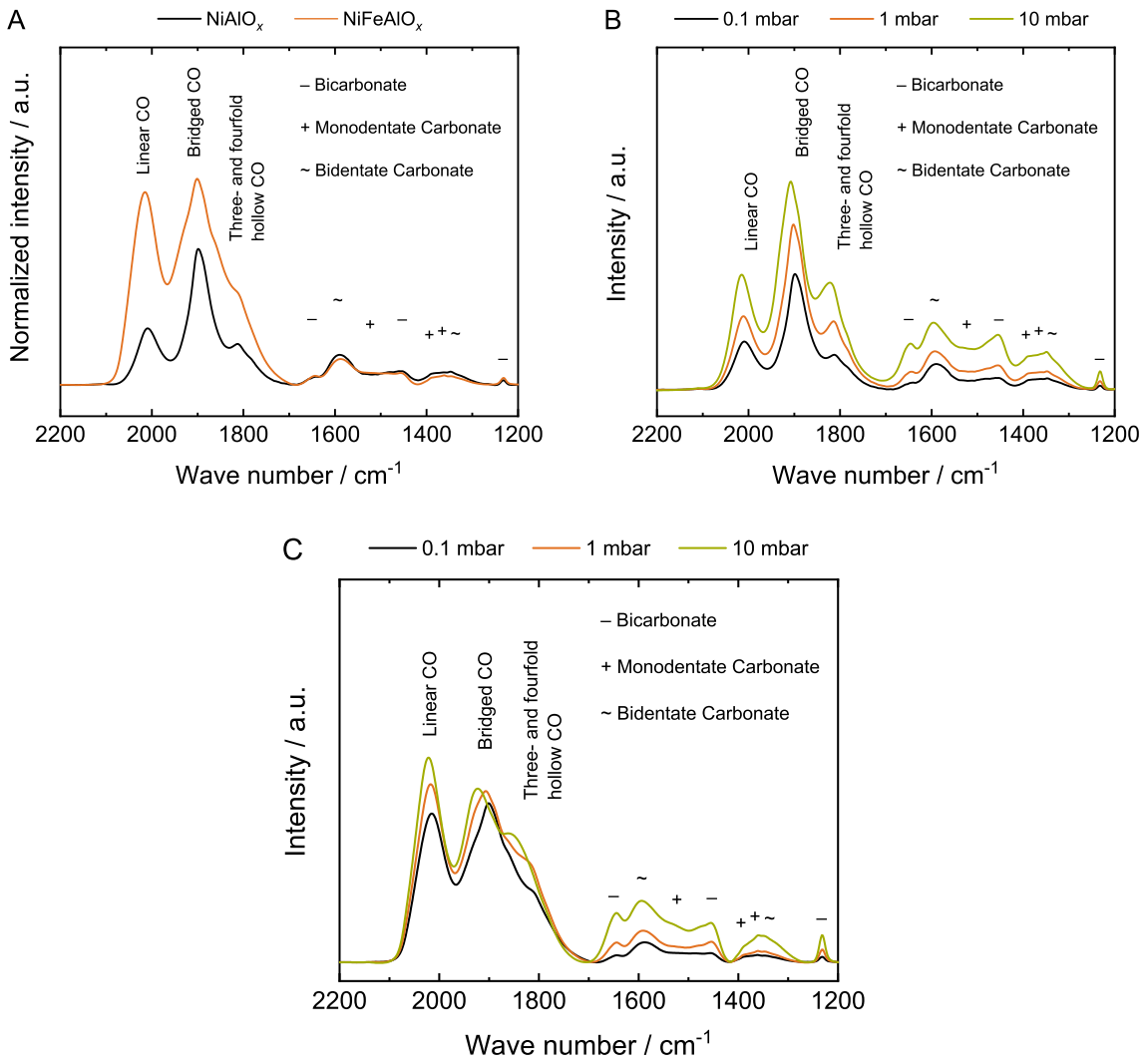


**Figure 7.12:** Infrared spectra of the *in situ* activated $NiAlO_x$ and $NiFeAlO_x$ at 40 °C, dosing pressure $p(CO_2)$ = 0.1 mbar, normalized to pellet mass and beam area (A), infrared spectra of $NiAlO_x$ for different dosing pressures at 40 °C (B), infrared spectra of $NiFeAlO_x$ for different $CO_2$ dosing pressures at 40 °C (C).

Significant differences evolve for the bands in the wavenumber range from 2100 to 1700 $cm^{-1}$, attributed to carbonyl bands originating from $CO_2$ dissociatively adsorbed on the metal sites. For $NiFeAlO_x$, the ratio of adsorbed carbonyl to adsorbed carbonate is much higher compared to $NiAlO_x$. This suggests that metallic Fe contributes to the dissociative adsorption of $CO_2$. However, when evaluating the binding mode, it seems like the proportion of CO being bound linearly (band at 2010 to 2000 $cm^{-1}$) is higher than for $NiAlO_x$, which indicates that Fe primarily contributes to linear binding of CO. Shoulders for bridged and three- as well as fourfold hollow adsorbed CO might be attributed to CO being simultaneously bound to Ni and Fe metal atoms. Furthermore, Fe might modify the electronic state of Ni, changing the $CO_2$ dissociation and/or CO binding properties of Ni. This becomes obvious from shifts of the three bands to higher wavenumbers by 6 $cm^{-1}$, which effectively indicates a higher bond strength of the C-O bond. However, it can be assumed that this shift is caused by adsorbate interactions due to the

higher amount of carbonyl adsorbed on $NiFeAlO_x$. This effect is similar to Figure 7.12 B–C, where the bands assigned to carbonyl on the metal sites are shifted to higher wavenumbers with increasing dosing pressure (increasing coverage). Similar shifts with increasing adsorption pressure can be observed for the band centers of the bidentate carbonate species.

The results from $CO_2$-TPD (*cf.* Figure 7.13) are in line with the observations from infrared spectroscopy. Four overlapping $CO_2$ desorption signals appear for both catalysts. The low-temperature signal with the maximum around 90 °C can be attributed to $CO_2$ evolved from bicarbonate species formed on weak basic sites. Bicarbonate formation is characteristic for $CO_2$ adsorption on transition aluminas [351] that expose both $Al^{IV}$ and hydroxyl groups [352], $CO_2$ is bound on these sites in a bridged configuration. In accordance to infrared spectroscopy from Figure 7.12 A, the density of weak basic sites seems to be increased for $NiFeAlO_x$. The signals in the medium temperature range from 120 to 300 °C can be assigned to $CO_2$ desorption from medium-strength basic sites, bound as monodentate or bidentate carbonate [269, 270].

Both, bidentate carbonate ($CO_2$ desorption peak centered at about 150 °C) and monodentate carbonate ($CO_2$ desorption peak centered at about 220 °C, order of assignment according to [141, 269, 270]) site densities are lower for $NiFeAlO_x$. Mono- and bidentate carbonate species were reported to form at coordinatively unsaturated exposed $O^{2-}$ sites [270], which may be created for reasons of charge compensation due to the incorporation of $Al^{3+}$ into NiO as found in XRD in Section 7.5.5.1, similar to the incorporation of $Al^{3+}$ in MgO in [269]. This is consistent to the observation that mono- and bidentate formation on transition aluminas is very scarce [352]. The proposed role of $Ni^{2+}$ for medium site density agrees well with [141] and Chapter 6, where an increase was observed with rising Ni loading in co-precipitated $NiAlO_x$ materials.

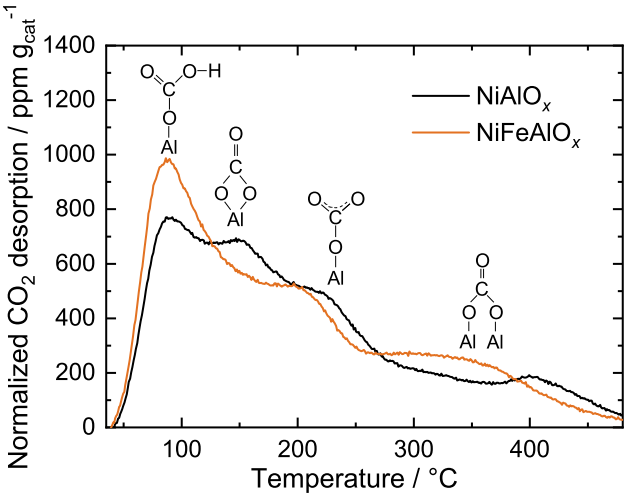


**Figure 7.13:** $CO_2$-TPD patterns of $NiAlO_x$ (black) and $NiFeAlO_x$ (orange), $CO_2$ adsorbed at 35 °C for 30 min, simplified structures according to [270], different binding configurations are given in [350].

The broad desorption signal at temperatures higher than 300 °C may be attributed to bridged/organic-like carbonate species bound to strong basic sites [270]. These carbonate structures are bridged across two adjacent $Al^{3+}$ coordination spheres [352]. From their investigations of various aluminum oxides, Morterra and Magnacca [352] deduced that bridged, "organic-like" carbonate does not form when only $Al^{IV}$ coordinated sites are present, but that hexagonally coordinated $Al^{3+}$ ions may give rise to the basicity of some surface oxygen sites in their coordination sphere.

Besides the differences in basic site densities, the binding energies of $CO_2$ on the medium and strong basic sites on $NiFeAlO_x$ seem to be decreased compared to $NiAlO_x$, obvious from the shift of the $CO_2$ desorption signals to lower desorption temperatures, possibly alleviating hydrogenation or decomposition and formation of carbonyl on the metal sites. Since the sites for (bi)carbonate formation, in contrast to carbonyl, are supposed to be exclusively located on the oxidic phase, the difference of basic sites densities on the oxidic phase is supposed to result from un- or partly reduced $Fe^{n+}$ ($n = 2, 3$) species, varying the properties for $CO_2$ adsorption on these sites. All observations in $CO_2$–TPD are consistent to previous studies on co-precipitated Ni-based co-precipitated catalysts in Chapters 4, 5, and 6.

### 7.5.6 Transmission Electron Microscopy

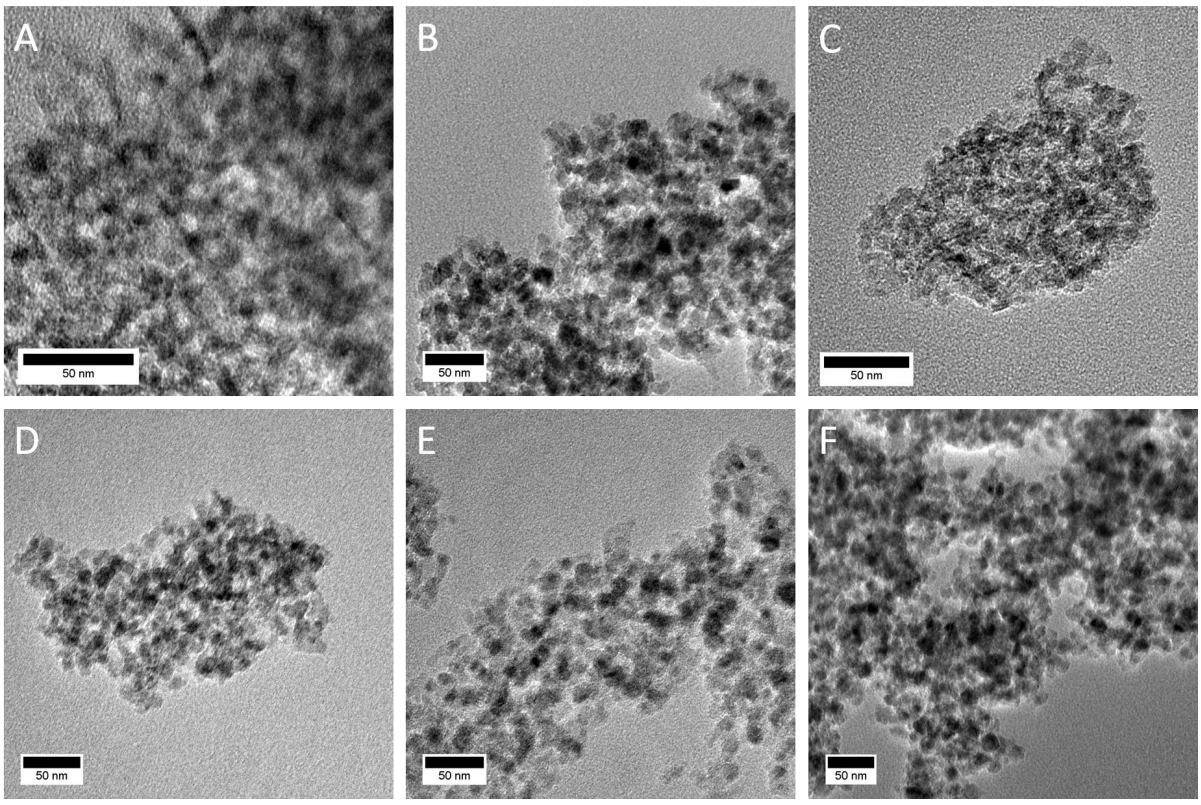


**Figure 7.14:** TEM images of $NiAlO_x$, freshly reduced (A) and aged for 72 h at 450 °C (B), and for $NiFeAlO_x$, freshly reduced (C), and aged for 6 (D), 40 (E), and 72 h (F) at 450 °C.

## 7.5.7 Mössbauer Spectroscopy

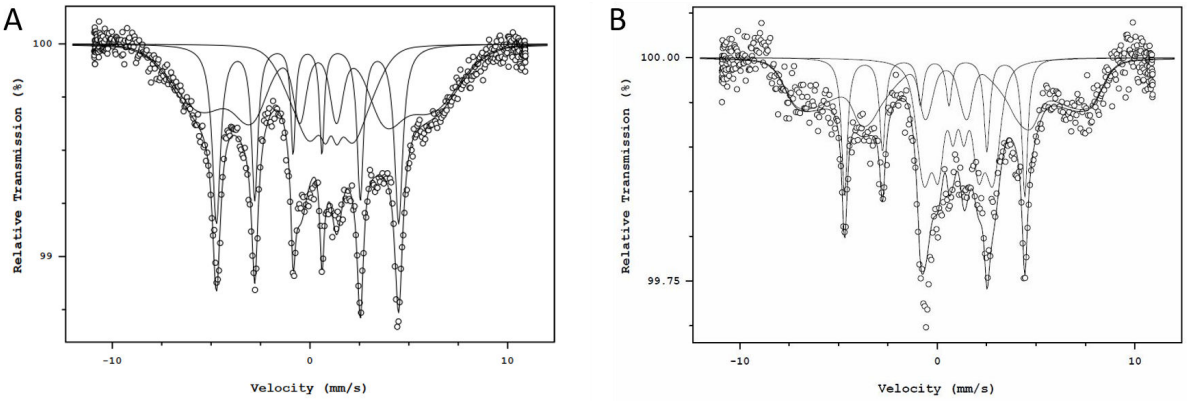


**Figure 7.15:** Mössbauer spectra of $NiFeAlO_x$, freshly reduced (A), and aged for 6 h at 450 °C (B). The spectra were recorded at 4.2 K with the $^{57}$Co/Rh source at the same temperature as the absorber.

## 7.5.8 Paramagnetic/Ferromagnetic Resonance Spectroscopy

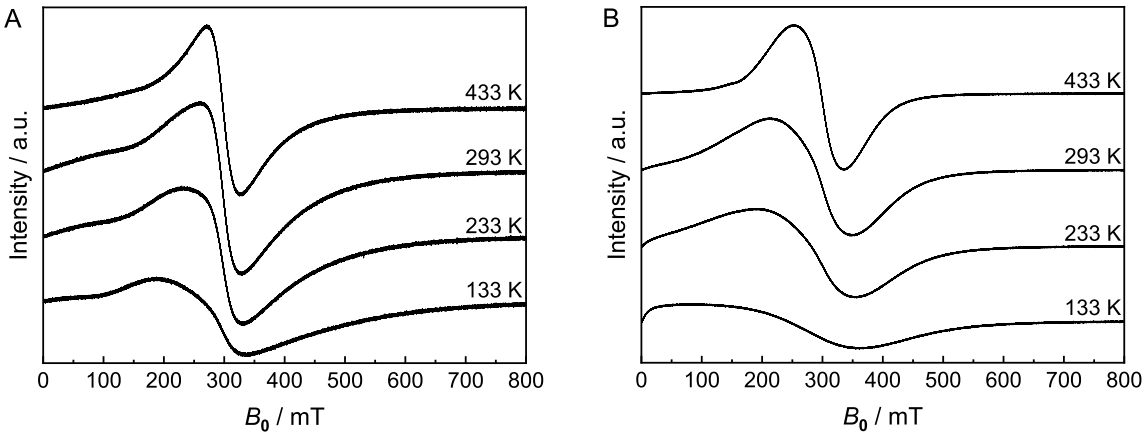


**Figure 7.16:** FMR spectra of $NiAlO_x$, freshly reduced (A) and aged for 72 h at 450 °C (B).

**Table 7.4:** Normalized magnetic intensities and linewidths from FMR of $NiAlO_x$ and $NiFeAlO_x$ in their freshly reduced and aged states.

| Catalyst | $t_a$ / h | $T_a$ / °C | Normalized intensity / - | $\Delta B_{pp}$ / mT |
|---|---|---|---|---|
| $NiAlO_x$ | 0 | - | 1 | 145 |
| | 72 | 450 | 1 | 270 |
| $NiFeAlO_x$ | 0 | - | 2.1 | 260 |
| | 6 | 450 | 4.0 | 265 |
| | 40 | 450 | 5.1 | 230 |
| | 72 | 450 | 4.0 | 170 |
| | 72 | 400 | 3.8 | 230 |

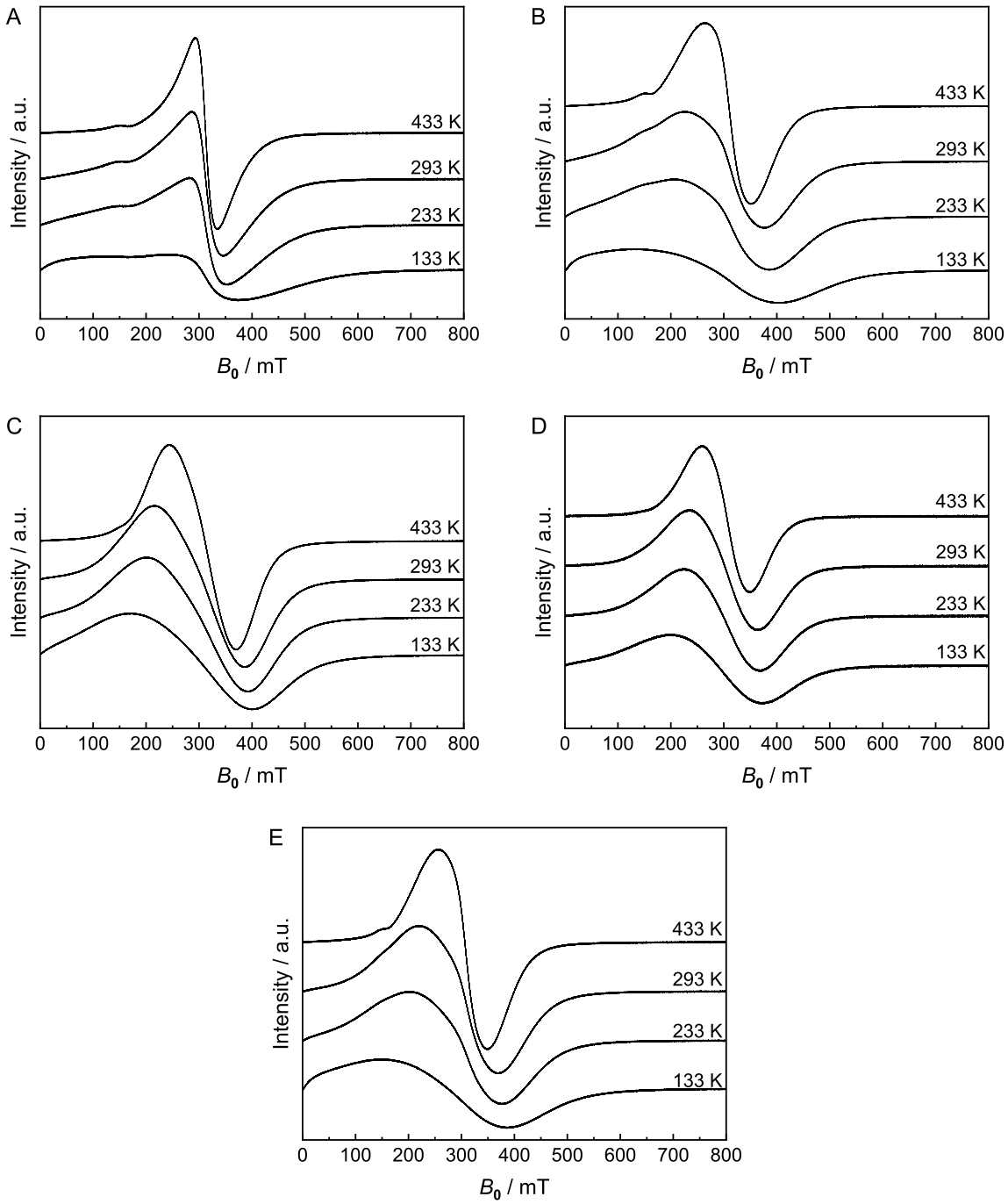


**Figure 7.17:** FMR spectra of $NiFeAlO_x$, freshly reduced (A), aged for 6 h (B), 40 h (C), 72 h (D) at 450 °C, and aged for 72 h at 400 °C (E).

### 7.5.9 Hydrogen Treatment of Aged $NiFeAlO_x$

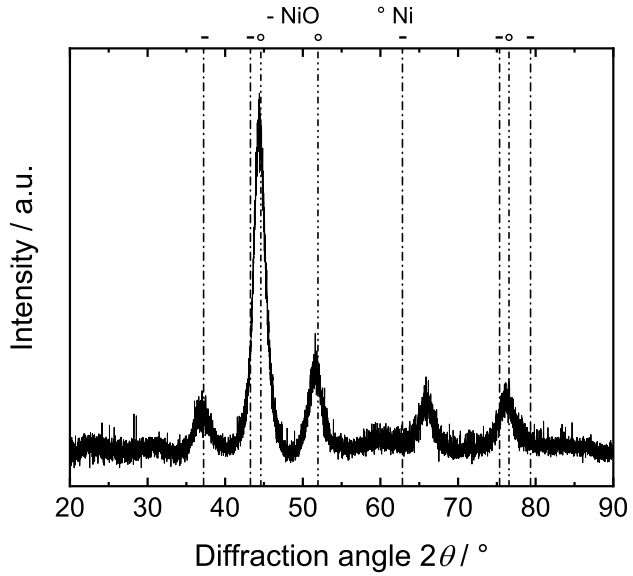


**Figure 7.18:** XRD pattern for $NiFeAlO_x$ after activation, aging at 450 °C and 8 bar for 6 h, re-activation at 485 °C in 5 % $H_2$ in Ar, repeated aging at 450 °C and 8 bar for 6 h, repeated re-activation at 485 °C in 5 % $H_2$ in Ar (JCPDS: NiO 78-0429, Ni 87-0712).

# 8 On the Kinetics of the Co-Methanation of CO and $CO_2$ on a Co-Precipitated Ni-Al Catalyst

This chapter was published in similar form in:

T. Burger[1], P. J. Donaubauer[1], O. Hinrichsen, On the kinetics of the co-methanation of CO and $CO_2$, *Applied Catalysis B: Environmental*, 2020, *282*, 119408, DOI 10.1016/j.apcatb.2020.119408



## Abstract

The kinetics of the gas-phase co-methanation reaction of carbon oxides over a co-precipitated 44 wt.% $NiAlO_x$ catalyst were modelled *via* competitive adsorption of CO and $CO_2$ and the subsequent methanation of a common surface intermediate. Steady-state isotope experiments and model discrimination suggest the decomposition of a hydrogenated $COH_y$ surface intermediate to be the kinetically relevant step in the methanation reaction. The best fit is obtained for hydroxycarbene ($y$ = 2). The presented kinetic model is the first to explicitly describe the full coupling of CO and $CO_2$ transformation. It is built on the basis of CO methanation, $CO_2$ methanation, steam reforming and water-gas shift experiments over a wide range of conditions. All model parameters are thermodynamically consistent and statistically relevant.

## 8.1 Introduction

The carbon oxides methanation reactions recently have re-gained interest due to an increase in environmental awareness and a change in energy policy, aiming to reduce greenhouse gas emissions and contain global warming [353]. In the power-to-gas process chain, $CO_x$, which may originate from waste gas streams of conventional power plants based on fossils or from gasification processes of biomass or coal, is converted to substitute natural gas (SNG) using $H_2$ derived by electrolysis using surplus renewable energy. The reaction system consisting of CO,

[1] The authors equally contributed to this work.

$CO_2$, $H_2O$, $CH_4$, and $H_2$ can be described by the reaction network comprising the methanation reactions of CO (*cf.* Reaction 8.I) and $CO_2$ (*cf.* Reaction 8.II) in combination with the water-gas shift reaction (*cf.* Reaction 8.III).

$$CO + 3\,H_2 \rightleftharpoons CH_4 + H_2O \qquad \Delta H_R^0 = -206.3\,\mathrm{kJ\,mol^{-1}} \quad \Delta G_R^0 = -142.2\,\mathrm{kJ\,mol^{-1}} \tag{8.I}$$

$$CO_2 + 4\,H_2 \rightleftharpoons CH_4 + 2\,H_2O \qquad \Delta H_R^0 = -165.1\,\mathrm{kJ\,mol^{-1}} \quad \Delta G_R^0 = -113.5\,\mathrm{kJ\,mol^{-1}} \tag{8.II}$$

$$CO + H_2O \rightleftharpoons CO_2 + H_2 \qquad \Delta H_R^0 = -41.2\,\mathrm{kJ\,mol^{-1}} \quad \Delta G_R^0 = -27.7\,\mathrm{kJ\,mol^{-1}} \tag{8.III}$$

In this work, it is focused on the kinetic description of the reaction network (Reactions 8.I-8.III), catalyzed by a co-precipitated, hydrotalcite-derived $NiAlO_x$ catalyst. Koschany *et al.* [24] recently developed a kinetic model for the description of $CO_2$ solo-methanation without considering the species CO as well as CO methanation and water-gas shift reaction. However, realistic feed gases derived from coal gasification or biomass plants contain significant amounts of CO, which is known to strongly inhibit the methanation reaction of $CO_2$ [169, 302] and, besides, can lead to significant catalyst deactivation by carbon deposition [28, 354, 355] or $Ni(CO)_4$ formation [356, 357]. Moreover, significant amounts of CO are formed in thermodynamic equilibrium at high methanation temperatures [27], caused by hotspot formation. Therefore, the kinetic description of CO methanation and the water-gas shift reaction are indispensable for the prediction of $CO_2$ methanation rates and to describe the reaction dynamics of CO-containing feed gas.

The different reaction pathways and mechanisms proposed in literature have extensively been discussed in Section 2.2.4, [73] and references therein. In the associative $CO_2$ methanation pathway, $CO_2$ is hydrogenated to formate, that is subsequently hydrogenated to $CH_4$ [126, 163]. The dissociative $CO_2$ methanation pathway, in comparison, involves the dissociation of $CO_2$ to CO* [80, 165, 166]. For associative CO methanation, CO adsorbs in the form of CO* and is hydrogenated *via* a hydrogenated surface intermediate $COH_y$ ($y$ = 1 to 3) [80, 166, 169–172, 174, 175], while for dissociative CO methanation CO* dissociates to C*, respectively, before hydrogenation to $CH_4$ [177–179].

Investigations by Weatherbee *et al.* [194] and Falconer *et al.* [115] give hints that the methanation reactions of CO and $CO_2$ proceed *via* the same mechanism. Falbo *et al.* investigated the mechanism of the methanation reaction over a $Ru/Al_2O_3$ catalyst in an IR study [57]. From the observations, they concluded that $CO_2$ is pre-activated on the oxidic phase in the form of carbonates that get hydrogenated to formate, while CO associatively adsorbs on the Ni centers. Formate then decomposes to CO* on the metal centers and is further hydrogenated. The hydrogenation step of CO* to $CH_4$ then was prosposed to take place *via* a common mechanism. As discussed in Section 2.2.4 (*cf.* references therein), state-of-the-art kinetic models on the methanation reactions comprise different mechanisms and kinetics for CO and $CO_2$ and do not reflect the competitive adsorption of CO and $CO_2$ [73, 186, 187, 191]. Instead, both CO and $CO_2$ adsorption processes are typically modelled *via* the assumption of quasi-equilibration with

surface-bound CO* [186, 193, 194], thus defining different CO* species for CO and $CO_2$, which may lead to the statistical irrelevance of the adsorption parameters for either CO or $CO_2$ [186], possibly resulting in inconsistencies among the remaining fitted kinetic and thermodynamic parameters. Also, models containing kinetic rate equations for CO methanation and water-gas shift reaction [73], or for $CO_2$ methanation and reverse of the water-gas shift reaction [191], therefore disregarding CO* originating from $CO_2$ or CO, respectively, do not give access to the surface coverage of CO* once the respective CO* precursor molecule is completely consumed and therefore may not be suitable for co-methanation feed gas.

Coupled methanation reactions *via* a common carbonyl reaction intermediate were kinetically described by Inoue *et al.* [176]. The rate-limiting step was assumed to be the hydrogenation of C* in an Eley-Rideal-type mechanism. However, they did neither include the adsorption of $H_2$, the repressive effect of $H_2O$ on the methanation rate, nor the water-gas shift reaction, which drastically simplified the resulting reaction network and rate equations. Still, the model could not be explicitly solved.

To resolve the interactions of CO*, $CO_{(g)}$ and $CO_{2(g)}$ in a mechanistically consistent approach, the model developed in this work, therefore, explicitly aims at describing the competitive adsorption of CO and $CO_2$ and their hydrogenation *via* the common reaction intermediate CO* in a common kinetically relevant step. For this reason, kinetic data points under CO and $CO_2$ co-methanation, water-gas shift as well as steam reforming conditions were gathered, providing over 1700 fitting responses. It is shown that the presented kinetic model cannot be discriminated from the model for $CO_2$ solo-methanation recently derived by Koschany *et al.* over the same catalyst [24].

## 8.2 Experimental

The $NiAlO_x$ catalyst used was the same as in [24] and prepared analogously to the one in Chapter 4 to provide data comparability. The detailed catalyst synthesis procedure can be found in Section 8.7.1.1. For characterization, inductively-coupled plasma-optical emission spectroscopy (ICP-OES), static gas sorption techniques, temperature-programmed reduction (TPR), temperature-programmed desorption of $H_2$ ($H_2$-TPD) and X-ray powder diffraction (XRD) were applied. The catalyst was characterized after reduction to capture the material characteristics describing its initial activity, as well as after an aging treatment (*cf.* Section 8.2.2) to evaluate deactivation mechanisms during the aging treatment and describe the material properties during kinetic data gathering. After activation, the catalyst featured a metal surface area of $21.4\,m^2\,g_{cat}^{-1}$ at a Ni crystallite size of 3.2 nm. The BET surface area was $294\,m^2\,g_{cat}^{-1}$. Static $CO_2$ chemisorption yielded a $CO_2$ uptake of $172\,\mu mol\,g_{cat}^{-1}$ (*cf.* Chapter 4). The calcined catalyst features a Ni loading of 44.3 wt.% and a mixed metal oxide structure. The experimental procedures and the characterization results are in detail reported in Section 8.7.1.2 and 8.7.2, respectively.

### 8.2.1 Experimental Setup

The setup described in [24] was modified (*cf.* Section 3.3) and used for all measurements. A carbonyl guard reactor was installed downstream the CO gas cylinder to capture carbonyls. All further piping was $SiO_2$-coated on the inside to prevent carbonyl formation. All gases were supplied by Westfalen. Gas purity was 5.0 for all gases except for CO (4.6). $H_2O$ was fed by a liquid phase mass flow controller and evaporated in a heat box before mixing with the reactant gas stream. All tubing was heated to prevent $H_2O$ condensation. Downstream the reactor, the gas flow was diluted with Ar in a ratio of 1:8. For $CO_2$, CO, $CH_4$, $H_2O$, and $H_2$, gas compositions were measured using an online Emerson MTL-4 process gas analyzer (PGA). Hydrocarbon and methanol byproducts were analyzed in a Clarus 580 gas chromatograph (GC, PerkinElmer) equipped with two FID detectors. For every reactant and product data point, the conditions were kept stable for at least 45 min. Gas composition was measured every second and averaged over the last 150 s. Volume contraction occurring in CO and $CO_2$ methanation (*cf.* Eq. 3.15) as well as volume expansion in the steam reforming reaction (*cf.* Eq. 3.17) were taken into account.

### 8.2.2 Catalyst Conditioning

25 mg of catalyst were mixed with 225 mg of purified SiC (ESK), placed in the isothermal zone of a $SiO_2$-coated tubular reactor of 4 mm diameter, and axially fixed by quartz wool plugs. To track catalyst bed temperature, a thermocouple with 1.5 mm diameter was put 1 mm into the catalyst bed at the reactor outlet.

The catalyst was activated at 485 °C (linear rate of $2\,\mathrm{K\,min^{-1}}$) in 5 % $H_2$ in Ar and held there for 11 h. The total space velocity was set to $30\,\mathrm{NL\,g_{cat}^{-1}\,h^{-1}}$. After cooling down to 250 °C, the aging procedure reported in [24] (*cf.* Section 8.7.3) was applied to obtain a stable catalyst performance over time and to decouple kinetic reaction rate data from deactivation phenomena. The stable activity level was obtained after 100 h of aging at 380 °C, 7 bar, and a feed gas composition of $H_2/CO_2/CH_4/H_2O/Ar$ = 4/1/1.25/2.5/1.25 at $Q = 120\,\mathrm{NL\,g_{cat}^{-1}\,h^{-1}}$. This gas composition reflects a fictive $CO_2$ conversion of 55.5 % at the reactor inlet, co-feeding of $H_2O$ proved to be effective for accelerating deactivation and reaching a constant activity level [24]. In addition, it leads to a uniformly aged catalyst bed. After aging, the Ni surface area was $13.3\,\mathrm{m^2\,g_{cat}^{-1}}$ at a mean crystallite size of 5.2 nm (calculated from XRD). The BET surface area amounted to $179\,\mathrm{m^2\,g_{cat}^{-1}}$ at a total pore volume of $0.89\,\mathrm{mL\,g_{cat}^{-1}}$, resulting in a mean hydraulic pore diameter of 19.8 nm (*cf.* Eq. 3.8). The total $CO_2$ uptake capacity after aging, determined by static chemisorption at $T$ = 35 °C, was $96\,\mathrm{\mu mol\,g_{cat}^{-1}}$ (*cf.* Section 8.7.2). Since no further catalyst deactivation was observed during the kinetic measurements, verified by activity measurements at various reference points (*cf.* Section 8.2.3), these material parameters reflect the state of the catalyst during the kinetic measurements. Compared to the catalyst properties initially after activation (*cf.* Section 8.7.2), the activity loss during aging (*cf.* Figure 8.12) seems to be caused by Ni particle sintering, decrease of the BET surface area (attributed to pore rupture, indicated

by an increase in pore volume and mean pore diameter) as well as the loss of basic sites. A comprehensive study on the deactivation processes of Ni-Al catalysts (also for a catalyst analogously prepared to the one in this study) was carried out in [134].

### 8.2.3 Kinetic Measurements

To avoid the formation of $Ni(CO)_4$ under reaction conditions, the temperature during parameter variation under CO-containing feed gas was kept higher than 230 °C. In analogy to [24], the maximum temperature was set 340 °C, the total pressure ranged from 1 to 10 bar. Moreover, steam reforming conditions were investigated at elevated temperatures up to 600 °C. The experiments were conducted for two space velocities, 180 and 240 NL $g_{cat}^{-1}$ $h^{-1}$. Kinetic measurements were carried out in differential and integral mode to cover the approximation to thermodynamic equilibrium. Besides, inhibition effects of the products $CH_4$ and $H_2O$ were investigated by co-feeding various stoichiometries. Limitation in the combination of experimental parameters, proved in and deduced from extensive pre-studies, arose from:

- carbon deposition under $H_2$-lean conditions free from $H_2O$ and $CO_2$ ($H_2/CO < 6$)
- excessive hotspot formation under space velocities higher than 240 NL $g_{cat}^{-1}$ $h^{-1}$ due to increased heat production
- short catalyst bed length to ensure isothermal temperature distribution, long enough to ensure plug flow behavior [358].

The catalyst particle fraction of 100 to 150 µm was used for the kinetic experiments. Experimental (by varying catalyst particle diameter at high space velocities as well as varying flow rate at fixed space velocities, respectively, and monitoring conversion and yields) and computational (by examining the heat and mass transfer criteria Eqs. A.1 to A.4, *cf.* Appendix A, for each component) investigations confirm the absence of heat and mass transport limitations for the kinetic measurements in the chosen parameter range.

To check for possible further catalyst deactivation during the kinetic measurements and parameter variation experiments, at least once per 24 h product gas compositions at the reference point $RF_1$ (for $CO_2$ methanation) and an additional reference point $RF_2$ (for CO methanation; $T$ = 270 °C, $p$ = 5 bar, $Q$ = 240 NL $g_{cat}^{-1}$ $h^{-1}$, $H_2/CO_2/CO/Ar$ = 21/3/3/13) were measured. At the reference point $RF_3$ ($T$ = 475 °C, $p$ = 5 bar and $Q$ = 180 NL $g_{cat}^{-1}$ $h^{-1}$ at a feed gas composition of $H_2/CH_4/H_2O/Ar$ = 2.5/10/15/72.5) possible deactivation under steam reforming conditions was tracked. All feed gas compositions and the respective parameters are listed in Table 8.3.

### 8.2.4 Steady-State $D_2$ Isotope Experiments

$D_2$ isotope experiments were carried out under steady-state flow conditions. To experimentally investigate the dissociation behavior of $H_2O$ on the Ni sites, $H_2O$ and $D_2$ ($H_2O/D_2/Ar$ = 1/5/9) were brought into contact over 25 mg of catalyst at a temperature of 260 °C and 4 bar. The total volumetric flow rate was 75 N mL $min^{-1}$. Reaction gas composition was monitored and analyzed *via* mass spectrometry (Pfeiffer-Vacuum Omnistar GSD301).

In a second experiment, $H_2$ in $H_2O/H_2/CO/Ar$ = 1/5/1/8 and $H_2/CO_2/Ar$ = 4/1/5, respectively, was replaced by $D_2$, while all other experimental parameters were kept constant as stated above. $CO_x$ conversions below 20 % verify that the reaction occurred in the kinetic regime away from thermodynamic equilibrium under these conditions. Reaction gas composition was monitored and analyzed *via* mass spectrometry (Pfeiffer-Vacuum Omnistar GSD301), the process gas analyzer (PGA), and the online gas chromatograph (GC). $CD_4$ was tracked *via* gas chromatography, applying a FID sensitivity factor of 1.0352 compared to $CH_4$ [359].

### 8.2.5 Determination of Apparent Activation Energies and Reaction Orders in CO Methanation

10 mg of catalyst were diluted with 90 mg of purified inert SiC. The apparent activation energy was determined under differential conditions by linearizing the Arrhenius equation in the temperature range from 240 to 290 °C and at absolute pressures of 4, 7, and 10 bar. The space velocity was 3000 NL $g_{cat}^{-1}$ $h^{-1}$ with a feed gas composition of $H_2/CO/Ar$ = 18/3/79. Errors were calculated according to Gaussian error propagation. The error of the temperature measurement was estimated to be 1.5 K (manufacturer's data, fuehlersysteme.net). The $CH_4$ formation rates were averaged over 150 single measurements per data point.

The apparent reaction orders were determined from linear regression of the logarithmic $CH_4$ formation rate versus the logarithmic CO partial pressure at constant $H_2$ partial pressure and *vice versa*. $CH_4$ conversion was held below 15 % to mimic differential conditions free from product or equilibrium limitations.

## 8.3 Model Development

The kinetic model presented was developed based on parameter estimation and model discrimination for literature-known methanation mechanisms. Additional information is provided in Section 8.7.6. A broad overview is given in [73] and the references therein. In addition, model development was based on the experiments described in Section 8.2.4.

## 8.3.1 Mechanistic Conclusions Based on Steady-State Isotope Experiments

### 8.3.1.1 Adsorption of $H_2O$

To evaluate the surface species formed upon the adsorption of $H_2O$ on the Ni sites (associative adsorption in the form of $H_2O$*, dissociative adsorption yielding OH* and H*), $H_2O$ was brought into contact with excess $D_2$ at 4 bar and 260 °C. The product gas contained significant amounts of HD and HDO clearly indicating that $H_2O$ dissociates on the Ni sites. Furthermore, only traces of $H_2$ were observed in the product gas. This is an indicator that $H_2O$ adsorption on Ni takes place *via* dissociation to OH* and H* and that dissociation of $H_2O$ to O* and H* can be neglected under the chosen conditions.

### 8.3.1.2 Nature of the Rate-Determining Step and the Surface Intermediate

When substituting $H_2$ by $D_2$, for both the CO- and the $CO_2$-containing methanation feed gas an inverse kinetic isotope effect was observed. The ratio of the $CH_4$ and the $CD_4$ formation rates $R_{CH_4,H_2}/R_{CD_4,D_2}$ was 0.78 for the $CO_2$-containing feed gas and 0.89 for the CO-containing feed gas. This is in line with a study on CO methanation of Mori *et al.* [170], who found an average inverse isotope effect of 0.75 for CO methanation over a supported $Ni/SiO_2$ catalyst in pulse surface reaction analysis experiments (PSRA) in the absence of $H_2O$.

The pure presence of a kinetic isotope effect clearly suggests that H atoms, either in the form of H* or bound in a surface complex, are involved in the rate-determining step. Any hydrogenation step that is positive in the reaction order of hydrogen should run faster in $H_2$ than in $D_2$, since D* formed on the active Ni sites features a higher stability on the catalyst surface due to a lower zero-point energy (related to its higher mass, common explanation for a kinetic isotope effect) [170]. The observed negative kinetic isotope effect thus contradicts the postulation a hydrogenation step being rate-limiting in methanation, but, instead, can be explained by assuming the decomposition of a H/D-containing (formyl Ni-CHO, hydroxycarbene Ni-CHOH, or hydroxymethyl Ni-$CH_2$OH) surface intermediate to be the kinetically relevant step in methanation. The replacement of H by D in the surface complex leads to a higher stabilization of the complex in the Ni surface due to the lower zero-point energy of O-D and C-D bonds compared to O-H and C-H bonds [170]. As a result of the resulting higher stability, a higher coverage for the deuterated surface species can be expected, leading to a higher decomposition rate.

The fact that the negative isotope effect is observed for both CO and $CO_2$ methanation is a strong hint that both methanation processes run *via* the same mechanism and feature the same rate-limiting step. The difference in the absolute kinetic isotope effects (0.78 for $CO_2$ methanation and 0.89 for CO methanation) can be explained by different coverages of the hydrogenated surface complex/CO*/OH* depending on feed gas composition. From transition state theory [360] and theoretical assumptions based on their experimental parameter, Mori *et al.* estimated a kinetic isotope effect of 0.74 when assuming the decomposition of a hydroxycarbene (CHOH*)

species to be rate-limiting, which was a good match to the experimental findings (0.75) [170].

The presence of H-containing surface intermediates in the methanation reaction and their involvement in the kinetically relevant reaction step has been claimed in different studies [80, 166, 169–172, 174, 175, 180], but experimental proof in IR experiments is lacking. However, this is not in contradiction of hydrogenated surface species being present. Andersson *et al.* estimated that the coverage of hydrogenated CHO* or COH* species being in equilibrium with CO* (which is a justified assumption based on the low barrier of formation compared to the desorption barrier of CO*) would amount to $< 10^{-7}$ [180], which explains their general non-appearance in IR spectra.

### 8.3.2 Mathematical Description of the Co-Adsorption of CO and $CO_2$

The main drawback of kinetic models for the methanation reaction available in literature is the assumption that surface-bound CO* may only arise from either $CO_{(g)}$ or $CO_{2(g)}$ (*cf.* Section 8.1). To couple the methanation reactions of CO and $CO_2$, however, instead it needs to be considered that CO* may be formed from the associative adsorption of $CO_{(g)}$, but also from the dissociative adsorption of $CO_{2(g)}$. Under pseudo steady-state conditions, the surface coverage of CO* is constant over time. $r_{ads}$ and $r_{des}$ describe the rate of ad- and desorption of CO and $CO_2$, respectively, $r_{met}$ the rate of methanation and $r_{SR}$ the rate of the steam reforming reaction:

$$\frac{\mathrm{d}\theta_{CO}}{\mathrm{d}t} = 0 = r_{ads,CO} - r_{des,CO} + r_{ads,CO_2} - r_{des,CO_2} - r_{met} + r_{SR}. \tag{8.1}$$

To describe the interactions of $CO_2$, CO, and $CH_4$ with CO* on the catalyst surface, the adsorption processes of CO or $CO_2$, respectively, can no longer be considered quasi-equilibrated, in contrast to literature-known kinetic model approaches [186, 191], but need to be balanced by the rate of the methanation reaction and its reverse. Assuming an associative adsorption mechanism for CO, the net rate of CO adsorption can be described by:

$$r_{ads,CO} - r_{des,CO} = k_{ads,CO} \cdot p'_{CO} \cdot \theta^* - k_{des,CO} \cdot \theta_{CO} = k_{ads,CO} \cdot p'_{CO} \cdot \theta^* - \frac{k_{ads,CO}}{K_{CO}} \cdot \theta_{CO}. \tag{8.2}$$

$K_{CO}$ denotes the adsorption constant of CO. For the mathematical description, all partial pressures are used in normalized form with a reference pressure of $p_{ref} = 1\,\mathrm{bar}$.[2]

$$p'_i = \frac{p_i}{p_{ref}} \tag{8.3}$$

The net rate of $CO_2$ adsorption contains the rate equation of the water-gas shift reaction (*cf.* Reaction 8.III). The rate-determining step in the water-gas shift reaction is commonly

[2] This procedure allows the definition of dimensionless equilibrium constants in accordance with thermodynamics (*cf.* Appendix C), rather than dividing the respective equilibrium constants by (powers of) the reference pressure.

considered to be the reaction of CO* with OH* or O* [73, 191]. Because of the results of the isotope experiments, disclosed in Section 8.3.1.1, it can be assumed that $H_2O$ dissociatively adsorbs to OH* and H*, while no O* is formed. Based on these results, the rate-determining step of the water-gas shift reaction then can be expressed as shown in Reaction 8.IV, in analogy to [191].

$$CO^* + OH^* \rightleftharpoons CO_2 + H^* + {}^* \tag{8.IV}$$

The rate of the reverse of the water-gas shift reaction is then equivalent to the H*-assisted adsorption of $CO_2$. The net rate of $CO_2$ adsorption therefore can be described by Eq. 8.4.

$$\begin{aligned} r_{\mathrm{ads,CO_2}} - r_{\mathrm{des,CO_2}} &= k_{\mathrm{ads,CO_2}} \cdot p'_{\mathrm{CO_2}} \cdot \theta_{\mathrm{H}} \cdot \theta^* - k_{\mathrm{des,CO_2}} \cdot \theta_{\mathrm{CO}} \cdot \theta_{\mathrm{OH}} \\ &= k_{\mathrm{ads,CO_2}} \cdot p'_{\mathrm{CO_2}} \cdot \theta_{\mathrm{H}} \cdot \theta^* - \frac{k_{\mathrm{ads,CO_2}}}{K_{\mathrm{CO_2}}} \cdot \theta_{\mathrm{CO}} \cdot \theta_{\mathrm{OH}} \end{aligned} \tag{8.4}$$

$K_{\mathrm{CO_2}}$ denotes the equilibrium constant for $CO_2$ adsorption. It should be mentioned that the adsorption of $CO_2$ may be a lumped process and may contain the pre-activation of $CO_2$ on the oxidic support in the form of carbonate. The assumption of a dual site mechanism, however, did not lead to an improvement of the data fits of any of the tested rate equations derived for different mechanisms. Based on the negative kinetic isotope effect discussed in Section 8.3.1.2, the rate-determining step in methanation is assumed to be the CO bond cleavage *via* the decomposition of a hydrogenated surface complex $COH_y$*, involving a second active site. $y$ denotes the degree of hydrogenation in $COH_y$. This hydrogenated surface complex $COH_y$* is assumed to be quasi-equilibrated with CO* [180].

$$CO^* + y\,H^* \rightleftharpoons COH_y{}^* + y^* \tag{8.V}$$

The coverage of $COH_y$ then can be expressed as

$$\theta_{\mathrm{COH}_y} = K_{\mathrm{COH}_y} \cdot \frac{\theta_{\mathrm{CO}} \cdot \theta_{\mathrm{H}}^y}{\theta^{*y}}. \tag{8.5}$$

With the rate-determining step of methanation

$$COH_y{}^* + {}^* \rightleftharpoons CH_{y-1}{}^* + OH^*, \tag{8.VI}$$

the net equation of the methanation reaction can then be written as shown in Eq. 8.6 [361].

$$\begin{aligned} r_{\mathrm{met}} - r_{\mathrm{SR}} &= k'_{\mathrm{met}} \cdot \theta_{\mathrm{COH}_y} \cdot \theta^* - k_{\mathrm{SR}} \cdot \theta_{\mathrm{CH}_{y-1}} \cdot \theta_{\mathrm{OH}} = k'_{\mathrm{met}} \cdot \theta_{\mathrm{COH}_y} \cdot \theta^* - \frac{k'_{\mathrm{met}}}{K'_{\mathrm{met}}} \cdot \theta_{\mathrm{CH}_{y-1}} \cdot \theta_{\mathrm{OH}} \\ &= k'_{\mathrm{met}} \cdot K_{\mathrm{COH}_y} \cdot \frac{\theta_{\mathrm{CO}} \cdot \theta_{\mathrm{H}}^y}{\theta^{*y}} \cdot \theta^* - \frac{k'_{\mathrm{met}}}{K'_{\mathrm{met}}} \cdot \theta_{\mathrm{CH}_{y-1}} \cdot \theta_{\mathrm{OH}} \\ &= k_{\mathrm{met}} \cdot \frac{\theta_{\mathrm{CO}} \cdot \theta_{\mathrm{H}}^y}{\theta^{*y}} \cdot \theta^* - \frac{k_{\mathrm{met}}}{K_{\mathrm{met}}} \cdot \theta_{\mathrm{CH}_{y-1}} \cdot \theta_{\mathrm{OH}} \end{aligned} \tag{8.6}$$

with $k_{met} = k'_{met} \cdot K_{COH_y}$ and $K_{met} = K'_{met} \cdot K_{COH_y}$. $K'_{met}$ is the equilibrium constant of Reaction 8.VI.

### 8.3.3 Formulation of Kinetic Expressions

The rates of dissociative adsorption of $H_2$, $H_2O$, and $CH_4$ are assumed to be considerably faster than the rate-determining step in methanation (*cf.* Reaction 8.VI) and therefore the surface species are treated to be in quasi-equilibrium with the partial pressure of the respective reactants (*cf.* Reactions 8.VII–8.IX).

$$H_2 + 2\,{}^* \rightleftharpoons 2\,H^* \tag{8.VII}$$

$$H_2O + 2\,{}^* \rightleftharpoons H^* + OH^* \tag{8.VIII}$$

$$CH_4 + (6\text{-}y)^* \rightleftharpoons CH_{y-1}{}^* + (5\text{-}y)H^* \tag{8.IX}$$

The respective coverages can be expressed by Eq. 8.7 to 8.9:

$$\theta_H = \left(K_{H_2} \cdot p'_{H_2}\right)^{0.5} \cdot \theta^* \tag{8.7}$$

$$\theta_{OH} = \frac{K_{H_2O} \cdot p'_{H_2O}}{\left(K_{H_2} \cdot p'_{H_2}\right)^{0.5}} \cdot \theta^* \tag{8.8}$$

$$\theta_{CH_{y-1}} = \frac{K_{CH_4} \cdot p'_{CH_4}}{\left(K_{H_2} \cdot p'_{H_2}\right)^{\frac{5-y}{2}}} \cdot \theta^*. \tag{8.9}$$

The closing condition for the coverages is given by the site balance:

$$1 = \theta_H + \theta_{OH} + \theta_{CH_{y-1}} + \theta_{CO} + \theta^*. \tag{8.10}$$

From the site balance in Eq. 8.10 and the steady-state condition for the surface coverage of CO* in Eq. 8.1, the surface coverage of $\theta_{CO}$ and the fraction of free sites $\theta^*$ can be determined using Eqs. 8.2, 8.4, and 8.6.

$$\theta_{CO} = \frac{A \cdot \theta^* + B \cdot \theta^{*2}}{C + D \cdot \theta^*} \tag{8.11}$$

$$\theta^* = \frac{-(A - D + C \cdot E) + \left[(A - D + C \cdot E)^2 - 4 \cdot (B + DE) \cdot (-C)\right]^{0.5}}{2 \cdot (B + D \cdot E)} \tag{8.12}$$

with

$$A = k_{\mathrm{ads,CO}} \cdot p'_{\mathrm{CO}} \tag{8.13}$$

$$B = k_{\mathrm{ads,CO_2}} \cdot p'_{\mathrm{CO_2}} \cdot \left(K_{\mathrm{H_2}} \cdot p'_{\mathrm{H_2}}\right)^{0.5} + \frac{k_{\mathrm{met}}}{K_{\mathrm{met}}} \cdot \frac{K_{\mathrm{CH_4}} \cdot p'_{\mathrm{CH_4}}}{\left(K_{\mathrm{H_2}} \cdot p'_{\mathrm{H_2}}\right)^{\frac{5-y}{2}}} \cdot \frac{K_{\mathrm{H_2O}} \cdot p'_{\mathrm{H_2O}}}{\left(K_{\mathrm{H_2}} \cdot p'_{\mathrm{H_2}}\right)^{0.5}} \tag{8.14}$$

$$C = \frac{k_{\mathrm{ads,CO}}}{K_{\mathrm{CO}}} \tag{8.15}$$

$$D = \frac{k_{\mathrm{ads,CO_2}}}{K_{\mathrm{CO_2}}} \cdot \frac{K_{\mathrm{H_2O}} \cdot p'_{\mathrm{H_2O}}}{\left(K_{\mathrm{H_2}} \cdot p'_{\mathrm{H_2}}\right)^{0.5}} + k_{\mathrm{met}} \cdot \left(K_{\mathrm{H_2}} \cdot p'_{\mathrm{H_2}}\right)^{\frac{y}{2}} \tag{8.16}$$

$$E = 1 + \frac{K_{\mathrm{H_2O}} \cdot p'_{\mathrm{H_2O}}}{\left(K_{\mathrm{H_2}} \cdot p'_{\mathrm{H_2}}\right)^{0.5}} + \left(K_{\mathrm{H_2}} \cdot p'_{\mathrm{H_2}}\right)^{0.5} + \frac{K_{\mathrm{CH_4}} \cdot p'_{\mathrm{CH_4}}}{\left(K_{\mathrm{H_2}} \cdot p'_{\mathrm{H_2}}\right)^{\frac{5-y}{2}}} \tag{8.17}$$

Using Eq. 8.2, 8.4, and 8.6, the net formation rates $R_i$ of the C-containing species $i$ can be written as

$$R_{\mathrm{CO}} = -\left(r_{\mathrm{ads,CO}} - r_{\mathrm{des,CO}}\right) \tag{8.18}$$

$$R_{\mathrm{CO_2}} = -\left(r_{\mathrm{ads,CO_2}} - r_{\mathrm{des,CO_2}}\right) \tag{8.19}$$

$$R_{\mathrm{CH_4}} = r_{\mathrm{met}} - r_{\mathrm{SR}}. \tag{8.20}$$

The net rates of $H_2$, and $H_2O$ formation are obtained from the elemental balances of H and O.

$$R_{\mathrm{H_2}} = 2 \cdot R_{\mathrm{CO_2}} + R_{\mathrm{CO}} - 2 \cdot R_{\mathrm{CH_4}} \tag{8.21}$$

$$R_{\mathrm{H_2O}} = -2 \cdot R_{\mathrm{CO_2}} - R_{\mathrm{CO}} \tag{8.22}$$

Thermodynamic consistency is ensured by the definition of the equilibrium constants $K_{\mathrm{met}}$ and $K_{\mathrm{CO_2}}$, respectively. $K_{\mathrm{met}}$ can be expressed *via*

$$K_{\mathrm{met}} = \frac{K_{\mathrm{CH_4}} \cdot K_{\mathrm{H_2O}} \cdot K_{\mathrm{eq,COmet}}}{K_{\mathrm{H_2}}^3 \cdot K_{\mathrm{CO}}}, \tag{8.23}$$

where $K_{\mathrm{eq,COmet}}$ denotes the equilibrium constant for the methanation reaction of CO (*cf.* Reaction 8.I). Furthermore, the equilibrium constant for $CO_2$ adsorption is coupled *via* the equilibrium constant of the water-gas shift reaction (*cf.* Reaction 8.III), $K_{\mathrm{eq,WGS}}$.

$$K_{\mathrm{CO_2}} = \frac{K_{\mathrm{CO}} \cdot K_{\mathrm{H_2O}}}{K_{\mathrm{H_2}} \cdot K_{\mathrm{eq,WGS}}} \tag{8.24}$$

The equilibrium constants $K_{eq,COmet}$ and $K_{eq,WGS}$ can be calculated by the corresponding enthalpy $\Delta_R H$ and entropy $\Delta_R S$ of reaction on the basis of reaction stoichiometry as well as enthalpy and entropy values of the reactants.

$$K_{eq}(T) = \exp\left(\frac{-\Delta_R G}{R \cdot T}\right) = \exp\left(\frac{T \cdot \Delta_R S(T) - \Delta_R H(T)}{R \cdot T}\right) \\ = \exp\left(\frac{\Delta_R S(T)}{R}\right) \cdot \exp\left(-\frac{\Delta_R H(T)}{R \cdot T}\right) \tag{8.25}$$

Following the principle of thermodynamic consistency [362], the adsorption parameters for $CO_2$ can be written as:

$$\Delta_{ads}H_{CO_2} = \Delta_{ads}H_{CO} + \Delta_{ads}H_{H_2O} - \Delta_{ads}H_{H_2} - \Delta_R H_{WGS}(T) \tag{8.26}$$

$$\Delta_{ads}S_{CO_2} = \Delta_{ads}S_{CO} + \Delta_{ads}S_{H_2O} - \Delta_{ads}S_{H_2} - \Delta_R S_{WGS}(T). \tag{8.27}$$

$K_{CO_2}$, therefore, can be expressed by Eq. 8.28.

$$K_{CO_2} = \exp\left(\frac{\Delta_{ads}S_{CO_2}}{R}\right) \cdot \exp\left(-\frac{\Delta_{ads}H_{CO_2}}{R \cdot T}\right) \tag{8.28}$$

At this point, it should be mentioned that, while generally enthalpies and entropies of adsorption are assumed to be independent from temperature, for $CO_2$ these adsorption parameters become a function of temperature due to the required coupling with the water-gas shift reaction. As stated in Section 8.3.2, $K_{CO_2}$ may be a lumped parameter describing the associative adsorption of $CO_2$ on the oxidic phase, and the consecutive reaction with H* on the Ni sites, which justifies this consideration. Details on calculation of thermodynamic properties are given in Appendix B. The resulting kinetic model is illustrated in Figure 8.1.

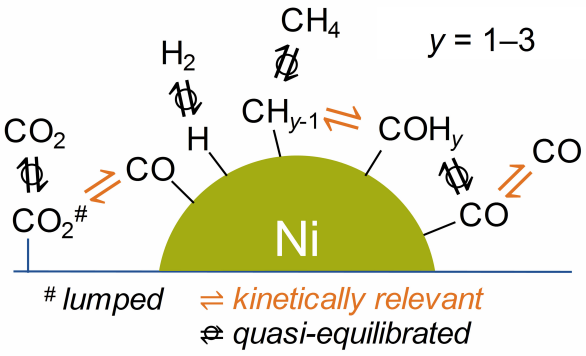


**Figure 8.1:** Sketch of the relevant steps and assumptions in the derived kinetic model.

## 8.4 Computational Methodology

All calculations were carried out in Matlab 2019a.

### 8.4.1 Thermodynamic Data

Enthalpy and entropy values for $CO_2$, CO, $CH_4$, $H_2$, and $H_2O$ were calculated using the expressions given in Appendix B.

### 8.4.2 Reactor Model

The experimental setup is described by a pseudo-homogeneous 1D isothermal and isobaric reactor model. Integration is carried out along the catalyst mass $m_{\mathrm{cat}}$.

$$\frac{\mathrm{d}\dot{n}_i}{\mathrm{d}m_{\mathrm{cat}}} = R_i \tag{8.29}$$

The molar flows $\dot{n}_i$ for each species were normalized to the total molar flow of C-containing species $i$ ($CO_2$, $CH_4$, CO) entering the reactor and catalyst mass $m_{\mathrm{cat}}$

$$\frac{\mathrm{d}Y_{i,j}}{\mathrm{d}x} = \frac{m_{\mathrm{cat},j}}{\dot{n}_{\mathrm{CH_4,in}} + \dot{n}_{\mathrm{CO_2,in}} + \dot{n}_{\mathrm{CO,in}}} \cdot R_{i,j} \tag{8.30}$$

for each experiment $j$. The equations are integrated numerically using a variable-step, variable-order solver [363].

### 8.4.3 Regression

Regression was carried out similar to the methodology published elsewhere [364]. The parameters $\phi_m$ were optimized to minimize the objective function $F$, which was described by the residuum of the weighted sums of squares of the experimental and calculated normalized net production rates at the reactor outlet for the responses CO, $CH_4$, and $CO_2$ ($n_{\mathrm{resp}} = 3$). $C_2$ and $C_3$ species were not included in the kinetic model. CO, $CH_4$, and $CO_2$ fulfilled the C mass balance by $\pm 3$ % for all data points used for kinetic modeling.

$$F = \sum_{k}^{n_{\mathrm{resp}}} \omega_k \sum_{j}^{n_{\mathrm{exp}}} \left( Y_{k,j}^{\mathrm{out,exp}} - Y_{k,j}^{\mathrm{out,calc}} \right)^2 \tag{8.31}$$

**Table 8.1:** Weighting factors used for parameter optimization.

| Species | $\omega_k$ / - |
|---|---|
| CO | 0.61885 |
| $CO_2$ | 0.15919 |
| $CH_4$ | 0.22196 |

The weighting factors $\omega_k$ were calculated according to [365] and are listed in Table 8.1.

$$\omega_k = \frac{\left(\sum_j^{n_{\text{exp}}} \dot{n}_{k,j}^{\text{out,exp}}\right)^{-1}}{\sum_k^{n_{\text{resp}}} \left(\sum_j^{n_{\text{exp}}} \dot{n}_{k,j}^{\text{out,exp}}\right)^{-1}} \tag{8.32}$$

The rate constants $k_l$ are described as Arrhenius-type, the adsorption constants $K_i$ *via* the respective equilibrium equations.

$$k_l = A_l \cdot \exp\left(\frac{E_{\text{A},l}}{R \cdot T}\right) \tag{8.33}$$

$$K_i = \exp\left(\frac{\Delta_{\text{ads}} S_i^{\text{o}}}{R}\right) \cdot \exp\left(-\frac{\Delta_{\text{ads}} H_i^{\text{o}}}{R \cdot T}\right) \tag{8.34}$$

To reduce the cross correlation between $A_l$ and $E_{\text{A},l}$ as well as between $\Delta_{\text{ads}} S_i^{\text{o}}$ and $\Delta_{\text{ads}} H_i^{\text{o}}$, the central temperature of the measured bed temperatures, $T_{\text{ref}} = \frac{T_{\text{min}}+T_{\text{max}}}{2} = 636.59\,\text{K}$, is chosen as reference value. To increase numerical stability, the model parameters were scaled and parametrized.

$$k_l = \exp\left(\phi_{k_l A_l} - \phi_{k_l E_{\text{A},l}} \left(\frac{T_{\text{ref}}}{T} - 1\right)\right) \tag{8.35}$$

$$\phi_{k_l A_l} = \ln\left(\frac{A_l}{\text{mol}\,\text{g}_{\text{cat}}^{-1}\,\text{h}^{-1}}\right) - \phi_{k_l E_{\text{A},l}} \tag{8.36}$$

$$\phi_{k_l E_{\text{A},l}} = \frac{E_{\text{A},l}}{R \cdot T_{\text{ref}}} \tag{8.37}$$

$$\ln K_i = \frac{\Delta_{\text{ads}} S_i^{\text{o}}}{R} - \frac{\Delta_{\text{ads}} H_i^{\text{o}}}{R \cdot T} = \phi_{K_i \Delta_{\text{ads}} S_i^{\text{o}}} - \phi_{K_i \Delta_{\text{ads}} H_i^{\text{o}}} \left(\frac{T_{\text{ref}}}{T} - 1\right) \tag{8.38}$$

$$\phi_{K_i \Delta_{\text{ads}} S_i^{\text{o}}} = \frac{\Delta_{\text{ads}} S_i^{\text{o}}}{R} - \phi_{K_i \Delta_{\text{ads}} H_i^{\text{o}}} \tag{8.39}$$

$$\phi_{K_i \Delta_{\text{ads}} H_i^{\text{o}}} = \frac{\Delta_{\text{ads}} H_i^{\text{o}}}{R \cdot T_{\text{ref}}} \tag{8.40}$$

In total, the presented mechanism involving three reaction rates and three C-containing species consists of six kinetic and eight adsorption parameters. Details on the regression procedure can be found elsewhere [364].

### 8.4.4 Model Evaluation

Based on the kinetic expressions introduced in Section 8.3.3, kinetic parameters are determined using the methodology given in Section 8.4. In a first step, the nature of the surface intermediate $COH_y$ is investigated by variation of the degree of hydrogenation $y$ from 1 to 3. Mechanistically, $y$ can only take discrete values of 1, 2, or 3. As stated in Section 8.1, several surface intermediates $COH_y$* have been reported to exist under the investigated conditions, allowing different levels of hydrogenation prior to the dehydroxylation to $CH_{y-1}$*, depending on the experimental parameters. Hence, the value of $y$ has to be regarded as an average value over the hydrogenation-dehydroxylation-series. With respect to this consideration, $y$ was varied from 1 to 3 in 0.2 steps while monitoring the value of the residuum of the weighted sums of squares (*cf.* Section 8.4.3). Figures 8.2 A–D illustrate the determined parameters for a varied degree of hydrogenation $y$. The minimum residuum was found for a degree of hydrogenation of $y$ = 2.1913 (*cf.* Figure 8.2 E).

In Figure 8.2 A–B, a strong impact of the degree of hydrogenation $y$ on the pre-exponential factor $A_{met}$ and activation energy $E_{A,met}$ for the methanation reaction can be observed. Both kinetic parameters increase for rising $y$-values. This coincides with the trend of the adsorption parameters for $CH_4$ and $H_2O$, which are coupled to the methanation reaction *via* thermodynamic equilibrium (*cf.* Eq. 8.23). Kinetic parameters for CO and $CO_2$ adsorption ($A_{CO/CO_2}$, $E_{A,CO/CO_2}$) as well as adsorption parameters for $H_2$ and CO are less affected by the variation of $y$. All adsorption parameters fulfill the strong criteria established by Boudart *et al.* [366]. For CO, small values for $\Delta_{ads}S_{CO}$ are observed. This could indicate that CO adsorption is not equally favored at each Ni site and, hence, less surface sites are active for CO adsorption, or that CO is very mobile on the catalyst surface. The results from $H_2$-TPD (*cf.* Section 8.7.2.6) clearly indicate Ni site heterogeneity.

The optimum value for the degree of hydrogenation $y$ = 2.1913 suggests that the majority of rate-determining steps for $CH_4$ formation occurs *via* dehydroxylation of $COH_2$* to CH*. Some of the $COH_2$* species undergo further hydrogenation to $COH_3$* before C-O bond cleavage to $CH_2$*, which is then the rate-limiting step. The extent of C-O bond cleavage in $COH_2$* and $COH_3$* thereby may be a function of reaction conditions. In contrast, the formation of surface carbon species C* *via* decomposition of COH* is unlikely to occur under the investigated conditions.

A closer investigation of the impact of $y$ on the kinetic description reveals two characteristic interrelations. First, under steam reforming conditions, the hydroxylation of $CH_2$* to $COH_3$* ($y$ = 3) is found to be the favorable pathway. Second, under CO methanation conditions featuring

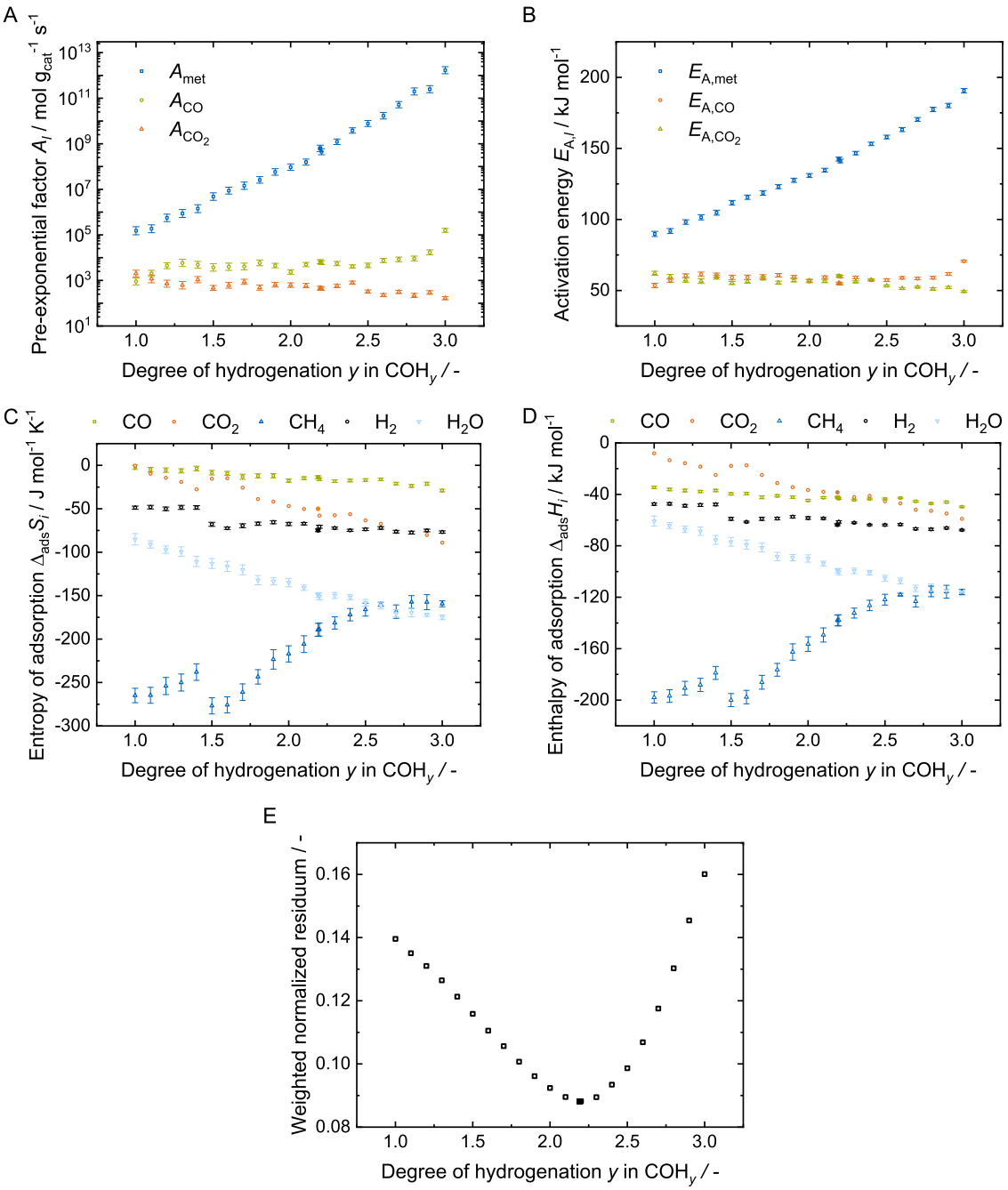


**Figure 8.2:** Determined kinetic parameters for varied degree of hydrogenation $y$: pre-exponential factors $A_l$ (A), activation energies $E_{A,l}$ (B), entropies of adsorption $\Delta_{ads}S_i$ (C), enthalpies of adsorption $\Delta_{ads}H_i$ (D), residuum value of objective function $F$ (*cf.* Eq. 8.31) (E). Void symbols: stepwise varied $y$; filled symbols: fitted value of $y = 2.1913$.

high $CO/H_2$ ratios, formation of surface carbon species ($y = 1$) becomes detectable. However, these reaction conditions also favor C-C bond formation (Fischer-Tropsch reaction) and have been discarded since $C_2$ and $C_3$ species were not included in the kinetic model. Hence, for $CO/CO_2$ co- methanation, as application of interest, the decomposition of $COH_2$* is determined as rate-determining step for the formation of $CH_4$. For this reason, the degree of hydrogenation is set to $y = 2$ in the subsequent sections. However, at this point it should be emphasized that

this is a significant simplification of the concurrent catalytic steps for $y$ = 1, 2, or 3, which are all functions of temperature, surface coverages, crystallite surface, *etc*. However, a closer investigation of this interplay of concurrent reaction pathways could only be achieved by first principle methods together with kinetic Monte-Carlo simulations, which, in turn, require idealized metal surfaces and are not able to fully describe the processes on and the morphology of an industrial-type catalyst used in this study. Besides, the presented model aims at describing the co-methanation reaction with limited computational effort to implement in process and reactor simulations.

In Table 8.2, the optimized parameters for $y$ = 2 are summarized together with their parameterized form $\phi_m$ (*cf.* Eqs. 8.35 to 8.40) including corresponding 95 % confidence intervals and statistic $t$-values. All 14 fitted parameters significantly surpass the critical $t$-value of 1.96, indicating their individual statistical relevance. This is further supported by the narrow 95 % confidence intervals. In addition, parameter interaction has been monitored. Only moderate to negligible correlations (*cf.* [364]) have been found. Moreover, the model is of high global significance, demonstrated by the respective $F$-test with 1612 degrees of freedom ($F_\mathrm{s}$ = 86 879 > $F_\mathrm{s,crit}$ = 1.70) [367]. This statistical evaluation holds for all other parameter sets shown in Figure 8.2. Analyses of the corresponding weighted residuals (*cf.* Section 8.7.7) yields

**Table 8.2:** Optimized parameter values for a degree of hydrogenation of $y$ = 2, in re-parameterized and parameterized ($\phi_m$) form, including corresponding 95 % confidence intervals (CI) and $t$-values: Degrees of freedom: 1612; $F$-test for global significance: $F_\mathrm{s}$ = 86 879 > $F_\mathrm{s,crit}$ = 1.70. Details on the statistical evaluation are given in [364]. Model parameters are based on a reference pressure of $p_\mathrm{ref}$ = 1 bar.

| | | $\phi_m$ | | |
|---|---|---|---|---|
| parameter | re-parameterized | value / - | 95 % CI | $t$ / - |
| $A_\mathrm{met}$ / mol $g_\mathrm{cat}^{-1}$ $s^{-1}$ | 9.39E+07 | 8.73 | 0.055 | 474.2 |
| $E_\mathrm{A,met}$ / kJ $mol^{-1}$ | 130.87 | 10.77 | 0.046 | 704.2 |
| $A_\mathrm{ads,CO_2}$ / mol $g_\mathrm{cat}^{-1}$ $s^{-1}$ | 6.23E+02 | 12.19 | 0.043 | 850.6 |
| $E_\mathrm{A,ads,CO_2}$ / kJ $mol^{-1}$ | 56.94 | 24.73 | 0.266 | 279.8 |
| $A_\mathrm{ads,CO}$ / mol $g_\mathrm{cat}^{-1}$ $s^{-1}$ | 2.35E+03 | 10.76 | 0.187 | 172.8 |
| $E_\mathrm{A,ads,CO}$ / kJ $mol^{-1}$ | 56.47 | 10.67 | 0.186 | 172.7 |
| $\Delta_\mathrm{ads}S_\mathrm{H_2}$ / J $mol^{-1}$ $K^{-1}$ | -67.51 | -11.03 | 0.193 | 171.6 |
| $\Delta_\mathrm{ads}H_\mathrm{H_2}$ / kJ $mol^{-1}$ | -58.38 | -29.56 | 1.068 | 83.2 |
| $\Delta_\mathrm{ads}S_\mathrm{CH_4}$ / J $mol^{-1}$ $K^{-1}$ | -217.02 | -16.98 | 0.540 | 94.4 |
| $\Delta_\mathrm{ads}H_\mathrm{CH_4}$ / kJ $mol^{-1}$ | -156.45 | -8.44 | 0.148 | 171.6 |
| $\Delta_\mathrm{ads}S_\mathrm{H_2O}$ / J $mol^{-1}$ $K^{-1}$ | -135.09 | 2.91 | 0.038 | 229.9 |
| $\Delta_\mathrm{ads}H_\mathrm{H_2O}$ / kJ $mol^{-1}$ | -89.85 | 3.46 | 0.045 | 229.0 |
| $\Delta_\mathrm{ads}S_\mathrm{CO}$ / J $mol^{-1}$ $K^{-1}$ | -17.56 | 0.73 | 0.031 | 70.4 |
| $\Delta_\mathrm{ads}H_\mathrm{CO}$ / kJ $mol^{-1}$ | -44.68 | 6.33 | 0.087 | 219.4 |

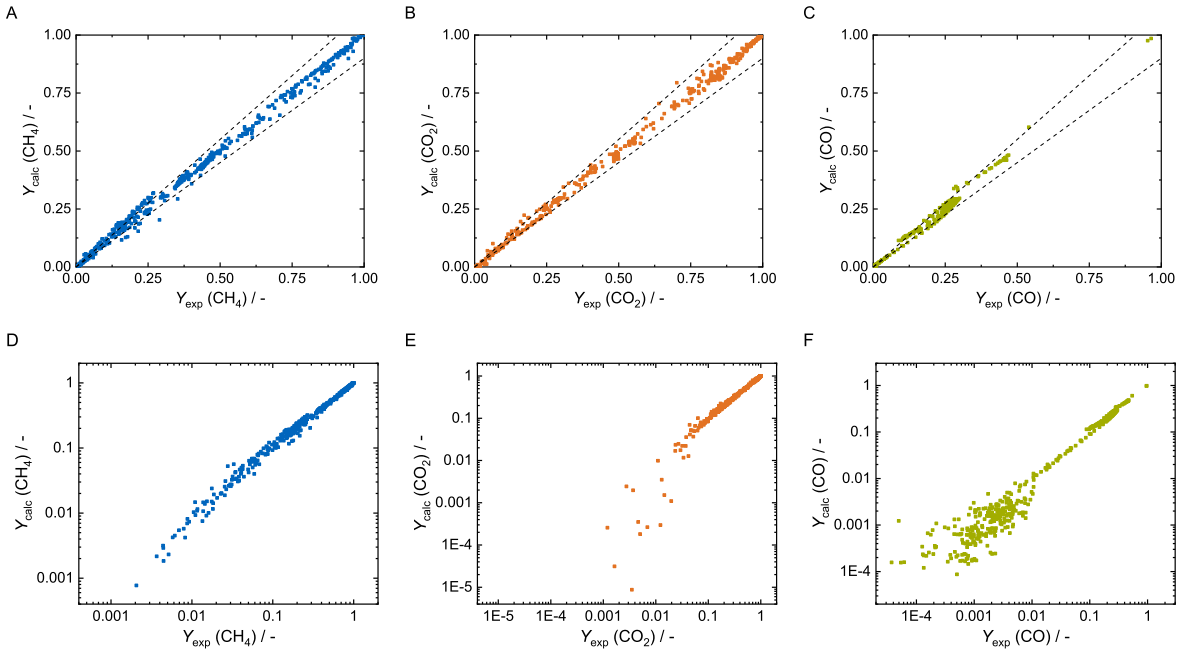


**Figure 8.3:** Linear (A, B, C) and logarithmic (D, E, F) parity plots comparing experimental and calculated normalized molar flows $Y_{i,j}$ (*cf.* Eq. 8.30) for $i = CH_4$ (A, D), CO (B, E), $CO_2$ (C, F). $j$ denotes number of experiment. Dashed lines indicate the $\pm 10\,\%$ region.

equally distributed residuals in terms of temperature, pressure, and space time.

From a mechanistic point of view, the resulting parameters all yield physically realistic and consistent values. The activation energy for methanation $E_{A,met} = 131\,kJ\,mol^{-1}$ is a good indication for the micro-kinetic border of the surface dehydroxylation of $COH_2$* to CH*. DFT studies investigating structure sensitivity of $H_2$-induced CO* cleavage on Ni surfaces yielded activation energies between 119 and $157\,kJ\,mol^{-1}$ depending on site geometry, coverage, and mechanism [180], which is in good agreement to the results presented in Figure 8.2 A. The energy barriers for the adsorption process of CO and $CO_2$ are fitted as 56 and $57\,kJ\,mol^{-1}$, respectively. $E_{A,CO}$ represents the pure sorption process onto the metal surface, while $E_{A,CO_2}$ describes the (lumped) process of the reverse of water-gas shift reaction on the surface (*cf.* Reaction 8.IV) and possible pre-activation of $CO_2$ on basic sites of the oxidic phase of the catalyst. A comparison of magnitude of the pre-exponential factors $A_i$ emphasizes the different character of surface methanation and the adsorption process for $CO_x$.

The determined adsorption enthalpy of $H_2$, $\Delta_{ads}H_{H_2}$, agrees well with experimentally determined isosteric heat of adsorption values (*cf.* Section 8.7.8) and literature. Redeal and Sweett found values between $86\,kJ\,mol^{-1}$ at low ($\theta_H = 0.4$) and $40\,kJ\,mol^{-1}$ at high ($\theta_H = 0.8$) hydrogen coverage [368]. Moreover, the determined $\Delta_{ads}H_{H_2}$ and $\Delta_{ads}S_{H_2}$ values are in line with data fitted from $H_2$-TPD data on Ni catalysts [369]. The fitted adsorption enthalpy of CO is on the lower end of data reported in an overview in [370] and may be attributed to the high CO coverage under CO-containing feed gas conditions [180]. It needs to be mentioned that the adsorption of $H_2$, $CH_4$, and $H_2O$ are treated as Langmuir-type in this study, meaning that the

determined adsorption parameters are averaged over all active sites and are independent from coverage and adsorbate interactions [223]. Sorption parameters for $H_2O$ and $CH_4$ represent combined processes of sorption and decomposition on the catalyst surface (*cf.* Reactions 8.VIII and 8.IX), and hence represent the superposition of these processes.

In Figure 8.3, the parity plots of the three fitting responses $CH_4$, $CO_2$, and CO are illustrated in linear and logarithmic form. The individual comparison demonstrates very good agreement of experiment and intrinsic kinetic model. All three carbon species can be described over a wide range of conditions. The logarithmic representation further highlights the excellent global accuracy of the model, which is able to adequately predict the full range of compositions and even traces of CO and $CO_2$.

## 8.4.5 Determination of Apparent Activation Energies and Reaction Orders

### 8.4.5.1 Apparent Activation Energy and Reaction Orders in CO Methanation

The Arrhenius plot for the determination of the apparent activation energy in CO methanation is shown in Figure 8.4. The apparent activation energy amounts to $109 \pm 3.9\,\mathrm{kJ\,mol^{-1}}$, which is in good agreement to literature studies [169, 172, 371, 372]. Dalmon and Martin [371] found apparent activation energy values ranging from 84 to $117\,\mathrm{kJ\,mol^{-1}}$ in the temperature range from 240 to 280 °C. Vannice measured an apparent activation energy of $105 \pm 5\,\mathrm{kJ\,mol^{-1}}$ over 5 % $Ni/Al_2O_3$ [172], Schoubye reported an apparent activation energy of approx. $100\,\mathrm{kJ\,mol^{-1}}$ for a catalyst containing 20 % NiO, 55 % MgO, and 25 % $Al_2O_3$ as well as for a 9 to 10 % $Ni/MgAl_2O_4$-spinel catalyst [372]. The apparent activation energy for CO methanation over the $NiAlO_x$ catalyst thereby is reported to be approximately $25\,\mathrm{kJ\,mol^{-1}}$ higher compared to $CO_2$ methanation [24].

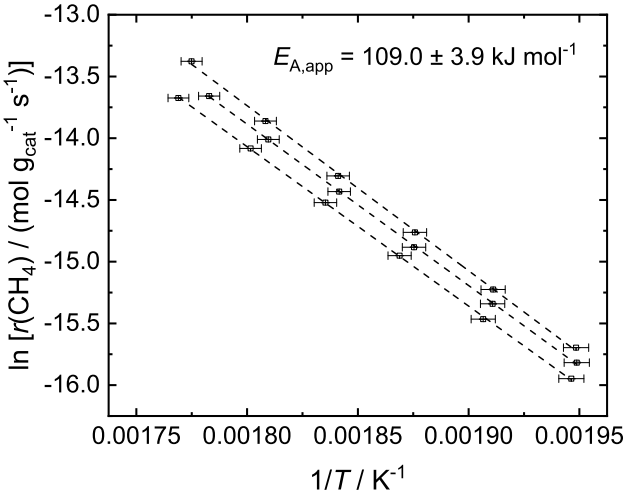


**Figure 8.4:** Arrhenius plot for CO methanation, data points taken at $3000\,\mathrm{NL\,g_{cat}^{-1}\,h^{-1}}$, $H_2/CO/Ar$ = 18/3/79, and pressures of 4, 7, and 10 bar, 240 to 290 °C.

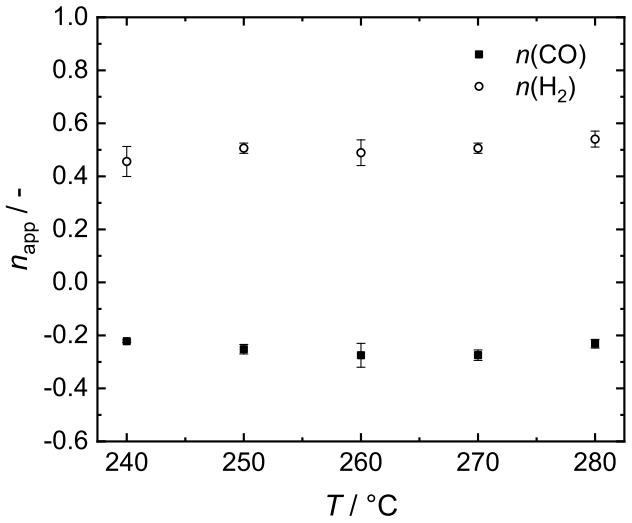


**Figure 8.5:** Apparent reaction orders of CO and $H_2$ for CO methanation, determined at 3000 NL $g_{cat}^{-1}$ $h^{-1}$ and pressures of 4, 7, and 10 bar.

The trends of the apparent reaction orders of $H_2$ and CO as a function of temperature are shown in Figure 8.5. The apparent reaction order of CO was found to be –0.3, the apparent reaction order of $H_2$ 0.5, both merely independent from temperature in the investigated range. The negative apparent reaction order in CO is well-known in literature [371, 372] and can be explained by the high coverage of CO under CO methanation conditions, limiting the availability of free active sites for $H_2$ adsorption. Schoubye reported a CO reaction order less than 0, reaching –0.5 at high CO concentrations [372]. The negative reaction order of –0.3 is consistent to results from Dalmon *et al.* [371]. However, they reported an apparent reaction order of approx. 1 in $H_2$.

#### 8.4.5.2 Derivation of Apparent Values from the Kinetic Model

The values for the apparent activation energies numerically derived from the kinetic model for $y$ = 2 and four reference cases are shown in Figure 8.6 A, C, E, G, the corresponding reaction orders of the species $i$ in 8.6 B, D, F, H. Under CO solo-methanation conditions (A, B, $CO/H_2/Ar$ = 10/60/30, 5 bar), the apparent activation energy of the methanation reaction decreases with increasing temperature and very well matches the value experimentally determined in the temperature range between 240 to 290 °C (109 ± 3.9 kJ $mol^{-1}$, *cf.* Figure 8.4). In strong accordance with the experimental results (*cf.* Figure 8.5), the apparent reaction order of CO is negative and gets positive at higher temperatures when CO surface coverage declines due to increasing CO conversion. At the same time, the apparent reaction order of $H_2$ decreases with increasing temperature, illustrating the competition of CO and $H_2$ for active Ni sites and highlighting the high CO* coverage in the low CO conversion region. For $CO_2$ solo-methanation (C, D, $CO_2/H_2/Ar$ = 10/40/50, 7 bar), the apparent activation energy decreases from 92 kJ $mol^{-1}$ at 200 °C to 83 kJ $mol^{-1}$ at 350 °C, which is in very good accordance with the value of approx. 83 kJ $mol^{-1}$ found by Koschany *et al.* in the temperature region from 240

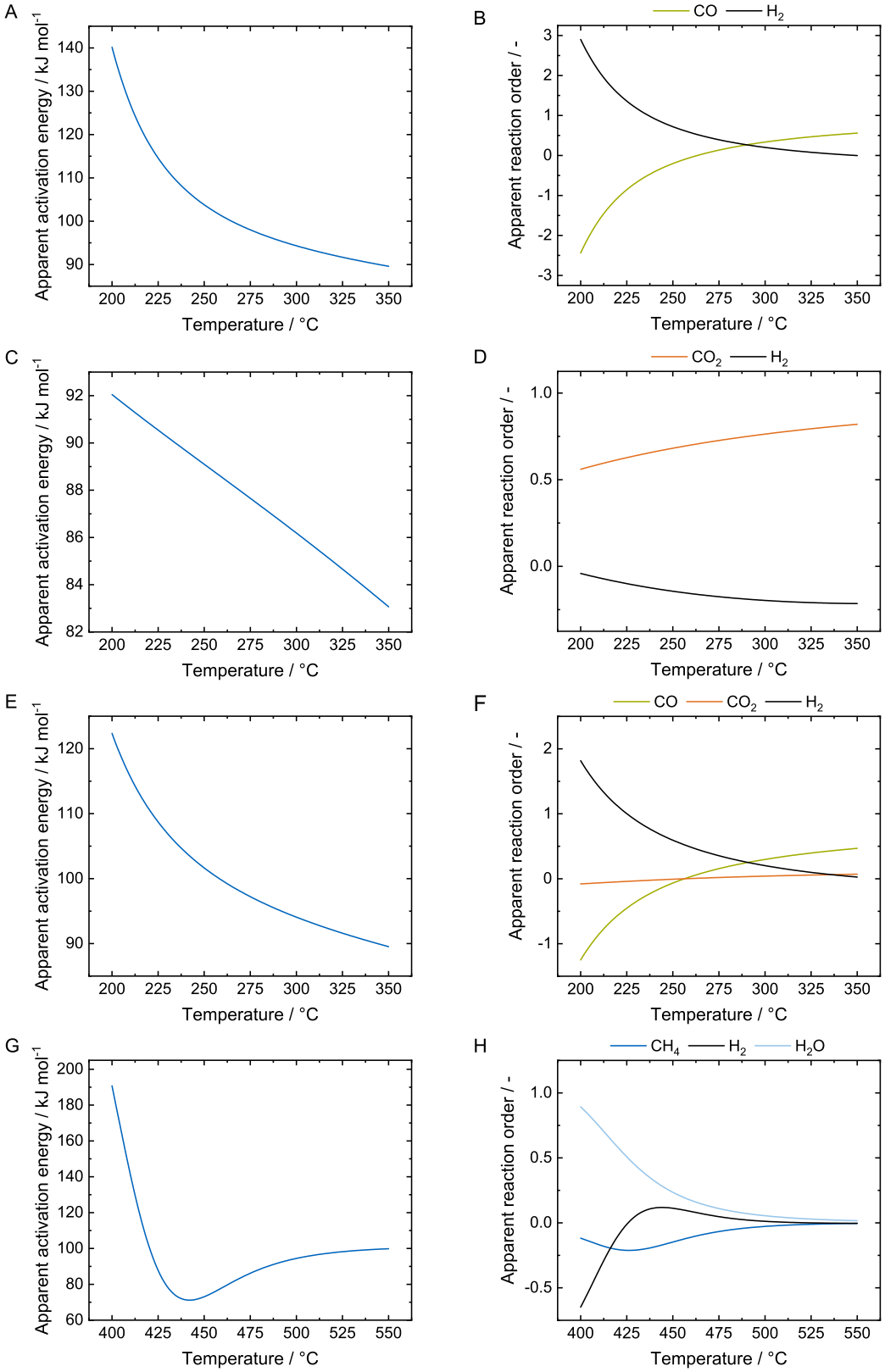


**Figure 8.6:** Apparent kinetic parameters calculated for the net rate of production of $CH_4$. Temperature dependence of apparent activation energies $E_{app,met}$ (A, C, E, G) and apparent reaction orders $n_{app,i}$ (B, D, F, H): CO solo-methanation ($CO/H_2/Ar$ = 10/60/30, 5 bar) (A, B), $CO_2$ solo-methanation ($CO_2/H_2/Ar$ = 10/40/50, 7 bar, *cf.* $RF_1$) (C, D), $CO/CO_2$ co-methanation ($CO/CO_2/H_2/Ar$ = 7.5/7.5/52.5/32.5, 5 bar, *cf.* $RF_2$) (E, F), steam reforming ($H_2/CH_4/H_2O/Ar$ = 2.5/10/15/72.5, 5 bar, *cf.* $RF_3$) (G, H).

to 300 °C [24] and literature studies over $Ni/Al_2O_3$ [373] and $Ni/SiO_2$ [194], where apparent values of 80 and 90 kJ mol$^{-1}$, respectively, have been reported. The numerical apparent reaction order for $CO_2$ increases from 0.6 at 200 °C to 0.8 at 350 °C, while the reaction order of $H_2$, in contrast to CO methanation (B), is slightly negative. Koschany *et al.* found reaction orders of 0.1 for $CO_2$ and 0.3 for $H_2$ in this temperature window [24]. The deviation hereby is owed to the H*-assisted $CO_2$ adsorption mechanism (*cf.* Section 8.3.2) and the repressive effect of $H_2O$ on $CO_2$ methanation [24]. The differences between numerical derivation and experiments can be explained by the influence of the $CO_2/H_2$ feed gas ratio (*cf.* Section 8.7.9). At a $CO_2/H_2$ ratio of 1, the apparent reaction order of $H_2$ is calculated to be 0.35, the one of $CO_2$ 0.18, which much better matches the experimental results [24].

The apparent kinetic values under co-methanation conditions (E, F, $CO/CO_2/H_2/Ar$ = 7.5/7.5/52.5/32.5, 5 bar) are very similar to the ones for the case of CO solo-methanation. The slightly lower apparent activation energy and absolute values of the reaction orders may again be caused by the lower $CO/H_2$ ratio.

$CO_2$ has negligible influence on the $CH_4$ formation rate in the whole temperature range under these conditions, which shows that the inhibition effect of CO on $CO_2$ methanation is successfully implemented in the kinetic model. Under steam reforming conditions (G, $H_2/CH_4/H_2O/Ar$ = 2.5/10/15/72.5, 5 bar), the apparent activation energy is approx. 190 kJ mol$^{-1}$ at 400 °C, then decreases to a minimum of 80 kJ mol$^{-1}$ at 430 °C before it rises back to approx. 100 kJ mol$^{-1}$ at high temperature. The high apparent activation energy at 400 °C (compared to the fitted value for the activation energy of the methanation reaction, *cf.* Table 8.2) indicates that under these conditions the sorption processes of CO and $CO_2$ play a major role, as the surface coverages are significantly reduced. In the kinetic model, both CO and $CO_2$ are modelled to be primary reaction products. However, the experimentally observed selectivity of $CH_4$ transformation towards $CO_2$ was found to be much higher than to CO. This indicates that the high apparent activation energy may be caused by an interaction between $CH_{y-1}$ hydrooxygenation and $CO_2$ desorption *via* the reverse of the water-gas shift reaction, while the decrease of the apparent activation energy can be interpreted by a rising influence of CO sorption at high temperatures. This consideration is in line with the trend of the apparent $H_2$ reaction order (H): At low temperatures it is negative and rises to 0.1 at 430 °C, at high temperatures the apparent reaction orders of all reactants level out at 0, reflecting the effect of chemical equilibrium.

For all reference points, the apparent activation energies and the apparent reaction orders deduced from the kinetic model are in good agreement with the experimentally determined values (*cf.* Section 8.4.5.1), which confirms that (a) the assumption of the decomposition of a hydrogenated surface complex $COH_y$ on the Ni surface being the critical step in the methanation reaction is consistent and seems justified, and that (b) the kinetics can be adequately described when setting the degree of hydrogenation $y$ to a value of 2.

### 8.4.6 Sensitivity Analysis

For deeper evaluation of the kinetic model and resolution of rate-determining steps under certain experimental conditions, a local sensitivity analysis following the 'degree of rate control' concept established by Campbell [374, 375] is performed. The details on the mathematical treatment are given elsewhere [364]. In the following approach, the net rate of production for $CH_4$ is treated as the characteristic rate for evaluation. Figure 8.7 shows the temperature dependence of $CH_4$ formation for the rate constants $k_l$ and equilibrium constants $K_i$ over a broad temperature range. In Figure 8.7 A, the degree of rate control of kinetic parameters $S(R_{CH_4}, k_l)$ for CO solo-methanation is demonstrated. At low and medium temperatures between 200 to 263 °C, the methanation reaction ($k_{met}$) is determining for the production of $CH_4$. At the same time, CO adsorption ($k_{ads,CO}$) has an inhibiting effect ($S(R_{CH_4}, k_{ads,CO}) < 0$), which correlates with experimentally (*cf.* Section 8.4.5.1) and numerically (*cf.* Section 8.4.5.2) determined apparent reaction orders. At elevated temperatures above 263 °C this inhibiting effect vanishes and both methanation and CO adsorption positively affect the formation of $CH_4$. At temperatures above 290 °C $k_{ads,CO}$ becomes the key kinetic constant.

For $CO_2$ solo-methanation in Figure 8.7 C, the surface methanation reaction only has a secondary effect on $CH_4$ formation. Instead, the overall rate for $CH_4$ formation is dominated by the initial $CO_2$ activation (H*-assisted dissociative adsorption of $CO_2$/reverse water-gas shift reaction, *cf.* Reaction 8.IV).

During $CO/CO_2$ co-methanation, displayed in Figure 8.7 E, parameter sensitivities are comparable to the ones during CO solo-methanation. However, the magnitude of $S(R_{CH_4}, k_l)$-values is damped by approximately 50 %. Moreover, $CO_2$ adsorption shows no significant effect on the overall $CH_4$ formation ($-0.1 \leq k_{ads,CO_2} \leq 0.1$). Overall, the trends of the degrees of rate control for $CO/CO_2$ co-methanation (Figure 8.6 E–F) are very similar to the ones for CO solo-methanation (Figure 8.6 A–B), which reflects the experimental observation that $CO_2$ methanation is strongly inhibited in the presence of CO and validates that the competitive adsorption of CO and $CO_2$ was successfully implemented in the kinetic model.

For temperatures and compositions mimicking steam reforming conditions (Figure 8.7 G), surface methanation plays a minor role. Here, the sorption properties of CO and $CO_2$ clearly dominate the consumption of $CH_4$. At the same time, this resembles the dominating effect of the chemical equilibrium, favoring the formation of $CO_2$ at low reforming temperatures (< 430 °C) and CO at elevated temperatures, respectively. For temperatures below 400 °C (not shown) the hydrooxygenation of $CH_{y-1}$ on the catalyst surface becomes the decisive factor.

Regarding the sorption equilibria, solely $K_{CH_4}$ shows an effect on the rate of $CH_4$ production (*cf.* Figures 8.7 B, D, F). However, for CO solo-methanation and $CO/CO_2$ co-methanation, $K_{CH_4}$ exhibits a positive effect on the formation of $CH_4$, while for $CO_2$ solo-methanation $K_{CH_4}$ slightly hinders the reaction. During steam reforming, $CH_4$ consumption is affected by $K_{CO}$, $K_{H_2O}$, and $K_{CH_4}$ up to temperatures of 450 °C (*cf.* Figure 8.7 H). At higher temperatures,

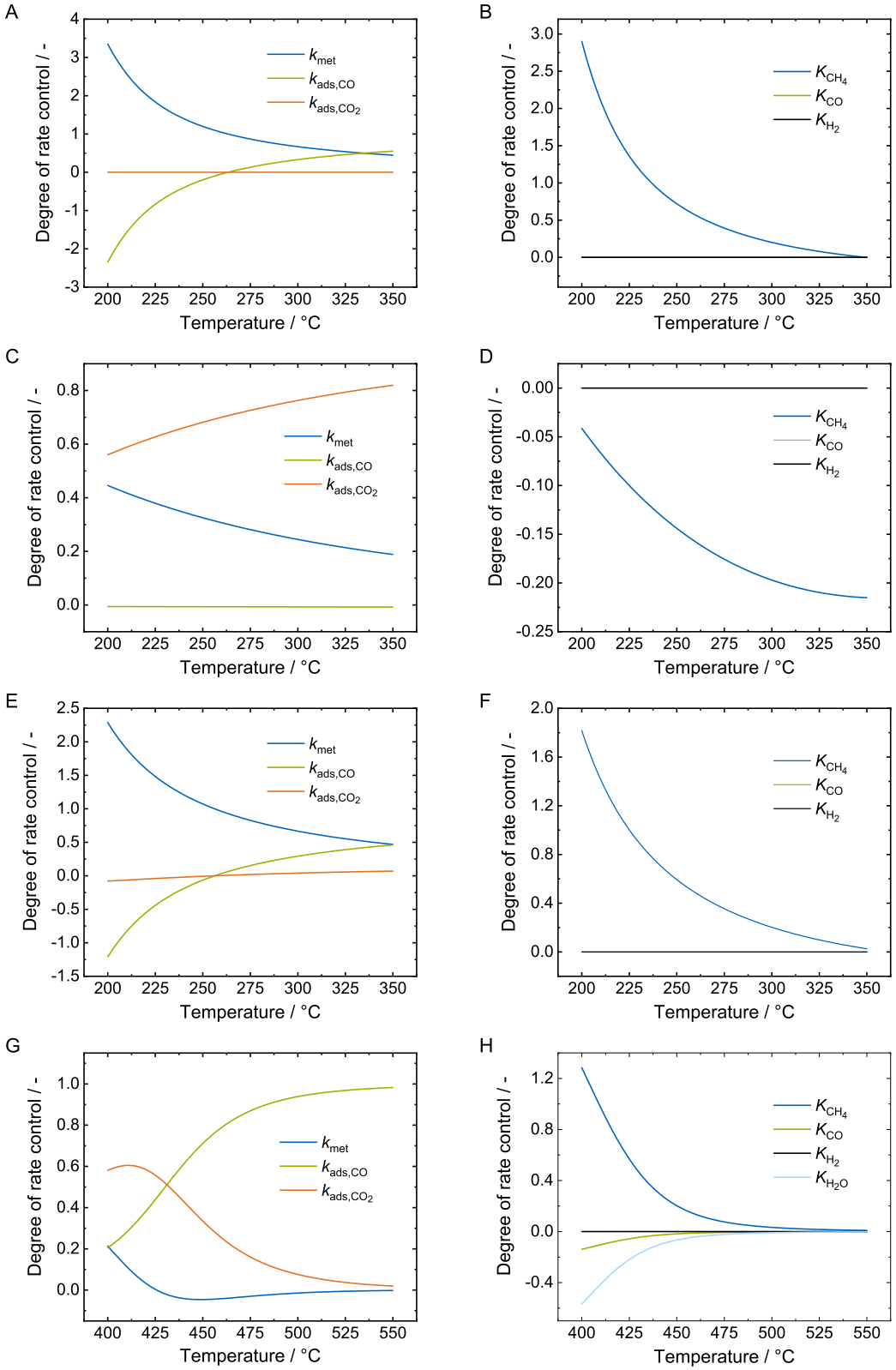


**Figure 8.7:** Local sensitivity of net rate of production of $CH_4$ on rate constants $k_l$ (A, C, E, G) and equilibrium constant $K_i$ (B, D, F, H) for varied reaction temperatures $T$: CO solo-methanation ($CO/H_2/Ar$ = 10/60/30, 5 bar) (A, B), $CO_2$ solo-methanation ($CO_2/H_2/Ar$ = 10/40/50, 7 bar, *cf.* $RF_1$) (C, D), $CO/CO_2$ co-methanation ($CO/CO_2/H_2/Ar$ = 7.5/7.5/52.5/32.5, 5 bar, *cf.* $RF_2$) (E, F); steam reforming ($H_2/CH_4/H_2O/Ar$ = 2.5/10/15/72.5, 5 bar, *cf.* $RF_3$) (G, H).

sorption equilibria do no longer affect the steam reforming reaction due to the dominance of chemical equilibria under these conditions.

## 8.5 Comparison to Kinetic Models Available in Literature

In Figure 8.8, the model predictions are compared to kinetic experiments and literature models applicable for the respective feed gas compositions. For $CO_2$ solo-methanation (A), the model agrees well with the one developed by Koschany *et al.* [24], clearly proofing data-consistency. In contrast to Koschany *et al.*, the model derived in this study predicts the experimentally observed formation of CO owed to the reverse of the water-gas shift reaction at medium $CO_2$ conversion ranges. $CO_2$ methanation kinetics are considerably faster than predicted by the model of Xu and Froment, which was developed for steam reforming over 15.2 wt.% $Ni/MgAl_2O_4$ [186] and by the recently developed kinetic model of Lalinde *et al.* [191], who used a 30 wt.% $NiO/Al_2O_3$ catalyst. Although the catalyst in this study was artificially aged prior to the kinetic experiments,

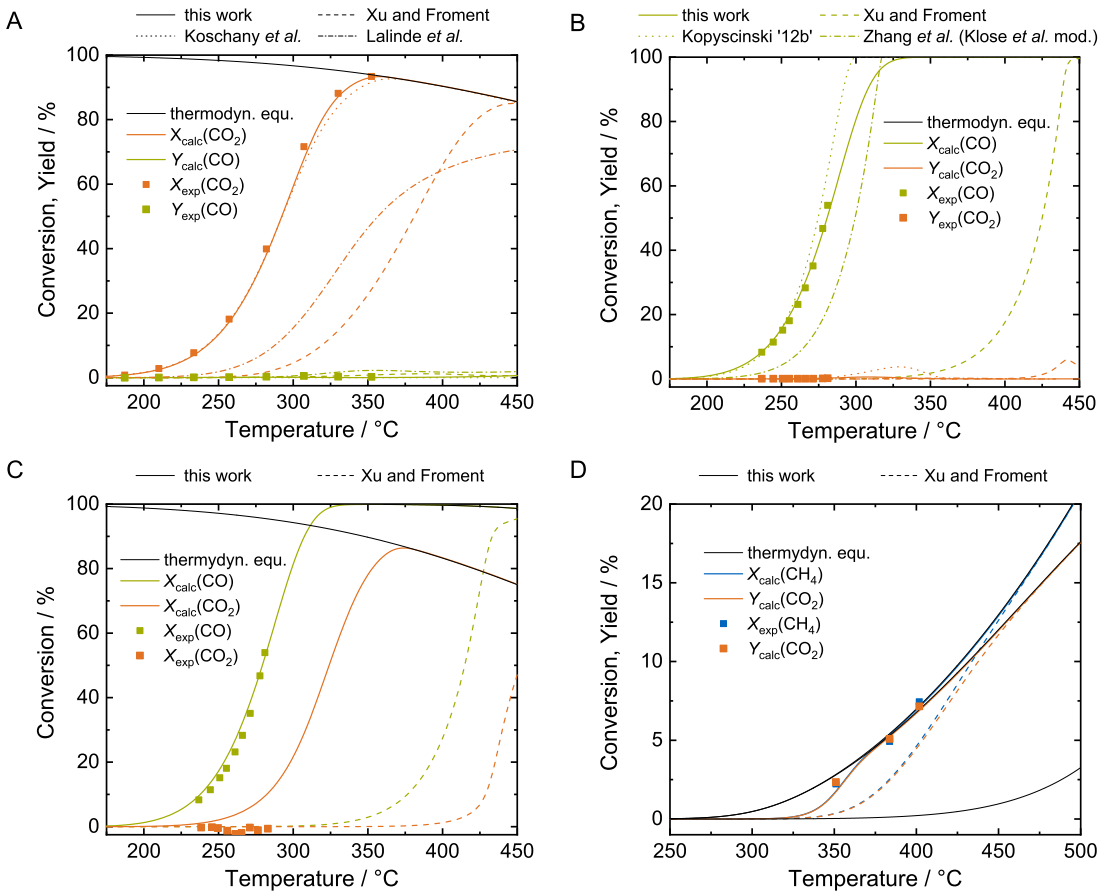


**Figure 8.8:** Comparison of the presented kinetic model to literature models and experimental data (filled symbols) for $CO_2$ solo-methanation ($CO_2/H_2/Ar$ = 10/40/50, 8 bar, *cf.* $RF_1$) (A), CO solo-methanation ($CO/H_2/Ar$ = 10/60/30, 5 bar) (B), $CO/CO_2$ co-methanation ($CO/CO_2/H_2/Ar$ = 7.5/7.5/52.5/32.5, 5 bar, *cf.* $RF_2$) (C), steam reforming ($H_2/CH_4/H_2O/Ar$ = 2.5/10/15/72.5, 5 bar, *cf.* $RF_3$) (D) conditions. Blue: $CH_4$, orange: $CO_2$, green: CO; black line: thermodynamic equilibrium conversion/yield.

this difference can be attributed to superior activity of the co-precipitated $NiAlO_x$. Similar gradients of the $X(CO_2)$ vs. temperature characteristics for the derived model and the one of Xu and Froment indicate similar apparent activation energies.

Under CO solo-methanation conditions (B), the kinetics predicted by the kinetic model derived in this study lie between the ones of Kopyscinski *et al.* [73] and Zhang *et al.* [74]. Kopyscinski *et al.* used a 50 wt.% $Ni/Al_2O_3$ methanation catalyst for their studies and derived three kinetic models that could not further be discriminated by statistical methods. The model used for comparison is named 'model 12b' in the original publication.

The model reported by Zhang *et al.* (50 wt.% Ni catalyst) is based on the kinetic model of Klose and Baerns [190], but while the kinetic parameters were fitted to own kinetic experiments, the adsorption parameters and the rate expression were kept constant [74]. It is noteworthy that for the model derived in this study the approach to equilibrium at high CO conversions is slightly slower compared to Kopyscinski *et al.* [73] and Zhang *et al.* [74] This may be caused by different deffects: First, in contrast to the presented model, both literature kinetic models do not consider thermodynamic equilibrium, which, however, may only play a minor role due to the high value of the equilibrium constant of CO methanation. Second, for higher degree of hydrogenation $y$, a faster approach to equilibrium was predicted by the model. As stated in Section 8.4.4, the minimum of the sum of the weighted residuals was found at $y = 2.1913$. This indicates that under CO methanation conditions at high CO conversion the decomposition of $COH_2$* and $COH_3$* may co-occur, both surface reactions being kinetically relevant and that for $y = 2$ the approach to equilibrium is slightly underestimated. Third, however, experimental data sets commonly do not include data points measured at high CO conversion ranges (also for this study), since under these conditions heat and mass transport limitations are very common, falsifying temperature measurements in the catalyst bed, exemplarily shown by Inui *et al.* [296]. With respect to this, this region is of very limited interest for industrial reactor simulations, since hotspot formation will occur due to heat transport limitations, endangering thermal runaway. The rapid increase of the reaction rate at high CO conversion can be attributed to the release of its self-limitation caused by the negative reaction order of CO.

Co-methanation (C) basically displays similar dependencies as found for solo-methanation. The presence of CO in the feed gas represses the methanation of $CO_2$, the adsorption of $CO_2$ then is the rate-limiting step for the overall process of $CO_2$ methanation (*cf.* Eq. 8.1). It is found that the model underestimates the repression of $CO_2$ methanation compared to the experimental data in Figure 8.8 C. As discussed for the approach to equilibrium in CO solo-methanation in Figure 8.8 B, the repressive effect of CO on $CO_2$ methanation is closely related to the degree of hydrogenation $y$ in $COH_y$. For $y = 3$, $CO_2$ is not converted up to the complete consumption of CO. Experimentally, a repression behavior between these two discrete cases was found, which is reflected of a fitted degree of hydrogenation of $3 > y = 2.1913 > 2$ (*cf.* Figure 8.2 E) and again indicates that under CO methanation conditions the hydrogenation of $COH_2$* to $COH_3$* (further processed *via* the consecutive decomposition of $COH_3$* to $CH_2$* and OH*) may compete with

the decomposition of $COH_2$* in the methanation pathway, especially at high CO conversion ranges.

For the steam reforming reference point (D), thermodynamic equilibrium is reached at 375 °C. Similar to the model by Xu and Froment [186], $CO_2$ is the primary reaction product, while CO evolution follows the thermodynamic equilibrium. This is consistent to faster kinetics of CO* reacting with OH* compared to CO* desorption and reflects the influence of CO and $CO_2$ sorption processes under these conditions found in Section 8.4.6.

For all four reference cases (A) to (D), the model predictions agree very well with the experimentally observed yield and conversion values. Moreover, as shown in Section 8.7.10, it can be demonstrated that the derived kinetic model for $CO_x$ co-methanation adequately describes the model of Koschany *et al.* [24] for $CO_2$ solo-methanation.

## 8.6 Conclusion

The presented kinetic model of the co-methanation of CO and $CO_2$ is based on the competitive adsorption of $CO_2$ (*via* the reverse of the water-gas shift reaction) and CO as well as on a common rate-determining step in the methanation process and provides an outstanding description of the experiments over a broad range of experimental conditions, including steam reforming and water-gas shift reaction. Model discrimination as well as steady state isotope experiments indicate that the decomposition of a hydrogenated surface complex $COH_y$ ($y$ = 1 to 3) is the critical step in the methanation reaction. The degree of hydrogenation $y$ thereby may be a function of gas composition and reaction conditions, under the constraint of a discrete value the best fit is obtained for $y$ = 2. It is the first kinetic model available in literature that fully couples the competitive transformation of CO and $CO_2$ to $CH_4$ on the basis of the same surface species and reaction kinetics. Moreover, thermodynamics are fully included and all fitting parameters fulfill statistical relevance and physical consistency.

## 8.7 Supplementary Material

### 8.7.1 Experimental

#### 8.7.1.1 Catalyst Synthesis

The catalyst was prepared by co-precipitation as described in [24], and is the same catalyst prepared in Chapter 4. The synthesis procedure is described in detail in Section 4.2.1. The calcined catalyst powder was pelletized using a Lightpath L-15 laboratory press with a pressure of 450 N cm$^{-2}$, crushed and sieved to obtain particle fractions of 100 to 150 µm. Any effect of the shaping procedure on the BET surface area or pore size distribution was excluded by $N_2$ physisorption reference experiments.

#### 8.7.1.2 Material Characterization

In this study, it is focused on the catalyst properties in the reduced state and after artificial aging to capture material characteristics relevant for the kinetic performance; data on the characteristics in the freshly co-precipitated and calcined states of the catalyst can be found in [24] and Chapter 4. For characterization of the aged catalyst sample, the catalyst from the reactor setup was transferred under Ar atmosphere.

##### Inductively Coupled Plasma-Optical Emission Spectroscopy

The Ni and Al contents of the catalyst were determined by inductively-coupled plasma-optical emission spectroscopy. 50 mg of catalyst were suspended in 1 M $H_3PO_4$ in a 50 mL volumetric flask and sonicated for 3 h at 60 °C. After cool-down, the volume of the solution was adjusted to 50 mL with 1 M $H_3PO_4$ and the so-prepared solution was diluted in a ratio of 1 to 10 with bi-distilled water. Metal standards (Merck standard IV) were prepared for 50, 10, 1, and 0.1 ppm metal ion concentrations. All data was collected five times and metal signal superimpositions in the emission spectra were excluded.

##### Volumetric $H_2$, $CO_2$, and CO Chemisorption Measurements

$H_2$, $CO_2$, and CO chemisorption experiments were carried out on a Quantachrome Autosorb 1. Approximately 100 mg of catalyst were placed in a U-shaped quartz reactor, the axial position was fixed by quartz wool plugs. For *in situ* activation, the catalyst was heated to 500 °C in 5 % $H_2$ in Ar with a linear heating rate of 2 K $min^{-1}$ and the temperature was held for 6 h. The catalyst sample was then evacuated for 1 h at 500 °C to remove all adsorbed H* and all $H_2$ from the cell. The sample was cooled down to 35 °C under vacuum and held there for another 15 min. The $H_2$ adsorption isotherm was measured in the range of 40 to 800 mmHg at 35 °C. Sorption equilibration time was set 2 min. A 1:1 Ni/H stoichiometric ratio, assuming dissociative adsorption of $H_2$ on Ni, was applied for the calculation of the Ni surface area [252]. The volumetric $H_2$ uptake was determined by extrapolation to zero pressure.

For the determination of the isosteric heats of adsorption of $H_2$, adsorption isotherms were recorded from 2 to 800 mmHg (in 2 mmHg steps from 2 to 20 mmHg, 20 mmHg steps from 20 to 80 mmHg, and 40 mmHg steps from 80 to 800 mmHg) at temperatures ranging from 200 to 425 °C in 25 K steps. From linearization and simplification of the Clausius-Clapeyron equation (*cf.* Eq. 8.41), the enthalpy of dissociative $H_2$ adsorption was calculated from the negative slope of the isosteres, assuming the enthalpy of adsorption to be independent from temperature in the investigated temperature region.

$$\frac{\mathrm{d}p}{\mathrm{d}T} = \frac{\Delta H_{\mathrm{m,v}}}{\Delta V_{\mathrm{m,v}} \cdot T} \tag{8.41}$$

With $\Delta V_{m,v} = V_{m(g)} - V_{m(l)}, V_{m(g)} \gg V_{m(l)}$ and the ideal gas law $V_{m(g)} = \frac{R \cdot T}{p}$, Eq. 8.42 can be deduced.

$$\frac{1}{p}\,\mathrm{d}p = \frac{\Delta H_{m,v}}{R \cdot T^2}\,\mathrm{d}T \tag{8.42}$$

For normalization and conversion of $H_2$ uptakes into coverages, the overall volumetric uptake was determined from the $H_2$ chemisorption measurement at 35 °C.

For $CO_2$ chemisorption, the equilibration time was set 10 min. Before recording the $CO_2$ adsorption isotherm, it was checked in reference experiments that the adsorption of $CO_2$ on the catalyst was not kinetically hindered by varying the equilibration time from 2 min min up to 2 h. The pretreatment of the catalyst was the same as applied for $H_2$ chemisorption.

CO chemisorption experiments were conducted at 0 °C [252] and 250 °C with an equilibration time of 2 min. For the high-temperature measurement, a strongly increased CO uptake was observed that could not be explained by simple CO adsorption on Ni, but rather suggests spill-over of CO on the oxidic phase, possibly adsorbing on unreduced $Ni^{2+}$ species [252] or forming formate species on mixed oxide hydroxyl sites [57]. Bartholomew and Pannell [252] showed that CO adsorption on Ni is rather complex, since the adsorption stoichiometry varies with temperature, metal dispersion/metal particle size, metal loading, and catalyst preparation procedure. Further CO adsorption experiments at high temperature to evaluate the isosteric heat of adsorption were therefore omitted.

For chemisorption experiments of the aged catalyst samples, the catalyst was heated in vacuum to 350 °C with a linear heating rate of 5 K $min^{-1}$ and held there for 2 h. After cool-down to 35 °C, the $H_2$ or $CO_2$ adsorption isotherms were recorded as described above.

### $N_2$ Physisorption

$N_2$ sorption isotherms were recorded on a Quantachrome NOVAtouch. Approximately 100 mg of catalyst were activated and degassed as described in Section 8.7.1.2. The total BET surface area was calculated from the data points at $\frac{p}{p_0}$ ranging from 0.05 to 0.3. The total pore volume was determined from the volumetric $N_2$ uptake at $\frac{p}{p_0} = 0.995$.

### X-ray Powder Diffraction

X-ray powder diffraction was carried out on a Panalytical Empyrean using Cu-$K_\alpha$ radiation. The X-ray source was equipped with a monochromator and a Ni filter. Diffractograms were taken in the $2\theta$ range from 5 to 90° with a resolution of 0.01 ° $step^{-1}$ and 45 steps $min^{-1}$. The activated (procedure *cf.* Section 8.7.1.2) and aged catalyst samples were sealed in 0.5 mm glass capillaries under Ar atmosphere to prevent oxidation of Ni. Line profiling was carried out in Highscore 3.0d. Mean crystallite sizes were determined by the Scherrer equation (*cf.* Eq. 3.4).

#### Temperature-Programmed Reduction

Temperature-programmed reduction (TPR) experiments were carried out on a Quantachrome ChemStar TPx. Approximately 100 mg of catalyst were heated to 1000 °C in a U-shaped quartz reactor with a linear heating rate of 5 K $min^{-1}$ in 5 % $H_2$ in Ar. The temperature was then held for 30 min. To mimic the reduction conditions prior to kinetic measurements and to calculate the degree of reduction under reaction conditions, in a second experiment approx. 100 mg of catalyst were heated to 485 °C in 5 % $H_2$ in Ar with a heating rate of 5 K $min^{-1}$ and held there for 300 min. The total gas flow was 100 mL $min^{-1}$, considering the recommendations of Monti and Baiker [219] and Malet and Caballero [218]. Gas exiting the reactor was tracked *via* a thermal conductivity detector. Evolving $CO_2$ and $H_2O$ during activation was removed in a acetone / liquid $N_2$ slurry trap. The $H_2$ consumption signal was smoothed applying a Loess filter with a span of 0.1 and fitted by Gaussian peaks. Calibration of the TCD was carried out with CuO.

#### Temperature-Programmed Desorption of $H_2$

For temperature-programmed desorption of $H_2$ ($H_2$-TPD), the setup described in [141] was used. 50 mg of catalyst were heated to 480 °C in flow of 5 % $H_2$ in He with a total flow rate of 100 mL $min^{-1}$ at a heating rate of 2 K $min^{-1}$ and held there for 8 h. The reactor was flushed and cooled to 84 K in He using liquid nitrogen, where $H_2$ was adsorbed at atmospheric pressure and total flow of 60 mL $min^{-1}$ for 30 min. After adsorption, the catalyst was purged in 100 mL $min^{-1}$ He flow for 30 min. $H_2$ desorption was carried out by heating from 84 to 753 K in 100 mL $min^{-1}$ He flow with a heating rate of 6 K $min^{-1}$. $H_2$ evolution was tracked *via* an online mass spectrometer (Omnistar GSD 301, Pfeiffer Vacuum). The purity of all gases was 6.0.

## 8.7.2 Characterization Results and Discussion

The relevant parameters for linking kinetic data and catalyst properties are the respective characterization data of the aged catalyst. In addition, a detailed analysis of the catalyst properties after reduction is reported in Chapter 4.

### 8.7.2.1 Inductively Coupled Plasma-Optical Emission Spectroscopy

The synthesis procedure aimed for a hydrotalcite-derived mixed metal oxide catalyst with a $n_{Ni}/n_{Al}$ composition of 1. By ICP-OES, the $n_{Ni}/n_{Al}$ ratio was determined to be 1.04, resulting in a Ni loading of 44.3 wt.% and an Al loading of 19.8 wt.% in the calcined catalyst. The Na content was below $10^{-3}$ wt.%; therefore synthesis-induced Na poisoning of the catalyst and effects on the catalytic performance can be excluded.

### 8.7.2.2 X-ray Powder Diffraction

The as-synthesized precipitate ($[Ni_{0.5}Al_{0.5}(OH)_2][(CO_3)_{0.25} \cdot n\,H_2O]$) features a takovite-like hydrotalcite structure. After calcination at 450 °C, a metastable mixed metal oxide structure of Ni and Al is formed. X-ray diffraction patterns and detailed discussion of these structures can be found in Chapters 4 and 5.

The XRD patterns recorded after reduction and after catalyst conditioning (*cf.* Section 8.2.2) are shown in Figure 8.9. Reflection signals at $2\theta$ = 44.4, 51.8, and 76.4° clearly show the presence of fcc Ni nanocrystallites generated from the Ni-Al mixed oxide structure under reducing conditions. From profile fitting, the mean crystallite size can be estimated to 3.2 nm (*cf.* Chapter 4). Due to the low crystallinity, obvious from peak broadening, this value should not be over-interpreted, but can be assumed as a lower boundary for the mean Ni particle diameter.

Besides, distinct reflections appear at $2\theta$ = 36.4 and 65.0°, which are attributed to the Al-containing oxidic phase. Comparison to literature data (JCPDS 10-0425) shows that reflection positions differ from the ones of crystalline $\gamma$-$Al_2O_3$, expected under the chosen calcination conditions, and any other pure aluminum oxide phase. This indicates that a significant amount of $Ni^{2+}$ is still present in the $Al^{3+}$-containing oxidic phase, which is not reduced under the chosen conditions. Alzamora *et al.* proposed that this semi-crystalline phase is in company of a second $Al^{3+}$-rich amorphous phase [139], which makes the determination of the composition of this oxidic phase difficult.

After aging, the FWHM of the reflections decrease while their intensities increase, which clearly indicates a rise in crystallinity. The mean crystallite diameter is fitted to 5.2 nm after aging, which, compared to the initial size of 3.2 nm, clearly indicates Ni particle sintering under the chosen aging conditions (*cf.* Section 8.2.2). Besides, a shift of the reflection attributed to the

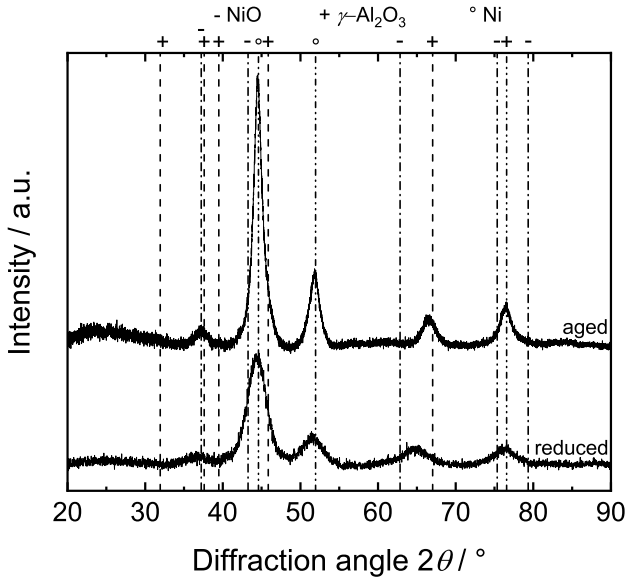


**Figure 8.9:** X-ray diffraction patterns of the freshly reduced and the aged $NiAlO_x$ catalyst (JCPDS: NiO 78-0429, Ni 87-0712, $\gamma$-$Al_2O_3$ 10-0425).

oxidic phase to higher diffraction angles (towards $\gamma$-$Al_2O_3$) can be observed (to $2\theta$ = 37.3 and 66.5°, respectively), indicating lattice contraction / a phase transformation occurring under aging condition. The oxidic phase evolved after aging may feature a higher relative $Al^{3+}$ content than the initial $Ni^{2+}$-containing oxidic phase, possibly originating from reconstruction processes involving the previous amorphous $Al^{3+}$-rich phase. These structural changes of the oxidic phase are non-trivial to resolve and consistent to Chapter 7.

### 8.7.2.3 Temperature-Programmed Reduction

The $H_2$ consumption profile recorded during temperature-programmed reduction (TPR) is shown in Figure 8.10. The maximum of $H_2$ consumption is reached at 440 °C. Gaussian peak fitting of the asymmetric peak shape for the sample reduced at 1000 °C resolves that two major $Ni^{2+}$ species exist in the $NiAlO_x$ catalyst. The low-temperature reduction peak centered at 420 °C makes up 45 % of the reduced $Ni^{2+}$ species, the high-temperature reduction peak is centered at 535 °C and makes up 55 % of the reducible $Ni^{2+}$ species. The presence of two different $Ni^{2+}$ species is in accordance with the results from XRD in Section 8.7.2.2. It is reflected in the structural model developed by Alzamora *et al.* [139], who postulated the co-existance of a crystalline $Al^{3+}$-containing, NiO-rich phase and a X-ray amorphous $Ni^{2+}$-containing, $Al^{3+}$-rich phase in the Ni-Al mixed metal oxide catalyst. The low-temperature reduction peak therefore can be attributed to the reduction of $Ni^{2+}$ species from the crystalline phase, while the peak centered at 535 °C is supposed to be caused by the reduction of $Ni^{2+}$ from the amorphous phase [137, 315, 316]. From Figure 8.10, the percentage of $Ni^{2+}$ reduced at 485 °C can be calculated to 57 %. At 1000 °C, 96 % of all Ni is in reduced state. Most noteworthy, in line with XRD in Figure 8.9, the presence of bulk spinel $NiAl_2O_4$ can be excluded. $Ni^{2+}$ from $NiAl_2O_4$ is expected to feature a reduction signal higher than 800 °C [92, 348, 349].

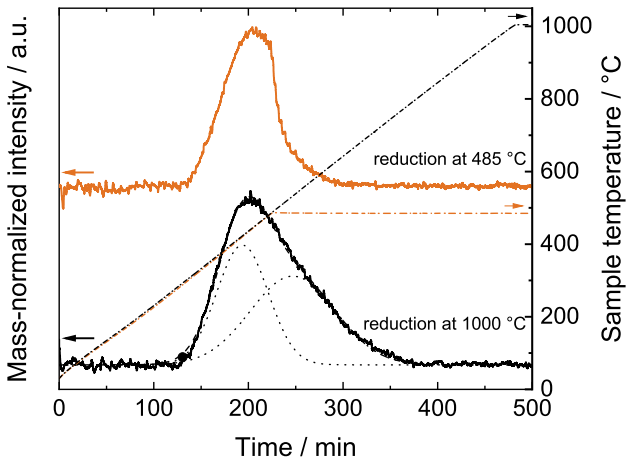


**Figure 8.10:** Temperature-programmed reduction pattern of the $NiAlO_x$ catalyst, reduced at 1000 °C, holding time 30 min, and at 485 °C, holding time 300 min. Heating rate 5 K $min^{-1}$. Dotted lines: Gaussian fits, dashed lines: cumulative curve, dash dotted lines: temperature profiles.

#### 8.7.2.4 $N_2$ Physisorption

Both the freshly reduced and the aged catalyst exhibit distinct type IV character featuring H3 hystereses, which is observed for mesoporous samples featuring aggregates of plate-like particles causing slit-shaped pores [225]. Deduced pore size distributions and values for the pore volume should not be over-interpreted for these samples [221]. The BET surface area decreases from 294 $m^2\,g_{cat}^{-1}$ initially after reduction to 179 $m^2\,g_{cat}^{-1}$ after aging. The pore volume, estimated from $N_2$ uptake at $p/p_0 = 0.995$, in contrast, increases from 0.68 to 0.89 $mL\,g_{cat}^{-1}$, which results in an increase of the mean hydraulic pore diameter (*cf.* Eq. 3.8) from 9.2 to 19.8 nm. The loss of BET surface area can be attributed to pore rupture under the (hydrothermal) aging conditions, possibly accompanied by sintering of the oxidic phase or reconstruction processes as evident from XRD in Figure 8.9.

#### 8.7.2.5 $H_2$ and $CO_2$ Chemisorption

The $H_2$ monolayer uptake was 270 $\mu mol\,g_{cat}^{-1}$, yielding a Ni surface area of 21.4 $m_{Ni}^2\,g_{cat}^{-1}$. The $CO_2$ monolayer uptake amounted to 172 $\mu mol\,g_{cat}^{-1}$ (*cf.* Chapter 4). While $H_2$ is assumed to selectively bind to the Ni sites, $CO_2$ may bind to the Ni sites or form carbonate / hydrogen carbonate species on the oxide material.

After aging (temperature program *cf.* Section 8.2.2), the $H_2$ uptake decreased to 170 $\mu mol\,g_{cat}^{-1}$, resulting in a reduction of the Ni surface area to 13.3 $m_{Ni}^2\,g_{cat}^{-1}$. This is a loss of 37 % and can be ascribed to Ni particle sintering under the hydrothermal aging conditions at 380 °C and 7 bar under $H_2O$ co-feed, in accordance with the increase of the Ni crystallite size from 3.2 to 5.2 nm as found in XRD in Figure 8.9. Simultaneously, the $CO_2$ uptake decreases from 172 $\mu mol\,g_{cat}^{-1}$ after reduction to 96 $\mu mol\,g_{cat}^{-1}$ after the aging treatment. Assuming that the majority of $CO_2$ associatively binds to basic sites on the oxidic phase of the catalyst, this decrease is consistent to the reduction of the BET surface area and can be explained by oxide phase sintering/restructuring and loss of basic sites during aging.

With a degree of reduction of 57 % as indicated by TPR, a mean Ni particle diameter of 8.1 nm can be calculated from the volumetric $H_2$ chemisorption uptake. Similarly, for the aged catalyst, assuming the degree of reduction stays constant under reaction conditions, a mean Ni particle diameter of 12.8 nm can be calculated.

#### 8.7.2.6 Temperature-Programmed Desorption of $H_2$

To evaluate the type of Ni sites in the reduced catalyst, temperature-programmed desorption of $H_2$ ($H_2$-TPD) was carried out. The $H_2$-TPD pattern is shown in Figure 8.11. The results from $H_2$-TPD are consistent to a previous study on Ni-Al catalyst focusing on the investigation of various Ni-Al catalysts by transient methods [141]. Four different Ni surface species can be distinguished. The low-temperature signal at 160 °C is supposed to arise from H bound in the subsurface area of the Ni crystallites ($\gamma$ signal), the signal at approx. 300 K ($\beta$ signal)

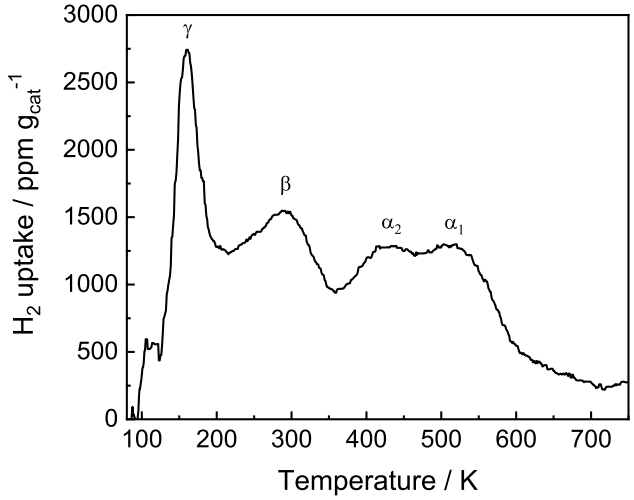


**Figure 8.11:** Temperature-programmed desorption pattern of $H_2$ from the $NiAlO_x$ catalyst.

is attributed to the desorption of H* bound to edges and corners of Ni crystallites as well as $H_2$ bound in multilayers [141, 376, 377]. The high-temperature signals at 420 K ($\alpha_2$) and 520 K ($\alpha_1$) can be assigned to the desorption of H bound to the surface of Ni crystallites [141, 376–379]. Under reaction conditions ($T > 450$ K), $\alpha_1$ and $\alpha_2$ are possible H occupation and reaction sites. The evolution of different desorption signals is an indicator for heterogeneity of the active Ni sites, featuring different sorption properties. Based on $H_2$ ad- and desorption experiments, Sehested *et al.* [380] calculated the adsorption constant of $H_2$ on a $Ni/MgAl_2O_4$ spinel catalyst for a kinetic model describing CO methanation under high $H_2$/CO ratios, but the catalyst used in their study exhibited homogeneity of H adsorption sites. Due to the Ni site heterogeneity of the catalyst observed in Figure 8.11, this approach is omitted in this study.

### 8.7.3 Catalyst Deactivation

Since no catalyst deactivation could be observed at low reaction temperatures and low partial pressures of steam (due to low $CO_2$ conversion) (*cf.* [24] and Section 4.5.8), artificial aging was carried out at 380 °C, 7 bar, and a reactant gas composition of $H_2/CO_2/CH_4/H_2O/Ar$ = 4/1/1.25/2.5/1.25 with a space velocity of $Q = 120\,\mathrm{NL\,g_{cat}^{-1}\,h^{-1}}$.

After 2 h of artificial aging in thermodynamic equilibrium at the conditions mentioned above, the catalyst bed was periodically cooled down to a reference point $RF_1$ (260 °C, 7 bar, $H_2/CO_2/Ar$ = 4/1/5, $Q = 150\,\mathrm{NL\,g_{cat}^{-1}\,h^{-1}}$) to track the extent of catalyst deactivation under kinetic conditions away from thermodynamic equilibrium. The deactivation behavior and the catalyst activity after aging are consistent to data reported earlier over this catalyst [24]. The trend of $CH_4$ yield over aging time at $RF_1$ is shown in Figure 8.12. A stable activity level was obtained after aging for 100 h at 380 °C.

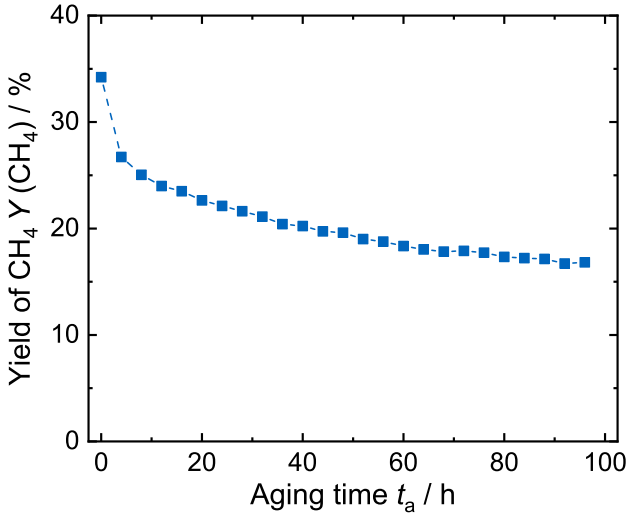


**Figure 8.12:** Trend of $CH_4$ yield over aging time, monitored at 260 °C, 7 bar, $H_2/CO_2/Ar$ = 4/1/5, $Q$ = 150 NL $g_{cat}^{-1}$ $h^{-1}$, aged at 380 °C, 7 bar, $H_2/CO_2/CH_4/H_2O/Ar$ = 4/1/1.25/2.5/1.25, $Q$ = 120 NL $g_{cat}^{-1}$ $h^{-1}$.

### 8.7.4 Evaluation of Heat and Mass Transport Criteria

Besides experimental verification of the absence of heat and mass transport criteria, all kinetic data points fulfil the heat (*cf.* appendix Eq. A.2 [381] and A.4 [311]) and mass transport (*cf.* appendix Eq. A.1 [312] and A.3 [312, 313]) correlations. For the determination of species gas concentrations, effective diffusion coefficients, and particle-to-fluid heat and mass transfer coefficients, Eq. A.5 to A.14 (*cf.* appendix) were applied. Catalyst pellet density was estimated from a bulk density of 500 kg $m^{-3}$ and a bed porosity of 0.5. Catalyst pellet conductivity was estimated to be 0.15 W $m^{-1}$ $K^{-1}$ [24], a conservative value for the high Ni loading of 44.3 wt.% (calcined catalyst). From the total pore volume estimated from $N_2$ physisorption data at $p/p_0$ = 0.995 (*cf.* Section 8.7.2.4) and the catalyst pellet density, pellet porosity $\varepsilon$ was calculated to be 0.6. The tortuosity factor $\tau^2$ was assumed to be 4.

In a conservative approach, the reaction orders $n$ for methanation and steam reforming were set to 1. The true activation energy of the methanation reaction was set 150 kJ $mol^{-1}$, for steam reforming 250 kJ $mol^{-1}$.

### 8.7.5 Kinetic Measurements

The experimental parameters for the kinetic measurements are listed in Table 8.3.

**Table 8.3:** Feed gas compositions and experimental parameters.

| No. | $y(CO_2)$ / - | $y(CO)$ / - | $y(CH_4)$ / - | $y(H_2O)$ / - | $y(H_2)$ / - | $y(Ar)$ / - | $T$ / °C | $p$ / bar | $m_{cat}$ / mg | $Q$ / NL $g_{cat}^{-1}$ $h^{-1}$ |
|---|---|---|---|---|---|---|---|---|---|---|
| 1[a] | - | 0.1 | - | - | 0.6 | 0.3 | 230–340 | 1, 5, 10, 15 | 25 | 180, 240 |
| 2[a] | 0.075 | 0.075 | - | - | 0.525 | 0.325 | 230–340 | 1, 5, 10, 15 | 25 | 180, 240 |
| 3[a] | 0.1 | 0.1 | 0.15 | 0.15 | 0.3 | 0.2 | 230–340 | 1, 5, 10, 15 | 25 | 180, 240 |
| 4[a] | 0.15 | 0.075 | 0.0375 | 0.075 | 0.375 | 0.2875 | 230–340 | 1, 5, 10, 15 | 25 | 180, 240 |
| 5[a] | 0.15 | 0.05 | 0.1 | - | 0.45 | 0.25 | 230–340 | 1, 5, 10, 15 | 25 | 180, 240 |
| 6[a] | - | 0.033 | - | - | 0.2 | 0.767 | 240–290 | 4, 7, 10 | 10 | 1200 |
| 7[a] | - | - | 0.1 | 0.15 | 0.025 | 0.725 | 310–530 | 2, 5, 8 | 25 | 180 |
| 8[a] | - | - | 0.15 | 0.3 | 0.0125 | 0.5375 | 310–530 | 2, 5, 8 | 25 | 214 |
| 9[b] | 0.1 | - | - | - | 0.4 | 0.5 | 180–240 | 2, 9, 15 | 75 | 36, 48 |
| 10[b] | 0.2 | - | - | - | 0.3 | 0.5 | 180–240 | 2, 9, 15 | 75 | 36, 48 |
| 11[b] | 0.25 | - | - | - | 0.25 | 0.5 | 180–240 | 2, 9, 15 | 75 | 36, 48 |
| 12[b] | 0.3 | - | - | - | 0.2 | 0.5 | 180–240 | 2, 9, 15 | 75 | 36, 48 |
| 13[b] | 0.4 | - | - | - | 0.1 | 0.5 | 180–240 | 2, 9, 15 | 75 | 36, 48 |
| 14[b] | 0.1 | - | - | - | 0.4 | 0.5 | 250, 265 | 3, 6, 9 | 25 | 120 |
| 15[b] | 0.2 | - | - | - | 0.2 | 0.6 | 250, 265, 285 | 3, 6, 9 | 25 | 120 |
| 16[b] | 0.4 | - | - | - | 0.1 | 0.5 | 250, 265 | 3, 6, 9 | 25 | 120 |
| 17[b] | 0.1 | - | - | - | 0.25 | 0.65 | 250–310 | 3, 6, 9 | 25 | 120 |
| 18[b] | 0.05 | - | - | - | 0.25 | 0.7 | 250 | 3, 6, 9 | 25 | 120 |
| 19[b] | 0.2 | - | - | - | 0.25 | 0.55 | 250–310 | 3, 6, 9 | 25 | 120 |
| 20[b] | 0.2 | - | - | - | 0.1 | 0.7 | 250, 265, 285 | 3, 6, 9 | 25 | 120 |
| 21[b] | 0.05 | - | - | - | 0.2 | 0.75 | 250, 265 | 3, 6, 9 | 25 | 120 |
| 22[b] | 0.1 | - | - | - | 0.1 | 0.8 | 335, 355 | 3, 6, 9 | 25 | 180 |
| 23[b] | 0.05 | - | 0.125 | 0.25 | 0.2 | 0.4 | 265, 310 | 3 | 25 | 120 |
| 24[b] | 0.2 | - | 0.125 | 0.25 | 0.2 | 0.225 | 265 | 3 | 25 | 120 |
| 25[b] | 0.1 | - | 0.125 | 0.25 | 0.4 | 0.125 | 250–310 | 3 | 25 | 120 |
| 26[b] | 0.1 | - | 0.1 | - | 0.4 | 0.4 | 250–310 | 3 | 25 | 120 |
| 27[b] | 0.1 | - | - | 0.125 | 0.4 | 0.375 | 265, 285, 310 | 3 | 25 | 120 |
| 28[b] | 0.1 | - | - | 0.3 | 0.4 | 0.2 | 250–310 | 3 | 25 | 120 |
| 29[b] | 0.025 | | 0.125 | 0.25 | 0.1 | 0.5 | 250, 310 | 3, 6 | 25 | 120 |
| 30[b] | 0.05 | - | 0.125 | 0.25 | 0.2 | 0.4 | 250–310 | 6 | 25 | 120 |
| 31[b] | 0.05 | - | 0.125 | 0.25 | 0.4 | 0.2 | 250–310 | 6 | 25 | 120 |
| 32[b] | 0.1 | - | 0.125 | 0.25 | 0.1 | 0.425 | 250–310 | 6 | 25 | 120 |
| 33[b] | 0.2 | - | 0.125 | 0.25 | 0.2 | 0.225 | 265–310 | 6 | 25 | 120 |
| 34[b] | 0.1 | - | 0.125 | 0.25 | 0.375 | 0.15 | 250–285 | 9 | 25 | 120 |
| 35[b] | 0.1 | - | 0.3 | - | 0.4 | 0.2 | 285 | 6 | 25 | 120 |
| 36[b] | 0.1 | - | 0.1 | - | 0.4 | 0.4 | 250, 265, 285 | 6 | 25 | 120 |
| 37[b] | 0.1 | - | - | 0.15 | 0.4 | 0.375 | 250, 265, 285 | 6 | 25 | 120 |
| 38[b] | 0.1 | - | - | 0.3 | 0.4 | 0.2 | 285 | 6 | 25 | 120 |
| 39[b] | 0.025 | - | 0.125 | 0.25 | 0.1 | 0.5 | 265 | 9 | 25 | 120 |
| 40[b] | 0.05 | - | 0.125 | 0.25 | 0.2 | 0.375 | 250–310 | 6 | 25 | 120 |
| 41[b] | 0.05 | - | 0.125 | 0.225 | 0,4 | 0.2 | 310 | 9 | 25 | 120 |
| 42[b] | 0.1 | - | 0.125 | 0.225 | 0,1 | 0.45 | 285, 310 | 9 | 25 | 120 |
| 43[b] | 0.2 | - | 0.125 | 0.25 | 0.2 | 0.225 | 265, 285, 310 | 9 | 25 | 120 |
| 44[b] | 0.1 | - | 0.125 | 0.25 | 0.4 | 0.125 | 250, 265, 285 | 6 | 25 | 120 |
| 45[b] | 0.1 | - | 0.1 | - | 0.4 | 0.4 | 250, 265, 285 | 9 | 25 | 120 |
| 46[b] | 0.025 | - | 0.125 | 0.25 | 0.15 | 0.45 | 355 | 9 | 25 | 120 |
| 47[b] | 0.025 | - | 0.125 | 0.25 | 0.1 | 0.5 | 335, 355 | 9 | 25 | 180 |
| 48[b] | 0.05 | - | 0.125 | 0.25 | 0.05 | 0.525 | 335, 355 | 9 | 25 | 180 |
| 49[b] | 0.05 | - | 0.125 | 0.25 | 0.15 | 0.425 | 335, 355 | 9 | 25 | 180 |
| 50[b] | 0.025 | - | 0.125 | 0.25 | 0.15 | 0.45 | 335, 355 | 6 | 25 | 180 |
| 51[b] | 0.05 | - | 0.125 | 0.25 | 0.1 | 0.5 | 335, 355 | 6 | 25 | 180 |
| 52[b] | 0.025 | - | 0.125 | 0.25 | 0.2 | 0.4 | 335, 355 | 6 | 25 | 180 |
| 53[b] | 0.05 | - | 0.125 | 0.25 | 0.05 | 0.5 | 335, 355 | 6 | 25 | 180 |
| 54[b] | 0.05 | - | 0.125 | 0.25 | 0.15 | 0.425 | 335, 355 | 6 | 25 | 180 |
| 55[b] | 0.025 | - | 0.125 | 0.275 | 0.15 | 0.425 | 335 | 3 | 25 | 180 |
| 56[b] | 0.025 | - | 0.125 | 0.275 | 0.2 | 0.375 | 335 | 3 | 25 | 180 |
| 57[b] | 0.05 | - | 0.125 | 0.275 | 0.15 | 0.4 | 335, 355 | 3 | 25 | 180 |

[a] temperature varied in 5 K steps from 240 to 300 °C, 10 K steps from 300 to 340 °C, 20 K steps from 310 to 530 °C (for No. 7 and No. 8).
[b] data points taken from Koschany *et al.* [24].

### 8.7.6 Model Derivation

Table 8.4 lists potential elementary steps and the deduced rate equations for the CO methanation reaction, formulated for rate inhibition by OH*. In an approach in accordance with the procedure of Koschany *et al.* [24] for $CO_2$ solo-methanation, these steps have been investigated as potentially rate-determining using the principles of Hougen and Watson [183] for Langmuir-Hinshelwood kinetics. In combination with the elementary steps in [73] and the references therein, this analysis resulted in 38 different kinetics models for CO methanation (19 for inhibition by OH*, 19 for inhibition by $H_2O$*). In this consideration, the water-gas shift reaction was neglected due to yields of less than 4 % and $CO_2$ was assumed as an inert, which is a justified simplification due to $CO_2$ conversions less than 1.5 %. Based on parameter estimation and model discrimination, the most suitable models were model 8, 6, 7, 16, and 17. For the models 6, 7, and 8, the equilibrium constant of the $COH_y$ surface intermediate as well as the adsorption enthalpy of $H_2$ could not be determined, which might arise from the low coverage of H and, above all, $COH_y$ [180] under reaction conditions. The best fit was obtained for model 8, the decomposition of a $COH_2$ surface complex, comprising seven fitting parameters. Except for models 9, 11, 12, and 19, assuming inhibition by OH* rather than $H_2O$* resulted in significantly lower fitting residua.

The models 6, 7, 16, and 17, however, involve a hydrogenation reaction as rate-determining step and therefore can be discarded due to the experimental observations in Section 8.3.1.2.

For co-methanation, competitive adsorption of CO and $CO_2$ has to be adequately described, which disqualifies the use of LHHW, or similar approaches, for model development. However, the investigations on $CO_2$ solo-methanation in [24] and the investigations on CO solo-methanation described above, in combination with the experimental observations in Section 8.3.1, are the fundament of the derived kinetic model comprising the competitive CO and $CO_2$ adsorption in Section 8.3.

**Table 8.4:** Elementary steps and rate equations for CO solo-methanation.

| Rate-determining step | LHHW rate equation |
|---|---|
| $CO + * \rightleftharpoons CO*$ | $r_1 = k \frac{p_{CO}\left(1-\frac{p_{CH_4}p_{H_2O}}{K_{eq,COmet}p_{CO}p_{H_2}^3}\right)}{\left(1+(K_{H_2}p_{H_2})^{0.5}+K_{CO}p_{CO}+K_{OH}\frac{p_{H_2O}}{p_{H_2}^{0.5}}\right)}$ |
| $CO* + * \rightleftharpoons C* + O*$ | $r_2 = k' \frac{p_{CO}\left(1-\frac{p_{CH_4}p_{H_2O}}{K_{eq,COmet}p_{CO}p_{H_2}^3}\right)}{\left(1+(K_{H_2}p_{H_2})^{0.5}+K_{CO}p_{CO}+K_{OH}\frac{p_{H_2O}}{p_{H_2}^{0.5}}\right)^2}$ |
| $CO* + H* \rightleftharpoons COH* + *$<br>$CO* + H* \rightleftharpoons C* + OH*$<br>$CO* + H* \rightleftharpoons CH* + O*$ | $r_3 = k' \frac{p_{H_2}^{0.5}p_{CO}\left(1-\frac{p_{CH_4}p_{H_2O}}{K_{eq,COmet}p_{CO}p_{H_2}^3}\right)}{\left(1+(K_{H_2}p_{H_2})^{0.5}+K_{CO}p_{CO}+K_{OH}\frac{p_{H_2O}}{p_{H_2}^{0.5}}\right)^2}$ |
| $CO* + 2H* \rightleftharpoons COH_2* + 2*$<br>$CO* + 2H* \rightleftharpoons CH* + OH* + *$<br>$CO* + 2H* \rightleftharpoons CH_2* + O* + *$ | $r_4 = k' \frac{p_{H_2}p_{CO}\left(1-\frac{p_{CH_4}p_{H_2O}}{K_{eq,COmet}p_{CO}p_{H_2}^3}\right)}{\left(1+(K_{H_2}p_{H_2})^{0.5}+K_{CO}p_{CO}+K_{OH}\frac{p_{H_2O}}{p_{H_2}^{0.5}}\right)^3}$ |
| $COH* + * \rightleftharpoons C* + OH*$<br>$COH* + * \rightleftharpoons CH* + O*$ | $r_5 = k' \frac{p_{H_2}^{0.5}p_{CO}\left(1-\frac{p_{CH_4}p_{H_2O}}{K_{eq,COmet}p_{CO}p_{H_2}^3}\right)}{\left(1+(K_{H_2}p_{H_2})^{0.5}+K_{CO}p_{CO}+K_{OH}\frac{p_{H_2O}}{p_{H_2}^{0.5}}+K_{COH}p_{H_2}^{0.5}p_{CO}\right)^2}$ |
| $COH* + H* \rightleftharpoons COH_2* + *$ | $r_6 = k' \frac{p_{H_2}p_{CO}\left(1-\frac{p_{CH_4}p_{H_2O}}{K_{eq,COmet}p_{CO}p_{H_2}^3}\right)}{\left(1+(K_{H_2}p_{H_2})^{0.5}+K_{CO}p_{CO}+K_{OH}\frac{p_{H_2O}}{p_{H_2}^{0.5}}+K_{COH}p_{H_2}^{0.5}p_{CO}\right)^2}$ |
| $COH* + 2H* \rightleftharpoons CH_2* + OH* + *$<br>$COH* + 2H* \rightleftharpoons COH_3* + 2*$ | $r_7 = k' \frac{p_{H_2}^{1.5}p_{CO}\left(1-\frac{p_{CH_4}p_{H_2O}}{K_{eq,COmet}p_{CO}p_{H_2}^3}\right)}{\left(1+(K_{H_2}p_{H_2})^{0.5}+K_{CO}p_{CO}+K_{OH}\frac{p_{H_2O}}{p_{H_2}^{0.5}}+K_{COH}p_{H_2}^{0.5}p_{CO}\right)^3}$ |
| $COH_2* + * \rightleftharpoons CH* + OH*$ | $r_8 = k' \frac{p_{H_2}p_{CO}\left(1-\frac{p_{CH_4}p_{H_2O}}{K_{eq,COmet}p_{CO}p_{H_2}^3}\right)}{\left(1+(K_{H_2}p_{H_2})^{0.5}+K_{CO}p_{CO}+K_{OH}\frac{p_{H_2O}}{p_{H_2}^{0.5}}+K_{COH_2}p_{H_2}p_{CO}\right)^2}$ |
| $COH_2* + H* \rightleftharpoons COH_3* + *$<br>$COH_2* + H* \rightleftharpoons CH_2* + OH*$ | $r_9 = k' \frac{p_{H_2}^{1.5}p_{CO}\left(1-\frac{p_{CH_4}p_{H_2O}}{K_{eq,COmet}p_{CO}p_{H_2}^3}\right)}{\left(1+(K_{H_2}p_{H_2})^{0.5}+K_{CO}p_{CO}+K_{OH}\frac{p_{H_2O}}{p_{H_2}^{0.5}}+K_{COH_2}p_{H_2}p_{CO}\right)^2}$ |
| $COH_2* + 2H* \rightleftharpoons CH_3* + OH* + *$ | $r_{10} = k' \frac{p_{H_2}^{2}p_{CO}\left(1-\frac{p_{CH_4}p_{H_2O}}{K_{eq,COmet}p_{CO}p_{H_2}^3}\right)}{\left(1+(K_{H_2}p_{H_2})^{0.5}+K_{CO}p_{CO}+K_{OH}\frac{p_{H_2O}}{p_{H_2}^{0.5}}+K_{COH_2}p_{H_2}p_{CO}\right)^3}$ |

| Rate-determining step | LHHW rate equation |
|---|---|
| $COH_3^* + * \rightleftharpoons CH_2^* + OH^*$ | $r_{11} = k' \frac{p_{H_2}^{1.5} p_{CO} \left(1 - \frac{p_{CH_4} p_{H_2O}}{K_{eq,COmet} p_{CO} p_{H_2}^3}\right)}{\left(1 + (K_{H_2} p_{H_2})^{0.5} + K_{CO} p_{CO} + K_{OH} \frac{p_{H_2O}}{p_{H_2}^{0.5}} + K_{COH_3} p_{H_2}^{1.5} p_{CO}\right)^2}$ |
| $COH_3^* + H^* \rightleftharpoons CH_3^* + OH^*$ | $r_{12} = k' \frac{p_{H_2}^{2} p_{CO} \left(1 - \frac{p_{CH_4} p_{H_2O}}{K_{eq,COmet} p_{CO} p_{H_2}^3}\right)}{\left(1 + (K_{H_2} p_{H_2})^{0.5} + K_{CO} p_{CO} + K_{OH} \frac{p_{H_2O}}{p_{H_2}^{0.5}} + K_{COH_3} p_{H_2}^{1.5} p_{CO}\right)^2}$ |
| $COH_3^* + 2H^* \rightleftharpoons CH_4^* + OH^* + *$ | $r_{13} = k' \frac{p_{H_2}^{2.5} p_{CO} \left(1 - \frac{p_{CH_4} p_{H_2O}}{K_{eq,COmet} p_{CO} p_{H_2}^3}\right)}{\left(1 + (K_{H_2} p_{H_2})^{0.5} + K_{CO} p_{CO} + K_{OH} \frac{p_{H_2O}}{p_{H_2}^{0.5}} + K_{COH_3} p_{H_2}^{1.5} p_{CO}\right)^3}$ |
| $C^* + H^* \rightleftharpoons CH^* + *$ | $r_{14} = k' \frac{p_{H_2}^{0.5} p_{CO}^{0.5} \left(1 - \frac{p_{CH_4} p_{H_2O}}{K_{eq,COmet} p_{CO} p_{H_2}^3}\right)}{\left(1 + (K_{H_2} p_{H_2})^{0.5} + K_{CO} p_{CO} + K_{OH} \frac{p_{H_2O}}{p_{H_2}^{0.5}} + K_{C} p_{CO}^{0.5}\right)^2}$ |
| $C^* + 2H^* \rightleftharpoons CH_2^* + 2^*$ | $r_{15} = k' \frac{p_{H_2} p_{CO}^{0.5} \left(1 - \frac{p_{CH_4} p_{H_2O}}{K_{eq,COmet} p_{CO} p_{H_2}^3}\right)}{\left(1 + (K_{H_2} p_{H_2})^{0.5} + K_{CO} p_{CO} + K_{OH} \frac{p_{H_2O}}{p_{H_2}^{0.5}} + K_{C} p_{CO}^{0.5}\right)^3}$ |
| $CH^* + H^* \rightleftharpoons CH_2^* + *$ | $r_{16} = k' \frac{p_{H_2} p_{CO}^{0.5} \left(1 - \frac{p_{CH_4} p_{H_2O}}{K_{eq,COmet} p_{CO} p_{H_2}^3}\right)}{\left(1 + (K_{H_2} p_{H_2})^{0.5} + K_{CO} p_{CO} + K_{OH} \frac{p_{H_2O}}{p_{H_2}^{0.5}} + K_{CH} p_{CO}^{0.5} p_{H_2}^{0.5}\right)^2}$ |
| $CH_2^* + H^* \rightleftharpoons CH_3^* + *$ | $r_{17} = k' \frac{p_{H_2}^{1.5} p_{CO}^{0.5} \left(1 - \frac{p_{CH_4} p_{H_2O}}{K_{eq,COmet} p_{CO} p_{H_2}^3}\right)}{\left(1 + (K_{H_2} p_{H_2})^{0.5} + K_{CO} p_{CO} + K_{OH} \frac{p_{H_2O}}{p_{H_2}^{0.5}} + K_{CH_2} p_{CO}^{0.5} p_{H_2}\right)^2}$ |
| $CH_2^* + 2H^* \rightleftharpoons CH_4^* + 2^*$ | $r_{18} = k' \frac{p_{H_2}^{2} p_{CO}^{0.5} \left(1 - \frac{p_{CH_4} p_{H_2O}}{K_{eq,COmet} p_{CO} p_{H_2}^3}\right)}{\left(1 + (K_{H_2} p_{H_2})^{0.5} + K_{CO} p_{CO} + K_{OH} \frac{p_{H_2O}}{p_{H_2}^{0.5}} + K_{CH_2} p_{CO}^{0.5} p_{H_2}\right)^3}$ |
| $CH_3^* + H^* \rightleftharpoons CH_4^* + *$ | $r_{19} = k' \frac{p_{H_2}^{2} p_{CO}^{0.5} \left(1 - \frac{p_{CH_4} p_{H_2O}}{K_{eq,COmet} p_{CO} p_{H_2}^3}\right)}{\left(1 + (K_{H_2} p_{H_2})^{0.5} + K_{CO} p_{CO} + K_{OH} \frac{p_{H_2O}}{p_{H_2}^{0.5}} + K_{CH_3} p_{CO}^{0.5} p_{H_2}^{1.5}\right)^2}$ |

## 8.7.7 Residuum Analysis

For the final model with $y = 2$, a comparison of weighted residuum values for the three fitting responses CO, $CO_2$, and $CH_4$ in terms of temperature, overall pressure, and space time of carbon containing reactants are given in the Figures 8.13–8.15, respectively.

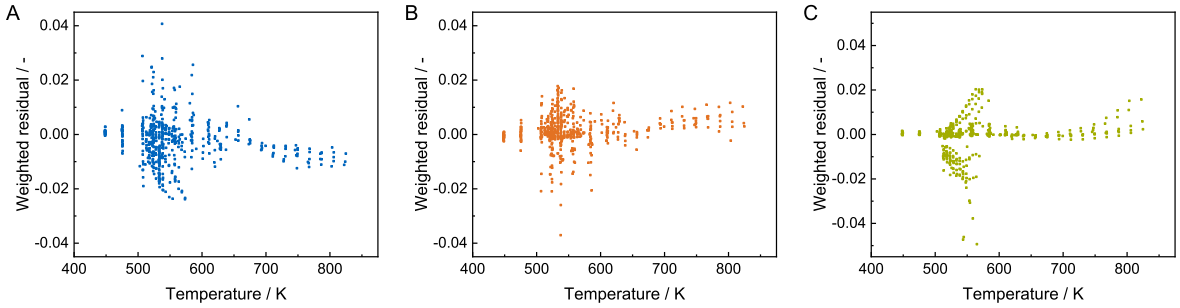


**Figure 8.13:** Dependency of weighted residuals on the reaction temperature for $CH_4$ (A), $CO_2$ (B), and CO (C).

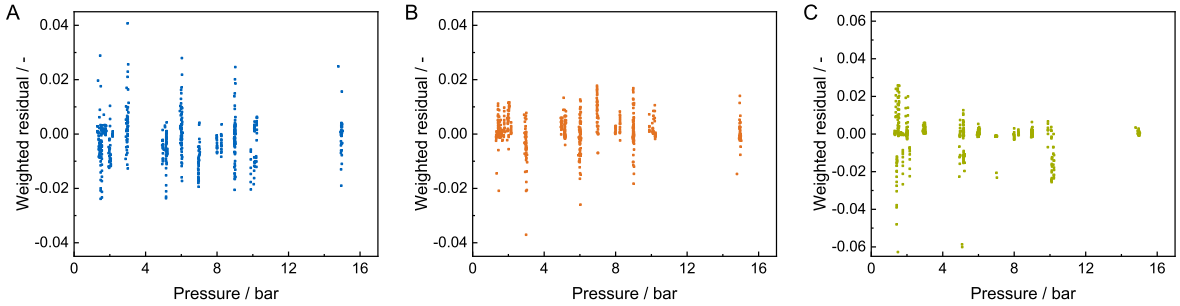


**Figure 8.14:** Dependency of weighted residuals on the overall pressure for $CH_4$ (A), $CO_2$ (B), and CO (C).

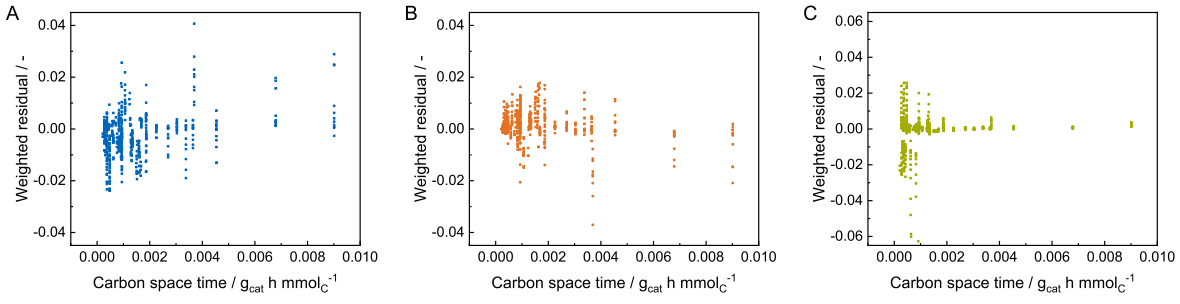


**Figure 8.15:** Dependency of weighted residuals on the carbon space time for $CH_4$ (A), $CO_2$ (B), and CO (C).

### 8.7.8 Experimental Determination of the Isosteric Heat of Adsorption of $H_2$

To exemplarily prove the fitted value of the enthalpy of $H_2$ adsorption on the Ni catalyst, the isosteric heat of adsorption was determined by $H_2$ chemisorption. For this, $H_2$ chemisorption experiments were carried out in 25 K steps from 200 to 425 °C. The hydrogen coverages were calculated by normalization to the $H_2$ monolayer uptake, determined *via* extrapolation to zero pressure of the sorption isotherm recorded at $T$ = 35 °C.

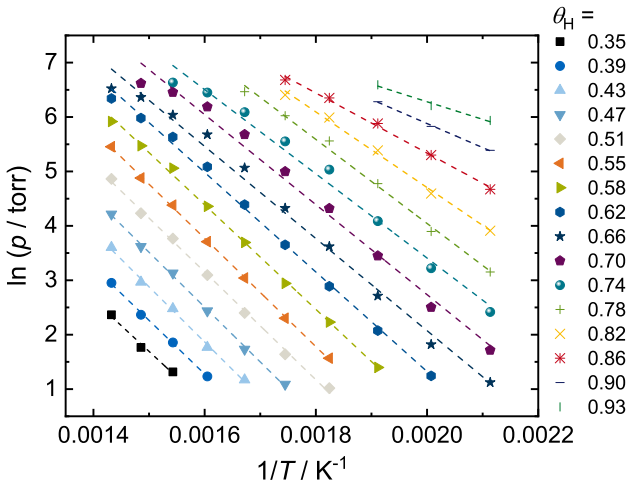


**Figure 8.16:** Plot of $\ln p$ vs. $\frac{1}{T}$, following the linearized simplified Clausius-Clapeyron equation (*cf.* Eq. 8.42) for the determination of the isosteric heat of adsorption as a function of hydrogen coverage.

From the slopes of the linearized lines in Figure 8.16, the isosteric heats of adsorption as a function of H coverage can be calculated, illustrated in Figure 8.17.

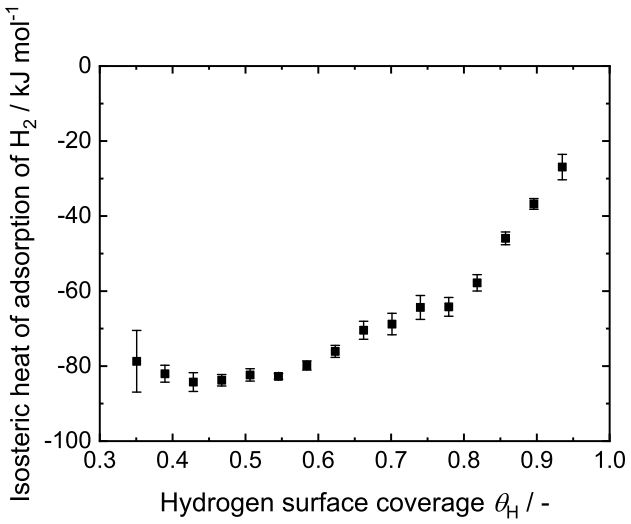


**Figure 8.17:** Trend of the isosteric heat of adsorption of $H_2$, $\Delta_{ads,V}H_{H_2}$ as a function of hydrogen surface coverage $\theta_H$.

### 8.7.9 Effect of the $CO_2/H_2$ Ratio on the Apparent Reaction Orders in $CO_2$ Methanation

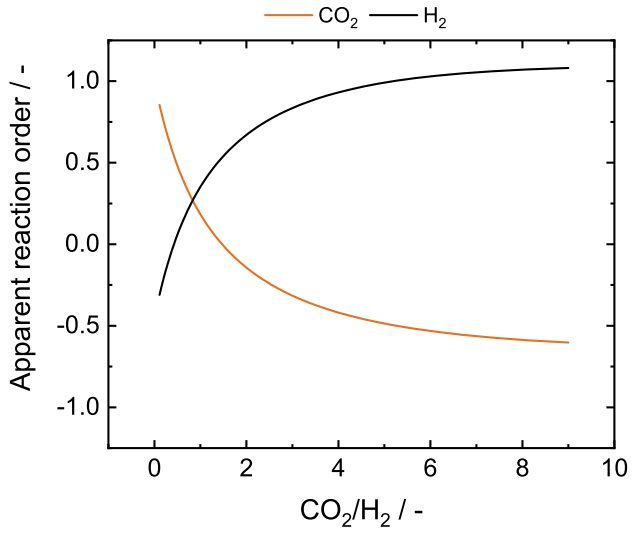


**Figure 8.18:** Influence of the stoichiometric $CO_2/H_2$ feed gas ratio on the apparent reaction orders $n_{app,i}$ for $CO_2$ solo-methanation (260 °C, 7 bar, *cf.* $RF_1$).

### 8.7.10 Transfer to $CO_2$ Solo-Methanation

Koschany *et al.* [24] reported a kinetic model for the solo-methanation of $CO_2$, the rate equation is shown in Eq. 8.43. The kinetic data pool lacked data on the steam reforming reaction and, when co-feeding $CH_4$ and $H_2O$ to $CO_2$ and $H_2$, was limited to a 1/2 stoichiometric ratio only. The water-gas shift reaction was not included in the model.

$$r_{CH_4} = k \cdot \frac{p_{CO_2}^{0.5} \cdot p_{H_2}^{0.5} \cdot \left(1 - \frac{p_{CH_4} \cdot p_{H_2O}^2}{p_{CO_2} \cdot p_{H_2}^4 \cdot K_{eq,CO_2 met}}\right)}{\left(1 + K_{H_2} \cdot p_{H_2}^{0.5} + K_{mix} \cdot p_{CO_2}^{0.5} + K_{OH} \cdot \frac{p_{H_2O}}{p_{H_2}^{0.5}}\right)^2} \tag{8.43}$$

They assumed a dissociative adsorption mechanism of $CO_2$, $H_2$ and $H_2O$. Furthermore, the hydrogenation of O* created by dissociation of $CO_2$ was considered as irreversible. Later, Marocco *et al.* confirmed that $CO_2$ methanation rates are adequately described by this form of rate equation [192].

However, based on the rate equation, three surface reactions, Reactions 8.X–8.XII, that cannot be mathematically discriminated, may potentially be rate-determining.

$$CO^* + H^* \rightleftharpoons COH^* + {}^* \tag{8.X}$$

$$CO^* + H^* \rightleftharpoons C^* + OH^* \tag{8.XI}$$

$$COH^* + {}^* \rightleftharpoons C^* + OH^* \tag{8.XII}$$

The negative isotope effect for $CO_2$ methanation effect discussed in Section 8.3.1.2 can only be explained when assuming Reaction 8.XII, the decomposition of COH*, as the rate-determining step. In addition, the authors did not consider mechanisms including higher order hydrogenation surface intermediates $COH_y$ ($y = 2, 3$). Furthermore, the rate equation was derived by assuming that the irreversible O* hydrogenation is as fast as the RDS: Transient studies show that, in contrast to CO methanation, the formation and desorption of water is considerably faster than for $CH_4$. Mori *et al.* [170] observed a maximum $H_2O/CH_4$ ratio of 8 when injecting $CO_2$ in a $H_2$-containing stream over a Ni/$\alpha$-$Al_2O_3$ catalyst. In addition, the fitted value for the adsorption enthalpy of $H_2$ was not significant and the adsorption enthalpy of $H_2O$ was positive. The kinetic model comprised two kinetic and six thermodynamic parameters for the description of one species and one reaction.

Figure 8.19 shows the parity plot of the kinetic model derived by Koschany *et al.* [24] and the model presented in this work. As already exemplarily illustrated in Figure 8.8 A, the parity plot confirms that the kinetic model developed in this study adequately describes the results of the kinetic model developed by Koschany *et al.* [24]. Therefore, the presented kinetic model can be regarded as an extension of the model derived by Koschany *et al.* to CO-containing feed gas as well as water-gas shift and mild stream reforming conditions.

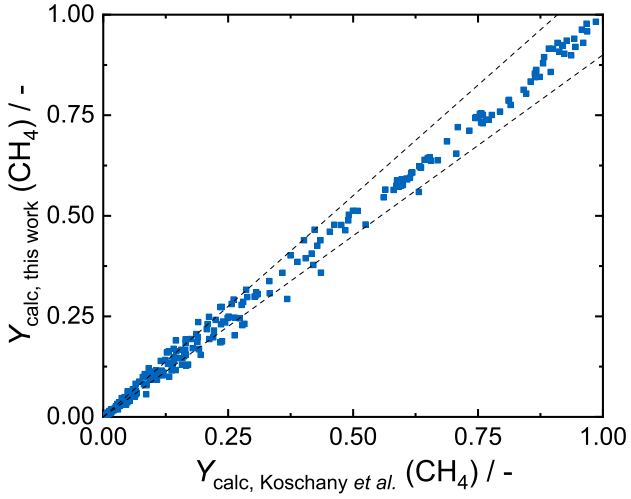


**Figure 8.19:** Parity plot comparing the normalized molar flows $Y_{calc}(CH_4)$ calculated from the kinetic model of Koschany *et al.* [24] and this study. Dashed lines indicate the ±10 % region.

# 9 Summary and Outlook

The $CO_2$ methanation reaction is one of the key steps in the power-to-gas concept, aiming at utilizing the greenhouse gas $CO_2$ as precursor substance for SNG to establish a chemical energy storage system. In this work, two basic requirements on $CO_2$ methanation catalysts, intrinsic catalytic activity to achieve high $CH_4$ yields at low reaction temperatures as well as high thermal stability under reaction conditions to increase catalyst life-time were addressed. The performance of an industrial-type co-precipitated $NiAlO_x$ ($n_{Ni}/n_{Al} = 1$) catalyst was significantly improved by doping the catalyst with appropriate amounts of Mn, Fe, or both elements.

The co-precipitated $NiAlO_x$ catalyst features a takovite-like distorted hydrotalcite structure. When added in small amounts during co-precipitation, neither Fe nor Mn have an impact on the structure of the precipitate, both ions seem to be incorporated into the brucite-like layers replacing $Ni^{2+}$ and $Al^{3+}$ in the hydroxide octahedra. After calcination, a mixed metal oxide of Ni and Al is formed, most likely consisting of two phases, an $Al^{3+}$-containing NiO phase and an $Al^{3+}$-rich, X-ray amorphous, possibly $Ni^{2+}$-containing phase. In X-ray powder diffraction, no impact of the promoters on the crystal structures in the catalyst can be observed. Therefore, it can be concluded that the promoters may form amorphous phases or be incorporated in the mixed metal oxide phases without significantly altering the lattice parameters. Catalyst activation is carried out at a medium temperature of 485 °C to maximize the metal surface area. Temperature-programmed reduction reveals two clear reduction signals for $NiAlO_x$, that can be assigned to the reduction of $Ni^{2+}$ species from the NiO-like phase and, most likely, the $Al^{3+}$-rich phase, respectively. The degree of reduction under these conditions amounts to 57 %.

For the Mn-containing catalyst samples, an additional low-temperature reduction signal can be identified, that can be assigned to the reduction of $Mn^{4+}$ to $Mn^{2+}$. Leaching of the catalyst in reducing environment indicates the presence of $Mn_3O_4$ after calcination, confirming the presence of $Mn^{2+}$ on the catalyst after activation at 485 °C. With increasing Mn loading, the reflection signal assigned to the oxidic Ni-Al phase after catalyst activation is shifted to lower diffraction angles, clearly suggesting that $Mn^{2+}$ is incorporated in this oxidic phase, leading to lattice distortion. While at low Mn loadings the Ni surface area is maintained, at high Mn loadings ($n_{Ni}/n_{Mn} < 4$) it significantly decreases. Temperature-programmed desorption, Fourier transform infrared spectroscopy, and $CO_2$ chemisorption experiments show an increasing $CO_2$ uptake capacity with rising Mn loading, which can be assigned to an increase of the density of weak ($CO_2$ bound as hydrogen carbonate) and medium ($CO_2$ bound as bidentate and monodentate carbonate) basic sites. In addition, the binding energy of $CO_2$ on these sites is decreased

compared to $NiAlO_x$. Steady-state methanation tests under stoichiometric feed gas composition at a total pressure of 8 bar show that Mn significantly increases the intrinsic catalytic activity of the $NiAlO_x$ catalyst. With rising Mn loading, the characteristic temperature for 50 % $CO_2$ conversion decreases from 266.6 K for $NiAlO_x$ to 240.6 K for an optimized $n_{Ni}/n_{Mn}$ ratio of 5.5. For higher Mn loadings, the effect of Mn is compensated by the negative contribution of the declining Ni surface area with decreasing Ni content in the catalyst. The beneficial effect of Mn on $NiAlO_x$ in $CO_2$ methanation thereby is attributed to the modification of basic sites upon the introduction of Mn. Especially a high density of medium basic sites as well as low binding energy of $CO_2$ on these sites may be beneficial for $CO_2$ methanation. This indicates that the pre-activation of $CO_2$ on the oxidic phase at the Ni particle perimeter may be an important step in $CO_2$ methanation. However, in addition, an electronic effect of Mn on the active Ni sites in the methanation reaction, modifying binding energies to reactants or intermediates, cannot be excluded.

Fe, in contrast, clearly interacts with the metallic Ni. In temperature-programmed reduction, $H_2$ consumption signals that can be attributed to the stepwise reduction of $Fe^{3+}$ to $Fe^0$ are observed. Besides, the reduction signal of Ni decreases to lower temperature, indicating a synergistic effect between Ni and Fe during catalyst activation. X-ray powder diffraction as well as ferromagnetic resonance spectroscopy confirms the formation of Ni-Fe alloy particles, forming a ($\gamma$Fe,Ni) phase in a fcc structure. Temperature-programmed desorption of $CO_2$ and $CO_2$ chemisorption experiments moreover reveal an increase of the $CO_2$ uptake that can be assigned to a higher density of weak basic sites. The binding energy of $CO_2$ on the basic sites seems to be slightly decreased compared to $NiAlO_x$. The effect of Fe on the basic sites on the oxidic phase is assigned to unreduced $Fe^{n+}$ ($n$ = 2, 3) species. Besides, IR spectroscopy shows that Fe contributes to the dissociation of $CO_2$ and/or modifies the $CO_2$ dissociation properties of Ni. The presence of exposed Fe atoms in ($\gamma$Fe,Ni) is consistent to $H_2$ chemisorption experiments, where a decrease of the $H_2$ uptake can be oberved caused by the kinetic limitation of $H_2$ adsorption on Fe at 35 °C.

In $CO_2$ methanation, a decrease of the characteristic temperature for 50 % $CO_2$ conversion from 266.6 K for $NiAlO_x$ to 254.5 K for an optimized $n_{Ni}/n_{Fe}$ ratio of 5.5 is observed. This effect may be caused by a modification of the reaction mechanism or the electronic properties of the active sites, affecting the C-O dissociation energy. The close interaction of Fe and the Ni sites is obvious from an increase of the apparent activation energy from approx. 77 kJ $mol^{-1}$ for $NiAlO_x$ to 89 kJ $mol^{-1}$ for $NiFeAlO_x$ with a $n_{Ni}/n_{Fe}$ promoter ratio of 5. In catalyst aging experiments at 500 °C for 32 h, $NiFeAlO_x$ features a much lower activity loss compared to $NiAlO_x$. Deactivation mechanisms comprise sintering of the active sites, sintering of the oxidic phase, and loss of basic sites. The decrease of the characteristic temperature for a $CO_2$ conversion of 50 % amounts to 24.0 K for $NiAlO_x$, but only 5.5 K for $NiFeAlO_x$ at an optimized $n_{Ni}/n_{Fe}$ ratio of 5.5. Time-resolved aging studies reveal that this increase of the apparent stability is caused by a temporal increase of the intrinsic catalytic activity of $NiFeAlO_x$ under aging conditions. The highest activity increase (129 % of the initial activity after catalyst activation) was observed after

aging at 450 °C for 16 h. Ferromagnetic resonance spectroscopy, X-ray powder diffraction, and Mössbauer spectroscopy reveal that this phenomenon is correlated to the partial segregation of Fe from the ($\gamma$Fe,Ni) particles. Mössbauer spectroscopy and total X-ray scattering experiments provide evidence that Fe segregation is accompanied by the oxidation of Fe, possibly resulting in the formation of wüstite closely located to the metal particles. The enhanced intrinsic catalytic activity thereby is accompanied by an increase of the apparent activation energy from approx. 89 to 102 kJ mol$^{-1}$. This compensation effect can be explained by assuming more than one kind of active sites on the catalyst surface. It is hypothesized that the *in situ* formed wüstite phase offers an additional reaction pathway for $CO_2$ activation by a $Fe^{2+}/Fe^{3+}$ redox mechanism, that features a higher activation energy but contributes to the overall methanation rate. The kinetic rate constant then can be expressed by the sum of two Arrhenius approaches, with the measured activation energy being lumped over the activation energies of both reaction pathways.

When co-doping Fe and Mn to $NiAlO_x$, catalysts with an improved activity and stability performance can be synthesized. The best trade-off for Ni-Fe-Mn-Al mixed metal oxide catalysts is achieved for a ratio of $n_{Ni}/n_{Fe} = 7$ and $n_{Ni}/n_{Mn} = 9.5$ (with $n_{Ni}/n_{Al} = 1$). However, the effects of Fe and Mn cannot be combined linearly. Doping them by subsequent incipient wetness impregnation of a co-precipitated calcined $NiAlO_x$ catalyst, the impregnation order plays a significant role on catalyst performance. The effect of the dopant added first prevails in the later catalyst performance. This offers the unique opportunity to tailor catalyst performance on the specific requirement. The trends of the performance of co-doped catalysts indicates that both promoters compete for the active sites. Since Mn clearly interacts with the oxidic phase and the effect of Fe can be deduced to a segregation-oxidation mechanism, it can be concluded that both promoters act at the perimeter of the metal particles.

The importance of the location of the Fe promoter in the Ni-Al mixed metal oxide catalyst was verified by selectively depositing Fe in proximity to $Ni^0$ sites *via* the surface redox reaction technique. The so-synthesized catalysts featured an improved apparent stability, comparable to the ones where Fe was doped during co-precipitation or by impregnation of the Ni-Al mixed metal oxide. Doping Fe *via* the surface redox reaction technique to a precipitated $Ni/Al_2O_3$ catalyst, in contrast, lead to a decrease of the apparent catalytic stability but an increase in activity, which highlights the importance of the oxidic phase on catalyst performance and (possibly synthesis-dependent) promoter effects.

For the $NiAlO_x$ catalyst, a kinetic model comprising $CO_x$ methanation, (reverse) water-gas shift reaction, and steam reforming was developed. In contrast to literature kinetic models, the methanation reactions of CO and $CO_2$ are described *via* one common kinetically relevant step by implementing competitive CO and $CO_2$ adsorption instead of assuming both adsorption processes to be quasi-equilibrated. Model discrimination and steady-state isotope experiments, which reveal an inverse isotope effect in both CO and $CO_2$ methanation, suggest that the dissociation of a hydrogenated $COH_y$ surface complex is the kinetically relevant step in $CO_x$ methanation. The best fit for over 1700 responses for CO, $CO_2$, and $CH_4$ is obtained for a

discrete value of $y = 2$ (hydroxycarbene). However, different $COH_y$ species may co-exist and their conversion may contribute to the overall methanation rate. Over the whole range of $y$ from 1 (formyl intermediate) to 3 (hydroxymethyl intermediate), the model and the parameters are thermodynamically consistent, statistically relevant, and physically meaningful. Nevertheless, the model and the kinetic parameters for $y = 2$ provide an average over reaction kinetics and describe the kinetic data points in excellent agreement. In CO-rich feed gas atmosphere, $CO_2$ methanation is inhibited by $CO_2$ adsorption on the catalyst surface, which is expressed *via* the reverse of the water-gas shift reaction in an H*-assisted reaction pathway becoming kinetically relevant. It is shown that the derived kinetic model cannot be discriminated from a kinetic model recently derived by Koschany *et al.* [24] for $CO_2$ solo-methanation over the same catalyst.

To get a deeper understanding of the elementary steps in $CO_x$ methanation, *ab initio* Monte-Carlo simulations coupled with transient techniques such as temporal analysis of products (TAP) or steady-state isotopic transient kinetic analysis (SSIKTA) may provide further insights. These investigations may also shine further light onto the impact on the Fe and Mn promoter on elementary step kinetics and the reaction mechanism. The kinetic model for $CO_x$ methanation was derived over only one kind of active sites. In real catalysts, different facets may feature different activities in methanation, especially considering the role of step and kink sites in this possibly structure-sensitive reaction. The presented kinetic model gives an average over the kinetics on different sites, which possibly involve different kinetically relevant steps. The assumption of a dual site mechanism for $CO_2$ adsorption and the methanation step, however, did not yield a better statistical description of the kinetic data than the presented model.

By promoting Fe and Mn, the catalytic performance of industrial type co-precipitated Ni-Al catalysts was significantly improved and a new generation of $CO_2$ methanation catalysts was introduced. The catalysts developed in this study may be applied in different reaction stages in a methanation process. In a two-stage methanation setup, one might utilize a Fe-promoted $NiAlO_x$ catalyst that features a long life-time under harsh methanation conditions in the first stage to convert the majority of the $CO_2$ at high temperature. In the second stage, one may rather apply a Mn-promoted catalyst operated at low temperature to achieve high $CH_4$ yields. However, the study was limited to a molar ratio of $n_{Ni}/n_{Al} = 1$ for all co-precipitated catalysts. One might wonder how the $n_{Ni}/n_{Al}$ ratio influences the promoter effects of Fe and Mn in terms of catalytic activity and catalyst stability. Current studies focus on the detailed investigation of the evolution of crystalline and possibly amorphous mixed metal oxide phases consisting of Ni and Al in various stoichiometries, highlighting the distribution and incorporation of Ni and Al therein. Moreover, it is manifest to try to apply the findings from the Mn promoter effect to other reactions that require $CO_2$ activation, such as $CH_3OH$ synthesis from $CO_2$ over Cu-Zn-Al mixed metal oxide catalysts. The methodology of coupling $CO_2$ and CO with the surface reaction of CO in the kinetic model for $CO_x$ methanation may be transferred to reactions involving similarly coupled adsorption steps such as the selective catalytic reduction of $NO_x$.

# A Heat and Mass Transport Limitation Criteria

For all kinetic data points, the heat and mass transport criteria Eqs. A.1 to A.4 were evaluated to exclude any influence of inter- or intra-particle mass and heat transport on the gathered kinetic data.

- Inter-particle mass transport: Mears criterion [312]

$$\frac{R_i \cdot \rho_\mathrm{P} \cdot d_\mathrm{P}}{\beta_i \cdot c_i} < \frac{0.3}{|n|} \tag{A.1}$$

- Inter-particle heat transport: Mears criterion [381]

$$\frac{|\sum R_i \cdot H_\mathrm{i}| \cdot \rho_\mathrm{P} \cdot d_\mathrm{P}}{\alpha \cdot T} < \frac{0.3 \cdot R \cdot T}{E_\mathrm{A}} \tag{A.2}$$

- Intra-particle mass transport: Weisz-Prater criterion [312, 313]

$$\frac{R_i \cdot \rho_\mathrm{P} \cdot d_\mathrm{P}^2}{4 \cdot c_i \cdot D_i^\mathrm{eff}} < \frac{1}{|n|} \tag{A.3}$$

- Intra-particle heat transport: Anderson criterion [311]

$$\frac{|\sum R_i \cdot H_\mathrm{i}| \cdot \rho_\mathrm{P} \cdot d_\mathrm{P}^2}{4 \cdot \lambda_\mathrm{P}^\mathrm{eff} \cdot T} < \frac{0.75 \cdot R \cdot T}{E_\mathrm{A}} \tag{A.4}$$

$R_i$ is the measured net consumption or formation rate of species $i$, $n$ the respective reaction order. $\alpha$ is the heat and $\beta_i$ the mass transfer coefficient for the particle-to-fluid transfer. $\lambda_\mathrm{P}^\mathrm{eff}$ denotes the effective heat conductivity of the pellet, $\rho_\mathrm{P}$ its density. The concentration $c_i$ of species $i$ can be calculated applying the universal gas law in Eq. A.5.

$$c_i = \frac{p_i}{R \cdot T} \tag{A.5}$$

The effective diffusion coefficient $D_i^\mathrm{eff}$ is calculated according to the Bosanquet equation (*cf.* Eq. A.6) [382] from pellet porosity $\varepsilon$, tortuosity $\tau^2$, the molecular diffusion coefficient $D_{i,\mathrm{m}}$

(*cf.* Eq. A.7) [383], and, to account for wall-effects in the mesopore system of the catalyst, the Knudsen diffusion coefficient $D_{i,\mathrm{Kn}}$ (*cf.* Eq. A.8).

$$D_i^{\mathrm{eff}} = \frac{\varepsilon}{\tau^2} \cdot \left( \frac{1}{D_{i,\mathrm{m}}} + \frac{1}{D_{i,\mathrm{Kn}}} \right)^{-1} \tag{A.6}$$

$$D_{i,\mathrm{m}} = \frac{1 - x_i}{\sum_{j \neq i} \frac{x_j}{D_{i,j}}} \tag{A.7}$$

$$D_{i,\mathrm{Kn}} = \frac{d_{\mathrm{Pore}}}{3} \cdot \sqrt{\frac{8 \cdot R \cdot T}{\pi \cdot M_i}} \tag{A.8}$$

The binary diffusion coefficient $D_{i,j}$ in Eq. A.7 can be calculated according to Fuller *et al.* [384, 385]:

$$\frac{D_{i,j}}{\mathrm{cm^2/s}} = \frac{0.001 \cdot \left(\frac{T}{\mathrm{K}}\right)^{1.75} \cdot \left( \left(\frac{M_i}{\mathrm{g/mol}}\right)^{-1} + \left(\frac{M_j}{\mathrm{g/mol}}\right)^{-1} \right)^{0.5}}{\frac{p}{\mathrm{atm}} \left( \left(\frac{\Delta v_i}{\mathrm{cm^3}}\right)^{\frac{1}{3}} + \left(\frac{\Delta v_j}{\mathrm{cm^3}}\right)^{\frac{1}{3}} \right)^2}. \tag{A.9}$$

The Nusselt number *Nu* and the Sherwood number *Sh*, that give access to the heat and mass transfer coefficients for the particle-to-fluid transfer, respectively, can be computed from suitable correlation equations, depending on the operational conditions. A commonly applied correlation valid for $0.1 < \mathrm{Re} < 100$ was determined by Wakao *et al.* [386].

$$Nu = \frac{\alpha \cdot d_{\mathrm{P}}}{\lambda} = 2 + 1.1 \cdot Pr^{\frac{1}{3}} \cdot Re^{0.6} = 2 + 1.1 \cdot \left( \frac{\eta \cdot c_p}{\lambda} \right)^{\frac{1}{3}} \cdot \left( \frac{\rho \cdot d_{\mathrm{P}} \cdot u}{\eta} \right)^{0.6} \tag{A.10}$$

$$Sh = \frac{\beta \cdot d_{\mathrm{P}}}{D_{i,\mathrm{m}}} = 2 + 1.1 \cdot Sc^{\frac{1}{3}} \cdot Re^{0.6} = 2 + 1.1 \cdot \left( \frac{\eta}{\rho \cdot D_{i,\mathrm{m}}} \right)^{\frac{1}{3}} \cdot \left( \frac{\rho \cdot d_{\mathrm{P}} \cdot u}{\eta} \right)^{0.6} \tag{A.11}$$

The viscosity $\eta$ and heat conductivity $\lambda$ of the fluid can be determined using the mixing relations of Wilke [387] in Eqs. A.12 to A.14. The density of the fluid $\rho$ can be calculated from the universal gas law with the mean molar mass of the fluid. The specific heat capacities of the different species $i$ can be computed using the Shomate equation (*cf.* Eq. B.1), giving access to the mean specific heat capacity of the fluid $c_p$.

$$\eta = \sum_i \frac{x_i \cdot \eta_i}{\sum_j x_j \cdot \psi_{\mathrm{ij}}} \tag{A.12}$$

$$\lambda = \sum_i \frac{x_i \cdot \lambda_i}{\sum_j x_j \cdot \psi_{\mathrm{ij}}} \tag{A.13}$$

$$\psi_{ij} = \frac{1}{2\sqrt{2}} \left( 1 + \left( \frac{\eta_i}{\eta_j} \right)^{\frac{1}{2}} + \left( \frac{M_j}{M_i} \right)^{\frac{1}{4}} \right)^2 + \left( 1 + \frac{M_i}{M_j} \right)^{-\frac{1}{2}} \tag{A.14}$$

# B Thermodynamic Data

The Shomate equation (*cf.* Eq. B.1) describes the specific molar heat capacity of a species $i$ as a polynomial function of temperature with the coefficients $a_i$ to $e_i$.

$$c_{p,i} = a_i + b_i \cdot T + c_i \cdot T^2 + d_i \cdot T^3 + e_i \cdot T^{-2} \tag{B.1}$$

The molar specific enthalpy (*cf.* Eq. B.2) and entropy (*cf.* Eq. B.3) values can be calculated according to

$$H_i^{\circ} = \int_{T_0}^{T} c_{p,i}(T)\mathrm{d}T + \Delta_f H_i^{\circ} = a_i \cdot T + \frac{b_i}{2} \cdot T^2 + \frac{c_i}{3} \cdot T^3 + \frac{d_i}{4} \cdot T^4 - e_i \cdot T^{-1} - (a_i \cdot T_0 + \frac{b_i}{2} \cdot T_0^2 + \frac{c_i}{3} \cdot T_0^3 + \frac{d_i}{4} \cdot T_0^4 - e_i \cdot T_0^{-1}) + \Delta_f H_i^{\circ} \tag{B.2}$$

$$S_i^{\circ} = \int_{T_0}^{T} \frac{c_{p,i}(T)}{T}\mathrm{d}T + S_{0,i}^{\circ} = a_i \cdot \ln(T) + b_i \cdot T + \frac{c_i}{2} \cdot T^2 + \frac{d_i}{3} \cdot T^3 - \frac{e_i}{2} \cdot T^{-2} - (a_i \cdot \ln(T_0) + b_i \cdot T_0 + \frac{c_i}{2} \cdot T_0^2 + \frac{d_i}{3} \cdot T_0^3 - \frac{e_i}{2} \cdot T_0^{-2}) + S_{0,i}^{\circ}. \tag{B.3}$$

$\Delta_f H_i^{\circ}$ describes the molar specific heat of formation, $S_{0,i}^{\circ}$ the molar specific entropy at the reference temperature $T_0$ = 298.15 K. They are listed in [388]. The coefficients $a_i$ to $e_i$ are tabulated for specific temperature intervals in the NIST Chemistry Web Book, based on [389] (used for studies in Chapters 4 to 7), and in [390] (used for studies in Chapters 2 and 8).

# C Thermodynamic Equilibrium

With the fundamental equation, the change of the total Gibbs free energy in an open flow system without external forces can be written as [391]

$$\mathrm{d}G' = \mathrm{d}H' - \mathrm{d}(T \cdot S') = \mathrm{d}U' + \mathrm{d}(p \cdot V) - \mathrm{d}(T \cdot S') = V \cdot \mathrm{d}p - S'\mathrm{d}T + \sum_i \mu_i \cdot \mathrm{d}n_i. \tag{C.1}$$

$\mu_i$ denotes the chemical potential of species $i$. Under isobaric and isothermal conditions, Eq. C.1 results in:

$$\mathrm{d}G' = \mathrm{d}H' - T \cdot \mathrm{d}S' = \sum_i \mu_i \cdot \mathrm{d}n_i. \tag{C.2}$$

The change of the molar Gibbs free energy therefore equals the change of the chemical potential and can be expressed by the change of the molar enthalpy and the molar entropy, as shown in Eq. C.3.

$$\mathrm{d}G = \mathrm{d}H - T \cdot \mathrm{d}S = \mathrm{d}\mu \tag{C.3}$$

The change of the total chemical potential in a chemical reaction is described by the chemical potentials of the species $i$ and their stoichiometric factors $\nu_i$.

$$\mathrm{d}\mu = \sum_i \nu_i \cdot \mu_i \tag{C.4}$$

The chemical potential of species $i$ can be expressed by Eq. C.5 with its standard chemical potential $\mu_i^{\mathrm{o}}$, its fugacity $f_i$, and its standard fugacity $f_i^{\mathrm{o}}$ [392].

$$\mu_i = \mu_i^{\mathrm{o}} + R \cdot T \cdot \ln\left(\frac{f_i}{f_i^{\mathrm{o}}}\right) \tag{C.5}$$

Thermodynamic equilibrium states in chemical reactions are characterized by a minimum in the Gibbs free energy $G$ along the reaction coordinate $\xi$. With Eqs. C.3 and C.4, this leads to the criterion [392]:

$$\left(\frac{\mathrm{d}G}{\mathrm{d}\xi}\right)_{p,T} = 0 = \mathrm{d}\mu = \sum_i \nu_i \cdot \mu_i. \tag{C.6}$$

With the definition of the Gibb's free energy of reaction

$$\Delta_R G = \sum_i \nu_i \cdot \mu_i = \sum_i \nu_i \cdot \left( \mu_i^o + R \cdot T \cdot \ln \left( \frac{f_i}{f_i^o} \right) \right) = \Delta_R G^o + \sum_i \nu_i \cdot R \cdot T \cdot \ln \left( \frac{f_i}{f_i^o} \right), \quad \text{(C.7)}$$

the equilibrium constant $K_{eq}$ for $\left( \frac{dG}{d\xi} \right)_{p,T} = \Delta_R G = 0$ can be defined:

$$\Delta_R G^o = \sum_i \nu_i \cdot \mu_i^o = -\sum_i \nu_i \cdot R \cdot T \cdot \ln \left( \frac{f_i}{f_i^o} \right) = -R \cdot T \cdot \ln \prod \left( \frac{f_i}{f_i^o} \right)^{\nu_i} = -R \cdot T \cdot \ln K_{eq} \quad \text{(C.8)}$$

$$\text{with } K_{eq} = \prod \left( \frac{f_i}{f_i^o} \right)^{\nu_i} = \exp \left( -\frac{\Delta_R G^o}{R \cdot T} \right). \quad \text{(C.9)}$$

The standard chemical potential $\mu_i^o$ of species $i$ thereby can be calculated from its standard enthalpy of formation and standard entropy (*cf.* Eqs. B.2 and B.3), respectively. In this study IUPAC SATP conditions ($T^o$ = 298.15 K, $p^o$ = 1 bar) are used as standard conditions.

$$\mu_i^o = \Delta_f H_i^o - T \cdot \Delta S_i^o \quad \text{(C.10)}$$

The fugacity $f_i$ for a gas species $i$ can be expressed *via* the fugacity coefficient $\varphi_i$, its molar fraction $y_i$ and the total pressure $p$ [392].

$$f_i = \varphi_i \cdot y_i \cdot p \quad \text{(C.11)}$$

With Eq. C.9 and Dalton's law, this leads to the expression:

$$K_{eq} = \exp \left( -\frac{\Delta_R G^o}{R \cdot T} \right) = \prod \left( \frac{\varphi_i \cdot y_i \cdot p}{f_i^o} \right)^{\nu_i} = \prod \varphi_i^{\nu_i} \cdot \prod p_i^{\nu_i} \cdot \prod \left( f_i^o \right)^{-\nu_i}. \quad \text{(C.12)}$$

The standard fugacity $f_i^o$ of an ideal gas at IUPAC SATP amounts to 1 bar. For ideal gases, furthermore, $\varphi_i$, per definition, is unity [392].

Alternatively, the equilibrium constants are often approximated by an empirical function of temperature. For CO methanation (*cf.* Reaction 2.I) and the water-gas shift reaction (*cf.* Reaction 2.III), they are given in Eqs. C.13 and C.14, respectively [279]. The equilibrium constant for $CO_2$ methanation (*cf.* Reaction 2.II) then can be calculated according to Eq. C.15.

$$K_{eq,COmet} = 810^{-1} \cdot \left( \frac{T}{K} \right)^{-3.3} \cdot \exp \left( \frac{202.3\,\text{kJ mol}^{-1}}{R \cdot T} \right) \quad \text{(C.13)}$$

$$K_{eq,WGS} = 9.01 \cdot 10^{-6} \cdot \left( \frac{T}{K} \right)^{0.968} \cdot \exp \left( \frac{43.6\,\text{kJ mol}^{-1}}{R \cdot T} \right) \quad \text{(C.14)}$$

$$K_{eq,CO_2met} = K_{eq,COmet} \cdot \left( K_{eq,WGS} \right)^{-1} \quad \text{(C.15)}$$

# D Bibliography


[1] GISTEMP Team: GISS Surface Temperature Analysis (GISTEMP), version 4. NASA Goddard Institute for Space Studies. Dataset accessed 2020-05-31 at data.giss.nasa.gov/gistemp/, **2020**.

[2] N. J. L. Lenssen, G. A. Schmidt, J. E. Hansen, M. J. Menne, A. Persin, R. Ruedy, D. Zyss, "Improvements in the GISTEMP Uncertainty Model", *Journal of Geophysical Research: Atmospheres* **2019**, *124*, 6307–6326, DOI 10.1029/2018jd029522.

[3] R. Gehrels, "Chapter 18 - Rising Sea Levels as an Indicator of Global Change" in *Climate Change*, (Ed.: T. M. Letcher), Elsevier, Amsterdam, NL, **2009**, pp. 325–336, DOI 10.1016/B978-0-444-53301-2.00018-X.

[4] C. Turley, "Chapter 2 - Ocean Acidification" in *Managing Ocean Environments in a Changing Climate*, (Eds.: K. J. Noone, U. R. Sumaila, R. J. Diaz), Elsevier, Burlington, MA, **2013**, pp. 15–44, DOI 10.1016/B978-0-12-407668-6.00002-1.

[5] A. J. Richardson, C. J. Brown, K. Brander, J. F. Bruno, L. Buckley, M. T. Burrows, C. M. Duarte, B. S. Halpern, O. Hoegh-Guldberg, J. Holding, C. V. Kappel, W. Kiessling, P. J. Moore, M. I. O'Connor, J. M. Pandolfi, C. Parmesan, D. S. Schoeman, F. Schwing, W. J. Sydeman, E. S. Poloczanska, "Climate change and marine life", *Biology Letters* **2012**, *8*, 907–909, DOI 10.1098/rsbl.2012.0530.

[6] E. S. Poloczanska, C. J. Brown, W. J. Sydeman, W. Kiessling, D. S. Schoeman, P. J. Moore, K. Brander, J. F. Bruno, L. B. Buckley, M. T. Burrows, C. M. Duarte, B. S. Halpern, J. Holding, C. V. Kappel, M. I. O'Connor, J. M. Pandolfi, C. Parmesan, F. Schwing, S. A. Thompson, A. J. Richardson, "Global imprint of climate change on marine life", *Nature Climate Change* **2013**, *3*, 919–925, DOI 10.1038/nclimate1958.

[7] Z. Şen, "Climate Change Impact on Floods" in *Flood Modeling, Prediction and Mitigation*, Springer International Publishing, Cham, CH, **2018**, pp. 337–379, DOI 10.1007/978-3-319-52356-9_8.

[8] A. Jentsch, C. Beierkuhnlein, "Research frontiers in climate change: Effects of extreme meteorological events on ecosystems", *Comptes Rendus Geoscience* **2008**, *340*, 621–628, DOI 10.1016/j.crte.2008.07.002.

[9] R. P. Core Writing Team, L. Meyer, Eds., Intergovernmental Panel on Climate Change (IPCC), "Climate Change 2014: Synthesis Report". Contribution of Working Groups I, II and III to the Fifth Assessment Report of the Intergovernmental Panel on Climate Change, IPCC, Geneva, CH, **2014**.

[10] European Commission, "A Clean Planet for all – A European strategic long-term vision for a prosperous, modern, competitive and climate neutral economy", COM (2018) 773, **2018**.

[11] European Commission, "United in delivering the Energy Union and Climate Action – Setting the foundations for a successful clean energy transition", COM (2019) 285, **2019**.

[12] Bundesministerium für Umwelt, Naturschutz und nukleare Sicherheit (BMU), "Klimaschutzplan 2050 – Klimaschutzpolitische Grundsätze und Ziele der Bundesregierung", 10029, **2019**.

[13] M. S. Guney, Y. Tepe, “Classification and assessment of energy storage systems”, *Renewable and Sustainable Energy Reviews* **2017**, *75*, 1187–1197, DOI 10.1016/j.rser.2016.11.102.

[14] Frontier Economics, "The Importance of the Gas Infrastructure for Germany’s Energy Transition – A model based analysis", **2018**.

[15] M. Sterner, "Bioenergy and renewable power methane in integrated 100 % renewable energy systems", PhD Thesis, Kassel University, Kassel, DE, **2009**.

[16] J. G. Speight, “5 - Recovery, storage, and transportation” in *Natural Gas (Second Edition)*, (Ed.: J. G. Speight), Gulf Professional Publishing, Boston, MA, **2019**, pp. 149–186, DOI 10.1016/B978-0-12-809570-6.00005-9.

[17] M. Götz, J. Lefebvre, F. Mörs, A. McDaniel Koch, F. Graf, S. Bajohr, R. Reimert, T. Kolb, “Renewable Power-to-Gas: A technological and economic review”, *Renewable Energy* **2016**, *85*, 1371–1390, DOI 10.1016/j.renene.2015.07.066.

[18] F. Ausfelder et al., “Energiespeicherung als Element einer sicheren Energieversorgung”, *Chemie Ingenieur Technik* **2015**, *87*, 17–89, DOI 10.1002/cite.201400183.

[19] J. V. Veselovskaya, P. D. Parunin, O. V. Netskina, L. S. Kibis, A. I. Lysikov, A. G. Okunev, “Catalytic methanation of carbon dioxide captured from ambient air”, *Energy* **2018**, *159*, 766–773, DOI 10.1016/j.energy.2018.06.180.

[20] D. Krekel, R. C. Samsun, R. Peters, D. Stolten, “The separation of $CO_2$ from ambient air – A techno-economic assessment”, *Applied Energy* **2018**, *218*, 361–381, DOI 10.1016/j.apenergy.2018.02.144.

[21] K. Z. House, A. C. Baclig, M. Ranjan, E. A. van Nierop, J. Wilcox, H. J. Herzog, "Economic and energetic analysis of capturing $CO_2$ from ambient air", *Proceedings of the National Academy of Sciences* **2011**, *108*, 20428–20433, DOI 10.1073/pnas.1012253108.

[22] S. Heyne, M. Seemann, T. J. Schildhauer, "Coal and Biomass Gasification for SNG Production" in *Synthetic Natural Gas from Coal, Dry Biomass, and Power-to-Gas Applications*, John Wiley & Sons, Ltd, Hoboken, NJ, **2016**, pp. 5–40, DOI 10.1002/9781119191339.ch2.

[23] C. R. Vitasari, M. Jurascik, K. J. Ptasinski, "Exergy analysis of biomass-to-synthetic natural gas (SNG) process via indirect gasification of various biomass feedstock", *Energy* **2011**, *36*, 3825–3837, DOI 10.1016/j.energy.2010.09.026.

[24] F. Koschany, D. Schlereth, O. Hinrichsen, "On the kinetics of the methanation of carbon dioxide on coprecipitated $NiAl(O)_{(x)}$", *Applied Catalysis B: Environmental* **2016**, *181*, 504–516, DOI 10.1016/j.apcatb.2015.07.026.

[25] P. Sabatier, J. Senderens, "Direct hydrogenation of oxides of carbon in presence of various finely divided metals", *Comptes rendus de l'Académie des sciences* **1902**, *134*, 689–691.

[26] L. Guo, J. Sun, Q. Ge, N. Tsubaki, "Recent advances in direct catalytic hydrogenation of carbon dioxide to valuable $C_{2+}$ hydrocarbons", *Journal of Materials Chemistry A* **2018**, *6*, 23244–23262, DOI 10.1039/C8TA05377D.

[27] J. J. Gao, Y. L. Wang, Y. Ping, D. C. Hu, G. W. Xu, F. N. Gu, F. B. Su, "A thermodynamic analysis of methanation reactions of carbon oxides for the production of synthetic natural gas", *RSC Advances* **2012**, *2*, 2358–2368, DOI 10.1039/c2ra00632d.

[28] D. C. Gardner, C. H. Bartholomew, "Kinetics of carbon deposition during methanation of carbon monoxide", *Industrial & Engineering Chemistry Product Research and Development* **1981**, *20*, 80–87, DOI 10.1021/i300001a007.

[29] F. Fischer, H. Tropsch, "Über die direkte Synthese von Erdöl-Kohlenwasserstoffen bei gewöhnlichem Druck. (Erste Mitteilung)", *Berichte der deutschen chemischen Gesellschaft (A and B Series)* **1926**, *59*, 830–831, DOI 10.1002/cber.19260590442.

[30] F. Fischer, H. Tropsch, "Über die direkte Synthese von Erdöl-Kohlenwasserstoffen bei gewöhnlichem Druck. (Zweite Mitteilung.)", *Berichte der deutschen chemischen Gesellschaft (A and B Series)* **1926**, *59*, 832–836, DOI 10.1002/cber.19260590443.

[31] J. C. J. Bart, R. P. A. Sneeden, "Copper-zinc oxide-alumina methanol catalysts revisited", *Catalysis Today* **1987**, *2*, 1–124, DOI 10.1016/0920-5861(87)80001-9.

[32] R.-P. Ye, J. Ding, W. Gong, M. D. Argyle, Q. Zhong, Y. Wang, C. K. Russell, Z. Xu, A. G. Russell, Q. Li, M. Fan, Y.-G. Yao, "$CO_2$ hydrogenation to high-value products via heterogeneous catalysis", *Nature Communications* **2019**, *10*, 5698, DOI 10.1038/s41467-019-13638-9.

[33] N. Abdoulmoumine, S. Adhikari, A. Kulkarni, S. Chattanathan, “A review on biomass gasification syngas cleanup”, *Applied Energy* **2015**, *155*, 294–307, DOI 10.1016/j.apenergy.2015.05.095.

[34] S. Faramawy, T. Zaki, A. A. E. Sakr, “Natural gas origin, composition, and processing: A review”, *Journal of Natural Gas Science and Engineering* **2016**, *34*, 34–54, DOI 10.1016/j.jngse.2016.06.030.

[35] J. G. Speight, *Natural Gas: A Basic Handbook*, Gulf Professional Publishing, San Diego, CA, **2018**.

[36] Deutsches Institut für Normung e.V., DIN EN 16723-1, "Erdgas und Biomethan zur Verwendung im Transportwesen und Biomethan zur Einspeisung ins Erdgasnetz – Teil 1: Festlegungen für Biomethan zur Einspeisung ins Erdgasnetz", **2017**.

[37] Deutscher Bundestag, Wissenschaftliche Dienste, "Grenzwerte für Wasserstoff ($H_2$) in der Erdgasinfrastruktur", Sachstand WD 8 - 3000 - 066/1, **2019**.

[38] Deutsches Institut für Normung e.V., DIN EN 16723-2, "Erdgas und Biomethan zur Verwendung im Transportwesen und Biomethan zur Einspeisung ins Erdgasnetz – Teil 2: Festlegungen für Kraftstoffe für Kraftfahrzeuge", **2017**.

[39] N. Söhngen, "Het onstaan en verdwijnen van waterstof en methaan onder den invloed van organisch leven", PhD Thesis, TU Delft, Delft, NL, **1906**.

[40] C. H. Bartholomew, “Mechanisms of catalyst deactivation”, *Applied Catalysis A: General* **2001**, *212*, 17–60, DOI 10.1016/S0926-860x(00)00843-7.

[41] A. Vita, C. Italiano, L. Pino, P. Frontera, M. Ferraro, V. Antonucci, “Activity and stability of powder and monolith-coated Ni/GDC catalysts for $CO_2$ methanation”, *Applied Catalysis B: Environmental* **2018**, *226*, 384–395, DOI 10.1016/j.apcatb.2017.12.078.

[42] D. Schlereth, P. J. Donaubauer, O. Hinrichsen, “Metallic Honeycombs as Catalyst Supports for Methanation of Carbon Dioxide”, *Chemical Engineering & Technology* **2015**, *38*, 1845–1852, DOI 10.1002/ceat.201400717.

[43] C. Fukuhara, K. Hayakawa, Y. Suzuki, W. Kawasaki, R. Watanabe, “A novel nickel-based structured catalyst for $CO_2$ methanation: A honeycomb-type Ni/$CeO_2$ catalyst to transform greenhouse gas into useful resources”, *Applied Catalysis A: General* **2017**, *532*, 12–18, DOI 10.1016/j.apcata.2016.11.036.

[44] S. Neuberg, H. Pennemann, V. Shanmugam, R. Thiermann, R. Zapf, W. Gac, M. Greluk, W. Zawadzki, G. Kolb, “$CO_2$ Methanation in Microstructured Reactors – Catalyst Development and Process Design”, *Chemical Engineering & Technology* **2019**, *42*, 2076–2084, DOI 10.1002/ceat.201900132.

[45] M.-M. Weiss, S. Schwinghammer, “Lurgi advanced Mk Plus coal gasifier technology applied for SNG production”, *Gasification Technologies Conference* **2012**.

[46] M. Sudiro, A. Bertucco, “Synthetic Natural Gas (SNG) from Coal and Biomass: a Survey of Existing Process Technologies, Open Issues and Perspectives” in *Natural Gas*, (Ed.: P. Potocnik), IntechOpen, Rijeka, HR, **2010**, Chapter 5, pp. 105–126, DOI 10.5772/9835.

[47] J. Kopyscinski, T. J. Schildhauer, S. M. A. Biollaz, “Production of synthetic natural gas (SNG) from coal and dry biomass - A technology review from 1950 to 2009”, *Fuel* **2010**, *89*, 1763–1783, DOI 10.1016/j.fuel.2010.01.027.

[48] A. L. Hausberger, G. A. Hammons, "Methanation process for the production of an alternate fuel for natural gas", U. S. Patent 4,005,996, **1977**.

[49] M. Lehner, R. Tichler, H. Steinmüller, M. Koppe, *Power-to-Gas: Technology and Business Models*, Springer International Publishing, Cham, CH, **2014**, DOI 10.1007/978-3-319-03995-4.

[50] S. Saha, K. P. Prasad, P. D. Chavan, G. Sahu, N. Kumari, S. Datta, “Methanation technology: Conversion of syngas into substitute natural gas (SNG)” in *NexGen Technologies for Mining and Fuel Industries (Volume I and II)*, *Vol. 1*, (Eds.: P. K. Singh, V. Singh, A. Singh, D. Kumbhakar, M. Roy), Allied Publishers Pvt. Ltd., New Delhi, IN, **2017**.

[51] A. Borgschulte, N. Gallandat, B. Probst, R. Suter, E. Callini, D. Ferri, Y. Arroyo, R. Erni, H. Geerlings, A. Züttel, “Sorption enhanced $CO_2$ methanation”, *Physical Chemistry Chemical Physics* **2013**, *15*, 9620–9625, DOI 10.1039/C3CP51408K.

[52] S. Walspurger, G. D. Elzinga, J. W. Dijkstra, M. Sarić, W. G. Haije, “Sorption enhanced methanation for substitute natural gas production: Experimental results and thermodynamic considerations”, *Chemical Engineering Journal* **2014**, *242*, 379–386, DOI 10.1016/j.cej.2013.12.045.

[53] G. D. Weatherbee, C. H. Bartholomew, “Hydrogenation of $CO_2$ on group VIII metals: IV. Specific activities and selectivities of silica-supported Co, Fe, and Ru”, *Journal of Catalysis* **1984**, *87*, 352–362, DOI 10.1016/0021-9517(84)90196-9.

[54] S. Scirè, C. Crisafulli, R. Maggiore, S. Minicò, S. Galvagno, “Influence of the support on $CO_2$ methanation over Ru catalysts: an FT-IR study”, *Catalysis Letters* **1998**, *51*, 41–45, DOI 10.1023/A:1019028816154.

[55] G. Garbarino, D. Bellotti, E. Finocchio, L. Magistri, G. Busca, “Methanation of carbon dioxide on $Ru/Al_2O_3$: Catalytic activity and infrared study”, *Catalysis Today* **2016**, *277*, 21–28, DOI 10.1016/j.cattod.2015.12.010.

[56] S.-T. Zhang, H. Yan, M. Wei, D. G. Evans, X. Duan, “Hydrogenation mechanism of carbon dioxide and carbon monoxide on Ru(0001) surface: a density functional theory study”, *RSC Advances* **2014**, *4*, 30241–30249, DOI 10.1039/C4RA01655F.

[57] L. Falbo, C. G. Visconti, L. Lietti, J. Szanyi, "The effect of CO on $CO_2$ methanation over $Ru/Al_2O_3$ catalysts: a combined steady-state reactivity and transient DRIFT spectroscopy study", *Applied Catalysis B: Environmental* **2019**, *256*, 117791, DOI 10.1016/j.apcatb.2019.117791.

[58] F. Solymosi, A. Erdöhelyi, M. Kocsis, "Methanation of $CO_2$ on supported Ru catalysts", *Journal of the Chemical Society Faraday Transactions 1: Physical Chemistry in Condensed Phases* **1981**, *77*, 1003–1012, DOI 10.1039/F19817701003.

[59] Z. Kowalczyk, K. Stołecki, W. Raróg-Pilecka, E. Miśkiewicz, E. Wilczkowska, Z. Karpiński, "Supported ruthenium catalysts for selective methanation of carbon oxides at very low $CO_x/H_2$ ratios", *Applied Catalysis A: General* **2008**, *342*, 35–39, DOI 10.1016/j.apcata.2007.12.040.

[60] F. Solymosi, A. Erdohelyi, T. Bansagi, "Methanation of $CO_2$ on Supported Rhodium Catalyst", *Journal of Catalysis* **1981**, *68*, 371–382, DOI 10.1016/0021-9517(81)90106-8.

[61] F. Solymosi, I. Tombácz, J. Koszta, "Effects of variation of electric properties of $TiO_2$ support on hydrogenation of CO and $CO_2$ over Rh catalysts", *Journal of Catalysis* **1985**, *95*, 578–586, DOI 10.1016/0021-9517(85)90136-8.

[62] M. Jacquemin, A. Beuls, P. Ruiz, "Catalytic production of methane from $CO_2$ and $H_2$ at low temperature: Insight on the reaction mechanism", *Catalysis Today* **2010**, *157*, 462–466, DOI 10.1016/j.cattod.2010.06.016.

[63] A. Karelovic, P. Ruiz, "Mechanistic study of low temperature $CO_2$ methanation over $Rh/TiO_2$ catalysts", *Journal of Catalysis* **2013**, *301*, 141–153, DOI 10.1016/j.jcat.2013.02.009.

[64] A. Karelovic, P. Ruiz, "$CO_2$ hydrogenation at low temperature over $Rh/\gamma$-$Al_2O_3$ catalysts: Effect of the metal particle size on catalytic performances and reaction mechanism", *Applied Catalysis B: Environmental* **2012**, *113-114*, 237–249, DOI 10.1016/j.apcatb.2011.11.043.

[65] A. Beuls, C. Swalus, M. Jacquemin, G. Heyen, A. Karelovic, P. Ruiz, "Methanation of $CO_2$: Further insight into the mechanism over $Rh/\gamma$-$Al_2O_3$ catalyst", *Applied Catalysis B: Environmental* **2012**, *113-114*, 2–10, DOI 10.1016/j.apcatb.2011.02.033.

[66] S. Tada, T. Shimizu, H. Kameyama, T. Haneda, R. Kikuchi, "$Ni/CeO_2$ catalysts with high $CO_2$ methanation activity and high $CH_4$ selectivity at low temperatures", *International Journal of Hydrogen Energy* **2012**, *37*, 5527–5531, DOI 10.1016/j.ijhydene.2011.12.122.

[67] H. L. Song, J. Yang, J. Zhao, L. J. Chou, "Methanation of Carbon Dioxide over a Highly Dispersed $Ni/La_2O_3$ Catalyst", *Chinese Journal of Catalysis* **2010**, *31*, 21–23, DOI 10.3724/Sp.J.1088.2010.90956.

[68] A. Erhan Aksoylu, Z. İlsen Önsan, "Hydrogenation of carbon oxides using coprecipitated and impregnated Ni/$Al_2O_3$ catalysts", *Applied Catalysis A: General* **1997**, *164*, 1–11, DOI 10.1016/S0926-860X(97)00151-8.

[69] H. Muroyama, Y. Tsuda, T. Asakoshi, H. Masitah, T. Okanishi, T. Matsui, K. Eguchi, "Carbon dioxide methanation over Ni catalysts supported on various metal oxides", *Journal of Catalysis* **2016**, *343*, 178–184, DOI 10.1016/j.jcat.2016.07.018.

[70] A. E. Aksoylu, A. N. Akin, Z. İ. Önsan, D. L. Trimm, "Structure/activity relationships in coprecipitated nickel-alumina catalysts using $CO_2$ adsorption and methanation", *Applied Catalysis A: General* **1996**, *145*, 185–193, DOI 10.1016/0926-860X(96)00143-3.

[71] S. Rahmani, M. Rezaei, F. Meshkani, "Preparation of promoted nickel catalysts supported on mesoporous nanocrystalline gamma alumina for carbon dioxide methanation reaction", *Journal of Industrial and Engineering Chemistry* **2014**, *20*, 4176–4182, DOI 10.1016/j.jiec.2014.01.017.

[72] J. Kopyscinski, T. J. Schildhauer, S. M. A. Biollaz, "Methanation in a fluidized bed reactor with high initial CO partial pressure : Part II – Modeling and sensitivity study", *Chemical Engineering Science* **2011**, *66*, 1612–1621, DOI 10.1016/j.ces.2010.12.029.

[73] J. Kopyscinski, T. J. Schildhauer, F. Vogel, S. M. A. Biollaz, A. Wokaun, "Applying spatially resolved concentration and temperature measurements in a catalytic plate reactor for the kinetic study of CO methanation", *Journal of Catalysis* **2010**, *271*, 262–279, DOI 10.1016/j.jcat.2010.02.008.

[74] J. Zhang, N. Fatah, S. Capela, Y. Kara, O. Guerrini, A. Y. Khodakov, "Kinetic investigation of carbon monoxide hydrogenation under realistic conditions of methanation of biomass derived syngas", *Fuel* **2013**, *111*, 845–854, DOI 10.1016/j.fuel.2013.04.057.

[75] W. Chen, R. Pestman, B. Zijlstra, I. A. W. Filot, E. J. M. Hensen, "Mechanism of cobalt-catalyzed CO hydrogenation: 1. Methanation", *ACS Catalysis* **2017**, *7*, 8050–8060, DOI 10.1021/acscatal.7b02757.

[76] T. A. Le, M. S. Kim, S. H. Lee, E. D. Park, "CO and $CO_2$ Methanation Over Supported Cobalt Catalysts", *Topics in Catalysis* **2017**, *60*, 714–720, DOI 10.1007/s11244-017-0788-y.

[77] M. A. Vannice, "The catalytic synthesis of hydrocarbons from $H_2$/CO mixtures over the group VIII metals", *Journal of Catalysis* **1975**, *37*, 449–461, DOI 10.1016/0021-9517(75)90181-5.

[78] F. S. Karn, J. F. Shultz, R. B. Anderson, "Hydrogenation of Carbon Monoxide and Carbon Dioxide on Supported Ruthenium Catalysts at Moderate Pressures", *I&EC Product Research and Development* **1965**, *4*, 265–269, DOI 10.1021/i360016a014.

[79] P. J. Lunde, F. L. Kester, “Carbon Dioxide Methanation on a Ruthenium Catalyst”, *Industrial & Engineering Chemistry Process Design and Development* **1974**, *13*, 27–33, DOI 10.1021/i260049a005.

[80] S. Eckle, H.-G. Anfang, R. J. Behm, “Reaction Intermediates and Side Products in the Methanation of CO and $CO_2$ over Supported Ru Catalysts in $H_2$-Rich Reformate Gases”, *The Journal of Physical Chemistry C* **2011**, *115*, 1361–1367, DOI 10.1021/jp108106t.

[81] A. Porta, L. Falbo, C. G. Visconti, L. Lietti, C. Bassano, P. Deiana, “Synthesis of Ru-based catalysts for $CO_2$ methanation and experimental assessment of intraporous transport limitations”, *Catalysis Today* **2020**, *343*, 38–47, DOI 10.1016/j.cattod.2019.01.042.

[82] É. Novák, K. Fodor, T. Szailer, A. Oszkó, A. Erdöhelyi, “$CO_2$ Hydrogenation on Rh/$TiO_2$ Previously Reduced at Different Temperatures”, *Topics in Catalysis* **2002**, *20*, 107–117, DOI 10.1023/A:1016359601399.

[83] J. C. Matsubu, V. N. Yang, P. Christopher, “Isolated Metal Active Site Concentration and Stability Control Catalytic $CO_2$ Reduction Selectivity”, *Journal of the American Chemical Society* **2015**, *137*, 3076–3084, DOI 10.1021/ja5128133.

[84] S. Ma, W. Song, B. Liu, H. Zheng, J. Deng, W. Zhong, J. Liu, X.-Q. Gong, Z. Zhao, “Elucidation of the high $CO_2$ reduction selectivity of isolated Rh supported on $TiO_2$: a DFT study”, *Catalysis Science & Technology* **2016**, *6*, 6128–6136, DOI 10.1039/C5CY02158H.

[85] U.S. Geological Survey, "Metal prices in the United States through 2010: Scientific Investigations report 2012-5188", **2013**.

[86] G. A. Mills, F. W. Steffgen, “Catalytic Methanation”, *Catalysis Reviews* **1974**, *8*, 159–210, DOI 10.1080/01614947408071860.

[87] C. K. Vance, C. H. Bartholomew, “Hydrogenation of Carbon-Dioxide on Group-VIII Metals: III, Effects of Support on Activity Selectivity and Adsorption Properties of Nickel”, *Applied Catalysis* **1983**, *7*, 169–177, DOI 10.1016/0166-9834(83)80005-0.

[88] S. Rönsch, J. Köchermann, J. Schneider, S. Matthischke, “Global Reaction Kinetics of CO and $CO_2$ Methanation for Dynamic Process Modeling”, *Chemical Engineering & Technology* **2016**, *39*, 208–218, DOI 10.1002/ceat.201500327.

[89] A. E. Aksoylu, Z. Misirli, Z. İ. Önsan, “Interaction between nickel and molybdenum in Ni-Mo/$Al_2O_3$ catalysts: I - $CO_2$ methanation and SEM-TEM studies”, *Applied Catalysis A: General* **1998**, *168*, 385–397, DOI 10.1016/S0926-860x(97)00369-4.

[90] R. Yadav, R. G. Rinker, “Steady-state methanation kinetics over a Ni/$Al_2O_3$ catalyst”, *The Canadian Journal of Chemical Engineering* **1993**, *71*, 202–208, DOI 10.1002/cjce.5450710206.

[91] K. O. Xavier, R. Sreekala, K. K. A. Rashid, K. K. M. Yusuff, B. Sen, "Doping effects of cerium oxide on Ni/$Al_2O_3$ catalysts for methanation", *Catalysis Today* **1999**, *49*, 17–21, DOI 10.1016/S0920-5861(98)00403-9.

[92] Z. X. Cheng, X. G. Zhao, J. L. Li, Q. M. Zhu, "Role of support in $CO_2$ reforming of $CH_4$ over a Ni/$\gamma$-$Al_2O_3$ catalyst", *Applied Catalysis A: General* **2001**, *205*, 31–36, DOI 10.1016/S0926-860X(00)00560-3.

[93] Y. Pan, C. Liu, Q. Ge, "Effect of surface hydroxyls on selective $CO_2$ hydrogenation over $Ni_4$/$\gamma$-$Al_2O_3$: A density functional theory study", *Journal of Catalysis* **2010**, *272*, 227–234, DOI 10.1016/j.jcat.2010.04.003.

[94] A. M. Zhao, W. Y. Ying, H. T. Zhang, H. F. Ma, D. Y. Fang, "Ni/$Al_2O_3$ catalysts for syngas methanation: Effect of Mn promoter", *Journal of Natural Gas Chemistry* **2012**, *21*, 170–177, DOI 10.1016/S1003-9953(11)60350-2.

[95] J. Li, L. Zhou, P. C. Li, Q. S. Zhu, J. J. Gao, F. N. Gu, F. B. Su, "Enhanced fluidized bed methanation over a Ni/$Al_2O_3$ catalyst for production of synthetic natural gas", *Chemical Engineering Journal* **2013**, *219*, 183–189, DOI 10.1016/j.cej.2013.01.005.

[96] G. Garbarino, P. Riani, L. Magistri, G. Busca, "A study of the methanation of carbon dioxide on Ni/$Al_2O_3$ catalysts at atmospheric pressure", *International Journal of Hydrogen Energy* **2014**, *39*, 11557–11565, DOI 10.1016/j.ijhydene.2014.05.111.

[97] Q. Liu, F. N. Gu, X. P. Lu, Y. J. Liu, H. F. Li, Z. Y. Zhong, G. W. Xu, F. B. Su, "Enhanced catalytic performances of Ni/$Al_2O_3$ catalyst *via* addition of $V_2O_3$ for CO methanation", *Applied Catalysis A: General* **2014**, *488*, 37–47, DOI 10.1016/j.apcata.2014.09.028.

[98] B. Legras, V. V. Ordomsky, C. Dujardin, M. Virginie, A. Y. Khodakov, "Impact and Detailed Action of Sulfur in Syngas on Methane Synthesis on Ni/$\gamma$-$Al_2O_3$ Catalyst", *ACS Catalysis* **2014**, *4*, 2785–2791, DOI 10.1021/cs500436f.

[99] A. Zhao, W. Ying, H. Zhang, H. Ma, D. Fang, "La and Mn Promotion of Ni/$Al_2O_3$ Catalysts for Syngas Methanation", *Energy Sources Part A: Recovery Utilization and Environmental Effects* **2014**, *36*, 1049–1056, DOI 10.1080/15567036.2012.666621.

[100] W. Zhen, B. Li, G. Lu, J. Ma, "Enhancing catalytic activity and stability for $CO_2$ methanation on Ni-Ru/$\gamma$-$Al_2O_3$ *via* modulating impregnation sequence and controlling surface active species", *RSC Advances* **2014**, *4*, 16472–16479, DOI 10.1039/C3RA47982J.

[101] Y. Wang, Y. Su, M. Zhu, L. Kang, "Mechanism of CO methanation on the $Ni_4$/$\gamma$-$Al_2O_3$ and $Ni_3Fe$/$\gamma$-$Al_2O_3$ catalysts", *International Journal of Hydrogen Energy* **2015**, *40*, 8864–8876, DOI 10.1016/j.ijhydene.2015.05.002.

[102] J. Zarfl, D. Ferri, T. J. Schildhauer, J. Wambach, A. Wokaun, "DRIFTS study of a commercial Ni/$\gamma$-$Al_2O_3$ CO methanation catalyst", *Applied Catalysis A: General* **2015**, *495*, 104–114, DOI 10.1016/j.apcata.2015.02.005.

[103] J. Yang Lim, J. McGregor, A. J. Sederman, J. S. Dennis, "Kinetic studies of $CO_2$ methanation over a Ni/$\gamma$-$Al_2O_3$ catalyst using a batch reactor", *Chemical Engineering Science* **2016**, *141*, 28–45, DOI 10.1016/j.ces.2015.10.026.

[104] K. Zhao, Z. Li, L. Bian, "$CO_2$ methanation and co-methanation of CO and $CO_2$ over Mn-promoted Ni/$Al_2O_3$ catalysts", *Frontiers of Chemical Science and Engineering* **2016**, *10*, 273–280, DOI 10.1007/s11705-016-1563-5.

[105] J. Y. Lim, J. McGregor, A. J. Sederman, J. S. Dennis, "Kinetic studies of the methanation of CO over a Ni/$\gamma$-$Al_2O_3$ catalyst using a batch reactor", *Chemical Engineering Science* **2016**, *146*, 316–336, DOI 10.1016/j.ces.2016.02.001.

[106] D. Lorito, H. Li, A. Travert, F. Maugé, F. C. Meunier, Y. Schuurman, C. Mirodatos, "Understanding deactivation processes during bio-syngas methanation: DRIFTS and SSITKA experiments and kinetic modeling over Ni/$Al_2O_3$ catalysts", *Catalysis Today* **2018**, *299*, 172–182, DOI 10.1016/j.cattod.2017.06.041.

[107] G. D. Weatherbee, C. H. Bartholomew, "Hydrogenation of $CO_2$ on group VIII metals: I. Specific activity of Ni/$SiO_2$", *Journal of Catalysis* **1981**, *68*, 67–76, DOI 10.1016/0021-9517(81)90040-3.

[108] T. Ishihara, K. Eguchi, H. Arai, "Hydrogenation of carbon monoxide over $SiO_2$-supported Fe-Co, Co-Ni and Ni-Fe bimetallic catalysts", *Applied Catalysis* **1987**, *30*, 225–238, DOI 10.1016/S0166-9834(00)84115-9.

[109] H. Lu, X. Yang, G. Gao, J. Wang, C. Han, X. Liang, C. Li, Y. Li, W. Zhang, X. Chen, "Metal (Fe, Co, Ce or La) doped nickel catalyst supported on $ZrO_2$ modified mesoporous clays for CO and $CO_2$ methanation", *Fuel* **2016**, *183*, 335–344, DOI 10.1016/j.fuel.2016.06.084.

[110] N. Perkas, G. Amirian, Z. Zhong, J. Teo, Y. Gofer, A. Gedanken, "Methanation of Carbon Dioxide on Ni Catalysts on Mesoporous $ZrO_2$ Doped with Rare Earth Oxides", *Catalysis Letters* **2009**, *130*, 455–462, DOI 10.1007/s10562-009-9952-8.

[111] J. Ren, X. Qin, J.-Z. Yang, Z.-F. Qin, H.-L. Guo, J.-Y. Lin, Z. Li, "Methanation of carbon dioxide over Ni–M/$ZrO_2$ (M = Fe, Co, Cu) catalysts: Effect of addition of a second metal", *Fuel Processing Technology* **2015**, *137*, 204–211, DOI 10.1016/j.fuproc.2015.04.022.

[112] M. Yamasaki, H. Habazaki, T. Yoshida, E. Akiyama, A. Kawashima, K. Asami, K. Hashimoto, M. Komori, K. Shimamura, "Compositional dependence of the $CO_2$ methanation activity of Ni/$ZrO_2$ catalysts prepared from amorphous NiZr alloy precursors", *Applied Catalysis A: General* **1997**, *163*, 187–197, DOI 10.1016/S0926-860X(97)00142-7.

[113] S. M. Lee, Y. H. Lee, D. H. Moon, J. Y. Ahn, D. D. Nguyen, S. W. Chang, S. S. Kim, "Reaction Mechanism and Catalytic Impact of Ni/$CeO_{2-x}$ Catalyst for Low-Temperature $CO_2$ Methanation", *Industrial & Engineering Chemistry Research* **2019**, *58*, 8656–8662, DOI 10.1021/acs.iecr.9b00983.

[114] J. Liu, C. Li, F. Wang, S. He, H. Chen, Y. Zhao, M. Wei, D. G. Evans, X. Duan, "Enhanced low-temperature activity of $CO_2$ methanation over highly-dispersed Ni/$TiO_2$ catalyst", *Catalysis Science & Technology* **2013**, *3*, 2627–2633, DOI 10.1039/C3CY00355H.

[115] J. L. Falconer, A. E. Zagli, "Adsorption and Methanation of Carbon-Dioxide on a Nickel-Silica Catalyst", *Journal of Catalysis* **1980**, *62*, 280–285, DOI 10.1016/0021-9517(80)90456-X.

[116] X. Guo, A. Traitangwong, M. Hu, C. Zuo, V. Meeyoo, Z. Peng, C. Li, "Carbon Dioxide Methanation over Nickel-Based Catalysts Supported on Various Mesoporous Material", *Energy & Fuels* **2018**, *32*, 3681–3689, DOI 10.1021/acs.energyfuels.7b03826.

[117] M. A. A. Aziz, A. A. Jalil, S. Triwahyono, R. R. Mukti, Y. H. Taufiq-Yap, M. R. Sazegar, "Highly active Ni-promoted mesostructured silica nanoparticles for $CO_2$ methanation", *Applied Catalysis B: Environmental* **2014**, *147*, 359–368, DOI 10.1016/j.apcatb.2013.09.015.

[118] M. A. A. Aziz, A. A. Jalil, S. Triwahyono, S. M. Sidik, "Methanation of carbon dioxide on metal-promoted mesostructured silica nanoparticles", *Applied Catalysis A: General* **2014**, *486*, 115–122, DOI 10.1016/j.apcata.2014.08.022.

[119] G. Du, S. Lim, Y. Yang, C. Wang, L. Pfefferle, G. L. Haller, "Methanation of carbon dioxide on Ni-incorporated MCM-41 catalysts: The influence of catalyst pretreatment and study of steady-state reaction", *Journal of Catalysis* **2007**, *249*, 370–379, DOI 10.1016/j.jcat.2007.03.029.

[120] C. Schüler, F. Betzenbichler, C. Drescher, O. Hinrichsen, "Optimization of the synthesis of Ni catalysts via chemical vapor deposition by response surface methodology", *Chemical Engineering Research and Design* **2018**, *132*, 303–312, DOI 10.1016/j.cherd.2018.01.015.

[121] X. Yan et al., "Nickel@Siloxene catalytic nanosheets for high-performance $CO_2$ methanation", *Nature Communications* **2019**, *10*, 2608, DOI 10.1038/s41467-019-10464-x.

[122] W. Gac, W. Zawadzki, G. Słowik, A. Sienkiewicz, A. Kierys, "Nickel catalysts supported on silica microspheres for $CO_2$ methanation", *Microporous and Mesoporous Materials* **2018**, *272*, 79–91, DOI 10.1016/j.micromeso.2018.06.022.

[123] G. Zhou, H. Liu, K. Cui, A. Jia, G. Hu, Z. Jiao, Y. Liu, X. Zhang, "Role of surface Ni and Ce species of Ni/$CeO_2$ catalyst in $CO_2$ methanation", *Applied Surface Science* **2016**, *383*, 248–252, DOI 10.1016/j.apsusc.2016.04.180.

[124] M. V. Konishcheva, D. I. Potemkin, S. D. Badmaev, P. V. Snytnikov, E. A. Paukshtis, V. A. Sobyanin, V. N. Parmon, "On the Mechanism of CO and $CO_2$ Methanation Over Ni/$CeO_2$ Catalysts", *Topics in Catalysis* **2016**, *59*, 1424–1430, DOI 10.1007/s11244-016-0650-7.

[125] B. Nematollahi, M. Rezaei, E. N. Lay, "Selective methanation of carbon monoxide in hydrogen rich stream over Ni/$CeO_2$ nanocatalysts", *Journal of Rare Earths* **2015**, *33*, 619–628, DOI 10.1016/S1002-0721(14)60462-2.

[126] Q. Pan, J. Peng, S. Wang, S. Wang, "In situ FTIR spectroscopic study of the $CO_2$ methanation mechanism on Ni/$Ce_{0.5}Zr_{0.5}O_2$", *Catalysis Science & Technology* **2014**, *4*, 502–509, DOI 10.1039/C3CY00868A.

[127] Q. Pan, J. Peng, T. Sun, D. Gao, S. Wang, S. Wang, "$CO_2$ methanation on Ni/$Ce_{0.5}Zr_{0.5}O_2$ catalysts for the production of synthetic natural gas", *Fuel Processing Technology* **2014**, *123*, 166–171, DOI 10.1016/j.fuproc.2014.01.004.

[128] Q. Pan, J. Peng, T. Sun, S. Wang, S. Wang, "Insight into the reaction route of $CO_2$ methanation: Promotion effect of medium basic sites", *Catalysis Communications* **2014**, *45*, 74–78, DOI 10.1016/j.catcom.2013.10.034.

[129] F. Ocampo, B. Louis, A. C. Roger, "Methanation of carbon dioxide over nickel-based $Ce_{0.72}Zr_{0.28}O_2$ mixed oxide catalysts prepared by sol-gel method", *Applied Catalysis A: General* **2009**, *369*, 90–96, DOI 10.1016/j.apcata.2009.09.005.

[130] F. Ocampo, B. Louis, L. Kiwi-Minsker, A.-C. Roger, "Effect of Ce/Zr composition and noble metal promotion on nickel based $Ce_xZr_{1-x}O_2$ catalysts for carbon dioxide methanation", *Applied Catalysis A: General* **2011**, *392*, 36–44, DOI 10.1016/j.apcata.2010.10.025.

[131] P. Fornasiero, R. Dimonte, G. R. Rao, J. Kaspar, S. Meriani, A. Trovarelli, M. Graziani, "Rh-Loaded $CeO_2$-$ZrO_2$ Solid-Solutions as Highly Efficient Oxygen Exchangers: Dependence of the Reduction Behavior and the Oxygen Storage Capacity on the Structural-Properties", *Journal of Catalysis* **1995**, *151*, 168–177, DOI 10.1006/jcat.1995.1019.

[132] S. Abate, C. Mebrahtu, E. Giglio, F. Deorsola, S. Bensaid, S. Perathoner, R. Pirone, G. Centi, "Catalytic Performance of $\gamma$-$Al_2O_3$–$ZrO_2$–$TiO_2$–$CeO_2$ Composite Oxide Supported Ni-Based Catalysts for $CO_2$ Methanation", *Industrial & Engineering Chemistry Research* **2016**, *55*, 4451–4460, DOI 10.1021/acs.iecr.6b00134.

[133] L. He, Q. Lin, Y. Liu, Y. Huang, "Unique catalysis of Ni-Al hydrotalcite derived catalyst in $CO_2$ methanation: cooperative effect between Ni nanoparticles and a basic support", *Journal of Energy Chemistry* **2014**, *23*, 587–592, DOI 10.1016/S2095-4956(14)60144-3.

[134] S. Ewald, M. Kolbeck, T. Kratky, M. Wolf, O. Hinrichsen, "On the deactivation of Ni-Al catalysts in $CO_2$ methanation", *Applied Catalysis A: General* **2019**, *570*, 376–386, DOI 10.1016/j.apcata.2018.10.033.

[135] S. Abate, K. Barbera, E. Giglio, F. Deorsola, S. Bensaid, S. Perathoner, R. Pirone, G. Centi, "Synthesis, Characterization, and Activity Pattern of Ni–Al Hydrotalcite Catalysts in $CO_2$ Methanation", *Industrial and Engineering Chemistry Research* **2016**, *55*, 8299–8308, DOI 10.1021/acs.iecr.6b01581.

[136] S. Abello, C. Berrueco, F. Gispert-Guirado, D. Montane, "Synthetic natural gas by direct $CO_2$ hydrogenation on activated takovites: effect of Ni/Al molar ratio", *Catalysis Science & Technology* **2016**, *6*, 2305–2317, DOI 10.1039/c5cy01200g.

[137] M. Gabrovska, R. Edreva-Kardjieva, D. Crişan, P. Tzvetkov, M. Shopska, I. Shtereva, "Ni–Al layered double hydroxides as catalyst precursors for $CO_2$ removal by methanation", *Reaction Kinetics Mechanisms and Catalysis* **2012**, *105*, 79–99, DOI 10.1007/s11144-011-0378-0.

[138] D. C. Puxley, I. J. Kitchener, C. Komodromos, N. D. Parkyns, "The Effect of Preparation Method upon the Structures, Stability and Metal/Support Interactions in Nickel/Alumina Catalysts" in *Studies in Surface Science and Catalysis*, *Vol. 16*, (Eds.: G. Poncelet, P. Grange, P. A. Jacobs), Elsevier, Amsterdam, NL, **1983**, pp. 237–271, DOI 10.1016/S0167-2991(09)60025-2.

[139] L. E. Alzamora, J. R. H. Ross, E. C. Kruissink, L. L. van Reijen, "Coprecipitated nickel–alumina catalysts for methanation at high temperature. Part 2.—Variation of total and metallic areas as a function of sample composition and method of pretreatment", *Journal of the Chemical Society Faraday Transactions 1: Physical Chemistry in Condensed Phases* **1981**, *77*, 665–681, DOI 10.1039/f19817700665.

[140] J. Zieliński, "Morphology of coprecipitated nickel/alumina catalysts with low alumina content", *Applied Catalysis A: General* **1993**, *94*, 107–115, DOI 10.1016/0926-860X(93)85001-6.

[141] S. Ewald, S. Standl, O. Hinrichsen, "Characterization of nickel catalysts with transient methods", *Applied Catalysis A: General* **2018**, *549*, 93–101, DOI 10.1016/j.apcata.2017.09.023.

[142] D. Beierlein, D. Häussermann, M. Pfeifer, T. Schwarz, K. Stöwe, Y. Traa, E. Klemm, "Is the $CO_2$ methanation on highly loaded Ni-$Al_2O_3$ catalysts really structure-sensitive?", *Applied Catalysis B: Environmental* **2019**, *247*, 200–219, DOI 10.1016/j.apcatb.2018.12.064.

[143] Y. Wu, J. Lin, G. Ma, Y. Xu, J. Zhang, C. Samart, M. Ding, "Ni nanocatalysts supported on mesoporous $Al_2O_3$–$CeO_2$ for $CO_2$ methanation at low temperature", *RSC Advances* **2020**, *10*, 2067–2072, DOI 10.1039/C9RA08967E.

[144] S. Hwang, J. Lee, U. G. Hong, J. C. Jung, D. J. Koh, H. Lim, C. Byun, I. K. Song, "Hydrogenation of carbon monoxide to methane over mesoporous nickel-M-alumina (M = Fe, Ni, Co, Ce, and La) xerogel catalysts", *Journal of Industrial and Engineering Chemistry* **2012**, *18*, 243–248, DOI 10.1016/j.jiec.2011.11.026.

[145] L. Znak, K. Stołecki, J. Zieliński, "The effect of cerium, lanthanum and zirconium on nickel/alumina catalysts for the hydrogenation of carbon oxides", *Catalysis Today* **2005**, *101*, 65–71, DOI 10.1016/j.cattod.2005.01.003.

[146] W. A. W. A. Bakar, R. Ali, N. S. Mohammad, "The effect of noble metals on catalytic methanation reaction over supported Mn/Ni oxide based catalysts", *Arabian Journal of Chemistry* **2015**, *8*, 632–643, DOI 10.1016/j.arabjc.2013.06.009.

[147] O. Thomys, "Entwicklung von Nickel-Trägerkatalysatoren für die Methanisierung von Kohlenstoffdioxid unter Anwendung von Parallelpräparation und statistischer Versuchsplanung", PhD Thesis, Technical University of Munich, Munich, DE, **2016**.

[148] M. P. Andersson, T. Bligaard, A. Kustov, K. E. Larsen, J. Greeley, T. Johannessen, C. H. Christensen, J. K. Nørskov, "Toward computational screening in heterogeneous catalysis: Pareto-optimal methanation catalysts", *Journal of Catalysis* **2006**, *239*, 501–506, DOI 10.1016/j.jcat.2006.02.016.

[149] F. H. Meng, P. Z. Zhong, Z. Li, X. X. Cui, H. Y. Zheng, "Surface Structure and Catalytic Performance of Ni-Fe Catalyst for Low-Temperature CO Hydrogenation", *Journal of Chemistry* **2014**, *2014*, 1–7, DOI 10.1155/2014/534842.

[150] S. Hwang, U. G. Hong, J. Lee, J. G. Seo, J. H. Baik, D. J. Koh, H. Lim, I. K. Song, "Methanation of carbon dioxide over mesoporous Ni-Fe-$Al_2O_3$ catalysts prepared by a coprecipitation method: Effect of precipitation agent", *Journal of Industrial and Engineering Chemistry* **2013**, *19*, 2016–2021, DOI 10.1016/j.jiec.2013.03.015.

[151] S. Hwang, U. G. Hong, J. Lee, J. H. Baik, D. J. Koh, H. Lim, I. K. Song, "Methanation of Carbon Dioxide Over Mesoporous Nickel–M–Alumina (M = Fe, Zr, Ni, Y, and Mg) Xerogel Catalysts: Effect of Second Metal", *Catalysis Letters* **2012**, *142*, 860–868, DOI 10.1007/s10562-012-0842-0.

[152] B. Mutz, M. Belimov, W. Wang, P. Sprenger, M.-A. Serrer, D. Wang, P. Pfeifer, W. Kleist, J.-D. Grunwaldt, "Potential of an Alumina-Supported $Ni_3Fe$ Catalyst in the Methanation of $CO_2$: Impact of Alloy Formation on Activity and Stability", *ACS Catalysis* **2017**, 6802–6814, DOI 10.1021/acscatal.7b01896.

[153] A. L. Kustov, A. M. Frey, K. E. Larsen, T. Johannessen, J. K. Nørskov, C. H. Christensen, "CO methanation over supported bimetallic Ni-Fe catalysts: From computational studies towards catalyst optimization", *Applied Catalysis A: General* **2007**, *320*, 98–104, DOI 10.1016/j.apcata.2006.12.017.

[154] J. Sehested, K. E. Larsen, A. L. Kustov, A. M. Frey, T. Johannessen, T. Bligaard, M. P. Andersson, J. K. Nørskov, C. H. Christensen, "Discovery of technical methanation catalysts based on computational screening", *Topics in Catalysis* **2007**, *45*, 9–13, DOI 10.1007/s11244-007-0232-9.

[155] T. Bligaard, J. K. Nørskov, S. Dahl, J. Matthiesen, C. H. Christensen, J. Sehested, "The Brønsted–Evans–Polanyi relation and the volcano curve in heterogeneous catalysis", *Journal of Catalysis* **2004**, *224*, 206–217, DOI 10.1016/j.jcat.2004.02.034.

[156] D. Pandey, G. Deo, "Promotional effects in alumina and silica supported bimetallic Ni–Fe catalysts during $CO_2$ hydrogenation", *Journal of Molecular Catalysis A: Chemical* **2014**, *382*, 23–30, DOI 10.1016/j.molcata.2013.10.022.

[157] D. Pandey, G. Deo, "Effect of support on the catalytic activity of supported Ni-Fe catalysts for the $CO_2$ methanation reaction", *Journal of Industrial and Engineering Chemistry* **2016**, *33*, 99–107, DOI 10.1016/j.jiec.2015.09.019.

[158] Z. Li, T. Zhao, L. Zhang, "Promotion effect of additive Fe on $Al_2O_3$ supported Ni catalyst for $CO_2$ methanation", *Applied Organometallic Chemistry* **2018**, *32*, e4328, DOI 10.1002/aoc.4328.

[159] M.-A. Serrer, K. F. Kalz, E. Saraci, H. Lichtenberg, J.-D. Grunwaldt, "Role of Iron on the Structure and Stability of $Ni_{3.2}Fe/Al_2O_3$ during Dynamic $CO_2$ Methanation for P2X Applications", *ChemCatChem* **2019**, *11*, 5018–5021, DOI 10.1002/cctc.201901425.

[160] B. Mutz, A. Gänzler, M. Nachtegaal, O. Müller, R. Frahm, W. Kleist, J.-D. Grunwaldt, "Surface Oxidation of Supported Ni Particles and Its Impact on the Catalytic Performance during Dynamically Operated Methanation of $CO_2$", *Catalysts* **2017**, *7*, 279, DOI 10.3390/catal7090279.

[161] C. Mebrahtu, F. Krebs, S. Perathoner, S. Abate, G. Centi, R. Palkovits, "Hydrotalcite based Ni-Fe/(Mg, Al)$O_x$ catalysts for $CO_2$ methanation - tailoring Fe content for improved CO dissociation, basicity, and particle size", *Catalysis Science & Technology* **2018**, *8*, 1016–1027, DOI 10.1039/C7CY02099F.

[162] J. Greeley, J. K. Nørskov, "A general scheme for the estimation of oxygen binding energies on binary transition metal surface alloys", *Surface Science* **2005**, *592*, 104–111, DOI 10.1016/j.susc.2005.07.018.

[163] P. A. U. Aldana, F. Ocampo, K. Kobl, B. Louis, F. Thibault-Starzyk, M. Daturi, P. Bazin, S. Thomas, A. C. Roger, "Catalytic $CO_2$ valorization into $CH_4$ on Ni-based ceria-zirconia. Reaction mechanism by operando IR spectroscopy", *Catalysis Today* **2013**, *215*, 201–207, DOI 10.1016/j.cattod.2013.02.019.

[164] A. Westermann, B. Azambre, M. C. Bacariza, I. Graça, M. F. Ribeiro, J. M. Lopes, C. Henriques, "Insight into $CO_2$ methanation mechanism over NiUSY zeolites: An operando IR study", *Applied Catalysis B: Environmental* **2015**, *174-175*, 120–125, DOI 10.1016/j.apcatb.2015.02.026.

[165] C. d. Leitenburg, A. Trovarelli, J. Kašpar, "A Temperature-Programmed and Transient Kinetic Study of $CO_2$ Activation and Methanation over $CeO_2$ Supported Noble Metals", *Journal of Catalysis* **1997**, *166*, 98–107, DOI 10.1006/jcat.1997.1498.

[166] S. Akamaru, T. Shimazaki, M. Kubo, T. Abe, "Density functional theory analysis of methanation reaction of $CO_2$ on Ru nanoparticle supported on $TiO_2$ (101)", *Applied Catalysis A: General* **2014**, *470*, 405–411, DOI 10.1016/j.apcata.2013.11.016.

[167] B. Miao, S. S. K. Ma, X. Wang, H. Su, S. H. Chan, "Catalysis mechanisms of $CO_2$ and CO methanation", *Catalysis Science & Technology* **2016**, *6*, 4048–4058, DOI 10.1039/C6CY00478D.

[168] G. E. Y. V. M. Vlasenko, "Mechanism of the Catalytic Hydrogenation of Oxides of Carbon to Methane", *Russian Chemical Reviews* **1969**, *38*, 728–739, DOI 10.1070/RC1969v038n09ABEH001829.

[169] T. van Herwijnen, H. van Doesburg, W. A. Jong, "Kinetics of the methanation of CO and $CO_2$ on a nickel catalyst", *Journal of Catalysis* **1973**, *28*, 391–402, DOI 10.1016/0021-9517(73)90132-2.

[170] T. Mori, H. Masuda, H. Imai, A. Miyamoto, S. Baba, Y. Murakami, "Kinetics, isotope effects, and mechanism for the hydrogenation of carbon monoxide on supported nickel catalysts", *The Journal of Physical Chemistry* **1982**, *86*, 2753–2760, DOI 10.1021/j100211a039.

[171] V. Sanchez-Escribano, M. A. Larrubia Vargas, E. Finocchio, G. Busca, "On the mechanisms and the selectivity determining steps in syngas conversion over supported metal catalysts: An IR study", *Applied Catalysis A: General* **2007**, *316*, 68–74, DOI 10.1016/j.apcata.2006.09.020.

[172] M. A. Vannice, "The catalytic synthesis of hydrocarbons from $H_2$/CO mixtures over the group VIII metals: II. The kinetics of the methanation reaction over supported metals", *Journal of Catalysis* **1975**, *37*, 462–473, DOI 10.1016/0021-9517(75)90182-7.

[173] C. P. Huang, J. T. Richardson, "Alkali promotion of nickel catalysts for carbon monoxide methanation", *Journal of Catalysis* **1978**, *51*, 1–8, DOI 10.1016/0021-9517(78)90232-4.

[174] J. W. E. Coenen, P. F. M. T. van Nisselrooy, M. H. J. M. de Croon, P. F. H. A. van Dooren, R. Z. C. van Meerten, "The dynamics of methanation of carbon monoxide on nickel catalysts", *Applied Catalysis* **1986**, *25*, 1–8, DOI 10.1016/S0166-9834(00)81215-4.

[175] G. I. Golodets, "Mechanism and kinetics of CO hydrogenation on metals", *Theoretical and Experimental Chemistry* **1985**, *21*, 525–529, DOI 10.1007/bf00944085.

[176] H. Inoue, M. Funakoshi, "Kinetics of Methanation of Carbon Monoxide and Carbon Dioxide", *Journal of Chemical Engineering of Japan* **1984**, *17*, 602–610, DOI 10.1252/jcej.17.602.

[177] M. Araki, V. Ponec, "Methanation of Carbon-Monoxide on Nickel and Nickel-Copper Alloys", *Journal of Catalysis* **1976**, *44*, 439–448, DOI 10.1016/0021-9517(76)90421-8.

[178] R. Z. C. van Meerten, J. G. Vollenbroek, M. H. J. M. de Croon, P. F. M. T. van Nisselrooy, J. W. E. Coenen, "The kinetics and mechanism of the methanation of carbon monoxide on a nickel-silica catalyst", *Applied Catalysis* **1982**, *3*, 29–56, DOI 10.1016/0166-9834(82)80221-2.

[179] I. Alstrup, "On the Kinetics of Co Methanation on Nickel Surfaces", *Journal of Catalysis* **1995**, *151*, 216–225, DOI 10.1006/jcat.1995.1023.

[180] M. P. Andersson, F. Abild-Pedersen, I. N. Remediakis, T. Bligaard, G. Jones, J. Engbæk, O. Lytken, S. Horch, J. H. Nielsen, J. Sehested, J. R. Rostrup-Nielsen, J. K. Nørskov, I. Chorkendorff, "Structure sensitivity of the methanation reaction: $H_2$-induced CO dissociation on nickel surfaces", *Journal of Catalysis* **2008**, *255*, 6–19, DOI 10.1016/j.jcat.2007.12.016.

[181] C. Zhi, Q. Wang, B. Wang, D. Li, R. Zhang, "Insight into the mechanism of methane synthesis from syngas on a Ni(111) surface: a theoretical study", *RSC Advances* **2015**, *5*, 66742–66756, DOI 10.1039/c4ra17096b.

[182] J. L. C. Fajín, J. R. B. Gomes, M. N. D. S. Cordeiro, "Mechanistic Study of Carbon Monoxide Methanation over Pure and Rhodium- or Ruthenium-Doped Nickel Catalysts", *The Journal of Physical Chemistry C* **2015**, *119*, 16537–16551, DOI 10.1021/acs.jpcc.5b01837.

[183] O. A. Hougen, K. M. Watson, *Chemical Process Principles*, *Vol. 3*, Wiley, New York, NY, **1943**.

[184] P. Mars, D. W. van Krevelen, "Oxidations carried out by means of vanadium oxide catalysts", *Chemical Engineering Science* **1954**, *3*, 41–59, DOI 10.1016/S0009-2509(54)80005-4.

[185] D. D. Eley, E. K. Rideal, "Parahydrogen Conversion on Tungsten", *Nature* **1940**, *146*, 401–402, DOI 10.1038/146401d0.

[186] J. Xu, G. F. Froment, "Methane steam reforming, methanation and water-gas shift: I. Intrinsic kinetics", *AIChE Journal* **1989**, *35*, 88–96, DOI 10.1002/aic.690350109.

[187] K. Hou, R. Hughes, "The kinetics of methane steam reforming over a Ni/$\alpha$-$Al_2O_3$ catalyst", *Chemical Engineering Journal* **2001**, *82*, 311–328, DOI 10.1016/S1385-8947(00)00367-3.

[188] P. C. L. Thorne, "Kapillarchemie: Eine Darstellung der Chemie der Kolloide und Verwandter Gebiete. By Prof. Dr. Herbert Freundlich. Third edition, enlarged. Pp. xvi+1225. Leipzig: Akademische Verlagsgesellschaft, 1923", *Journal of the Society of Chemical Industry* **1924**, *43*, 70–71, DOI 10.1002/jctb.5000430306.

[189] K. Yang, O. Hougen, "Determination of Mechanism of Catalyzed Gaseous Reactions", *Chemical Engineering Progress* **1950**, *46*, 146–157.

[190] J. Klose, M. Baerns, "Kinetics of the methanation of carbon monoxide on an alumina-supported nickel catalyst", *Journal of Catalysis* **1984**, *85*, 105–116, DOI 10.1016/0021-9517(84)90114-3.

[191] J. A. Hernandez Lalinde, P. Roongruangsree, J. Ilsemann, M. Bäumer, J. Kopyscinski, "$CO_2$ methanation and reverse water gas shift reaction. Kinetic study based on *in situ* spatially-resolved measurements", *Chemical Engineering Journal* **2020**, *390*, 124629, DOI 10.1016/j.cej.2020.124629.

[192] P. Marocco, E. A. Morosanu, E. Giglio, D. Ferrero, C. Mebrahtu, A. Lanzini, S. Abate, S. Bensaid, S. Perathoner, M. Santarelli, R. Pirone, G. Centi, "$CO_2$ methanation over Ni/Al hydrotalcite-derived catalyst: Experimental characterization and kinetic study", *Fuel* **2018**, *225*, 230–242, DOI 10.1016/j.fuel.2018.03.137.

[193] I. Champon, A. Bengaouer, A. Chaise, S. Thomas, A.-C. Roger, "Carbon dioxide methanation kinetic model on a commercial Ni/$Al_2O_3$ catalyst", *Journal of $CO_2$ Utilization* **2019**, *34*, 256–265, DOI 10.1016/j.jcou.2019.05.030.

[194] G. D. Weatherbee, C. H. Bartholomew, "Hydrogenation of $CO_2$ on group VIII metals: II. Kinetics and mechanism of $CO_2$ hydrogenation on nickel", *Journal of Catalysis* **1982**, *77*, 460–472, DOI 10.1016/0021-9517(82)90186-5.

[195] D. W. Goodman, R. D. Kelley, T. E. Madey, J. T. Yates, "Kinetics of the hydrogenation of CO over a single crystal nickel catalyst", *Journal of Catalysis* **1980**, *63*, 226–234, DOI 10.1016/0021-9517(80)90075-5.

[196] R. S. Polizzotti, J. A. Schwarz, "Hydrogenation of CO to methane: Kinetic studies on polycrystalline nickel foils", *Journal of Catalysis* **1982**, *77*, 1–15, DOI 10.1016/0021-9517(82)90140-3.

[197] H. Knözinger, E. Taglauer, "Spreading and Wetting" in *Preparation of Solid Catalysts*, Wiley-VCH, Weinheim, DE, **2008**, Chapter 4.8, pp. 501–526, DOI 10.1002/9783527619528.ch4h.

[198] M. D. Argyle, C. H. Bartholomew, "Heterogeneous Catalyst Deactivation and Regeneration: A Review", *Catalysts* **2015**, *5*, 145–269, DOI 10.3390/catal5010145.

[199] J. H. Sinfelt, "Bifunctional Catalysis" in *Advances in Chemical Engineering*, *Vol. 5*, (Eds.: T. B. Drew, J. W. Hoopes, T. Vermeulen, G. R. Cokelet), Academic Press, New York, NY, London, UK, **1964**, pp. 37–74, DOI 10.1016/S0065-2377(08)60006-X.

[200] A. Trovarelli, "Catalytic Properties of Ceria and $CeO_2$-Containing Materials", *Catalysis Reviews* **1996**, *38*, 439–520, DOI 10.1080/01614949608006464.

[201] T. Sakpal, L. Lefferts, "Structure-dependent activity of $CeO_2$ supported Ru catalysts for $CO_2$ methanation", *Journal of Catalysis* **2018**, *367*, 171–180, DOI 10.1016/j.jcat.2018.08.027.

[202] F. Wang, S. He, H. Chen, B. Wang, L. Zheng, M. Wei, D. G. Evans, X. Duan, "Active Site Dependent Reaction Mechanism over Ru/$CeO_2$ Catalyst toward $CO_2$ Methanation", *Journal of the American Chemical Society* **2016**, *138*, 6298–6305, DOI 10.1021/jacs.6b02762.

[203] J. F. LePage, R. Schlögl, M. S. Wainwright, F. Schüth, K. Unger, E. I. Ko, H. Jacobsen, P. Kleinschmit, R. G. Menon, B. Delmon, K. Y. Lee, M. Misino, S. T. Oyama, "Preparation of Solid Catalysts: Sections 2.0 and 2.1" in *Handbook of Heterogeneous Catalysis*, Wiley-VCH, Weinheim, DE, **1997**, pp. 49–138, DOI 10.1002/9783527619474.ch2a.

[204] W. M. H. Sachtler, G. Schulz-Ekloff, S. Ernst, J. J. Friplat, K. Tanabe, H. Hattori, J. F. Le Page, M. Baerns, E. Körting, "Preparation of Solid Catalysts: Sections 2.3.4 – 2.6" in *Handbook of Heterogeneous Catalysis*, Wiley-VCH, Weinheim, DE, **1997**, Chapter 2, pp. 365–426, DOI 10.1002/9783527619474.ch2d.

[205] B. E. Koel, J. Kim, "Promoters and Poisons" in *Handbook of Heterogeneous Catalysis*, Wiley-VCH, Weinheim, DE, **2008**, Chapter 5.3.4, pp. 1593–1624, DOI 10.1002/9783527610044.hetcat0087.

[206] M. Wolf, L. H. Wong, C. Schüler, O. Hinrichsen, "$CO_2$ methanation on transition-metal-promoted Ni-Al catalysts: Sulfur poisoning and the role of $CO_2$ adsorption capacity for catalyst activity", *Journal of $CO_2$ Utilization* **2020**, *36*, 276–287, DOI 10.1016/j.jcou.2019.10.014.

[207] P. H. Karpinski, J. S. Wey, "6 - Precipitation processes" in *Handbook of Industrial Crystallization (Second Edition)*, (Ed.: A. S. Myerson), Butterworth-Heinemann, Woburn, MA, **2002**, pp. 141–160, DOI 10.1016/B978-075067012-8/50008-2.

[208] M. Lok, "Coprecipitation" in *Synthesis of Solid Catalysts*, Wiley-VCH, Weinheim, DE, **2009**, Chapter 7, pp. 135–151, DOI 10.1002/9783527626854.ch7.

[209] J. W. Geus, "Process for homogeneous deposition precipitation of metal compounds on support or carrier materials", U. S. Patent 4,113,658, **1978**.

[210] C. Louis in *Catalyst Preparation: Science and Engineering*, (Ed.: J. Regalbuto), CRC Press, Boca Raton, FL, **2007**.

[211] F. Caruso, S. Mantellato, M. Palacios, R. J. Flatt, "ICP-OES method for the characterization of cement pore solutions and their modification by polycarboxylate-based superplasticizers", *Cement and Concrete Research* **2017**, *91*, 52–60, DOI 10.1016/j.cemconres.2016.10.007.

[212] X. Hou, R. S. Amais, B. T. Jones, G. L. Donati, "Inductively Coupled Plasma Optical Emission Spectrometry" in *Encyclopedia of Analytical Chemistry*, John Wiley & Sons, Ltd, Hoboken, NJ, **2016**, pp. 1–25, DOI 10.1002/9780470027318.a5110.pub3.

[213] Y. Waseda, E. Matsubara, K. Shinoda, *X-Ray Diffraction Crystallography : Introduction, Examples and Solved Problems*, Springer, Berlin, Heidelberg, DE, **2011**.

[214] L. Spieß, G. Teichert, R. Schwarzer, H. Behnken, C. Genzel, "Zellparameterbestimmung" in *Moderne Röntgenbeugung: Röntgendiffraktometrie für Materialwissenschaftler, Physiker und Chemiker*, Springer Fachmedien Wiesbaden, Wiesbaden, DE, **2019**, pp. 275–290, DOI 10.1007/978-3-8348-8232-5_7.

[215] U. Holzwarth, N. Gibson, "The Scherrer equation versus the 'Debye-Scherrer equation'", *Nature Nanotechnology* **2011**, *6*, 534, DOI 10.1038/nnano.2011.145.

[216] P. Scherrer, "Bestimmung der Größe und der inneren Struktur von Kolloidteilchen mittels Röntgenstrahlen", *Mathematisch-Physikalische Klasse* **1918**, *2*, 98–100.

[217] A. Gervasini, "Temperature Programmed Reduction/Oxidation (TPR/TPO) Methods" in *Calorimetry and Thermal Methods in Catalysis*, (Ed.: A. Auroux), Springer, Berlin, Heidelberg, DE, **2013**, pp. 175–195, DOI 10.1007/978-3-642-11954-5_5.

[218] P. Malet, A. Caballero, "The selection of experimental conditions in temperature-programmed reduction experiments", *Journal of the Chemical Society Faraday Transactions 1* **1988**, *84*, 2369–2375, DOI 10.1039/F19888402369.

[219] D. A. M. Monti, A. Baiker, "Temperature-programmed reduction. Parametric sensitivity and estimation of kinetic parameters", *Journal of Catalysis* **1983**, *83*, 323–335, DOI 10.1016/0021-9517(83)90058-1.

[220] V. Rakić, L. Damjanović, "Temperature-Programmed Desorption (TPD) Methods" in *Calorimetry and Thermal Methods in Catalysis*, (Ed.: A. Auroux), Springer, Berlin, Heidelberg, DE, **2013**, pp. 131–174, DOI 10.1007/978-3-642-11954-5_4.

[221] K. S. Singh, J. Rouquerol, G. Bergeret, P. Gallezot, M. Vaarkamp, D. C. Koningsberger, A. K. Datye, J. W. Niemantsverdriet, T. Butz, G. Engelhardt, G. Mestl, H. Knözinger, H. Jobic, "Characterization of Solid Catalysts: Sections 3.1.1 – 3.1.3" in *Handbook of Heterogeneous Catalysis*, Wiley-VCH, Weinheim, DE, **1997**, pp. 427–582, DOI 10.1002/9783527619474.ch3a.

[222] K. S. W. Sing, D. H. Everett, R. A. W. Haul, L. Moscou, R. A. Pierotti, J. Rouquerol, T. Siemieniewska, "Reporting Physisorption Data for Gas/Solid Systems" in *Handbook of Heterogeneous Catalysis*, Wiley-VCH, Weinheim, DE, **2008**, Chapter 3.3.1, pp. 1217–1230, DOI 10.1002/9783527610044.hetcat0065.

[223] I. Langmuir, "The Adsorption of Gases on Plane Surfaces of Glass, Mica and Platinum", *Journal of the American Chemical Society* **1918**, *40*, 1361–1403, DOI 10.1021/ja02242a004.

[224] S. Brunauer, P. H. Emmett, E. Teller, "Adsorption of Gases in Multimolecular Layers", *Journal of the American Chemical Society* **1938**, *60*, 309–319, DOI 10.1021/ja01269a023.

[225] K. S. W. Sing, “Reporting physisorption data for gas/solid systems with special reference to the determination of surface area and porosity (Recommendations 1984)”, *Pure and Applied Chemistry* **1985**, *57*, 603–619, DOI 10.1351/pac198557040603.

[226] M. Thommes, K. Kaneko, A. V. Neimark, J. P. Olivier, F. Rodriguez-Reinoso, J. Rouquerol, K. S. Sing, “Physisorption of gases, with special reference to the evaluation of surface area and pore size distribution (IUPAC Technical Report)”, *Pure and Applied Chemistry* **2015**, *87*, 1051, DOI 10.1515/pac-2014-1117.

[227] E. P. Barrett, L. G. Joyner, P. P. Halenda, “The Determination of Pore Volume and Area Distributions in Porous Substances. I. Computations from Nitrogen Isotherms”, *Journal of the American Chemical Society* **1951**, *73*, 373–380, DOI 10.1021/ja01145a126.

[228] P. A. Sermon, G. C. Bond, “Hydrogen Spillover”, *Catalysis Reviews* **1974**, *8*, 211–239, DOI 10.1080/01614947408071861.

[229] M. Kraus, G. M. Pajonk, W. M. H. Sachtler, Z. Paál, G. A. Somorjai, J. H. Block, D. L. Cocke, N. Kruse, D. S. Santilli, B. Gates, J. A. Martens, P. A. Jacobs, C. R. A. Catlow, A. T. Bell, E. J. Maginn, D. N. Theodorou, “Elementary Steps and Mechanisms: Sections 5.3 – 5.5” in *Handbook of Heterogeneous Catalysis*, Wiley-VCH, Weinheim, DE, **1997**, pp. 1051–1188, DOI 10.1002/9783527619474.ch5b.

[230] Deutsches Institut für Normung e.V., DIN 66136-2, "Bestimmung des Dispersionsgrades von Metallen durch Chemisorption - Teil 2: Volumetrisches Verfahren", **2007**.

[231] H. Günzler, H. Gremlich, “Absorption und Molekülbau” in *IR-Spektroskopie*, Wiley-VCH, Weinheim, DE, **2013**, Chapter 2, pp. 9–37, DOI 10.1002/9783527662852.ch2.

[232] A. Vimont, F. Thibault-Starzyk, M. Daturi, “Analysing and understanding the active site by IR spectroscopy”, *Chemical Society Reviews* **2010**, *39*, 4928–4950, DOI 10.1039/B919543M.

[233] H. Günzler, H. Gremlich, “Das Spektrometer” in *IR-Spektroskopie*, Wiley-VCH, **2013**, Chapter 3, pp. 39–71, DOI 10.1002/9783527662852.ch3.

[234] O. Yalcin, “Ferromagnetic Resonance” in *Ferromagnetic Resonance*, (Ed.: O. Yalcin), IntechOpen, Rijeka, HR, **2013**, Chapter 1, DOI 10.5772/56134.

[235] T. Mitsui, “Chapter 7 - Synchrotron Mössbauer Spectroscopy Measurement” in *Magmas Under Pressure*, (Eds.: Y. Kono, C. Sanloup), Elsevier, Amsterdam, NL, **2018**, pp. 179–210, DOI 10.1016/B978-0-12-811301-1.00007-1.

[236] S. Oswald, “X-Ray Photoelectron Spectroscopy in Analysis of Surfaces, Update based on the original article by Steffen Oswald, Encyclopedia of Analytical Chemistry, © 2000, John Wiley & Sons, Ltd.” in *Encyclopedia of Analytical Chemistry*, John Wiley & Sons, Hoboken, NJ, **2013**, DOI 10.1002/9780470027318.a2517.pub2.

[237] B. J. Inkson, “2 - Scanning electron microscopy (SEM) and transmission electron microscopy (TEM) for materials characterization” in *Materials Characterization Using Nondestructive Evaluation (NDE) Methods*, (Eds.: G. Hübschen, I. Altpeter, R. Tschuncky, H.-G. Herrmann), Woodhead Publishing, Duxford, UK, **2016**, pp. 17–43, DOI 10.1016/B978-0-08-100040-3.00002-X.

[238] W. Dietz, “Response factors for gas chromatographic analyses”, *Journal of Chromatographic Science* **1967**, 68–71, DOI 10.1093/chromsci/5.2.68.

[239] T. Burger, "Experimental and theoretical investigations on the methanation reaction of $CO_2$", *not published*, Master’s Thesis, Technical University of Munich, Munich, DE, **2015**.

[240] S. V. Krupa, R. N. Kickert, “The Greenhouse Effect: Impacts of Ultraviolet-B (UV-B) Radiation, Carbon Dioxide ($CO_2$), and Ozone ($O_3$) on Vegetation”, *Environmental Pollution* **1989**, *61*, 263–393, DOI 10.1016/0269-7491(89)90166-8.

[241] M. Specht, J. Brellochs, V. Frick, B. Stürmer, U. Zuberbühler, M. Sterner, G. Waldstein, “Speicherung von Bioenergie und erneuerbarem Strom in Erdgasnetz”, *Erdöl Erdgas Kohle* **2010**, *126*, 342–346.

[242] A. Varone, M. Ferrari, “Power to liquid and power to gas: An option for the German Energiewende”, *Renewable and Sustainable Energy Reviews* **2015**, *45*, 207–218, DOI 10.1016/j.rser.2015.01.049.

[243] M. Thema, M. Sterner, T. Lenck, P. Götz, “Necessity and Impact of Power-to-gas on Energy Transition in Germany”, *Energy Procedia* **2016**, *99*, 392–400, DOI 10.1016/j.egypro.2016.10.129.

[244] S. Rönsch, J. Schneider, S. Matthischke, M. Schluter, M. Götz, J. Lefebvre, P. Prabhakaran, S. Bajohr, “Review on methanation - From fundamentals to current projects”, *Fuel* **2016**, *166*, 276–296, DOI 10.1016/j.fuel.2015.10.111.

[245] M. Frey, T. Romero, A.-C. Roger, D. Edouard, “Open cell foam catalysts for $CO_2$ methanation: Presentation of coating procedures and *in situ* exothermicity reaction study by infrared thermography”, *Catalysis Today* **2016**, *273*, 83–90, DOI 10.1016/j.cattod.2016.03.016.

[246] S. Rönsch, S. Matthischke, M. Müller, P. Eichler, “Dynamische Simulation von Reaktoren zur Festbettmethanisierung”, *Chemie Ingenieur Technik* **2014**, *86*, 1198–1204, DOI 10.1002/cite.201300046.

[247] G. Q. Zhang, T. J. Sun, J. X. Peng, S. Wang, S. D. Wang, “A comparison of Ni/SiC and Ni/$Al_2O_3$ catalyzed total methanation for production of synthetic natural gas”, *Applied Catalysis A: General* **2013**, *462*, 75–81, DOI 10.1016/j.apcata.2013.04.037.

[248] H. Li, Y. Xu, C. Gao, Y. Zhao, “Structural and textural evolution of Ni/$\gamma$-$Al_2O_3$ catalyst under hydrothermal conditions”, *Catalysis Today* **2010**, *158*, 475–480, DOI 10.1016/j.cattod.2010.07.015M4-Citavi.

[249] S. Abello, C. Berrueco, D. Montane, "High-loaded nickel-alumina catalyst for direct $CO_2$ hydrogenation into synthetic natural gas (SNG)", *Fuel* **2013**, *113*, 598–609, DOI 10.1016/j.fuel.2013.06.012.

[250] X.-Z. Jiang, S. A. Stevenson, J. A. Dumesic, "Mössbauer spectroscopy and methanation kinetics studies of nickel-iron alloy particles supported on titania and alumina", *Journal of Catalysis* **1985**, *91*, 11–24, DOI 10.1016/0021-9517(85)90283-0.

[251] D. Schlereth, O. Hinrichsen, "A fixed-bed reactor modeling study on the methanation of $CO_2$", *Chemical Engineering Research and Design* **2014**, *92*, 702–712, DOI 10.1016/j.cherd.2013.11.014.

[252] C. H. Bartholomew, R. B. Pannell, "The Stoichiometry of Hydrogen and Carbon-Monoxide Chemisorption on Alumina-Supported and Silica-Supported Nickel", *Journal of Catalysis* **1980**, *65*, 390–401, DOI 10.1016/0021-9517(80)90316-4.

[253] Z. Yu, D. Chen, M. Rønning, T. Vrålstad, E. Ochoa-Fernández, A. Holmen, "Large-scale synthesis of carbon nanofibers on Ni–Fe–Al hydrotalcite derived catalysts", *Applied Catalysis A: General* **2008**, *338*, 136–146, DOI 10.1016/j.apcata.2008.01.003.

[254] H. J. Jung, M. A. Vannice, L. N. Mulay, R. M. Stanfield, W. N. Delgass, "The characterization of carbon-supported iron catalysts: Chemisorption, magnetization, and Mössbauer spectroscopy", *Journal of Catalysis* **1982**, *76*, 208–224, DOI 10.1016/0021-9517(82)90250-0.

[255] H. Topsøe, N. Topsøe, H. Bohlbro, J. A. Dumesic, "Supported Iron Catalysts: Particle Size Dependence of Catalytic and Chemisorptive Properties" in *Studies in Surface Science and Catalysis*, *Vol. 7*, (Eds.: T. Seivama, K. Tanabe), Elsevier, Amsterdam, NL, **1981**, pp. 247–265, DOI 10.1016/S0167-2991(09)60275-5.

[256] M. Boudart, A. Delbouille, J. A. Dumesic, S. Khammouma, H. Topsøe, "Surface, catalytic and magnetic properties of small iron particles: I. Preparation and characterization of samples", *Journal of Catalysis* **1975**, *37*, 486–502, DOI 10.1016/0021-9517(75)90184-0.

[257] T. Matsumoto, J. Kubota, J. N. Kondo, C. Hirose, K. Domen, "Adsorption Structures of Carbon Dioxide on NiO(111) and Hydroxylated NiO(111) Studied by Infrared Reflection Adsorption Spectroscopy", *Langmuir* **1999**, *15*, 2158–2161, DOI 10.1021/la9810298.

[258] P. H. M. De Korte, E. B. M. Doesburg, C. P. J. De Winter, L. L. Van Reijen, "Characterization of the interaction between nickel oxide and aluminium oxide in coprecipitated catalysts", *Solid State Ionics* **1985**, *16*, 73–80, DOI 10.1016/0167-2738(85)90026-8.

[259] R. B. Shalvoy, B. H. Davis, P. J. Reucroft, "Studies of the metal-support interaction in coprecipitated nickel on alumina methanation catalysts using X-ray photoelectron spectroscopy (XPS)", *Surface and Interface Analysis* **1980**, *2*, 11–16, DOI 10.1002/sia.740020104.

[260] B. J. Tan, K. J. Klabunde, P. M. A. Sherwood, "X-ray photoelectron spectroscopy studies of solvated metal atom dispersed catalysts. Monometallic iron and bimetallic iron-cobalt particles on alumina", *Chemistry of Materials* **1990**, *2*, 186–191, DOI 10.1021/cm00008a021.

[261] B. J. Tan, K. J. Klabunde, P. M. A. Sherwood, "XPS studies of solvated metal atom dispersed (SMAD) catalysts. Evidence for layered cobalt-manganese particles on alumina and silica", *Journal of the American Chemical Society* **1991**, *113*, 855–861, DOI 10.1021/ja00003a019.

[262] G. C. Allen, S. J. Harris, J. A. Jutson, J. M. Dyke, "A Study of a Number of Mixed Transition-Metal Oxide Spinels Using X-Ray Photoelectron-Spectroscopy", *Applied Surface Science* **1989**, *37*, 111–134, DOI 10.1016/0169-4332(89)90977-X.

[263] C. J. Wright, C. G. Windsor, D. C. Puxley, "Paracrystallinity in a coprecipitated nickel/alumina catalyst", *Journal of Catalysis* **1982**, *78*, 257–261, DOI 10.1016/0021-9517(82)90306-2.

[264] E. A. Owen, E. L. Yates, "LXVI. X-ray measurement of the thermal expansion of pure nickel", *The London Edinburgh and Dublin Philosophical Magazine and Journal of Science* **1936**, *21*, 809–819, DOI 10.1080/14786443608561628.

[265] A. Fischer, R. Hosemann, W. Vogel, J. Koutecky, J. Pohl, M. Ralek, "Microparacrystals as Catalysts", *Studies in Surface Science and Catalysis* **1981**, *7*, 341–354, DOI 10.1016/S0167-2991(09)60282-2.

[266] T. V. Reshetenko, L. B. Avdeeva, V. A. Ushakov, E. M. Moroz, A. N. Shmakov, V. V. Kriventsov, D. I. Kochubey, Y. T. Pavlyukhin, A. L. Chuvilin, Z. R. Ismagilov, "Coprecipitated iron-containing catalysts (Fe-$Al_2O_3$, Fe-Co-$Al_2O_3$, Fe-Ni-$Al_2O_3$) for methane decomposition at moderate temperatures", *Applied Catalysis A: General* **2004**, *270*, 87–99, DOI 10.1016/j.apcata.2004.04.026.

[267] T. Li, Y. Yang, C. Zhang, X. An, H. Wan, Z. Tao, H. Xiang, Y. Li, F. Yi, B. Xu, "Effect of manganese on an iron-based Fischer–Tropsch synthesis catalyst prepared from ferrous sulfate", *Fuel* **2007**, *86*, 921–928, DOI 10.1016/j.fuel.2006.10.019.

[268] F. Guo, J.-Q. Xu, W. Chu, "$CO_2$ reforming of methane over Mn promoted Ni/$Al_2O_3$ catalyst treated by $N_2$ glow discharge plasma", *Catalysis Today* **2015**, *256*, 124–129, DOI 10.1016/j.cattod.2015.02.036.

[269] J. I. Di Cosimo, V. K. Díez, M. Xu, E. Iglesia, C. R. Apesteguía, "Structure and Surface and Catalytic Properties of Mg-Al Basic Oxides", *Journal of Catalysis* **1998**, *178*, 499–510, DOI 10.1006/jcat.1998.2161.

[270] X. Wang, M. Shen, L. Song, Y. Su, J. Wang, "Surface basicity on bulk modified phosphorus alumina through different synthesis methods", *Physical Chemistry Chemical Physics* **2011**, *13*, 15589–15596, DOI 10.1039/C1CP21299K.

[271] M. del Arco, P. Malet, R. Trujillano, V. Rives, "Synthesis and Characterization of Hydrotalcites Containing Ni(II) and Fe(III) and Their Calcination Products", *Chemistry of Materials* **1999**, *11*, 624–633, DOI 10.1021/cm9804923.

[272] S. Gil, J. Garcia-Vargas, L. Liotta, G. Pantaleo, M. Ousmane, L. Retailleau, A. Giroir-Fendler, "Catalytic Oxidation of Propene over Pd Catalysts Supported on $CeO_2$, $TiO_2$, $Al_2O_3$ and M/$Al_2O_3$ Oxides (M = Ce, Ti, Fe, Mn)", *Catalysts* **2015**, *5*, 671–689, DOI 10.3390/catal5020671.

[273] J. A. Duffy, "A Review of Optical Basicity and Its Applications to Oxidic Systems", *Geochimica Et Cosmochimica Acta* **1993**, *57*, 3961–3970, DOI 10.1016/0016-7037(93)90346-X.

[274] J. K. Nørskov, T. Bligaard, A. Logadottir, S. Bahn, L. B. Hansen, M. Bollinger, H. Bengaard, B. Hammer, Z. Sljivancanin, M. Mavrikakis, Y. Xu, S. Dahl, C. J. H. Jacobsen, "Universality in heterogeneous catalysis", *Journal of Catalysis* **2002**, *209*, 275–278, DOI 10.1006/jcat.2002.3615.

[275] D. L. Trimm, "Deactivation and Regeneration" in *Handbook of Heterogeneous Catalysis*, Wiley-VCH, Weinheim, DE, **1997**, Chapter 7, pp. 1263–1282, DOI 10.1002/9783527619474.ch7.

[276] D. J. Duvenhage, N. J. Coville, "Deactivation of a precipitated iron Fischer-Tropsch catalyst - A pilot plant study", *Applied Catalysis A: General* **2006**, *298*, 211–216, DOI 10.1016/j.apcata.2005.10.009.

[277] M. E. Dry, "Fischer-Tropsch synthesis over iron catalysts", *Catalysis Letters* **1991**, *7*, 241–251, DOI 10.1007/bf00764506.

[278] M. A. A. Aziz, A. A. Jalil, S. Triwahyono, A. Ahmad, "$CO_2$ methanation over heterogeneous catalysts: recent progress and future prospects", *Green Chemistry* **2015**, *17*, 2647–2663, DOI 10.1039/c5gc00119f.

[279] L. M. Aparicio, "Transient isotopic studies and microkinetic modeling of methane reforming over nickel catalysts", *Journal of Catalysis* **1997**, *165*, 262–274, DOI 10.1006/jcat.1997.1468.

[280] M.-D. Lee, J.-F. Lee, C.-S. Chang, T.-Y. Dong, "Effects of addition of chromium, manganese, or molybdenum to iron catalysts for carbon dioxide hydrogenation", *Applied Catalysis* **1991**, *72*, 267–281, DOI 10.1016/0166-9834(91)85055-Z.

[281] E. Schweda, G. Jander, E. Blasius, *Jander, Blasius anorganische Chemie*, Hirzel Verlag, Stuttgart, DE, **2012**.

[282] A. H. Reidies, “Manganese Compounds” in *Ullmann’s Encyclopedia of Industrial Chemistry*, Wiley-VCH, Weinheim, DE, **2000**, DOI 10.1002/14356007.a16_123.

[283] M. K. Titulaer, J. B. H. Jansen, J. W. Geus, “The quantity of reduced nickel in synthetic takovite: effects of preparation conditions and calcination temperature”, *Clays and clay minerals* **1994**, *42*, 249–258, DOI 10.1346/CCMN.1994.0420303.

[284] E. C. Kruissink, L. L. van Reijen, J. R. H. Ross, “Coprecipitated nickel-alumina catalysts for methanation at high temperature. Part 1.-Chemical composition and structure of the precipitates”, *Journal of the Chemical Society Faraday Transactions 1: Physical Chemistry in Condensed Phases* **1981**, *77*, 649–663, DOI 10.1039/F19817700649.

[285] S. J. Mills, A. G. Christy, J. M. R. Genin, T. Kameda, F. Colombo, “Nomenclature of the hydrotalcite supergroup: natural layered double hydroxides”, *Mineralogical Magazine* **2012**, *76*, 1289–1336, DOI 10.1180/minmag.2012.076.5.10.

[286] J. Soria, M. T. Blasco, J. C. Conesa, “Metal-support interactions in supported nickel catalysts: a FMR study”, *Surface Science Letters* **1991**, *251*, A373, DOI 10.1016/0167-2584(91)91015-O.

[287] E. G. Derouane, A. Simoens, C. Colin, G. A. Martin, J. A. Dalmon, J. C. Védrine, “Effects of particle size and degree of reduction on the magnetic properties of dispersed nickel catalysts”, *Journal of Catalysis* **1978**, *52*, 50–58, DOI 10.1016/0021-9517(78)90122-7.

[288] V. K. Sharma, A. Baiker, “Superparamagnetic effects in the ferromagnetic resonance of silica supported nickel particles”, *The Journal of Chemical Physics* **1981**, *75*, 5596–5601, DOI 10.1063/1.441997.

[289] E. G. Derouane, A. J. Simoens, J. C. Védrine, “Ferromagnetic resonance investigation of dispersed Ni catalysts: epitaxial and textural effects from the support”, *Chemical Physics Letters* **1977**, *52*, 549–553, DOI 10.1016/0009-2614(77)80507-1.

[290] A. A. Andreev, P. W. Selwood, “Ferromagnetic resonance of supported nickel with adsorbed hydrogen, oxygen, and ethylene”, *Journal of Catalysis* **1967**, *8*, 375–382, DOI 10.1016/0021-9517(67)90334-X.

[291] Y. Öner, B. Aktaş, F. Apaydin, E. A. Harris, “Ferromagnetic resonance study of $Ni_{79}Mn_{21}$ alloy”, *Physical Review B* **1988**, *37*, 5866–5869, DOI 10.1103/PhysRevB.37.5866.

[292] Y.-C. Lee, A. B. Pakhomov, K. M. Krishnan, “Size-driven magnetic transitions in monodisperse MnO nanocrystals”, *Journal of Applied Physics* **2010**, *107*, 09E124, DOI 10.1063/1.3366611.

[293] M. Bailera, P. Lisbona, L. M. Romeo, S. Espatolero, “Power to Gas projects review: Lab, pilot and demo plants for storing renewable energy and $CO_2$”, *Renewable & Sustainable Energy Reviews* **2017**, *69*, 292–312, DOI http://doi.org/10.1016/j.rser.2016.11.130.

[294] F. Gutiérrez-Martín, L. M. Rodríguez-Antón, "Power-to-SNG technology for energy storage at large scales", *International Journal of Hydrogen Energy* **2016**, *41*, 19290–19303, DOI 10.1016/j.ijhydene.2016.07.097.

[295] H. Harms, B. Höhlein, A. Skov, "Methanisierung kohlenmonoxidreicher Gase beim Energie-Transport", *Chemie Ingenieur Technik* **1980**, *52*, 504–515, DOI 10.1002/cite.330520605.

[296] T. Inui, M. Funabiki, M. Suehiro, T. Sezume, "Methanation of $CO_2$ and CO on supported nickel-based composite catalysts", *Journal of the Chemical Society Faraday Transactions 1: Physical Chemistry in Condensed* **1979**, *75*, 787–802, DOI 10.1039/F19797500787.

[297] M. Boudart, B. H. Davis, H. Heinemann, "Introduction" in *Handbook of Heterogeneous Catalysis*, Wiley-VCH, Weinheim, DE, **1997**, pp. 1–48, DOI 10.1002/9783527619474.ch1.

[298] R. Dębek, M. Motak, T. Grzybek, M. Galvez, P. Da Costa, "A Short Review on the Catalytic Activity of Hydrotalcite-Derived Materials for Dry Reforming of Methane", *Catalysts* **2017**, *7*, 32, DOI 10.3390/catal7010032.

[299] C. Forano, U. Costantino, V. Prévot, C. T. Gueho, "Chapter 14.1 - Layered Double Hydroxides (LDH)" in *Handbook of Clay Science*, (Eds.: F. Bergaya, G. Lagaly), Developments in Clay Science, Elsevier, Amsterdam, NL, **2013**, pp. 745–782, DOI 10.1016/B978-0-08-098258-8.00025-0.

[300] E. E. Unmuth, L. H. Schwartz, J. B. Butt, "Iron alloy Fischer-Tropsch catalysts: I. Oxidation-reduction studies of the Fe-Ni system", *Journal of Catalysis* **1980**, *61*, 242–255, DOI 10.1016/0021-9517(80)90360-7.

[301] C. N. R. Rao, G. U. Kulkarni, K. R. Kannan, S. Chaturvedi, "In-situ Moessbauer and EXAFS investigations of the structural and magnetic properties of bimetallic iron-nickel/silica and iron-copper/silica catalysts", *The Journal of Physical Chemistry* **1992**, *96*, 7379–7385, DOI 10.1021/j100197a045.

[302] H. Habazaki, M. Yamasaki, B.-P. Zhang, A. Kawashima, S. Kohno, T. Takai, K. Hashimoto, "Co-methanation of carbon monoxide and carbon dioxide on supported nickel and cobalt catalysts prepared from amorphous alloys", *Applied Catalysis A: General* **1998**, *172*, 131–140, DOI 10.1016/S0926-860X(98)00121-5.

[303] A. E. Zagli, J. L. Falconer, C. A. Keenan, "Methanation on supported nickel catalysts using temperature programmed heating", *Journal of Catalysis* **1979**, *56*, 453–467, DOI 10.1016/0021-9517(79)90136-2.

[304] C. Schild, A. Wokaun, R. A. Koeppel, A. Baiker, "Carbon dioxide hydrogenation over nickel/zirconia catalysts from amorphous precursors: on the mechanism of methane formation", *The Journal of Physical Chemistry* **1991**, *95*, 6341–6346, DOI 10.1021/j100169a049.

[305] A. Erdöhelyi, M. Pásztor, F. Solymosi, "Catalytic hydrogenation of $CO_2$ over supported palladium", *Journal of Catalysis* **1986**, *98*, 166–177, DOI 10.1016/0021-9517(86)90306-4.

[306] F. Solymosi, A. Erdöhelyi, "Hydrogenation of $CO_2$ to $CH_4$ over alumina-supported noble metals", *Journal of Molecular Catalysis* **1980**, *8*, 471–474, DOI 10.1016/0304-5102(80)80086-1.

[307] S. V. Ho, P. Harriott, "The kinetics of methanation on nickel catalysts", *Journal of Catalysis* **1980**, *64*, 272–283, DOI 10.1016/0021-9517(80)90502-3.

[308] J. Gu, Y.-W. Zhang, F. Tao, "Shape control of bimetallic nanocatalysts through well-designed colloidal chemistry approaches", *Chemical Society Reviews* **2012**, *41*, 8050–8065, DOI 10.1039/C2CS35184F.

[309] G. Zhang, X. Liu, Y. Wang, C. Liu, S. Xing, "Achieving $MnO_2$ Nanosheets through Surface Redox Reaction on Nickel Nanochains for Catalysis and Energy Storage", *Chemistry – A European Journal* **2017**, *23*, 5557–5564, DOI 10.1002/chem.201700185.

[310] L. Swartzendruber, V. Itkin, C. Alcock, "Phase diagrams of binary nickel alloys" in *Phase diagrams of binary nickel alloys*, *Vol. 6*, (Ed.: P. Nash), ASM International, Materials Park, OH, **1991**, pp. 110–132.

[311] J. B. Anderson, "A criterion for isothermal behaviour of a catalyst pellet", *Chemical Engineering Science* **1963**, *18*, 147–148, DOI 10.1016/0009-2509(63)80023-8.

[312] D. E. Mears, "Tests for Transport Limitations in Experimental Catalytic Reactors", *Industrial & Engineering Chemistry Process Design and Development* **1971**, *10*, 541–547, DOI 10.1021/i260040a020.

[313] P. B. Weisz, C. D. Prater, "Interpretation of Measurements in Experimental Catalysis" in *Advances in Catalysis*, *Vol. 6*, (Eds.: W. Frankenburg, V. I. Komarewsky, E. K. Rideal), Academic Press, New York, NY, **1954**, pp. 143–196, DOI 10.1016/S0360-0564(08)60390-9.

[314] E. C. Kruissink, E. B. M. Doesburg, L. L. van Reijen, L. E. Alzamora, S. Orr, J. R. H. Ross, G. van Veen, "The Preparation and Pretreatment of Coprecipitated Nickel-Alumina Catalysts for Methanation at High Temperatures" in *Studies in Surface Science and Catalysis*, *Vol. Volume 3*, (Eds.: P. G. P. J. B. Delmon, G. Poncelet), Elsevier, Amsterdam, NL, **1979**, pp. 143–157, DOI 10.1016/S0167-2991(09)60210-X.

[315] J. Zhang, H. Xu, X. Jin, Q. Ge, W. Li, "Characterizations and activities of the nano-sized $Ni/Al_2O_3$ and $Ni/La–Al_2O_3$ catalysts for $NH_3$ decomposition", *Applied Catalysis A: General* **2005**, *290*, 87–96, DOI 10.1016/j.apcata.2005.05.020.

[316] B. Vos, E. Poels, A. Bliek, "Impact of Calcination Conditions on the Structure of Alumina-Supported Nickel Particles", *Journal of Catalysis* **2001**, *198*, 77–88, DOI 10.1006/jcat.2000.3082.

[317] E. Cremer, "The Compensation Effect in Heterogeneous Catalysis" in *Advances in Catalysis*, *Vol. 7*, (Eds.: W. G. Frankenburg, V. I. Komarewsky, E. K. Rideal), Academic Press, New York, NY, **1955**, pp. 75–91, DOI 10.1016/S0360-0564(08)60525-8.

[318] H. Eyring, "The Activated Complex and the Absolute Rate of Chemical Reactions", *Chemical Reviews* **1935**, *17*, 65–77, DOI 10.1021/cr60056a006.

[319] H. Eyring, "The Activated Complex in Chemical Reactions", *The Journal of Chemical Physics* **1935**, *3*, 107–115, DOI 10.1063/1.1749604.

[320] S. M. Kim, P. M. Abdala, T. Margossian, D. Hosseini, L. Foppa, A. Armutlulu, W. van Beek, A. Comas-Vives, C. Copéret, C. Müller, "Cooperativity and Dynamics Increase the Performance of NiFe Dry Reforming Catalysts", *Journal of the American Chemical Society* **2017**, *139*, 1937–1949, DOI 10.1021/jacs.6b11487.

[321] T. Inui, M. Funabiki, "Methanation of Carbon Dioxide and Carbon Monoxide on Supported Ni-$La_2O_3$-Ru catalysts", *Chemistry Letters* **1978**, *7*, 251–252, DOI 10.1246/cl.1978.251.

[322] E. Zagli, J. L. Falconer, "Carbon-Dioxide Adsorption and Methanation on Ruthenium", *Journal of Catalysis* **1981**, *69*, 1–8, DOI 10.1016/0021-9517(81)90122-6.

[323] S. I. Fujita, N. Takezawa, "Difference in the selectivity of CO and $CO_2$ methanation reactions", *Chemical Engineering Journal* **1997**, *68*, 63–68, DOI 10.1016/S1385-8947(97)00074-0.

[324] W. L. Vrijburg, E. Moioli, W. Chen, M. Zhang, B. J. P. Terlingen, B. Zijlstra, I. A. W. Filot, A. Züttel, E. A. Pidko, E. J. M. Hensen, "Efficient Base-Metal NiMn/$TiO_2$ Catalyst for $CO_2$ Methanation", *ACS Catalysis* **2019**, *9*, 7823–7839, DOI 10.1021/acscatal.9b01968.

[325] J. Kirchner, J. K. Anolleck, H. Lösch, S. Kureti, "Methanation of $CO_2$ on iron based catalysts", *Applied Catalysis B: Environmental* **2018**, *223*, 47–59, DOI 10.1016/j.apcatb.2017.06.025.

[326] M.-D. Lee, J.-F. Lee, C.-S. Chang, "Catalytic Behavior and Phase Composition Change of Iron Catalyst in Hydrogenation of Carbon Dioxide", *Journal of Chemical Engineering of Japan* **1990**, *23*, 130–136, DOI 10.1252/jcej.23.130.

[327] J. Fournier, L. Carreiro, Y. T. Qian, S. Soled, R. Kershaw, K. Dwight, A. Wold, "Methanation studies: Characterization of some iron catalysts by X-ray diffraction and Curie point determinations", *Journal of Solid State Chemistry* **1985**, *58*, 211–220, DOI 10.1016/0022-4596(85)90237-3.

[328] S. De, J. Zhang, R. Luque, N. Yan, "Ni-based bimetallic heterogeneous catalysts for energy and environmental applications", *Energy & Environmental Science* **2016**, *9*, 3314–3347, DOI 10.1039/C6EE02002J.

[329] S. A. Theofanidis, V. V. Galvita, H. Poelman, G. B. Marin, "Enhanced Carbon-Resistant Dry Reforming Fe-Ni Catalyst: Role of Fe", *ACS Catalysis* **2015**, *5*, 3028–3039, DOI 10.1021/acscatal.5b00357.

[330] J. Cai, Y. Han, S. Chen, E. J. Crumlin, B. Yang, Y. Li, Z. Liu, "$CO_2$ Activation on Ni(111) and Ni(100) Surfaces in the Presence of $H_2O$: An Ambient-Pressure X-ray Photoelectron Spectroscopy Study", *The Journal of Physical Chemistry C* **2019**, *123*, 12176–12182, DOI 10.1021/acs.jpcc.8b11698.

[331] S.-G. Wang, D.-B. Cao, Y.-W. Li, J. Wang, H. Jiao, "Chemisorption of $CO_2$ on Nickel Surfaces", *The Journal of Physical Chemistry B* **2005**, *109*, 18956–18963, DOI 10.1021/jp052355g.

[332] C. Liu, T. R. Cundari, A. K. Wilson, "$CO_2$ Reduction on Transition Metal (Fe, Co, Ni, and Cu) Surfaces: In Comparison with Homogeneous Catalysis", *The Journal of Physical Chemistry C* **2012**, *116*, 5681–5688, DOI 10.1021/jp210480c.

[333] S. Farsi, W. Olbrich, P. Pfeifer, R. Dittmeyer, "A consecutive methanation scheme for conversion of $CO_2$ – A study on $Ni_3Fe$ catalyst in a short-contact time micro packed bed reactor", *Chemical Engineering Journal* **2020**, *388*, 124233, DOI 10.1016/j.cej.2020.124233.

[334] U. Gonser, S. Nasu, W. Kappes, "Mössbauer spectroscopy of Fe-Ni and Fe-Pt alloys", *Journal of Magnetism and Magnetic Materials* **1979**, *10*, 244–251, DOI 10.1016/0304-8853(79)90185-9.

[335] C. Wilkinson, A. K. Cheetham, G. J. Long, P. D. Battle, D. A. O. Hope, "Polarized neutron diffraction and Moessbauer effect study of the magnetic ordering in wustite, $Fe_yO$", *Inorganic Chemistry* **1984**, *23*, 3136–3141, DOI 10.1021/ic00188a023.

[336] C. A. McCammon, "Magnetic properties of $Fe_xO$ ($x > 0.95$): Variation of Néel temperature", *Journal of Magnetism and Magnetic Materials* **1992**, *104-107*, 1937–1938, DOI 10.1016/0304-8853(92)91612-W.

[337] C. A. McCammon, D. C. Price, "Mössbauer spectra of $Fe_xO$ ($x > 0.95$)", *Physics and Chemistry of Minerals* **1985**, *11*, 250–254, DOI 10.1007/BF00307402.

[338] R. A. Guirado-López, M. C. Desjonquères, D. Spanjaard, "Role of the chemical ordering on the magnetic properties of Fe–Ni cluster alloys", *European Physical Journal D* **2005**, *36*, 67–78, DOI 10.1140/epjd/e2005-00182-9.

[339] C. A. McCammon, L. Liu, "The effects of pressure and temperature on nonstoichiometric wustite, $Fe_xO$: The iron-rich phase boundary", *Physics and Chemistry of Minerals* **1984**, *10*, 106–113, DOI 10.1007/BF00309644.

[340] L. S. Darken, R. W. Gurry, "The System Iron-Oxygen. I. The Wüstite Field and Related Equilibria", *Journal of the American Chemical Society* **1945**, *67*, 1398–1412, DOI 10.1021/ja01224a050.

[341] M. Tsuji, H. Kato, T. Kodama, S. G. Chang, N. Hesegawa, Y. Tamaura, "Methanation of $CO_2$ on $H_2$-reduced Ni(II)-or Co(II)-bearing ferrites at 200 °C", *Journal of Materials Science* **1994**, *29*, 6227–6230, DOI 10.1007/BF00354564.

[342] Y. Tamaura, M. Tahata, "Complete reduction of carbon dioxide to carbon using cation-excess magnetite", *Nature* **1990**, *346*, 255–256, DOI 10.1038/346255a0.

[343] H. Kato, T. Sano, Y. Wada, Y. Tamaura, M. Tsuji, T. Tsuji, S. Miyazaki, "Methanation of $CO_2$ with the oxygen-deficient Ni(II)-ferrite under dynamic conditions", *Journal of Materials Science* **1995**, *30*, 6350–6354, DOI 10.1007/BF00369687.

[344] K. Nishizawa, H. Kato, K. Mimori, T. Yoshida, N. Hasegawa, M. Tsuji, Y. Tamaura, "Methanation of carbon deposited directly from $CO_2$ on rhodium-bearing activated magnetite", *Journal of Materials Science* **1994**, *29*, 768–772, DOI 10.1007/BF00445992.

[345] K. Nishizawa, T. Kodama, M. Tabata, T. Yoshida, M. Tsuji, Y. Tamaura, "Adsorption of $CO_2$ on oxygen-deficient magnetite: adsorption enthalpy and adsorption isotherm", *Journal of the Chemical Society Faraday Transactions* **1992**, *88*, 2771–2773, DOI 10.1039/FT9928802771.

[346] M. Tsuji, K. Nishizawa, T. Yoshida, Y. Tamaura, "Methanation reactivity of carbon deposited directly from $CO_2$ on to the oxygen-deficient magnetite", *Journal of Materials Science* **1994**, *29*, 5481–5484, DOI 10.1007/BF01171565.

[347] T. Yoshida, K. Nishizawa, M. Tabata, H. Abe, T. Kodama, M. Tsuji, Y. Tamaura, "Methanation of $CO_2$ with $H_2$-reduced magnetite", *Journal of Materials Science* **1993**, *28*, 1220–1226, DOI 10.1007/BF01191956.

[348] G. H. Li, L. J. Hu, J. M. Hill, "Comparison of reducibility and stability of alumina-supported Ni catalysts prepared by impregnation and co-precipitation", *Applied Catalysis A: General* **2006**, *301*, 16–24, DOI 10.1016/j.apcata.2005.11.013.

[349] H.-S. Roh, K.-W. Jun, S.-E. Park, "Methane-reforming reactions over Ni/Ce-$ZrO_2$/$\theta$-$Al_2O_3$ catalysts", *Applied Catalysis A: General* **2003**, *251*, 275–283, DOI 10.1016/S0926-860X(03)00359-4.

[350] W. Taifan, J.-F. Boily, J. Baltrusaitis, "Surface chemistry of carbon dioxide revisited", *Surface Science Reports* **2016**, *71*, 595–671, DOI 10.1016/j.surfrep.2016.09.001.

[351] G. Busca, V. Lorenzelli, "Infrared spectroscopic identification of species arising from reactive adsorption of carbon oxides on metal oxide surfaces", *Materials Chemistry* **1982**, *7*, 89–126, DOI 10.1016/0390-6035(82)90059-1.

[352] C. Morterra, G. Magnacca, "A case study: surface chemistry and surface structure of catalytic aluminas, as studied by vibrational spectroscopy of adsorbed species", *Catalysis Today* **1996**, *27*, 497–532, DOI 10.1016/0920-5861(95)00163-8.

[353] C. Golling, R. Heuke, H. Seidl, J. Uhlig, "Roadmap Power to Gas", Deutsche Energie-Agentur GmbH (dena), **2017**.

[354] X. B. Bai, S. Wang, T. J. Sun, S. D. Wang, “Influence of Operating Conditions on Carbon Deposition Over a Ni Catalyst for the Production of Synthetic Natural Gas (SNG) from Coal”, *Catalysis Letters* **2014**, *144*, 2157–2166, DOI 10.1007/s10562-014-1379-1.

[355] J. Barrientos, M. Lualdi, M. Boutonnet, S. Jaras, “Deactivation of supported nickel catalysts during CO methanation”, *Applied Catalysis A: General* **2014**, *486*, 143–149, DOI 10.1016/j.apcata.2014.08.021.

[356] J. Barrientos, N. Gonzalez, M. Lualdi, M. Boutonnet, S. Jaras, “The effect of catalyst pellet size on nickel carbonyl-induced particle sintering under low temperature CO methanation”, *Applied Catalysis A: General* **2016**, *514*, 91–102, DOI 10.1016/j.apcata.2015.12.034.

[357] W. M. Shen, J. A. Dumesic, C. G. Hill, “Criteria for Stable Ni Particle-Size under Methanation Reaction Conditions - Nickel Transport and Particle-Size Growth Via Nickel Carbonyl”, *Journal of Catalysis* **1981**, *68*, 152–165, DOI 10.1016/0021-9517(81)90048-8.

[358] D. E. Mears, “The role of axial dispersion in trickle-flow laboratory reactors”, *Chemical Engineering Science* **1971**, *26*, 1361–1366, DOI 10.1016/0009-2509(71)80056-8.

[359] T. Holm, “Aspects of the mechanism of the flame ionization detector”, *Journal of Chromatography A* **1999**, *842*, 221–227, DOI 10.1016/S0021-9673(98)00706-7.

[360] S. Glassstone, K. J. Laidler, H. Eyring, *The Theory of Rate Processes*, McGraw-Hill, New York, NY, **1941**.

[361] T. Burger, P. Donaubauer, O. Hinrichsen, “Corrigendum to “On the kinetics of the co-methanation of CO and $CO_2$ on a co-precipitated Ni-Al catalyst” [Appl. Catal. B 282 (2021) 119408]”, *Applied Catalysis B: Environmental* **2021**, *296*, 120366, DOI 10.1016/j.apcatb.2021.120366.

[362] A. B. Mhadeshwar, H. Wang, D. G. Vlachos, “Thermodynamic Consistency in Microkinetic Development of Surface Reaction Mechanisms”, *The Journal of Physical Chemistry B* **2003**, *107*, 12721–12733, DOI 10.1021/jp034954y.

[363] L. F. Shampine, M. W. Reichelt, “The MATLAB ODE Suite”, *SIAM Journal on Scientific Computing* **1997**, *18*, 1–22, DOI 10.1137/s1064827594276424.

[364] P. J. Donaubauer, D. M. Melzer, K. Wanninger, G. Mestl, M. Sanchez-Sanchez, J. A. Lercher, O. Hinrichsen, “Intrinsic kinetic model for oxidative dehydrogenation of ethane over MoVTeNb mixed metal oxides: A mechanistic approach”, *Chemical Engineering Journal* **2019**, 123195, DOI 10.1016/j.cej.2019.123195.

[365] T.-Y. Park, G. F. Froment, “Kinetic Modeling of the Methanol to Olefins Process. 2. Experimental Results, Model Discrimination, and Parameter Estimation”, *Industrial & Engineering Chemistry Research* **2001**, *40*, 4187–4196, DOI 10.1021/ie000854s.

[366] M. Boudart, D. Mears, M. Vannice, “Kinetics of Heterogeneous Catalytic Reactions”, *Industrie Chimique Belge* **1967**, *32*, 2811–284.

[367] K. Toch, J. W. Thybaut, G. B. Marin, “A systematic methodology for kinetic modeling of chemical reactions applied to n-hexane hydroisomerization”, *AIChE Journal* **2015**, *61*, 880–892, DOI 10.1002/aic.14680.

[368] E. K. Rideal, F. Sweett, “The chemisorption of hydrogen on nickel”, *Proceedings of the Royal Society of London. Series A. Mathematical and Physical Sciences* **1960**, *257*, 291–301, DOI 10.1098/rspa.1960.0152.

[369] J. A. Konvalinka, P. H. Van Oeffelt, J. J. F. Scholten, “Temperature programmed desorption of hydrogen from nickel catalysts”, *Applied Catalysis* **1981**, *1*, 141–158, DOI 10.1016/0166-9834(81)80002-4.

[370] I. Toyoshima, G. A. Somorjai, “Heats of Chemisorption of $O_2$, $H_2$, CO, $CO_2$, and $N_2$ on Polycrystalline and Single Crystal Transition Metal Surfaces”, *Catalysis Reviews* **1979**, *19*, 105–159, DOI 10.1080/03602457908065102.

[371] J. A. Dalmon, G. A. Martin, “The kinetics and mechanism of carbon monoxide methanation over silica-supported nickel catalysts”, *Journal of Catalysis* **1983**, *84*, 45–54, DOI 10.1016/0021-9517(83)90084-2.

[372] P. Schoubye, “Methanation of CO on some Ni catalysts”, *Journal of Catalysis* **1969**, *14*, 238–246, DOI 10.1016/0021-9517(69)90431-X.

[373] R. Maatman, S. Hiemstra, “A kinetic study of the methanation of $CO_2$ over nickel-alumina”, *Journal of Catalysis* **1980**, *62*, 349–356, DOI 10.1016/0021-9517(80)90463-7.

[374] C. T. Campbell, “Future Directions and Industrial Perspectives Micro- and macro-kinetics: Their relationship in heterogeneous catalysis”, *Topics in Catalysis* **1994**, *1*, 353–366, DOI 10.1007/BF01492288.

[375] H. Rabitz, M. Kramer, D. Dacol, “Sensitivity Analysis in Chemical Kinetics”, *Annual Review of Physical Chemistry* **1983**, *34*, 419–461, DOI 10.1146/annurev.pc.34.100183.002223.

[376] L. Znak, J. Zieliński, “Interaction of Hydrogen with Unsupported and Supported Nickel”, *Langmuir* **2006**, *22*, 8758–8763, DOI 10.1021/la0605541.

[377] L. Znak, J. Zieliński, “Effects of support on hydrogen adsorption/desorption on nickel”, *Applied Catalysis A: General* **2008**, *334*, 268–276, DOI 10.1016/j.apcata.2007.10.015.

[378] S. Smeds, T. Salmi, L. P. Lindfors, O. Krause, "Chemisorption and TPD studies of hydrogen on Ni/$Al_2O_3$", *Applied Catalysis A: General* **1996**, *144*, 177–194, DOI 10.1016/0926-860X(96)00103-2.

[379] J. M. Kanervo, K. M. Reinikainen, A. O. I. Krause, "Kinetic analysis of temperature-programmed desorption", *Applied Catalysis A: General* **2004**, *258*, 135–144, DOI 10.1016/j.apcata.2003.08.019.

[380] J. Sehested, S. Dahl, J. Jacobsen, J. R. Rostrup-Nielsen, "Methanation of CO over nickel: Mechanism and kinetics at high $H_2$/CO ratios", *The Journal of Physical Chemistry B* **2005**, *109*, 2432–8, DOI 10.1021/jp040239s.

[381] D. E. Mears, "Diagnostic criteria for heat transport limitations in fixed bed reactors", *Journal of Catalysis* **1971**, *20*, 127–131, DOI 10.1016/0021-9517(71)90073-X.

[382] C. H. Bosanquet, "The Optimum Pressure for a Diffusion Separation Plant", *British Technical Assistance Report BR 507* **1944**.

[383] D. F. Fairbanks, C. R. Wilke, "Diffusion Coefficients in Multicomponent Gas Mixtures", *Industrial & Engineering Chemistry* **1950**, *42*, 471–475, DOI 10.1021/ie50483a022.

[384] E. N. Fuller, P. D. Schettler, J. C. Giddings, "New Method for Prediction of Binary Gas-Phase Diffusion Coefficients", *Industrial & Engineering Chemistry* **1966**, *58*, 18–27, DOI 10.1021/ie50677a007.

[385] E. N. Fuller, K. Ensley, J. C. Giddings, "Diffusion of halogenated hydrocarbons in helium. The effect of structure on collision cross sections", *The Journal of Physical Chemistry* **1969**, *73*, 3679–3685, DOI 10.1021/j100845a020.

[386] N. Wakao, S. Kaguei, T. Funazkri, "Effect of fluid dispersion coefficients on particle-to-fluid heat transfer coefficients in packed beds", *Chemical Engineering Science* **1979**, *34*, 325–336, DOI 10.1016/0009-2509(79)85064-2.

[387] C. R. Wilke, "A Viscosity Equation for Gas Mixtures", *The Journal of Chemical Physics* **1950**, *18*, 517–519, DOI 10.1063/1.1747673.

[388] W. Haynes, *CRC Handbook of Chemistry and Physics*, 95th ed., CRC Press, Hoboken, NJ, **2015**.

[389] J. Chase, M.W., "NIST-JANAF Themochemical Tables, Fourth Edition", *J. Phys. Chem. Ref. Data Monograph 9* **1998**, 1–1951, DOI 10.18434/T42S31.

[390] M. Kleiber, R. Joh, "Stoffwerte von sonstigen chemisch einheitlichen Flüssigkeiten und Gasen" in *VDI Wärmeatlas*, (Ed.: S. Kabelac), Springer, Berlin, Heidelberg, DE, **2006**, pp. 249–294, DOI 10.1007/978-3-540-32218-4_18.

[391] S. M. Walas, "2 - Thermodynamic Functions and Equilibrium" in *Phase Equilibria in Chemical Engineering*, (Ed.: S. M. Walas), Butterworth-Heinemann, Stoneham, MA, **1985**, pp. 109–137, DOI 10.1016/B978-0-409-95162-2.50010-5.

[392] A. Behr, A. Renken, J. Gmehling, M. Baerns, A. Brehm, J. Gmehling, K.-O. Hinrichsen, H. Hofmann, U. Onken, R. Palkovits, *Technische Chemie*, Wiley-VCH, Weinheim, DE, **2013**.

# Nomenclature

## Latin Symbols

| | | |
|---|---|---|
| $A$ | area | $m^2$ |
| $A$ | Arrhenius constant | depends on model |
| $a, b, c$ | unit cell constants | Å |
| $a$–$e$ | fitting values in Shomate equation | depends on exponent in polynomial |
| $B$ | magnetic flux density | T |
| $\Delta B_{pp}$ | linewidth in FMR/EPR spectrum | T |
| $c$ | velocity of light | $m\,s^{-1}$ |
| $c$ | concentration | $mol\,L^{-1}$ |
| $c_p$ | specific heat capacity | $J\,kg^{-1}\,K^{-1}$ |
| $D$ | diffusion coefficient | $m^2\,s^{-1}$ |
| $D$ | dispersion | - |
| $d$ | diameter | m |
| $d$ | $d$ spacing | Å |
| $d_{red}$ | degree of reduction | - |
| $E$ | energy | $J\,mol^{-1}$ |
| $E_a$ | activation energy | $J\,mol^{-1}$ |
| $E_{bin}$ | binding energy | $J\,mol^{-1}$ |
| $\Delta E_q$ | quadrupole splitting | $J\,mol^{-1}$ |
| $F$ | objective function | - |
| $F_s$ | significance parameter for F-test | - |
| $f$ | fugacity | Pa |
| $G$ | molar Gibbs's free energy | $J\,mol^{-1}$ |
| $G'$ | Gibbs's free energy | J |
| $g$ | nuclear $g$-factor | - |
| $GHSV$ | gas hourly space velocity | $h^{-1}$ |
| $H$ | molar enthalpy | $J\,mol^{-1}$ |
| $H$ | magnetic field strength | $A\,m^{-1}$ |
| $H'$ | enthalpy | J |
| $h, k, l$ | Miller indices | - |
| $I$ | nuclear spin | - |

| | | |
|---|---|---|
| $I$ | intensity | a.u. |
| $i,j,k$ | species | - |
| $j$ | number of experiment | - |
| $K$ | shape factor | - |
| $K$ | equilibrium constant | depends on model |
| $k$ | reaction rate constant | depends on model |
| $k$ | number of response | - |
| $M$ | molar mass | $\mathrm{g\,mol^{-1}}$ |
| $m$ | mass | kg |
| $m$ | nuclear magnetic spin quantum number | - |
| $m_\mathrm{n}$ | nuclear Bohr magnetron | $\mathrm{J\,T^{-1}}$ |
| $mb$ | mass balance | - |
| $N$ | number of atoms | - |
| $n$ | molar amount | mol |
| $n$ | order of maximum | - |
| $n$ | total number | - |
| $n$ | reaction order | - |
| $\dot{n}$ | molar flow | $\mathrm{mol\,s^{-1}}$ |
| $Nu$ | Nusselt number | - |
| $P$ | characteristic value for TPR experiments in [218] | K |
| $p$ | pressure | Pa |
| $p_i$ | partial pressure of species $i$ | Pa |
| $p_i'$ | reduced partial pressure of species $i$ | |
| $Pr$ | Prandtl number | - |
| $Q$ | mass-normalized volumetric flow rate at standard conditions | $\mathrm{NL\,g_{cat}^{-1}\,h^{-1}}$ |
| $R_i$ | net formation rate of species $i$ | $\mathrm{mol\,g_{cat}^{-1}\,s^{-1}}$ |
| $r$ | radius | m |
| $r$ | reaction rate | $\mathrm{mol\,g_{cat}^{-1}\,s^{-1}}$ |
| $Re$ | Reynolds number | - |
| $S$ | molar entropy | $\mathrm{J\,mol^{-1}\,K^{-1}}$ |
| $S$ | specific surface area | $\mathrm{m^2\,g_{cat}^{-1}}$ |
| $S$ | selectivity | - |
| $S$ | degree of rate control | - |
| $S'$ | entropy | $\mathrm{J\,K^{-1}}$ |
| $s$ | adsorption stoichiometry | - |
| $Sc$ | Schmidt number | - |
| $Sh$ | Sherwood number | - |
| $SV$ | space velocity | $\mathrm{h^{-1}}$ |

| | | |
|---|---|---|
| $T$ | temperature | K |
| $t$ | time | s |
| $t$ | statistic t-value | - |
| $U$ | adsorption uptake | $\mathrm{mol\,g_{cat}^{-1}}$ |
| $u$ | velocity | $\mathrm{m\,s^{-1}}$ |
| $V$ | volume | $\mathrm{m^3}$ |
| $\dot{V}$ | volumetric flow rate | $\mathrm{m^3\,s^{-1}}$ |
| $w$ | loading | - |
| $WTY$ | weight time yield | $\mathrm{mol\,kg_{cat}^{-1}\,h^{-1}}$ |
| $X$ | conversion | - |
| $x, y$ | molar fraction | - |
| $Y$ | yield | - |
| $Y$ | normalized molar flow | - |
| $y$ | degree of hydrogenation in $\mathrm{COH}_y$ | - |
| $z$ | degree of hydrogenation in $\mathrm{CH}_z$ | - |
| $z$ | charge | C |
| $*$ | free site | - |

## Greek Symbols

| | | |
|---|---|---|
| $\alpha$ | heat transfer coefficient | $\mathrm{W\,m^{-2}\,K^{-1}}$ |
| $\alpha$ | exponent for statistical and thermodynamic consistency in [187] | - |
| $\alpha, \beta, \gamma$ | angle in crystal lattice | $^\circ$ |
| $\beta$ | mass transfer coefficient | $\mathrm{m\,s^{-1}}$ |
| $\beta$ | full width at half maximum | $^\circ$ |
| $\gamma, \delta$ | fitting parameters in [192] | - |
| $\delta$ | isomer shift in Mößbauer spectrum | $\mathrm{mm\,s^{-1}}$ |
| $\varepsilon$ | pellet porosity | - |
| $\eta$ | dynamic viscosity | Pa s |
| $\theta$ | diffraction angle | $^\circ$ |
| $\theta$ | surface coverage | - |
| $\lambda$ | wavelength | nm |
| $\lambda$ | heat conductivity | $\mathrm{W\,m^{-1}\,K^{-1}}$ |
| $\mu$ | chemical potential | $\mathrm{J\,mol^{-1}}$ |
| $\nu$ | frequency | Hz |
| $\nu$ | stoichiometric factor | - |
| $\tilde{\nu}$ | wavenumber | $\mathrm{cm^{-1}}$ |
| $\rho$ | density | $\mathrm{kg\,m^{-3}}$ |
| $\sigma$ | cross sectional area | $\mathrm{m^2}$ |
| $\tau^2$ | tortuosity | - |

| | | |
|---|---|---|
| $\Phi$ | work function | eV |
| $\phi_m$ | dimensionless parameter | - |
| $\varphi_i$ | fugacity coefficient of species *i* | - |
| $\psi$ | Wilke-Chang parameter | - |
| $\omega$ | weighting factor | - |

## Constants

| | | |
|---|---|---|
| $C$ | constant | - |
| $h$ | Planck constant | J s |
| $N_A$ | Avogadro's constant | $mol^{-1}$ |
| $R$ | universal gas constant | $J\,mol^{-1}\,K^{-1}$ |

## Superscript

| | |
|---|---|
| o | standard state (at 25 °C and 1 bar) |
| * | adsorbed |
| ′ | lumped parameter |
| exp | experimental |
| calc | calculated |
| out | at reactor outlet |

## Subscript

| | |
|---|---|
| A | adsorptive |
| a | aging |
| ads | adsorbed, adsorption |
| app | apparent |
| Au | Auger |
| B | bulk |
| BET | determined by BET theory |
| C | crystallite |
| c | calcined |
| calc | calculated |
| cat | catalyst |
| crit | critical |
| COmet | CO methanation |
| $CO_2$met | $CO_2$ methanation |
| des | desorption |
| dil | dilution |

| | |
|---|---|
| eff | effective |
| el | electrical |
| eq | equilibrium |
| ex | exposed |
| exp | experiment |
| f | formation |
| g | gas |
| Hüttig | Hüttig |
| i | impregnated, derived from impregnated catalyst |
| in | entering the reactor, bypass measurement |
| int | internal |
| kin | kinetic |
| Kn | Knudsen |
| L | liquefaction |
| l | liquid |
| M | metal |
| m | melting |
| m | molar |
| m | molecular |
| max | maximum |
| met | methanation |
| min | minimum |
| ML | monolayer |
| Néel | Néel temperature |
| out | leaving the reactor, reactor measurement |
| P | particle |
| P | pellet |
| pore | pore |
| R | reaction |
| ref | reference |
| rel | relative |
| resp | response |
| S | surface |
| SR | steam reforming |
| Tammann | Tammann |
| th | thermal |
| V | isosteric |
| v | vaporization |
| x | derived from co-precipitated catalyst |
| 0 | reference |

| | |
|---|---|
| 1 | first layer |
| 50 | at 50 % $CO_2$ conversion |
| (I) | impregnated first |
| (II) | impregnated second |

### Abbreviations

| | |
|---|---|
| BET | Brunauer-Emmett-Teller |
| BJH | Barrett-Joyner-Halenda |
| BSE | backscattered secondary electron |
| CI | confidence interval |
| CVD | chemical vapor deposition |
| DFT | density functional theory |
| DoE | design of experiments |
| EDX | energy-dispersive X-ray spectroscopy |
| EPR | electron paramagnetic resonance spectroscopy |
| FMR | ferromagnetic resonance spectroscopy |
| FT-IR | Fourier transform infrared spectroscopy |
| ICP-OES | inductively coupled plasma-optical emission spectroscopy |
| IR | infrared |
| LHHW | Langmuir-Hinshelwood-Hougen-Watson |
| PGA | process gas analyzer |
| PSRA | pulse surface reaction analysis |
| RDS | rate-determining step |
| RF | reference point |
| S | temperature variation cycle |
| SE | secondary electron |
| SSITKA | steady-state isotopic transient kinetic analysis |
| TEM | transmission electron microscopy |
| TOS | time on stream |
| TPD | temperature-programmed desorption |
| TPO | temperature-programmed oxidation |
| TPR | temperature-programmed reduction |
| WGS | water-gas shift reaction |
| XPS | X-ray photoelectron spectroscopy |
| XRD | X-ray diffraction |

# List of Figures

# List of Tables

# List of Publications

## Paper Publications

- K.J. Carroll[1], T. Burger[1], L. Langenegger, S. Chavez, S.T. Hunt, Y. Román-Leshkov, F.R. Brushett, "Electrocatalytic Hydrogenation of Oxygenates using Earth-Abundant Transition-Metal Nanoparticles under Mild Conditions", ChemSusChem, 2016, *9*, 1904–1910.

- T. Burger[1], F. Koschany[1], O. Thomys, K. Köhler, O. Hinrichsen, "$CO_2$ methanation over Fe- and Mn-promoted co-precipitated Ni-Al catalysts: Synthesis, characterization and catalysis study", Applied Catalysis A: General, 2018, *558*, 44–54.

- T. Burger, F. Koschany, A. Wenng, O. Thomys, K. Köhler, O. Hinrichsen, "Simultaneous activity and stability increase of co-precipitated Ni-Al $CO_2$ methanation catalysts by synergistic effects of Fe and Mn promoters", Catalysis Science & Technology, 2018, *8*, 5920–5932.

- T. Burger, H. M. S. Augenstein, F. Hnyk, M. Döblinger, K. Köhler, O. Hinrichsen, "Targeted Fe-Doping of Ni-Al Catalysts *via* the Surface Redox Reaction Technique for Unravelling its Promoter Effect in the $CO_2$ Methanation Reaction", ChemCatChem, 2020, *12*, 649–662.

- M. I. Arz, T. Kratky, S. Günther, K. Rodewald, T. Burger, M. Heuberger, B. Rieger, "Sequential immobilization of ansa-hafnocene complexes for propene polymerization", Journal of Organometallic Chemistry, 2020, *909*, 121075.

- T. Burger, S. Ewald, A. Niederdränk, O. Hinrichsen, "Unraveling the promotional effect of Fe on the stability of co-precipitated Ni-Al catalysts in the methanation reaction of $CO_2$", Applied Catalysis A: General, 2020, *604*, 117778.

- T. Burger[1], P. J. Donaubauer[1], O. Hinrichsen, "On the kinetics of the co-methanation of CO and $CO_2$", Applied Catalysis B: Environmental, 2020, *282*, 119408.

[1] The authors equally contributed to this work.

# Publications of Patent Applications

- K. Köhler, O. Thomys, K.-O. Hinrichsen, F. Koschany, T. Burger, "Manganese-doped nickel-methanation catalysts", European Patent Office, 2018, publication number WO/2018/141649, international application number PCT/EP2018/051996.[1]

- K. Köhler, O. Thomys, K.-O. Hinrichsen, F. Koschany, T. Burger, "Iron-doped nickel methanation catalysts", European Patent Office, publication number WO/2018/141648, international application number PCT/EP2018/051995.[1]

- K. Köhler, O. Thomys, K.-O. Hinrichsen, F. Koschany, T. Burger, "Nickel methanation catalysts doped with iron and manganese", European Patent Office, publication number WO/2018/141646, international application number PCT/EP2018/051993.[1]

# Conference Contributions

## Oral Presentations

- T. Burger, F. Koschany, O. Hinrichsen, "Production of Synthetic Natural Gas by $CO_2$ Methanation: Synthesis and Characterization of Highly Active Catalysts", Natural Gas Conversion Symposium 11, 2016, Tromsø.

- T. Burger, F. Koschany, O. Hinrichsen, "Second Generation $CO_2$ Methanation Catalysts", 7th Energy Colloquium of the Munich School of Engineering, 2017, Munich.

- T. Burger, H.M.S. Augenstein, K. Köhler, O. Hinrichsen, "Unravelling the Improved $CO_2$ Methanation Performance of Ni-Fe-Al Catalysts by Targeted Doping at Ni Sites", 52. Jahrestreffen Deutscher Katalytiker, 2019, Weimar.

- T. Burger, S. Ewald, K. Köhler, O. Hinrichsen, "Effect of Ni-Fe Segregation on the Deactivation Behavior of Co-Precipitated $NiFeAlO_x$ Catalysts in the $CO_2$ Methanation Reaction", Natural Gas Conversion Symposium 12, 2019, San Antonio.

## Poster Presentations

- C. Schüler, S. Ewald, T. Burger, "Characterization of $CO_2$ Methanation Catalysts", 6th Energy Colloquium of the Munich School of Engineering, 2016, Munich.

- T. Burger, O. Hinrichsen, "Kinetic investigations on the co-methanation of CO and $CO_2$", 50. Jahrestreffen Deutscher Katalytiker, 2017, Weimar.

- T. Burger, O. Hinrichsen, "Kinetic investigations on the co-methanation of CO and $CO_2$", Europacat, 2017, Florence.
- T. Burger, A. Niederdränk, O. Hinrichsen, "Effect of Ni-Fe segregation on the deactivation behavior of Fe-promoted $NiAlO_x$ catalysts in the $CO_2$ methanation reaction", 51. Jahrestreffen Deutscher Katalytiker, 2018, Weimar.
- T. Burger, O. Hinrichsen, "Catalyst Development for $CO_2$ Methanation", 8th Energy Colloquium of the Munich School of Engineering, 2018, Munich.
- M. Wolf, C. Schüler, T. Burger, O. Hinrichsen, "Sulfur poisoning of co-precipitated Ni-Al catalysts for the methanation of $CO_2$", 52. Jahrestreffen Deutscher Katalytiker, 2019, Weimar.
- S. Ewald, T. Burger, O. Hinrichsen, "Unravelling promoter effects on Ni-Al catalysts by TPD", 52. Jahrestreffen Deutscher Katalytiker, 2019, Weimar.
- T. Burger, P. Reuschl, O. Hinrichsen, "Activity Increase and Aging Behavior of Mn-Doped Hydrotalcite-Derived Ni-Al Catalysts for the Methanation Reaction of $CO_2$", Europacat, 2019, Aachen.
- T. Burger, P. Donaubauer, O. Hinrichsen, "On the kinetics of the co-methanation of CO and $CO_2$", 53. Jahrestreffen Deutscher Katalytiker, 2020, virtual poster presentation.